Structural basis of positive modulation of type-A GABA receptors



Suzanne Scott

Merton College

University of Oxford

A thesis submitted for the degree of

Doctor of Philosophy

Trinity 2018

Acknowledgements

It is said to take a village to raise a child, and this is true then it certainly takes an academic community to complete a thesis. Assistance has come from all sides, and I am truly grateful to have had the opportunity to study in these collaborative environments. I would like to thank the entire staff, academic and support, and students at STRUBI, the MRC-LMB and DPAG.

I am thankful, first and foremost, to my supervisors and mentors Radu Aricescu and Michael Kohl. In the more difficult periods of my DPhil, their boundless optimism helped show me a path forward. Not only have given me seemingly endless mentorship, guidance and support, but also the memories of many interesting discussions on the drive to Harwell to visit DLS and eBIC (Radu), races up the stairs of the LMB (Radu) and post-midnight rides through Copenhagen (Michael). I deeply appreciate the time and effort they have put into my training.

I would also like to thank the $GABA_AR$ crew in the Aricescu lab, and in particular my first mentor in the lab Paul Miller, as well as Simonas Masiulis and Duncan Laverty, who all provided me with a huge amount of support. Other members of the Aricescu lab, Holly Sun, Christina Heroven, Lina Malinauskaite, Veronica Chang, Jonathan Egleheert, Ester Biehels, Nikos Mitakidis, Patricial Brown and Andrija Sente, all provided me with useful assistance, including collaborative Titan Krios sessions, providing much-needed reagents at a minute's notice, and companionship for long nights and weekends at the lab.

Colleagues at STRUBI, DPAG and the MRC-LMB have also given me innumerable assistance. In particular, I would like to thank the facility staff that I have collaborated with, including Tom Walter and Karl Harlos at STRUBI; Giuseppe Cannone, Joanna Brown and Shaoxia Chen at the LMB EM facility; Chris Johnson and Stephen McLaughlin at the LMB Biophysics facility; Maria Daly, Fan Zhang, Martyn Balmont from the LMB flow cytometry facility, as well as Patricia Edwards and Jianguo Shi for assistance with mammalian and insect cell tissue culture. Furthermore, without our collaborators at VUB, Nele Buys, Els Pardon, Tomasz Uchanski and Jan Stayert, who raised nanobodies for us, this project would not have been possible. The administrative staff, including Andy King and Debbie Clarke from the Neuroscience DPhil programme, and Merton College academic office, have also been greatly helpful. I am also grateful to the Wellcome Trust, the Clarendon Fund, and Merton College for enabling this work through the provision of funding.

Finally, I would like to thank my friends and family, near and far, for their love and support during this period. In particular, Jonathan has provided tireless enthusiasm during difficult times, for which I will always be grateful.

Abstract

The $GABA_AR$ is the main inhibitory neurotransmitter receptor in the brain, and is primarily responsible for maintaining the excitatory-inhibitory balance in neurons on which normal function of the nervous system depends. This receptor is subject to modulation by several endogenous and pharmacological agents, which can have dramatic effects on the brain and behaviour. Common examples of drugs affecting $GABA_ARs$ include anaesthetics, anxiolytics and sedatives. In particular, there has been great interest in developing drugs against the α2- and α3-containing $GABA_ARs$ because of their roles in pain and anxiety. The aim of the work described in this thesis was to investigate modulation of $GABA_ARs$ by positive modulators. In particular, because nanobodies raised against $GABA_ARs$ have previously been shown to positively modulate the α1β3γ2L receptor, new nanobodies were raised against the α2β3 and α3β3 $GABA_ARs$, in the hope of obtaining specific modulators. These were characterised for affinity and modulatory activity at their respective $GABA_ARs$, and several high-affinity nanobodies that act as positive allosteric modulators were identified. In order to investigate the structural effect of these nanobodies, methods for expression and purification of full-length heteromeric $GABA_ARs$ were then investigated. A comparison of transient transfection, BacMam and stable cell lines indicated that the highest expression was obtained from HEK293 cells stably transduced with triheteromeric $GABA_ARs$. After developing a method for purification of these receptors, the interaction of the α3β3γ2L $GABA_AR$ with one nanobody, α3β3nb173, was investigated by single-particle cryo-EM. Several datasets were collected, and the best map had a nominal resolution of 3.8 Å. This map revealed a novel modulatory site on the $GABA_AR$, at the top of the β+/α- interfaces and above the GABA binding site. These findings have implications for the discovery of novel drugs against the $GABA_AR$, potentially of major clinical importance, either by using nanobodies directly or developing compounds to mimic their activity at this novel site.

Contents

List of Figures **ix**

List of Tables **xii**

List of Abbreviations **xiv**

1 Introduction **1**

1.1 GABAergic neurotransmission and the inhibitory synapse 2
1.1.1 GABA synthesis and release 2
1.1.2 GABA-mediated Cl^- flux 2
1.1.3 GABA removal 3
1.1.4 GABA catabolism 3
1.1.5 Variants of 'classical' GABAergic neurotransmission 3
1.2 $GABA_A$ receptor biophysical properties 4
1.2.1 The family of pentameric ligand-gated ion channels 4
1.2.2 Types of $GABA_A$Rs and their stoichiometry 6
1.2.3 Assembly and post-translational modification of $GABA_A$Rs . . . 10
1.2.4 Trafficking and synaptic anchoring 10
1.2.5 Single-channel conductance and ion selectivity 11
1.2.6 Mechanisms of channel gating and desensitisation 12
1.3 $GABA_A$R pharmacology 14
1.3.1 GABA 16
1.3.2 Benzodiazepines 16
1.3.3 Other ECD ligands 17
1.3.4 Neurosteroids 18
1.3.5 Anaesthetics 18
1.3.6 Pore-binding antagonists 19
1.4 Distinct roles for types of $GABA_A$Rs in the brain 19
1.4.1 Expression of the α2 and α3 subunits in the brain 20
1.4.2 Pain 21
1.4.3 Anxiety 23
1.4.4 Addiction 25

1.5 Nanobodies as tools for (structural) biology . . . 25
1.5.1 Nanobody structure . . . 26
1.5.2 Applications of nanobodies in structural biology . . . 26
1.6 Aims of this thesis . . . 28

2 Materials and Methods **29**
2.1 Molecular biology . . . 29
2.1.1 Expression vectors . . . 29
2.1.2 cDNA and construct design . . . 31
2.1.3 PCR . . . 32
2.1.4 Restriction digests . . . 35
2.1.5 Ligations . . . 35
2.1.6 Gibson assembly . . . 36
2.1.7 *In vitro* assembly . . . 36
2.1.8 Transformations . . . 37
2.1.9 DNA preparation . . . 37
2.1.10 Sanger sequencing . . . 38
2.2 Protein expression . . . 38
2.2.1 Protein expression in *E. coli* . . . 39
2.2.2 Transient transfection of mammalian cells . . . 40
2.2.2.1 Mammalian cell lines used and their maintenance . . . 40
2.2.2.2 Adherent, small scale . . . 42
2.2.2.3 Adherent, large scale . . . 43
2.2.2.4 Suspension, large scale . . . 44
2.2.3 Generation of recombinant baculoviruses . . . 45
2.2.4 Baculovirus transduction of mammalian cells (BacMam) . . . 48
2.2.5 Generation of stable cell lines . . . 48
2.2.6 Induction of stable cell lines . . . 49
2.2.7 Fluorescence activated cell sorting (FACS) . . . 50
2.2.8 Light microscopy . . . 51
2.3 Protein purification and characterisation . . . 51
2.3.1 SDS-PAGE and western blots . . . 51
2.3.2 Immunoaffinity media preparation . . . 53
2.3.3 Purification of soluble proteins from the *E. coli* periplasm . . . 53
2.3.4 Purification of soluble proteins from the *E. coli* cytoplasm . . . 55
2.3.5 Preparation of lysates for FSEC . . . 56
2.3.6 Small-scale membrane protein purification . . . 56
2.3.7 Fluorescence size exclusion chromatography (FSEC) screening . . . 57
2.3.8 Large-scale membrane protein purification . . . 58

2.3.9 Exchange of membrane proteins to amphipols or nanodiscs . . . 60
2.3.10 Purification of soluble proteins from expression media 60
2.3.11 *In vitro* biotinylation of purified proteins 61
2.3.12 Deglycosylation of purified proteins 61
2.4 Biophysical characterisation of $GABA_AR$-nanobody interactions 61
2.4.1 Surface plasmon resonance 61
2.4.2 Biolayer interferometry 62
2.5 Electrophysiology 64
2.6 Electron microscopy 66
2.6.1 Introduction to the theory and practice of single particle cryo-EM 66
2.6.1.1 Sample preparation 66
2.6.1.2 Data collection 69
2.6.1.3 Data analysis 75
2.6.1.4 Model building, refinement and validation 80
2.6.2 Electron microscopy performed 82
2.6.2.1 Addition of drugs and formation of nanobody- or -megabody-$GABA_AR$ complexes 82
2.6.2.2 Grid preparation for negative stain electron microscopy 82
2.6.2.3 Data collection for negative stain electron microscopy 82
2.6.2.4 Graphene oxide deposition on grids 83
2.6.2.5 Cryo-EM grid preparation 83
2.6.2.6 Data collection for cryo-EM 83
2.6.2.7 EM data processing 84

3 Generation and screening of nanobodies against α(2/3)-containing $GABA_ARs$ 86
3.1 Introduction 86
3.1.1 Nanobody properties and uses 86
3.1.2 Existing $GABA_AR$ nanobodies and aims of this chapter 88
3.2 Characterisation of nanobodies against α1β3 $GABA_AR$ 89
3.3 Preparation of α(2/3)β3 $GABA_ARs$ for nanobody generation 91
3.4 Purification of nanobodies against α(2/3)β3 $GABA_ARs$ 95
3.5 Kinetic characterisation of nanobodies against α(2/3)β3 $GABA_ARs$ 97
3.6 Functional characterisation of nanobodies against α(2/3)β3 $GABA_ARs$ . . 102
3.7 Discussion 104

4 Optimisation of triheteromeric $GABA_AR$ expression and purification 110
4.1 Introduction . . . 110
4.1.1 Expression systems . . . 110
4.1.2 Protein purification . . . 112
4.1.3 Aims . . . 113
4.2 Transient transfection of full-length αβγ $GABA_ARs$ . . . 113
4.3 The BacMam expression system . . . 117
4.4 $GABA_AR$-expressing cell lines and comparison with BacMam . . . 122
4.5 Purification optimisation . . . 129
4.6 Discussion . . . 132
4.6.1 Constructs and stoichiometry . . . 133
4.6.2 Expression systems . . . 135
4.6.3 $GABA_AR$ purification . . . 137

5 Structural studies of an α3β3γ2L $GABA_AR$-nanobody complex 139
5.1 Introduction . . . 139
5.1.1 Aims . . . 141
5.2 Optimisation of grids for cryo-EM . . . 141
5.3 α3β3 $GABA_AR$ in complex with α3β3mb173 and GABA . . . 143
5.4 α3β3γ2L $GABA_AR$ in complex with α3β3mb173 and GABA . . . 147
5.5 α3β3γ2L $GABA_AR$ in complex with α3β3mb173, GABA and picrotoxin . 151
5.5.1 Nanodisc dataset . . . 151
5.5.2 Amphipol dataset . . . 154
5.5.3 Combined amphipol and nanodisc datasets . . . 158
5.6 Discussion . . . 163
5.6.1 Grid optimisation . . . 163
5.6.2 Datasets collected . . . 164
5.6.3 Data processing strategies . . . 167
5.6.4 Structure of the α3β3γ2L $GABA_AR$, in complex with α3β3γ2L, GABA and picrotoxin . . . 168

6 General discussion 172

Appendices

A Expression vectors used for cloning 176

B Constructs 181

C Oligonucleotide primers 187

D MATLAB scripts used for data analysis and presentation 190
D.1 FSEC data analysis . . . 190
D.1.1 plot_data.m . . . 192
D.1.2 analyse_lysates.m . . . 194
D.2 BLI data analysis . . . 197
D.2.1 SCK_fit . . . 197
D.2.2 SCK_sim_fit_preset_R0 . . . 200
D.2.3 SCK_sim_fit_drift_preset_R0 . . . 203
D.2.4 import_octet.m . . . 206
D.3 Electrophysiology data analysis . . . 211
D.3.1 load_ionflux . . . 211
D.3.2 analyze_ionflux_screen.m . . . 220

E Supplementary data 234

F Published work 268

References 323

List of Figures

1.1 An overview of $GABA_AR$ structure 5
1.2 $GABA_AR$ subunits and pentameric arrangement 7
1.3 Alignment of $GABA_AR$ subunits 9
1.4 $GABA_AR$ ligands 15
1.5 A comparison of IgG and HC antibodies, FAbs and nanobodies 26
1.6 Nanobody structure 27

2.1 Endpoint dilution assay for virus titration 47
2.2 96-well plate layout for BLI experiments 63
2.3 Ionflux plate layout 65
2.4 Workflow for cryo-EM data collection and processing 67

3.1 Purification of α1β3nb138 90
3.2 Kinetics of $GABA_AR$-α1β3nb138 binding assessed by SPR 91
3.3 Electrophysiological characterisation of α1β3nb138 92
3.4 α2β3 $GABA_AR$ stability is negatively affected by concentration by ultrafiltration 93
3.5 α2β3, α3β3, β3 $GABA_AR$ purifications 94
3.6 Purification of α1β3 and α2β3 nanobodies 96
3.7 Purification of α1β3 and α2β3 nanobodies 97
3.8 α1β3nb125 binding to a α2β3 $GABA_AR$ investigated using BLI and SPR . 98
3.9 Example fits of BLI screening for αβ $GABA_AR$-nanobody interactions . . 100
3.10 Responses of α2β3γ2 and α3β3γ2 $GABA_ARs$ to EC_{10} doses of GABA and increasing concentrations of nanobody 105

4.1 Transient small-scale transfection and purification of 1D4-tagged αβγ and β3 $GABA_ARs$ 115
4.2 Optimisation of 1D4-tagged αβγ $GABA_AR$ purification. 116
4.3 Purification of 1D4-tagged α2β3γ2L $GABA_AR$ 116
4.4 Lysate FSEC with transfected pEZT constructs 117
4.5 PCR verification of correct bacmid recombination 118
4.6 Lysate FSEC with cells transduced by BacMam 119
4.7 Lysate FSEC with cells transduced by BacMam in PEM and FreeStyle 293 121

4.8 The mV-β3-1D4 cell line . . . 123
4.9 Characterisation of cell lines expressing heteromeric $GABA_A$Rs . . . 125
4.10 Lysate FSEC screening of expression conditions for heteromeric cell lines 126
4.11 Three-colour FACS with $GABA_A$R IRES-FP cell lines . . . 127
4.12 One-colour FACS with $GABA_A$R cell lines . . . 128
4.13 Affinity purification of α2β3γ2L $GABA_A$R from a stable cell line in detergent 130
4.14 Affinity purification and exchange to nanodiscs of α2β3γ2L $GABA_A$R from a stable cell line . . . 131
4.15 Reconstitution of a α3β32L $GABA_A$R into amphipols and nanodiscs . . . 133

5.1 Characterisation of FLAG-purified $GABA_A$R from a stable cell line by EM 142
5.2 Optimisation of cryo grids for $GABA_A$Rs . . . 144
5.3 Data collection for FLAG-purified $GABA_A$R from a stable cell line . . . 146
5.4 3D reconstruction of a FLAG-purified α3β3γ2L $GABA_A$R in complex with α3β3γmb173 . . . 148
5.5 Likely subunit assignment and α3β3mb173 binding site for a FLAG-purified α3β3γ2L $GABA_A$R . . . 149
5.6 Data collection for 1D4-purified $GABA_A$R from a stable cell line . . . 151
5.7 2D classes and 3D reconstruction for 1D4-purified $GABA_A$R from a stable cell line in the presence of 1 mM GABA and α3β3mb173 . . . 152
5.8 Data collection for 1D4-purified $GABA_A$R in MSP2N2 nanodiscs from a stable cell line in the presence of 1 mM picrotoxin, 1 mM GABA and α3β3mb173 . . . 154
5.9 Data processing for 1D4-purified α2β32L $GABA_A$R in MSP2N2 nanodisc from a stable cell line in the presence of 1 mM picrotoxin, 1 mM GABA and α3β3mb173 . . . 155
5.10 Data collection for 1D4-purified $GABA_A$R in amphipols from a stable cell line in the presence of 1 mM picrotoxin, 1 mM GABA and α3β3mb173 . . . 156
5.11 Data processing for 1D4-purified α2β32L $GABA_A$R in amphipols from a stable cell line in the presence of 1 mM picrotoxin, 1 mM GABA and α3β3mb173 . . . 159
5.12 Data processing for combined datasets of 1D4-purified α2β32L $GABA_A$R in amphipols and MSP2N2 nanodiscs from a stable cell line in the presence of 1 mM picrotoxin, 1 mM GABA and α3β3mb173 . . . 160
5.13 α1β3γ2L $GABA_A$R in complex with GABA, picrotoxin, and α1β3nb138, docked into the map for the α3β3γ2L $GABA_A$R . . . 161
5.14 Possible α3β3mb173-$GABA_A$R interface . . . 162
5.15 Relative positions of agonist and modulatory sites at $GABA_A$R and GlyRs 169

A.1 Features of the pHLsec vector . . . 177

A.2 Features of the pEZT-BM vector 178
A.3 Features of the pHR-CMV-TetO$_2$-IRES-EmGFP vector 179
A.4 Features of the pMESy4 vector 180

E.1 Full SDS-PAGE gels for purification of α1β3 and α2β3 nanobodies 237
E.2 Full SDS-PAGE gels for purification of α3β3 nanobodies 238

List of Tables

2.1 Uniprot accession codes and domain boundaries of human $GABA_AR$ subunits used . . . 31
2.2 Standard reaction components for Pyrobest, Phusion, Q5 and *Taq* polymerases . . . 33
2.3 Standard reaction conditions for Pyrobest, Phusion, Q5 and *Taq* polymerases 34
2.4 Components for typical one- and two-enzyme restriction digests . . . 35
2.5 Typical components for a ligation . . . 36
2.6 Antibiotic concentrations for *E. coli* selection . . . 37
2.7 Sequencing primers . . . 38
2.8 Cell lines and media typically used for adherent mammalian tissue culture 41
2.9 Cell lines and media typically used for mammalian suspension tissue culture 42
2.10 Reagents for western blotting . . . 52
2.11 Buffers for coupling to CNBr-activated Sepharose 4B . . . 53
2.12 Buffers used for purification of proteins from *E. coli* periplasmic space . . 54
2.13 Buffers used for purification of proteins from *E. coli* cytoplasm . . . 55
2.14 Detergents used for membrane protein purification . . . 56
2.15 Affinity chromatography conditions . . . 57
2.16 Buffers used in membrane protein purifications . . . 57
2.17 Excitation and emission wavelengths for FSEC . . . 58
2.18 Preparation of grids used for cryo-EM . . . 83

3.1 Nanobodies previously raised against an α1β3 $GABA_AR$ . . . 88
3.2 Investigating nanobody-α2β3 $GABA_AR$ binding by kinetic titration using BLI: results of fits from MATLAB . . . 99
3.3 α(2/3)β3nbs with increased affinity in the presence of 1 mM GABA . . . 101
3.4 Comparison of nanobody and megabody binding to α(2/3)β3 $GABA_ARs$ in the presence or absence of 1 mM GABA . . . 102
3.5 Compound application protocol used for nanobody screening . . . 103
3.6 Hits from Ionflux screen for positive modulation . . . 104

4.1 Titres for baculovirus production optimisations . . . 118
4.2 FSEC screening of lysates from HEK293S GnTI$^-$ cells transduced with α2/β3/mEGFP-γ2L-1D4 using BacMam (first round) . . . 120

4.3 FSEC screening of lysates from HEK293S GnTI$^-$ cells transduced with α2/β3/mEGFP-γ2L-1D4 using BacMam (second round) 121
4.4 Top 10 expression conditions for mV-β3-1D4 using a stable cell line or the BacMam expression system 124

5.1 Data collection parameters for α3β3 $GABA_AR$ (in MSP2N2 nanodiscs, FLAG purification) + α3β3mb173, 1 mM GABA 145
5.2 Data collection parameters for α3β3γ2L $GABA_AR$ (in MSP2N2 nanodiscs, 1D4 purification) + α3β3mb173, 1 mM GABA 150
5.3 Data collection parameters for α3β3γ2L $GABA_AR$ (in MSP2N2 nanodiscs, 1D4 purification) + α3β3mb173, 1 mM GABA, 1 mM picrotoxin 153
5.4 Data collection parameters for α3β3γ2L $GABA_AR$ (in amphipols, 1D4 purification) + α3β3mb173, 1 mM GABA, 1 mM picrotoxin 157

B.1 Constructs used in this work 182
B.2 Cloning methods for constructs 185

C.1 Oligonucleotide primers used in this work 188
C.1 Oligonucleotide primers used in this work 189

E.1 α2β3 $GABA_AR$ nanobody selection conditions 234
E.2 α3β3 $GABA_AR$ nanobody selection conditions 239
E.3 Investigating α2β3nb-$GABA_AR$ binding by kinetic titration using BLI: results of fits from MATLAB 241
E.4 Investigating α3β3nb-$GABA_AR$ binding by kinetic titration using BLI: results of fits from MATLAB 244
E.5 Investigating α2β3nb-$GABA_AR$ binding in the presence of 1 mM GABA by kinetic titration using BLI: results of fits from MATLAB 247
E.6 Investigating α3β3nb-$GABA_AR$ binding in the presence of 1 mM GABA by kinetic titration using BLI: results of fits from MATLAB 251
E.7 Investigating α2β3nb-$GABA_AR$ binding in the presence of 10 μM gabazine by kinetic titration using BLI: results of fits from MATLAB 254
E.8 Investigating α3β3nb-$GABA_AR$ binding in the presence of 10 μM gabazine by kinetic titration using BLI: results of fits from MATLAB 258
E.9 Results of ionflux screen for positive modulation 261
E.10 Lysate FSEC results comparing mV-β3-1D4 expression using BacMam and a stable cell line in various conditions 263
E.11 Optimisation of expression conditions for cell lines expressing heteromeric $GABA_ARs$, ranked by peak height 266

List of Abbreviations

4-PIOL . . . . . 5-(4-piperidyl)isoxazol-3-ol

5-HT_3R . . . . . Serotonin type 3 receptor

AChBP . . . . . Acetylcholine binding protein

AChR . . . . . Acetylcholine receptor

AcMNPV . . . . *Autographa californica* multiple nuclear polyhedrosis virus

Allopregnanolone 5α-pregan-3α-ol-20-one

ATP . . . . . Adenosine triphosphate

BacMam . . . . . Baculovirus-mediated transfection of mammalian cells

BBE . . . . . Bovine brain lipid extract

BiP . . . . . Binding immunoglobin protein

BirA . . . . . Biotin ligase

BLI . . . . . Biolayer interferometry

CAG (promoter) See legend for figure A.1

CCD . . . . . Charge-coupled device

CDR . . . . . Complementarity determining region

CHS . . . . . Cholesterol hemisuccinate

CI . . . . . Confidence interval

Clptm1 . . . . . Cleft lip and palate transmembrane protein 1

CMC . . . . . Critical micellar concentration

CMOS . . . . . Complementary metal oxide semiconductor

CMV . . . . . Cytomegalovirus

cryo-EM . . . . . Cryo-electron microscopy

CTF . . . . . Contrast transfer function

DDM . . . . . n-Dodecyl-β-D-Maltopyranoside

DDTM . . . . . n-Dodecyl-β-D-Thiomaltopyranoside

DED . . . . . Direct electron detector

DHA . . . . . Docosahexaenoic acid

DMCM Methyl-6,7-dimethoxy-4-ethyl-beta-carboline-3-carboxylate

DMEM . . . . . Dulbecco's Modified Eagle Medium

DMEM/F12 . . . Dulbecco's Modified Eagle Medium/Nutrient Mixture F-12

DMNG . . . . . Decyl Maltose Neopentyl Glycol

DQE . . . . . Detective quantum efficiency

DRG . . . . . Dorsal root ganglia

DTT . . . . . Dithiothreitol

ECD . . . . . Extracellular domain

ECL . . . . . Enhanced chemiluminescence

EDTA . . . . . Ethylenediaminetetraacetate

E_{GABA} . . . . . Reversal potential for GABA currents

EGFP . . . . . Enhanced green fluorescent protein

ELIC . . . . . *Erwinia chrysanthemi* ligand-gated ion channel

ELISA . . . . . Enzyme-linked immunosorbent assay

EM . . . . . Electron microscopy

EmGFP . . . . . Emerald monomeric green fluorescent protein

EPSC . . . . . Excitatory post-synaptic potential

ER . . . . . Endoplasmic reticulum

Fab . . . . . Antigen binding fragment of an IgG

FACS . . . . . Fluorescence activated cell sorting

FBS . . . . . Fetal bovine serum

fc . . . . . Flow cell

FEG . . . . . Field emission gun

FL . . . . . Full-length

FP . . . . . Fluorescent protein

FSC . . . . . Fourier shell correlation

FSC area . . . . . Forward-scattered area

FSEC . . . . . Fluorescence size exclusion chromatography

GABA . . . . . γ-amino butyric acid

GABA-ρ . . . . . $GABA_AR$ /$GABA_CR$ composed of ρ subunits

GABARAP . . . $GABA_AR$-associated protein

$GABA_AR$ . . . . γ-amino butyric acid type A receptor

$GABA_BR$ . . . . γ-amino butyric acid type B receptor

$GABA_CR$ . . . . γ-amino butyric acid type C receptor

GAD . . . . . Glutamate decarboxylase

GAD_{65} . . . . . 65 kDa isoform of glutamate decarboxylase

GAD_{67} . . . . . 67 kDa isoform of glutamate decarboxylase

GABA-T . . . . . GABA aminotransferase

GAT . . . . . GABA transporter

GFP . . . . . Green fluorescent protein

GLIC . . . . . *Gloeobacter violaceus* ligand-gated ion channel

GluCl . . . . . Glutamate-gated chloride channel

GlyR . . . . . Glycine receptor

GnTI . . . . . N-acetylglucosaminyltransferase I

GO . . . . . Graphene oxide

GPCR . . . . . G-protein coupled receptor

GPU . . . . . Graphical processing unit

GS . . . . . Glutamine synthetase

GST . . . . . Glutathione-S-Transferase

HA (tag) . . . . . Influenza hamagglutinin (tag)

HCAb . . . . . Heavy chain antibody

HEK293 cell . . . Human embryonic kidney 293 cell

HEK293T cell . . Human embryonic kidney 293 cell expressing the SV-40 T-antigen

HEPES . . . . . 4-(2-hydroxyethyl)-1-piperazineethanesulfonic acid

HIV . . . . . Human immunodeficiency virus

HopQ . . . . . Extracellular adhesin domain of *H. pylori*

HRP . . . . . Horseradish peroxidase

HRV . . . . . Human rhinovirus

ICD . . . . . Intracellular domain

IgG . . . . . Immunoglobin-γ

IMAC . . . . . Immobilised metal ion chromatography

IPSC . . . . . Inhibitory postsynaptic current

IPSP . . . . . Inhibitory postsynaptic potential

IPTG . . . . . Isopropyl β-D-1-thiogalactopyranoside

IRES . . . . . Internal ribosome entry sequence

IVA . . . . . *In vitro* assembly

KCC2 . . . . . K^+-Cl^- contransporter 2

LB . . . . . Lysogeny Broth

LHFPL4 . . . . . Lipoma HMGIC fusion partner-like 4

LN_2 . . . . . Liquid nitrogen

mAb . . . . . Monoclonal antibody

MAPS . . . . . Monolithic active pixel sensor

mb . . . . . Megabody

MCS . . . . . Multiple cloning site

mEGFP . . . . . Monomeric enhanced green fluorescent protein

MES . . . . . 2-(N-morpholino)ethanesulfonic acid

MOI . . . . . Multiplicity of infection

MOPS . . . . . 3-(N-morpholino)propanesulfonic acid

MSP . . . . . Membrane scaffold protein

MSP1D1 . . . . . Membrane scaffold protein 1D1

MSP2N2 . . . . . Membrane scaffold protein 2N2

MTF . . . . . Modulation transfer function

mVenus, mV . . Monomeric Venus (fluorescent protein)

nAChR . . . . . Nicotininc acetylcholine receptor

nb . . . . . Nanobody

NEAA . . . . . Non-essential amino acids

NKCC1 . . . . . Na^+-K^+-Cl^- contransporter 1

NL2 . . . . . Neuroligin 2

PAG . . . . . Phosphate activated glutaminase

PAGE . . . . . Polyacrylamide gel electrophoresis

PBS . . . . . Phosphate buffered saline

PCR . . . . . Polymerase chain reaction

PEI . . . . . Polyethylenimine

PEM . . . . . Protein Expression Medium

PKC . . . . . Protein kinase C

pLGIC . . . . . Pentameric ligand-gated ion channel

Plic-1 . . . . . Protein that links integrin-associated protein with the cytoskeleton-1

POPC 1-palmitoyl-2-oleoyl-sn-glycero-3-phosphocholine

Pregnanolone . . 5β-pregan-3α-ol-20-one

PSF . . . . . Point spread function

rpm . . . . . Revolutions per minute

RPTP . . . . . Receptor type protein tyrosine phosphatase

RT . . . . . Room temperature

RU . . . . . Response units

SBP . . . . . Streptavidin binding protein

SCK . . . . . Single cycle kinetics

SDS . . . . . Sodium dodecyl sulfate

SDS-PAGE . . . Sodium dodecyl sulfate polyacrylamide gel electrophoresis

SEC . . . . . Size exclusion chromatography

SEM . . . . . Standard error of the mean

SGD . . . . . Stochastic gradient descent

SMA . . . . . Styrene–maleic acid

SMALP . . . . . Styrene–maleic acid lipid particle

SPR . . . . . Surface plasmon resonance

SSA . . . . . Succinic semialdehyde

SSC area . . . . . Side-scattered area

SV40 . . . . . Simian virus 40

svg . . . . . Scalable Vector Graphics

TBPS . . . . . Tert-butylbicyclophoporothionate

TEM . . . . . Transmission electron microscope

TetR, TR . . . . . Tetracycline repressor protein

TETS . . . . . Tetramethylenedisulfotetramine

TEV . . . . . Tobacco Etch Virus

THDOC 5α-pregan-3α,21-diol-20-one; 3α,5α-THDOC

THIP . . . . . 4,5,6,7-tetrahydroisoxazolo[5,4-c]pyridin-3-ol

TCA . . . . . Tricarboxylic acid

TMD . . . . . Transmembrane domain

VH . . . . . IgG heavy chain variable region

VHH . . . . . Variable domain of a heavy-chain antibody

VIAAT . . . . . Vesicular inhibitory amino acid transporter

VGAT . . . . . Vesicular GABA transporter

VL . . . . . IgG heavy chain variable region

VPA . . . . . Valproic acid

VPP . . . . . Volta phase plate

v/v . . . . . Volume per volume

WPRE . . . . . Woodchuck hepatitis virus posttranscriptional regulatory element

w/v . . . . . Weight (g) per volume (ml)

ZAC . . . . . Zinc activated ion channel

1 Introduction

Contents

1.1 **GABAergic neurotransmission and the inhibitory synapse** 2
1.2 **$GABA_A$ receptor biophysical properties** 4
1.3 **$GABA_AR$ pharmacology** 14
1.4 **Distinct roles for types of $GABA_ARs$ in the brain** 19
1.5 **Nanobodies as tools for (structural) biology** 25
1.6 **Aims of this thesis** 28

Activity in the brain is a delicate balance of excitatory and inhibitory events. These events are key to the normal function of the brain, and disruption of neurotransmission at the cellular and molecular level can have disastrous consequences. The focus of this thesis is the inhibitory γ-amino butyric acid (GABA) type A receptor ($GABA_AR$), and in this section a 'classical' view of GABAergic neurotransmission will be first outlined (Section 1.1) before details of the biophysical characteristics (Section 1.2), pharmacology of $GABA_ARs$ (Section 1.3) and role of specific $GABA_ARs$ in the brain (Section 1.4) are discussed. Finally, nanobodies will be introduced as tools for structural biology and beyond (Section 1.5).

1.1 GABAergic neurotransmission and the inhibitory synapse

1.1.1 GABA synthesis and release

The first suggestion that GABA may play an important role in the brain was in the 1950 report from Roberts and Frankel [1], who noted that large quantities of GABA were present in protein-free extracts from mouse, rat, rabbit, guinea pig, frog and human brains. This first report suggested the formation of GABA from L-glutamate by the enzyme glutamic acid decarboxylase (GAD). Two isoforms of GAD were later found to exist in the brain: GAD_{67} and GAD_{65}, named for their corresponding molecular weights [2]. These isoforms have a slightly different distribution within neurons, with GAD_{67} being diffuse throughout the cytosol and GAD_{65} being primarily confined to synaptic terminals [2].

After synthesis, GABA is packaged into synaptic vesicles for release by VIAAT (vesicular inhibitory amino acid transporter)/VGAT (vesicular GABA transporter), which was simultaneously cloned by two different groups and hence given two different names [3], [4]. This protein is located on synaptic vesicles [5] where it transports GABA from the cytosol into the vesicle using a proton gradient [6].

Release of GABA from the synaptic terminal is evoked by an action potential in a Ca^{2+}-dependent manner [7]. The machinery involved in release is complex, but release occurs via SNARE-mediated vesicle fusion events [7].

1.1.2 GABA-mediated Cl^- flux

GABA released from the presynaptic terminal diffuses across the synaptic cleft to bind to $GABA_A$Rs embedded in the postsynaptic membrane. This binding results in a flow of Cl^- ions through the channel according to their electrochemical gradient. Thus the result of GABA agonism is a flow of negatively charged ions into the cell, known as an inhibitory postsynaptic current (IPSC). This results in hyperpolarisation of the postsynaptic membrane, reducing the impact of coincident excitatory postsynaptic currents (EPSCs), as well as shunting inhibition due to the increase in membrane conductance [8].

1.1.3 GABA removal

The continued presence of GABA in the synaptic cleft would result in continued inhibition of the postsynaptic cell; in order to prevent this, neurotransmitter is actively removed by GABA transporters (GATs) located on neurons and astrocytes. These take up one GABA molecule into the cell along with two sodium ions and one chloride ion [9]. The time scale for elevated GABA concentration in the synaptic cleft is estimated to be on the order of hundreds of microseconds [10].

1.1.4 GABA catabolism

When taken back up into neurons, GABA is metabolised to succinic semialdehyde (SSA) through the action of GABA transaminase (GABA-T) [11]. SSA is oxidised to succinate, which can re-enter the tricarboxylic acid (TCA) cycle. When taken up into astrocytes, after re-entering the TCA cycle and emerging as glutamate, GABA can be converted to glutamine by the action of glutamine synthetase (GS) [12]. Glutamine can be exchanged between astrocytes and neurons, and converted back to glutamate in neurons by phosphate-activated glutaminase (PAG) [13].

1.1.5 Variants of 'classical' GABAergic neurotransmission

There are variations to almost every step in this outline of GABAergic neurotransmission; only a few notable examples are described here.

Although glutamate is thought to be the main GABA precursor in most of the brain, in some regions putrescine can be a significant precursor for GABA synthesis [14].

$GABA_A$Rs may be positioned opposed to a GABA release site (synaptic receptors), in the region of the synapse (perisynaptic), or outside of the synapse (extrasynaptic) [8]. Phasic inhibition is said to occur when a temporal relationship exists between GABA release and inhibitory events. This is true when $GABA_A$Rs opposed to sites of GABA release are activated, as described above. Furthermore, simultaneous or near-simultaneous multivesicular release can result in spillover and activation of both synaptic and perisynaptic receptors. Extrasynaptic receptors mediate a tonic inhibition, and are spontaneously active and/or activated by tonic levels of GABA [10]. Additionally,

presynaptic $GABA_A$Rs are located in the axonal compartment, where they can mediate presynaptic inhibition [15].

Although GABA is usually thought of as an inhibitory neurotransmitter, the direction of chloride flow through $GABA_A$Rs depends on the local electrochemical gradient. This gradient is maintained by chloride transporters, particularly the Na^+-K^+-Cl^- contransporter NKCC1, and the K^+-Cl^- contransporter KCC2, which use Na^+ and K^+ gradients to transport Cl^- ions across the membrane [16]. Changes in expression of these transporters can modulate the intracellular Cl^- concentration, which determines the reversal potential for GABA currents (E_{GABA}). This, in turn, can modulate neuronal excitability and network function [16]. Changes in E_{GABA} are likely to underlie reported cases of an excitatory effect of GABA at axo-axonal synapses [17], [18]. Furthermore, during development changes in Cl^- transporter expression have been documented, resulting in changes to E_{GABA} [19].

The flow of GABA through GATs is not always unidirectional; under certain circumstances reversal of neuronal or astrocytic GABA transport can occur. As an alternative to Ca^{2+}-evoked release, GABA can be extruded due to reversal of the Na^+ gradient, increased cytoplasmic GABA concentration, or through the action of GAT inhibitors [9].

In addition to ionotropic $GABA_A$Rs, GABA also acts at metabotropic GABA type-B receptors ($GABA_B$R). These are G-protein coupled receptors (GPCRs) and can be located pre- or postsynaptically, and can be excitatory or inhibitory.

Finally, $GABA_A$Rs are also expressed in non-neuronal cell types and outside the nervous system. Examples include expression of $GABA_A$Rs in pancreatic islet α cells. Here, GABA is co-released with insulin from neighbouring βcells causing inhibition of glucagon secretion [20].

1.2 $GABA_A$ receptor biophysical properties

1.2.1 The family of pentameric ligand-gated ion channels

The $GABA_A$R is part of a larger family of pentameric ligand-gated ion channels (pLGICs). In humans, this family includes other anion-selective channels such as the glycine receptor (GlyR), as well as the cation-selective acetylcholine receptor (AChR) and nicotinic AChR (nAChR), serotonin type 3 receptor (5-HT_3R), and the zinc-activated ion channel (ZAC). A

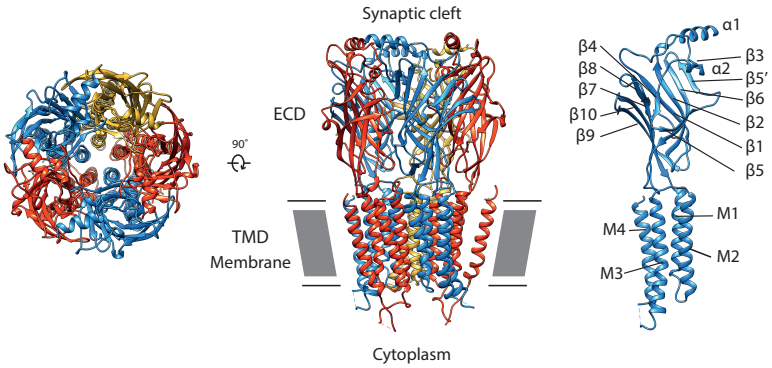

Figure 1.1: An overview of $GABA_AR$ structure. The $GABA_AR$ is displayed from the top (left) and side (middle). The secondary structure elements are shown for one subunit on the right.

number of homologs exist in other species including the *Caenorhabditis elegans* glutamate-gated chloride channel (GluCl), and ion channels from the bacteria *Gloeobacter violaceus* (GLIC) and *Erwinia chrysanthemi* (ELIC) [21]. Although the latter has been reassigned as *Dickeya dadantii*, its ligand-gated ion channel continues to be referred to as ELIC. Several structures of family members have now been solved by X-ray crystallography and cryo-electron microscopy (cryo-EM), including acetylcholine binding protein (AChBP) [22], [23], nAChR [24]–[26], GLIC [27]–[29], ELIC [30], GluClα [31], [32], 5-HT_3R [33], [34], GlyR [35], [36] and $GABA_AR$ [37]–[42].

Family members share a common topology, with five subunits arranged pseudo-symmetrically around a central pore to form an approximate cylinder with height 110Å and diameter 60-80Å (Figure 1.1). Each subunit is comprised of three main domains: the extracellular domain (ECD), transmembrane domain (TMD) and intracellular domain (ICD) (Figure 1.1), with the latter omitted in prokaryotic family members [21]. The modular subunit design is confirmed by studies which have constructed functional ECD/TMD chimeras of different family members, including AChBP/GlyR, AChBP/5-HT_3R, nAChRα7/5-HT_{3R}, and GLIC/GlyR [43], [44]. Indeed, chimeras between receptors with disparate pharmacological or biophysical properties is a common strategy to narrow down the regions involved in a particular aspect of function (for example, [45], [46]).

The ECD is composed of ten β-sheets (β1-10) arranged into a twisted β-sandwich. By convention each of the loops in the ECD is named for the β-sheet it precedes, so the β1-2 loop is called loop 2, and so forth. The ECD harbours the neurotransmitter binding

site, with the regions involved in coordination on the principal (+) and complementary (-) faces given the names loops A-C and loops D-F, respectively [47]. These names are historical, with portions of these binding 'loops' corresponding to β-sheets. Eukaryotic family members have a conserved disulfide bond in loop 7, the Cys-loop, which is not present in prokaryotic family members [21].

The TMD is composed of four transmembrane helices, M1-4. Each subunit contributes one M2 helix to form the pore. Given the large degree of homology in the family, a common numbering system is used for the M2 helix, which designates 0' as the residue at the cytoplasmic end of M2 (α1 Arg255, β2 Arg250, and γ2 Arg265). Conduction of ions is prevented while the receptor is in closed states by gates located in M2. A dual-gate model has been proposed for pLGICs, with an 'activation gate' in the 9' to 13' region, and the 'desensitisation gate' in the cytoplasmic -2' to 2' region [48].

The ICD is comprised of the long loop between M3 and M4, and is the most sequence-diverse region of the receptor. It is not present in prokaryotic family members [21] and is not necessary to form functional channels [49]. This domain is mainly implicated in trafficking to and anchoring in the synaptic membrane, as well as receptor modulation by intracellular proteins and post-translational modifications [48]. In the nAChR and 5-HT_3R, this domain is ordered [33], [34], whereas the majority of the ICD was unresolved in recent cryo-EM studies of a full-length heteromeric $GABA_A$R [41], [42].

1.2.2 Types of $GABA_A$Rs and their stoichiometry

$GABA_A$Rs were first purified using a benzodiazepine column [50], which led to the cloning of the first subunits [51]. In humans, eight families of subunits are known to exist, creating a palette of 19 subunits: α1-6, β1-3, γ1-3, δ, ε, θ, π, ρ1-3 (Figure 1.2A). Several subunits are alternatively spliced which can have functional consequences [52]; for example γ2 exists in short (γ2S) and long (γ2L) forms with the inserted eight amino acids (LLRMFSF) in the ICD containing a protein kinase C (PKC) phosphorylation site [53], [54]. Other aspects of mRNA processing can be developmentally regulated, such as RNA editing of the α3 subunit DNA (I→M at position 314), which increases in prevalence in adults [55], [56].

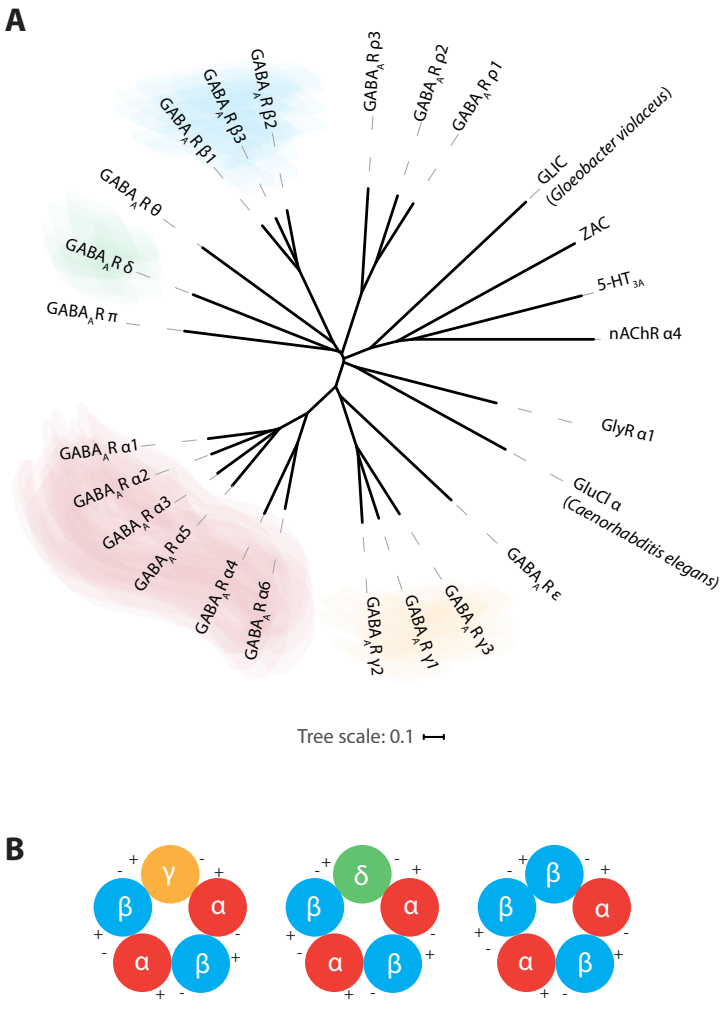

Figure 1.2: GABA$_A$R subunits and pentameric arrangement. **A**: A phylogenetic tree of GABA$_A$R subunits, as well as other pLGIC subunits. The tree was created with interactive Tree of Life (iTOL; [57]) after the alignment of subunit sequences using Clustal Omega [58]. The sequences used for alignment can be found at Uniprot accession codes P14867 (human α1), P47869 (human α2), P34903 (human α3), P48169 (human α4), P31644 (human α5), Q16445 (human α6), P18505 (human β1), P47870 (human β2), P28472 (human β3), Q8N1C3 (human γ1), P18507 (human γ2), Q99928 (human γ3), O13764 (human δ), P78334 (human ε), Q9UN88 (human θ), O00591 (human π), P24046 (human ρ1), P28476 (human ρ2), A9MPY1 (human ρ3), G5EBR3 (*GluCl* α), P23415 (human GlyR α1), P43681 (human nAChR α4), P46098 (human 5-HT$_{3A}$), Q401N2 (human ZAC), and Q7NDN8 (GLIC). **B**: Likely subunit arrangement of αβγ, αβδ, αβ receptors [59] The principle (+) and complementary (-) interfaces are indicated for each subunit.

There is ~70% sequence identity of subunits within families, and ~20% sequence identity between subunit families [60] (Figure 1.3). In humans, most genes are located in clusters of different subunit types, for example at 4p12 (γ1, α2, α4, β1), 5q34 (β2, α6, α1, γ2), 6q15 (ρ1, ρ2), Xq28 (ε, α3, θ) and 15q13 (β3, α5, γ3) [52]. Clustering is thought to stem from duplication of an ancestral gene to form a group, and then subsequent translocation to elsewhere in the genome [61].

$GABA_A$Rs are known to be pentameric from studies by negative stain electron microscopy [62], sucrose density gradient centrifugation [63] and the functionality of concatameric constructs [64]. Given the existence of 19 different subunits, if all combinations were allowed there could be 19^5 different kinds of $GABA_A$Rs. This is not the case, with some combinations disallowed, and others preferred [59], [65]. Criteria for the existence of particular types of $GABA_A$Rs have been suggested, and pertain to the properties of recombinant and native receptors of the putative type [59]. Recombinant receptors should unambiguously be shown to form with a particular subunit composition, stoichiometry and arrangement, with unique biophysical and pharmacological properties. Colocalisation of the subunits should be shown in animals at the tissue, cell and subcellular levels, and a physical demonstration (e.g. by co-immunoprecipitation) and functional characterisation (e.g. based on unique pharmacology) should be made.

A majority of native $GABA_A$Rs are composed of two α subunits, two β subunits, and one non-α, non-β subunit (Figure 1.2B) [59], [65], [66]. A predominant form of $GABA_A$Rs is that of αβγ, which exist in a 2α:2β:1γ ratio with a clockwise subunit arrangement of α-β-γ-α-β [63], [64], [67]–[70]. It is possible that other stoichiometries and arrangements may exist when subunits are expressed heterologously, but these are not likely to be physiologically relevant [71]. Major types of αβγ receptors include α1β2γ2, α1β3γ2, α2βγ2, α3βγ2, α4βγ2, α5βγ2, and α6βγ [59]. There may be two different alpha subunits in a pentamer; for example α1α6βγ [72]–[74]. αβγ receptors are thought to be primarily resident in synapses, and mediate phasic inhibition [10].

Other physiologically relevant types of $GABA_A$Rs include αβδ and αβ, which are both mainly extrasynaptic [10], [75]. There has been some disagreement about the stoichiometry of both (αβδ[76]–[80], αβ[63]–[65], [69], [81]), but the most likely arrangement seems

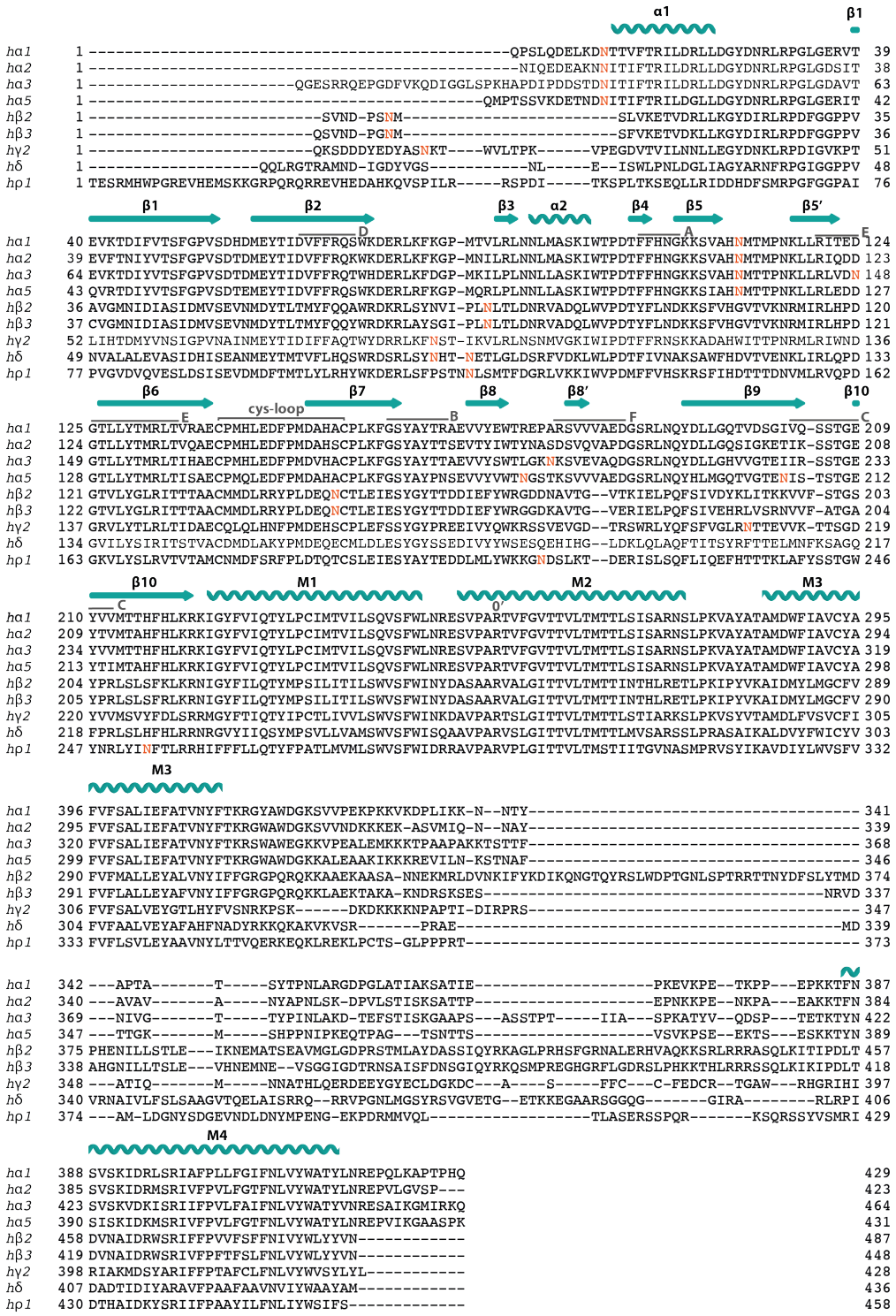

Figure 1.3: Alignment of GABA$_A$R subunits. Clustal omega alignment of several synaptic human GABA$_A$R subunits (mature peptide only), with secondary structure above as symbols (labelled β1-10, M1-4). Neurotransmitter binding loops are indicated (A-F) and the cys-loop are also indicated above. N-linked glycosylation sites are indicated in red. Aligned sequences, with signal sequences removed, are from Uniprot, with the following accession numbers: P14867, human α1; P47869, human α2; P34903, human α3; P31644, human α5; P47870, human β2; P28472, human β3; P18507, human γ2; O14764, human δ; P24046, human ρ1. Alignment was conducted with Clustal Omega [58]. Secondary structure information derived from [37], binding loop information from [47].

to be substitution of either δ or β for γ [59]. A similar arrangement has been proposed for αβθ and αβε receptors [82], [83].

Additionally, some subunits can form homomeric receptors, most notably ρ [84]. These are strongly expressed in the retina [59], and were previously classified as a distinct group of $GABA_C$Rs based on their distinct pharmacology and biophysical properties [85]. The current recommendation of the International Union of Pharmacology is for the disuse of the $GABA_C$R terminology in favour of a reclassification of ρ subunits as part of the $GABA_A$R family [59].

An additional type of homomeric receptor is formed from β3 subunits [86], [87]. As these do not contain a β+/α- interface they are not gated by GABA, but can instead be gated by histamine [88], [89].

1.2.3 Assembly and post-translational modification of $GABA_A$Rs

$GABA_A$R assembly occurs in the endoplasmic reticulum (ER), facilitated by luminal and cytoplasmic chaperones, including binding immunoglobin protein (BiP) and calnexin [65], [90]. In most cases single subunits are retained in the ER upon heterologous expression [65]. The receptor is stabilised in the ER by Plic-1 (protein that links integrin-associated protein with the cytoskeleton-1) [91].

The ECD has been suggested to harbor several motifs that are particularly important for assembly [92], [93], including a conserved α subunit N-linked glycan in the vestibule which interacts with a tyrosine residue on the opposite γ subunit in αβγ receptors to constrain the stoichiometry of $GABA_A$Rs [38]–[40].

$GABA_A$Rs are also the subject of other post-translational modifications, including phosphorylation, which can modify channel behaviour [94]. Palmitoylation of γ subunits is also thought to be important for their accumulation at synapses [91].

1.2.4 Trafficking and synaptic anchoring

Many proteins have been shown in proteomic studies to interact with $GABA_A$Rs [95]–[97] and can have an impact on GABAergic transmission. For example, a role in forward trafficking has been suggested for $GABA_A$R-associated protein (GABARAP) [98], whereas Cleft

lip and palate transmembrane protein 1 (Clptm1) was shown to interact with $GABA_A$Rs to slow their trafficking to the synapse [97].

Furthermore, several interacting proteins are thought to be involved in anchoring $GABA_A$Rs at the synapse. One such protein is gephyrin, which is thought to bind to $GABA_A$R ICDs and oligomerise to form clusters of receptors at postsynaptic sites, although some degree $GABA_A$R clustering and inhibitory neurotransmission is preserved upon knockdown of gephyrin expression in neurons [99]. Gephyrin also binds collybistin and the postsynaptic adhesion molecule neuroligin 2 (NL2), which are also thought to be involved in clustering $GABA_A$Rs at inhibitory synapses [100]. Recently, lipoma HMGIC fusion partner-like 4 (LHFPL4) has also been shown to interact with the γ subunit as an 'auxiliary subunit' and is essential for clustering [101], [102]. Although the term 'auxiliary subunit' may not be appropriate given that LH4 does not seem to modulate the functional properties of $GABA_A$Rs, this protein seems to play a critical role in stabilising the receptor at the synapse through formation of a tripartite complex along with NL2 [101], [102].

1.2.5 Single-channel conductance and ion selectivity

Like other biophysical properties, $GABA_A$R single channel conductance is dependent on subunit combination. For example, α1β1 receptors have a main conductance level of 15 pS and a subconductance level of 10 pS, while α1β1γ2S receptors have a main conductance level of 29 pS and a subconductance level of 21 pS [103]. In patch-clamp experiments, different conductances can also be observed in patches pulled from neurons, consistent with the view that neurons contain multiple types of $GABA_A$Rs [10].

M2 residues are thought to be the major determinant of conductance and selectivity in pLGICs. This was first established in other family members, and initial studies in a cation-selective pLGIC, the nAChR, showed that mutations to polar and charged residues in M2 play a major role in determining single-channel conductance [104]. In line with this view, rapid and reversible changes in single-channel conductance can be observed by manipulating extracellular pH and engineering protonatable residues along the nAChR M2 [105]. Such transitions between conductance levels can also be observed within clusters of activation in $GABA_A$Rs [106]. An effect on conductance can be observed at side chains

that do not directly face into the pore, presumably due to an effect on the electrostatic environment [105], [107], and these principles illustrated in other pLGIC family members are presumed to also apply to the $GABA_AR$.

Additional determinants of conductance in pLGICs lie along the ion permeation path in the ECD vestibule and the ICD. Residues in the external vestibule, through which ions flow into M2, are thought to play a role in concentrating permeant ions relative to bulk solution [108], although in $GABA_ARs$ mutations to different subunits do not sum linearly [109]. In the $5\text{-}HT_3R$, the ICD from each subunit forms a helix (MX) that together form a cone pointing downwards into the cell. Portals through which ions flow are formed in the gaps between these helices, and the residues lining these portals also contain important determinants of single-channel conductance [110]. However, this region does not appear to be ordered in the $GABA_AR$, at least in the absence of interaction partners, since it is not resolved in cryo-EM density of a full-length heteromeric $GABA_AR$ [41], [42].

The main determinants of ion permeability for pGLICs are also thought to reside in the M2 helix, as was first demonstrated for the nAChR [104]. $GABA_ARs$ are anion-permeable, with the main permeant ion being chloride. They also possess a smaller permeability for bicarbonate ions ($P_{Cl^-}/P_{HCO_3^-} \approx 0.2$) [111]. In homomeric ρ1 $GABA_ARs$, the double mutants (ΔPro-2'/Ala-1'Glu) and (ΔP-2'/R-0'E) had reversed permeabilities ($P_{Na^+}:P_{K^+}:P_{Cl^-}=0:0.03:1$) to (2.79:3.59:1) and (2.4:3.0:1), respectively [112]. In heteromeric $GABA_ARs$, similar mutations could affect permeability but with asymmetric effects, with mutations in β3 having a larger effect than equivalent mutations in α2 or γ2 [113]. This could be due to the fact that the contribution of charged side chains to selectivity depends on their protonation state, which can depend in complex ways upon the local environment, as has been shown for other pGLIC family members [46].

1.2.6 Mechanisms of channel gating and desensitisation

During $GABA_AR$ activation, binding of GABA to a site in the extracellular domain causes opening of a distant channel gate in the TMD. The main steps in channel gating have been explored in the $GABA_AR$ as well as other pLGIC family members. Each stage forms part of a continuous process in an energy landscape which may be visited regardless of

ligand binding, but the association of pharmacological agents can shift the landscape so as to favour particular states [114].

GABA binds to the β+/α- interface, of which there are two per pentamer (Figure 1.2B; see also Section 1.3.1 for more detail). Two GABA molecules are necessary to fully activate the channel [90]. Closure of loop C over the agonist ('capping') is thought to be an important step in receptor activation [47] (but see [114]). Consistent with this, a relatively large difference is seen in $GABA_AR$ structures with and without GABA [41]. Binding of GABA results in a reorganisation of the intersubunit interfaces in the ECD, encapsulated in a recently posited 'lock and pull' mechanism [41]. In this model, closure of loop C in the β subunits results in rotation of the ECD of this subunit. A rearrangement of the β+/α- interface results in a 'lock' of these two adjacent subunits, and the β subunit rotation is transmitted to other subunits ('pull'), to result in overall rotation of the five ECDs. This is consistent with an 'un-blooming' motion deduced from comparisons between conducting and nonconducting states of other homomeric pLGICs [114].

Since pLGICs have a modular structure, these changes in the ECD need to be transmitted to the TMD in order to open the gate. This communication between the two domains is proposed to be bi-directional [115]. Coupling occurs via several interactions at the ECD/TMD interface, including between loop 7 and loop 2, which interact with the M2-3 linker [114], [116]. This linker is displaced outwards, causing outward tilting and anti-clockwise rotation of the TMD helices and thus moving the Leu9' residue towards the intersubunit interfaces [114] [41]. These concerted motions result in widening of the activation gate, permitting ions to flow through the channel.

In the continued presence of agonist, pLGICs enter a nonconducting desensitised state that is distinct from the closed state [48]. In this state the M2 helices are tilted to a narrow constriction at the cytoplasmic end where the desensitisation gate is located [37]. The assignment of this state is consistent with functional evidence that localises the desensitisation gate at the bottom of the pore [117], and the M2 conformation is likely to result from a further tilting after activation [48].

In addition to the desensitised β3 homomeric $GABA_AR$, structures of heteromeric $GABA_ARs$ with truncated M3-4 have recently been solved by cryo-EM [38]–[40], as well

as several full-length receptor structures in desensitised and closed states [41], [42]. One of these truncated $GABA_AR$ structures is in a putative open state [40], while the pore conformations observed in the other two are best characterised by a collapse of the γ subunit into the pore [38], [39]. Given that a full-length heteromeric $GABA_AR$ exhibits a five-fold pseudo-symmetric arrangement of its TMDs when reconstituted into a lipid bilayer [42], the physiological relevance of these heteromeric structures is unclear.

Distinct intermediate states between these three conformations (closed, open, desensitised) have also been proposed. In an analysis of GlyR single-channel kinetics, Burzomato and colleagues [118] proposed that in the course of opening, a closed channel briefly rests in a nonconducting pre-activation ('flip') state. In this framework, the flip-open transition is independent of ligand efficacy, whereas partial agonists differ from full agonists in their ability to promote a resting state-flip transition [119]. It has been further proposed that flipping or 'priming' is linked to capping of loop C [115].

GLIC has recently been crystallised in what the authors propose as a distinct desensitised state from that of the $GABA_AR$ [120]. The basis for this claim is the presence of a bound fatty acid docosahexaenoic acid (DHA), which the authors suggest accelerates the rate and extent of desensitisation. However, after further analysis of the functional data presented by Basak and colleagues [120], others have suggested this structure to represent a pre-activation state stabilised by DHA [120]. However, given that pre-activation states are thought to represent brief intermediates [119], a third interpretation is that the introduction of DHA induces a non-physiological conformation in detergent-solubilised GLIC.

1.3 $GABA_AR$ pharmacology

$GABA_ARs$ have a diverse pharmacology, binding a large array of endogenous and clinically relevant ligands (see Figure 1.4) including sedatives, anxiolytics, anticonvulsants, and hypnotics [121]. Many of these ligands exert differing effects, giving each known subtype a unique profile of active pharmacological agents. A complete review of all $GABA_AR$ ligands is beyond the scope of this thesis, and indeed some drugs, such as topiramate, atiripentol, and losigamone have unknown sites of action [122]. Instead, this section will be limited to a discussion of the main known orthosteric and allosteric sites.

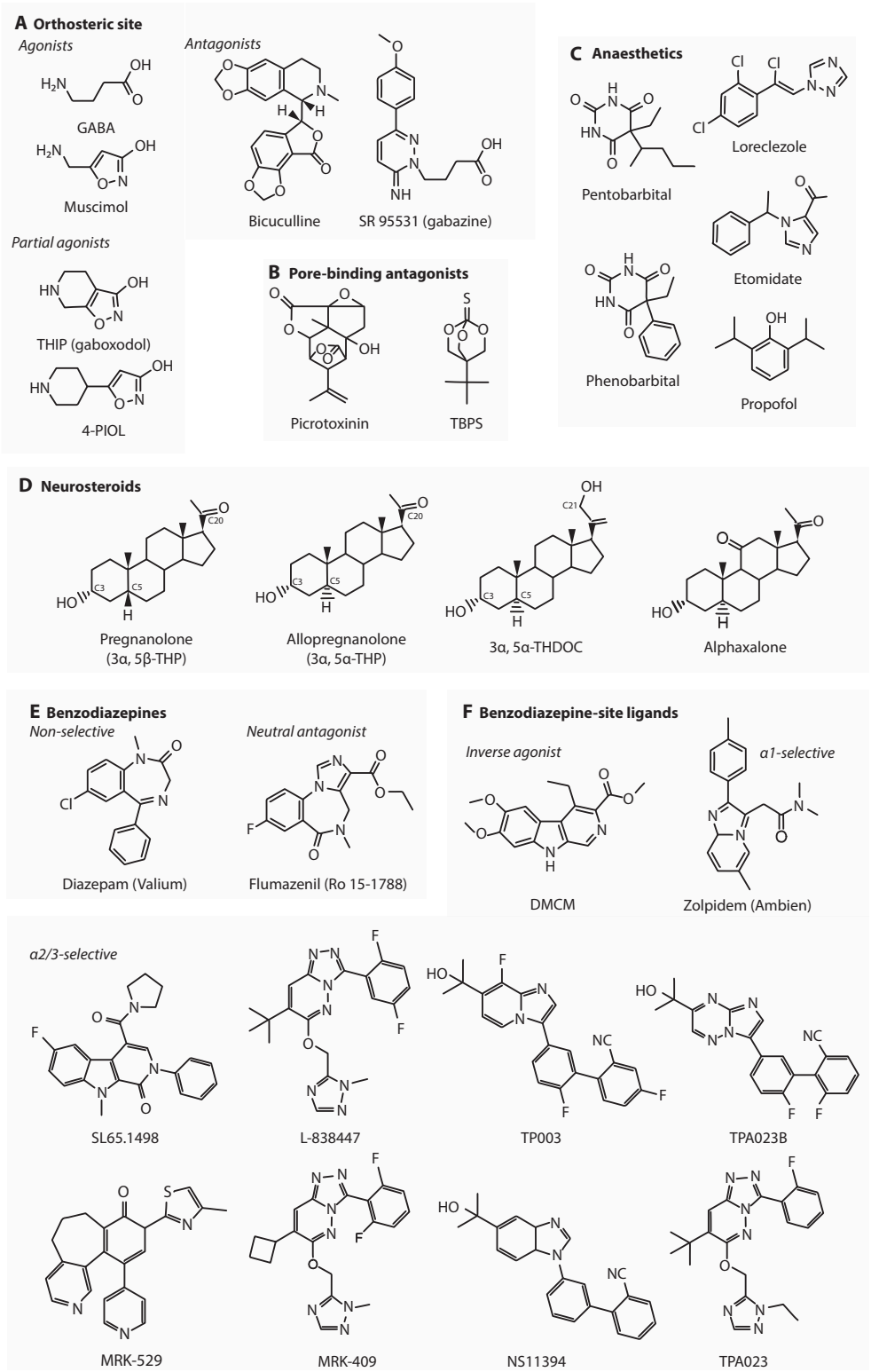

Figure 1.4: $GABA_AR$ ligands. A selection of orthosteric and allosteric $GABA_AR$ ligands, organised by binding site and efficacy. Figure modified from [123].

1.3.1 GABA

GABA binds at the orthosteric site, located at the β+/α- interface, to activate the receptor (Figure 1.4A) [124]. Several aromatic residues line this site leading to its characterisation as an 'aromatic box', and cation-π interactions are common in agonist binding at orthosteric sites within the pLGIC family [125]. Indeed, the interactions between GABA and its binding site have been visualised in recent $GABA_AR$ structures, revealing multiple putative cation-π interactions, as well as salt bridges and hydrogen bonds [38], [39] [41].

Several other agonists and antagonists bind at the GABA site, including the agonist muscimol; the partial agonists 4,5,6,7-tetrahydroisoxazolo[5,4-c]pyridin-3-ol (THIP, gaboxadol), and 5-(4-piperidyl)isoxazol-3-ol (4-PIOL); and the antagonists bicuculline and SR 95531 (gabazine) [121], [123] (Figure 1.4A).

There are differences in the sensitivity of different subtypes for ligands at this site. Most notably, δ-containing receptors are more sensitive to agonists such as GABA, muscimol and gaboxadol, while γ-containing receptors are less sensitive [121]. In addition, GABA has been suggested to be a partial agonist at δ-containing receptors, while THIP is a partial agonist at γ-containing subunits but a full agonist at αβδ receptors [126]. Homomeric β3 receptors cannot bind GABA due to the absence of an α subunit, but agonistic activity at this site can be imparted by histamine and benzamidine [37], [89].

1.3.2 Benzodiazepines

A second important site is located at a homologous position to the GABA site at the α+/γ- interface in α1βγ, α2βγ, α3βγ and α5βγ receptors, where the first documented ligands were the benzodiazepines (Figure 1.4E) [121]. These are best known as positive allosteric modulators such as diazepam (marketed as Valium), midazolam (Versed, Hypnovel), alprazolam (Xanax) and, flunitrazepam (Rohypnol) [127]. Other ligands at the benzodiazepine site can be negative allosteric modulators, which reduce GABA-mediated $GABA_AR$ gating; or neutral antagonists, which have no effect on $GABA_AR$ activation but competitively inhibit modulation by other benzodiazepine-site ligands [123]. Methyl-6,7-dimethoxy-4-ethyl-beta-carboline-3-carboxylate (DMCM) is an example of a negative allosteric modulator, whereas Ro15-1788 (flumazenil) is an example of a neutral antagonist.

Benzodiazepines are unable to bind to the equivalent α+/γ- interface in α4βγ and α4βγ receptors due to the substitution of an arginine (α4Arg99, α4Arg100) for a histidine (α1His101, α2His101, α3His126, α5His126) [128].

The mode of benzodiazepine binding has been the subject of much investigation, and recent structural studies with bretazenil (which has lower potency than diazepam [129]) and flumazenil [39], [40] showed a different orientation to alprazolam and diazepam (both potent positive modulators) [41]. One possible interpretation of this data is that benzodiazepines with different functional effects adopt different binding poses.

Furthermore, benzodiazepine-site ligands with differing activities at specific $GABA_A$Rs have been characterised (Figure 1.4E, F). For example, the z-drugs zolpidem, zopiclone and zalpeon are non-benzodiazepines that have some selectivity for α-containing $GABA_A$Rs over other subunit combinations [130]. Ocinaplon is another α1-preferring positive allosteric modulator [123]. A large effort has been made to identify α2/3 selective positive allosteric modulators and partial agonists, which include NS11394, TP003, L-838477, SL65.1498, TPA023, TPA023B, MRK-049, HZ-166, MRK-623, KRM-II-81, MP-III-024, AZD7325, and PF-06372865 although the degree of selectivity varies considerably between these compounds, and often activity is retained at α5-containing receptors [123], [131]–[137]. For example, NS11394 is a positive allosteric modulator with potency α5 > α3, > α2 > α1 [138]; SL65.1498 is as potent as diazepam at α2- and α3-containing $GABA_A$Rs but has lower potency at α1- and α5-containing receptors [139]; α3IA is an inverse agonist with selectivity for α3-containing receptors [140].

1.3.3 Other ECD ligands

There is increasing evidence for the existence of an allosteric site at the α+/β- interface at a position homologous to the GABA site, and the drugs CGS 9895 and LAU 177 have been proposed to bind there [141], [142]. This site is also bound by a nanobody recently shown to selectively positively modulate α1-containing $GABA_A$Rs [40]. This site is referred to as 'benzodiazepine site 2' by Olsen [121].

The ECD is also proposed to harbour a high-affinity ethanol binding site, although this is controversial [143]. It is clear that ethanol can modulate $GABA_A$Rs at high concentrations

(<50 mM) [60], has also been suggested to modulate extrasynaptic α4/6βδ receptors at low millimolar concentrations, leading to their characterisation as 'one glass of wine receptors' [143]. Results in heterologous expression systems have yielded conflicting results about the potentiation of these $GABA_A$Rs by low concentrations of ethanol [126], [144], [145]. It was suggested that differences in the level of incorporation of the δ subunit into pentamers may have caused these discrepancies [143], but one study using concatameric receptors also reported no potentiation of α4β2δ receptors by low concentrations of ethanol [126]. Nevertheless, it has been reported that cerebellar granule cells, known to express extrasynaptic α6βδ receptors [72], [73], are potentiated by low ethanol concentrations [146] and a role for α4-containing receptors in the nucleus accumbens was implicated in rat ethanol self-administration by region-specific knockout [147].

1.3.4 Neurosteroids

The neurosteroids are metabolites of progesterone and deoxycorticosterone that form a class of endogenous $GABA_A$R modulators [148]. Examples include 5α-pregan-3α-ol-20-one (3α, 5α-THP, allopregnanolone), 5β-pregan-3α-ol-20-one (3β, 5α-THP, pregnanolone), and 5α-pregan-3α, 21-diol-20-one (3α, 5α-THDOC), as well as synthetic steroids such as 5α-pregane-3α-ol-11,20-dione (alphaxalone) (Figure 1.4D). These modulate $GABA_A$R currents at low concentrations, and have agonist activity at high concentration [149]–[151].

Neurosteroids have some degree of subunit selectivity, with slightly higher potency at δ-containing receptors compared to γ-containing receptors, but little selectivity amongst αβγ receptors [152]. They are proposed to bind to site(s) in the TMD, with mutagenesis and photolabelling studies identifying between one and three sites [45], [153], [154]. In addition to positively modulating neurosteroids, $GABA_A$Rs are inhibited by sulphated steroids such as pregnanolone sulphate [151], with a likely binding site in the TMD [155].

1.3.5 Anaesthetics

Another clinically important class of ligands at $GABA_A$Rs are anaesthetics, including the barbiturates (e.g. pentobarbitone, phenobarbitone), as well as propofol, etomidate and loreclezole (Figure 1.4C). These modulators can also have anxiolytic, sedative and

anticonvulsant activity, depending on their pharmacokinetics [123]. Most compounds at this site are positive allosteric modulators, for example etomidate at low (< 100 μM) concentrations; although this drug can also activate the receptor at higher concentrations (100 μM - 1 mM) and at higher still concentrations (> 1 mM) it blocks the channel [156]. Anaesthetics also potentiate different subunit combinations to differing degrees, with some most notably preferring β2/3-containing receptors over those containing β1 [47]. This has been shown to stem from the M2 15' residue, which in its β1 form (serine) markedly reduces potentiation compared to its β2/3 form (asparagine) [47], [157]. Photolabeling studies have identified an intersubunit site for anaesthetics [158], and in heteromeric receptors different compounds have been proposed to bind to homologous sites with differing affinities [121], [157].

The anti-parasite drug ivermectin binds *C. elegans* GluClα and the GlyR at a similar site [31], [159]. It has recently been shown that ivermectin also modulates the $GABA_AR$ in a similar manner [160], so it would appear to bind at the same site.

1.3.6 Pore-binding antagonists

The convulsant picrotoxin has long been known as noncompetitive antagonists at $GABA_ARs$ [161], [162] (Figure 1.4B). This drug binds in the $GABA_AR$ pore to stabilize the receptor in a nonconducting state [163], by preventing desensitization and stabilising the receptor in a resting state [48]. The binding site for picrotoxinin, the more active component of picrotoxin, is between the 2' and 9' positions of M2, with the exocyclic oxygen atoms of picrotoxinin forming hydrogen bonds with the Thr6' [41]

Other ligands binding at this site include tert-butylbicyclophoporothionate (TBPS), thujoine, lindane, dieldrin, fipronil, pitrazepin, tetramethylenedisulfotetramine (TETS) [121].

1.4 Distinct roles for types of $GABA_ARs$ in the brain

As the major mediators of inhibitory neurotransmission, $GABA_ARs$ are of central importance in the nervous system. One topic that has been of central interest in the field is the matter of assigning roles to particular types of $GABA_ARs$ [128], [164]–[166]. Common tools for the assignment of roles to particular $GABA_AR$ types include an examination of

$GABA_AR$ subunit expression, particularly in behaviourally relevant brain areas [167], the use of pharmacologically selective agents [168], as well as examining the consequences of genetic manipulations of $GABA_AR$ subunits in animal models [128]. These approaches are not mutually exclusive, as exemplified by benzodiazepine-site knockin mice (αHis101Arg, α2His101Arg, α3His126Arg, α5His102Arg) in which an α subunit histidine critical for benzodiazepine modulation is mutated to knock out the affinity for ligands at this site (see Section 1.3.2), whilst other properties of the receptor remain intact [128], [169], [170]. These mice lines have been used extensively to investigate the basis of the sedative, anxiolytic, analgesic, addictive and myorelaxant properties of diazepam [128], [169]–[172]. Other studies have used mice with a particular subunit knocked out, however in the case of $GABA_ARs$ this is often accompanied by compensatory changes in expression levels of other subunits [128].

The importance of different $GABA_AR$ types is underscored in the approach of 'circuit pharmacology', which focuses on $GABA_AR$ types in circuit- and cell-specific locations in understanding the behavioural effects of pharmacological agents [147]. This is of particular importance because of the large array of diseases in which GABAergic neurotransmission is implicated, including addiction, anxiety, autism, epilepsy, insomnia, pain, schizophrenia and depression [90], [130], [166], [172]–[175]. It is beyond the scope of this thesis to give details of all these, and this section will be limited to a few example processes in which α2/3-containing $GABA_ARs$ are implicated.

1.4.1 Expression of the α2 and α3 subunits in the brain

Of the synaptic α subunits (α1, α2, α3, α5), the α2 and α3 subunits have a more limited distribution in the brain compared with the predominant α1 [176]–[178]. In adult rats, α2 is abundant in the olfactory bulb, allocortex, hippocampus, amygdala, striatum and cranial nerve motor nuclei and moderately expressed in the neocortex, hypothalamus and pontine nuclei; α3 is abundant in the olfactory bulb, allocortex, amygdala, septum, intralaminar and reticular thalamic nuclei, and moderately expressed in the neocortex, basal forebrain, hypothalamus and brainstem [178]. $GABA_AR$ subunit expression is known to be developmentally regulated, with a decrease in α2 expression and an increase in α1

expression evident during early postnatal development [179], [180]. This is particularly striking in the cortex, with different cortical regions switching expression at different stages in development [179].

It has also been suggested that $GABA_AR$ subunits are located on neurons in an input-specific manner. For example, hippocampal pyramidal neurons express α1, α2, α3 and α5, but these subunits have been proposed to segregate to distinct subcellular locations. The α1 subunit is largely expressed postsynaptically in somatodendritic locations, whereas α2 is enriched at the axon initial segment and is present only at a small number of somatodendritic synapses, and α5 is mainly located outside the synapse [181]. Furthermore, somatic synapses from parvalbumin-positive (PV+) basket cells onto pyramidal cells tend to be enriched in α1-containing $GABA_ARs$, whereas cholecystokinin-positive (CCK+) basket cells tend to make synapses containing α2 subunits [182], [183] (but see [184]).

1.4.2 Pain

A role in pain for spinal $GABA_ARs$ follows from the pain gate theory of nociception [174]. Two major classes of nociceptors, Aδ and C, have their cell bodies in the dorsal root ganglia (DRG) and trigeminal ganglia. Their axons mainly terminate in superficial layers of the spinal dorsal horn (laminae I and II), where incoming nociceptive information is processed and relayed to higher brain centres. Pain gate theory describes how interneurons control the flow of nociceptive information such that they act as an inhibitor at the spinal output system when activated by mechanoreceptive fibres, but nociceptive fibres cause disinhibition of output to higher centres. Thus, inhibition of dorsal horn interneurons is proposed to underlie types of pathological pain such as hyperalgesia, an exaggerated response to painful stimuli; whereas enhancing inhibition in the spinal cord can suppress relay of information about noxious stimuli.

A particular role for the α2 and α3 subunits can be inferred from their expression in the spinal cord. A detailed study was made by Paul and colleagues [185], who found that α2/3 subunits are most abundant in lamina II, while α1/5 subunits are more prominent in laminae III-IV. An analysis of the cell bodies in lamina II and III suggests significant

expression of α2 and α3 on glutamatergic, GABAergic and glycinergic neurons. Furthermore, putative GABAergic synapses onto primary afferent terminals predominately contain α2 and α3 subunits, suggesting a presynaptic form of inhibition of incoming sensory information. A functional role for these subunits is implied by findings from electrophysiology experiments conducted by Knabl and co-workers [169], who found that diazepam does not potentiate GABA currents in primary afferent DRG neurons in α2His101Arg mice, and in intrinsic dorsal horn neurons in α3His126Arg mice.

Furthermore, results from studies using genetically engineered mice also support the claim that α2 and α3 are particularly involved in pain. Knabl and colleagues [169] showed that intrathecal administration of diazepam is antihyperalgesic in models of neuropathic and inflammatory hyperalgesia, but this effect is ablated in α2His101Arg mice. Systemically administered diazepam is not usually antinociceptive, presumably because its sedative effects prevent it from being used at an appropriate concentration. However, the sedative actions of systemic diazepam are abolished in α1His101Arg mice, and on this background diazepam was also antinociceptive in a model of C-fibre induced nociception [186]. A role for α2 and α3 is implied by the finding that diazepam has significantly less antihyperalgesic activity in double knockin α1His101Arg/α2His101Arg and α1His101Arg/α3His126Arg mice, but not α1His101Arg/α5H105R mice [186].

A role in pain for $GABA_A$Rs has long been suggested by the effects of intrathecal applications of $GABA_A$R agonists such as muscimol [187]. Several α2/3 selective compounds have been investigated for their efficacy in animal models of hyperalgesia. Since these are α1-sparing, they can be administered systemically without significant sedation [188]. NS11394 and L-838417 (Figure 1.4E) are positive allosteric modulators at the benzodiazepine site, with activity at α5, α3 and α1-containing αβγ receptors [131], [138] (see also Section 1.3.2). When delivered systemically, these drugs are effective in a number of different rodent hyperalgesia models [169], [189]–[191]. More selective drugs such as SL-65.1498 and HZ-166, which are more potent at α2- and α3-containing αβγ receptors compared with α1- and α5-containing receptors [133], [192], have also been shown to be effective [186], [188].

A combination of pharmacology and genetics was used by Paul and colleagues [193], who investigated a specific role for spinal α2-containing $GABA_A$Rs in rodent models of

pain. They found that HZ-166 is antihyperalgesic in wild-type mice in two models of hyperalgesia, but when a binding site for this drug is removed by either a cre-mediated spinal-specific knockout of the floxed α2 subunit, or a spinal specific α2His101Arg knockin, the effect of this drug is abolished. Interestingly, they found that there was no significant difference between drug naïve cre-negative mice and their α2 spinal-specific knockout mice, and their mouse lines had responses to HZ-166 that were intermediate between vehicle administration and the drug in cre-negative mice. These findings are consistent with a role for the α3 subunit as well as α2.

Based on the promise of these pre-clinical studies, a recent trial was conducted by Pfizer with a positive modulator PF-06372865 with a profile of selectivity α3 > α2 > α5 >> α1 [137]. The results of phase II clinical trials with this compound as a treatment for low back pain were recently published, and show no significant effect on the primary outcome parameter and only small effects on the secondary outcome parameter [194]. The lack of effect of this drug has been attributed to a lower level of receptor occupancy than might have been necessary to see an effect, as well as the differences between the clinical indication (low back pain) and the rodent pain models in which efficacy of α2/3-selective drugs are observed (inflammatory and neuropathic hyperalgesia, rather than acute nociceptive stimuli) [195].

1.4.3 Anxiety

A link between $GABA_A$Rs and anxiety, which is distinct from fear in that it involves a response to a perceived (rather than concrete) threat, has long been drawn from the anxiolytic effects of diazepam. Indeed, administration of diazepam directly into the amygdala, a brain region implicated in anxiety and fear, was shown to have an impact on conditioned anxiety by Nagy and colleagues in 1979 [196].

Although the α2 subunit has a limited distribution in the brain, it is highly expressed in the amygdala [178], and a specific role for α2- and α3-containing $GABA_A$Rs has been implied by experiments with benzodiazepine-insensitive knockin mice. Low and colleagues [172] investigated the action of diazepam in α2His101Arg and α3His126Arg mice, finding that its anxiolytic effect was abolished in the elevated plus maze and the light-dark choice test, both tests of innate anxiety, in the α2 knockin mice. A similar investigation

found that the anxiolytic effects of diazepam in a model of conditioned anxiety were reduced in α2His101Arg mice [197].

A further study investigated the effects of knocking out the α2 subunit on anxiety, finding a significant effect on a model of conditioned anxiety [198]; however this study failed to show a lack of adaptive changes in the expression of other $GABA_AR$ subunits in this mouse. In an effort to avoid the complications of global subunit knockouts, and to narrow down the circuitry involved in anxiety, Engin and co-workers [199] created mice in which the α2 subunit was knocked out only in particular regions of the hippocampus. In these animals, the effects of diazepam in innate anxiety (elevated plus maze, light-dark choice test) were abolished when α2 was knocked out in CA3 and the dentate gyrus.

On the basis of this work, pharma companies have striven to develop α2-selective drugs in the search for non-sedative anxiolytics, and many of the drugs later shown to be effective in pain (see Section 1.4.2) were developed in this quest [168]. These include MRK-409, MRK-529, L-838447, TP003, TPA023, TPA023B, and NS11394 (Figure 1.4E). These compounds all have some degree of selectivity for α2/3-containing receptors, and had promising outcomes in pre-clinical trials [168]. However, none were successful in clinical trials for a variety of reasons including poor pharmacokinetics [123], unexpected sedative and amnesic effects [200] and toxicity [201]. However, there appears to be continued interest in such compounds, as exemplified by recently developed examples such as KRM-II-81 [135] and MP-III-024 [136].

Although there are clear indications of a link between $GABA_AR$ subtypes and behaviours linked to anxiety, recent studies have revealed some complications that are indicative of the complex basis of behaviour. Anxiety has a complex aetiology, and anxiolytic drugs can have a variety of targets in the brain including the serotonergic, glutamatergic, neuropeptide and endocannabinoid systems [200]. Furthermore, later tests of benzodiazepine site knockin animals with only one intact binding site suggested that the α2, α3 and α5 subunits may be involved in anxiety in a task-specific manner [202]. Although only the α1 subunit was initially assigned a role in diazepam-mediated sedation [171], a study using some of the above-mentioned α2/3 selective compounds in

rhesus monkeys identified a role for the α2/3 subunits in a mild form of sedation and for the α1 subunit in deep sleep [203].

1.4.4 Addiction

The basis of the addictive properties of benzodiazepines is another example of a re-consideration of initial assignments of $GABA_AR$ subunit function.

The α1 subunit has been implicated in the addictive properties of benzodiazepines based on the properties of the α1-preferring ligand, zolpidem. A common test for addictive properties in animal models is that of self-administration, and zolpidem has not only been shown to be self-administered by primates [204], but is also addictive in humans [205]. A specific role for α1 was also suggested by experiments with α1His101Arg mice in which self-administration of midazolam is abolished [170].

However, some results indicate a possible role for the α2 and α3 subunits in addictive behaviour. For example, self-administration of the mainly α1-sparing compounds L-838417, TPA023B, MRK-623 and TP003 has been described in primates [204], [206], and diazepam reduces self-stimulation in the intracranial self-stimulation test in wild-type mice but not α2His101R or α3His126Arg mice [207]. Again, subunit involvement may be task-specific, with another study finding a role for the α3 subunit in reduction of intracranial self-stimulation by midazolam, but the α1 and α2 subunits in midazolam preference a two-bottle choice task [208].

1.5 Nanobodies as tools for (structural) biology

Heavy chain antibodies (HCAbs), consisting of only the heavy chain of conventional immunoglobin-γ (IgG) antibodies, were first described by Hamers-Casterman and colleagues in 1993 [209] (Figure 1.5). Originally discovered in camel sera by enterprising undergraduate students as part of a practical class [210], these unusual antibodies are also found in other species of camelids including the llama, as well as several species of shark [211]. Nanobodies, the antigen-binding fragment of HCAbs, have several useful properties, leading to their application not only as research tools, but also as diagnostic tools and theraputics [212].

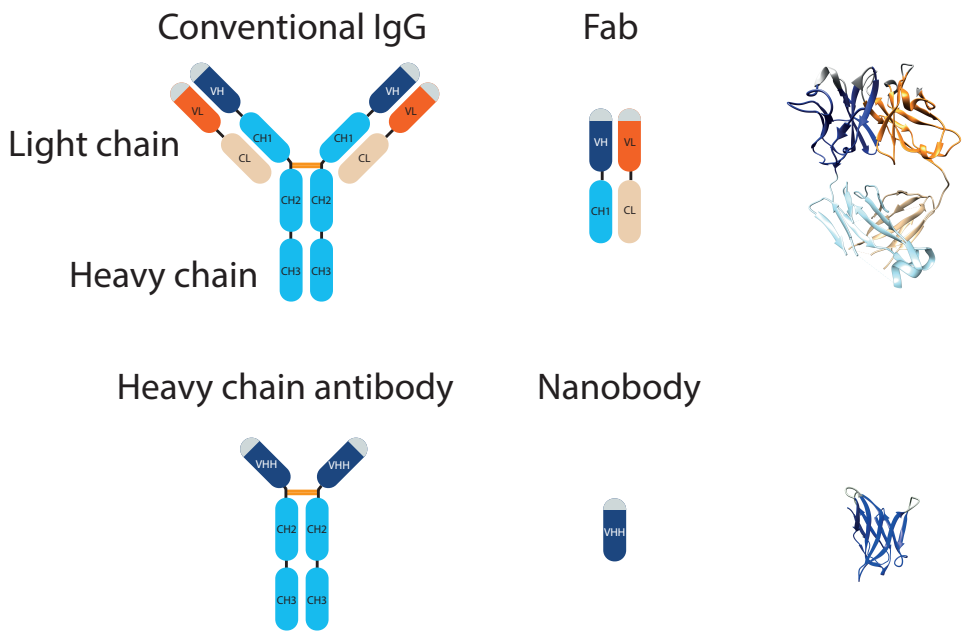

Figure 1.5: A comparison of IgG and HC antibodies, FAbs and nanobodies. The structure of an IgG antibody, a heavy chain antibody, and their antigen binding fragments (FAb, nanobody). FAb from PDB entry 3RIF, nanobody from PDB entry 4PIR.

1.5.1 Nanobody structure

The overall structure of a nanobody, the antigen binding fragment of an HCAb (VHH, nanobody), is illustrated in Figure 1.6. Nanobodies are composed of nine β-sheets (A-B-C-C'-C"-D-E-F-G), with three hypervariable loops (complementarity-determining regions, CDR1-3) that form the paratope. VHH structure is reminiscent of the heavy chain variable region (VH) of IgGs, but with some key differences that allow them to exist without association with an IgG light chain variable region (VL). Most notably, several highly conserved residues that in VH contribute to the interaction with VL are replaced in VHH with smaller or hydrophilic amino acids [212].

1.5.2 Applications of nanobodies in structural biology

Nanobodies have favourable biochemical properties, rendering them useful in structural studies. A streamlined process to raise nanobodies in llamas, generate a nanobody library, select for binders using multiple rounds of phage display, and express and purify

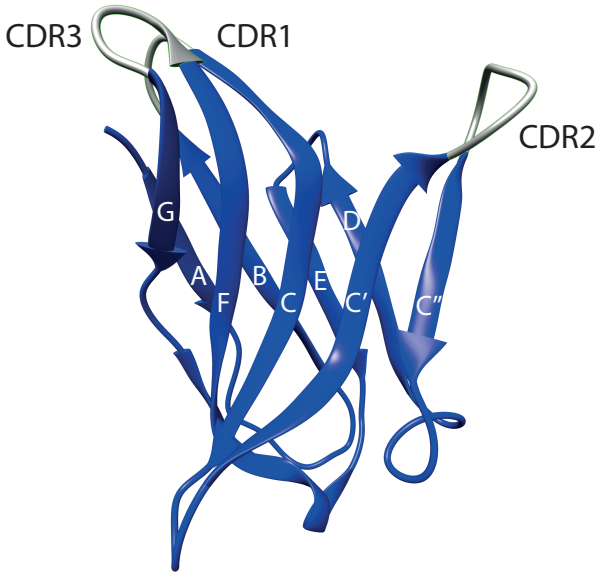

Figure 1.6: Nanobody structure. he general structure of a nanobody, showing the nine β-strands (A-G) and three hypervariable complementarity-determining regions (CDR1-3). Structure from PDB entry 4PIR.

selected nanobodies in *E. coli* has been developed with a total timeline of about three months [213], [214].

Nanobodies are small(~15 kDa), and tend to have high solubility, stability, and resistance to harsh conditions [213]. Typically, nanobodies are stable during purification and can be expressed with high yields. They tend to recognise different kinds of epitopes compared with Fabs, particularly three-dimensional regions of protein surfaces such as cavities, due to their protruding complementarity determining region (CDR) loops and monomeric nature [212]. Nanobodies are promising as theraputics as they can have functional effects on their targets; for example nanobodies raised against GPCRs have been shown to stabilize distinct conformational states [215]. Methods have been developed to engineer nanobodies that can cross cell membranes, allowing access to intracellular targets [216]. They are also useful reagents for basic research, for example they also often aid crystallisation of their target proteins through the formation of favourable crystal contacts [33], [217]. They can also be useful for immunoaffinity chromatography; a notable example is the GFP

nanobody which can be coupled to resin and used to capture GFP-tagged protein [218].

A further use of nanobodies in structural biology is for the construction of megabodies, chimeras created by grafting other proteins into the nanobody backbone. One example is that created by fusing a circularised version extracellular adhesin domain of /textitHeliobacter pylori (HopQ) into the first β-turn connecting strands A and B the nanobody [42]. Such a megabody created from the $GABA_AR$ α1-binding nanobody Nb38, termed Mb38, has been observed to broaden the distribution of orientations observed in cryo-EM studies of α1β3γ2 $GABA_ARs$ which greatly assisted the determination of structures of this receptor [41], [42].

1.6 Aims of this thesis

Since $GABA_ARs$ are of crucial importance in brain function and the target of several clinically relevant drugs, understanding the structural mechanisms through which they are modulated is critical for developing new, more selective drugs to target these receptors. Towards this aim, in this thesis I describe the generation and screening of nanobodies against α2- and α3-containing $GABA_ARs$ (Chapter 3). After optimising the expression and purification of triheteromeric $GABA_ARs$ (Chapter 4), I outline structural studies of an α3β3γ2L $GABA_AR$-nanobody complex using cryo-EM (Chapter 5). Furthermore, the structural basis for neurosteroid binding was also explored, and is detailed in Appendix F.

2
Materials and Methods

Contents

2.1 Molecular biology 29
2.2 Protein expression 38
2.3 Protein purification and characterisation 51
2.4 Biophysical characterisation of $GABA_AR$-nanobody interactions . . 61
2.5 Electrophysiology 64
2.6 Electron microscopy 66

2.1 Molecular biology

2.1.1 Expression vectors

For mammalian expression, the pHLsec (Figure A.1), pEZT-BM (Figure A.2) and pHR vectors (Figure A.3) and variants thereof were used [219], [220] [221]. The pHLsec vector was used mainly for large- and small-scale transient transfections of mammalian cells (Section 2.2.2). The plasmid pEZT-BM was used to generate recombinant baculoviruses (Section 2.2.4) as well as small-scale transient transfection of mammalian cells. The vector pHR was used to generate recombinant lentiviruses for polyclonal stable cell line generation (Section 2.2.5), as well as small-scale transient transfection of mammalian cells.

pHLsec and pHR contain a multiple cloning site (MCS) which follows the promoter and any regulatory elements, and is organised as follows: *EcoRI* - signal sequence - 5' tag

- *AgeI* - insert - *KpnI* - 3' tag - stop codons - *XhoI*. The signal sequence in pHR comes from pHLsec, and is the chicken receptor type protein tyrosine phosphatase (RPTP)σ sequence. In all constructs the native $GABA_AR$ signal sequences were not used, and the pHLsec signal sequence was used instead. A modified version of pEZT-BM was used, created by Dr Duncan Laverty. In this vector these MCS features were recapitulated and other backbone restriction sites (*EcoRI*, *AgeI*, *KpnI* and *XhoI*) removed. For the plasmid pHR, in some cases a version containing an internal ribosome entry site (IRES) and fluorescent protein (FP) in between the 3' tag and stop codons was used [221] (Figure A.3) The shared MCS of these vectors permits easy transfer of inserts between vectors, or addition and subtraction of N- and C-terminal tags, by digestion with the appropriate enzymes and ligation into a compatible vector.

Peptide tags appended to constructs for western blotting and protein purification include rho-1D4 (TETSQVAPA) [222], FLAG (DYKDDDDK) [223], influenza hamagglutinin (HA, YPYDVPDYA), twin-strep (WSHPQFEK-GGGSGGGSGG-SA-WSHPQFEK) [224], streptavidin binding protein (SBP, MDEKTTGWRGGHVVEGLAGELEQLRAR-LEHHPQGQREP) [225], and polyhistidine tags.

The *E. coli* periplasmic expression plasmid pMESy4 was used for expression of nanobodies in the periplasmic space (Figure A.4).

A green fluorescent protein (GFP) nanobody was used for the production of immunoaffinity media (Section 2.3.2). The plasmid pOPINE-GFP_nanobody was used for expression of this nanobody in *E. coli* [226], and was provided by Brett Collins (Addgene plasmid #49172).

For MSP2N2 and MSP1D1, the pMSP1D1 and pMSP2D2 plasmids were used, and were provided by Stephen Sligar (Addgene plasmids #20061 and #29520, respectively).

For *in vivo* biotinylation, biotin ligase (BirA) was retained in the ER through the use of an ER-retention sequence. The plasmid pDisplay-BirA-ER was used for this purpose [227]. This plasmid was provided by Alice Ting (Addgene plasmid #20856).

Table 2.1: Uniprot accession codes and domain boundaries of human $GABA_AR$ subunits used

Subunit	Uniprot entry	First residue in mature peptide	Mature peptide		
			ECD	TMD	M3-4 loop
α1	P14867	Q28 (Uniprot)	1 - 222 (QPSL…LKRK)	223 - 429 (IGYF…TPHQ)	313 - 390 (RGYA…NSVS)
α2	P47869	N29 (Uniprot)	1 - 221 (NIQE…LKRK)	222 - 423 (IGYF…GVSP)	312 - 387 (RGWA…NSVS)
α3	P34903	Q30 (Uniprot)	1 - 246 (QGES…LKRK)	247 - 464 (IGYF…IRKQ)	337 - 425 (RSWA…NSVS
α4	P48169	Q36 (Uniprot)	1 - 220 (QNQK…LRRK)	221- 519 (MGYF…ESLM)	311 - 481 (IQME…SGTS)
α5	P31644	Q32 (Uniprot)	1 - 225 (QMPT…LKRK)	226 - 431 (IGYF…ASPK)	316 - 392 (RGWA…NSIS)
α6	Q16445	K20 (Uniprot)	1 - 220 (KLEV…LQRK)	221 - 434 (MGYF…SSVE)	311 - 396 (LQTQ…GGTS)
β3	P28472 (isoform 1)	Q26 (Uniprot)	1 - 217 (QSVN…LKRN)	218 - 448 (IGYF…YYVN)	308 - 421 (GRGP…TDVN)
γ2L	P18507 (isoform 2)	Q40 (Uniprot)	1 - 232 (QKSD…LSRR)	233 - 436 (MGYF…YLYL)	323 - 408 (NRKP…IRIA)

2.1.2 cDNA and construct design

The boundaries for the human $GABA_AR$ subunits used are shown in in Table 2.1. In this thesis, the convention in the field of numbering residues from the first amino acid after signal sequence cleavage will be maintained. For example, in this system α1Gln28 from Uniprot entry P14867 is designated α1Gln1. This first residue of the mature peptide and its equivalent in the Uniprot numbering system (from the beginning of the signal peptide) are also listed in Table 2.1.

Full-length (FL) constructs are comprised of the entire mature peptide for each subunit. Unless otherwise stated, all constructs are full-length. To increase expression, in some cases the M3-4 loop was replaced with the equivalent linker from GLIC (SQPARAA) [37], [49]. These constructs were termed 'glvi', after the nomenclature of Jansen and colleagues [49].

cDNAs for human $GABA_AR$ subunits α1-6 (glvi), α1 (FL) β3 (glvi), β3 (FL) were provided by Dr Paul Miller. The cDNA for the FL β3 subunit contained an extra *KpnI* site in the M3-4 loop, resulting in an extra two residues (GT). cDNA for the FL human γ2 (long isoform, γ2L) subunit was provided by Dr Duncan Laverty. This cDNA contained a substitution of Ala for Thr at position 11, in the region prior to the first helix of the extracellular domain, likely having a minimal effect on protein structure. cDNAs for human $GABA_AR$ subunits α2-6 (FL) were synthesised as 'GeneArt Strings' by Life Technologies.

Sequences for these were codon-optimised for mammalian expression and based on the mature peptide sequences from Uniprot as detailed in Table 2.1.

Nanobody constructs were provided by Els Pardon and Jan Stayert. These consisted of the pelB leader sequence for periplasmic targeting, the nanobody sequence, and hexa-histidine and EPEA tags for purification [214]. Megabodies were created from the nanobody sequences by Tomas Uchanski and Jan Stayert. A circular permutant of the extraceullular adhesin domain of *Heliobacter pylori* (HopQ, uniprot B5Z8H1) was inserted into the first β-turn of the nanobody (which connects strands A and B). The entire megabody sequence consists of the conserved first thirteen residues of the parent nanobody (strand A), then the C-terimal portion of HopQ (residues 227-449), a three-residue linker connecting the amino and carboxyl termini of HopQ, then the N-terminal portion of HopQ (residues 49-221), followed by the remainder of the nanobody, as well as hexa-histidine and EPEA purification tags [42].

Typically, new constructs were created by polymerase chain reaction (PCR) or overlap PCR, and products were digested with the appropriate enzymes and ligated into the appropriate vector (Sections 2.1.4, 2.1.5), then transformed into DH5α5 cells. Occasionally, constructs were assembled into plasmids by Gibson assembly [228] (Section 2.1.6) or *in vitro* assembly (IVA) [229] (Section 2.1.7).

See Appendix B for a full list of constructs used.

Record-keeping and primer design were carried out using the Benchling web application.

2.1.3 PCR

Polymerase chain reaction (PCR) was carried out using DNA polymerase from Takara (Pyrobest polymerase) and New England Biotechnology (NEB; Phusion and Q5 polymerases). The components for a typical reaction for Pyrobest, Phusion, Q5 and *Taq* polymerases are listed in Table 2.2, and the conditions in Table 2.3

Typically Pyrobest, Phusion and Q5 were used for cloning new constructs, whereas the lower-fidelity enzyme *Taq* polymerase was used only for colony PCR. For Pyrobest, the dNTP mix included in the kit was used; for Phusion, Q5 and *Taq* polymerases dNTPs

Table 2.2: Standard reaction components for Pyrobest, Phusion, Q5 and *Taq* polymerases

Pyrobest polymerase (50 µl reaction)		
Component	Concentration	Volume (µL)
Template DNA	100 ng µL^{-1}	50-500 ng
Pyrobest buffer II	5X	5
dNTP mixture	2.5 mM each	4
Primer 1	10 µM	2.5
Primer 2	10 µM	2.5
Pyrobest polymerase	5 UµL^{-1}	0.25
Ultrapure water		to 50 µl

Phusion polymerase (50 µl reaction)		
Component	Concentration	Volume (µL)
Template DNA	100 ng µL^{-1}	50-500 ng
Phusion HF reaction buffer	5X	5
dNTP mixture	10 mM	1
Primer 1	10 µM	2.5
Primer 2	10 µM	2.5
Phusion polymerase	100 UµL^{-1}	0.5
Ultrapure water		to 50 µl

Q5 polymerase (50 µl reaction)		
Component	Concentration	Volume (µL)
Template DNA	100 ng µL^{-1}	50-500 ng
Q5 reaction buffer	5X	5
dNTP mixture	10 mM	1
Primer 1	10 µM	2.5
Primer 2	10 µM	2.5
Q5 polymerase	2 UµL^{-1}	0.5
Ultrapure water		to 50 µl

Taq polymerase (20 µl reaction)		
Component	Concentration	Volume (µL)
Template DNA	Single *E. coli* colony	
Taq reaction buffer	10X	2
dNTP mixture	10 mM	0.4
Primer 1	10 µM	0.4
Primer 2	10 µM	0.4
Taq polymerase	250 UµL^{-1}	0.25
Ultrapure water		to 20 µl

were purchased as a set from GE Healthcare (dNTP Set, 100 mM each A,C,G,T), mixed in equal proportions and diluted with ultrapure water to a final concentration of 10 mM, then aliquoted and stored at -20 °C until use. Oligonucleotide primers were ordered from Eurofins or Sigma-Aldrich, and were typically designed to be 15-30 nucleotides long with a GC content of 40-60%, T_m of 55-65 °C, and ending in 1-3 G or C bases (See Appendix C for a complete list of primers used). Primers were made up in ultrapure water to a stock concentration of 100 µM, and diluted to 10 µM prior to use. Colony PCR with *Taq* polymerase was used to verify the likely success of cloning for new constructs. Primers were chosen to give a product of approximately 1 kb; the presence of a product indicated a positive colony and constructs were also sequence-verified by Sanger sequencing (Section 2.1.10) before use.

In the case of difficult PCR where a product was not observed, the reaction was repeated with the addition of 3% DMSO (Phusion and Q5), 1 M betaine (Phusion and Q5), 1X Q5 High GC Enhancer (Q5), or with the replacement of GC buffer for HF buffer (Phusion), or combinations thereof (final concentrations listed).

PCR success was verified by agarose gel electrophoresis. Typically gels were cast with 1% agarose in TBE buffer (typically made up as a 20X stock, 1X solution contains 90 mM Tris base, 90 mM boric acid, 2.5 mM disodium ethylenediaminetetraacetate [EDTA], pH

Table 2.3: Standard reaction conditions for Pyrobest, Phusion, Q5 and *Taq* polymerases

Pyrobest polymerase		
Step	Temperature (°C)	Duration (s)
1	95	60
2	98	10
3	3 °C below lowest primer T_m	30
4	72	30 per kb of template
5	Repeat steps 2-4 for 20-25 cycles	
6	72	600
7	4	hold

Phusion polymerase		
Step	Temperature (°C)	Duration (s)
1	98	30
2	98	10
3	3 °C below lowest primer T_m	15
4	72	15 per kb of template
5	Repeat steps 2-4 for 20-25 cycles	
6	72	600
7	4	hold

Q5 polymerase		
Step	Temperature (°C)	Duration (s)
1	95	30
2	98	5
3	3 °C below lowest primer T_m	10
4	72	20 per kb of template
5	Repeat steps 2-4 for 20-25 cycles	
6	72	120
7	4	hold

Taq polymerase		
Step	Temperature (°C)	Duration (s)
1	95	600
2	95	15
3	50	15
4	68	60
5	Repeat steps 2-4 for 25-30 cycles	
6	68	60
7	4	hold

adjusted to 8.3 with concentrated HCl). DNA was mixed with 6X purple gel loading dye (NEB) before being placed in wells, and 1X TBE buffer was also used as the running buffer.

For overlap PCR, primers were designed to anneal to the template as described above, but with the following modifications: for mutagenesis, a pair of primers were designed with the desired mutation in the middle; for insertions, a pair of primers at each border of the insertion was designed, facing outwards from the insertion, with approximately 15 base pairs of each of the fragments to be joined; for deletions, a pair of primers flanking the deletion site was designed with approximately 15 base pairs of each of the regions either side of the region to be deleted.

The first round of overlap PCR was conducted as two separate reactions, each with one of the pair of primers around the change with an appropriate sequencing primer (Table 2.7), conducted as described in Tables 2.2 and 2.3.

Following verification of a successful PCR by gel electrophoresis (typically with 5 ul of the reaction), a PCR cleanup was conducted, using buffers and spin columns from the Qiagen Gel Extraction kit. Five volumes of buffer PB from this kit was added to each reaction, and then the mixture was transferred to a spin column. The column was spun at 16000*g*, the flow-through discarded and 500 µl buffer PE was added. After another identical

Table 2.4: Components for typical one- and two-enzyme restriction digests

One-enzyme reaction		
Component	Concentration	Amount
DNA	Varies	0.5-3 µg
NEB CutSmart buffer	10X	2 µl
Enzyme	Varies	5-10 U
Ultrapure water		Up to 20 µl

Two-enzyme reaction		
Component	Concentration	Amount
DNA	Varies	0.5-3 µg
NEB CutSmart buffer	10X	2 µl
Enzyme 1	Varies	5-10 U
Enzyme 2	Varies	5-10 U
Ultrapure water		Up to 20 µl

centrifugation step, the top of the spin column was placed in a fresh 1.5 ml tube, and 40 µl of ultrapure water added. The eluate was collected after a third identical centrifugation step.

A second round of PCR was then conducted to create the full construct. This reaction was composed of the same components as listed in Table 2.2, except that the template and the two primers were replaced by 3 µl of each reaction product. This reaction proceeded for 3-5 cycles as per the parameters in Table 2.3. Then 2.5 µl of the forward and reverse sequencing primers used in the first reaction were added to this second reaction to amplify the final product. This reaction proceeded as per the parameters listed in Table 2.3.

2.1.4 Restriction digests

Restriction digests of PCR products or vectors were typically conducted at 37 °C, as appropriate for the enzyme used. Enzymes were purchased from (NEB). The components (Table 2.4) were assembled into an 0.2 ml tube, and incubated for 2 h. Reaction products were typically run on a 1% agarose gel after the addition of 6X purple loading dye (NEB) to separate DNA fragments of different sizes, with the desired fragments excised from the gel and subjected to extraction using the Qiagen Gel Extraction kit as per the manufacturer's instructions.

2.1.5 Ligations

Ligations were carried out with T4 ligase from NEB. Typical reaction components are listed in Table 2.5. Typically, a 1:3 molar ratio of vector:insert was used. The reaction was assembled in a 0.2 ml tube, and proceeded for 15 min at room temperature. The mixture was then placed on ice.

Table 2.5: Typical components for a ligation

Component	Concentration	Amount
T4 DNA ligase buffer	10X	2 µl
Vector DNA	Varies	50 ng
Insert DNA	Varies	3X vector DNA (molar ratio)
T4 DNA ligase	400000 UmL^{-1}	1 µl
Ultrapure water		To 20 µl

2.1.6 Gibson assembly

As an alternative to traditional restriction enzyme-based cloning, Gibson assembly was occasionally used [228]. Gibson assembly tended not to be successful for cloning into pHLsec due to difficulty in amplifying the backbone; varying degrees of success were achieved with other vectors. Primers for Gibson assembly at the boundaries of DNA fragments to be joined or deleted were designed using the Benchling web application, typically with 20 overlapping base pairs from each fragment. Following successful PCR, agarose gel electrophoresis and gel extraction of each of the fragments, the reaction was carried out using the NEB Gibson Assembly Master Mix. This mix contains an exonuclease to create 3' overhangs at the homologous boundary regions allowing them to anneal, a polymerase to fill in gaps between annealed overhangs, and a DNA ligase to seal nicks. Equimolar amounts of each fragment were used, typically 0.05-0.2 pmol. Typically 10 µl of Master Mix was used in a total reaction volume of 20 µl, and the reaction proceeded at 50 °C for 30 min.

2.1.7 *In vitro* assembly

Occasionally, *in vitro* assembly (IVA) was used, which is similar to Gibson assembly in terms of primer design (see Section 2.1.6 for details). Following a succesful PCR of each fragment, template DNA was digested with FastDigest *DpnI* (Thermo Fisher Scientific) at 37 °C for 15 min. Typically 2-3 µl of each PCR product was then used to transform DH5α cells (Section 2.1.8), relying on endogenous DNA repair mechanisms to recombine homologous regions to recreate a circular plasmid [229].

Table 2.6: Antibiotic concentrations for *E. coli* selection

Antibiotic	Solvent	Stock concentration (mg ml^{-1})	Working concentration (µg ml^{-1})
Ampicillin	Ultrapure water	100	100
Chloramphenicol	Ethanol	25	25
Kanamycin	Ultrapure water	50	50
Gentamycin	Ultrapure water	10	10
Tetracycline	Ultrapure water	10	10

2.1.8 Transformations

Transformations were typically conducted with 30 µl of library-efficiency competent DH5α5 cells (Thermo Fisher Scientific). These were stored at -80 °C and thawed on ice. Typically 2-5 µl of product from ligation (Section 2.1.5), Gibson assembly (Section 2.1.6) or *DpnI*-digested PCR products in the case of IVA (Section 2.1.7) was introduced to the thawed competent cells and the mixture was incubated on ice for 5 min. The mixture was then placed at 42 °C for 40 s, then incubated on ice again for 2 min. 100 µl of S.O.C. medium (Thermo Fisher Scientific) was then added to the mixture and it was placed in an incubator at 37 °C, 180 rpm for 1 h. The mixture was then plated on LB-agar plates (Melford Lysogeny broth [LB] premix supplemented with 2% agar, autoclaved and then additionally supplemented with appropriate antibiotics [Table 2.6]), which were incubated overnight at 37 °C.

2.1.9 DNA preparation

Following tranformation of a new construct, typically several colonies were each used to inoculate 5 ml of LB broth (Melford premix), supplemented with the appropriate antibiotics (Table 2.6 lists the concentrations used). This culture was used to prepare plasmid DNA using the Qiagen Miniprep kit according to the manufacturer's instructions. Constructs were sequence-verified before use (Section 2.1.10). Where a larger amount of DNA was required (for example, for large-scale transient transfections [Section 2.2.2]), Qiagen Endotoxin-free Midiprep, Maxiprep, Megaprep and Gigaprep kits were used as per the manufacturer's instructions.

Table 2.7: Sequencing primers

Sequencing primers		
Name	Target	Sequence (5' to 3')
pHLSec F	pHLsec	GCTCTAGAGCCTCTGCTAACC
pHLsec R	pHLsec	CACCAGCCACCACCTTCTGAT
pMESy4 F	pMESy4	CGATAAGCTTAAGGAGACAGTACATATG
pMESy4 R	pMESy4	TTTTGTCGTCTTTCCAGACG
pEZT-BM F	pEZT-BM, pHR (CMV promoter)	CAACGGGACTTTCCAAAATG
pEZT-BM R	pEZT-BM, pHR (WPRE)	ATACCAGTCAATCTTTCAC
pHR R	pHR (IRES)	CCCTCACATTGCCAAAAGACGG
mEGFP_ct F	mEGFP	CCAATGAGAAGCGTGACC

2.1.10 Sanger sequencing

Sanger sequencing was performed by GATC or Source Bioscience. Plasmid DNA and primers were supplied, and the reaction and analysis were carried out by the company. Common sequencing primers are listed in Table 2.7. Analysis of the results was conducted in the Benchling web application.

2.2 Protein expression

Depending on the protein of interest, either *E. coli* or mammalian expression systems were used. Soluble proteins, such as nanobodies and membrane scaffold proteins (MSPs) were expressed in *E. coli* (Section 2.2.1), and occasionally by transient transfection of mammalian cells (Section 2.2.2.3).

$GABA_A$Rs were expressed in human embryonic kidney 293 (HEK293) cell lines (Section 2.2.2). Small-scale screening of constructs was conducted either by transient transfection of adherent HEK293T or HEK293S GnTI$^-$ cells in suspension. For large-scale expression, HEK293S GnTI$^-$ cells were grown in suspension and protein expression was induced by either transient transfection of DNA (Section 2.2.2.4), transduction using recombinant baculoviruses (Section 2.2.4), or in the case of stable cell lines, induced by the addition of doxycycline (Section 2.2.6).

2.2.1 Protein expression in *E. coli*

For periplasmic protein expression in *E. coli*, the WK6*su*$^-$ strain was used [214], [230]. For cytoplasmic protein expression, competent BL21(DE3)pLysS cells (Promega), or BL21 Gold cells (Aligent) were used.

WK6 cells were rendered competent by treatment with $CaCl_2$. In this procedure, a pre-culture of WK6 cells was created by inoculating 5 ml of LB medium with a small amount of cells from a glycerol stock stored at -80 °C. This pre-culture was incubated at 37 °C and 180 rpm overnight, before being added to 100 ml fresh LB medium. This mixture was incubated at 37 °C and 180 rpm until it reached an absorbance at 600 nm (A_{600}) of 0.2-0.6 in a standard cuvette. The mixture was then centrifuged at 3200*g* at 4 °C for 10 min. The supernatant was discarded and the cells resuspended in 40 ml ice-cold 100 mM $CaCl_2$. This mixture was incubated for 25 min on ice, then centrifuged again at 3200*g* and 4 °C for 10 min. The supernatant was discarded and the cells resuspended in 1.2 ml of ice-cold 80 mM $CaCl_2$, 15% (v/v) glycerol, aliquoted, snap-frozen in liquid nitrogen (LN_2), and stored at -80 °C until use.

30 µl of WK6 cells were thawed on ice and typically transformed with 100-200 ng of the appropriate plasmid using the same procedure as for DH5α cells (Section 2.1.8), except that they were plated on LB-agar supplemented with 100 µg ml^{-1} and 2% (w/v) glucose. For expression of MSPs, a glycerol stock of transformed BL21 Gold cells provided by Christiane Kowatsch was used to streak an LB-agar plate supplemented with 30 µg ml^{-1} kanamycin. Following overnight incubation at 37 °C, a single colony was used to inoculate 10 ml of LB supplemented with 100 µg ml^{-1}ampicillin, 2% (w/v) glucose and 1 mM $MgCl_2$ in the case of WK6 cells, or 50 ml of 2XTY broth (premix purchased from Formedium) supplemented with 30 µg ml^{-1} kanamycin in the case of BL21 cells. This pre-culture was grown overnight at 37 °C and 180 rpm.

The following morning, this pre-culture was added to TB (Terrific Broth, Melford Premix, supplemented with 0.4% [v/v] glycerol, typically 0.5-2 l) supplemented with 100 µg ml^{-1} ampicillin, 1 mM $MgCl_2$ and 0.1% (w/v) glucose in the case of WK6 cells, or TB supplemented with 30 µg ml^{-1} kanamycin in the case of Bl21 cells. The mixture

was incubated at 37 °C and 180 rpm until the A_{600} in a standard cuvette reached 0.6-0.8 (WK6) or 2.5-3(BL21). At this point, expression was induced by addition of 1 mM isopropyl β-D-1-thiogalactopyranoside (IPTG). For WK6 cells expression proceeded either overnight at 28 °C and 180 rpm or at 37 °C, 180 rpm for 4 h. For BL21 cells, 3-4 h at 28 °C and 180 rpm for BL21 cells. Bacteria were then harvested by centrifugation at 4500*g* and RT, for 15 min. Protein purification was typically performed directly following expression, however occasionally bacterial pellets were snap-frozen in LN_2 and stored at -80 °C for purification at a later date.

2.2.2 Transient transfection of mammalian cells

2.2.2.1 Mammalian cell lines used and their maintenance

$GABA_A$Rs were expressed in HEK293 cells [231]. For small-scale construct screening and electrophysiology, $GABA_A$Rs were expressed in adherent HEK293T cells containing a mutant version of the SV40 T-antigen, which maintain a high copy number of vectors containing the SV40 origin of replication [232], [233]. Chimeric $GABA_A$Rs were exclusively expressed by transient transfection in HEK293S *GnTI*$^-$ cells. These cells are adapted to growth in suspension and lack N-acetylglucosaminyltransferase I (GnTI) activity, resulting in homogenous $Man_5GlcNAc_2$ N-linked glycans [234]. All stable cell lines created using the lentivirus system [221] were created using the HEK293S GnTI$^-$ TetR (HEK293S/TR) cells, which retain the features of HEK293S GnTI$^-$ cells, and additionally express the tetracycline repressor protein (TetR) through stable transfection of the pcDNA6/TR vector [234]. To produce lentiviruses at high titre, the HEK293 Lenti-X cell line (Clontech) was used.

Mammalian cell lines were typically maintained in pre-warmed (37 °C) Dulbecco's Modified Eagle Medium (DMEM) or a mixture of DMEM and nutrient mixture F-12 (DMEM/F-12) with appropriate supplements (see Table 2.8) in T25, T75 or T175 flasks as necessary. All media and supplements were obtained from Gibco except for blasticidin S hydrochloride which was obtained from Thermo Fisher Scientific. Flasks were kept in a humidified incubator operated at 37 °C and 5% CO_2.

Cells were typically passaged every 2-4 days (when ~70-90% confluent). For a typical passage of cells in a T175 flask, after removing the medium, cells were washed with 15 ml

Table 2.8: Cell lines and media typically used for adherent mammalian tissue culture

Cell line	Medium	Additives	Reference
HEK293S GnTI$^-$	DMEM	10% FBS, 2 mM L-glutamine, 1X NEAA	[234]
HEK293T	DMEM	10% FBS, 2 mM L-glutamine, 1X NEAA	[232]
HEK293S/TR GnTI$^-$	DMEM/F-12	10% FBS, 1X NEAA, 5 µg ml^{-1} Blasticidin	[234]
HEK293 Lenti-X	DMEM	10% FBS, 2 mM L-glutamine, 1X NEAA	Obtained from Clontech

sterile phosphate-buffered saline (PBS; 175 mM NaCl, 16.6 mM $Na_2HPO_4.2H_2O$, 9.5 mM $NaH_2PO_4.2H20$, pH = 7.2). 4 ml of 0.05% (w/v) trypsin-EDTA (Gibco) was added and incubated with the cells at 37 °C for 1-2 min. The cells were gently dislodged and 21 ml of supplemented medium appropriate for the cell type (Table 2.8) was then added and the cells resuspended. Optionally, cells were pelleted at 100*g*, the supernatant removed, and the cells resuspended in 25 ml medium. Either with or without this extra centrifugation step, the appropriate amount of cell suspension (typically 4-6 ml) was transferred into a new flask and topped up to 25 ml with fresh medium. Flasks were returned to the incubator (humidified, and set at 37 °C and 5% CO_2). Cells were typically kept for 25-30 passages or 3 months.

Suspension-adapted lines of HEK293 cells, including HEK293S GnTI$^-$, HEK293S GnTI$^-$ TetR, or derivatives, were also grown in suspension. After passaging as described above, cells were transferred into bottles rather than flasks. Either 500 ml empty DMEM bottles (Sigma), or 125 ml, 250 ml, or 500 ml Corning Erlenmeyer flasks (Thermo Fisher Scientific), or 1 l roller bottles (Biofil) were used, typically with no more than 40% of the total volume filled. Cells were incubated at 37 °C, 8% CO_2 and 130 rpm. In the first passage in suspension, cells were typically grown in supplemented FreeStyle 293 medium (Gibco) (Table 2.9). After this first passage, cells for transient transfection were transferred into Protein Expression Medium (PEM, Gibco) [40], whereas cells for BacMam and stable cell lines remained in FreeStyle 293 medium [220], [235] [221]. Cells were counted with a haemocytometer and passaged 1:2-1:6 when they reached a density of 2-3x10^6 mL^{-1}.

As an alternative to bottles and flasks, suspension-adapted cells were grown in a WAVE Bioreactor 20/50 (GE Healthcare), in a 20 l WAVE CellBag (GE Healthcare). Typically, 1-2 l of suspension cells at 2-3x10^6 mL^{-1} were used to seed another 3-4 l of medium (Table 2.9) in the bag. The CellBag was maintained at 37 °C and 5% CO_2, with a rocking speed and

Table 2.9: Cell lines and media typically used for mammalian suspension tissue culture

First passage in suspension		
Cell line	Medium	Supplements
HEK293S GnTI$^-$	FreeStyle 293	1% FBS, 2 mM L-glutamine, 1X NEAA
HEK293S GnTI$^-$ TetR	FreeStyle 293	1% FBS, 2 mM L-glutamine, 1X NEAA, 5 µg ml^{-1} blasticidin
Subsequent passages		
Cell line	Medium	Supplements
HEK293S GnTI$^-$	FreeStyle 293	1% FBS, 2 mM L-glutamine, 1X NEAA
HEK293S GnTI$^-$	Protein Expression Medium	1% FBS, 2 mM L-glutamine, 1X NEAA
HEK293S GnTI$^-$ TetR	FreeStyle 293	1% FBS, 2 mM L-glutamine, 1X NEAA, 5 µg ml^{-1} blasticidin
WAVE CellBag growth		
Cell line	Medium	Supplements
HEK293S GnTI$^-$ TetR	FreeStyle 293	5% FBS, 2 mM L-glutamine, 1X NEAA

angle of 26 rpm and 6°. Cell density was monitored as cells were expanded, and rocking speed and angle were increased to 30 rpm and 7° as the volume increased to ~ 10 l.

Where necessary, cell lines were cryopreseved for long-term storage. Typically, one confluent T175 flask was washed with 15 ml PBS, then 0.05% trypsin was added. The cells were incubated at 37 °C for 2-3 min, then gently dislodged. 20 ml of the appropriate medium was added, and the cells were pelleted by centrifugation at 200*g* for 2 min. Cells were then resuspended in 3 ml freezing medium (90% fetal bovine serum [FBS], 10% sterile DMSO) and distributed between three 1 ml labelled cryovials per T175 flask. These cryovials were transfered to a freezing chamber ('Mr. Frosty', Thermo Scientific) which was placed at -80 °C. The following morning cryovials were transferred to a vapour phase cell bank.

To revive cells from long-term storage, a vial of cells was thawed in a 37 °C waterbath. 1 ml of pre-warmed medium appropriate for the cell line was added dropwise, and the cells were transferred to a tube containing 20 ml pre-warmed medium. The cells were pelleted at 200*g* for 2 min, then resuspended in 25 ml fresh medium and transferred to a T175 flask.

2.2.2.2 Adherent, small scale

Small-scale transfections for screening constructs were typically conducted with HEK293T cells in 6-well plates. To seed cells, a 70-90% confluent T175 flask of cells was washed with 15 ml PBS, then 4 ml of 0.05% trypsin was added. After incubation at 37 °C for 2-3 min, the cells were gently dislodged and 21 ml of the appropriate medium (Table 2.8)

was added. 3 ml of this cell suspension per 6-well plate was transferred to a 50 ml tube, and 9.5 ml of fresh medium was added per 3 ml of cell suspension. This mixture was distributed amongst the required number of 6-well plates, with 2 ml per well. These plates were placed in a humidified incubator set at 37 °C and 5% CO_2 for up to 24 h. Typically cells were ~60-80% confluent upon transfection.

Cells were transfected using Lipofectamine 2000 (Thermo Fisher Scientific). Lipofectamine (6 µl per well) was diluted in 250 µl of the appropriate medium (Table 2.8), but without FBS. 4 µg per well of plasmid DNA was also diluted in 250 µl of the appropriate medium (Table 2.8), but without FBS. These two mixtures were combined and incubated for 10 min at room temperature. During this period, the medium in the 6-well plates was replaced with fresh medium appropriate for the cell line (Table 2.8), but with 2% FBS instead of 10% FBS. Following the incubation period, the DNA/lipofectamine mixture was added to the cells.

For *in vivo* biotinylation, avi-tagged constructs were used and 10% of the total DNA was replaced with pDisplay-BirA-ER [227] and media were supplemented with 50 µM D-biotin.

Transfected cells were harvested 24-72 h after transfection. Typically cells were first washed with 2 ml PBS, then dislodged by pipetting in a further 1 ml of PBS. Cells were collected by centrifugation at 500*g*, and cell pellets were either processed immediately (Section 2.3.6) or snap-frozen in LN_2 and stored at -80 °C until use.

2.2.2.3 Adherent, large scale

For large-scale adherent transient transfections, HEK293 cell lines were grown in roller bottles with a ribbed surface (2125 cm^2, Greiner Bio-One) [219]. Typically, HEK293T cells were used. Cells were first expanded in T175 flasks (Section 2.2.2.1) until one flask per roller bottle reached ~70-90% confluency. To seed cells, 70-90% confluent T175 flasks of cells were washed with 15 ml PBS, then 4 ml per flask of 0.05% trypsin was added. After incubation at 37 °C for 2-3 min, the cells were gently dislodged and 21 ml per flask of the appropriate medium (Table 2.8) was added. 25 ml of cell suspension was added to each roller bottle, along with 225 ml fresh medium. Cells were incubated at 37 °C and 5% CO_2, with gentle rotation, until ~80-90% confluent, typically 3-4 days.

To transfect cells (quantities listed are per roller bottle and were scaled accordingly), 0.5 mg plasmid DNA was chloroform-extracted, then mixed with 50 ml medium without FBS. 6 mg 25 kDa branched polyethylenimine (1 mg ml^{-1} stock, pH = 7) was added to the DNA/medium mixture, and then incubated for 10 min at room temperature. During the incubation period, the medium in the roller bottles was replaced with 200 ml fresh medium as appropriate for the cell line (Table 2.8), but with 2% FBS instead of the usual 10%. The transfection mixture was then added to the roller bottles and they were returned to the incubator.

For *in vivo* biotinylation, avi-tagged constructs were used and 10% of the total DNA was replaced with pDisplay-BirA-ER [227] and media were supplemented with 50 µM D-biotin.

The medium, containing secreted protein, was harvested 3-5 days after transfection. The medium was collected into 1 l centrifuge tubes (Beckman Coulter) and centrifuged at 5000*g* for 20 min. The supernatant was vacuum-filtered (0.22 µm) into sterile glass bottles and stored at 4 °C until purification (Section 2.3.10).

2.2.2.4 Suspension, large scale

Suspension-adapted lines of HEK293 cells, including HEK293S GnTI$^-$, HEK293S GnTI$^-$ TetR, or derivatives, were used for large-scale expression of $GABA_A$Rs. For transient transfection, cells were expanded in PEM until the desired volume of cells was reached, typically 9 l. The transfection was performed at a high cell density [236], so cells were first pelleted in 1.5 l batches at 400*g* for 7 min. For each 1.5 l batch, a 1:1 mix of the construct to be transfected and empty pHLsec, with an extra 2% GFP to assess transfection efficiency, was chloroform-extracted and mixed with 20 ml FreeStyle 293 medium (supplemented with 2 mM L-glutamine, and 1X non-essential amino acids [NEAA], but no FBS). 2.4 mg Polyethylenimine (PEI) Max (linear, 40 kDa, in water at 1 mg ml^{-1}, pH = 7) was added to another 20 ml of similarly-supplemented FreeStyle 293 medium, and then the two mixtures were combined and incubated for 5 min. After centrifugation of the cells, the supernatant was decanted into flasks for later reuse and cells were resuspended in the DNA/PEI/FreeStyle 293 mixture. The cells were then split equally between two 2 l

Erlenmeyer flasks, each containing 100 ml FreeStyle 293 supplemented with 2 mM L-glutamine, and 1X NEAA and 5 mM valproic acid [237]. These flasks were incubated at 37 °C, 8% CO_2 and 160 rpm for 3-5 h. Following this incubation period cells were diluted back to their original volume with re-used PEM (resupplemented with 1 mM L-glutamine and 0.5X NEAA) and transferred back into their original growth bottles. Cells were incubated at 37 °C, 8% CO_2 and 130 rpm, and harvested 48-72 h after transfection by centrifugation at 400*g* for 7 min. Transfection efficiency was assessed by visualising GFP fluorescence prior to harvesting, and was typically 30-60%. Cell pellets were typically snap-frozen in LN_2 and stored at -80 °C until needed.

For *in vivo* biotinylation, avi-tagged constructs were used and 10% of the total DNA was replaced with pDisplay-BirA-ER [227]. All media were supplemented with 50 µM D-biotin.

2.2.3 Generation of recombinant baculoviruses

For generation of recombinant baculoviruses, constructs were subcloned into pEZT-BM (Section 2.1) [220].

Recombinant bacmids were prepared as previously described [220], [235]. Plasmid DNA was first transformed into competent DH10Bac *E. coli* (Thermo Fisher Scientific) to generate a recombinant bacmid. An aliquot of cells was thawed on ice, and 50 ng of plasmid DNA was added. The cells were incubated on ice for 5 min, then placed in a 42 °C water bath for 40 s. Cells were then placed back on ice for 2 min. 300 µl of 2XTY broth was added and cells were incubated at 37 °C and 200 rpm for 4 h. 20, 40 and 80 µl of this mixture was plated on LB-agar plates supplemented with 7 µg ml^{-1} gentamycin, 50 µg ml^{-1} kanamycin, 10 µg ml^{-1} tetracycline, 40 µg ml^{-1} IPTG and 300 µg ml^{-1} Blue Gal. Plates were incubated at 37 °C for 48 h. A mixture of white colonies, indicating the replacement of a *LacZ* gene with the expression casette from pEZT-BM in the parental DH10α bacmid, and blue colonies, indicating a retained *LacZ* gene, were typically observed.

One white colony was used to inoculate 10 ml of LB broth supplemented with 4 µg ml^{-1} gentamicin, 25 µg ml^{-1} kanamycin, and 5 µg ml^{-1} tetracycline. Typically, two cultures were prepared for each construct and these were incubated at 37 °C and 200 rpm for 24 h. Recombinant bacmids were purified using buffers from the Qiagen Miniprep kit.

Cells were first pelleted by centrifugation at 3900*g* for 10 min, then resuspended in 200 µl buffer P1. 200 µl buffer P2 was added and the tube was repeatedly inverted to mix the contents. 200 µl buffer N3 was then added and the mixture was again inverted to mix. The tube was then spun at 15000*g* for 10 min, and the supernatant transferred into a new 2 ml tube. 1 ml isopropanol was added and the tube was incubated at -20 °C for 10 min. The mixture was then spun at 15000*g* for 15 min at 4 °C and the supernatant discarded. The pellet was washed with 1 ml 70% (v/v) ethanol and then spun again at 15000*g* for 15 min at 4 °C. The supernatant was again removed and the pellet air-dried for 5 min and then dissolved in 50 µl ultrapure water.

Correct recombination of the expression cassette into the bacmid was verified by PCR (Section 2.1.3).

Insect Sf9 cells were passaged in Insect-XPRESS medium (Lonza), and provided when necessary by Dr Jianguo Shi. For generation of a P1 virus, $1x10^6$ Sf9 cells were seeded per well in a 6-well plate, and incubated at 27 °C for 30 min. In the meantime, 80 µl medium and 20 µl Cellfectin II (Thermo Fisher Scientific) per well were combined and incubated for 5 min. 4 µg bacmid DNA was added to another 100 µl media per well and the two mixtures were combined and incubated for 30 min. 1.3 ml more media was added and this transfection mixture was used to replace the media in the 6-well plates.

Since the pEZT-BM vector contains an insect expression cassette with mEGFP under the p10 promoter, the transfection and subsequent virus amplification was monitored by visualising mEGFP expression. The supernatant containing P1 virus was harvested once the majority of cells were fluorescent (typically 5-7 days). P2 virus was generated by adding P1 virus to 50 ml Sf9 cells at a density of $1.5x10^6$ mL^{-1}. Cell count and viability were monitored daily using a Countess automated cell counter (Invitrogen) and P2 virus was harvested once cell viability dropped below 70% (typically 3-4 days). The virus-containing medium was collected as the supernatant after centrifugation at 3500*g* for 15 min, and was sterile-filtered (0.45 µm), supplemented with 2% FBS and stored at 4 °C in foil-wrapped sterile bottles.

Virus titre was determined by endpoint dilution assay (Figure 2.1) [220], [235] . Sf9 cells were plated in a 96-well clear-bottom plate ($7.5x10^4$ per well) and allowed to adhere at 27 °C for 15 min. A 1/10 serial dilution ranging from 10^0 to 10^{-8} of virus stock was prepared,

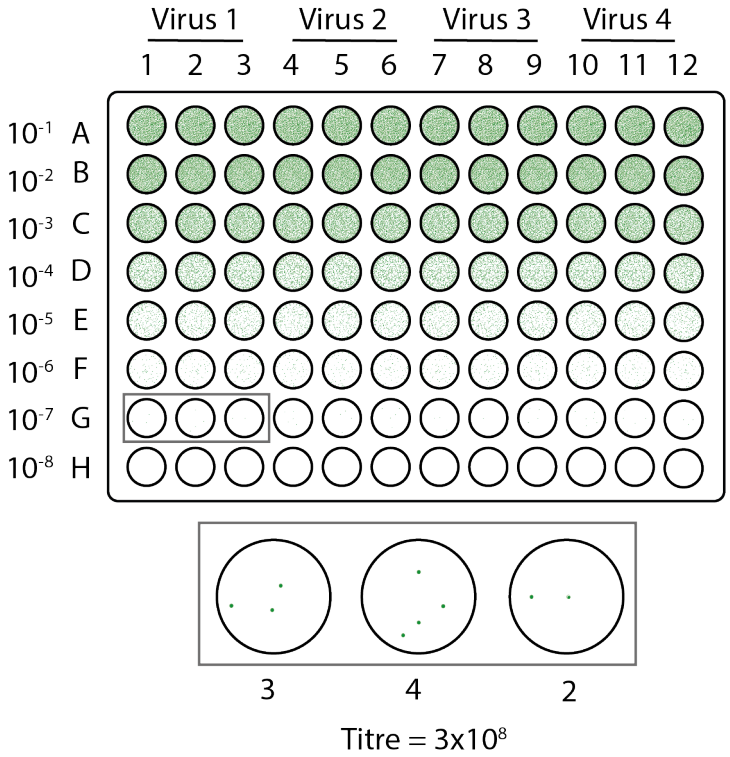

Figure 2.1: Endpoint dilution assay for virus titration. Assays were conducted in 96-well plates, with dilutions added to Sf9 cells in triplicate for each virus. Grey inset shows the cells counted for one virus.

with 100 µl of each dilution, in triplicate. The medium of the cells in the 96-well plate was then replaced with this triplicate serial dilution. GFP expression was monitored 48 h later, and the limiting dilution that resulted in a minimal number of fluorescent cells was identified. The number of cells in the well corresponding to this limiting dilution were counted and averaged across the triplicate wells. Assuming that each fluorescent cell results from one infection particle, for an average number of cells n, at a dilution d, the titre was calculated according to Equation (2.1).

$$titre = n \times d \times 10 \tag{2.1}$$

Once the titre of a P2 stock was established, typically the multiplicity of infection (MOI) and time for optimal production of P3 virus were optimised. 50 ml of Sf9 cells at a density of 1.5×10^6 mL^{-1} were infected at a MOI of 10^{-1}, 10^{-2} and 10^{-3}. Cell count and viability were monitored each day for four days, and samples were taken on days 2, 3 and 4. The titre of these samples was determined by endpoint dilution assay, and the optimal time

point and MOI were determined. For large-scale P3 production, P2 virus at the optimal MOI was introduced to Sf9 cells at a density of 1.5x10^6 mL^{-1}, and at the optimal time point the virus-containing medium was collected as the supernatant after centrifugation at 3500*g* for 15 min. This supernatant was filtered (0.45 µm) and supplemented with 2% FBS, then stored in foil-wrapped bottles at 4 °C until use. The titre of P3 stocks was also determined by endpoint dilution assay.

2.2.4 Baculovirus transduction of mammalian cells (BacMam)

Prior to transduction of mammalian cells with recombinant baculovirus, insect cell medium was removed by precipitation of the virus with PEG solution (4X solution comprised of 32% PEG 6000, 40 mM NaCl, 4 mM 4-(2-hydroxyethyl)-1-piperazineethanesulfonic acid (HEPES), pH = 7.4, autoclaved). The mixture was incubated overnight at 4 °C and precipitated virus was collected the following day by centrifugation at 3900*g* for 30 min. The supernatant was discarded and the virus resuspended in 1/10 volume of FreeStyle 293. The titre was again verified by endpoint dilution assay.

HEK293S GnTI$^-$ cells were grown in suspension as described in Section 2.2.2.1. Cells were typically transduced at a density of 2x10^6 mL^{-1} with an MOI of 1-10. For heteromeric $GABA_AR$, viruses for each subunit were mixed during transduction. Valproic acid (1-10 mM) or sodium butyrate (1-10 mM) were added to enhance expression if small-scale tests showed them to be efficacious. After transduction, cells were incubated at 30 or 37 °C, 8% CO_2 for 24-72 h, then harvested by centrifugation at 400*g* for 7 min. Cell pellets were typically snap-frozen in LN_2 and stored at -80 °C until needed.

2.2.5 Generation of stable cell lines

Polyclonal stable cell lines were generated by transduction with recombinant lentiviruses [221]. First, constructs were subcloned into the transfer vector pHR as described in Section 2.1. Lenti-X were cells passaged as described in Section 2.2.2.1, except that in the last passage before transfection they were grown in media appropriate for the target cell line (typically DMEM/F-12 for HEK293S GnTI$^-$ TetR cells), except that any antibiotics were omitted.

All steps in the generation of lentiviral particles were carried out at biosafety level 2. Recombinant lentiviruses were generated by co-transfection of the pHR transfer vector with second-generation envelope and packaging plasmids (pMD2.G and psPAX2, respectively, both provided by Dr Jonathan Elgeehert). A 1:1:1 mix of pHR, psPAX2 and pMD2.G was used to transfect Lenti-X cells, typically in a ~90% confluent T175 flask. For heteromeric $GABA_A$Rs, each subunit was co-transfected with the total amount of transfer plasmid kept constant. 70 µg total plasmid DNA was mixed with 500 µl medium, with FBS omitted, and in a separate tube 175 µl PEI stock (25 kDa branched, 1 mg ml^{-1} stock) was mixed with 500 µl medium without FBS. The two mixtures were combined and incubated at room temperature for 10 min. The medium in the flask of Lenti-X cells was then replaced with 29 ml fresh medium supplemented with 2% FBS rather than 10%, and the transfection mixture added. The flask was then incubated at 37 °C and 5% CO_2 in a humidifed environment.

The expression medium containing lentiviral particles was harvested 3 days after transfection. This was then filtered (0.45 µm), 10 ml of fresh medium and 40 µl polybrene (10 mg ml^{-1} stock, Merck) added, and then used to replace the medium in a ~90% confluent T175 flask of the target cell line, typically HEK293S GnTI$^-$ TetR. This flask was placed back into a humidified incubator set at 37 °C and 5% CO_2.

After 3 days, the cells were washed five times with 15 ml PBS; then the new polyclonal stable cell line was passaged as usual. At this point, cells could be transferred back to a biosafety level 1 tissue culture facility. New cell lines were also cryopreserved (Section 2.2.2.1) for future use.

2.2.6 Induction of stable cell lines

Cell lines were expanded until the desired cell volume was reached, with a density of 2-3x10 ^{6} mL^{-1}. For cell lines stably expressing the tetracycline repressor, expression of the transgene was then induced by the addition of 1-10 µg ml^{-1} to the culture medium. After induction, cells were typically incubated at 30 °C, 130 rpm and 8% CO_2. Optionally, sodium butyrate (1-10 mM) or valproic acid (1-10 mM) were added to enhance expression.

Cells were incubated for 24-72 h, then harvested by centrifugation at 400*g* for 7 min. Cell pellets were typically snap-frozen in LN_2 and stored at -80 °C until needed.

2.2.7 Fluorescence activated cell sorting (FACS)

Polyclonal stable lines expressing proteins fused to fluorescent proteins (mVenus, mEGFP) or made with pHR variants containing IRES-FP sequences were additionally sorted to boost yield by removing non-transduced cells. Fluorescence-activated cell sorting (FACS) was carried out with the assistance of Dr Jonathan Elegheert (Oxford), Maria Daly, Fan Zhang and Martyn Balmont (Cambridge).

Cells were grown for sorting in T175 flasks, and transgene expression was induced 12-24 h before sorting with 1 $\mu g\,ml^{-1}$ doxycycline (Section 2.2.6). Induced cells were washed with 15 ml PBS, then 4 ml 0.05% trypsin was added and the cells incubated at 37 °C for 1-2 min. 21 ml of the appropriate (adherent) medium was added and then the cells were pelleted by centrifugation at 100*g* for 2 min. The cell pellet was gently resuspended in 50 ml FreeStyle 293 medium and allowed to recover at 37 °C, 8% CO_2 and 130 rpm for 2-4 h. Prior to sorting, cells were again pelleted by centrifugation at 100*g* for 2 min, resuspended in PBS supplemented with 2% FBS at a density of 5-10x10^6 mL^{-1}, and passed through a 40 µm cell strainer (Corning).

Sorting was conducted on a SH800S Cell Sorter (Sony Biotechnology) or Synergy Cell Sorter (Sony Biotechnology). For one-colour sorts, typically two gates were drawn, one based on forward-scattered area (FSC area) and side-scattered area (SSC area) to separate single cells from debris and cell clumps, and a second gate to separate fluorescent from non-fluorescent cells. The boundaries for the second gate were identified based on negative controls (cells treated identically but not containing a transgene). One-colour sorts were typically conducted based on GFP fluorescence, with a 488 nm laser used for excitation and a 525±50 nm bandpass emission filter. For three-colour sorts, the same FSC area/SSC area gate was drawn, and two additional gates to select for triple-positive cells. Blue, green and red gates were based on fluorescence measured with a 405 nm laser and 455±50 nm bandpass emission filter, a 488 nm laser and a 525±50 nm bandpass emission

filter, and a 561 nm laser and a 615±30 nm bandpass filter. Fluorescence in each channel was compensated based on the signal from cells expressing a single fluorescent protein.

Cells were sorted into tubes pre-filled with the appropriate adherent media, supplemented with penicillin-streptomycin (50 UmL^{-1}, Gibco). After 3-4x10^6 positive cells had been collected, cells were returned to adherent tissue culture in T25 flasks.

FACS data was analysed using FCS Express 6 Flow.

2.2.8 Light microscopy

Where cells were transfected with fluorescent proteins, expression was verified by light microscopy.

A Nikon TE2000U fluorescence inverted microscope, equipped with CoolLED pE-300, DAPI, FITC, TRITC, and CY5 filter sets and a Hamamatsu C4742-96 CCD camera were used to visualise transmitted light as well as transfected fluorescent proteins. Alternatively, an EVOS Fluorescence Cell Imaging System (Invitrogen) with DAPI, GFP and RFP Light Cubes was used.

Light microscopy data were analysed in FIJI.

2.3 Protein purification and characterisation

2.3.1 SDS-PAGE and western blots

Expression of new constructs and presence of the protein of interest in purification steps was verified by sodium dodecyl sulfate-polyacrylamide gel electrophoresis (SDS-PAGE) and/or western blot. For membrane protein lysates, cells transfected with the construct of interest (Section 2.2.2.2) were first resuspended in 150 mM NaCl, 10 mM HEPES (pH = 7.2) and solubilised in 1% detergent (typically DDM, see Section 2.3.6, Table 2.14) for 60 min. For SDS-PAGE, 4X NuPage LDS Sample Buffer (Life Technologies), supplemented with 200 mM dithiothreitol (DTT) was added to protein samples prior to loading on a precast Nupage 4-12% Bis Tris Gel (Life Technologies). Membrane protein samples were loaded directly onto the gel; soluble protein samples were heated at 98 °C for 5 min prior to loading. Gels were run in a Bolt Mini Gel Tank (Invitrogen) at room temperature, filled with 1X NuPage 3-(N-morpholino)propanesulfonic acid (MOPS) running buffer

Table 2.10: Reagents for western blotting

Primary antibodies					
Target	Species raised in	Dilution	Supplier	Catalogue number	Other information
Penta-his peptide	Mouse	1:1000	Qiagen	34660	
1D4 peptide	Mouse	1:5000	University of British Columbia	N/A	
$GABA_AR$ β2/3	Mouse	1:500	Merck	MAB341	
GFP	Rabbit	1:1000	Abcam	ab290	
FLAG peptide	Rabbit	1:1000	Sigma	F7425	
HA peptide	Rabbit	1:500	Sigma	H6908	
Secondary antibodies					
Mouse IgG Fc fragment	Goat	1:2000	Sigma	A0168	HRP conjugate
Rabbit IgG Fc fragment	Goat	1:3000	Abcam	ab6721	HRP conjugate
Other					
Streptavidin-HRP	N\A	1:100000	Sigma	S2438	No secondary antibody required

or 1X NuPage 2-(N-morpholino)ethanesulfonic acid (MES) running buffer (purchased from Formedium) at 180 V for 35 min. The Amersham ECL rainbow molecular weight markers (GE Healthcare) or Precision Plus Protein Dual Color Standards (Bio-Rad) were used to estimate the molecular weight of protein bands.

To directly visualise proteins, the gel was placed in ~15 ml of InstantBlue Protein Stain (Expedeon) and incubated at room temperature and 30 rpm for 60 min, then washed in water 2-3 times. Stained SDS-PAGE gels were visualised with a Gel Documentation System (Bio-Rad).

For western blots, proteins in an SDS-PAGE gel were first transferred to a nitrocellulose membrane in the Blot Module of the Bolt Mini Gel Tank filled with 1X NuPage Transfer Buffer (Invitrogen). The transfer proceeded at 30 V and 150 mA for 70 min. Membranes were blocked by incubation in PBST (PBS with 0.1% Tween20) containing 3% BSA at room temperature for 30 min at 30 rpm. The membrane was then incubated with a primary antibody (Table 2.10) diluted in PBST containing 3% BSA for 60 min at 30 rpm. Following three 15 min washes in PBST at 30 rpm, the membrane was then incubated with the secondary antibody (Table 2.10) diluted in PBST containing 3% BSA. Following three more 15 min washes in PBST at 30 rpm, horseradish peroxidase (HRP) was detected with the Clarity Western Enhanced Chemiluminescence (ECL) Substrate (Bio-Rad) and visualised with a Gel Documentation System (Bio-Rad).

Table 2.11: Buffers for coupling to CNBr-activated Sepharose 4B

Buffer	Components
1	1 mM HCl
2	100 mM $NaHCO_3$, 500 mM NaCl, pH = 8.5
3	100 mM Tris-HCl, pH = 8.0
4	100 mM Tris-HCl, 500 mM NaCl, pH =8.5
5	100 mM NaOAc, 500 mM NaCl, pH = 4.0

2.3.2 Immunoaffinity media preparation

Immunoaffinity media were prepared by coupling an antibody or nanobody to CNBr-activated Sepharose 4B (GE Healthcare). Typically, 3-4 g of Sepharose 4B was used, which resulted in 10.5-14 ml of immunoaffinity medium. Buffers used are listed in Table 2.11. Sepharose was first washed in 100 ml buffer 1, then 100 ml buffer 2. 1D4 antibody (14 mg, University of British Columbia), or GFP nanobody (3.5 mg, homemade, Sections 2.2.1 and 2.3.4, [218]) per 1 g of Sepharose was added to buffer 2 and incubated with Sepharose 4B with gentle end-on-end rotation for 2-4 h at room temperature or overnight at 4 °C. After verifying coupling of the protein via A_{280} measurement of the flow-through, the Sepharose 4B was then washed with 100 ml buffer 3, then incubated with buffer 3 for 2 h at room temperature. The Sepharose 4B was washed three times, alternating between 100 ml buffer 4 and 100 ml buffer 5. Finally, the freshly-prepared immunoaffinity media were washed with 100 ml more buffer 5, and stored in buffer 5 at 4 °C until use.

After use, immunoaffinity media were collected and regenerated 1-2 times. Media were regenerated by 5-6 2 h incubations with a regeneration buffer. This buffer consisted of 1X PBS, plus 20 mM Tris (pH = 7.5), 1 M NaCl, 1 mM EDTA and 50% 1,2-propanediol.

2.3.3 Purification of soluble proteins from the *E. coli* periplasm

Proteins expressed in *E. coli* and targeted to the periplasmic space (Section 2.2.1) were released from the periplasm by osmotic shock, and polyhistidine-tagged proteins were then purified by immobilised metal ion chromatography (IMAC). Buffers used are listed in Table 2.12, where the pH of buffers NiA and NiB were chosen to be at least 0.5 pH units away from the theoretical protein pI (calcuated with the ExPASy ProtParam web server),

Table 2.12: Buffers used for purification of proteins from *E. coli* periplasmic space

Buffer	Components
TES	200 mM Tris-HCl, 0.5 mM EDTA, 500 mM sucrose, pH = 8
TES/4	TES buffer diluted 1/4
NiA	50 mM HEPES, 500 mM NaCl, 10 mM imidazole, pH = 7.2 or pH = 7.8
NiB	50 mM HEPES, 200 mM NaCl, 400 mM imidazole, pH = 7.2 or pH = 7.8
SEC	PBS or 10 mM HEPES, 150 mM NaCl, pH = 7.2 or pH = 7.8

and volumes listed are for 1 l of *E. coli* culture volume. For osmotic shock, cell pellets were resuspended in 15 ml TES buffer per 1 l of culture volume, and incubated on ice at 130 rpm for 3-5 h. 30 ml TES/4 was then added and the mixture incubated on ice at 130 rpm for a further 2-3 h. Debris was removed by centrifugation at 1000*g* and 4 °C for 30 min.

For IMAC, 600 µl of Ni-NTA resin (HisPur, Thermo Fisher Scientific) per 1 l of culture was added to the supernatant containing the protein released from the periplasmic space. The mixture was rotated gently end-on-end for 2 h at room temperature or 4 °C overnight. The beads were then packed in a gravity flow column (Bio-Rad) and washed with 50 ml 10 mM imidazole (buffer NiA), 50 ml 25 mM imidazole (3.8% NiA, 96.2% NiB), and 50 ml 50 mM imidazole (72.5% NiA, 27.5% NiB), then eluted using 5 ml NiB buffer, rotating gently end-on-end for 15 min. A total of three eluates were collected in this manner. The eluates were pooled and concentrated by ultrafiltration. Optionally, size exclusion chromatography (SEC) was performed, in which case the sample was concentrated to ~3 ml and injected onto an appropriate SEC column (typically Superdex 75 16/600) connected to an Äkta system and equilibrated in SEC buffer. The Äkta system was controlled with UNICORN software (GE Healthcare), which was also used to record chromatograms. Fractions were pooled based on the chromatogram and SDS-PAGE analysis of fractions, and then further concentrated by ultrafiltration. If SEC was not performed, the high-imidazole buffer was exchanged by three successive rounds of concentration by ultrafiltration to ~2 ml and dilution with SEC buffer to 10 ml. Purified proteins were aliquoted, snap-frozen in LN_2 and stored at -80 °C until use. The purification was monitored by SDS-PAGE and western blot with samples collected at each stage.

Table 2.13: Buffers used for purification of proteins from *E. coli* cytoplasm

Buffer	Components
Lysis buffer (MSP)	20 mM $NaPO_4$, 1% Trition-X100, 1% protease inhibitor cocktail for histidine-tagged proteins (Sigma)
Lysis buffer (other proteins)	300 mM NaCl, 50 mM Tris-HCl, pH 8, 1% protease inhibitor cocktail for histidine-tagged proteins (Sigma)
NiA	50 mM HEPES, 500 mM NaCl, 10 mM imidazole, pH = 7.2 or pH = 7.8
NiB	50 mM HEPES, 200 mM NaCl, 400 mM imidazole, pH = 7.2 or pH = 7.8
MSP-W1	40 mM Tris-HCl, 300 mM NaCl, 1% Triton-X100, pH = 8.0
MSP-W2	40 mM Tris-HCl, 300 mM NaCl, 50 mM cholate, pH = 8.0
MSP-W3	40 mM Tris-HCl, 300 mM NaCl, pH = 8.0
MSP-W4	40 mM Tris-HCl, 300 mM NaCl, 50 mM imidazole for MSP1D1 or 20 mM imidazole for MSP2N2, pH = 8.0
MSP-E	40 mM Tris-HCl, 300 mM NaCl, 300 mM imidazole
SEC	PBS or 10 mM HEPES, 150 mM NaCl, pH = 7.2 or pH = 7.8

2.3.4 Purification of soluble proteins from the *E. coli* cytoplasm

For proteins expressed in *E. coli* cytoplasm (Section 2.2.1), cells were first lysed by sonication (Sonics Vibra-cell), and then polyhistidine-tagged proteins were purified from the lysate by IMAC. Buffers are listed in Table 2.13, with the pH of buffers NiA, NiB and SEC chosen to be 0.5 pH units away from the theoretical protein pI (calculated with the ExPASy ProtParam web server), and volumes listed are for 1 l of culture.

Cell pellets (Section 2.2.1) were resuspended in 50 ml of lysis buffer and lysed by sonication. Debris was cleared by centrifugation at 30000*g* and 4 °C for 30 min.

Polyhistidine-tagged proteins were purified by IMAC. For MSPs, 2.5 ml of Ni-NTA resin was added to the supernatant and the mixture was rotated at 65 rpm for 4 h at 4 °C. The resin was collected in a gravity flow column (Bio-Rad) and washed with 25 ml MSP-W1, 15 ml MSP-W2, 25 ml MSP-W3 and 50 ml MSP-W4. MSPs were then eluted with 5 ml MSP-E buffer, rotating gently end-on-end for 15 min. A total of three eluates were collected in this manner. The eluates were pooled and dialysed into SEC buffer using a 10 kDa cutoff Slide-A-Lyzer casette (Thermo Fisher Scientific). Purified protein was then concentrated by ultrafiltration, aliquoted, snap-frozen in LN_2 and stored at -80 °C until use. For other proteins, IMAC was carried out as described in Section 2.3.3. The purification was monitored by SDS-PAGE and western blot with samples collected at each stage.

Table 2.14: Detergents used for membrane protein purification

Name	Molecular weight (Da)	CMC in H_2O (uM)	(%)	Aggregation number
n-Dodecyl-β-D-Maltopyranoside (DDM)	510.6	170	0.0000087	~78-149
n-Dodecyl-β-D-Thiomaltoside (DDTM)	526.6	50	0.0026	~126
Decyl Maltose Neopentyl Glycol (DMNG)	949.1	36	0.0034	
Lauryl Maltose Neopentyl Glycol (LMNG)	1005.2	10	0.001	

2.3.5 Preparation of lysates for FSEC

For lysate fluorescence size exclusion chromatography (FSEC), cell pellets (typically from 1 ml [2x10^6) suspension cells] were thawed briefly in a room-temperature metal block, and then placed on ice. Cells were resuspended in 200 µl ice-cold resuspension buffer containing 300 mM NaCl, 50 mM HEPES, 1 mM $CaCl_2$, 1 mM $MgCl_2$, 5 Uml^{-1} benzonase nuclease (Novagen) and 1% mammalian protease inhibitors (Sigma), pH 7.2. Detergent (Table 2.14) and cholesterol hemisuccinate (CHS, Anatrace) were added to a final concentration of 1% and 0.1%, respectively. The cell suspensions were rotated for 2 h at 4 °C, and then cleared of debris by centrifugation at 129000*g* at 4 °C for 20 min. The supernatant was analysed by FSEC (Section 2.3.7).

2.3.6 Small-scale membrane protein purification

Small-scale protein purification was used to screen constructs in combination with FSEC (Section 2.3.7). All samples were kept on ice and all buffers and centrifuge rotors were pre-chilled. Cells used were typically from one well of a confluent 6-well plate, or 1 ml (2x10^6) suspension cells. Cell pellets were thawed in a room temperature metal block, then placed on ice and then resuspended in 400 µl resuspension buffer (Table 2.16). Detergent (Table 2.14) was added to a final concentration of 1.5% and the mixture was rotated gently end-on-end for 90-120 min at 4 °C. Cholesterol hemisuccinate (CHS, Anatrace), was often added throughout at a concentration of 10% of the detergent concentration (i.e 0.15% for detergent at 1.5%). Debris was removed by centrifugation at 25000*g* for 10 min at

Table 2.15: Affinity chromatography conditions

Tag	Media	Source	Buffer A supplement for elution	Elution conditions
1D4	Anti-1D4 antibody-agarose	Homemade (Section 2.3.2)	0.5-2 mM 1D4 peptide	Overnight at 4 °C
FLAG	Anti-FLAG M2 affinity gel	Sigma	50 μg ml^{-1} 3x FLAG peptide	15 min at 4°C
GFP	Anti-GFP nanobody agarose	Homemade (Section 2.3.2)	TEV or 3C protease	Overnight at 4 °C
SBP	Pierce high-capacity streptavidin agarose	Thermo Fisher Scientific	1 mM D-biotin	Overnight at 4 °C
Twin-strep	Strep-TactinXT	IBA	TEV or 3C protease	Overnight at 4 °C

Table 2.16: Buffers used in membrane protein purifications

Buffer	Components
Buffer A	300 mM NaCl, 50 mM HEPES pH 7.2
Resuspension buffer	Buffer A supplemented with 1% mammalian protease inhibitor cocktail (Sigma)
Wash-1 buffer	Buffer A supplemented with 0.1% detergent and 0.01% CHS
Wash-2 buffer	Buffer A supplemented with 0.01% detergent and 0.001% CHS
Elution buffer	Buffer A supplemented with detergent at 2-3x CMC, CHS at 0.2-0.3% detergent CMC, and appropriate elution reagent (Table 2.15)

4 °C. The supernatant was transferred to a new tube and topped up with 400 μl buffer A. 30 μl of the appropriate affinity media (Table 2.15) were added and incubated with the lysate for 90-120 min at 4 °C with gentle end-on-end rotation. The beads were pelleted by centrifugation at 30*g* and 4 °C and washed twice with 1 ml of wash-1 buffer and 1 ml of wash-2 buffer (Table 2.16). For each wash, the supernatant was removed after centrifugation at 30*g* and 4 °C. Protein was eluted from affinity media in 100 μl of elution buffer (Table 2.16) with the appropriate elution condition (Table 2.15). In the case of protease cleavage, 1:100 (v/v) dilution of Tobacco Etch Virus (TEV) protease (provided by Christina Heroven) (6 mg ml^{-1}), or human rhinovirus (HRV) 3C protease (provided by Dr Lina Malinauskaite) (1.5 mg ml^{-1}) were used. All elution buffers were made with buffer A and also contained detergent at 2-3x CMC and CHS at 0.2-0.3% detergent CMC if appropriate. Eluates were typically analysed by fluorescence size exclusion chromatography (Section 2.3.7), SDS-PAGE and/or western blot (Section 2.3.1).

2.3.7 Fluorescence size exclusion chromatography (FSEC) screening

Purified proteins or lysates were loaded onto a Superose 6 Increase 3.2/300 column (GE Healthcare) equilibrated in a buffer composed of 150 mM NaCl and 25 mM HEPES (pH = 7.2) attached to a high-performance liquid chromatography system with automated micro-

Table 2.17: Excitation and emission wavelengths for FSEC

Fluorochrome	Excitation wavelength (nm)	Emission wavelength (nm)
Tryptophan	295	315
mVenus	515	528
mEGFP	488	520

volume loader and in-line fluorescence detection (Shimadzu). If the protein remained in detergent, this was also included in the running buffer at 2-3x CMC. Separate columns were used for lysates, membrane proteins that remained in detergent, and membrane proteins that had been exchanged into amphipol or nanodiscs. For lysate samples, a pre-filter was attached before the SEC column to prevent any debris from entering the column. Typically 5-20 µl of sample was injected onto the column. Fluorescence was monitored at the wavelengths listed in Table 2.17. Typically, mVenus or mEGFP fluorescence was monitored for lysates, and for purified proteins A_{280} as well as FP (if applicable) and tryptophan fluorescence was recorded.

FSEC data were typically analysed with custom MATLAB scripts to detect the height of the $GABA_AR$ peak (Appendix D.1). The peak height was assumed to be proportional to the mass of protein present in the injected sample, which was to be optimzed by comparing different protein expression and purification conditions. In the scripts, first FSEC data was loaded from a .ascii file exported fromt the Shimadzu software, and subtracted a linear baseline. Then, local maxima with a prominence above a certain threshold around an elution time of 23-26 minutes (known to correspond to the $GABA_AR$ peak from preliminary tests) were detected. The threshold for peak prominence was manually tuned so as to only detect one peak for each chromatogram in this time frame. The height, elution time and prominence of this peak were the primary outputs for each FSEC chromatogram; additional features such as peak width and the presence of shoulders were not considered. These were then exported as an excel spreadsheet for further analysis.

2.3.8 Large-scale membrane protein purification

Membrane protein purifications were carried out as described by Miller and Aricescu [37]. All samples were kept on ice and all buffers and centrifuge rotors were pre-chilled. For some

purifications, $GABA_AR$ ligands such as 1 mM GABA or 1 mM picrotoxin were included in all buffers. The composition of buffers used is listed in Table 2.16, and detergents used are listed in Table 2.14.

Cell pellets were thawed briefly in room-temperature water and then placed on ice. Thawed cells were resuspended in 6 ml per 200 ml cell culture of resuspension buffer. Detergent was added to a final concentration of 1-1.5% and the mixture was incubated at 4 °C with gentle end-on-end rotation for 90-120 min. The cell debris was cleared by centrifugation at 10000*g* and 4 °C for 15 min, and the supernatant was incubated with immunoaffinity resin (Table 2.15, typically FLAG or 1D4). For homomeric $GABA_ARs$, 100 µl of resin was used per 200 ml of cell culture, and for heteromeric $GABA_ARs$ 50 µl of resin was used per 200 ml of cell culture. The mixture was incubated at 4 °C with genle end-on-end rotation for 90-120 min. The immunoaffinity resin was collected, typically in a gravity flow column, but occasionally by centrifugation at 45*g* and 4 °C for 5 min. The beads were washed first in wash-1 buffer, and then in wash-2 buffer (Table 2.16), typically with 50 resin volumes of each. Optionally, exchange of membrane proteins into amphipols or nanodiscs was carried out (Section 2.3.9), otherwise protein was eluted with buffer A containing detergent at 2-3% CMC and CHS at 0.2-0.3% detergent CMC, with the appropriate supplement for the appropriate amount of time (Table 2.15). If the sample was to be used for electron microscopy (EM), buffer A was typically diluted 1/4 to lower the salt content of the solution. A sample of the eluate was subjected to FSEC to assess its quality (Section 2.3.7). If the protein was to be used for crystallography, it was concentrated by ultrafiltration and injected on to a 10/300 Superose-6 increase column (GE Healthcare) that had previously been equilibrated with buffer A diluted 1/2, supplemented with detergent at 2-3% CMC and CHS at 0.2-0.3% detergent CMC if appropriate. Peak fractions were pooled and concentrated by ultrafiltration, and either used immediately or snap-frozen in LN_2 and stored at -80 °C. The purification was monitored by SDS-PAGE and western blot with samples collected at each stage.

2.3.9 Exchange of membrane proteins to amphipols or nanodiscs

When used for EM studies, membrane proteins were often exchanged into amphipols or nanodiscs. This exchange step was carried out while the protein was still bound to immunoaffinity media [41], [42]. Typically, lipids and MSP or amphipols were added in excess, and after reconstitution this excess was removed by extensive washing of the media.

1-palmitoyl-2-oleoyl-sn-glycero-3-phosphocholine (POPC, Avanti) and bovine brain lipid extract (BBE, Folch Fraction I, Sigma) were both dissolved in 150 mM NaCl, 20 mM HEPES (pH = 7.4), 3% DDM at 10 mg ml^{-1} (POPC) or 20 mg ml^{-1} (BBE) for two weeks and then stored at -20 °C. Before use, POPC and BBE were mixed with a final concentration of 8.5 mg ml^{-1} (POPC) and 2.5 mg ml^{-1} (BBE) and underwent gentle end-on-end rotation at 4 °C for 30 min. Insoluble material was removed by centrifugation at 15000*g* and 4 °C for 15 min. This lipid mix was first added at a 1:1 ratio with resin volume and the mixture was incubated for 30 min at 4 °C with gentle end-on-end rotation. Typically, lipids were added to immunoaffinity media in ~4 resin volumes of buffer in the wash-2 buffer (Table 2.16). Excess lipids were removed with the supernatant after centrifugation at 30 *g*, 4 °C for 2 min. 4 resin volumes of wash-2 buffer were added, along with 0.4 mg A8-35 (from a 100 mg ml^{-1} stock in water, Anatrace) or 4 mg MSP per 100 µl immunoaffinity resin. This mixture was incubated with gentle end-on-end rotation for 30 min at 4 °C. 30 mg BioBeads SM-2 resin (Bio-Rad) equilibrated in buffer A were then added and the mixture was incubated with gentle end-on-end rotation for 2 h at 4 °C. The immunoaffinity resin was then washed 6-8 times in 4 immunoaffinity resin volumes of buffer A and then protein was eluted as per Section 2.3.8, but with detergent omitted from the elution buffer.

2.3.10 Purification of soluble proteins from expression media

Media containing soluble proteins were first diafiltrated (QuixStand, 10 kDa membrane). When media were reduced to at least 1/10 the original volume, the system was topped up to the original volume with NiA buffer (Table 2.12) and then diafiltrated again to at least 1/10 the original volume. Typically proteins harboured a polyhistidine tag and were subjected to IMAC with 1 ml of Ni-NTA resin per 1.5 l medium volume (prior to diafiltration) and SEC (usually on a Superdex 16/600 column) as described in Section 2.3.3. After SEC, peak

fractions were pooled and concentrated by ultrafiltration, and then snap-frozen in LN_2 and stored at -80 °C until required. The purification was monitored by SDS-PAGE and western blot with samples collected at each stage.

2.3.11 *In vitro* biotinylation of purified proteins

In vitro biotinylation of $GABA_A$Rs was carried out using purified BirA provided by Dr Ross Robinson. The concentration of avi-tagged substrate was ~4 μM, and 2.5 μg BirA was used per 1 nmol substrate. 50 mM HEPES (pH = 8), 10 mM MgOAc, 10 mM ATP and 100 μM D-biotin were added (final concentrations) and the reaction proceeded overnight at 4 °C.

2.3.12 Deglycosylation of purified proteins

Prior to crystallisation, homomeric $GABA_A$Rs were deglycosylated by the addition of 1:100 (v/v) Endoglycosidase H (provided by Dr Paul Miller). The reaction proceeded at room temperature for 2 h, and then samples were placed back on ice.

In some cases heteromeric $GABA_A$Rs were deglycosylated by the addition of 1:100 (v/v) Endoglycosidase F1 (provided by Christina Heroven) just prior to vitrification on grids. The reaction proceeded at room temperature for 2 h, and then samples were placed back on ice.

2.4 Biophysical characterisation of $GABA_A$R-nanobody interactions

2.4.1 Surface plasmon resonance

Surface plasmon resonance (SPR) experiments were conducted with a Biacore T200 instrument (GE Healthcare) and were conducted to characterise nanobody-$GABA_A$R interactions by kinetic titration series (called single-cycle kinetics [SCK] in Biacore software). Biotinylated $GABA_A$Rs were used as the ligand and deposited onto one flow cell of a streptavidin-coated sensor chip (Sensor Chip SA, GE Healthcare) to a level of ~1000 response units (RU). A second flow cell was used as a reference, without deposition of the ligand. SCK was then conducted with a two-fold dilution series of the analyte from 0.25x K_D to 8x K_D (the dissociation constant [K_D] was estimated from pilot experiments), with a 120 s contact time for each analyte concentration and a 600 s dissociation time at the

end of the cycle. Analyte dilutions were made in running buffer, which contained 150 mM NaCl, 10 mM HEPES (pH = 7.2), 0.007% DMNG, 0.0007% CHS. Data were analysed with Biacore T200 Evaluation Software (GE Healthcare), and SCK data was typically fitted using a 1:1 Langmuir binding model. For each fit, the evaluation software reports a χ^2 value as a goodness-of-fit measure. This is a measure of the average squared residual, calculated based on the fitted value at a given point, r_x, the experimental value at the same point, r_x, the number of data points, n, and the number of fitted parameters, p (Equation 2.2).

$$\chi^2 = \frac{\sum_1^n r_f - r_x{}^2}{n - p} \tag{2.2}$$

2.4.2 Biolayer interferometry

Biolayer interferometery (BLI) was used as an alternative to SPR when a large number of interactions were to be characterised. Kinetic titration series were also used to investigate nanobody-$GABA_AR$ interaction kinetics [238], [239] on an Octet RED96 or RED384 system (ForteBio). Biotinylated $GABA_ARs$ were adsorbed onto SA Dip and Read Biosensors (ForteBio) to a thickness of 3-4 nm. Ten-fold serial dilutions were prepared for each nanobody from 0.1 nM to 1000 nM in a 96-well or 384-well plate. Dilutions were made in a buffer containing 150 mM NaCl, 10 HEPES (pH = 7.2 or 7.8 depending on nanobody pI), 0.007% DMNG and 0.0007% CHS. The $GABA_AR$ ligands GABA (agonist, 1 mM) and gabazine (antagonist, 10 μM) were added to this buffer for some experiments. An example plate layout for a 96-well plate is shown in Figure 2.2. After adsorption of biotinylated $GABA_ARs$, biosensors were placed in increasing concentrations of nanobody for 180 s (each concentration), with each concentration followed by a short 20 s dissociation, and a longer 600 s dissociation after the final assocation.

For data analysis, a 1:1 binding model was assumed in which a receptor (R) and ligand (L) form a receptor-ligand complex (RL) (Equation (2.3))

$$\mathrm{R} + \mathrm{L} \underset{k_d}{\overset{k_a}{\rightleftharpoons}} \mathrm{RL} \tag{2.3}$$

The rate of association can then be written as Equation (2.4).

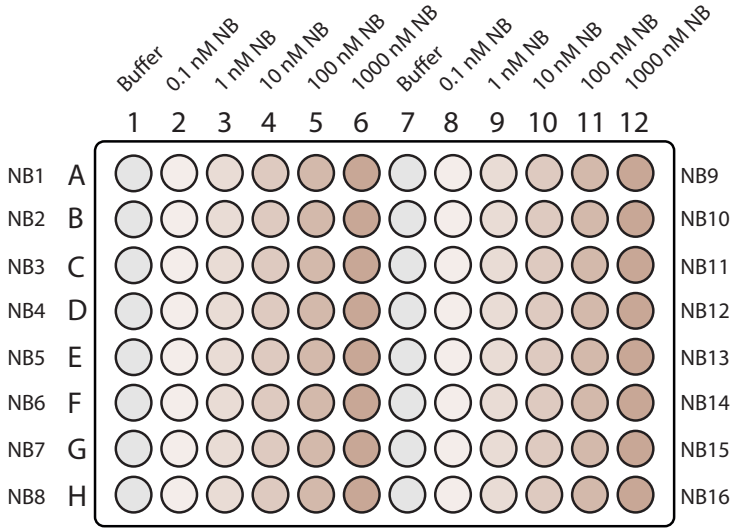

Figure 2.2: 96-well plate layout for biolayer interferometry (BLI) experiments. Organisation of a serial dilution of 16 nanobodies per 96-well plate for a typical BLI experiment.

$$\frac{\mathrm{d[RL]}}{\mathrm{dt}} = \mathrm{k}_a[\mathrm{R}][\mathrm{L}] - \mathrm{k}_d[\mathrm{RL}] \tag{2.4}$$

This can be written in terms of the signal, S observed (with $S \propto [RL]$), with S_{max} being the signal observed when all available receptor is associated with ligand [240] (Equation (2.5)).

$$\frac{\mathrm{dS}}{\mathrm{dt}} = \mathrm{k}_a[\mathrm{L}](\mathrm{S}_{\mathrm{max}} - \mathrm{S}) - \mathrm{k}_d\mathrm{S} \tag{2.5}$$

BLI data were analysed with a MATLAB script that implements Euler's method to numerically solve Equation (2.5) and fit values of k_a, k_d and S_{max} (details and the scripts can be found in Appendix D.2). A goodness-of-fit parameter, R^2, was also calculated based on the difference between the fitted curves and the data. Equilibrium dissociation constants were then calculated as $K_D = \frac{k_d}{k_a}$.

Additionally, to assess the goodness-of-fit for each kinetic titration, the coefficient of determination (R^2) statistic was calculated in MATLAB:

$$R^2 = \frac{\sum_{i=1}^{n}(\hat{y}_i - \bar{y}_i)^2}{\sum_{i=1}^{n}(y_i - \bar{y}_i)^2} \tag{2.6}$$

Where n is the number of data points, y_i is the ith experimental value, $\bar{y}_i$ is the ith model value $\hat{y}_i$

2.5 Electrophysiology

Electrophysiology was performed using an IonFlux 16 automated patch-clamp system (Fluxion Biosciences).

On the day prior to electrophysiology experiments, HEK293T cells (Section 2.2.2) were transfected with the relevant $GABA_AR$ subunits. Cells were transfected in a T175 flask at 30-40% confluency with a total of 48 µg of DNA and 96 µl of lipofectamine by scaling up the lipofectamine transfection method described in Section 2.2.2.2. Typically 3% GFP plasmid DNA was included in the total DNA to assess transfection efficiency. 3-5 h after the transfection mixture was introduced to the flask, the medium was replaced with 24 mL DMEM (supplemented with 10% FBS but no NEAA or L-glutamine).

Cells were used for electrophysiology 24 h after transfection. The efficiency of transfection was verified by fluorescence microscopy, and cell preparation only proceeded if this efficiency was greater than 50%. Cells were briefly washed in 15 ml PBS, and then 4 ml 1X trypLE (Gibco) was added to the flask, which was incubated at 37 °C for 7 min. Cells were gently dislodged and then 21 ml DMEM (supplemented with 10% FBS but no NEAA or L-glutamine) was added. Cells were pelleted by centrifugation at 100*g* for 90 s, then resuspended in 50 ml FreeStyle 293 and recovered in an incubator operated at 37 °C and 8% CO_2, 130 rpm for 30-60 min.

During this recovery period, Ionflux microfluidic plates were prepared. These contain eight patterns per plate, each with two cell traps that can accommodate 20 cells. Thus, 16 recordings were obtained from each plate, and each recording resulted from the current through an ensemble of 20 trapped cells. Up to 8 channels for drugs (200 µl per well) are available per pattern. The layout of a 96-well format Ionflux plate is illustrated in Figure 2.3 Typically one of the drug channels was reserved for extracellular solution, and the remaining channels contained drugs made up in extracellular solution. The extracellular solution was composed of 137 mM NaCl, 4 mM KCl, 1 mM $MgCl_2$, 1.8 mM $CaCl_2$, 10 mM HEPES and 10 mM glucose, (pH = 7.4), osmolarity 300-310 mOsm. The intracellular

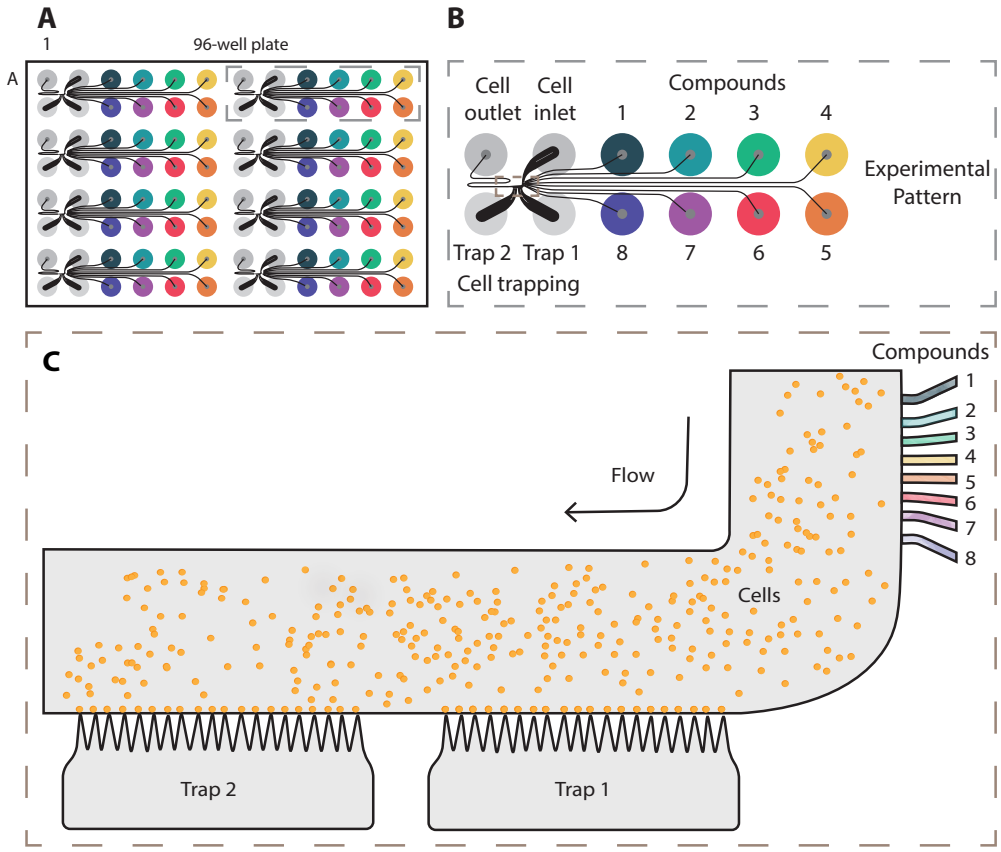

Figure 2.3: Ionflux plate layout. A: The layout of a 96-well format Ionflux plate, illustrating the eight patterns per plate. **B**: One experimental pattern, with the function of each well illustrated. During an experiment, cells are placed in the the 'cell inlet' well, internal solution is placed in the two trap wells, and drugs made up in extracellular solution are placed in the eight compound wells. Currents are recorded by electrodes that are placed in the two trap wells. **C:** An enlarged view of the trap and compound addition area of the plate. Cells initially flow past the traps, where an ensemble is trapped. Later in the experiment, drugs in solution flow out of the eight compound outlets (right) past the trapped cells. Figure modified from the Fluxion website (https://ionflux.fluxionbio.com/)

solution was placed into the appropriate well for each pattern and contained 155 mM CsCl, 5 mM NaCl, 1 mM $MgCl_2$, 10 mm HEPES and 5 mM EGTA, (pH = 7.35, osmolarity = 295-200 mOsm). Following the incubation period, cells were collected from 25 ml of FreeStyle 293 medium by centrifugation at 100 *g* for 90 s, and then resuspended in extracellular solution at a density of 4-5x10^6 mL^{-1}.

The IonFlux instrument was operating using Ionflux (v4) software. Cells were held at -60 mV, and series resistance compensation was set at 80%. The recording was divided into 20 s 'sweeps', with the drugs applied during each sweep pre-set in Ionflux software before the start of each experiment. Electrophysiology data were analysed in IonFlux v4

software, or using custom MATLAB scripts (Appendix D.3)

2.6 Electron microscopy

Single-particle electron microscopy (EM) was used to investigate the structure of purified heteromeric $GABA_A$Rs. This section first gives an introduction to the theory and practice of EM, particularly EM at cryogenic temperatures (cryo-EM) (Section 2.6.1), and then gives details how these processes were conducted (Section 2.6.2).

2.6.1 Introduction to the theory and practice of single particle cryo-EM

The field of cryo electron microscopy (cryo-EM) is currently undergoing a rapid expansion [241], [242]. Although progress in the field has developed steadily, recent developments in both data collection and processing have increased the reach of the technique, both in terms of the resolution achieved and the kinds of samples that can be investigated. It is particularly useful for macromolecular complexes that are difficult to crystallise, such as membrane proteins, and equivalent resolutions to X-ray crystallography have become achievable. Although not without its unique challenges, cryo-EM now presents a viable alternative to X-ray crystallography for determination of macromolecular structure. A basic workflow for cryo-EM is outlined in Figure 2.4.

2.6.1.1 Sample preparation

Once protein has been purified and is ready for visualisation, the sample first needs to be prepared for imaging in an electron microcope. This involves transfer to a support, usually a disc of fine metal mesh called a grid. This grid is usually coated with a carbon support of various kinds, depending on the type of experiment.

Negative stain For negative stain experiments, a layer of continuous carbon is used. This layer of carbon is normally hydrophobic, but can be rendered more hydrophilic by the deposition of charged particles in a glow discharger [243]. The sample is then applied to the grid and embedded in a layer of heavy metal atoms. These envelope the sample

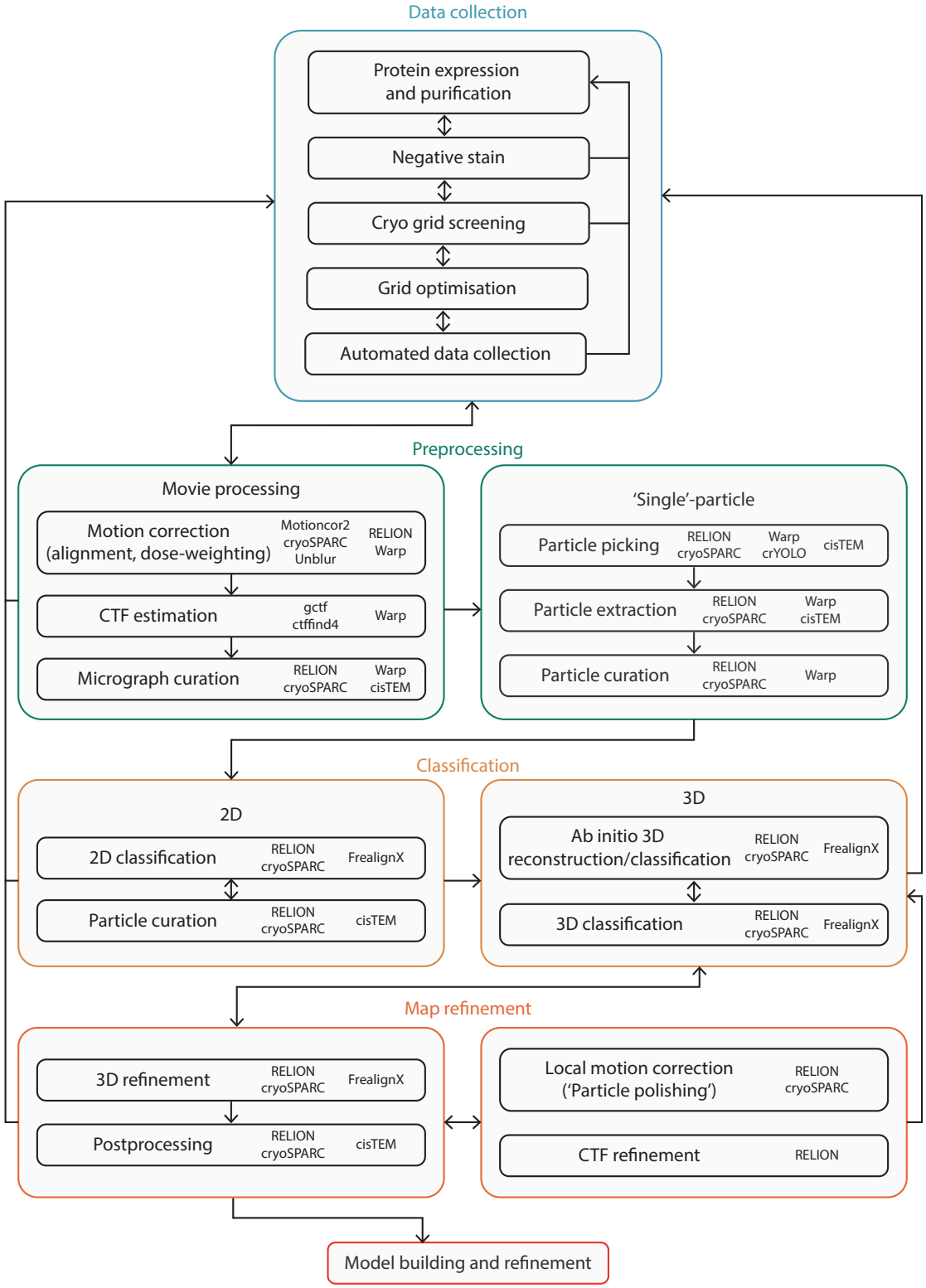

Figure 2.4: Workflow for cryo-EM data collection and processing. The main steps are shown, highlighting transitions between data collection, preprocessing, processing and postprocessing steps. Software used for processing steps are indicated; this are by no means an exhaustive list but indicate of some packages and tools used in this work. Figure modified from the cryoSPARC v2 website (https://v2.cryosparc.com/)

to provide enhanced contrast (hence the name, 'negative staining'). This technique is relatively fast and easy, but the disadvantages of this method are that the crystals formed of the heavy metal enforce a limit on the resolution that can be achieved to ~20Å, and the process of negative staining often introduces artefacts such as flattening of the specimen [244]. Negative stain is often used to screen samples before proceeding to cryo-EM.

Vitrification by plunge-freezing Higher resolution data can be collected by vitrification of the protein of interest in an aqueous buffer. In this process, a grid containing a thin film of liquid is quickly plunged into liquid ethane or propane at around 100 K, typically cooled by liquid nitrogen [245]. Care must be taken to maintain the grid at a temperature below 135 K, since vitreous ice will transition to crystalline ice at temperatures above this threshold [245]. When this technique was developed, samples were deposited on the grid by a nebuliser which generates a fine spray of droplets [245]. However, it is presently more common to apply a larger droplet of sample to the grid (a few µl), blot away the excess liquid with filter paper, and then directly plunge the grid into liquid ethane [246]. This usually results in a thin film of vitreous ice containing the protein of interest, which is sometimes referred to as being in a 'frozen-hydrated' state.

Vitrification allows proteins to exist in the high vacuum of the electron microscope in a near-native state [246], as well as providing some degree of protection from sample degradation as a result of irradiation [247]. However, it is important to optimise the ice thickness present on the grid. If the ice is too thin, proteins will be excluded, and ice that is too thick will reduce contrast in the micrograph [248]. Ice thickness therefore requires optimisation; however, ice is often variable within a single grid and between batches of grids produced at the same time. Some control over the thickness of ice on a grid can be excercised by modifying blotting and glow-discharge conditions, or by adding a small amount of detergent to the sample [248].

Several different kinds of grids can be used for cryo-EM of vitrified samples. Commonly a thin amorphous carbon film with regularly spaced holes is present on the grid, and upon plunge-freezing a thin layer of vitreous ice is formed in these holes [243]. Another alternative is to use 'lacey' carbon, an irregular mesh of thin carbon that provides similar

holes for the formation of thin films of ice. However, carbon is a poor conductor at low temperature and is prone to charging and beam-induced movement, particularly in the z-direction (along the column axis). More structurally stable gold holey films to replace carbon were introduced to combat these difficulties [249].

In cases where it is difficult to obtain a concentration of protein that would result in a reasonable density of particles suspended in ice, it is possible to use thin support substrates to which particles may adhere [248]. Typical supports include thin layers of amorphous carbon, graphene, or graphene oxide [248], [250]–[252]. Except for graphene, these may reduce contrast in micrographs. An alternative method for increasing particle density is to undergo multiple rounds of sample application and blotting before vitrification [253].

One issue with the preparation of cryo-EM grids is the exposure of proteins to a number of surfaces with which they may interact. These include the metal grid bars, holey support, air-water interface and the blotting paper. Of these, the air-water interface tends to create the most issues since the particles lie very close to it just prior to vitrification, and its hydrophobic nature can induce denaturation of proteins [254].

Interaction with the air-water interface can also result in issues with preferential orientation of the protein, where all particles are in the same orientation. A sterotypical view of particles creates issues during data processing, since in order to obtain a faithful reconstruction of a three-dimensional object, a complete sampling of all possible orientations is necessary [255]. Several methods for overcoming this issue have been proposed, including the addition of detergents to change the properties of this interface, by using a support as mentioned above, by modifying the hydrophobicity of the grid by altering glow-discharging parameters, or by modifying the protein itself (e.g. through the addition or removal of affinity tags) [254]. An alternative strategy is to collect datasets with differing tilts; however, the optimal angle for tilted collection must be determined and the tilt must be accounted for during data processing [256].

2.6.1.2 Data collection

Image formation and the contrast transfer function In the microscope, the specimen is exposed to a beam of electrons. Interacting electrons are scattered by the Coulomb

potential of the sample, and scattering events can be elastic or inelastic. In elastic scattering events, momentum is conserved, and these electrons are useful for forming an image of the object. Contrast arises from the fact that some regions of the specimen scatter electrons more strongly than others, and thus fewer electrons arrive at the corresponding portion of the image [246]. This is known as amplitude contrast. Phase contrast, where path differences between unscattered and scattered electrons create interference, is another source of contrast [246]. The application of defocus provides an additional source of phase contrast [257], and is typically required to visualise vitrified macromolecular specimens.

Inelastic scattering occurs when some of the energy carried by the electron is transferred to the sample, and thus momentum is not conserved. This energy deposition damages the specimen, creating radiation damage [247], and was originally observed through the fading of diffraction spots in electron diffraction experiments [258]. The ratio of elastic to inelastic scattering is given by the scattering cross-section, and for carbon atoms which comprise most biological macromolecules of interest, the inelastic scattering section is larger than the elastic one. For example, for every electron that is scattered elastically, three electrons will be scattered inelastically, depositing energy into the sample and contributing to radiation damage [241].

Due to the physical properties of any imaging device, a point source in the sample plane will be imperfectly recreated at the image plane. The function characterising the spread of a delta function during imaging is called the point spread function (PSF). The image acquired of a finite object is thus a convolution of the object with the PSF. The Fourier space equivalent of the PSF is the contrast transfer function (CTF), which describes how contrast is modulated in the microscope, and is a function of spatial frequency, defocus and astigmatism [259].

The effect of the CTF can be visualised in a Fourier transform of the image, manifesting as oscillations with increasing spatial frequency. The presence of partial coherence (a spread of energy of electrons) dampens the CTF at higher frequencies, resulting in a loss of resolution; this can be described by an envelope function [259]. The presence of alternating bright and dark bands with increasing frequency (Thon rings) in the Fourier transform of a micrograph is a consequence of the CTF and its dependence on spatial

frequency, and the decay of these rings with increasing spatial frequency is a consequence of the envelope function.

Since the frequency of CTF oscillation depends on the defocus applied, collection of micrographs at only one defocus would result in a loss of particular spatial frequencies where the CTF is zero. To collect information for these spatial frequencies, typically a range of defoci are applied during data collection.

Microscope components In the microscope, electrons are emitted at the top of the column by the cathode. Older and lower-end microscopes use tungsten filaments for this purpose, whereas this process has been improved by the use of field emission guns (FEGs). These provide a more intense source of electrons, and thus a brighter and more coherent beam [260]. Since the envelope function of the CTF is determined by beam coherence, a more coherent source contributes to the preservation of high resolution information in images.

The cathode is kept at high negative potential, whereas the rest of the microscope is at ground potential [259]. This provides an accelerating voltage (also known as 'high tension'), which is typically 120-300 keV. Usually high-resolution data is collected at 300 keV, since at higher voltages the microscope resolution, depth-of-focus, aberrations, and beam penetration improve [261].

If air were present inside the microscope column, the emitted electrons would be immediately scattered. Therefore, a high vacuum is maintained inside the microscope at all times, and samples are introduced through an airlock. This presents a problem for the examination of specimens containing or suspended in liquid water. The solution is vitrification and maintenance of samples at liquid nitrogen temperatures (see Section 2.6.1.1). Under these conditions, the vapour pressure of water is negligible [259], and maintenance of the vacuum also becomes necessary to prevent contamination of the sample by water vapour which can deposit on the cryo-specimen to form crystalline ice.

Electrons exiting the cathode are focused by a system of condenser lenses, typically two or three. These are magnetic lenses that can modulate the path of the electron beam as it passes through. A three condenser lens system provides a larger set of conditions under

which the beam incident on the specimen is parallel; if only two are present then their strengths must be carefully adjusted to achieve parallel illumination [262]. In practice, care is only taken to adjust the optics to obtain parallel illumination for high-resolution data collection, and for screening this practice is rare.

The beam then enters the objective lens, which is the first image-forming lens of the microscope. Typically these have small focal lengths, so the specimen must be placed inside the lens itself [259]. Here, an image is formed by the interaction of electrons with the specimen. For a thin sample, the majority of electrons remain unscattered and pass through the object.

Objective lens aberrations are one of the limiting factors on microscope resolution [259]. Spherical aberration creates the effect that the focal length for rays further from the optical axis is different than for those that are closer. Chromatic aberration results in focusing of electrons with slightly different energies (and hence different wavelengths). Axial astigmatism is due to imperfections in magnetic lenses, resulting in differences in the way specimen features are imaged depending on their orientation in the specimen plane.

An objective aperture is located at the back focal plane. This aperture determines the portion of scattered rays that form the image, and screening out highly scattered electrons increases amplitude contrast [259].

As an alternative to an objective aperture, a phase plate can be placed at the back focal plane. Early types were comprised of a thin film of amorphous carbon with a small central hole, and the interaction of the beam with the carbon results in a phase shift. Although these devices increase the contrast present in the images, they do not alter the signal to noise ratio [263]. Devices of this type such as the Zernike and Hilbert phase plates have been used [264]. However, these suffered from issues with short lifetimes before degradation, fringing artefacts and practical difficulties in the precise alignment of the plate [265].

The Volta phase plate (VPP) is also comprised of a thin (~10 nm) film of amorphous carbon, but without the central hole [266]. When placed at the back focal plane of the microscope, a Volta potential develops immediately above the surface of the carbon which causes a phase advance that increases with the overall dose on the film, although the mechanisms underlying this potential are unknown [266]. This causes a phase shift,

which increases in magnitude with the length of time that the VPP is exposed to the beam. Data can be collected with a VPP in focus, but the accuracy required for focusing presents practical difficulties that hinder this approach [267]. On the other hand, the introduction of a small (around -500 nm) defocus has been successfully used to collect high-resolution (>3 Å) data [268].

Finally, after the beam passes through the sample and the projector lens system that project the image of the specimen onto a detector or fluorescent screen. Changes in strength of the projector lenses change the magnification of the projected image, and thus the Nyquist frequency (discussed in further detail below) and resolution that can be achieved.

Direct electron detectors Finally, the recent rapid development of cryo-EM is in large part due to the development of much-improved detectors [261]. Two measures of detector fidelity are detective quantum efficiency (DQE) and modulation transfer function (MTF).

DQE is a measure of how the physics of the detector degrades the signal, and is calculated as the ratio of the squares of the signal to noise ratios (S/N) entering (in) and exiting (out) the device [269] (Equation 2.7).

$$\mathrm{DQE}=\frac{(\mathrm{S/N})^2_{\mathrm{out}}}{(\mathrm{S/N})^2_{\mathrm{in}}} \tag{2.7}$$

A DQE of unity would imply a perfect detector; that is, all incoming information is preserved perfectly. However, since detectors are pixelated, the maximum spatial frequency that can be sampled is a function of the pixel size. The Nyquist frequency (f_N) is the maximum resolvable spatial frequency (Equation 2.8).

$$f_N=\frac{1}{2\cdot \mathrm{pixel\,size}} \tag{2.8}$$

The pixelated nature of detectors fundamentally limits their fidelity; for example, the DQE at the Nyquist frequency of a perfect pixel detector is 0.405 [270].

The MTF is another measure of detector performance, and specifies how strongly the various spatial frequencies in an image are recorded. The MTF of a detector is determined by factors such as pixel size and spread of electrons through the active layer of the detector [261].

The first detector used in electron microscopy was photographic film. Although inconvenient in terms of processing steps required, the DQE of film at half-Nyquist (30-35%) is significantly better than that of early digital detectors using charge-coupled devices (CCDs; 7-10%) at 300 keV [270]. This is in part due to the inefficiency in CCD-based detectors: film directly detects electrons though their interaction with silver halide crystals (grains) [271], whereas CCDs can only indirectly detect electrons after their conversion to photons by a scintillator [261]. Therefore, until quite recently, high-resolution cryo-EM structures were solved with data captured with film [261].

Presently, complementary metal oxide semiconductor/monolithic active pixel sensor (CMOS/MAPS)-based detectors have improved sensitivity due to their direct detection of electrons. Commonly used are the Falcon III from FEI/Thermo Fisher Scientific [272] and K2 Summit from Gatan [273], which both have DQE at half-Nyquist significantly higher than film (40-60%) in 'linear' mode [269].

DQE is further improved for these detectors by the use of 'counting' mode, in which the dose rate is low and individual electrons can be detected and replaced by a delta function [261]. The high frame rate afforded by the use of CMOS technology is cruical for reducing missed or overlapping events, and greatly improving the signal-to-noise ratio. In principle, the use of counting mode allows collection of data retaining information beyond the Nyquist frequency.

A second advantage of the higher frame rates made possible by these detectors is that fractionation of the entire exposure is made possible such that a 'movie', rather than a micrograph, is collected. This allows alignment of individual frames to account for both instability in the stage and motion induced by the electron beam to restore high-resolution information [273] (see also Section 2.6.1.3).

Microscope alignments To have the best chance of collecting high-resolution data, the optical elements of the microscope must be carefully chosen and aligned. The condenser aperture removes electrons with a large angular spread from the beam, with a corresponding improvement in coherence. However, a smaller aperture also results in a weaker beam, so the smallest aperture giving the desired fluence should be chosen [243]. To align the

microscope, the apertures are centred with respect to the optical axis of the microscope, working from the top of the column downwards. Astigmatism in each of the lenses should also be minimised as much as possible. Care should be taken to align the electron beam parallel to the optical axis of the objective lens; failure to do so results in axial coma, an image aberration that is difficult to account for computationally and can degrade the high-resolution information in the projected image [274].

2.6.1.3 Data analysis

After a dataset has been collected, further processing steps are required to generate a 3D density map from the 2D projections recorded. The first of these are the preprocessing steps, in which frames from movies collected during the exposure are aligned, motion-corrected and flattened into a single micrograph; the CTF for each micrograph is estimated; and the locations of the individual particles in the micrographs are recorded. Next the data is processed to reconstruct a 3D density map of the imaged particle. Several software packages are available that provide a 'pipelined approach' to data processing, performing all steps necessary for 3D reconstruction. These include RELION (REgularised LIkelihood OptimisatioN) [255], cryoSPARC [275], and cisTEM [276]. Furthermore, several useful standalone software perform one or a few processing steps, such as Warp for preprocessing steps [277], MotionCor2 and Unblur for motion correction [241], [278], gctf and CTFFIND4 for CTF estimation [279], [280], crYOLO for particle picking [281]. Many other software exist, but the discussion here will be limited to only packages used in the work described in this thesis.

Preprocessing: motion correction, CTF estimation, particle picking and extraction
The first step in preprocessing is necessitated by the use of a direct electron detector to collect data. As elaborated upon in Section 2.6.1.2, these can collect 'movies' with fractionation of the total exposure into frames. Current processing regimes require micrographs, rather than movies, as input, so at a minimum the frames from the movie must be compressed into a micrograph. However, given that beam-induced motion can blur the micrograph, a more efficient use of movie data is to align the frames to

minimise motion in the compressed micrograph [282]. Several algorithms to achieve this goal have been implemented.

The program Unblur iteratively aligns whole frames against an average of other frames, and smoothes the trajectories by fitting with a cubic spline to prevent sudden changes in trajectory [241]. This program also performs exposure weighting while summing over the frames, to correct for the loss of information due to radiation damage [241]. An alternative to Unblur is MotionCor2 [278]. During alignment, this program divides each frame into patches, and iteratively determines the motion of each patch. If the patches are too small to be reliably aligned, larger patches are used. This provides some degree of local motion correction, since the beam-induced motions are not usually uniform over the whole micrograph. MotionCor2 can also perform radiation-damage weighting during summation. Since radiation damage affects high resolution features more quickly than it affects lower resolution features, frames are assigned B-factors and then these are used to weight the averaged micrograph. Newer versions of packages such as Warp, RELION-3 and cryoSPARC v2 also provide their own implementation of these algorithms. At the time of writing, only the RELION-3 and Warp implementations have been described, which are both only slightly different to that of MotionCor2 [277], [283].

After movie frames have been integrated into a micrograph, the next step is to estimate the CTF for each image. Two programs, gctf and CTFFIND4, are typically used for this task [279], [280]. These compute the power spectrum of micrographs, in which the effect of the CTF can been seen in Thon rings, and attempt to fit the parameters of a mathematical function describing the CTF. In gctf, eqiphase averaging, which is a kind of rotational averaging that considers astigmatism, is employed to improve the visibility of Thon rings so as to better fit them [280]. Both programs can now fit micrographs acquired with a phase plate, which introduces additional terms into the description of the CTF [268].

Typically, at this stage micrographs unsuitable for analysis are removed, such as those with defects of the sample such as empty holes, cracks in the ice, large aggregations or particles or significant ice contamination; or of imaging such as large drift or astigmatism. Some packages such as Warp, RELION and cryoSPARC v2 provide automated methods to removed micrographs based on, for example, CTF fit parameters. Visual inspection of

the micrographs and CTF fits is nevertheless important to obtain an overall feel of the dataset and to remove any bad micrographs that have escaped detection.

In a process known as 'particle picking', individual particles are identified in the micrographs and their locations recorded. In early software this was achieved by manually clicking on particles. However, it has become the norm to collect large datasets consisting of thousands of images, so allowing for a few hundred particles per micrograph, this soon becomes a long and laborious process. An alternative is to use an automated method of picking. The simplest of these search for correlations in the images with a simple function such as a Gaussian or a Laplacian-of-Gaussian. This operation is performed by convolution of the image with one of these functions, and then by searching for peaks in the convoluted image [276]. This approach is implemented in RELION and cisTEM.

An extension of this method is to use projections of the imaged particle as templates. However, this approach warrants caution, since using a template to pick only random noise can result in a reconstruction of the original template (known as the 'Einstein-from-noise' [284]). To overcome this issue, references are low-pass filtered and good practice dictates that after picking only 2D classes (see Section 2.6.1.3) that contain higher resolution features should be used [255]. When particles from the dataset are used to produce these references, this process can be considered a from of supervised learning. Recently, developments in the field of machine learning have resulted in more sophisticated methods for particle picking. These also learn features of the particles and background from fully picked micrographs, and have been implemented in Warp and crYOLO [277], [281]

Finally, individual particles are extracted from the whole micrograph along with a small amount of background. A box size of at least 1.5-2 times the largest axis of the particle is required to prevent CTF aliasing in Fourier space due to finite box sizes. Particles extracted in certain packages such as RELION also undergo normalisation of the background, and inversion to convert black particles on a white background to white particles on a black background [255].

Processing: 2D and 3D classification, 3D refinement In theory, the Fourier slice theorem makes the reconstruction of a 3D density map from 2D projections through that map relatively trivial. This theorem states that the Fourier transform of 2D projections through an object are equivalent to a slice through the 3D Fourier space representation of this object. Thus, all that is required is to take the Fourier transform of all the 2D particle images, align them in Fourier space, and then take the inverse Fourier transform to reconstruct the 3D object. These mathematical operations are relatively easy to implement.

However, in practice there are several complicating factors that make this operation decidedly non-trivial. The most significant of these is that the relative orientations of the particles must be known in order to reproduce the macromolecular complex of interest in this way. However, since particles (usually) tumble randomly in solution prior to vitrification, this information is not present in the experimental data. The problem of the reconstruction of a 3D density map has therefore been characterised as an incomplete data problem [285]. If the particle adopts a preferential orientation on grids, a true 3D reconstruction is unlikely to be computed, unless the particle possess significant symmetry which can make up for the lost orientations.

The general approach to finding the relative orientations of single particles is to optimise a likelihood function, which quantifies the agreement between the experimental data and a model, while marginalising over the unknown parameters. However, since the data is noisy and there are many unknown parameters, there are many noisy models that can describe the data equally well [285]. Regularisation is one way to address this issue, in which additional information is used to determine orientations. This additional information is the assumption that the reconstruction is smooth, such that all Fourier components of the data are independent, with a mean of zero and an unknown variance τ [285]. The value of τ is input by the user during the process of classification, and is generally between 2 and 4 [255].

Although 2D classification can proceed without initial references for each class, a 3D reference is required for the optimisation of particle orientations in 3D. This requires generation of an initial model that resembles the 3D structure of the particle, since the results of orientation optimisations can be sensitive to the choice of initial model. Arguably the best algorithm for *ab inito* model generation is stochastic gradient descent (SGD),

as implemented in cryoSPARC. Instead of gradual maximisation of a single likelihood function, which quantifies how well the experimental images explain a 3D density map, many approximate structures are first generated from random subsets of the data. Each iteration involves only a small subset of the data, and so is relatively computationally inexpensive [275]. The 'gradual maximisation' approach is sensitive to initial conditions due to the presence of local minima, but the SGD approach is less insensitive to these and is thus more likely to find the optimal solution.

A complication in cryo-EM data processing is sample heterogeneity. Almost all current methods for 3D reconstruction assume that the 2D projections come from identical copies of the same particle. However, real macromolecular complexes often have substantial conformational heterogeneity which complicates the process of reconstruction. This is usually dealt with through the process of classification, in which a clustering algorithm is applied to separate the particles into distinct classes. In 2D these classes can represent projections of the particle from different angles, or can represent different objects such as different conformations of the protein, or spurious particles such as ice contamination or empty areas of ice. As such, a first round (or two) of unsupervised 2D classification is usually undertaken to remove 'junk' particles from the dataset. Sample heterogeneity is then addressed by undertaking rounds of 3D classification, making use of a reference generated by SGD [255].

3D refinement is used to calculate a final map once a relatively homogenous subset of the data has been obtained [285]. Cryo-EM data are extremely noisy, and overfitting is a danger in refinement. This occurs when the reconstruction describes noise in the data rather than the underlying signal. Since refinement is iterative, these noisy features are often reinforced during refinement [285]. To overcome this, the 'gold standard' is to divide the data into two half-sets, refine each separately, and assess the resolution of the final merged reconstruction as the Fourier shell correlation (FSC) between the two half-maps [285]. The resolution at which the FSC drops below 0.143 is the commonly accepted standard for the nominal resolution of the map [255], [286].

Another method of dealing with heterogeneity that results from the relative movement of rigid portions of the protein is multibody refinement. This involves separate refinement

of user-defined domains of a particle by way of iteratively subtracting out one domain at a time and refining the remaining domains [287]. This can result in better overall reconstructions of large, flexible macromolecular complexes. A similar approach is taken in cryoSPARC, where a new kind of refinement called non-uniform refinement was introduced. At the time of writing, this method is unpublished, however, the v2 documentation (https://cryosparc.com/docs/reference/jobs/) describes this type of refinement as taking into account flexible and disordered regions by dynamically estimating their locations.

Post-processing and per-particle preprocessing refinement Resolution is often underestimated during 3D refinement, since noise in the solvent regions is still present. To extract the most information upon convergence, in post-processing the solvent-noise is removed by the multiplication of the map with a mask that defines the boundaries of the protein, excluding noise from the reconstruction. A new FSC is calculated and the map is filtered ('sharpened') to this new resolution.

Refinement of the preprocessing steps can be undertaken on a per-particle basis. For example, 'particle polishing' fits the beam-induced trajectories of individual particles, rather than whole frames or patches [283], and is implemented in RELION-3 and cryoSPARC v2. Refinement of the CTF parameters on a per-particle basis is also implemented in RELION, although at the time of writing the algorithm for this refinement has not been described in the literature. Although these refinements can be conducted before any other processing, they are also often undertaken after a 3D reconstruction has been obtained, which allows a clear assessment of their putative benefit. In RELION these steps require 3D-refined data as input, and so can be conducted after initial 2D and 3D classification, and 3D refinement. In cryoSPARC, local motion correction can be conducted directly after particle picking. The refined particles after CTF refinement and particle polishing are then subjected to additional rounds of classification and/or refinement.

2.6.1.4 Model building, refinement and validation

Once the final 3D density map has been reconstructed, a molecular model can be built. Unlike in X-ray crystallography, the refined 3D density map does not change during refinement of the model since it does not contribute any information to the calculation

of the map. The aim of model building and refinement is to maximise the real space correlation between the experimental map and one that would be generated by the model [288]. This process is generally undertaken by rounds of manual adjustment in a visualisation program such as Coot [289], and automated refinement in software packages such as Phenix (using phenix.real_space_refine [290]).

Since the number of parameters in the atomic model are large, care should be taken to avoid overfitting. One method proposed to cross-validate a refined atomic model is as follows [288]:

1. Use the final, sharpened (full) density map to build and refine the atomic model.
2. Randomly displace the coordinates of the atoms in the refined atomic model by 0.5-1.0 Å, or as much as reasonably possible.
3. Refine the randomised model against both half-maps.
4. Calculate differences between models refined against each half-map.

Divergence between these models indicates some overfitting, although this method may underestimate the degree of overfitting present.

Model quality assesment A way of assessing the quality of a refined model is by applying prior knowledge of likely chemical structure. One example of this approach is the Ramachandran plot, which refers to the torsion angle of the N-Cα (φ) and Cα-C (ψ) bonds for each residue in the main polypeptide chain. Based on knowledge of chemical structure, certain angles are favoured, allowed or disallowed. Measuring these angles for each of the residues in the model and inspecting the resulting Ramachandran plot provides another way of assessing the plausibility of a refined model [291].

Further validation can be obtained from a consideration of all atoms in the model, as exemplified by the analysis carried out by MolProbity. This package also considers model features such as atoms that have been built too close to one another (clashes) and likelihood of rotamers. This provides another useful tool for assessing model quality before the final task of interpreting a refined model begins.

2.6.2 Electron microscopy performed

2.6.2.1 Addition of drugs and formation of nanobody- or -megabody-$GABA_AR$ complexes

The addition of drugs and nanobodies or megabodies occurred just prior to making EM grids. Nanobodies were purified as described in Section 2.3.3, and megabodies [42] were provided by Tomas Uchanski and Jan Stayert.

2.6.2.2 Grid preparation for negative stain electron microscopy

Uranyl formate was made up at a stock concentration of 2% (w/v), dissolved in ultrapure water by vigorous agitation. NaOH was added at a final concentration of 0.01 N, and the mixture was filtered (0.2 µm), aliquoted and stored at -20 °C, protected from light, until use. This uranyl formate solution was typically diluted to 0.5-1% before use.

To make negative stain grids, 300 mesh copper grids with a carbon coating (Agar Scientific) were glow-discharged in an Edwards Sputter Coater S150B at 0.2 mBar and 30 mA for 30 s. 4 µl protein (typically $GABA_ARs$ at a concentration of 0.02-0.03 mg ml^{-1}) was applied to the carbon side of the grid and incubated for 30-60 s, then removed by blotting with filter paper (Whatman No. 1). This was quickly followed three washes, touching the grid to a 40 µl drop of ultrapure water then blotting the liquid away with filter paper. The grid was then washed with the prepared uranyl formate solution in the same manner, before incubation with uranyl formate solution for 30-60 s. Grids were air-dried and then stored until use.

2.6.2.3 Data collection for negative stain electron microscopy

Negative stain grids were imaged on an FEI Tecnai Spirit transmission electron microscope (TEM) equipped with a Gatan Orius S C200B camera. The microscope was operated at 120 keV and images were collected at a nominal magnification of 15,000-30,000X, corresponding to a pixel size of 3.5-1.78 Å, with a defocus between -2 µm and -4 µm, and a fluence of 20-80 $e^- Å^{-2}$. Micrographs were collected with Digital Micrograph software (Gatan).

Table 2.18: Preparation of grids used for cryo-EM

Grid type	Mesh	Holes (µm)	Glow discharge settings	Blot time (s)	Blot force
Quantifoil Au	400	1.2/1.3	0.2 mBar, 30 mA for 30 s	5-6	-15
UltrAuFoil	400	1.2/1.3	0.2 mBar, 30 mA for 30 s	5-6	-15
Ultrathin carbon Cu	300	Lacey	0.2 mBar, 30 mA for 30 s	8-9	-15
UltrAuFoil, GO coated	400	1.2/1.3	N\A	5-6	-15

2.6.2.4 Graphene oxide deposition on grids

Where protein concentration was low, graphene oxide (GO) was deposited on grids as a support before sample application [250], [251]. Grids were glow-discharged in an Edwards Sputter Coater S150B at 0.2 mBar and 30 mA (Quantifoil) or 40 mA (UltrAuFoil) for 30 s. 3 µl of GO solution (Sigma, diluted to 0.2 mg ml^{-1}) was applied to the top side of the grid and incubated for 60 s. The grid was then washed twice on the top side with 10 µl drops of ultrapure water (which was removed with filter paper, Whatman No. 1), then washed on the back side of the grid in the same way. Coated grids were air-dried and then stored in a sealed chamber with a desiccant until use (at least 4-5 h).

2.6.2.5 Cryo-EM grid preparation

Cryo grids were prepared with a Vitrobot (Mark IV, FEI) operated at 4 °C and 100% humidity. 3.5 µl of purified $GABA_AR$ (0.1-0.5 mg ml^{-1}) was applied to the grid as detailed in Table 2.18. Where sample concentration was low, 2-3 rounds of blotting were sometimes conducted, or graphene oxide-coated grids were used [253]. This took place with the grid inside the vitrobot chamber, with sample applied through the side port as normal, and all but the final blot done manually with blotting paper (Whatman No. 1) inserted through the side port. The final blot was conducted as usual with the vitrobot, except that the blot time usually increased by 2-3 s. After blotting, the grid was vitrified by plunging into liquid ethane cooled by LN_2, then quickly transferred to LN_2 and stored in a grid box under cryogenic conditions.

2.6.2.6 Data collection for cryo-EM

Cryo grids were screened on an FEI Tecnai Spirit TEM equipped with a Gatan Ultrascan 1000 CCD and operated at 120 keV, or an FEI Technai G^2 F20 TEM equipped with

an FEI Falcon II direct electron detector (DED) and operated at 200 keV. Grids were transferred to a 626 single tilt liquid nitrogen cryo-transfer holder (Gatan) which was placed inside the microscope. Data were acquired using low dose mode in the Techani User Interface to limit the exposure of the specimen to the electron beam before imaging. Digital Micrograph (Gatan) or Technai Imaging and Analysis (FEI) were used to collect micrographs. Typically, data were collected at a nominal magnification of 26,000X (pixel size 3.95 Å, Spirit) or 50,000X (pixel size 2.08 Å, F20), with a defocus between -2 µm and -4 µm, a fluence of 20 e^{-} $Å^{-2}$ and exposure time of 2 s. During initial screening, grids were assessed for ice thickness and particle distribution.

For higher resolution reconstructions, data were collected in 24-72 h shifts on an FEI Titan Krios equipped with a Volta Phase Plate (VPP) and Falcon III detector (FEI). Data collection proceeded using EPU (FEI), and after microscope alignments, grid squares and holes with an appropriate thickness of ice were selected for automated data acquisition. The VPP was then aligned and data were acquired with autofocusing typically once every 10 µm, drift measurement once per grid square, and a defocus in the range of -0.5 µm to -0.7 µm. A nominal magnification of 75,000X was used, resulting in a calibrated pixel size of 1.055-1.084 Å (depending on the particular microscope used), and a total fluence of 30 electrons/$Å^2$ was used over an exposure time 60 s. A total of 75 frames were collected, and the detector was operated in counting mode.

2.6.2.7 EM data processing

Preprocessing steps for EM data processing were carried out making use of the pipelined approach and wrappers provided by the RELION [292], cryoSPARC [275], cisTEM [276] or Warp [277] packages. Occasionally, single software tools such as Motioncor2 [278], Gctf [280] or crYOLO [281] were used for motion correction, CTF estimation or particle picking, respectively.

Further processing of extracted particles was mainly conducted in RELION and cryoSPARC. Generally, 1-4 rounds of 2D classification was carried out, followed by further rounds of 3D classification and gold-standard refinement. Further correction for local particle motion was optionally carried out in RELION ('bayesian particle polishing') [283]

and cryoSPARC ('local motion correction'), and per-particle refinement of CTF parameters was carried out in RELION. More details of the processing of individual datasets can be found in Chapter 5, and of individual packages in Appendix 2.6.1.3.

3

Generation and screening of nanobodies against α(2/3)-containing $GABA_AR$s

Contents

3.1 Introduction 86
3.2 Characterisation of nanobodies against α1β3 $GABA_AR$ 89
3.3 Preparation of α(2/3)β3 $GABA_AR$s for nanobody generation 91
3.4 Purification of nanobodies against α(2/3)β3 $GABA_AR$s 95
3.5 Kinetic characterisation of nanobodies against α(2/3)β3 $GABA_AR$s 97
3.6 Functional characterisation of nanobodies against α(2/3)β3 $GABA_AR$s 102
3.7 Discussion 104

3.1 Introduction

3.1.1 Nanobody properties and uses

Nanobodies, the binding domain (VHH) of heavy-chain antibodies (HCAbs, see Figure 1.5), have been found to be useful reagents in a variety of applications [293]. These include their use for protein purification and immunoprecipitation, by attaching a specific nanobody to agarose beads to form an immunoaffinity column. Nanobodies can also act as negative or positive allosteric modulators, and so can be useful to trap a protein in a particular conformation for structural studies, or to study the functional properties of the receptor.

They can also facilitate protein crystallisation as chaperones, helping a protein-nanobody complex to pack into a crystal form through the formation of favourable crystal contacts. Finally, nanobodies have been used as tracers for *in vivo* intracellular target localisation studies, or as tools that enable sensitive detection of biomarkers or diagnostic imaging.

One example in basic research is the use of nanobodies fused to fluorescent proteins, which can be transfected and expressed in cells to visualise target proteins [294]. Another example is the 'CaptureSelect C-tag' VHH, a nanobody recognising a C-terminal EPEA motif which can be used for protein purification. Although there appears to be a preference for nanobodies to bind to concave surfaces in folded proteins, the EPEA nanobody demonstrates the possibility of binding to small linear epitopes [293]. Approaches have also been developed to generate nanobodies that can cross cell membranes and therefore the blood-brain barrier, based on an electrostatic interaction between a cationic protein and the anionic charges present on the cell surface [295]. An extension of this method is the addition of cleavable arginine-rich peptides to nanobodies, which results in their accumulation in intracellular compartments [216]. There is also considerable interest in developing nanobodies as therapies, with companies such as Ablynx and Theranyx pursuing several leads to develop nanobody drugs.

Nanobody properties that are of prime interest for structural biology include their utility as crystallisation chaperones [33], [217], and their use to break the pseudo-symmetry of objects in cryo-EM studies [40]. This can enable the high-resolution determination of structures for proteins that have previously been difficult to study. In the present work, nanobodies were made use of for both protein crystallography and cryo-EM, and more details on these applications is given in Chapter 5.

Nanobodies that have functional effects upon binding have also been observed, such as those raised against the β_2-adrenergic receptor (β_2-AR) [215]. These nanobodies were shown to stabilize various active and inactive states of this receptor by allosteric effects. This modulation led to the determination of modulated states of the receptor by X-ray crystallography. Nanobodies performing the same function for $GABA_A$Rs would be of great interest, not only for determining the structure of functional states of the receptor as for the β_2-AR, but also as potential leads for therapeutics.

Table 3.1: Nanobodies previously raised against an α1β3 $GABA_AR$

Family	Original reference number	Reference in this work	Other notes
	CA8125	α1β3nb125	β3-specific
1	CA8126	α1β3nb126	
	CA8127	α1β3nb127	
2	CA8137	α1β3nb137	
3	CA8143	α1β3nb143	
4	CA8129	α1β3nb129	β3-specific
5	CA8130	α1β3nb130	α1-specific, positive modulator
6	CA8134	α1β3nb134	
7	CA8135	α1β3nb135	
8	CA8139	α1β3nb139	
9	CA8124	α1β3nb124	
10	CA8131	α1β3nb131	
11	CA8132	α1β3nb132	
12	CA8136	α1β3nb136	
13	CA8138	α1β3nb138	α1-specific positive modulator; referred to as 'Nb38' by Miller and colleagues [40]
14	CA8141	α1β3nb141	
15	CA8142	α1β3nb142	
16	CA8128	α1β3nb128	

3.1.2 Existing $GABA_AR$ nanobodies and aims of this chapter

The aims of the work described in this chapter were: 1) to further characterise existing nanobodies raised against an α1β3 $GABA_AR$, and 2) to raise and characterise new nanobodies against the α2β3 and α3β3 $GABA_ARs$.

Prior to the commencement of this work, nanobodies had previously been raised and characterised against α1β3-containing $GABA_ARs$ by Paul Miller and Simonas Masiulis [40], [296]. Nanobodies were raised against an α1β3 $GABA_AR$ by immunisation of a llama and construction and screening of a nanobody display library, in collaboration with Els Pardon and Jan Stayert. This resulted in the identification of 18 nanobodies binding this $GABA_AR$ (Table 3.1). These nanobodies were originally given the designations CA8xxx; however, in order to clearly identify these nanobodies as raised against a α1β3 $GABA_AR$, and to facilitate comparisons between these nanobodies and others discussed in this chapter, they will be referred to as α1β3nbxxx, where xxx is the last three digits of the original designation. Similarly, nanobodies raised against α2β3 and α3β3 $GABA_ARs$ will be referred to as α2β3nbxxx and α3β3nbxxx.

Some of these nanobodies had interesting properties [296]. Some were found to be β3- or α1-specific, on the basis of their binding at β3 and α1β3 $GABA_ARs$. These include

α1β3nb125 and α1β3nb129. Others were found not to bind β3 homomers, and were therefore considered α1-specific. These include α1β3nb130 and α1β3nb138. In line with previous reports of functionally active nanobodies [297], [298], these two α1-specific nanobodies were also found to be positive modulators of α1-containing $GABA_A$Rs.

In regard to the second aim, α(2/3)-containing $GABA_A$Rs were chosen as new nanobody targets because of their physiological properties. α1-, α2-, and α3-containing $GABA_A$Rs are thought to be the main $GABA_A$Rs in the synapse [10]; and as discussed at length in Section 1.4, α(2/3)-containing receptors play important roles in physiological processes such as pain and anxiety [147].

Several methods have been described to raise HCAbs, for nanobody production [214], [299], [300]. Nanobodies can, in theory, be raised in any animal that naturally develops HCAbs against antigens, including camelids such as camels, llamas and alpacas, as well as certain species of shark [209], [211]. In practice, llamas are commonly used to generate nanobodies, and sera from immunised animals can be used to generate a display library [214], [299]. This library can then be screened for nanobodies binding the protein of interest, for example by phage display and selection against the protein of interest [214]. An alternative to Llama immunisation is *in vitro* evolution of an existing nanobody by alternate rounds of error-prone PCR and selection by a display technique [299]. In the present work, the former approach was taken, because of the demonstrated success of this method [214], and the availability of expert collaborators to carry it out.

3.2 Characterisation of nanobodies against α1β3 $GABA_A$R

As a first step, the characteristics of nanobodies against an α1β3 $GABA_A$R that had been raised previously were examined. Previous work by Simonas Masiulis and Paul Miller had identified α1β3nb138 as a tight binder at α1β3 receptors with functional effects [296]. To study the properties of this nanobody, it was first expressed by transfection of pHLsec-α1β3nb138-avi-his into HEK293T cells grown in roller bottles. The polyhistidine-tagged nanobody was then purified by IMAC after buffer exchange by diafiltration. The IMAC eluate was then subjected to SEC (Figure 3.1A) on a Superdex 75 16/600 column. SDS-PAGE analysis identified a main band of ~20 kDa, consistent with the theoretical molecular

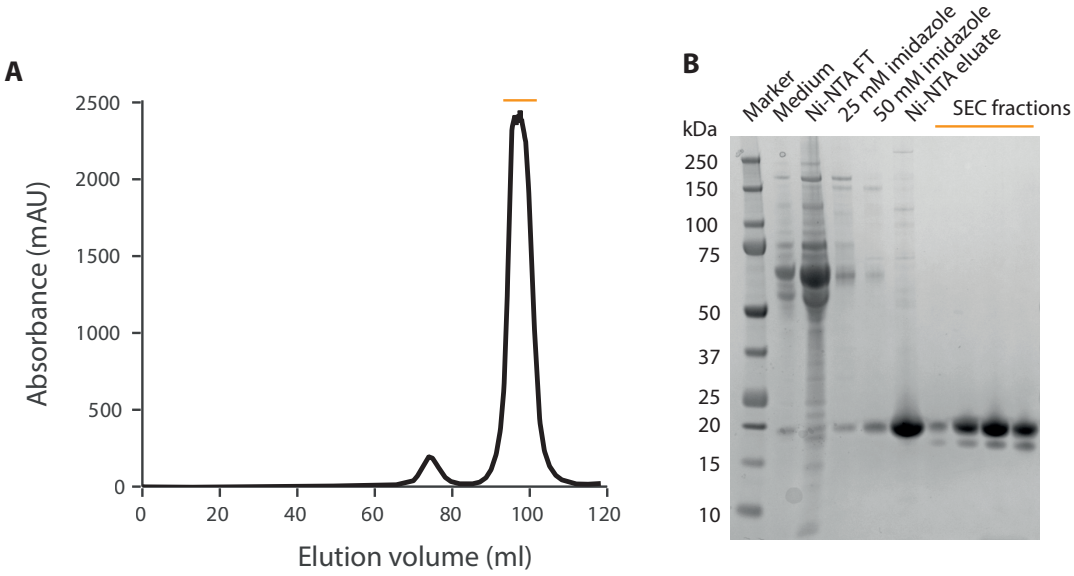

Figure 3.1: Purification of α1β3nb138. A,B: SEC chromatogram (**A**) and Coomassie SDS-PAGE (**B**) from the purification of α1β3nb138 after expression in HEK293T cells (six roller bottles).

weight of 19.5 kDa, as well as a less prominent band of ~18 kDa, presumably the result of proteolytic cleavage (Figure 3.1B). Consistent with the favourable biochemical properties of nanobodies, yields of 3-6 mg per litre of medium were obtained, and the protein could be concentrated to ~1 mM.

The binding of α1β3nb138 to a biotinylated α1β3γ2 $GABA_AR$ (sample provided by Simonas Masiulis) was assessed by kinetic titration using surface plasmon resonance (SPR). The $GABA_AR$ was applied to one flow cell (fc2) of the chip to a level of ~8300 RU, but not to a reference cell (fc1). A two-fold dilution series of α1β3nb138 was then applied to both flow cells and the fc2-1 response was monitored (Figure 3.2). A 1:1 Langmuir binding model was used to fit this data, making the assumption that if multiple sites are present on each $GABA_AR$, these are equivalent and so binding at each site is independent. This model gave a k_a of (4.83 ± 0.08)x10^5 M^{-1} s^{-1}, k_d of (3.20 ± 0.04)x10^{-3} s^{-1}, and R_{max} of 28.0 ± 0.1 RU (χ^2 = 1.15 RU^2). Based on this fit, a K_D of 6.6 ± 0.2 nM was calculated.

The functional effects of purified α1β3nb138 were then examined using an Ionflux machine to conduct automated patch-clamp electrophysiology (Figure 3.3). $GABA_ARs$ were expressed in HEK293T cells by transfection of a 1:1:2 mixture of full-length α1-6, β3 and γ2L subunits. For the α subunit, untagged α1 (pHLsec-α1) or 1D4-tagged α2-6

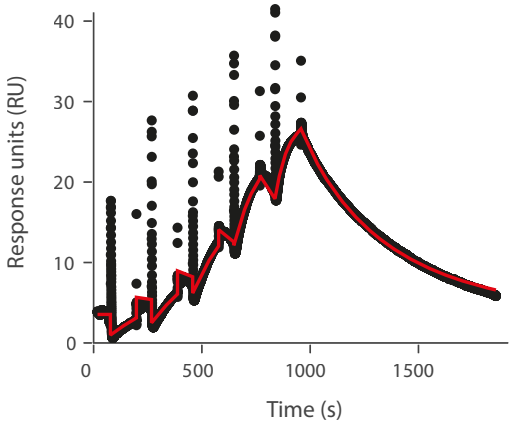

Figure 3.2: Kinetics of $GABA_AR$-α1β3nb138 binding assessed by SPR. Response (fc2-1) of the analyte α1β3nb138 applied to the ligand α1β3γ2 $GABA_AR$ (adsorbed to the chip at a level of 8300 RU). Black points indicate the sensorgram, and in red is the fit from Biacore Evaluation T200 software. See text for details of fit.

(pHLsec-α2-1D4 through pHLsec-α6-1D4) were used. For the β subunit, untagged pHLsec-β3 was used, and for the γ subunit, pHLsec-SBP-γ2L-1D4 was used. α1β3nb138 was diluted in external solution and applied at concentrations of 0.3-30 μM.

When co-applied with an EC_{10} dose of GABA, α1β3nb138 showed strong potentiation of α1β3γ2 receptors (Figure 3.3A, C), with an EC_{50} of 1.0±0.4 μM, but no potentiation at α2β32 receptors up to concentrations of 30 μM (Figure 3.3B, C). The potentiation of α1-6β3γ2 receptors in response to a 1 μM and 10 μM dose of α1β3nb138 was also examined, with only α1β3γ2 receptors showing significant potentiation (mean fold-change from EC_{10} GABA dose alone > 1, one-sample t-test, $p<0.05$). The fold-changes for α1β32 receptors were 2.5±0.6 (n=7) and 4.8±1.5 (n=6) for 1 μM and 10 μM, respectively.

3.3 Preparation of α(2/3)β3 $GABA_ARs$ for nanobody generation

To raise HCAbs in llamas, α2β3 and α3β3 $GABA_ARs$ were first purified. These receptors were expressed by transfecting HEK293S GnTI$^-$ cells in suspension with a 1:1 mixture of pHLsec-α2glvi-1D4 or pHLsec-α3glvi-1D4 with pHLsec-β3glvi. The 1D4 purification tag was placed only on the α subunit to avoid purification of homomeric β3 channels.

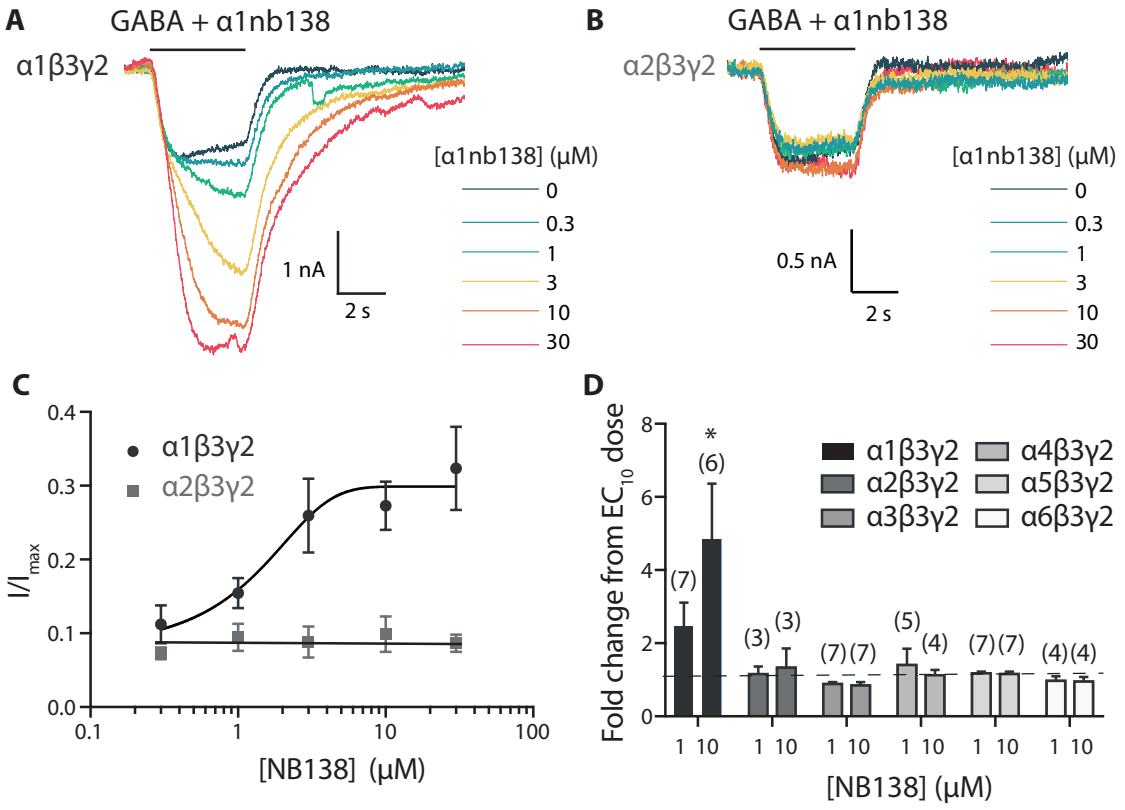

Figure 3.3: Electrophysiological characterisation of α1β3nb138. A,B: α1β3nb138 potentiation of EC_{10} GABA at α1β3γ2 (A) and α2β3γ2 (B) receptors. **C**: Dose-response for α1β3nb138 potentiation at α1β3γ2 (n=5) and α2β3γ2 (n=3) receptors. Currents were normalised to a dose of GABA that evoked a maximal current (I_{max}). **D**: Potentiation of EC_{10} GABA at α1-6β3γ2 receptors. n given above each bar * indicates the mean is significantly different to 1 (indicating no change), $p<0.05$. All data are mean ± SEM.

GABA$_A$Rs were purified using DMNG and CHS to solubilise the cells, followed by 1D4 affinity chromatography. After elution from 1D4 resin, initially the protein was concentrated and injected onto a Superose-6 Increase (10/300) column (Figure 3.4A). However, the sample appeared to be polydisperse after concentration and only a small peak was observed (c.f. a homomeric β3 channel in Figure 3.5F); instead, in future purifications the eluate was loaded directly onto a larger Superdex 200 16/600 column (Figure 3.4B). Under these conditions, the sample appeared more monodispersed, with only a small shoulder visible in the chromatogram.

α2β3 and α3β3 GABA$_A$Rs were then purified using this method (Figure 3.5). ~1 mg each of α2β3 and α3β3 GABA$_A$Rs were required for llama immunisation. The GABA$_A$Rs α2glvi-1D4/β3glvi (Figure 3.5A, B) and α3glvi-1D4/β3glvi (Figure 3.5D, E) were purified

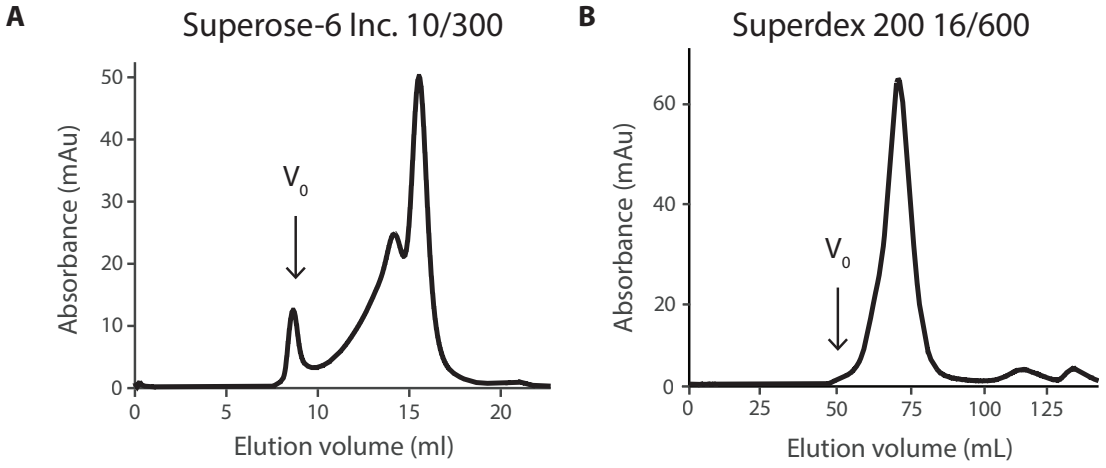

Figure 3.4: α2β3 $GABA_AR$ stability is negatively affected by concentration by ultrafiltration. Protein stability was negatively affected by concentration by ultrafiltration. **A**: SEC chromatogram for an α2β3 $GABA_AR$ after concentration on a Superose-6 Increase 10/300 column. **B**: SEC chromatogram for an α2β3 $GABA_AR$ without concentration on a Superdex 200 16/600 column.

for this purpose. To enhance the probability of finding functional modulators in the raised antibodies, both αβ $GABA_ARs$ were purified in the presence of 1 mM GABA.

Furthermore, biotinylated protein was required for selection of each nanobody library. Therefore, pHLsec-α2glvi-1D4 or pHLsec-α3glvi-1D4 were co-transfected with pHLsec-β3glvi-avi, and biotinylated *in vitro* before SEC. The success of the biotinylation reaction was then verified by western blot (Figure 3.5). Typical yields for αβ $GABA_ARs$ were ~0.2 mg for each litre of suspension cells.

Amongst the α1β3 nanobodies, those that bound the α1 subunit tended to functionally modulate the receptor. Therefore, a biotinylated β3 $GABA_AR$ was purified in order to select for β3-specific nanobodies (and by a process of elimination, α2- and α3-specific nanobodies). A biotinylated β3 $GABA_AR$ was expressed with a 1:1 mixture of pHLsec-β3glvi-avi and pHLsec-β3glvi-1D4 DNA. This protein was biotinylated *in vivo* by cotransfection with BirA-ER and inclusion of D-biotin in all media. This protein was better behaved during purification as compared to αβ $GABA_ARs$, and could be concentrated and subjected to SEC on a Superose-6 Increase 10/300 column (Figure 3.5F, G). Biotinylation was again confirmed by western blot with streptavidin-HRP (Figure 3.5H).

The purified α(2/3)β3 and β3 $GABA_AR$ proteins were then sent to Nele Buys, Els Pardon and Jan Steyaert, collaborators at Vrije Universiteit Brussel (VUB), who raised HCAbs

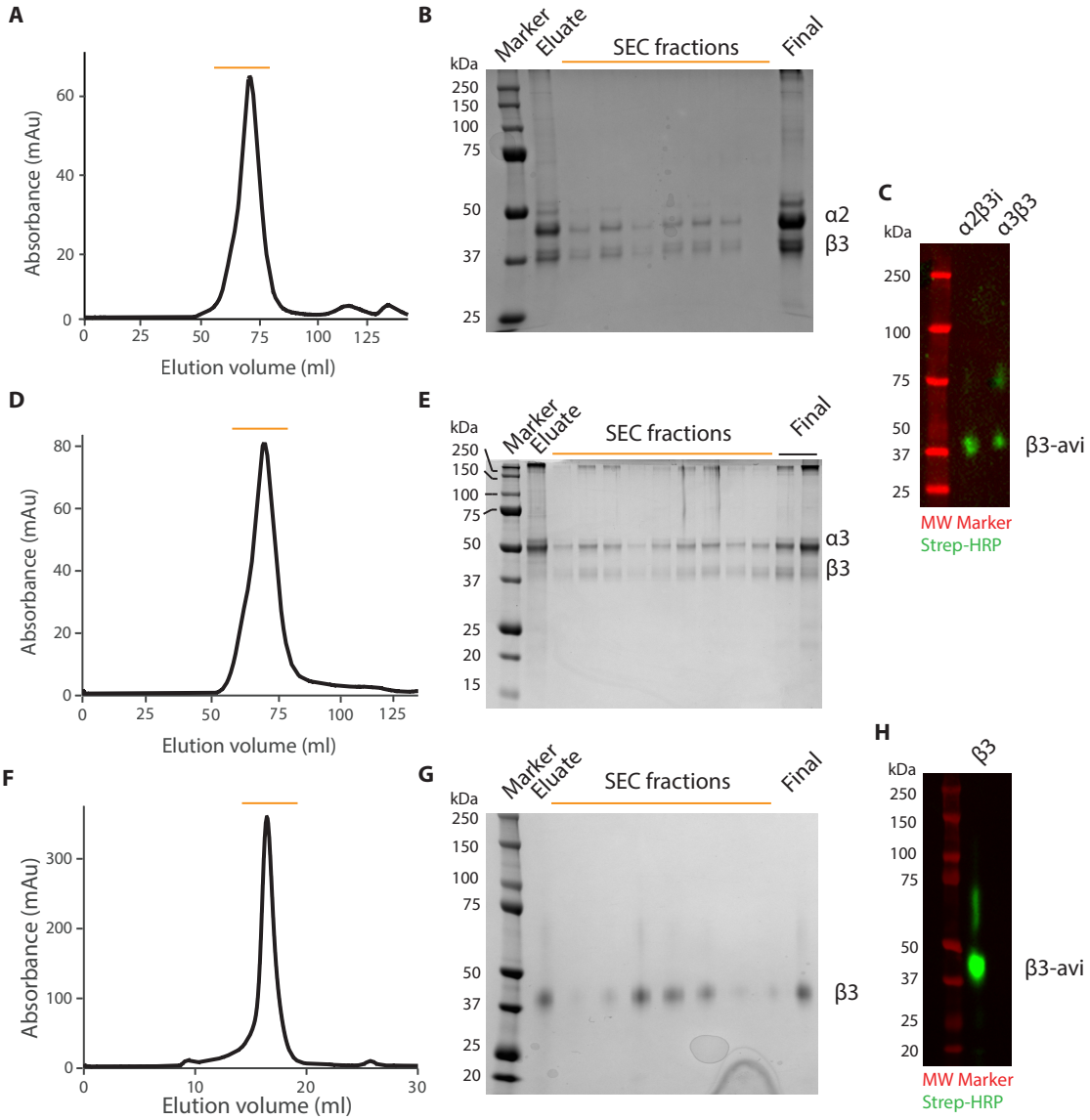

Figure 3.5: α2β3, α3β3, β3 $GABA_AR$ purifications. **A, B**: Purification of an α2β3 $GABA_AR$, showing a typical chromatogram (**A**) and Coomassie SDS-PAGE (**B**). **C**: Detection of biotinylated protein in a western blot of α2glvi-1D4β3-avi and α3glvi-1D4β3-avi $GABA_ARs$ with streptavidin-HRP. **D, E**: Purification of an α3β3 $GABA_AR$, showing a typical chromatogram (**D**) and Coomassie SDS-PAGE (**E**). **F, G**: Purification of a β3 $GABA_AR$, showing a typical chromatogram (**F**) and Coomassie SDS-PAGE (**G**). **H**: Detection of biotinylated protein in a western blot of β3-1D4β3-avi $GABA_AR$ with streptavidin-HRP. For **B**, **E** and **G**, samples taken from the eluate from 1D4 resin, SEC fractions and pooled fractions ('Final') are indicated. For **C** and **H**, the green channel quantifies the chemiluminescence, and the red channel was used for visualising the molecular weight markers.

against α(2/3)β3 $GABA_A$Rs in llamas, constructed a cDNA library of nanobodies, and screened this library by phage display [214]. The screening steps were conducted in the presence of 1 mM GABA or 10 μM gabazine; for each of these conditions, selections were carried out after adsorption of α(2/3)β3 receptors onto an enzyme-linked immunosorbent assay (ELISA) plate, or by capture of biotinylated α(2/3)β3 receptors on an ELISA plate with adsorbed NeutrAvidin. To select for α-specific nanobodies, selections were carried out in competition with the β3 homomeric $GABA_A$R.

For the α2β3 nanobodies, 176 clones were screened, and of these 126 were found to bind in selections and were sequence-analysed. This gave 65 unique nanobodies, α2β3nb88-152 (Table E.1). These 65 nanobodies were grouped into 48 families based on similarity in the CDR3 region. The occurence of nanobodies in each family is listed in Table E.1.

For the α3β3 nanobodies, 176 clones were screened, and of these 117 were found to bind in selections and were sequence-analysed. This gave 54 nanobodies, α3β3nb153-206 (Table E.2). These 54 unique nanobodies were grouped into 38 families based on similarity in the CDR3 region. The occurence of nanobodies in each family is listed in Table E.2.

3.4 Purification of nanobodies against α(2/3)β3 $GABA_A$Rs

To characterise the new α2β3 and α3β3 nanobodies, all nanobodies were first expressed in *E. coli* and purified in batches of 24. In addition, three nanobodies raised against α1β3 (α1β3nb125, α1β3nb129 and α1β3nb138) were also purified to act as controls during screening. Previous work by Simonas Masiulis and Paul Miller identified α1β3nb125 and α1β3nb129 as binding the β3 subunit, and α1β3nb138 as binding the α1 subunit [296].

The plasmids for each nanobody were provided by Nele Buys, Els Pardon and Jan Steyaert. Each plasmid encoded the nanobody, with an N-terminal PelB leader sequence for targeting to the periplasm, and C-terminal hexa-histidine and CaptureSelect (EPEA) tags for purification. Each nanobody was expressed in WK6 cells as described in Section 2.2.1, in a 500 ml culture volume. Nanobodies were released from the periplasm by osmotic shock, and purified by IMAC as described in Section 2.3.3. Since there were many nanobodies to purify, SEC was not conducted, but instead the high-imidazole buffer was exchanged after multiple rounds of concentration by ultrafiltration and dilution with

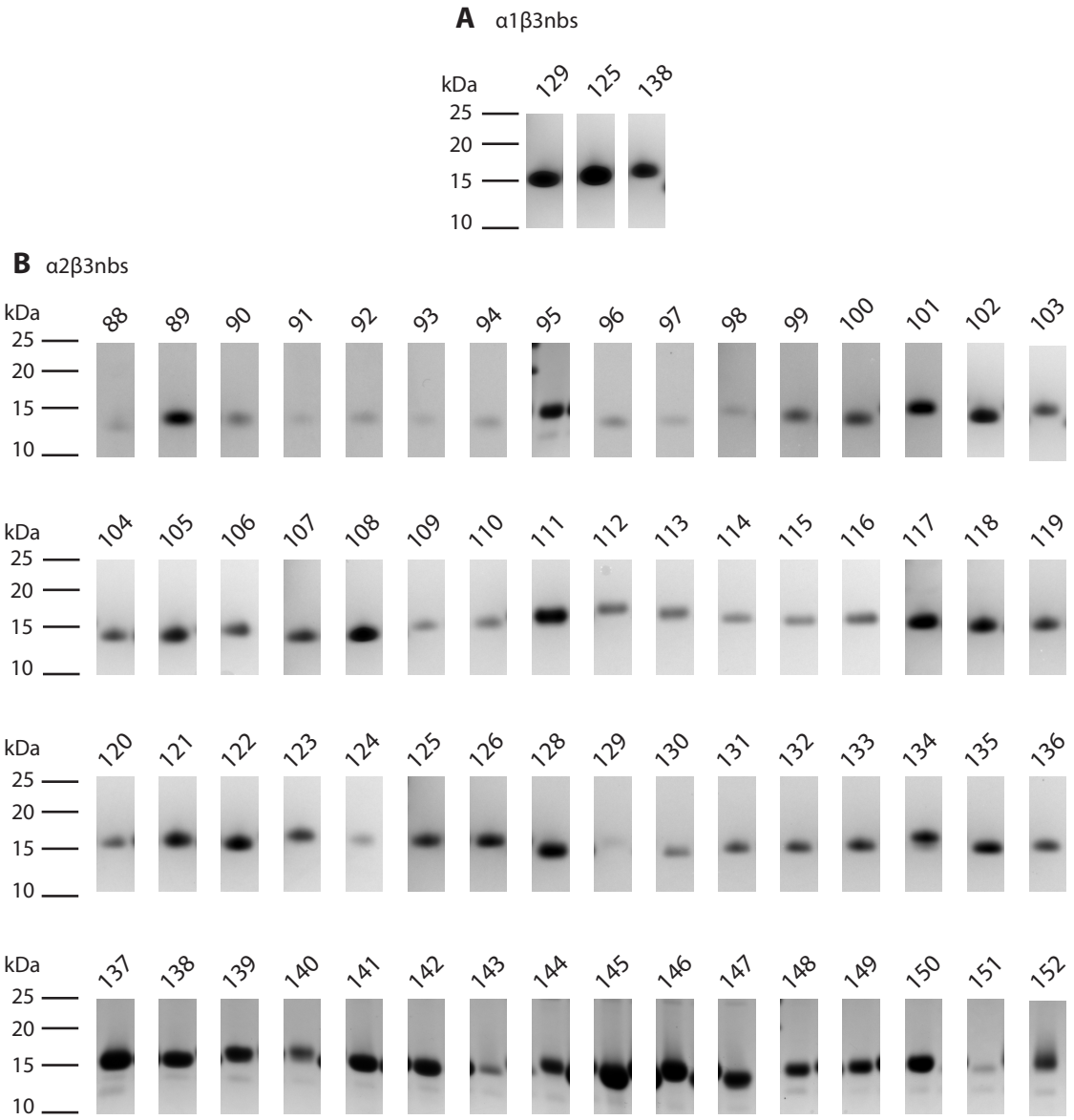

Figure 3.6: Purification of α1β3 and α2β3 nanobodies. A, B: Coomassie-stained SDS-PAGE gel bands for purified α1β3 (**A**) and α2β3 (**B**) nanobodies. Molecular weights (25-10 kDa) are indicated on the left. See Figure E.1 for uncropped SDS-PAGE gels.

another buffer (150 mM NaCl, 10 mM HEPES pH 7.2 or 7.8, depending on nanobody pI).

SDS-PAGE gels were run to identify the success of each purification (Figures 3.6, 3.7).

Yields were quite variable, but were typically 0.1-5 mg per 500 ml of culture.

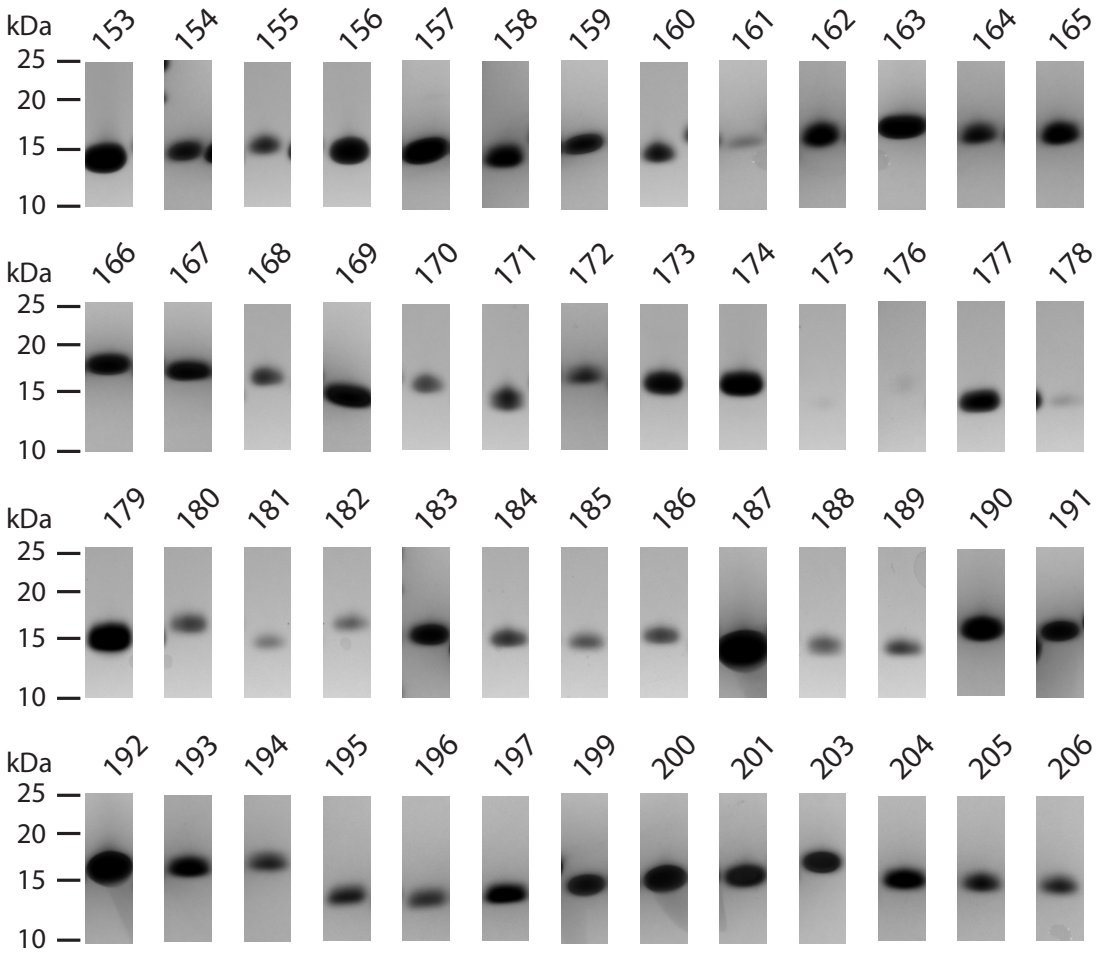

Figure 3.7: Purification of α3β3. Coomassie-stained SDS-PAGE gel bands for purified α3β3. Molecular weights (25-10 kDa) are indicated on the left. See Figure E.2 for uncropped SDS-PAGE gels.

3.5 Kinetic characterisation of nanobodies against α(2/3)β3 $GABA_ARs$

To verify the quality of the purified nanobodies and to investigate possible ways of characterising their kinetics, the interaction between one β3-specific nanobody (α1β3nb125) and a biotinylated α2β3 $GABA_AR$ was investigated with SPR and BLI (Figure 3.8). For this and all other SPR and BLI experiments described in this section, biotinylated α(2/3)glvi-1D4β3glvi-avi $GABA_ARs$ were used, and these were purified as described in Section 3.3 above. First, the interaction was investigated by SPR using kinetic titration (Figure 3.8A). After immobilisation of biotinylated α2β3 $GABA_AR$ to one flow cell (fc2) of a streptavidin

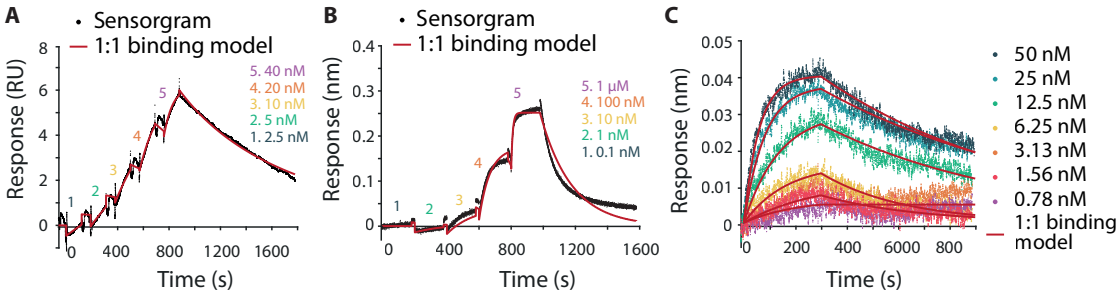

Figure 3.8: α1β3nb125 binding to a α2β3 $GABA_AR$ investigated using BLI and SPR. A: SPR with biotinylated α2β3 $GABA_AR$ adsorbed onto a streptavidin chip to a level of 1000 RU. Kinetic titration was then conducted with nanobody concentrations from 2.5 nM to 40 nM while the response (fc2-1) was monitored. **B:** Kinetic titration of α1β3nb125 using BLI, with α2β3 first immobilised on a streptavidin tip to a thickness of 3.5 nm. **C:** 'Classical' kinetic investigation of α1β3nb125 using BLI, with α2β3 first immobilised on a streptavidin tip to a thickness of 3 nm.

sensor chip to a level of 1000 RU, a two-fold dilution series of α2β3nb125 from 2.5 nM to 40 nM was applied to two flow cells (fc2, fc1), and the fc2-1 signal was monitored. Fitting a 1:1 binding model gave a k_a of (4.2 ± 0.6)x10^5 M^{-1} s^{-1}, k_d of (1.4 ± 0.1)x10^{-3} s^{-1}, and R_{max} of 6.83 ± 0.01 (χ^2 = 0.036 RU^2). Based on these values, a K_D of 3.23 ± 0.05 nM was calculated.

For the BLI kinetic titration experiment (Figure 3.8B), a fit of a 1:1 binding model in MATLAB (see details below) gave a k_a of 9.9x10^4 M^{-1} s^{-1} (95% CI (9.7-10.0)x10^4 M^{-1} s^{-1}), k_d of 5.1x10^{-3} s^{-1} (95% CI (5.1-5.2)x10^{-3} s^{-1}), and R_{max} of 0.265 (95% CI 0.264-0.266) (R^2=0.97), from which a K_D of 52 nM was calculated. For the 'traditional' kinetics experiment conducted using BLI (Figure 3.8C), fitting a 1:1 binding model gave a k_a of (3.80 ± 0.05)x10^5 M^{-1} s^{-1}, and k_d of (1.21 ± 0.01)x10^{-3} s^{-1} (χ^2 = 0.027), giving a K_D of 3.2 ± 0.05 nM

To maximise throughput, purified nanobodies were screened using kinetic titration on a BLI instrument (OctetRED 96 or 384) [239]. Biotinylated α2β3 or α3β3 $GABA_AR$ was adsorbed to streptavidin (SA) tips to a thickness of 3-4 nm. Since there was no previous knowledge of nanobody affinity, a wide range of dilutions were used: a ten-fold dilution series from 0.1 nM to 1 μM was prepared as shown in Figure 2.2. The $GABA_AR$-coated tips were then placed in increasing concentrations of nanobody, and binding was monitored by a change in thickness of the biolayer on the tip. An association time of 180 s and dissociation time of 20 s were used for each concentration of nanobody, and a final dissociation length of 600 s was used.

Table 3.2: Investigating nanobody-α2β3 $GABA_A$R binding by kinetic titration using BLI: results of fits from MATLAB

α1β3nb	k_a (M^{-1} s^{-1}) [95% CI]	k_d (s^{-1}) [95% CI]	R_{max} (nm) [95% CI]	K_D (nM) [95% CI]	R^2
125	$9.86x10^4$ [(9.70-10.0)$x10^4$]	$5.13x10^{-3}$ [(5.08-5.18)$x10^{-3}$]	0.265 [0.264-0.266]	52.0 [51.1-53.0]	0.970
129	$7.24x10^4$ [(6.85-7.63)$x10^4$]	$1.72x10^{-4}$ [(1.56-1.87)$x10^{-4}$]	0.01 [0.00-0.01]	2.37 [2.12-2.62]	0.975
138	45.1 [(-2.37-2.46)$x10^3$]	$1.67x10^{-4}$ [(1.49-1.86)$x10^{-4}$]	0.90 [-47-49]	$3.71x10^3$ [(-1.95-2.02)$x10^5$]	0.959

Since the Octet data analysis software has no capacity to analyse kinetic titration data, and a version of BiaEvaluation that supports data import was not available [239], data were analysed in MATLAB. A script was written which takes as inputs the data exported from Octet data analysis software, as well as the concentrations and timings of nanobody applications, and fits the parameters of a 1:1 binding model as previously described [238] (see Appendix D.2). Some example fits are shown in Figure 3.9 (red lines). The fits were visually inspected and only data were considered for which all of the following criteria were met: the coefficient of determination (R^2) was greater than 0.9, the R_{max} was greater than 0.1, and 95% confidence intervals (CIs) on model parameters did not include zero.

As positive and negative controls, the binding of some α1β3nbs to an α2β3 $GABA_A$R was first investigated. α1β3nb125 and α1β3nb129 had been previously identified to bind the β3 subunit, and α1β3nb138 binds the α1 subunit (see Section 3.2 above). These were purified along with the other nanobodies (Figure 3.6), and then their interaction with biotinylated α2β3 was characterised by BLI kinetic titration (Table 3.2).

Next, all the α2β3 and α3β3 nanobodies were screened against a biotinylated α2β3 and α3β3 $GABA_A$R, respectively. Some example sensorgrams are shown in Figure 3.9. Table E.3 lists the fit parameters for the α2β3 nanobodies, and Table E.4 lists the fit parameters for the α3β3 nanobodies. The fits that were considered are listed at the top of each table; for the sake of completeness, poor fits are also listed at the bottom of each table.

A wide variety of behaviours were observed in the binding of these nanobodies to their respective $GABA_A$Rs. Many bound with a K_D in the low nanomolar range: for the α2β3 nanobodies (33 good fits) the lowest K_D was 0.34 nM, the largest K_D was 480 nM,

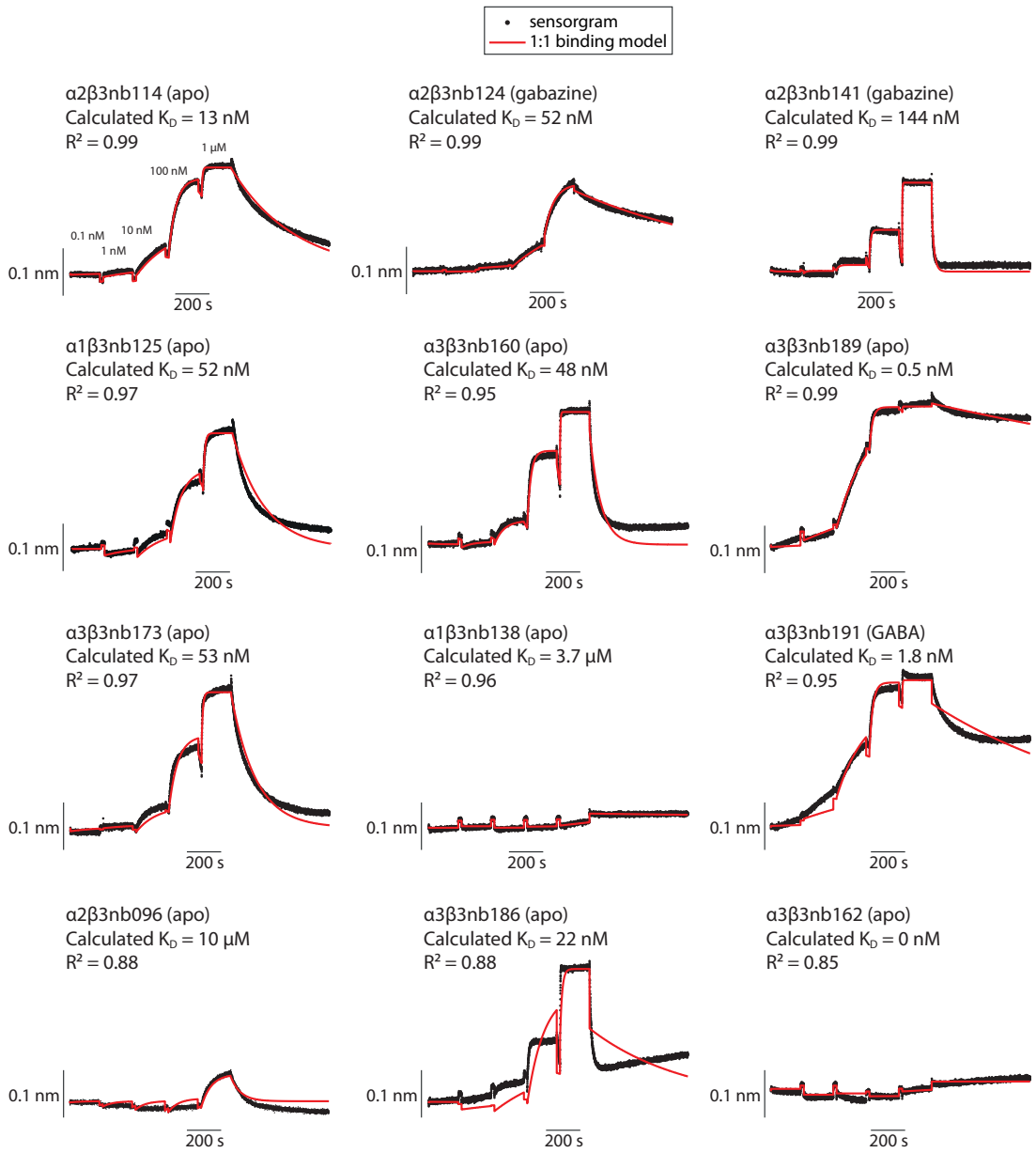

Figure 3.9: Example fits of BLI screening for αβ $GABA_A$R-nanobody interactions. Biotinylated α2β3 or α3β3 $GABA_A$Rs were adsorbed onto streptavidin (SA) tips, and then exposed to a ten-fold dilution series of nanobody (increasing from 0.1 nM to 1 μM), followed by a longer dissociation. The sensorgram is displayed in black dots. Fits (red lines) were conducted in MATLAB (see text for details).

Table 3.3: α(2/3)β3nbs with increased affinity in the presence of 1 mM GABA

α(2/3)β3nb	Apo			1 mM GABA		
	k_a (M^{-1} s^{-1}) [95% CI]	k_d (s^{-1}) [95% CI]	K_D (nM) [95% CI]	k_a (M^{-1} s^{-1}) [95% CI]	k_d (s^{-1}) [95% CI]	K_D (nM) [95% CI]
091	$4.37x10^4$ [$4.25x10^4$-$4.48x10^4$]	$1.42x10^{-2}$ [$1.40x10^{-2}$-$1.44x10^{-2}$]	325 [315-335]	$5.34x10^4$ [$5.30x10^4$-$5.38x10^4$]	$9.79x10^{-4}$ [$9.73x10^{-4}$-$9.86x10^{-4}$]	18.3 [18.1-18.5]
094	$1.11x10^4$ [$1.08x10^4$-$1.15x10^4$]	$5.19x10^{-3}$ [$5.16x10^{-3}$-$5.21x10^{-3}$]	466 [452-480]	$1.78x10^4$ [$1.77x10^4$-$1.80x10^4$]	$4.35x10^{-4}$ [$4.32x10^{-4}$-$4.38x10^{-4}$]	24.4 [24.1-24.7]
099	$8.77x10^4$ [$8.60x10^4$-$8.94x10^4$]	$7.65x10^{-3}$ [$7.56x10^{-3}$-$7.73x10^{-3}$]	87.2 [85.3-89.1]	$2.14x10^5$ [$2.13x10^5$-$2.15x10^5$]	$6.46x10^{-4}$ [$6.42x10^{-4}$-$6.51x10^{-4}$]	3.02 [2.99-3.05]
100	$6.74x10^4$ [$6.59x10^4$-$6.88x10^4$]	$2.43x10^{-3}$ [$2.40x10^{-3}$-$2.47x10^{-3}$]	36.1 [35.2-37.1]	$1.49x10^5$ [$1.48x10^5$-$1.51x10^5$]	$6.14x10^{-4}$ [$6.07x10^{-4}$-$6.22x10^{-4}$]	4.12 [4.06-4.18]
101	$1.07x10^5$ [$1.06x10^5$-$1.09x10^5$]	$2.76x10^{-3}$ [$2.74x10^{-3}$-$2.77x10^{-3}$]	25.7 [25.3-26.0]	$1.27x10^5$ [$1.26x10^5$-$1.29x10^5$]	$3.50x10^{-4}$ [$3.44x10^{-4}$-$3.56x10^{-4}$]	2.75 [2.69-2.80]
125	$1.02x10^4$ [$1.00x10^4$-$1.04x10^4$]	$1.11x10^{-3}$ [$1.10x10^{-3}$-$1.11x10^{-3}$]	108 [106-110]	$8.93x10^4$ [$8.89x10^4$-$8.97x10^4$]	$5.31x10^{-4}$ [$5.28x10^{-4}$-$5.33x10^{-4}$]	5.94 [5.90-5.98]
128	$5.78x10^4$ [$5.62x10^4$-$5.94x10^4$]	$4.96x10^{-3}$ [$4.89x10^{-3}$-$5.03x10^{-3}$]	85.8 [83.1-88.4]	$5.17x10^4$ [$5.14x10^4$-$5.20x10^4$]	$4.58x10^{-4}$ [$4.53x10^{-4}$-$4.63x10^{-4}$]	8.85 [8.75-8.96]
150	$3.45x10^4$ [$3.43x10^4$-$3.47x10^4$]	$1.98x10^{-4}$ [$1.95x10^{-4}$-$2.01x10^{-4}$]	5.74 [5.65-5.83]	$8.74x10^4$ [$8.70x10^4$-$8.79x10^4$]	$3.01x10^{-5}$ [$2.76x10^{-5}$-$3.26x10^{-5}$]	0.34 [0.32-0.37]
160	$3.07x10^5$ [$3.00x10^5$-$3.15x10^5$]	$1.48x10^{-2}$ [$1.45x10^{-2}$-$1.51x10^{-2}$]	48.2 [46.7-49.7]	$3.09x10^5$ [$3.01x10^5$-$3.17x10^5$]	$1.59x10^{-3}$ [$1.54x10^{-3}$-$1.64x10^{-3}$]	5.16 [4.95-5.38]
173	$1.20x10^5$ [$1.19x10^5$-$1.22x10^5$]	$6.66x10^{-3}$ [$6.61x10^{-3}$-$6.72x10^{-3}$]	55.4 [54.5-56.3]	$4.26x10^5$ [$4.18x10^5$-$4.34x10^5$]	$1.99x10^{-3}$ [$1.96x10^{-3}$-$2.01x10^{-3}$]	4.66 [4.56-4.77]
174	$1.67x10^3$ [$4.22x10^2$-$2.92x10^3$]	$7.42x10^{-4}$ [$7.12x10^{-4}$-$7.72x10^{-4}$]	444 [112-776]	$1.79x10^4$ [$1.72x10^4$-$1.86x10^4$]	$8.03x10^{-4}$ [$7.75x10^{-4}$-$8.30x10^{-4}$]	44.8 [42.4-47.2]
186	$2.32x10^5$ [$2.27x10^5$-$2.37x10^5$]	$4.64x10^{-2}$ [$4.55x10^{-2}$-$4.73x10^{-2}$]	200 [194-206]	$7.68x10^5$ [$7.50x10^5$-$7.85x10^5$]	$5.65x10^{-3}$ [$5.56x10^{-3}$-$5.75x10^{-3}$]	7.37 [7.16-7.57]

and the median K_D was 26 nM. For the α3β3 nanobodies (35 good fits) the lowest, highest and median K_Ds were 0.07 nM, 646 nM and 6.6 nM, respectively. However, it should be noted that the median K_D is skewed by the exclusion of poorly fitted data, which is largely comprised of poor binders.

To identify nanobodies that may have a functional effect, the screening was repeated in the presence of either 1 mM GABA or 10 μM gabazine. The results of these screens are summarised in Tables E.5, E.6, E.7, and E.8. Of particular interest in this screening were nanobodies for which affinity increased in the presence of GABA and gabazine, that may be candidates for positive or negative allosteric modulators, respectively. Some examples of nanobodies that increased in affinity in the presence of 1 mM GABA are shown in Table 3.3.

Megabodies, chimeras created by fusing nanobodies to a larger protein, have recently been shown to be useful for cryo-EM studies of $GABA_A$Rs [41], [42]. Therefore, a megabody was generated by fusing the nanobody with a larger scaffold protein, cHopQ, for selected nanobodies (α2β3nb095, α2β3nb148, α3β3nb173 and α3β3nb183). Megabody design, cloning and purification were performed by Tomasz Uchanski, Els Pardon and Jan

Table 3.4: Comparison of nanobody and megabody binding to α(2/3)β3 $GABA_A$Rs in the presence or absence of 1 mM GABA

α(2/3)β3nb/mb	k_a (95% CI) (M^{-1} s^{-1})	k_d (95% CI) (s^{-1})	R_{max} (95% CI) (nm)	K_D (95% CI) (nM)	R^2
nb095 (apo)	$2.99x10^4$ [$(2.96\text{-}3.03)x10^4$]	$9.82x10^{-4}$ [$(9.74\text{-}9.90)x10^{-4}$]	0.32 [0.32-0.32]	32.8 [32.3-33.3]	0.988
mb095 (apo)	$3.96x10^4$ [$(3.90\text{-}4.02)x10^4$]	$2.45x10^{-3}$ [$(2.43\text{-}2.47)x10^{-3}$]	0.28 [0.28-0.28]	61.9 [60.8-62.9]	0.974
nb173 (apo)	$5.60x10^4$ [$(5.41\text{-}5.78)x10^4$]	$3.18x10^{-2}$ [$(3.09\text{-}3.27)x10^{-2}$]	0.29 [0.29-0.29]	569 [544-593]	0.897
mb173 (apo)	$8.54x10^4$ [$(8.21\text{-}8.87)x10^4$]	$5.87x10^{-2}$ [$(5.69\text{-}6.06)x10^{-2}$]	0.23 [0.23-0.23]	688 [654-722]	0.896
nb183 (apo)	$5.32x10^4$ [$(5.23\text{-}5.42)x10^4$]	$1.77x10^{-3}$ [$(1.75\text{-}1.80)x10^{-3}$]	1.08 [1.08-1.08]	33.4 [32.6-34.1]	0.951
mb183 (apo)	$4.29x10^4$ [$(4.25\text{-}4.33)x10^4$]	$5.19x10^{-4}$ [$(5.11\text{-}5.27)x10^{-4}$]	1.23 [1.23-1.23]	12.1 [11.9-12.3]	0.988
nb095 (GABA)	$1.60x10^5$ [$(1.58\text{-}1.62)x10^5$]	$7.91x10^{-5}$ [$(7.09\text{-}8.73)x10^{-5}$]	0.35 [0.35-0.35]	0.49 [0.44-0.55]	0.985
mb095 (GABA)	$7.21x10^5$ [$(7.16\text{-}7.25)x10^5$]	$6.28x10^{-5}$ [$(5.93\text{-}6.63)x10^{-5}$]	0.43 [0.43-0.43]	0.09 [0.08-0.09]	0.997
nb148 (GABA)	$6.59x10^4$ [$(6.57\text{-}6.61)x10^4$]	$1.04x10^{-4}$ [$(1.02\text{-}1.06)x10^{-4}$]	1.12 [1.12-1.12]	1.6 [1.5-1.6]	0.999
mb148 (GABA)	$4.02x10^4$ [$(3.98\text{-}4.05)x10^4$]	$1.04x10^{-4}$ [$(1.00\text{-}1.09)x10^{-4}$]	0.77 [0.76-0.77]	2.6 [2.5-2.7]	0.997
nb173 (GABA)	$1.46x10^6$ [$(1.42\text{-}1.49)x10^6$]	$2.12x10^{-2}$ [$(2.08\text{-}2.16)x10^{-2}$]	0.33 [0.33-0.33]	14.5 [14.1-15.0]	0.948
mb173 (GABA)	$1.82x10^6$ [$(1.77\text{-}1.87)x10^6$]	$2.60x10^{-2}$ [$(2.55\text{-}2.66)x10^{-2}$]	0.34 [0.34-0.34]	14.3 [13.8-14.8]	0.936
nb183 (GABA)	$1.18x10^5$ [$(1.16\text{-}1.20)x10^5$]	$2.35x10^{-3}$ [$(2.33\text{-}2.38)x10^{-3}$]	1.06 [1.05-1.06]	19.9 [19.5-20.3]	0.947
mb183 (GABA)	$1.01x10^5$ [$(9.97\text{-}1.03)x10^5$]	$9.68x10^{-4}$ [$(9.51\text{-}9.84)x10^{-4}$]	1.25 [1.24-1.25]	9.6 [9.3-9.8]	0.959

Stayert at VUB. Binding of these megabodies was compared to the equivalent nanobody in Octet, which was performed with a 3-fold dilution series based on findings from the initial screening. Four dilutions either side of the previously determined K_D were prepared for nanobodies and megabodies, and used to perform a kinetic titration with α2β3 or α3β3 $GABA_A$Rs using BLI in the presence or absence of 1 mM GABA. The data were fit in MATLAB as before (Table 3.4). The K_D values determined were similar for pairs of nanobodies and megabodies in equivalent conditions.

3.6 Functional characterisation of nanobodies against α(2/3)β3 $GABA_A$Rs

High-affinity binders were screened for functional activity by automated patch-clamp in an Ionflux machine. Since screening the whole library of nanobodies in this manner

Table 3.5: Compound application protocol used for nanobody screening

Sweep	Drug	Application times within sweep (s) [total time (s)]
3	I_{max} GABA	2-3 s [1 s]
4	EC_{10} GABA	2-5 s [3 s]
5	EC_{10} GABA	2-11 s [9 s]
7	EC_{10} GABA + 100 nM nb	2-11 s [9s]
9	EC_{10} GABA + 300 nM nb	2-11 s [9s]
11	EC_{10} GABA	2-5 s [3 s]
11	EC_{10} GABA EC_{10} GABA + 1 μM nb EC_{10} GABA + 3 μM nb EC_{10} GABA + 10 μM nb	2-4 s [2 s] 4-8 s [4 s] 8-11 s [3 s] 11-14 s [3 s]
14	I_{max} GABA	2-3 s [1 s]
16	I_{max} GABA	2-4 s [2 s]

would not have been practical, the results from the BLI screen were used to inform this functional screen. In particular, nanobodies that increased in affinity in the presence of GABA, including those for which a good fit was not obtained in the apo condition, were prioritised in screening.

For α2β3 and α3β3 nanobodies, cells transfected with full-length α2β3γ2L and α3β3γ2L receptors were used, respectively. The constructs used for transfection were the same as those used for the Ionflux experiments with α1β3nb138 described above (Section 3.2).

The protocol used for screening is shown in Table 3.5. Typically one experimental pattern (see Figure 2.3) was used per nanobody. Since some nanobodies had slow off rates, especially in the presence of GABA (see Tables E.5 and E.6), the higher 1 μM, 3 μM and 10 μM doses of nanobody were applied sequentially in one sweep (Table 3.5, sweep 11).

The data were analysed in MATLAB (see Section D.3.2), and the results of the screen for all nanobodies are given in Table E.9. In this analysis, the fold-change (FC) from an EC_{10} dose of GABA alone was calculated for each dose of nanobody co-applied with the same EC_{10} dose of GABA. Some examples of currents recorded in the presence of increasing concentrations of nanobodies are shown in Figure 3.10. Dose-response curves

Table 3.6: Hits from Ionflux screen for positive modulation: fold-change from EC_{10} GABA dose (FC), standard deviation (SD) and number of recordings (n) for each dose of nanobody

α2/3β3nb	0.1 μM nb			0.3 μM nb			1 μM nb			3 μM nb			10 μM nb		
	FC	SD	n	FC	SD	n	FC	SD	n	FC	SD	n	FC	SD	n
095	0.95	0.07	6	0.73	0.12	6	1.01	0.43	6	1.67	0.18	6	2.26	0.44	6
148	0.96	0.08	4	0.84	0.15	4	0.91	0.05	4	1.89	0.25	4	2.64	0.71	4
172	1.09	0.09	4	1.24	0.55	4	1.30	0.31	4	2.14	0.68	4	3.15	1.18	4
173	2.66	0.15	3	2.13	0.35	3	2.37	0.94	5	3.99	1.69	5	3.26	1.30	5
183	1.26	0.28	6	2.83	2.44	6	1.90	0.45	6	3.19	0.98	6	4.29	1.50	6

were not fitted to the data because it was unclear if saturation had been reached at the highest nanobody concentration.

Nanobodies that were found to be modulatory in an initial screen with one nanobody per pattern in an Ionflux plate were then tested again. The results of these follow-ups are displayed in Table 3.6.

3.7 Discussion

The main aim of the work described in this chapter was to characterise nanobodies against $GABA_A$Rs. This included work with nanobodies previously raised against an α1β3 $GABA_A$R, as well as new nanobodies created in collaboration with Nele Buys, Els Pardon and Jan Steyaert at VUB.

First, the properties α1β3nb138 were examined. Consistent with previous reports that nanobodies have favourable biochemical properties [293], α1β3nb138 was well expressed and could be concentrated to millimolar concentrations. Importantly for any further *in vivo* nanobody use, α1β3nb138 was well expressed in a mammalian expression system, as well as a previously described *E. coli* expression system [214]. A primary concern for proteins expressed in *E. coli* is contamination with endotoxins derived from the outer cell membrane [301], [302]. These can be carried through during protein purification [302], and if they enter the blood can cause sepsis [301]. Alternative endotoxin-free expression systems are therefore more desirable in the case of proteins to be used *in vivo*, so the viability of the mammalian expression system in this case may be important for further work.

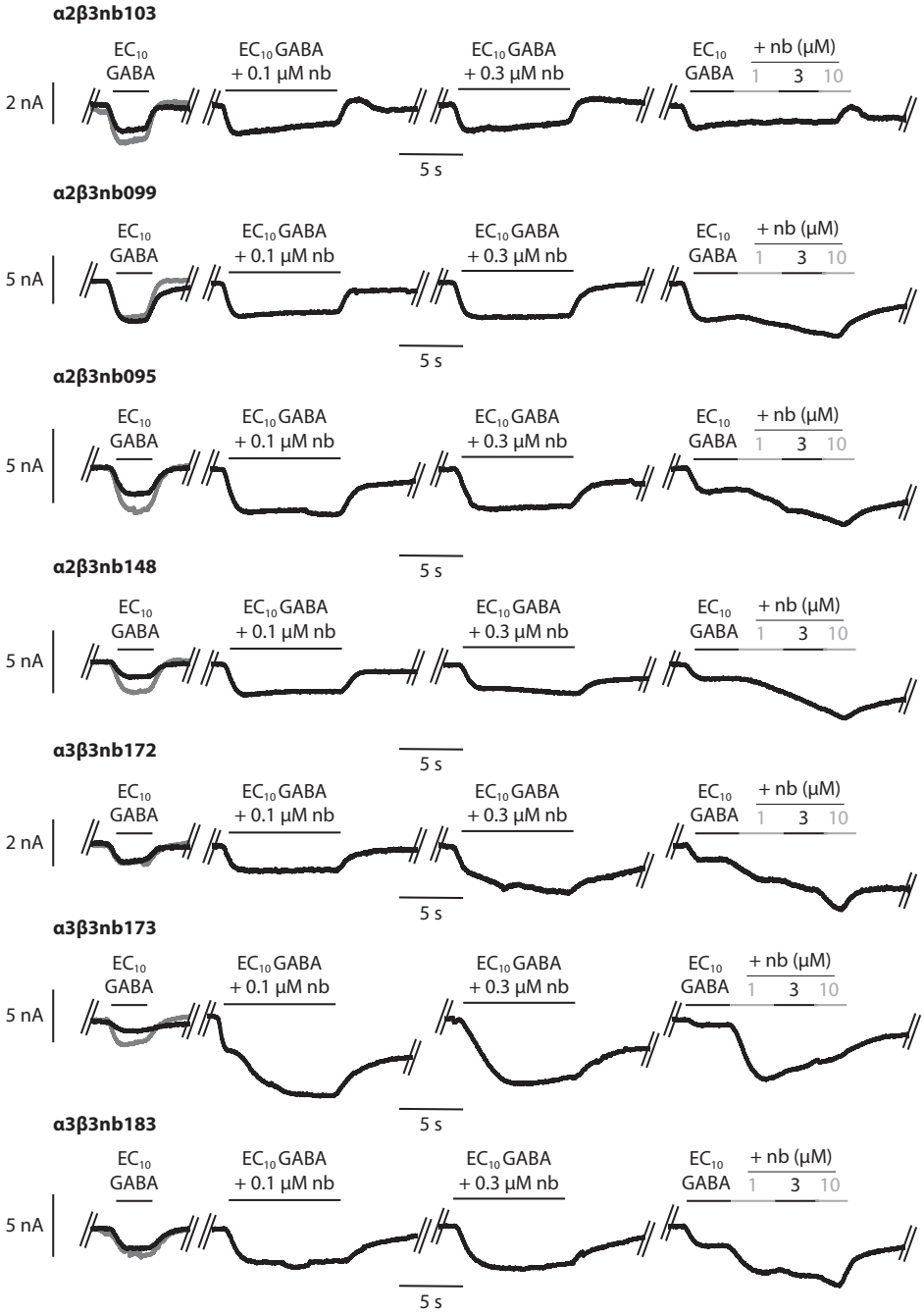

Figure 3.10: [Responses of α2β3γ2 and α3β3γ2 $GABA_A$Rs to EC_{10} doses of GABA and increasing concentrations of nanobody. Nanobodies (0.1-10 μM) were screened for modulatory activity at αβγ $GABA_A$Rs using automated patch-clamp electrophysiology (Ionflux). Nanobodies were applied together with an EC_{10} dose of GABA, and the resulting currents were compared against an EC_{10} dose of GABA alone (two replicates shown, grey and black). Many nanobodies had no (α2β3nb103) or weak (α2β3nb099) modulatory activity at doses up to 10 μM. α2β3nb095, α2β3nb148, α3β3nb172, α3β3nb173 and α3β3nb183 were found to be potent modulators of their respective αβγ $GABA_A$Rs (see also Table E.9).

Next the properties of purified α1β3nb138 were examined. This nanobody was found to be a tight binder, with a K_D of 6 nM as determined by SPR kinetic titration. This value varies slightly from a previous finding of K_D=1 nM [40]. Similarly, the potent modulation of a α1β3γ2 GABA$_A$R by this nanobody is consistent with the previous finding that 10 μM α1β3nb138 potentiated EC_{10} GABA currents by 300%. This previous study found that the postive modulation was more potent than diazepam, a comparison not made here. Furthermore, this nanobody was found to be selective for α1β3γ2 receptors over α(2-6)β3γ2 receptors. α1β3nb138 is therefore a potentially useful pharmacological tool for further research. Given that α1-containing receptors are also targets for sedative drugs [165], this nanobody may also have therapeutic potential.

Next, α2β3 and α3β3 GABA$_A$Rs were purified in order to raise new nanobodies. In line with previous work with GABA$_A$Rs [37], [40], as well as other pLGICs [31], [33], [35], the long intracellular M2-3 loop was removed and replaced with a short linker. Since this domain is likely unstructured in GABA$_A$Rs [41], [42], it is unclear if nanobodies binding to this domain would be discovered, or what functional effect such nanobodies would have. If ICD nanobodies were found, they may compete with proteins thought to bind the intracellular domain, such as gephyrin or GABRAP[303], and therefore could be useful research tools. However, the present work was restricted to nanobodies binding the ECD.

Furthermore, some difficulties were experienced when purifying αβ GABA$_A$Rs, which appeared to be less well-behaved than a homomeric β3 GABA$_A$R. The reason for this difference is unclear, but the difficulties associated with purification of αβ GABA$_A$Rs could be overcome by omitting the concentration step prior to SEC.

A large number of nanobodies binding α2β3 (65 nanobodies) and α3β3 (54 nanobodies) GABA$_A$Rs were found during selection. When the α1β3 nanobodies were raised, 18 nanobodies were found to bind during selection with solid phase coated or 1D4 mAb-captured α1β3 GABA$_A$R. The α(2/3)β3 nanobodies were found in four different selection conditions, so a larger number of selection conditions may partially explain the larger number of nanobodies. The other difference was the sample itself: in the case of the α(2/3)β3 GABA$_A$Rs the sample used for immunisation had 1 mM GABA included in the buffer, whereas this was not the case for α1β3. However, since GABA likely dissociated

from the receptor quite quickly after injection, it is unclear if this could be responsible for the difference.

Since many nanobodies were obtained, it was necessary to screen in the most efficient way. One possible approach could have been to take representative nanobodies from each family (Tables E.1, E.2). However, most families consisted of only one or two members, so this approach would not have eliminated many nanobodies. Instead, all nanobodies were purified and care was taken to design the most efficient screening strategy. This consisted of two stages: first, all the nanobodies were screened using BLI kinetic titration; and second, the high-affinity nanobodies were screened using automated patch-clamp electrophysiology.

For the initial BLI screen, kinetic titration (using one tip per nanobody) was more efficient than a traditional kinetic experiment (using up to 8 tips per nanobody). Although a traditional kinetic experiment can be conducted in less time (~20 minutes), only one (OctetRED 96, which can use up to 8 tips) or two (OctetRED 384, using 16 tips) nanobodies could be investigated in parallel. Similarly, SPR can only characterise one nanobody at a time, and extra time is associated with preparing the chip for each experiment. However, one kinetic titration experiment took ~35 minutes and can be performed for 8 (OctetRED 96) or 16 (OctetRED 384) nanobodies in parallel. This approach was therefore the most time-efficient of the available alternatives, and given that one BLI tip is a fraction of the cost of an SPR chip, also the most cost-effective.

To screen the whole set of nanobodies for which no previous information about affinity was available, a wide range of concentrations were used for the kinetic titration. This made it possible to determine a wide range of affinities, but with a likely trade-off for accuracy. This is illustrated by three experiments in which the affinity of α1β3nb125 was determined for an α2β3 $GABA_A$R. With a traditional method of kinetics by BLI, and SPR kinetic titration, the K_Ds determined were identical (3.2 nM for BLI, 3.2 nM for SPR). The same range of concentrations were used for these two experiments (1.25-50 nM). In a third experiment, a wider range of concentrations (0.1 nM-1 μM) was used, and the K_D was 52 nM, suggesting that an appropriate range of concentrations may be important for an accurate determination of K_D. Therefore, there is likely to be some inaccuracy in

the screening results and the calculated K_D values should be interpreted with caution. However, these results are still useful as a guide to the likely affinity of each nanobody, and for filtering out nanobodies that do not bind.

The range in nanobody behaviour is illustrated in the results for α1β3nb125, 129 and 138 binding at α2β3 $GABA_A$Rs. The fit to the α1β3nb125 data is consistent with high-affinity binding, as would be expected for a β3-specific nanobody. Similarly, the wide confidence intervals for the α1β3nb138 indicate a poor fit of the data, which was typically observed for poor binders. Since this nanobody is α1-specific, this result was again expected. The fit for the α1β3nb129 data, with a $R_{max}\approx 0$, is also indicative of poor binding. The reason for this result is less clear, since this nanobody can bind homomeric β3 $GABA_A$Rs [296]. Repetition of the experiment may shed light on this issue. These results highlight the importance of not over-interpreting the screening results, and the lack of binding for α1β3nb129 suggests the possible presence of other false negatives in this dataset.

Nevertheless, it is clear that some high-affinity binders are present amongst the nanobodies screened , and the megabodies created from a few of these appeared to bind with very similar affinities as their parent nanobodies. This can be seen by inspection of the raw sensorgrams (for example, Figure 3.9), as well as in the fits of the data. More accurate numbers could be obtained for affinity parameters by repeated measurements, however, the objective of the present work was only to screen for possible tight binders and exclude weak binders. Several promising leads were found, and thus although another pass through the entire complement of nanobodies would be useful for placing better bounds on the k_a and k_d for each, it was not judged necessary in the present work.

A comparison between the nanobodies that increased in affinity in the presence of GABA (Table 3.3), and the nanobodies found to be positive modulators in the Ionflux screen (Table 3.6) again hints at limitations of the screening procedure. The rationale for screening in the presence and absence of GABA was that nanobodies that recognise activated states may bind more tightly in the presence of GABA. However, of the nanobodies that were identified in this screen, only α3β3nb173 was later found to be a positive modulator.

Despite these limitations of the screening process, the end result was the discovery of several promising nanobodies that are positive modulators of α(2-3)β3γ2 $GABA_A$Rs. The

decision was made to screen against αβγ receptors because these are the main physiological receptor type [59]. It is possible that the lack of modulatory activity of nanobodies identified by BLI screening is due to the use of αβγ $GABA_A$Rs in Ionflux screening; however, this seems unlikely since the only difference is the substitution of one γ2 subunit for β3.

Nevertheless, these modulatory nanobodies could be useful for structural studies of $GABA_A$Rs, as previously demonstrated for Nb38 which binds the α1β3γ2 $GABA_A$R [40]. In particular, the megabodies characterised may be useful for cryo-EM work, since this modification was shown to improve the orientation distribution when for a α1β3γ2 $GABA_A$R-Mb38 complex [41], [42]. A description of the use of nanobodies and megabodies in cryo-EM can be found in Chapter 5. Furthermore, these nanobodies may have further applications in physiological investigations. Given the important role played by α(2/3)-containing $GABA_A$Rs in anxiety and pain [147], [169], if the obstacle presented by the blood-brain barrier can be overcome, these nanobodies also have potential as therapeutics.

4

Optimisation of triheteromeric $GABA_AR$ expression and purification

Contents

4.1 Introduction 110
4.2 Transient transfection of full-length αβγ $GABA_ARs$ 113
4.3 The BacMam expression system 117
4.4 $GABA_AR$-expressing cell lines and comparison with BacMam 122
4.5 Purification optimisation 129
4.6 Discussion 132

4.1 Introduction

Once nanobodies suitable for structural studies had been identified (Chapter 3), the next task was to express and purify a suitable $GABA_AR$ in order to examine the structural effect of nanobody binding. Since the majority of synaptic $GABA_ARs$ are αβγ heteromers [59], the α2β3γ2L and α3β3γ2L receptor types were the focus of this work.

4.1.1 Expression systems

Various expression systems are available for the heterologous expression of proteins. Mammalian expression systems are a popular choice for the expression of membrane

glycoproteins, due to their capacity to express proteins that are correctly folded and functional, as well as the favourable lipid composition of their cell membrane [304]. A further advantage of HEK293S GnTI$^-$ cells over other mammalian cell lines and insect cells is their homogenous N-linked glycans, which can be advantageous for deglycosylation with enzymes such as EndoF [234], [305]. In particular, HEK293 cells have been successfully used to express homomeric and heteromeric $GABA_ARs$ by transient transfection [37], [40], by making use of the BacMam system [38], [39], or by the generation of stable cell lines [306]–[308].

Of these three methods, the most rapid is transient transfection. Requiring only the purification of cDNA for the constructs of interest, once cells have been grown to the desired volume transient transfection can be used to express the protein of interest within a few days [219]. HEK293 cells can be grown and transfected in suspension to increase biomass [236]. However, a disadvantage of transient transfection is that high transfection efficiencies can be difficult to obtain. However, expression enhancers such as valproic acid (VPA) and sodium butyrate can be used to increase protein expression further [237]. These are histone deacetylase inhibitors that are thought to increase protein expression though reversal of DNA association with histones resulting from the introduction of extra-chromosomal DNA [237].

A second method to induce transient expression in mammalian cell lines is the BacMam system. This method makes use of the Autographa californica nuclear polyhedrosis virus (AcMNPV) to transduce mammalian cells [309]. This virus is a large enveloped member of the Baculoviridae family, with a double-stranded, circular DNA genome of ~130 kb [309]. Although first known for its ability to infect and replicate in insect cells, AcMNPV was later discovered to also infect mammalian cells, but without the ability to replicate in this host [309]. A combination of commercially available systems to produce AcMNPV, such as the Bac-to-Bac system from Invitrogen, with vectors containing a mammalian expression cassette have enabled the BacMam system to be used for high-level protein expression [220], [235].

A third method for the expression of proteins in mammalian cells is the generation of stable cell lines. Although their generation can be time-consuming using traditional

methods for clonal selection, they have the advantage of being easy to use once created, and capable of high-level homogeneous expression [304]. Recently, a faster method for the generation of stable cell lines has been described, that makes use of recombinant lentiviruses capable of integrating genetic material into the host cell genome [221]. If a high lentiviral titre is achieved, the resulting high efficiency of transduction allows the new polyclonal cell line to be used without isolating single clones, saving many months of work. If the lentiviral titre is lower and fluorescent proteins are also expressed, FACS can be used to isolate the transduced population of cells. Expression of a fluorescent protein for FACS can be achieved by either fusion with the protein of interest, or by making use of an internal ribosome entry site (IRES) sequence; a recently generated suite of vectors based on pHR allows for both these possibilities [221].

4.1.2 Protein purification

Once an integral membrane protein has been expressed, it must be first purified before use in any downstream structural biology studies. In this process, the protein is solubilised either directly from cells or from pelleted membranes after cell disruption, generally by using a detergent. The protein of interest is then enriched and separated from other cellular components, typically by affinity chromatography. After affinity chromatography, other purification steps such as size exclusion chromatography (SEC) or ion exchange chromatography can be carried out. These can also provide information about the structural integrity of the sample, and for membrane proteins fluorescence size exclusion chromatography (FSEC) is useful as an analytical technique to screen large numbers of different constructs in small amounts [310].

Various tags are available for affinity chromatography, from fusion proteins such as glutathione-S-transferase (GST) to small epitope tags such as FLAG and 1D4 [311]. In the past, several strategies have been used to successfully purify $GABA_AR$s, such as 1D4 [37], [40], FLAG [306] and twin-strep [39] affinity chromatography. Another type of affinity chromatography makes use of a GFP-binding nanobody [218], [226], which may be particularly useful because of the utility of GFP fusions for FSEC and FACS.

For integral membrane proteins, one optional step in purification is removal of the detergent used for solubilisation. Detergent can be replaced in a variety of detergent-free systems, including amphipols, nanodiscs, and liposomes [312], [313]. Depending on the downstream application this can be highly desirable; for example, detergents can have detrimental effects on protein distribution and ice thickness in cryo-EM [243].

4.1.3 Aims

The aim of the work described in this chapter was to explore methods of expression and purification of triheteromeric α2/3-containing $GABA_A$Rs. Efforts to express these receptors in a variety of expression systems are described. Additionally, methods for purification of expressed receptors are also discussed.

4.2 Transient transfection of full-length αβγ $GABA_A$Rs

To purify α2/3β3γ2L heteromers, rather than homomeric β3 or heteromeric αβ $GABA_A$Rs, the purification tag for affinity chromatography was placed on the γ subunit. Full-length α2 and α3 were cloned into pHLsec, and a full-length β3 construct in pHLsec was provided by Paul Miller. In order to perform FSEC, and for purification of αβγ receptors, a construct was created with monomeric enhanced green fluorescent protein (mEGFP) fused to the N-terminus of γ2L and a 1D4 tag placed at the C-terminus (mEGFP-γ2L-1D4). This construct was also subcloned into pHLsec; for more details of cloning methods used, see Appendix B.

As a first attempt at purifying full-length heteromeric $GABA_A$Rs, small-scale transfections were conducted with HEK293T cells in 6-well plates. Full-length pHLsec-α2 or pHLsec-α3, pHLsec-β3, and pHLsec-mEGFP-γ2L-1D4 were cotransfected in a 1:1:1 ratio using lipofectamine. Transfection of cells with only pHLsec-mV-β3-1D4 or pHLsec-mV-β3glvi-1D4 was also carried out for comparison.

Fluorescence (mEGFP or mVenus) could be observed in all transfected cells (Figure 4.1A-D). 1D4-tagged $GABA_A$Rs were then purified from the cells by solubilisation in 1% DDTM, DDM or DMNG, followed by 1D4 affinity chromatography. 5 μl of the eluate was then subjected to FSEC on a Superose-6 Increase 3.2/300 column. However, only

the homomeric β receptors had prominent $GABA_AR$ peaks (25 min, Figure 4.1E). αβγ heteromer peaks were barely above noise, regardless of the detergent used (Figure 4.1E, F).

First, the transfection and purification was repeated with a larger amount of transfected cells, and modifications to the protocol were made in an attempt to optimise the yield and sample quality. A range of salt concentrations (100-500 mM NaCl) and buffer pH (20 mM HEPES, pH 6.8-7.8), as well as various additives (1 mM GABA; and the high-affinity nanobodies α2β3nb111, α2β3nb119, α2β3nb146, all used at 10 μM) were explored for buffer A (used for solubilisation and binding to 1D4 affinity media). These tests were conducted with HEK293S GnTI$^-$ cells transiently transfected with a 1:1:1 ratio of pHLsec-α2, pHLsec-β3 and pHLsec-mEGFP-γ2L-1D4. Cells were harvested 72 h after transfection and 25 ml of cell suspension was used for each condition. The eluates (80 μl) from 1D4 affinity media (25 μl for each sample) were then subjected to FSEC, and the tryptophan fluorescence (excitation wavelength 295 nm, emission wavelength 315 nm) was monitored (Figure 4.2). A double peak was observed around 25 min, with one main peak at 25 min (typical for $GABA_ARs$) and a small shoulder in some conditions and two clear peaks in others. The condition in which this shoulder was least prominent was when a buffer composed of 300 mM NaCl and 20 mM HEPES (pH = 7.2) was used, so this buffer was used for future purifications. The additives had little effect on the protein quality, so were omitted from future purifications.

Based on these results, a larger volume (1.5 L) of cells (HEK293S GnTI$^-$) were transfected in suspension, and then purified using a buffer containing 300 mM NaCl and 20 mM HEPES (pH = 7.2) (and using DDTM as a detergent). After elution, a 5 μl sample was subjected to FSEC (Figure 4.3A), and the remainder of the sample was exchanged into amphipols by incubation with 1:10 (w/w) A8-35 at 4 °C with gentle rotation for 2 h, and then incubation with 10 mg biobeads with gentle rotation for 2 h to remove the detergent. This sample was injected (40 μl) onto a Superdex-6 Increase 3.2/300 column and fractions were collected, but no distinct $GABA_AR$ peak was observed in the UV (280 nm) absorbance channel (Figure 4.3A, B). Furthermore, the $GABA_AR$ peak observed in the GFP fluorescence channel indicated a heterogenous sample, and this is consistent with negative stain EM conducted with fractions collected of this sample after FSEC (Figure 4.3C).

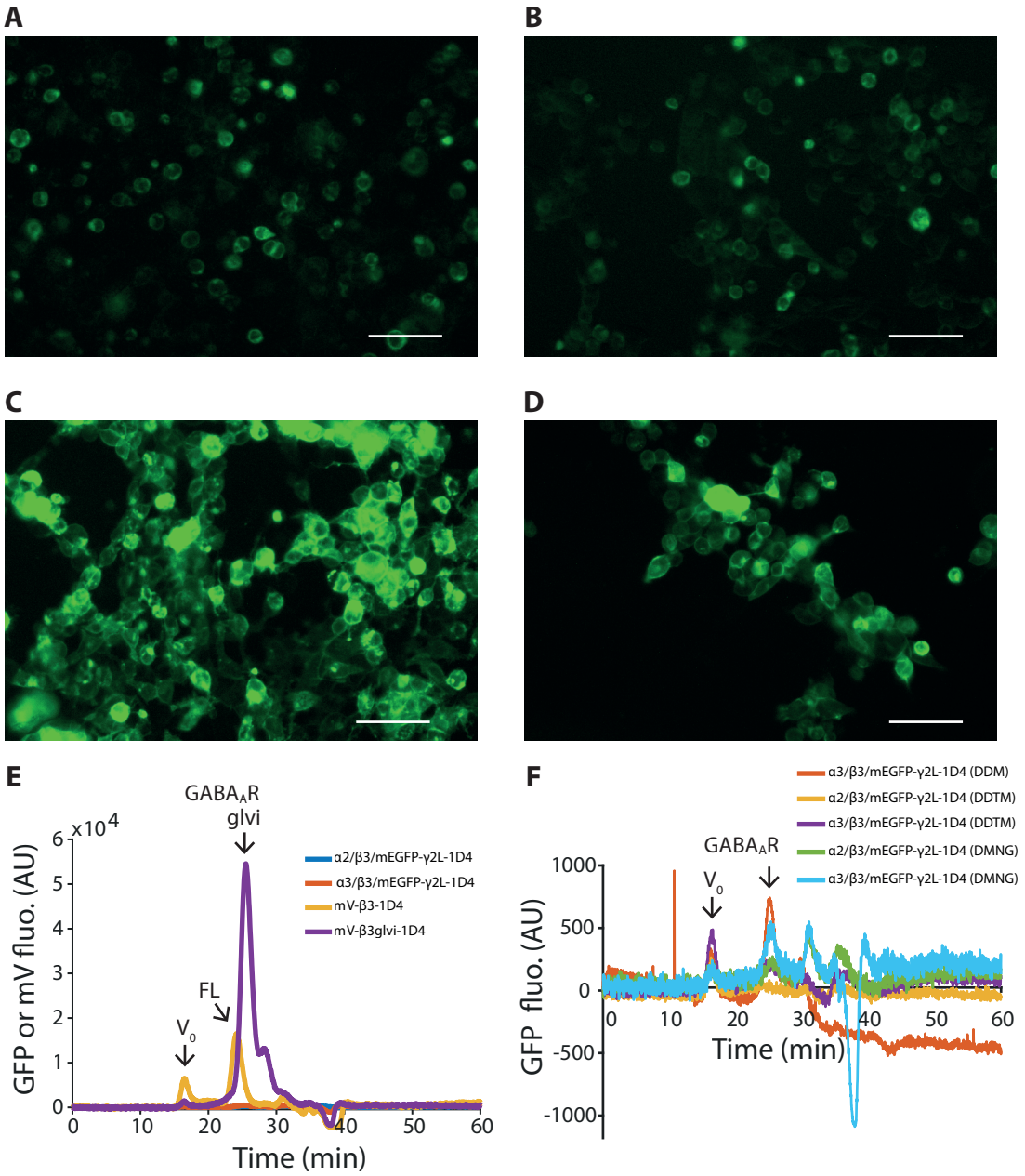

Figure 4.1: Transient small-scale transfection and purification of 1D4-tagged αβγ and β3 $GABA_ARs$. **A-D**: Epifluorescence images of cells transfected with the α2/β3/mEGFP-γ2L-1D4 (**A**), α3/β3/mEGFP-γ2L-1D4 (**B**), mV-β3glvi (**C**), or mV-β3 (**D**) subunits. mVenus (β3 homomers) or mEGFP (αβγ heteromers) were fused to the N-terminus of the β3 or γ2L subunits, respectively. Scale bars: 100 µm. **E, F**: FSEC analysis of 1D4-purified proteins in DMNG (**E**); or DMNG, DDTM or DDM (**F**). The void (V_0) and $GABA_AR$ peaks (full-length, FL; and glvi) are indicated with arrows. These typically eluted at ~25 min under typical SEC conditions (flow rate 0.06 ml min^{-1}) The y-axis plots GFP (excitation 488 nm, emission 507 nm) or mVenus (excitation 515 nm, emission 508 nm), as appropriate.

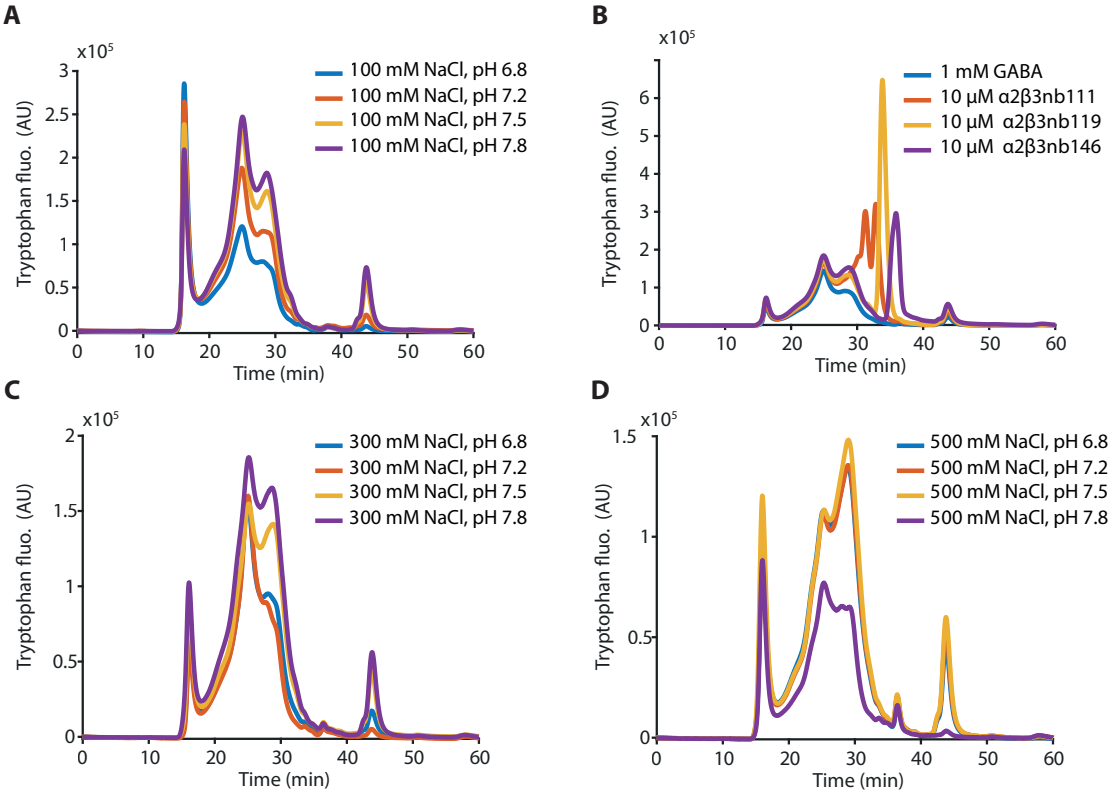

Figure 4.2: Optimisation of 1D4-tagged αβγ $GABA_AR$ purification. Tryptophan fluorescence from FSEC with the eluates from 1D4 affinity media. The purification was conducted using buffers with varying salt concentration and pH (**A, C, D**). All buffers contained 20 mM HEPES. Additives to a buffer composed of 300 mM NaCl and 20 HEPES (pH = 7.2) were also explored (**B**).

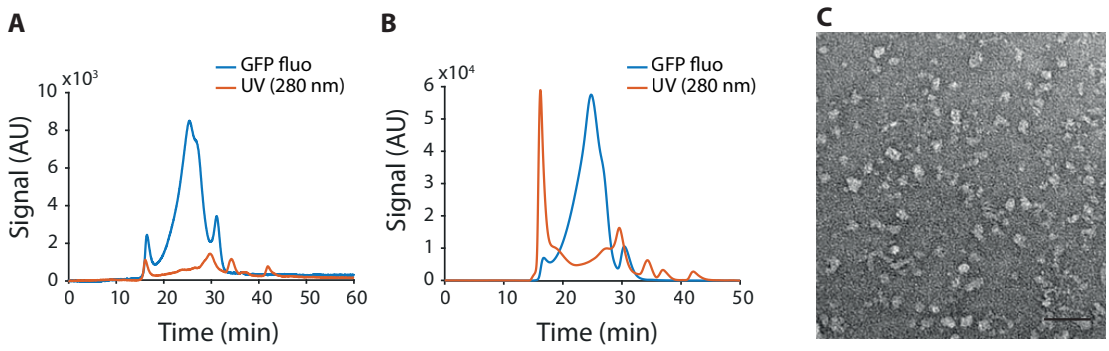

Figure 4.3: Purification of 1D4-tagged α2β3γ2L $GABA_AR$. A,B: Shimadzu chromatograms (Superdex-6 Increase 3.2/300 column) of GFP fluorescence (blue) and UV_{280} absorbance (orange) for α2β3γ2L $GABA_AR$ purified in the presence of DDTM (**A**, 5 µl injected), or exchanged into A8-35 after purification in the presence of DDTM (**B**, 40 µl injected). **C**: Negative stain electron microscopy with purified α2β3γ2L $GABA_AR$ after exchange into A8-35. Scale bar: 50 nm.

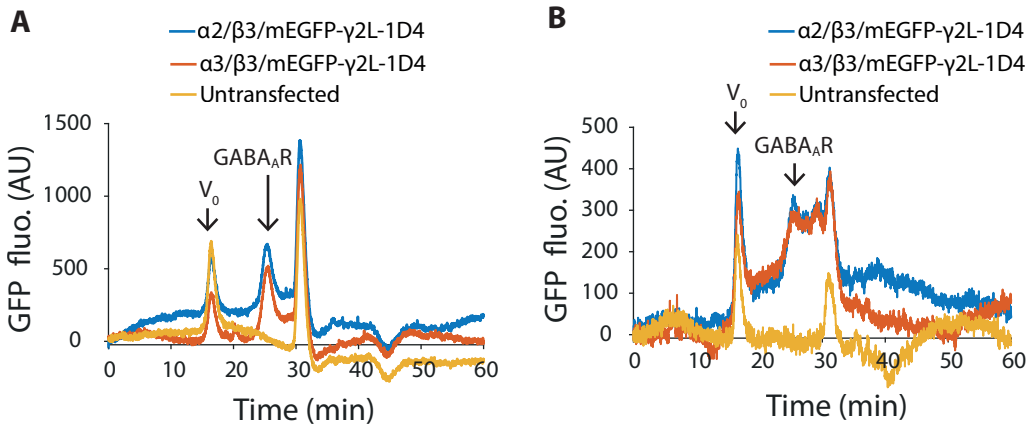

Figure 4.4: Lysate FSEC with transfected pEZT constructs. **A,B**: Shimadzu chromatograms (Superdex-6 Increase 3.2/300 column) showing GFP fluorescence for cell lysates from HEK293T cells transfected with α(2/3)β3γ2L $GABA_AR$s, using pEZT-BM constructs. Cell lysates were created by solubilisation in 1% DDM (**A**) or 1% DDTM (**B**). A $GABA_AR$ peak at ~25 min is clearly visible in transfected cells (blue, orange), but absent in untransfected cells (yellow). The void volume (V_0) is also indicated by an arrow.

4.3 The BacMam expression system

Since full-length, heteromeric $GABA_AR$s were not amenable to transient expression and purification strategies developed for the β3 homomer, alternative strategies were sought.

First, the BacMam expression system was used to express $GABA_AR$s by making use of the pEZT-BM plasmid [220]. The α2, α3, β3 and γ2L subunits were subcloned into the mammalian expression cassette of this vector to create the vectors pEZT-α2, pEZT-α3, pEZT-β3 and pEZT-mEGFP-γ2L-1D4.

These constructs were cotransfected into HEK293T cells in 6-well plates as before, and expression was verified by FSEC with cell lysates after solubilisation with 1% DDM (Figure 4.4A) or 1% DDTM (Figure 4.4B). A $GABA_AR$ peak at ~25 min was visible for transfected cells, but not untransfected cells.

Recombinant baculoviruses were created by transfection of insect Sf9 cells with recombinant bacmids from transformed *E. coli* DH10Bac cells. Correct transposition of the expression cassette into the bacmid was verified by PCR (using forward and reverse sequencing primers for pEZT-BM; Figure 4.5). Then the recombinant bacmid was used to transfect Sf9 cells in a 6-well plate. The resulting P1 virus was amplified once more by addition to 50 ml of Sf9 cells at 1.5x10^6 ml^{-1}. The titre of the P2 virus was determined

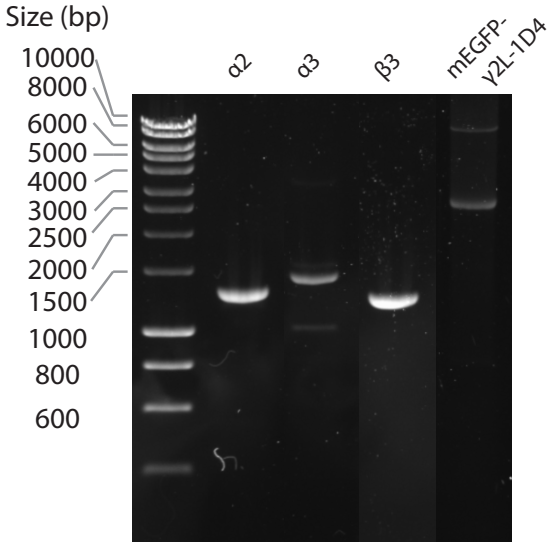

Figure 4.5: PCR verification of correct bacmid recombination. PCR products were subjected to agarose gel electrophoresis. Expected bands were: α2, 1.3 kb; α3, 1.5 kb; β3, 1.4 kb; mEGFP-γ2L-1D4, 2.4 kb

Table 4.1: Titres for baculovirus production optimisations. The highest titre achieved is in bold.

Virus	MOI	Day 2			Day 3			Day 4		
		Titre	Count (x10^6)	Viability (%)	Titre	Count (x10^6)	Viability (%)	Titre	Count (x10^6)	Viability (%)
α2	10^{-1}	7x10^5	1.4	9.10x10^1	**2x10^7**	1	76	4x10^6	1.2	28
	10^{-2}	2x10^6	1.4	9.50x10^1	6x10^6	1.4	79	3x10^6	1.4	22
	10^{-3}	9x10^6	1.5	9.30x10^1	1x10^7	1.8	91	8x10^6	2.3	31
β3	10^{-1}	4x10^6	1.2	8.80x10^1	**3x10^7**	1.3	87	3x10^6	1.1	14
	10^{-2}	2x10^6	1.7	9.20x10^1	6x10^6	1.8	81	2x10^6	1.7	17
	10^{-3}	2x10^6	1.5	9.50x10^1	4x10^6	1.8	86	8x10^6	1.9	27
mEGFP-γ2L-1D4	10^{-1}	6x10^6	0.92	8.70x10^1	6x10^6	1.9	56	6x10^6	1.3	8
	10^{-2}	1x10^7	1.9	9.70x10^1	5x10^6	1.1	59	1x10^7	1.3	12
	10^{-3}	2x10^6	2.7	9.70x10^1	2x10^7	3	91	**6x10^7**	3.7	25

by endpoint titration assay, and P3 production conditions (MOI, time) were optimised. Typically three MOIs (10^{-1}, 10^{-2} and 10^{-3}) and three time points (48, 72, 96 h) were used to test conditions for P3 virus generation. Table 4.1 shows the results of the optimisation of three viruses. The optimal time and MOI varied for each virus, and these conditions were used for larger-scale (500 ml) infection of Sf9 cells to produce larger quantities of baculovirus.

Next, baculoviruses for individual subunits were mixed to transduce expression of $GABA_ARs$ in HEK293S GnTI$^-$ cells. Initially, the viruses for α2, β3 and mEGFP-γ2L-1D4 were each used at an MOI of 1 to transduce HEK293S GnTI$^-$ cells in suspension at a density of 2x10^6 ml^{-1}. Transduced cells displayed clear green fluorescence (Figure 4.6A). 1 ml of cells was collected after 72 h, and cells were solubilised in 1% DDTM for lysate FSEC. A clear

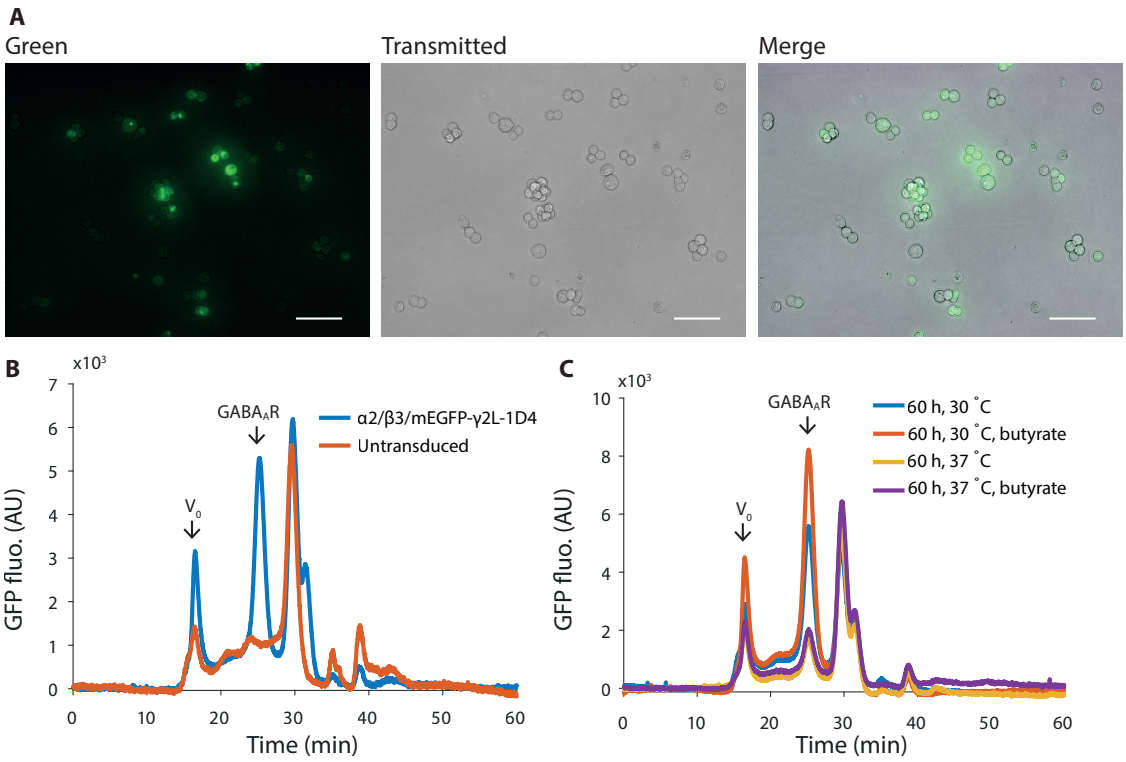

Figure 4.6: Expression of $GABA_AR$s using BacMam and lysate FSEC. A: Fluorescence images of cells transduced with α2, β3 and mEGFP-γ2L-1D4 subunits using BacMam. Scale bars: 100 µm **B**: A $GABA_AR$ peak was clearly visible in the GFP signal from lysate FSEC with cells transduced with α2, β3 and mEGFP-γ2L-1D4 subunits (blue), but not untransduced cells (orange). **C**: Example chromatograms from a test of BacMam expression conditions using lysate FSEC.

$GABA_AR$ peak was present in the GFP signal (excitation wavelength of 488 nm, emission wavelength of 507 nm) for transduced cells, but not untransduced cells (Figure 4.6B).

In order to optimise expression of $GABA_AR$s in the BacMam system, HEK293S GnTI$^-$ cells in suspension ($2x10^6$ ml^{-1}) were transduced with the α2, β3 and mEGFP-γ2L-1D4 subunits, each at a MOI of 1. Cells were incubated at 30°C or 37°C, and with or without the addition of 5 mM sodium butyrate. A 1 ml sample of cells was taken after 60, 72, 84 and 96 h, and these were subjected to lysate FSEC as described above. Chromatograms were analysed in MATLAB to identify the height of the $GABA_AR$ peak (around ~25 min, see Section D.1 for scripts). These heights for various expression conditions are shown in Table 4.2, and some example chromatograms are shown in Figure 4.6C. The highest peak was observed when cells were incubated at 30 °C, with the addition of 5 mM sodium butyrate, for 60 h.

A second round of optimisation was conducted to further optimise $GABA_AR$ expres-

Table 4.2: FSEC screening of lysates from HEK293S GnTI$^-$ cells transduced with α2/β3/mEGFP-γ2L-1D4 using BacMam (first round)

Time (h)	Temperature (°C)	Sodium butyrate	$GABA_AR$ peak height (AU)	$GABA_AR$ peak elution volume (min)
60	30		$5.63x10^3$	25.3
60	30	x	$8.29x10^3$	25.3
60	37		$1.68x10^3$	25.3
60	37	x	$1.95x10^3$	25.2
72	30		$5.27x10^3$	25.3
72	30	x	$6.87x10^3$	25.3
72	37		$1.99x10^3$	25.3
72	37	x	$1.82x10^3$	25.3
84	30		$5.11x10^3$	25.3
84	30	x	$5.65x10^3$	25.3
84	37		$1.39x10^3$	25.5
84	37	x	$8.87x10^2$	25.3
96	30		$3.89x10^3$	25.3
96	30	x	$3.87x10^3$	25.2
96	37		$1.06x10^3$	25.3
96	37	x	$7.75x10^2$	25.1

sion. Cells were transduced as before, incubated at 30 °C and a 1 ml sample of cells was collected 60 h after transduction. A range of ratios and MOIs of viruses for each subunit were used, from 1/4:1/4:1/4 to 4:4:4 (α2 MOI:β3 MOI:mEGFP-γ2L-1D4 MOI). A wider range of additives was also explored: 1-10 mM sodium butyrate, and 5 mM VPA. The data were analysed in MATLAB as before, and the results are shown in Table 4.3.

All transductions described so far were conducted with HEK293S GnTI$^-$ cells grown in Protein Expression Medium (PEM), since this medium was also used to grow cells for transient transfections [37]. However, other protocols suggest growing cells in FreeStyle 293 medium [220], [235], so these two types of media were also trialled for BacMam, using α2, β3, mEGFP-γ2L-1D4 viruses at an MOI of 1:1:1 (α:β:γ) to transduce HEK293S GnTI$^-$ cells in suspension. Cells were incubated at 30 °C for 72 h, then a 1 ml sample was taken and subjected to lysate FSEC as before (Figure 4.7). The results from this experiment showed an increase in $GABA_AR$ expression when cells were transduced in Freestyle 293, so this media was used in all later experiments.

Table 4.3: FSEC screening of lysates from HEK293S GnTI$^-$ cells transduced with α2/β3/mEGFP-γ2L-1D4 using BacMam (second round)

Additive (mM)	MOI (α:β:γ)	Peak height (AU)	Peak time (min)
—	1/4:1/4:1/4	$9.48x10^2$	25.5
—	1/2:1/2:1/2	$1.01x10^3$	25.4
—	1:1:1	$1.40x10^3$	25.0
—	1:1:2	$2.62x10^3$	25.4
—	1:2:1	$2.29x10^3$	25.2
—	1:2:2	$3.67x10^3$	25.2
—	2:1:1	$4.28x10^3$	25.1
—	2:1:2	$6.21x10^3$	25.0
—	2:2:1	$4.92x10^3$	25.1
—	2:2:2	$3.59x10^3$	25.2
—	4:4:4	$2.76x10^3$	25.2
10 butyrate	1:1:1	$1.10x10^3$	25.6
3 butyrate	1:1:1	$2.04x10^3$	25.2
5 butyrate	1:1:1	$1.56x10^3$	25.4
5 VPA	1:1:1	$4.51x10^3$	25.1

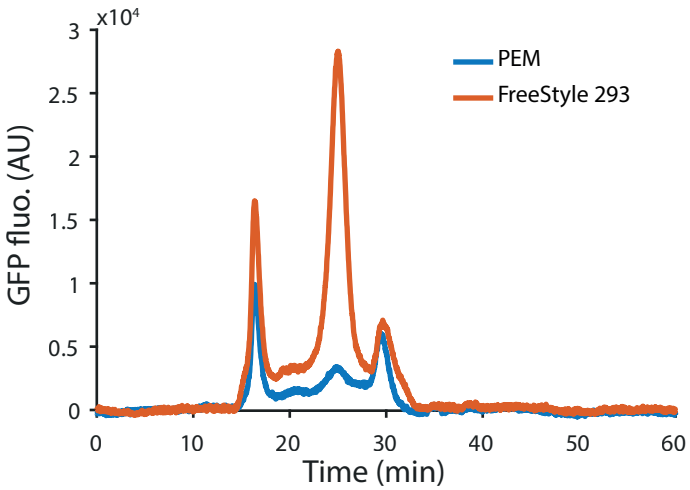

Figure 4.7: Lysate FSEC with cells transduced by BacMam in PEM and FreeStyle 293.

4.4 $GABA_AR$-expressing cell lines and comparison with BacMam

As an alternative to the BacMam expression system, polyclonal cell lines stably expressing $GABA_ARs$ were also created [221]. To first compare the relative expression of the BacMam expression system with induced expression in a stable cell line, both were used to express homomeric β3 $GABA_ARs$. To create a stable cell line, full-length β3 with an N-terminal mVenus and C-terminal 1D4 tag (mV-β3-1D4) was subcloned into the transfer vector pHR to create the plasmid pHR-mV-β3-1D4. Recombinant lentiviruses were then generated by cotransfection of this vector with psPAX2 and pMD2.G into HEK293 LentiX cells, which were then used to transduce HEK293S GnTI$^-$ TetR cells. Thus, an inducible polyclonal cell line expressing mV-β3-1D4 was created. mV-β3-1D4 expression could be observed after induction with 10 μg ml^{-1} doxycycline for 48 h by western blot (Figure 4.8A), fluorescence microscopy (Figure 4.8B-D) and lysate FSEC (Figure 4.8E).

This cell line was then used to compare mV-β3-1D4 expression with that achieved in the BacMam expression system. The mV-β3-1D4 construct was subcloned into the pEZT-BM vector, and recombinant baculovirus was produced. Expression of mV-β3-1D4 by induction of the stable cell line or transduction of HEK293S GnTI$^-$ cells was then compared in various expression conditions. Both cell types were grown in suspension to a density of 2x10^6 ml^{-1}. For BacMam, cells were induced using an MOI of 1, 4 or 10; with the addition (or omission) of 5 mM sodium butyrate or 5 mM VPA. Cells were incubated at 30 °C or 37 °C. For the stable cell lines, protein expression was induced by the addition (or omission) of 5 or 10 μg l^{-1} doxycycline, and with the addition (or omission) of 5 mM sodium butyrate or 5 mM VPA, and cells were incubated at 30 °C or 37 °C. A 1 ml sample of all cells was taken at 24, 48 and 72 h after induction, and subjected to lysate FSEC. These data were then analysed again in MATLAB; the peak heights for all samples are given in Table E.10, and the top 10 conditions and their overall ranks for each expression system are given in Table 4.4.

These results indicated that the stable cell line had higher expression than that achieved in the BacMam system, so cell lines expressing heteromeric $GABA_ARs$ were then created. In order to achieve this, FLAG tags were added at the α2 and α3 N-termini, and an HA tag was added at the β3 N-terminus; these constructs were subcloned into pHR to create the

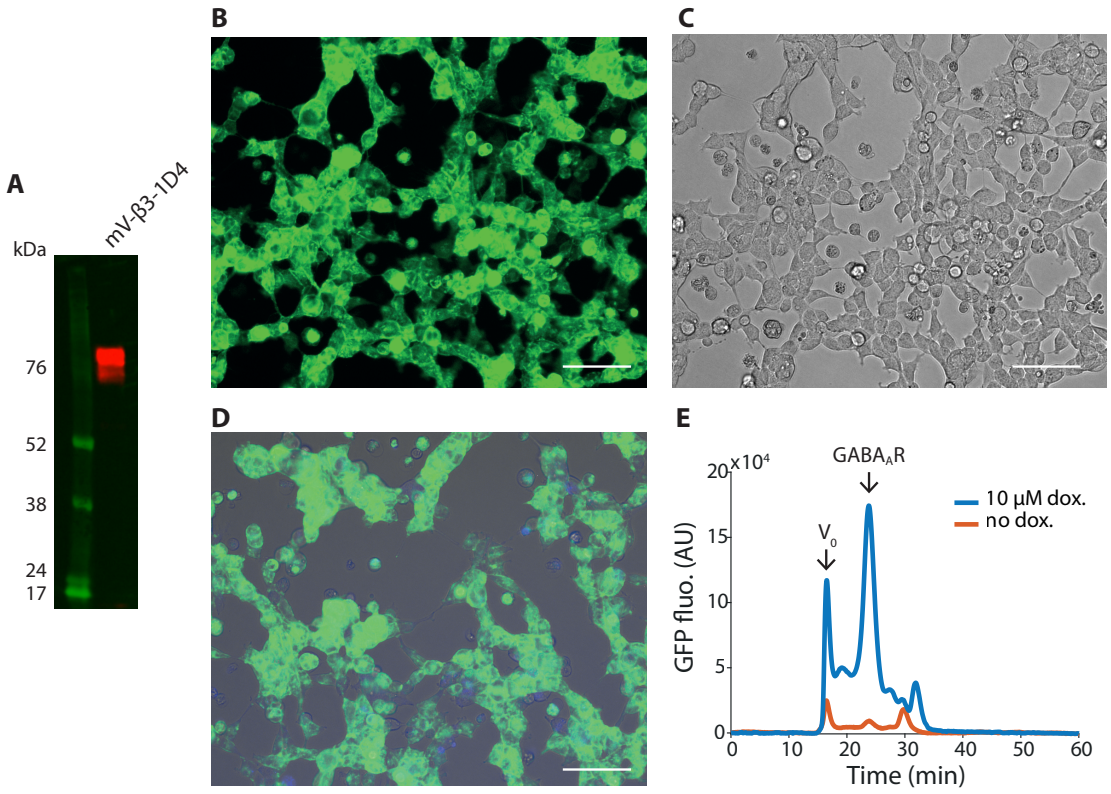

Figure 4.8: The mV-β3-1D4 cell line. **A**: Anti-1D4 western blot showing expression of mV-β3-1D4. Chemiluminescence is in the red channel, and the molecular weight markers are displayed in green. **B-D**: Fluorescence images showing mVenus fluorescence in induced cells (24 h, 10 µg ml^{-1} doxycycline), showing a green channel (**B**), transmitted light (**C**) and a merge (**D**). Scale bars: 50 µm. **E**: Lysate FSEC chromatograms (mVenus fluorescence) showing a clear $GABA_AR$ peak for induced cells (10 µM doxycycline, 48 h) but not for non-induced cells.

plasmids pHR-FLAG-α2, pHR-FLAG-α3 and pHR-HA-β3. In addition, a TEV protease cleavage site was added between the mEGFP and γ2L sequences, and a 3x(GGS) linker added between the γ2L and 1D4 sequences in mEGFP-γ2L-1D4; the resulting construct was also subcloned into pHR to create pHR-mEGFP-TEV-γ2L-3x(GGS)-1D4. To facilitate FACS later, these same constructs were also subcloned into pHR-IRES-FP vectors to create the constructs pHR-FLAG-α2-IRES-mRuby2, pHR-FLAG-α3-IRES-mRuby2, pHR-HA-β3-IRES-mTurquoise2 and pHR-mEGFP-TEV-γ2L-3x(GGS)-1D4-IRES-EmGFP.

These constructs were co-transfected (1α:1β:1γ) into HEK293 LentiX cells, and the resulting lentiviral particles were used to transduce HEK293S GnTI$^-$ TetR cells to give four cell lines: FLAG-α2/HA-β3/mEGFP-TEV-γ2L-3x(GGS)-1D4, FLAG-α3/HA-β3/mEGFP-TEV-γ2L-3x(GGS)-1D4, FLAG-α2-IRES-mRuby2/HA-β3-IRES-mTurquoise2/mEGFP-TEV-

Table 4.4: Top 10 expression conditions for mV-β3-1D4 using a stable cell line or the BacMam expression system

Rank	Expression system	VPA (mM)	Sodium butyrate (mM)	Temperature (°C)	Time (h)	MOI	Doxycycline concentration (mg ml^{-1})	Peak height (AU)	Elution time (min)
1	Stable	0	0	37	72	-	5	2.58x10^5	23.7
2	Stable	0	0	37	48	-	5	2.56x10^5	23.7
3	Stable	0	0	37	48	-	10	2.41x10^5	23.8
4	Stable	0	5	30	72	-	10	2.26x10^5	23.8
5	Stable	0	5	30	72	-	5	2.17x10^5	23.8
6	Stable	0	0	30	72	-	10	2.16x10^5	23.8
7	Stable	0	0	37	24	-	5	2.08x10^5	23.8
8	Stable	0	5	30	48	-	10	2.01x10^5	23.7
9	Stable	0	0	30	72	-	5	2.01x10^5	23.8
10	Stable	0	5	30	48	-	5	2.01x10^5	23.8
36	BacMam	0	5	30	72	10	-	6.13x10^4	23.9
38	BacMam	0	5	37	48	10	-	3.80x10^4	23.9
39	BacMam	0	5	30	72	4	-	3.52x10^4	23.9
40	BacMam	0	5	37	24	10	-	3.39x10^4	23.6
41	BacMam	0	5	30	48	10	-	3.34x10^4	23.9
42	BacMam	0	5	37	72	10	-	2.73x10^4	23.9
43	BacMam	0	5	30	48	4	-	1.99x10^4	23.9
44	BacMam	0	5	37	48	4	-	1.87x10^4	23.9
45	BacMam	5	0	37	24	10	-	1.67x10^4	23.7
46	BacMam	5	0	37	48	10	-	1.66x10^4	23.9

γ2L-3x(GGS)-1D4-IRES-EmGFP, and FLAG-α3-IRES-mRuby2/HA-β3-IRES-mTurquoise2/mEGFP-TEV-γ2L-3x(GGS)-1D4-IRES-EmGFP. Expression of all three subunits in all cell lines was verified by western blot after 24 h of induction by the addition of 10 μg ml^{-1} doxycycline (Figure 4.9).

An optimisation of expression conditions for the FLAG-α2/HA-β3/mEGFP-TEV-γ2L-3x(GGS)-1D4 and FLAG-α3/HA-β3/mEGFP-TEV-γ2L-3x(GGS)-1D4 cell lines was then conducted. Cells were grown in suspension in FreeStyle 293 media to a density of 2x10^6 ml^{-1}, and then induced with 5 or 10 μg ml^{-1} doxycycline. Optionally, 5 mM sodium butyrate or 5 mM VPA was added, and cells were incubated at 30 °C or 37 °C. A 1 ml sample of the cell suspension was then collected for lysate FSEC, in which cells were solubilised with 1% DDM (supplemented with 0.1% CHS) and run as before. The data were analysed in MATLAB to find the height of the $GABA_AR$ peak (Table E.11). Some example chromatograms (the best and worst for each cell line) are shown in Figure 4.10. For both cell lines, the best expression condition was 30 °C, 48 h, no additives, and 5 μg ml^{-1} doxycycline; and

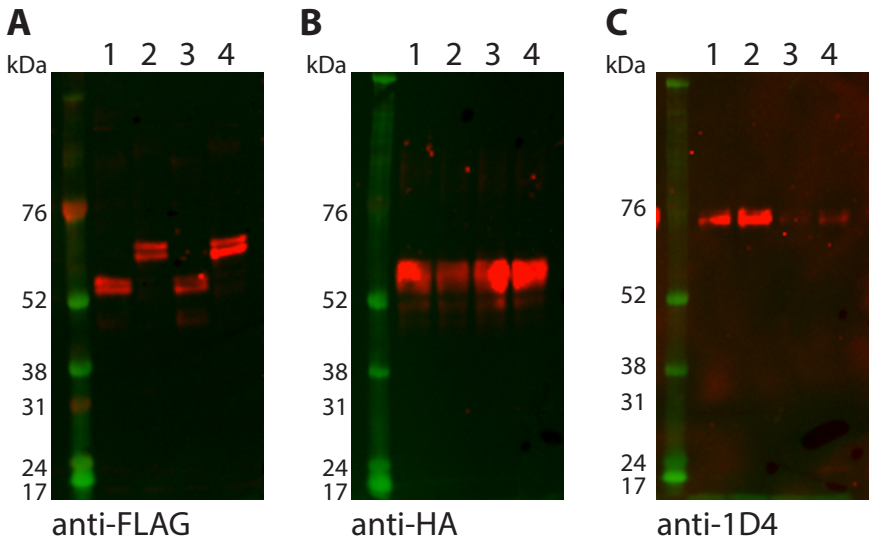

Figure 4.9: Characterisation of cell lines expressing heteromeric $GABA_A$Rs. A-C: Anti-FLAG (**A**), anti-HA (**C**) and anti-1D4 (**C**) western blots showing expression of FLAG-, HA- and 1D4- tagged subunits. Chemiluminescence is in the red channel, and the molecular weight markers are displayed in green. 1: FLAG-α2/HA-β3/mEGFP-TEV-γ2L-3x(GGS)-1D4, 2: FLAG-α3/HA-β3/mEGFP-TEV-γ2L-3x(GGS)-1D4, 3: FLAG-α2-IRES-mRuby2/HA-β3-IRES-mTurquoise2/mEGFP-TEV-γ2L-3x(GGS)-1D4-IRES-EmGFP, 4: FLAG-α3-IRES-mRuby2/HA-β3-IRES-mTurquoise2/mEGFP-TEV-γ2L-3x(GGS)-1D4-IRES-EmGFP.

the worst expression condition was 37 °C, 48 h, 5 mM VPA, and 5 μg ml^{-1} doxycycline. Furthermore, in both cases incubation at 30 °C for 48 h resulted in higher expression. If both of these conditions were met, doxycycline concentration seemed to be of less consequence, with both 5 μg ml^{-1} and 10 μg ml^{-1} doxycycline and both additives (or no additive) all resulting in high expression levels.

These cell lines are polyclonal; therefore, the expression level of heteromeric $GABA_A$Rs will vary from cell to cell. To further optimise $GABA_A$R expression, cells were sorted using FACS by Martyn Balmont, Fan Zhang and Maria Daly from the LMB flow cytometry facility. First, the FLAG-α2-IRES-mRuby2/HA-β3-IRES-mTurquoise2/mEGFP-TEV-γ2L-3x(GGS)-1D4-IRES-EmGFP and FLAG-α3-IRES-mRuby2/HA-β3-IRES-mTurquoise2/mEGFP-TEV-γ2L-3x(GGS)-1D4-IRES-EmGFP cell lines were sorted for triple-positive (mRuby2, mTurquoise2, and EmGFP) cells (Figure 4.11A-F). For the FLAG-α2-IRES-mRuby2/HA-β3-IRES-mTurquoise2/mEGFP-TEV-γ2L-3x(GGS)-1D4-IRES-EmGFP cell line, 15.9% of cells were triple-positive; and for FLAG-α3-IRES-mRuby2/HA-β3-IRES-mTurquoise2/mEGFP-TEV-γ2L-3x(GGS)-1D4-IRES-EmGFP, 12.5% of cells were triple-positive. Sorted and

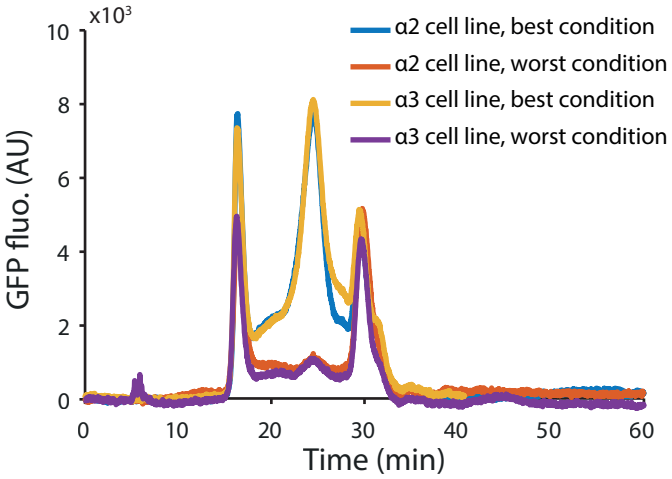

Figure 4.10: Lysate FSEC screening of expression conditions for heteromeric cell lines. The best and worst expression conditions for FLAG-α2/HA-β3/mEGFP-TEV-γ2L-3x(GGS)-1D4 (α2 cell line) and FLAG-α3/HA-β3/mEGFP-TEV-γ2L-3x(GGS)-1D4 (α3 cell line) as judged by lysate FSEC. For both cell lines the best condition was 30 °C, 48 h, no additives, and 5 µg ml^{-1} doxycycline and the worst expression condition was 37 °C, 48 h, 5 mM VPA, and 5 µg ml^{-1} doxycycline.

unsorted cells were then expanded, and when an appropriate culture volume with a density of 2x10^6 ml^{-1} was reached, $GABA_AR$ expression was induced with 10 µg ml^{-1} doxycycline and incubated at 30 °C. A 1 ml sample was taken of each cell type at 48 h and 72 h; cells were then solubilised in 1% DDM and 0.1% CHS, and then subjected to lysate FSEC (Figure 4.11G-H). The sorted cells gave approximately two- to four-fold higher $GABA_AR$ peaks (in the GFP channel, around 25 min) compared with the unsorted cells.

The non-IRES-FP (FLAG-α2/HA-β3/mEGFP-TEV-γ2L-3x(GGS)-1D4 and FLAG-α3/HA-β3/mEGFP-TEV-γ2L-3x(GGS)-1D4) cell lines were also sorted for mEGFP-positive cells by Dr Jonathan Elegheert (Figure 4.12A-F). For the α2 cell line 36.6% of cells were positive, whereas 30.1% of the α3 cells were positive. Sorted and unsorted cells were then also expanded, and when a density of 2x10^6 ml^{-1} was reached, induced with 10 µg ml^{-1} doxycycline and incubated at 30 °C. A 1 ml sample was taken of each cell type at 48 h and 72 h; cells were then solubilised in 1% DDM and 0.1% CHS, and then subjected to lysate FSEC (Figure 4.11G-H). The sorted cells again gave approximately two-fold higher $GABA_AR$ peaks (in the GFP channel, around 25 min) compared with the unsorted cells.

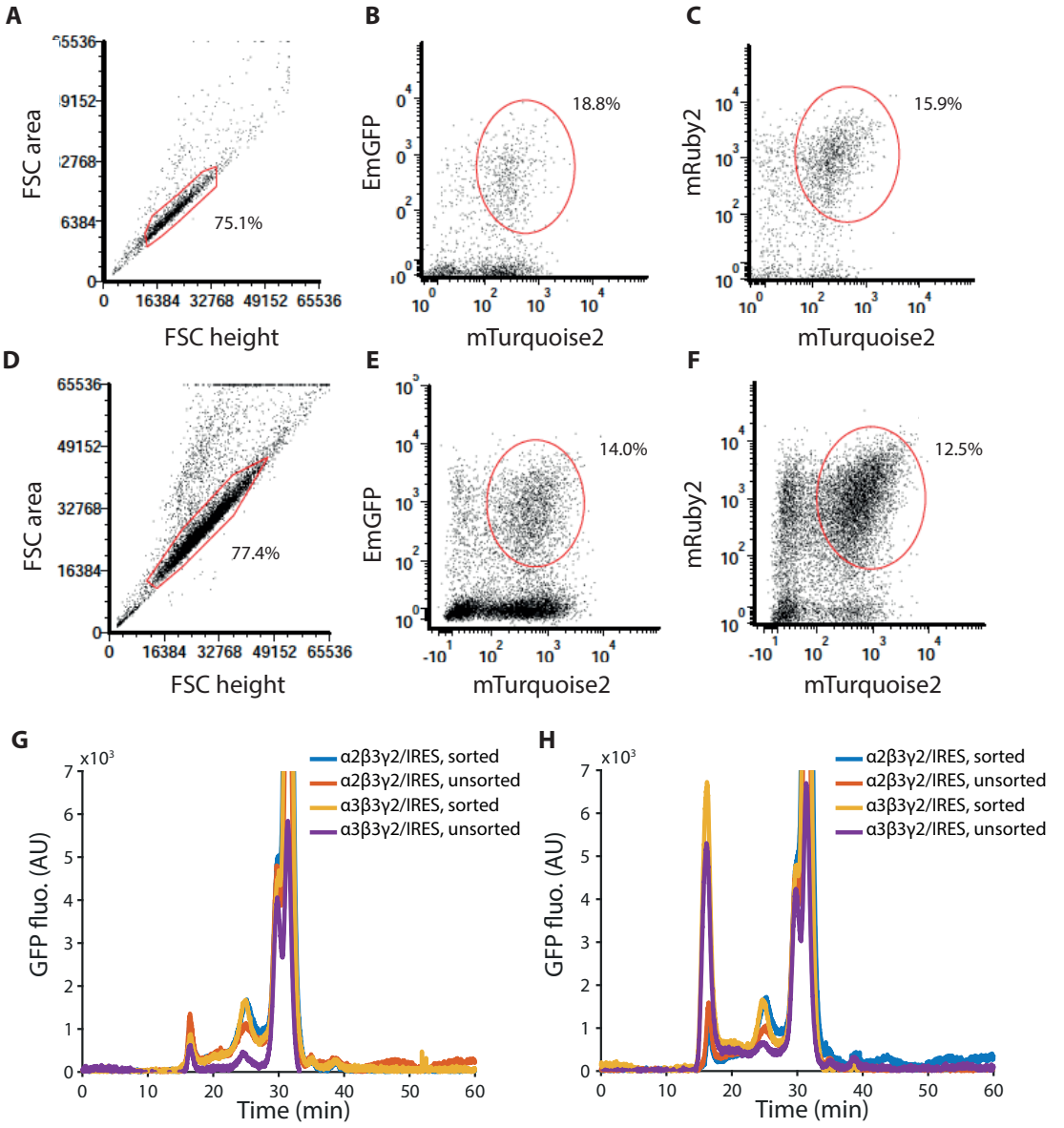

Figure 4.11: Three-colour FACS with $GABA_AR$ IRES-FP cell lines. **A-F**: FACS with the FLAG-α2-IRES-mRuby2/HA-β3-IRES-mTurquoise2/mEGFP-TEV-γ2L-3x(GGS)-1D4-IRES-EmGFP (**A-C** and FLAG-α3-IRES-mRuby2/HA-β3-IRES-mTurquoise2/mEGFP-TEV-γ2L-3x(GGS)-1D4-IRES-EmGFP (**D-F**) cell lines. Cells were first sorted using one gate in the forward-scattered area (FSC area) and forward-scattered height (FSC height) to isolate single cells (**A, D**), and then with two more gates to sort triple-positive mRuby2, mTurquoise2 and EmGFP positive cells (**B, C, E, F**). Percentages shown are after applying all gates to the left (i.e. for the gate in **C**, the value refers to triple-positive singlet cells as a percentage of all cells, i.e. after applying all gates). **G, H**: Lysate FSEC with sorted and unsorted cells after solubilisation of 1 ml of induced cells (10 µg ml^{-1} doxycycline), collected after 48 h (**G**) or 72 h (**H**) in 1% DDM, 0.1% CHS.

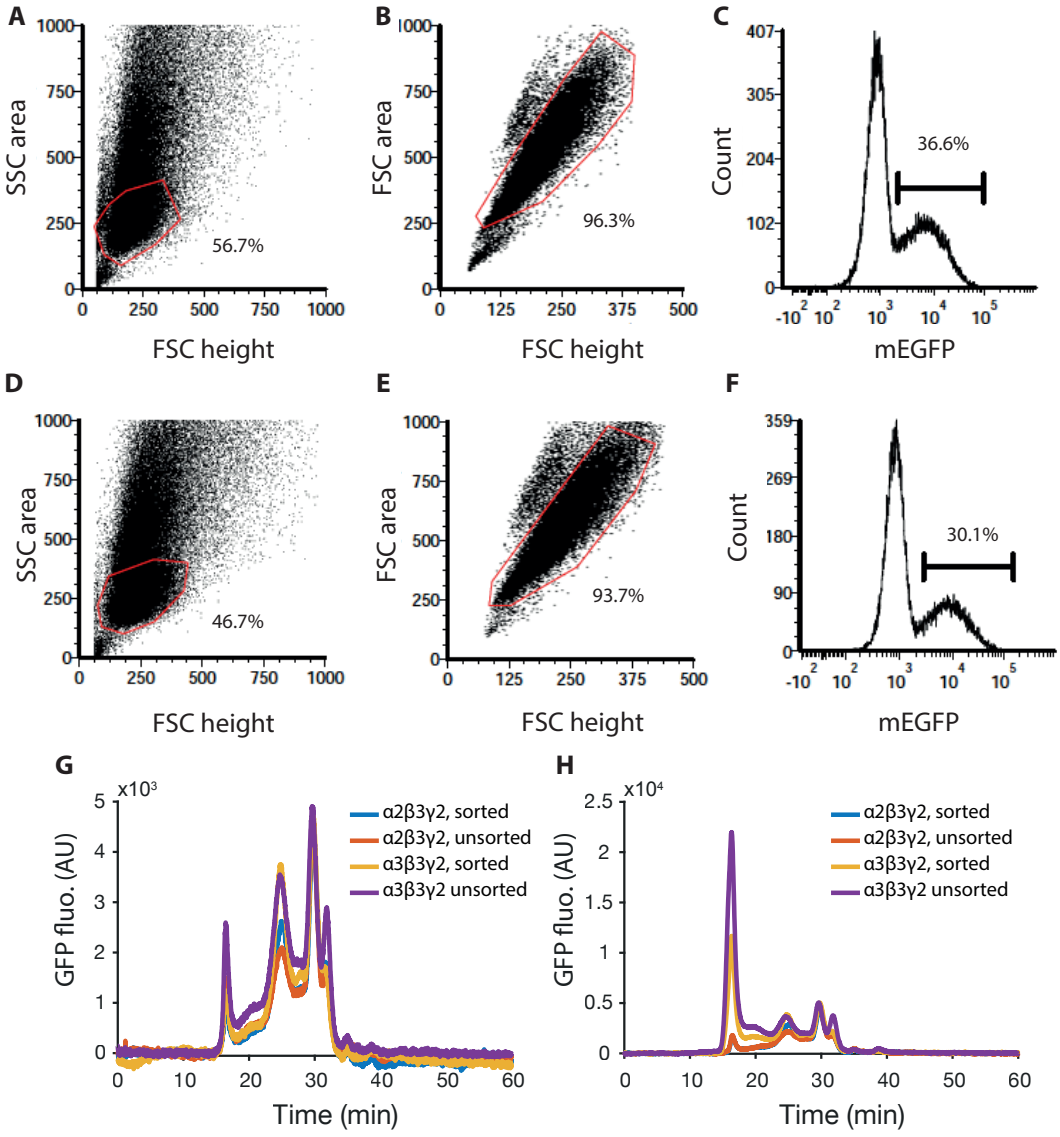

Figure 4.12: One-colour FACS with $GABA_AR$ cell lines. **A-F**: FACS with the FLAG-α2/HA-β3/mEGFP-TEV-γ2L-3x(GGS)-1D4 (**A-C** and FLAG-α3/HA-β3/mEGFP-TEV-γ2L-3x(GGS)-1D4 (**D-F**) cell lines. Cells were first sorted using a gate in the side-scattered area (SSC area) and forward-scattered height (FSC height), and then a second gate in the forward-scattered area (FSC area) and forward-scattered height (FSC height) to isolate single cells (**A, B, D, E**), and then with a third gate to sort mEGFP-positive from negative cells (**C, F**). Percentages shown are after applying all gates to the left (i.e. for the gate in **C**, the value refers to mEGFP-positive singlet cells as a percentage of all cells, i.e. after applying all gates). **G, H**: Lysate FSEC with sorted and unsorted cells after solubilisation of 1 ml of induced cells (10 µg ml^{-1} doxycycline), collected after 48 h (**G**) or 72 h (**H**) in 1% DDM, 0.1% CHS.

4.5 Purification optimisation

Next, the possibility of purification of expressed $GABA_ARs$ was investigated. The stable cell lines expressed $GABA_ARs$ with FLAG (α subunit) and 1D4 (γ subunit) tags, as well as a cleavable N-terminal GFP fusion (γ subunit). Therefore, the use of anti-FLAG, anti-1D4 and anti-GFP affinity media was explored. The sorted FLAG-α2/HA-β3/mEGFP-TEV-γ2L-3x(GGS)-1D4 cell line was grown in suspension and induced at a density of $2x10^6$ ml^{-1} with 10 μg ml^{-1} doxycycline. 250 ml of suspension cells was solubilised in 1% LMNG, 0.1% CHS, and then split into three. To each third, 100 μl of affinity media was added (anti-1D4, anti-FLAG, anti-GFP). After incubation with the media, $GABA_ARs$ were eluted from the 1D4 and FLAG resins using 100 μl of elution buffer (150 mM NaCl, 20 mM HEPES (pH = 7.2), 0.01% LMNG, 0.01% CHS, plus 2 mM 1D4 peptide for 1D4 resin or 1.5 μg ml^{-1} 3xFLAG peptide for FLAG resin). For GFP resin, the protein was cleaved by the addition of 1 mg ml^{-1} TEV protease to the same buffer. Eluates were collected after incubation with the elution buffer for 15 minutes (FLAG), or overnight (1D4, GFP). A further two incubations with the same volume of elution buffer were also conducted for 15 min (FLAG) or 2 h (GFP, 1D4).

To remove TEV protease from the GFP affinity sample, the three eluates were pooled and incubated with 10 μl TALON Co^{2+} affinity resin at 4°C for 30 minutes. Each sample was then subjected to FSEC (Figure 4.13A, B) and analysed by SDS-PAGE (Figure 4.13C). Both of these analyses revealed the most efficient means of purification was using FLAG affinity resin. For the GFP eluate, much of the protein cleaved from the GFP affinity resin seemed to have bound to the TALON resin (Figure 4.13C, lanes 13 and 14).

A comparison of the tryptophan fluorescence and GFP fluorescence for the FLAG and 1D4 samples revealed a much larger peak in the tryptophan signal compared with the GFP signal in the case of FLAG affinity purification (4.13D), but almost identical height peaks in the case of 1D4 purification (4.13E).

Additionally, protein purified using FLAG, 1D4 or GFP affinity media was reconstituted into nanodiscs. After washing the affinity media, 50 μl lipid mix (85% 10 mg ml^{-1} 1-palmitoyl-2-oleoyl-sn-glycero-3-phosphocholine [POPC] dissolved in 150 mM NaCl, 20 mM HEPES pH 7.4, and 3% DDM and 15% 20 mg ml^{-1} bovine brain extract dissolved in 150 mM NaCl, 20 mM HEPES pH 7.4, and 3% DDM) were added to each sample and

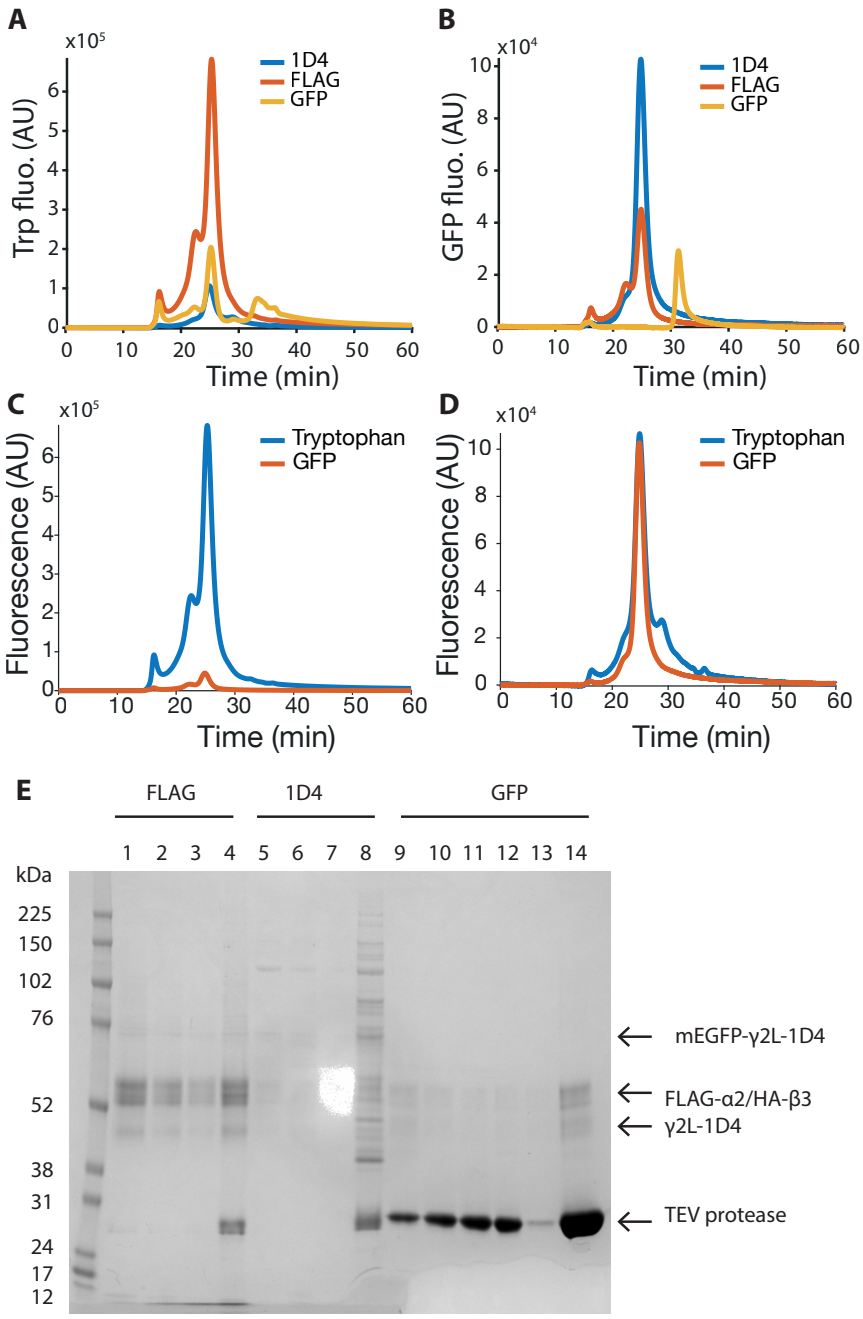

Figure 4.13: Affinity purification of α2β3γ2L $GABA_AR$ from a stable cell line in detergent. **A-D**: FSEC chromatograms for purified α2β3γ2L $GABA_AR$ from FLAG, 1D4 and GFP affinity chromatography. Both tryptophan (**A**) and GFP fluorescence (**B**) were monitored. A comparison of the tryptophan and GFP fluorescence for the FLAG (**C**) and 1D4 (**D**) samples. **E**: Coomassie SDS-PAGE of samples collected during affinity purifications: three eluates (lanes 1-3, 5-7, 9-11) were collected from each type of affinity media. Samples of the media after elution (lanes 4, 8, 12) were also run on the gel. Additionally, eluates from GFP affinity media were pooled and incubated with TALON metal affinity resin; the flow-through was run in lane 13 and a sample of the TALON resin was run in lane 14.

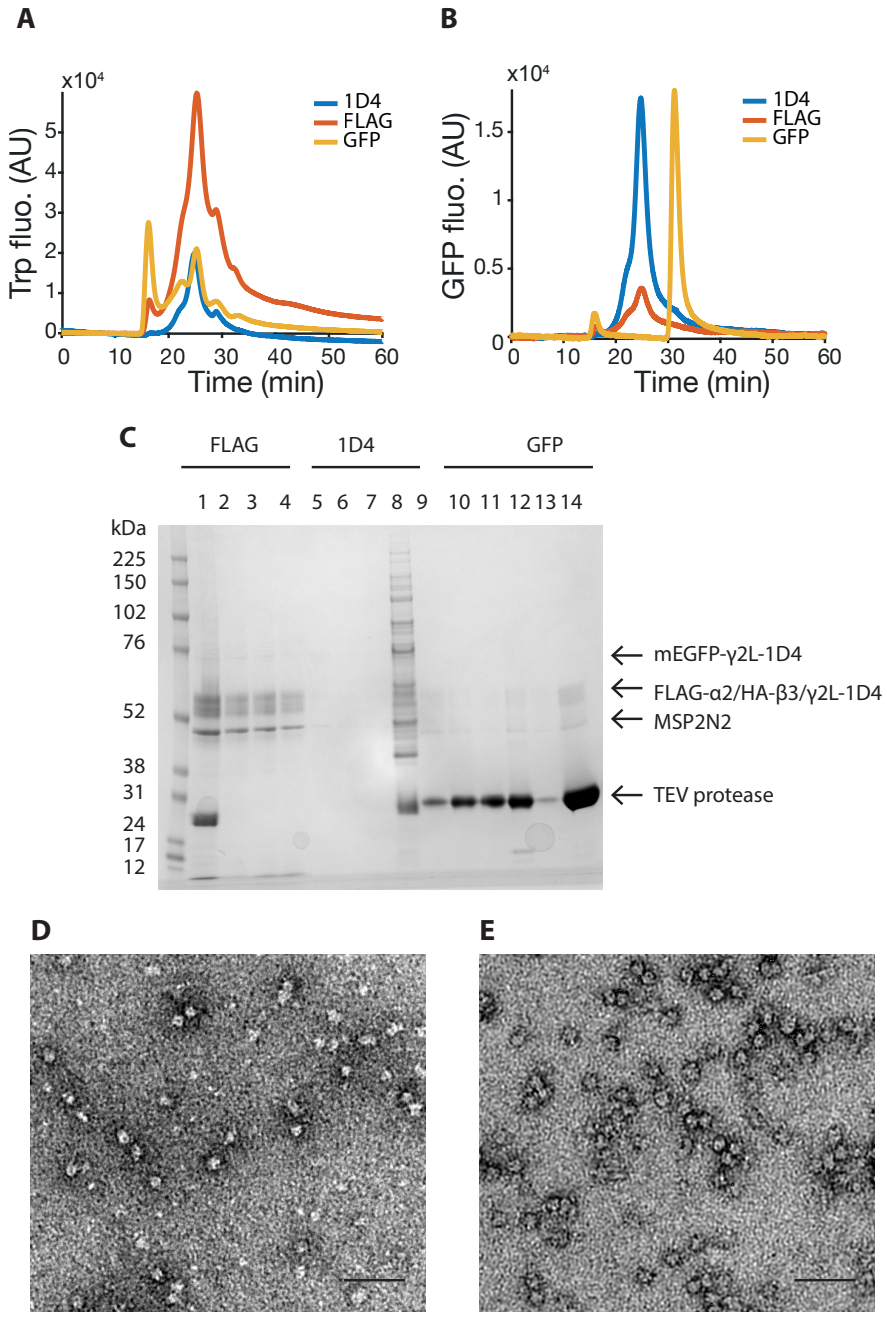

Figure 4.14: Affinity purification and exchange to nanodiscs of α2β3γ2L $GABA_AR$ from a stable cell line. **A, B**: FSEC chromatograms for purified α2β3γ2L $GABA_AR$ from FLAG, 1D4 and GFP affinity chromatography. **C**: Coomassie SDS-PAGE of samples collected during affinity purifications: three eluates (lanes 2-4, 5-7, 9-11) were collected from each type of affinity media. Samples of the media after elution (lanes 1, 8, 12) were also run on the gel. Additionally, eluates from GFP affinity media were pooled and incubated with TALON metal affinity resin; the flow-through was run in lane 13 and a sample of the TALON resin was run in lane 14. **D, E**: Negative stain EM with the eluates from 1D4 (**D**) and FLAG (**E**) affinity media. Scale bar 50 nm.

incubated for 30 minutes at 4 °C. 250 µg MSP2N2 was then added to each sample and incubated for 30 minutes 4 °C. Finally, 15 mg biobeads were added to each sample and incubated for two h at 4 °C. The affinity media were then washed extensively with buffer (without detergent; 8 x 1 ml washes), and $GABA_ARs$ were eluted as before.

The eluates were subjected to FSEC (Figure 4.14A, B) and Coomassie SDS-PAGE (Figure 4.14C) as before. Again, FLAG affinity purification gave the highest $GABA_AR$ peak in the tryptophan fluorescence channel, but 1D4 affinity purification gave the highest peak in the GFP fluorescence channel.

Negative stain EM was also conducted with the eluate from both FLAG and 1D4 affinity chromatography (Figure 4.14D, E). The sample appeared a little heterogenous, but resembled a cylindrical object with roughly the dimensions that would be expected for a $GABA_AR$ reconstituted into a nanodisc.

Reconstitution of heteromeric $GABA_ARs$ into amphipols (A8-35) was also explored. To compare these two systems, the $GABA_ARs$ were purified from the FLAG-α3/HA-β3/mEGFP-TEV-γ2L-3x(GGS)-1D4 cell line by 1D4 affinity chromatography as described above. For this purification, 1 mM picrotoxin, which binds in the pore, was included in all buffers, in an effort to rigidify the protein during purification. After washing the affinity medium (25 µl resin per 100 ml cells), the same lipid mix was added as before (1:1 [v/v] with resin volume). After a 30 min incubation, either A8-35 (2 µg per µl resin) or MSP2N2 (4 µg per µl resin) was added and incubated for a further 30 min. Biobeads (10 mg per 50 µl resin) were then added and the mixture was incubated for 2 h at 4 °C. After extensive washing and elution as before, the eluates were subjected to FSEC (Figure 4.15A, B) and negative stain EM (Figure 4.15C, D). The amphipol sample appeared to have a more monodisperse FSEC profile, and appeared more homogenous in negative stain EM compared with the nanodisc sample.

4.6 Discussion

In this chapter, various approaches were taken to purify triheteromeric $GABA_ARs$. Various expression systems were explored, including transient transfection, BacMam and stable cell lines. Several purification tags were also explored in search of the most efficient purification.

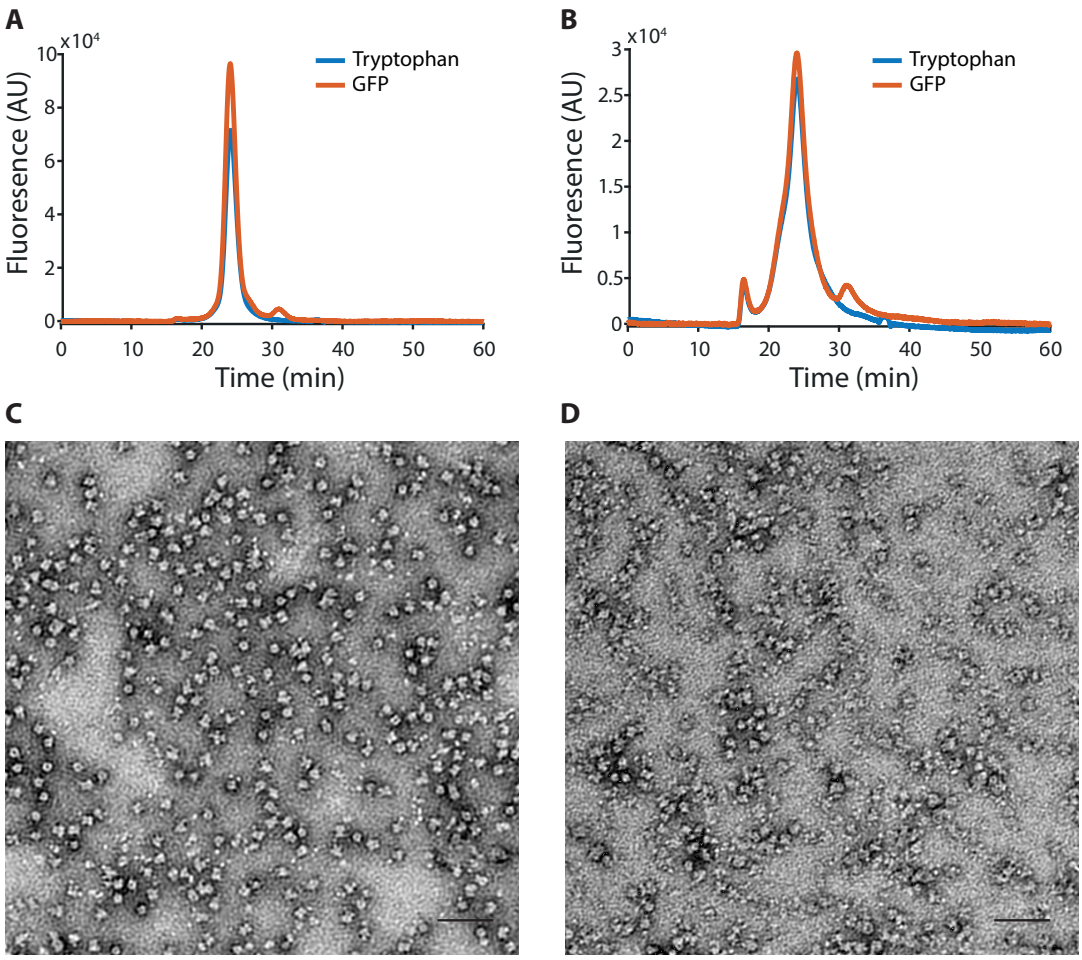

Figure 4.15: Reconstitution of a α2β32L $GABA_AR$ into amphipols and nanodiscs. A, B: FSEC chromatograms for purified α2β3γ2L $GABA_AR$ after reconstitution into amphipols (**A**, A8-35) or nanodiscs (**B**, MSP2N2). Negative stain EM of purified α2β3γ2L $GABA_AR$ after reconstitution into amphipols (**C**, A8-35) or nanodiscs (**D**, MSP2N2). Scale bar: 50 nm.

4.6.1 Constructs and stoichiometry

Although other studies have explored engineering $GABA_ARs$ to increase protein expression [37], [314], the focus of this work was to find conditions under which wild-type receptors could be expressed and purified, since recent structures of heteromeric $GABA_ARs$ solved by cryo-EM have adopted confirmations for which the physiological relevance is unclear [38], [39]. Particularly striking is the asymmetry of the pore region in these structures, a characteristic not observed in any other pLGIC family member, even in the heteromeric α4β2 nAChR [26]. To avoid possible artefacts of protein engineering and purification, full-length

wild-type subunits were used, with only the addition of small epitope tags for purification, or in the case of γ2L, an N-terminal GFP fusion which facilitated purification and FSEC.

The oligomeric state of purified $GABA_ARs$ was not extensively examined in the present work. It is well established that pLGICs are pentameric [22], [24], [31], [33], [35], including $GABA_ARs$ [37]–[40], although in some FSEC chromatograms, peaks other than the $GABA_AR$ and void peaks were present. It is unclear if these represent alternative oligomeric states or contaminants. After optimisation of expression and reconstitution into amphipols or nanodiscs, purified $GABA_ARs$ appeared relatively homogenous by negative stain EM, and will be later shown by high-resolution cryo-EM to be pentameric (Chapter 5).

The stoichiometry of purified receptors was also not examined. Methods have been developed to express heteromeric ion channels and manipulate their stoichiometry, including the construction of expression vectors with multiple subunits [315], or mixing expression vectors for different subunits in various ratios [26]. However, given that recent structures of triheteromeric $GABA_ARs$ have all indicated a 2α:2β:1γ subunit ratio (notably, after purification with a tag on the γ subunit) [38]–[40], which is consistent with previous functional evidence [59], the stoichiometry of purified αβγ receptors was assumed to also be 2α:2β:1γ. This was later examined by cryo-EM (see Chapter 5).

However, there are likely to be at least two populations of $GABA_ARs$ present in the αβγ stable cell lines generated in the present work. This inference comes from a comparison of the GFP (fused to γ2L-1D4) and tryptophan (total protein) fluorescence for receptors purified by FLAG and 1D4 affinity chromatography. When purified with 1D4 affinity chromatography, the peaks in GFP and tryptophan fluorescence were of a similar height, but when purified with FLAG affinity chromatography, the tryptophan fluorescence peak was at least ten times larger than the GFP peak. Therefore, purification using the FLAG tag (on the α subunit) likely resulted in enrichment of αβ as well as αβγ $GABA_ARs$, whereas a 1D4 purification (with a tag on the γ subunit) could only result in isolation of the αβγ receptor. Since a GFP signal is still present in the FLAG-purified sample, it is likely that this is a mixture of mostly αβ heteromers, with a small amount of αβγ receptors.

Although the α, β and γ subunits were transfected in a 1:1:1 ratio when producing lentiviral particles, viral titre tends to decrease with increasing construct size [221], so

the larger size of the γ subunit due to mEGFP fusion may have decreased its packaging efficiency. It is tempting to suggest that this resulted in lower expression of the γ subunit and therefore could be the reason for the larger proportion of αβ receptors. A previous study which developed a high-expressing α1β3γ2 cell line by 2:2:1 transfection of all three subunits found that only four of ten clones had the expected 2:1 ratio of agonist to benzodiazepine radioligand sites, suggesting some heterogeneity of stoichiometry [307]. However there is some functional evidence to the contrary, that suggests altering the ratio of subunit cDNA during transfection of αβγ $GABA_ARs$ does not change the functional properties of the expressed channels [67]. One possible interpretation of these data is that incorporation of γ into pentamers is less efficient, such that under low-level heterologous expression αβγ heteromers predominate, but when $GABA_ARs$ are highly expressed αβ heteromers are more prevalent.

4.6.2 Expression systems

In this work, mammalian cell lines were used exclusively to express $GABA_ARs$. Mammalian expression is preferable to other expression systems such as *E. coli* and yeast due to the capacity of mammalian cells for overexpression of 'complex' membrane proteins with native-like post-translational modifications [304]. Therefore, HEK293S GnTI$^-$ cells and derivatives were used to express $GABA_ARs$. In previous work transient transfection [37] or BacMam [38], [39] were used to express homomeric and heteromeric receptors with truncations to the intracellular M3-4 loop, however full-length receptors appeared to be poorly expressed when expressed in HEK293S GnTI$^-$ cells by transient transfection.

One other popular mammalian expression system is the BacMam system, which has been successfully used to express membrane proteins, including pLGICs such as GluCl and nAChR [220], [235]. In the present work, BacMam resulted in an appreciable level of expression of $GABA_AR$ expression in lysate FSEC. The level of expression seemed to be variable (compare peak heights around 25 minutes in Figures 4.7, 4.6, and Table 4.3), although it is unclear if this variability is inherent or due to incidental factors such as inaccurate estimation of viral titre.

The advantage of the pEZT-BM plasmid used here is that it allows easy titration of baculovirus stocks [220]. However, interpreting the results of the end-point assay for determining viral titre requires the assumption that each virus infects only one Sf9 cell, resulting in an observable level of GFP expression. If GFP expression is not sufficiently high to be observed in some cells, or if the virus replicates during the course of the assay, this assumption is invalidated. A further assumption is that the susceptibility to infection is the same for Sf9 cells, with which the assay was performed, and HEK293 cells that were used to express $GABA_ARs$. The validity of these assumptions was not examined in the present work, but if not met this could explain the variability observed in $GABA_AR$ expression.

To further explore possible expression systems, a comparison of β3 $GABA_AR$ expression using BacMam and a polyclonal stable cell line was conducted. The lysate FSEC results indicated better expression in the stable cell line, although the reasons for this difference were not examined. The vectors used for these two systems make use of the same promoter (CMV), but differ in their 3' elements: pEZT-BM contains WPRE and polyA sequences, whereas pHR contains only a WPRE sequence. Although this difference could affect mRNA stability, which is a determinant of protein expression level [304], if this were the main factor then one would expect to obtain higher expression of $GABA_ARs$ with the BacMam system. In contrast, the titre of the lentiviral particles was not determined, but a very high titre resulting in many copies of the transgene in each cell could explain these results. Another possible explanation is an enhancement of expression after integration of the transgene into the genome upon lentiviral transduction, or a combination of these last two factors.

Based on the high expression level observed in the $GABA_AR$ β3 cell line, heteromeric αβγ cell lines were then created. These cell lines were also polyclonal, so a range of expression levels would be expected across the population. To select for cells expressing all three subunits, a three-colour FACS sort was conducted with cell lines containing an IRES-FP. The expression of a fluorescent protein indicated positive cells, but only appeared to correlate weakly with $GABA_AR$ expression; only 10-15% cells were sorted as triple-positive for all fluorescent proteins, but the lysate FSEC peak was only about two- to four-fold higher for the sorted cells compared with the unsorted cells. When cells were sorted based on a GFP directly fused to the protein of interest (mEGFP-γ2L), around 30-35%

of cells were found to be positive but again the improvement in expression was less than three-fold. The reason for this difference is unclear, although the high level of αβ $GABA_AR$ expression in these cells is a confounding factor.

The advantage of the lentivirus approach to creating a cell line is time-efficiency. Other approaches, such as the creation of monoclonal cell lines, have also been used to express $GABA_ARs$; for example α1β3, α1β3γ2L and α4β3δ$GABA_ARs$ [306]–[308]. Although these monoclonal cell lines exhibit high levels of expression of functional $GABA_ARs$, each cell line takes many months to establish, and is labour-intensive. In contrast, the approach taken here can be completed within a month and is relatively hands-off. It is also possible to test many constructs at once, as done here with four heteromeric $GABA_AR$ cell lines (α2β3γ2L and α3β3γ2L, with and without IRES-FP).

4.6.3 $GABA_AR$ purification

During purification, two different approaches to reconstitute $GABA_ARs$ into detergent alternatives were taken. From recent results with α1β2γ2 $GABA_ARs$, it is clear that detergents can have a detrimental effect on the integrity of the $GABA_AR$ transmembrane domain [38]–[40]. Membrane proteins in detergent can also be difficult to work with when making cryo-EM grids because of changes in surface tension and concentration of protein required [243]. Therefore, purified $GABA_ARs$ were reconstituted into amphipols (A8-35) or nanodiscs (MSP2N2). This was performed while protein was still bound to affinity chromatography media by adding an excess of lipids and A8-35 or MSP2N2, in order to facilitate removal of this excess [41], [42]. This method is different to the usual approach of adding particular ratios of lipids and MSP or amphipols, and then removing a small excess by size exclusion chromatography [313], [316]. However, the low yield of $GABA_ARs$ made collecting a size exclusion eluate difficult, and therefore the present approach was used.

Despite the lack of a size exclusion 'polishing' step in the purification, purified $GABA_ARs$ in amphipols appeared relatively homogenous as judged by FSEC negative stain EM. Purified $GABA_ARs$ in nanodiscs appeared less homogenous, with a broader FSEC peak and some possible degradation visible in negative stain EM (Figure 4.15). The reason for this difference is unclear. While other alternatives area available, for example SMALP

(styrene–maleic acid lipid particles) and Salipro [317], [318], these are less well characterised and therefore were left for future work.

After optimisation of expression and purification of $GABA_ARs$ in this work, cryo-EM studies using purified protein are discussed in the next chapter.

5

Structural studies of an α3β3γ2L $GABA_A$R-nanobody complex

Contents

5.1 Introduction 139
5.2 Optimisation of grids for cryo-EM 141
5.3 α3β3 $GABA_A$R in complex with α3β3mb173 and GABA 143
5.4 α3β3γ2L $GABA_A$R in complex with α3β3mb173 and GABA 147
5.5 α3β3γ2L $GABA_A$R in complex with α3β3mb173, GABA and picrotoxin 151
5.6 Discussion 163

5.1 Introduction

After developing methods for purification of triheteromeric $GABA_A$Rs (Chapter 4), the structure of this receptor, and in particular its interaction with potentiating nanobodies (Chapter 3) was investigated by cryo-EM.

In recent years, single-particle cryo-EM has become a viable technique for high-resolution structure determination, particularly for large macromolecular complexes that are unlikely to crystallise [243]. Recent developments both in hardware, including better microscopes, direct electron detectors and phase plates [265], [272]; as well as data processing software, including new algorithms, better implementations of existing algorithms,

and the use of graphical processing units (GPUs) to accelerate data analysis [275], [319], [320], have enabled the determination of protein structures that were previously difficult to characterise. Improvements have also been made in sample preparation, including the introduction of more stable grids with a gold support (commercialised by Quantifoil as UltrAuFoil grids) that are more resistant to movement in the electron beam [249]. Further details of the theory and practice of cryo-EM can be found in Section 2.6.1.

Despite these advances, challenges still remain for structure determination by cryo-EM. In particular, if a homogeneous and stable sample has been obtained, making good grids which contain well-distributed particles in thin ice can still be difficult [243]. The air-water interface, which is extensive in the thin films created just prior to vitrification, can induce preferential orientation or denaturation (full or partial) of exposed proteins [254], [321]. This issue is greater for some proteins than others, in a seemingly unpredictable manner. Previous work has found that $GABA_ARs$ can have issues with selective orientation on cryo-EM grids [296], although less so for samples in detergent [38], [39] and nanodiscs [41], [42]. However, the use of detergents presents additional issues with sample quality [38], [39] as well as particle distribution in freestanding ice [243]. Therefore, approaches to reconstitute $GABA_ARs$ into alternative supports such as nanodiscs and amphipols were explored (Chapter 4), and approaches to making cryo-EM grids are described in this chapter.

In addition to grid preparation, the $GABA_AR$ presents additional difficulties for cryo-EM because of its relatively small size. The full-length pentameric receptor is ~250 kDa, which is on the low end of particle size practically observable by traditional cryo-EM. Although theoretical calculations indicate that averaging ~10000 particles of a protein of size ~100 kDa should be enough to obtain 'atomic' resolution [263], reconstructions from data such as this were difficult to obtain for many years [322]. In addition to developments in hardware related to optics and detectors (discussed in Section 2.6.1), one additional factor that has improved the reach of cryo-EM into the range of smaller proteins (even to those below 100 kDa) has been the development of the Volta Phase Plate (VPP) [266], [268], [323]. When placed in the back focal plane, this device produces phase contrast which enhances the visible features of particles in micrographs. The VPP has been successfully

used to determine the structure of other small proteins by cryo-EM, such as GPCRs [324], [325] and even haemoglobin (64 kDa) [326].

5.1.1 Aims

Cryo-EM is thus a useful technique for structural determination of $GABA_ARs$, as illustrated by several recent structures of heteromeric $GABA_ARs$ solved using this technique [38], [39], [41], [42], [327]. The aim of the work described in this chapter was to investigate the interaction of nanobodies identified earlier as positive modulators of $GABA_ARs$ (Chapter 3) with full-length heteromeric $GABA_ARs$, from a structural perspective.

5.2 Optimisation of grids for cryo-EM

First, the behaviour of purified $GABA_ARs$ on cryo-EM grids was explored. Since sample concentration was often low (~0.1 mg ml^{-1}), the particle density on grids was increased in these cases by multiple rounds of sample application and blotting before vitrification [253]. The effect of this method was explored with an α3β3γ2L purified with FLAG affinity chromatography (see Chapter 4 for details of a typical purification). A 10 µl sample of the eluate (diluted 1/5 to conserve sample) was subjected to FSEC (Figure 5.1A) and negative stain EM (Figure 5.1B).

A megabody version of the nanobodies α3β3nb173 and α3β3nb183, here termed α3β3mb173 and α3β3mb183, kindly provided by Tomasz Uchanski and Jan Stayert, were added to $GABA_AR$ samples. α3β3mb173 was added to the $GABA_AR$ at a calculated molar ratio of 4:1 (mb to pentamer). GABA was also added to a final concentration of 1 mM, since this increases the affinity of this nanobody for the receptor (see Chapter 3). This sample, at a concentration of 0.1 mg ml^{-1}, was used to make vitrified cryo-EM grids. Initially, when the sample was applied to UltrAuFoil 1.2/1.3 grids (400 mesh), blotted and vitrified, the particles appeared sparsely distributed (Figure 5.1C). Therefore, additional grids were vitrified after two rounds of sample application and blotting (Figure 5.1D), which improved the density of particles in ice. For grids prepared this way, the first round of blotting was performed manually with filter paper inserted through the side port of the vitrobot, and the final round was performed using the vitrobot itself.

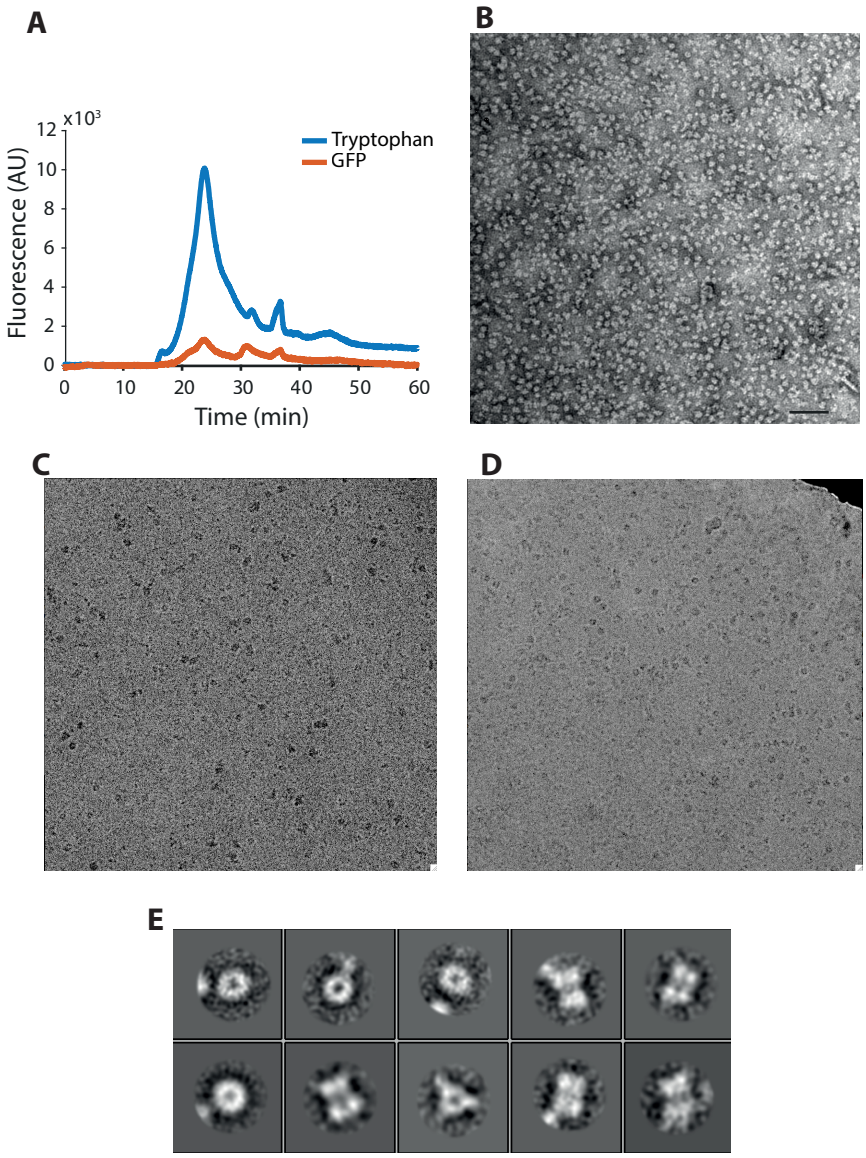

Figure 5.1: Characterisation of FLAG-purified GABA$_A$R from a stable cell line, reconstituted into MSP2N2 nanodiscs by EM. A: Analytical FSEC with FLAG-purified GABA$_A$R from an α3β3γ2L stable cell line. The tryptophan (blue) and GFP (red) fluorescence was recorded **B**: Negative stain EM with the same sample. **C, D**: Vitrified FLAG-purified GABA$_A$R from an α3β3γ2L stable cell line on UltrAuFoil 1.2/1.3 grids, after one (**C**) or two (**D**) sample applications. **E**: 2D classification of 2749 particles from 13 micrographs from cryo-EM showing top and side views of purified GABA$_A$Rs. Scale bars: 40 nm

Next, the behaviour of purified $GABA_ARs$ on other types of grids was explored, and in particular the distribution of orientations adopted by receptors in vitrified ice. α3β3γ2L $GABA_AR$ was purified from the FLAG-α3/HA-β3/mEGFP-TEV-γ2L-3x(GGS)-1D4 cell line using 1D4 affinity chromatography as previously described (Chapter 4). Where necessary, sample was applied to grids multiple times as described above. Figure 5.2 shows micrographs and 2D classes for various samples (α3β3γ2L reconstituted into amphipols [A8-35; Figure 5.2A-E] or nanodiscs [MSP2N2; Figure 5.2F], and deglycosylated with EndoF1 [Figure 5.2D, E] or not [Figure 5.2A-C, F]), on various types of grids (UltrAuFoil 1.2/1.3 [5.2A-C, E, F], optionally coated with graphene oxide [Figure 5.2C]; or ultrathin continuous carbon with overlaid lacey carbon on copper grids [Figure 5.2D]).

$GABA_ARs$ reconstituted into amphipols in the presence of 1 mM GABA and α3β3mb173 or α3β3mb183 were first investigated (Figure 5.2A, B). After the collection of 20 (α3β3mb173) or 21 (α3β3mb183) micrographs, particles were picked and two rounds of 2D classification were conducted in cryoSPARC (v2). This analysis revealed that most particles seem to be preferentially oriented, with a predominant 'top' view with a characteristic toroid shape. Coating UltrAuFoil (1.2/1.3) grids with graphene oxide seemed to have only a small effect on the distribution of orientations (Figure 5.2C). However, when $GABA_ARs$ in amphipols were deglycosylated with EndoF1 after elution and applied to either UltrAuFoil 1.2/1.3 or copper grids coated with ultrathin continuous carbon and lacey carbon, likely side and tilt views were observed in 2D classes (Figure 5.2D, E, white asterisks). Similarly, when $GABA_ARs$ were reconstituted into nanodiscs (MSP2N2), some likely side or tilt views were visible (Figure 5.2F).

5.3 α3β3 $GABA_AR$ in complex with α3β3mb173 and GABA

The grids containing FLAG-purified α3β3γ2L $GABA_AR$, reconstituted into nanodiscs (MSP2N2), in complex with α3β3mb173 and 1 mM GABA were then used for a data collection session on an FEI Titan Krios (Figure 5.3), using the settings detailed in Table 5.1. Figure 5.3A shows a typical micrograph from this dataset. After motion correction using MotionCor2 [278], the CTF was estimated for each micrograph using gctf [280], and an example power spectrum is shown in Figure 5.3B. The phase shifts and range of

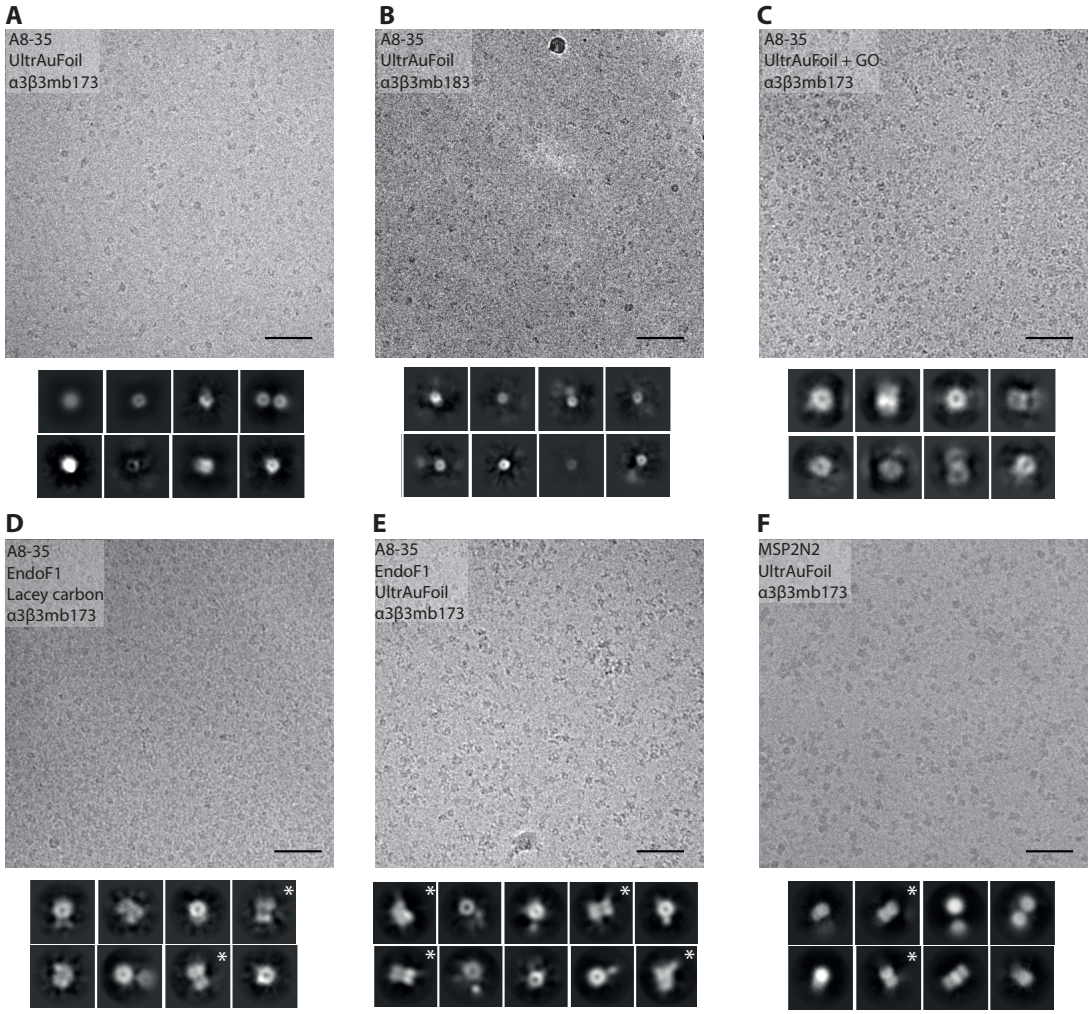

Figure 5.2: Optimisation of cryo grids for $GABA_AR$s. Micrographs (top) and 2D classes (bottom) for various $GABA_AR$ samples and grid types. All $GABA_AR$s here are α3β3γ2L purified from a polyclonal stable cell line, and all are in the presence of 1 mM GABA. **A**: A micrograph taken of plunge-frozen grids (UltrAuFoil 1.2/1.3) for a $GABA_AR$ reconstituted into amphipols (A8-35), in the presence of α3β3mb173; 2D classes for 7523 particles picked from 20 micrographs. **B**: A micrograph taken of vitrified grids (UltrAuFoil 1.2/1.3) for a $GABA_AR$ reconstituted into amphipols (A8-35), in the presence of α3β3mb183; 2D classes for 2354 particles picked from 21 micrographs. **C**: A micrograph taken of cryo-EM grids (UltrAuFoil 1.2/1.3, coated with graphene oxide) for a $GABA_AR$ reconstituted into amphipols (A8-35), in the presence of α3β3mb173; 2D classes for 6138 particles picked from 13 micrographs. **D**: A micrograph taken of plunge-frozen grids (Ultrathin lacey carbon, copper grid bars) for EndoF1-treated $GABA_AR$ reconstituted into amphipols (A8-35), in the presence of α3β3mb173; 2D classes for 4674 particles picked from 18 micrographs. **E**: A micrograph taken of cryo-EM grids (UltrAuFoil, 1.2/1.3) for EndoF1-treated $GABA_AR$ reconstituted into amphipols (A8-35), in the presence of α3β3mb173; 2D classes for 3337 particles picked from 20 micrographs. **F**: A micrograph taken of vitrified grids (UltrAuFoil, 1.2/1.3) for a $GABA_AR$ reconstituted into nanodiscs (MSP2N2), in the presence of α3β3mb173; 2D classes for 3337 particles picked from 20 micrographs. White asterisks in the top right hand corner of 2D classification boxes indicate likely side views (in the plane of the membrane). Note: 2D classes appear to be different sizes because the pixel size varies between datasets. Scale bars: 50 nm

Table 5.1: Data collection parameters for α3β3 $GABA_AR$ (in MSP2N2 nanodiscs, FLAG purification) + α3β3mb173, 1 mM GABA

Data collection parameters	
Microscope	Titan Krios (LMB Krios II)
Volta Phase Plate used	x
Detector	Falcon III (Counting)
Nominal magnification	75,000X
Voltage (kV)	300
Fluence ($e^- Å^{-2}$)	30
Frames	75
Defocus range (μm)	-0.5 to -0.7
Pixel size (Å)	1.07
Number of micrographs	372
Processing	
Micrographs used	269
Number of picked particles	189787
Particles in final reconstruction	15132
Type of refinement	Homogenous refinement (cryoSPARC v2)
Symmetry imposed	C1
Map resolution (Å)	11.9
FSC threshold	0.143

defocus values are as would be expected (Figure 5.3C, D). After autopicking in RELION-2 (117929 particles), and two rounds of 2D classification, the 2D classes shown in Figure 5.3E were obtained (40417 particles). A variety of orientations are visible in these classes, and the extracellular domain, transmembrane domain and nanodisc belt protein are distinguishable. Two megabodies appear to be bound to the extracellular domain in these classes (Figure 5.3E, white arrows), with approximately a 145° angle between the two nanobodies (Figure 5.3E, inset).

Various data processing strategies were pursued using the software packages Warp, RELION-3, and cryoSPARC. Most efforts to process this data resulted in 'streaky' maps (Figure 5.4B), indicative of anisotropy; the best reconstruction was obtained in cryoSPARC (v2) using non-uniform refinement (Figure 5.4). This cryo-EM density map was obtained using 8730 particles, after auto-picking in RELION-3 (179289 particles), two rounds of 2D classification (40417 particles selected), and one round of 3D classification (into 3 classes, 1 class selected).

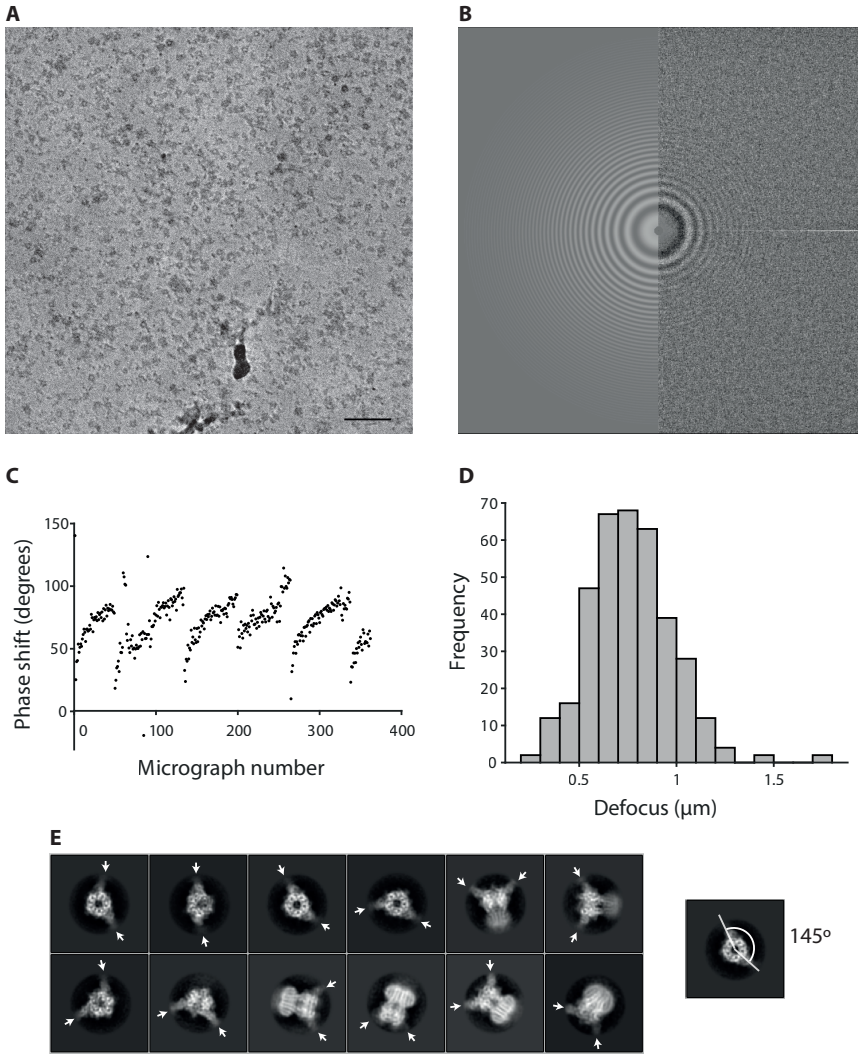

Figure 5.3: Data collection for FLAG-purified $GABA_AR$ from a stable cell line. **A**: Example motion-corrected, dose-weighted micrograph for vitrified FLAG-purified $GABA_AR$ from an α3β3γ2L stable cell line in complex with α3β3mb173. Scale bar: 50 nm. **B**: Example fitted power spectrum. **C, D**: Phase shifts (**C**) and defocus (**D**) for 372 motion-corrected micrographs, estimated using gctf. **E**: 2D classification (in RELION-3) of 40417 particles picked from motion-corrected micrographs. Two bound megabodies were visible in this dataset, with an angle of approximately 145° between them.

This map had a nominal resolution of 6.6 Å (Figure 5.4F), and accommodated the structure of a α1β3γ2L $GABA_AR$, solved in complex with α1β3nb138 (Figure 5.5), and two nanobodies (two copies of α1β3nb138 from the $GABA_AR$ structure was here docked into the map) [41]. Density for the receptor, the nanobody portion of two megabodies, and the nanodisc are clearly visible, but the low resolution of the map prevented further interpretation. However, it is clear that the megabody used, α3β3nb173, binds in a distinct location from the binding site of α1β3nb138 for the α1β3γ2L $GABA_AR$, at the top of the ECD.

This binding site appears to be at the top of the interface between adjacent subunits, above loop C (5.5E, F). Although the resolution is too poor to unambiguously identify individual subunits, an inspection of density unaccounted for by the main chain of the docked model reveals likely N-linked glycans (Figure 5.5). Given that the three subunits have different patterns of N-linked glycosylations (Figure 5.5A), this allows the tentative assignment of the subunits on either side of the nanobody binding interface, although the identity of the fifth subunit is unclear (Figure 5.5B-F). Based on the apparent presence of N-linked glycans close to β3N80 and β3N149 on the principal (+) subunit, and α3N148 and α3N200 on the complementary (-) subunit, it would appear that α3β3mb173 binds at the same interface as GABA (β+/α-), but at the top of the ECD.

5.4 α3β3γ2L $GABA_AR$ in complex with α3β3mb173 and GABA

Since the FLAG-purified sample did not yield a high-resolution map, the behaviour of 1D4-purified samples were next explored. Since the 1D4 purification tag is on the γ subunit, these must contain at least one of these subunits, and are likely to be αβγ heteromers.

The FLAG-α3/HA-β3/mEGFP-TEV-γ2L-3x(GGS)-1D4 cell line was grown in suspension, and induced at a density of $2.5x10^6$ ml^{-1} and volume of 1 l. After solubilisation in 1% LMNG, 0.1% CHS, receptors were incubated with 1D4 affinity resin (400 µl), and reconstituted into MSP2N2 while bound. 1 mM GABA was added to the eluate (500 µl), as well as α3β3mb173 at a calculated 4mb:1 pentamer molar ratio, and then the sample was concentrated by ultrafiltration (100 kDa cutoff membrane) to approximately 0.25 mg ml^{-1}. This complex was used to make cryo grids (UltrAuFoil 1.2/1.3) and these grids were used

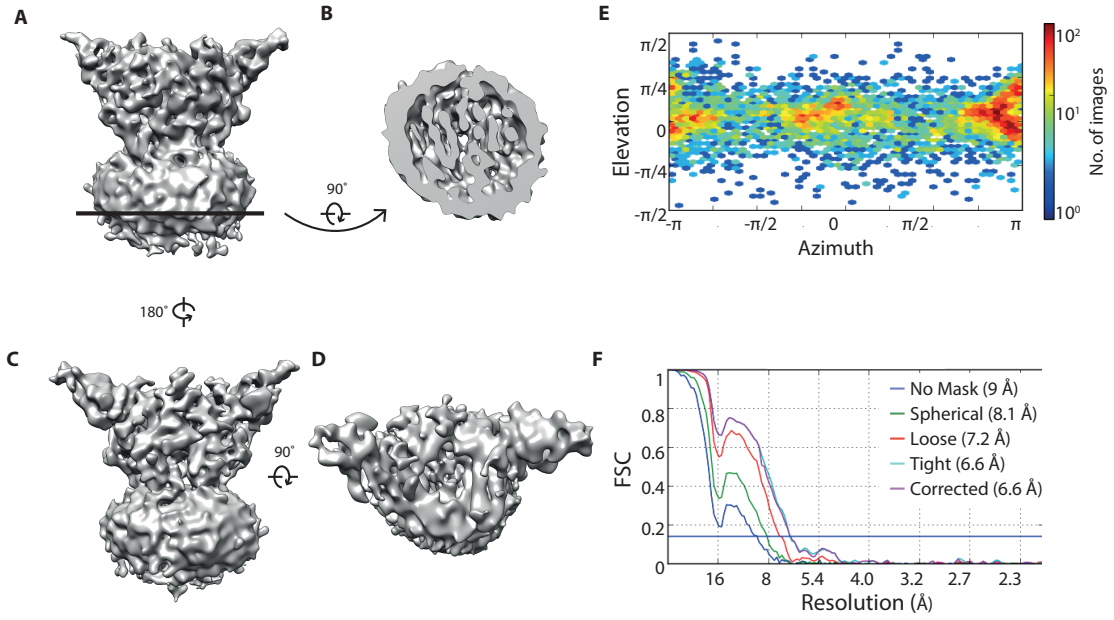

Figure 5.4: 3D reconstruction of a FLAG-purified α3β3γ2L $GABA_AR$ in complex with α3β3γmb173. **A-D**: Views of the reconstructed $GABA_AR$ cryo-EM map after non-uniform refinement in cryoSPARC from the side (**A**, **C**), top (**D**), and as a slice through the TMD (**B**). **E**: Density of the distribution of angles (elevation and azimuth) assigned to particles during refinement. Red hexagons represent many particles with that combination of elevation and azimuth, and blue indicates few particles. **F**: Fourier-shell correlations between two half-maps using various masks (indicated in top right hand corner).

for data collection on a Titan Krios (Figure 5.6) using the setup detailed in Table 5.2 . These data were of reasonable quality (Figure 5.6C, D), except for the last 100 micrographs which could not be motion-corrected, likely due to motion in the stage during collection or irregularities in the phase plate for this position.

These data were processed in the same way as the previous dataset, using MotionCor2 for motion-correction, gctf for CTF estimation, RELION for reference-free auto-picking (using the Laplacian of Gaussian option in RELION-3) and particle extraction. A total of 18978 auto-picked particles were extracted, and then imported into cryoSPARC (v2). Three rounds of 2D classification were conducted in cryoSPARC (Figure 5.7A). The megabodies are not as prominent in these classes, but two faint nanobodies in the same location as the FLAG-purified sample are visible in some side views (5.7). There also appears to be some heterogeneity in nanodisc size in these classes.

The best particles (34660) from 2D classification were used for *ab initio* 3D recon-

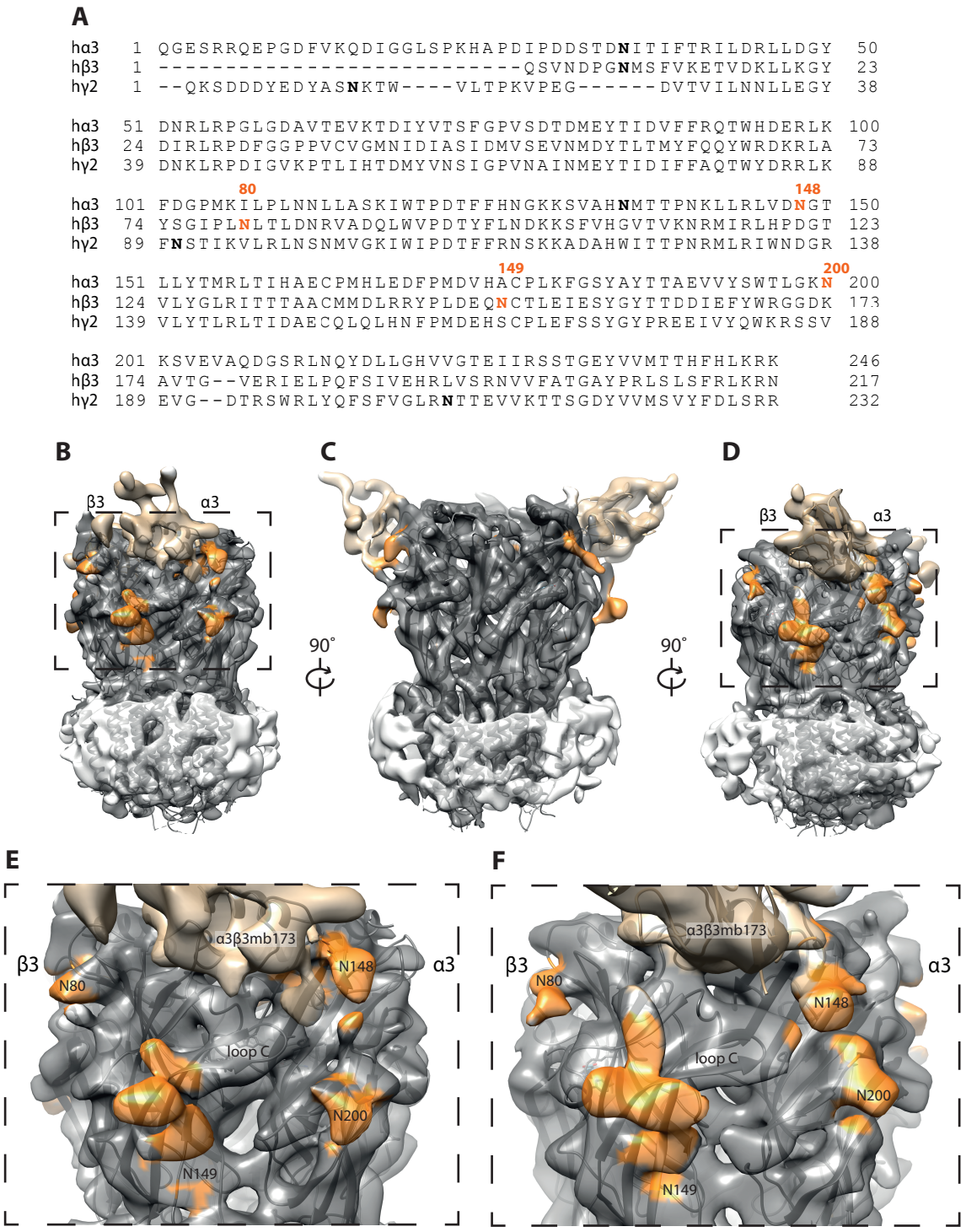

Figure 5.5: Likely subunit assignment and α3β3mb173 binding site for a FLAG-purified α3β3γ2L GABA$_A$R. A: Alignment of α3, β3 and γ2 ECDs, with N-linked glycosylation sites indicated in bold. **B-D**: Side views of the 3D reconstruction of a FLAG-purified α3β3γ2L GABA$_A$R in complex with α3β3mb173, with density likely to correspond to N-linked glycans in orange. **E, F**: Closer views of the ECD near the nanobody binding sites, with density likely corresponding to N-linked glycans (orange) at β3N80, β3N149, α3N148 and α3N200 indicated.

Table 5.2: Data collection parameters for α3β3γ2L $GABA_AR$ (in MSP2N2 nanodiscs, 1D4 purification) + α3β3mb173, 1 mM GABA

Data collection parameters	
Microscope	Titan Krios (LMB Krios II)
Volta Phase Plate used	x
Detector	Falcon III (Counting)
Nominal magnification	75,000X
Voltage (kV)	300
Fluence ($e^- Å^{-2}$)	30
Frames	75
Defocus range (μm)	-0.5 to -0.7
Pixel size (Å)	1.07
Number of micrographs	408
Processing	
Micrographs used	346
Number of picked particles	40417
Particles in final reconstruction	8730
Type of refinement	Non-uniform refinement (cryoSPARC v2)
Symmetry imposed	C1
Map resolution (Å)	6.6
FSC threshold	0.143

struction. After further heterogenous and homogenous refinement in cryoSPARC, the map displayed in Figure 5.7B-D was obtained. This map had a nominal resolution of 13 Å (Figure 5.7E). Since this map is low resolution, caution should be taken when interpreting its features. For example, this map has oval-shaped density for the nanodisc/TMD (5.7B-D), likely due to apparent heterogeneity in the disc size that is also evident in the 2D classes (Figure 5.7A). However, one similarity between maps derived from this dataset and the previous one (for FLAG-purified $GABA_AR$) is the presence of two features at the top of the ECD, in roughly the same position, which are likely to correspond to two bound megabodies. Only part of the nanobody portion of these megabodies was resolved in both cases, with density at one site slightly stronger than the other.

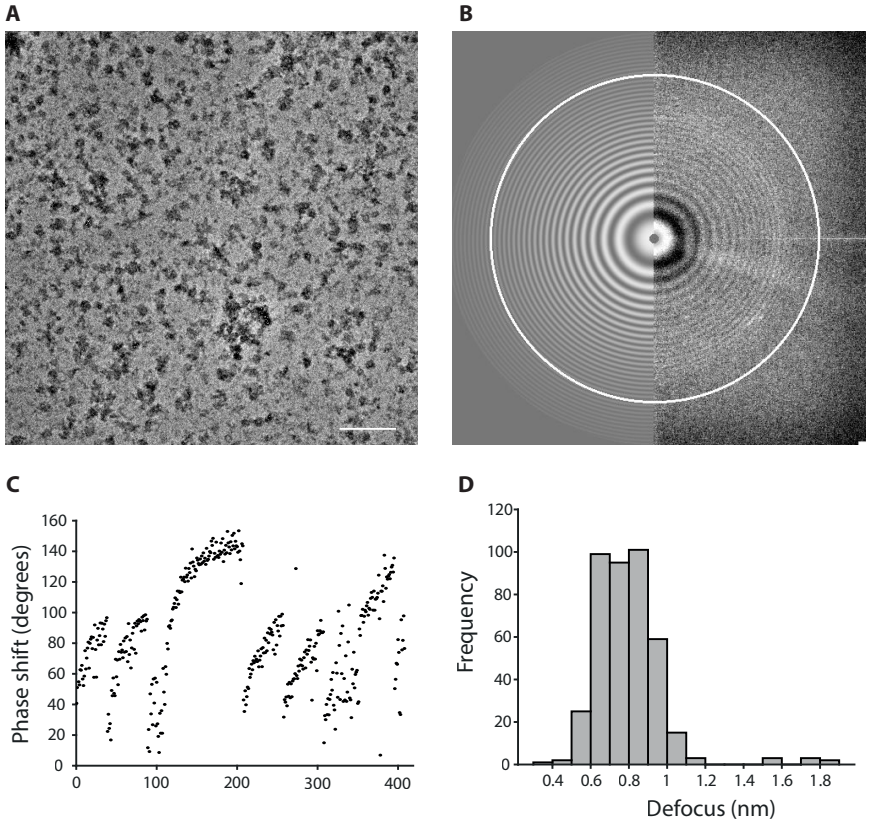

Figure 5.6: Data collection for 1D4-purified GABA$_A$R from a stable cell line. **A**: Example motion-corrected, dose-weighted micrograph for vitrified 1D4-purified GABA$_A$R from an α3β3γ2L stable cell line in complex with α3β3mb173. Scale bar: 50 nm **B**: Example fitted power spectrum from this dataset. **C, D**: Phase shifts (**C**) and defocus (**D**) for 408 motion-corrected micrographs, estimated using gctf.

5.5 α3β3γ2L GABA$_A$R in complex with α3β3mb173, GABA and picrotoxin

5.5.1 Nanodisc dataset

In an effort to further improve sample quality, GABA$_A$Rs were purified from the FLAG-α3/HA-β3/mEGFP-TEV-γ2L-3x(GGS)-1D4 cell line with the inclusion of 1 mM picrotoxin in all buffers throughout purification. Since picrotoxin is a pore-binding antagonist [48], it was included in the hope that its presence would rigidify the receptor during purification. After detergent solubilisation, GABA$_A$R was enriched using 1D4 affinity chromatography and reconstituted into MSP2N2 nanodiscs, and 1 mM GABA and α3β3mb173 was added at a ~2:1 (mb:pentamer) ratio before vitrification on UltrAuFoil 1.2/1.3 grids. These grids

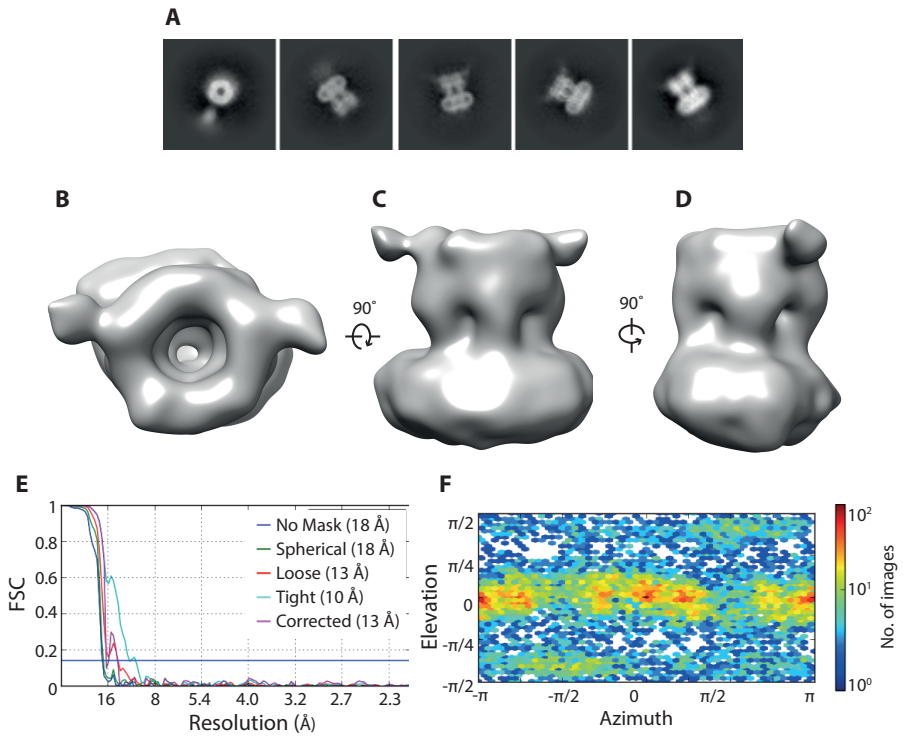

Figure 5.7: 2D classes and 3D reconstruction for 1D4-purified $GABA_AR$ from a stable cell line in the presence of 1 mM GABA and α3β3mb173. **A**: 2D classes for 1D4-purified $GABA_AR$ from an α3β3γ2L stable cell line in complex with α3β3mb173. 189787 particles were picked and extracted using RELION, and then subjected to two rounds of 2D classification in cryoSPARC. These five selected classes contained 23552 particles. **B-D**: 3D reconstruction generated from 15132 particles in cryoSPARC. **E, F**: FSC for two half-maps (**E**) and angular distribution of all particles (**F**) for the reconstruction shown in **B-D**.

were used for a data collection session on a Titan Krios, using a Volta Phase Plate and a Falcon III detector operated in counting mode (Figure 5.8). A total of 1068 movies were collected; the range of phase shifts (Figure 5.8C) and defocus values (Figure 5.8D) indicated by CTF estimation using gctf are roughly what would be expected; the fact that the range of defocus values was larger than the set values (5.8D, Table 5.3) is due to the fact that autofocusing was carried out only every 9 µm.

Again, various data processing strategies were pursued using the software packages gctf, crYOLO, RELION-3, and cryoSPARC (v2). Movies were motion-corrected and dose-weighted using the RELION-3 implementation of motion correction, the CTF for each micrographs was estimated using gctf, particles were picked using crYOLO and extracted using RELION-3 (135316 particles from 644 micrographs). These extracted particles were

Table 5.3: Data collection parameters for α3β3γ2L $GABA_AR$ (in MSP2N2 nanodiscs, 1D4 purification) + α3β3mb173, 1 mM GABA, 1 mM picrotoxin

Data collection	
Microscope	Titan Krios (Strubi)
Volta Phase Plate used	x
Detector	Falcon III (Counting)
Nominal magnification	75,000X
Voltage (kV)	300
Fluence ($e^- Å^{-2}$)	30
Frames	75
Defocus range (μm)	-0.5 to -0.7
Pixel size (Å)	1.07
Number of micrographs	1068
Processing	
Micrographs used	644
Number of picked particles	135316
Particles in final reconstruction	20563
Type of refinement	Non-uniform refinement (cryoSPARC v2)
Symmetry imposed	C1
Map resolution (Å)	3.9
FSC threshold	0.143

then subjected to two rounds of 2D classification in RELION-3. The remaining particles after 2D classification (54000 particles) were subjected to Bayesian particle polishing in RELION-3, and the resulting 'shiny' particles were imported into cryoSPARC v2. Further classification and refinement in cryoSPARC is illustrated in Figure 5.9. After one further round of 2D classification in cryoSPARC, *ab initio* reconstruction was used to generate two different 3D models. Heterogenous refinement was used to classify particles into one of three classes, and the particles from the best of these were subjected to non-uniform refinement which yielded the final model.

This model had a nominal resolution of 3.9 Å. The features visible in this map are typical of this resolution, with partial resolution of β-sheets in the ECD, α-helices visible in the TMD, and density for the MSP also visible (Figure 5.9B). The TMD shows five-fold pseudosymmetry, with the four α-helices from each subunit arranged around a central pore. A feature is visible in the lower portion of the pore, likely to be due to the presence

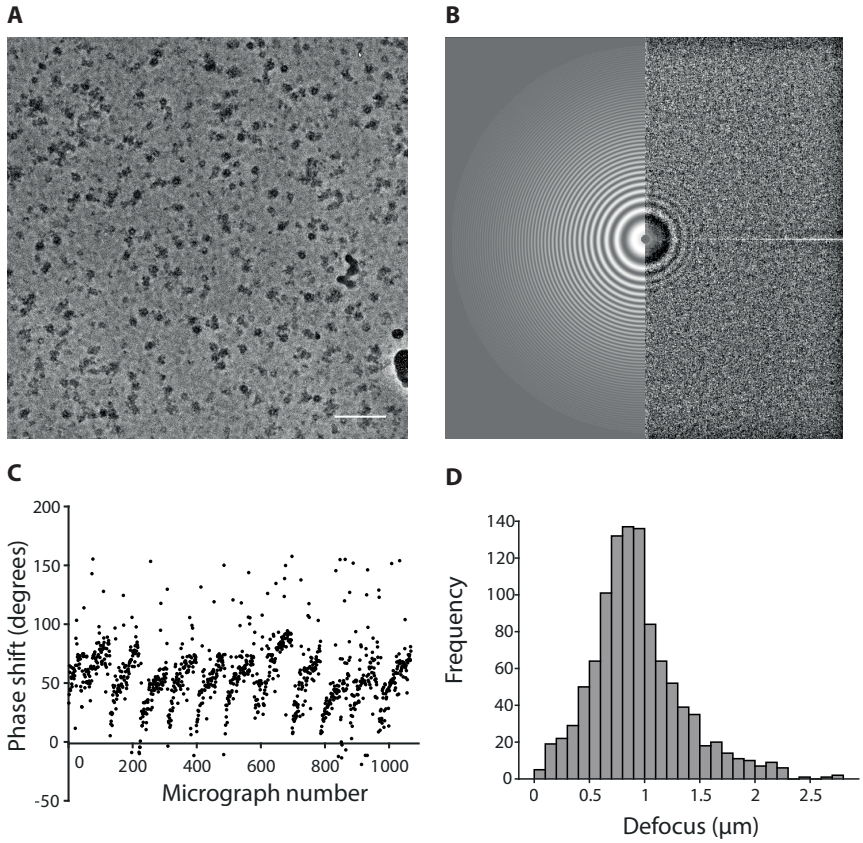

Figure 5.8: Data collection for 1D4-purified $GABA_AR$ in MSP2N2 nanodiscs from a stable cell line in the presence of 1 mM picrotoxin, 1 mM GABA and α3β3mb173. **A**: Example motion-corrected, dose-weighted micrograph for vitrified 1D4-purified $GABA_AR$ in nanodiscs from an α3β3γ2L stable cell line in complex with α3β3mb173, in the presence of 1 mM GABA and 1 mM picrotoxin. Scale bar: 50 nm **B**: Example fitted power spectrum. **C, D**: Phase shifts (**C**) and defocus (**D**) for 1068 motion-corrected micrographs, estimated using gctf.

of picrotoxin bound to the receptor. Only one megabody was visible in this map, as before, and only the nanobody portion of the megabody was resolved. The megabody appears to be bound to the same site as observed in the previous two datasets, at the top of the ECD.

5.5.2 Amphipol dataset

Since $GABA_ARs$ reconstituted into amphipols looked promising in initial screening (see Chapter 4.5), data was next collected from $GABA_ARs$ reconstituted into A8-35 (in the presence of lipids). α3β3γ2L $GABA_AR$ was purified from the FLAG-α3/HA-β3/mEGFP-TEV-γ2L-3x(GGS)-1D4 cell line as for the previous sample in the presence of 1 mM picrotoxin. $GABA_ARs$ were reconstituted into A8-35 in the presence of POPC and bovine

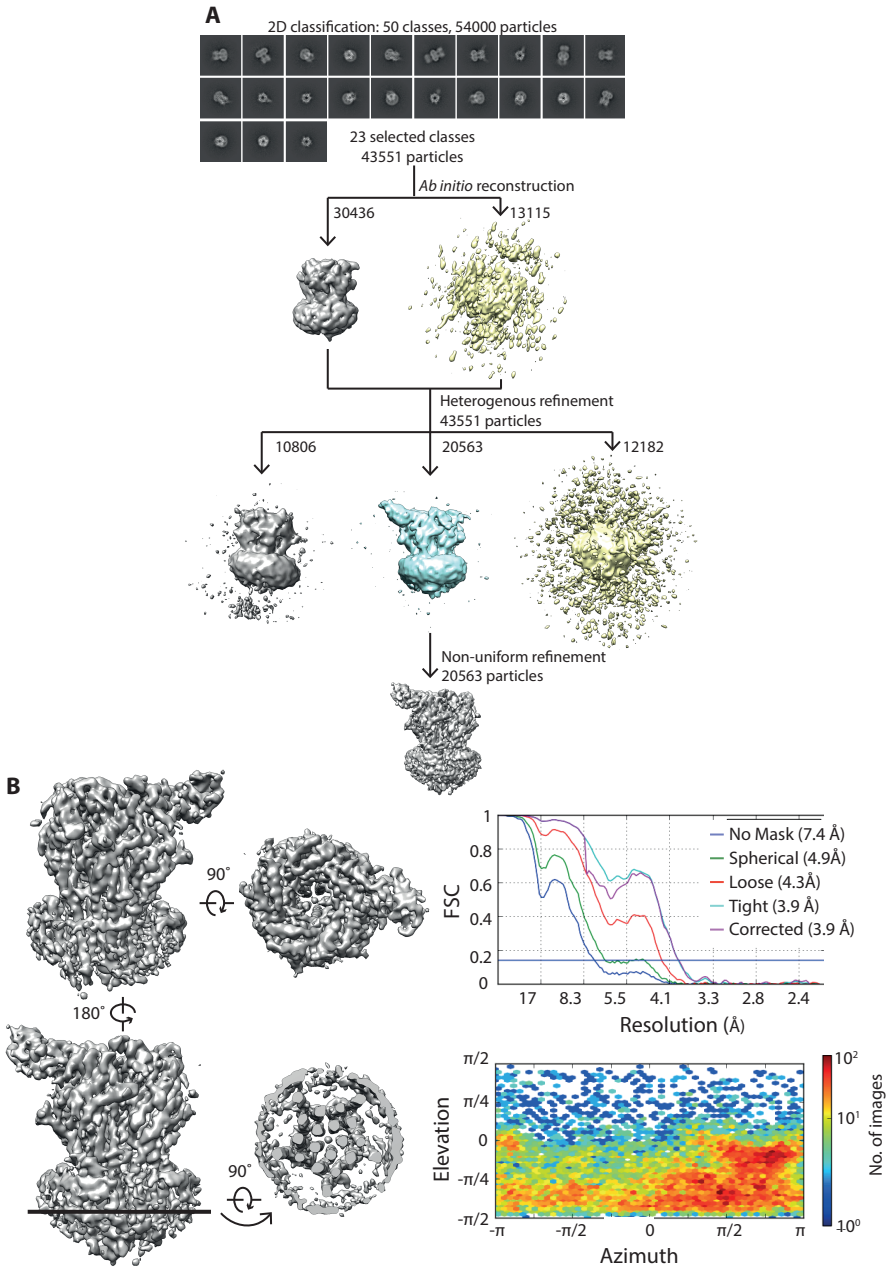

Figure 5.9: Data processing for 1D4-purified α2β32L GABA$_A$R in MSP2N2 nanodisc from a stable cell line in the presence of 1 mM picrotoxin, 1 mM GABA and α3β3mb173. **A**: Initial preprocessing was conducted using RELION-3, gctf and crYOLO. After Bayesean particle polishing in RELION-3, 'shiny' particles were imported into cryoSPARC (v2) for further 2D classification, *ab initio* reconstruction, heterogenous refinement, and finally non-uniform refinement. The number of particles in 3D classes are indicated next to arrows. **B**: The map obtained from non-uniform refinement as viewed from the side (top left, bottom left), top (top middle) and as a slice through the TMD (bottom middle). Fourier shell correlation and distribution of particle orientations are shown on the top right and bottom right, respectively.

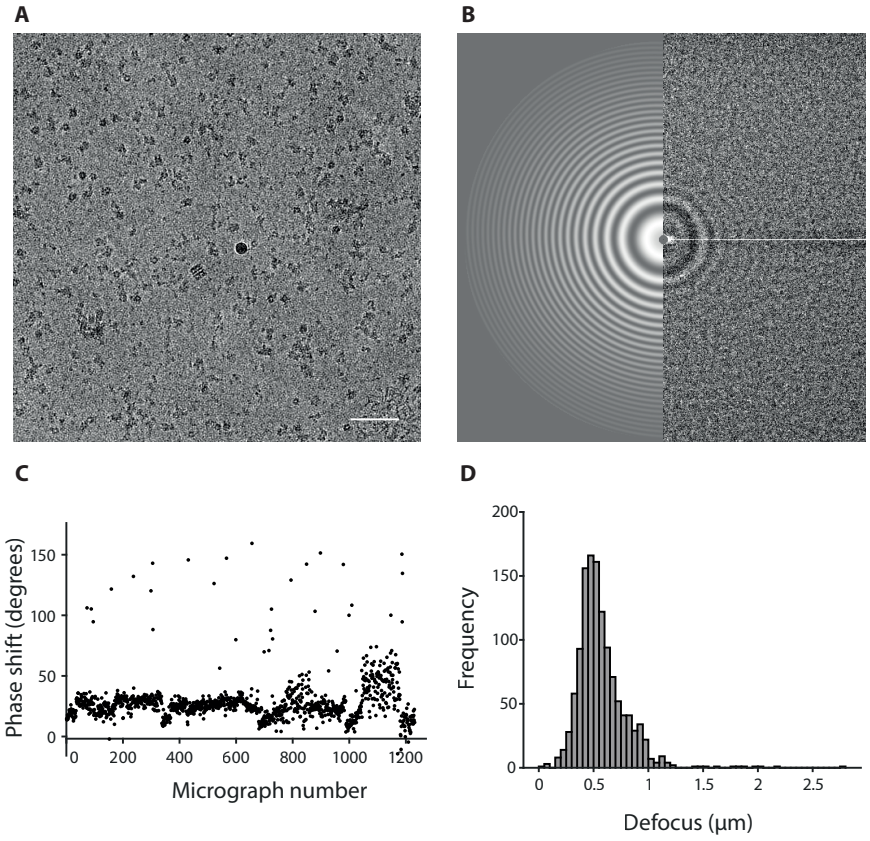

Figure 5.10: Data collection for 1D4-purified $GABA_AR$ in amphipols from a stable cell line in the presence of 1 mM picrotoxin. **A**: Example motion-corrected, dose-weighted micrograph for vitrified 1D4-purified $GABA_AR$ in amphipols from an α3β3γ2L stable cell line in complex with α3β3mb173, in the presence of 1 mM GABA and 1 mM picrotoxin. Scale bar: 50 nm **B**: Example fitted power spectrum. **C, D**: Phase shifts (**C**) and defocus (**D**) for 1231 motion-corrected micrographs, estimated using gctf.

brain lipid extract while bound to 1D4 affinity resin, and after elution and deglycosylation with EndoF1, were mixed with 1mM GABA (final concentration) and α3β3mb173 in a 4:1 (mb to pentamer) ratio. This mixture was applied on UltrAuFoil 1.2/1.3 grids and plunge-frozen in liquid ethane. Data were collected using a Titan Krios microscope as described in Table 5.4 (see also Figure 5.10). For this dataset, the phase shifts were lower than would usually be expected (Figure 5.10C), and as a result there was less constrast in the aligned micrographs (Figure 5.10A).

The data for this sample were processed in a similar manner to previous datasets. Movies were motion corrected and dose-weighted using MotionCor2, the CTF for each aligned micrograph was estimated using gctf, and then a small number of particles were

Table 5.4: Data collection parameters for α3β3γ2L $GABA_AR$ (in amphipols, 1D4 purification) + α3β3mb173, 1 mM GABA, 1 mM picrotoxin

Data collection parameters	
Microscope	Titan Krios (eBIC Krios I)
Volta Phase Plate used	x
Detector	Falcon III (Counting)
Nominal magnification	75,000X
Voltage (kV)	300
Fluence ($e^- Å^{-2}$)	30
Frames	75
Defocus range (μm)	-0.5
Pixel size (Å)	1.084
Number of micrographs	1231
Processing	
Micrographs used	861
Number of picked particles	346787
Particles in final reconstruction	43402
Type of refinement	Non-uniform refinement (cryoSPARC v2)
Symmetry imposed	C1
Map resolution (Å)	4.2
FSC threshold	0.143

manually picked and used to generate templates for autopicking in RELION-3. A total of 346787 particles were picked from 861 micrographs, and extracted using RELION-3. Figure 5.11 shows processing of these particles after their import into cryoSPARC (v2). After two rounds of 2D classification, *ab initio* reconstruction was used to generate initial models. These were used as references for one round of heterogenous refinement into two classes, using all the particles selected after the first round of 2D classification. Particles from the best class was then divided further into three classes by heterogenous refinement, and the best subset of particles was then subjected to non-uniform refinement. This resulted in a map with a nominal resolution of 4.2 Å (Figure 5.11B), reconstructed from 43402 particles.

This map is slightly less well resolved than for the previous dataset collected for α3β3γ2L in nanodiscs (compare Figure 5.9B with Figure 5.11B). The most striking differences are the presence of two, rather than one, bound megabodies; and the difference in density surrounding the TMD, with the density for A8-35 adhering tightly to the TMD, rather

than forming a circular ring like MSP2N2.

5.5.3 Combined amphipol and nanodisc datasets

Since the two datasets for the α3β3γ2L $GABA_AR$ in complex with α3β3mb173, 1 mM GABA and 1 mM picrotoxin differed only in the support for the TMD and number of bound megabodies, these two datasets were pooled and processed together in an effort to obtain a better resolution map. The motion-corrected micrographs for $GABA_AR$ in amphipols was re-processed in Warp (CTF estimation and particle picking) to give 262422 particles; these were combined with 184897 particles extracted in RELION-3 after motion correction (MotionCor2), CTF estimation (gctf) and particle picking (RELION-3 autopicking) from the dataset for $GABA_ARs$ in nanodiscs. The pixel size for the nanodisc dataset was 1.07 Å, whereas the pixel size for the amphipol dataset was 1.084 Å, so particles from the nanodisc dataset were downscaled during extraction so that all particles had the same box size (306 pixels) and pixel size (1.084 Å).

These two sets of particles were then imported into cryoSPARC (v2) and processed together (Figure 5.12). After several rounds of 2D and 3D classification (Figure 5.12A), non-uniform refinement of 40666 particles gave a map with a nominal resolution of 3.8 Å (Figure 5.12B). Since this map has a MSP-like circular density in the TMD, and only one visible megabody, it is likely that the contribution of particles from the nanodisc dataset is larger than that of the amphipol dataset.

Since the structure of a α1β3γ2L $GABA_AR$ was recently solved in the presence of GABA and picrotoxin [41], a good model was available for rigid body docking into this map. This model was well-accommodated in the map (Figure 5.13), and subunits were assigned based on the pattern of density not accounted for by the main chain of the model, presumed to be N-linked glycans (Figure 5.13A, B, orange density; see also Figure 5.5A). This indicated a stoichiometry of 2α:2β:1γ, with a subunit arrangement of α-β-α-β-γ. The β3N149 and γ2LN90 N-linked glycans previously observed in a crystal structure of the β3 homomer [37] are particularly prominent (Figure 5.13B).

Of primary interest is the location of the α3β3mb173 binding site (Figure 5.14). Although the density at this interface is too weakly resolved to confidently identify the

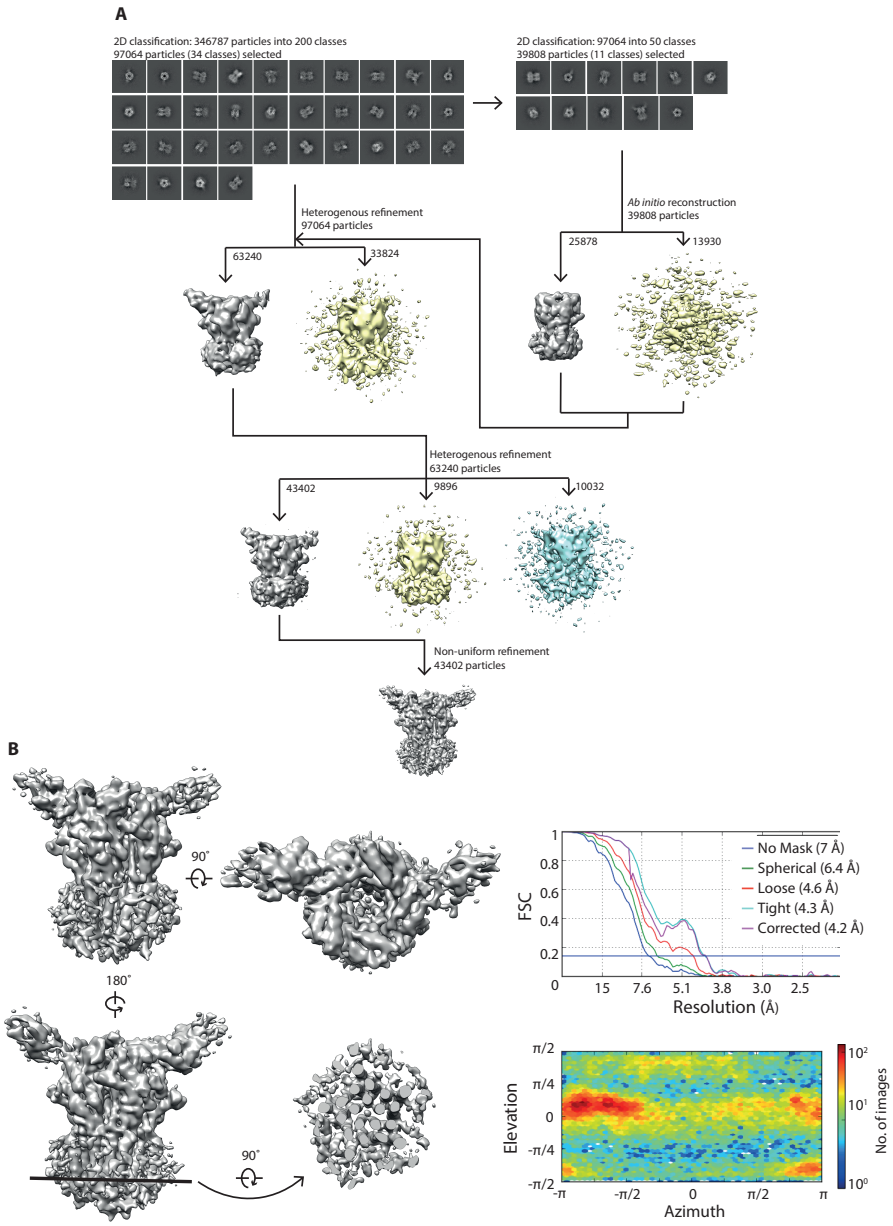

Figure 5.11: Data processing for 1D4-purified α2β32L GABA$_A$R in amphipols from a stable cell line in the presence of 1 mM picrotoxin, 1 mM GABA and α3β3mb173. A: Initial preprocessing was conducted using RELION-3 and gctf. Extracted particles were imported into cryoSPARC (v2) for further 2D classification, *ab initio* reconstruction, heterogenous refinement, and finally non-uniform refinement. The number of particles in 3D classes are indicated next to arrows. **B**: The map obtained from non-uniform refinement as viewed from the side (top left, bottom left), top (top middle) and as a slice through the TMD (bottom middle). Fourier shell correlation and distribution of particle orientations are shown on the top right and bottom right, respectively.

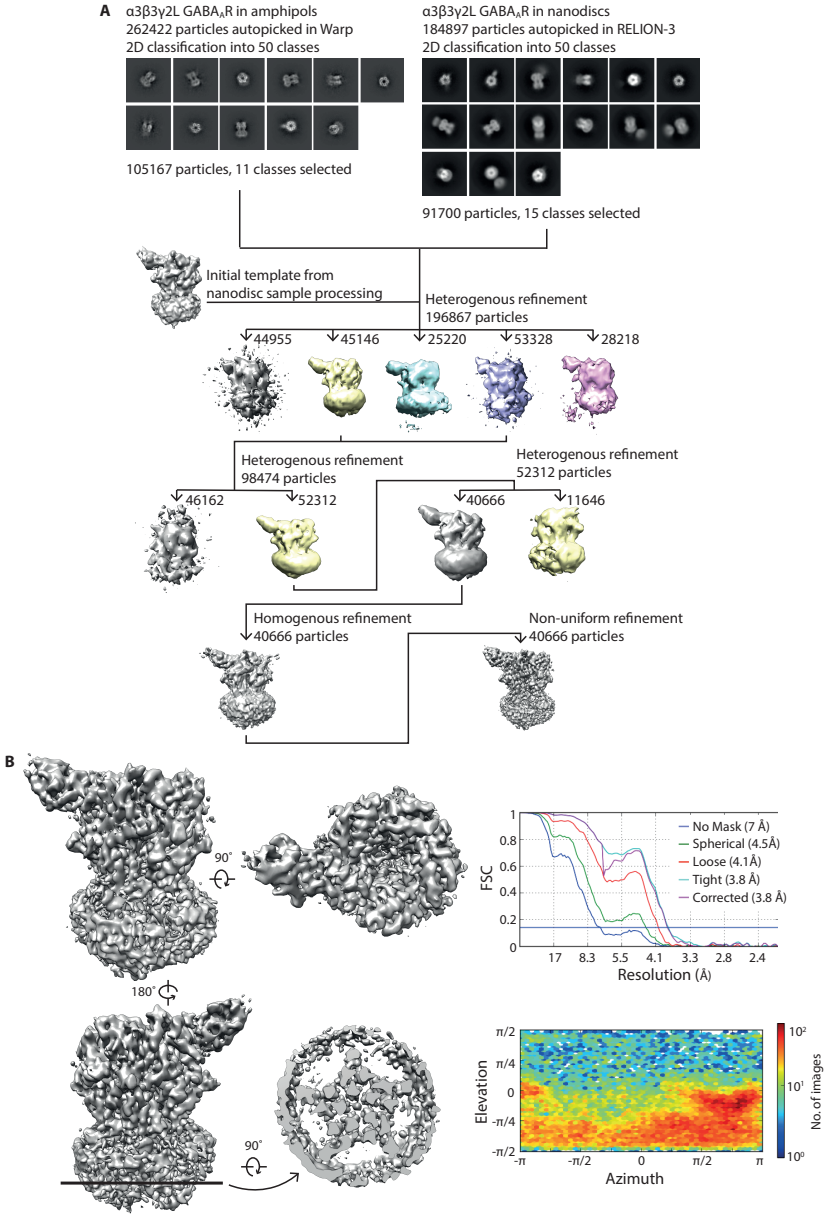

Figure 5.12: Data processing for combined datasets of 1D4-purified α2β32L GABA$_A$R in amphipols and nanodiscs from a stable cell line in the presence of 1 mM picrotoxin, 1 mM GABA and α3β3mb173. A: 2D and 3D classification of the combined particles. The two datasets were first separately subjected to one round of 2D classification, then combined for one round of 3D classification into 5 classes (using a map generated from the nanodisc dataset as an initial reference). The particles from two of these classes were further classified into two classes, and the best of these were classified further into two more classes. Finally, homogenous refinement and non-uniform refinement were conducted with the best particles. The number of particles in each 3D class is shown next to the arrows. **B**: The map obtained from non-uniform refinement as viewed from the side (top left, bottom left), top (top middle) and as a slice through the TMD (bottom middle). Fourier shell correlation and distribution of particle orientations are shown on the top right and bottom right, respectively.

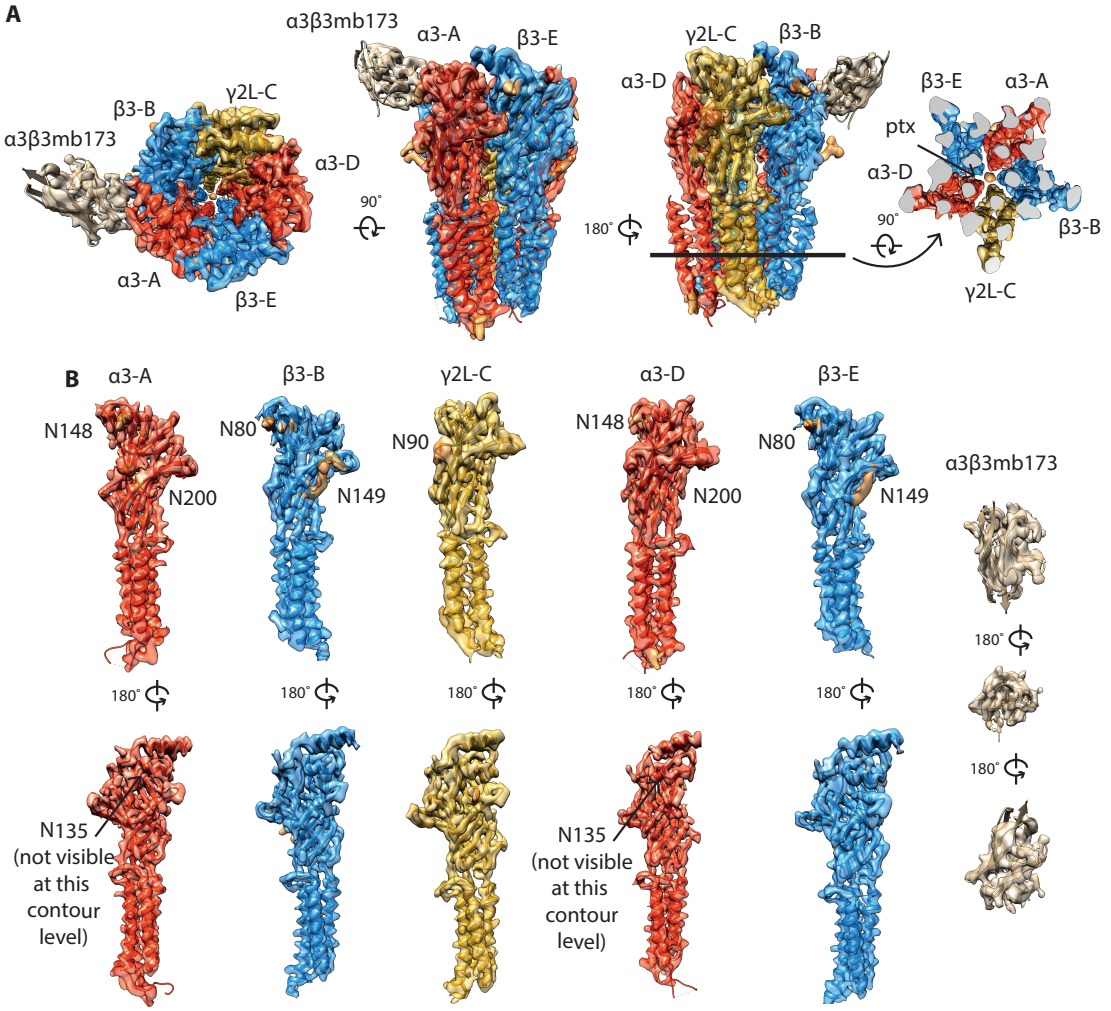

Figure 5.13: α1β3γ2L $GABA_AR$ in complex with GABA, picrotoxin, and α1β3nb138, docked into the map for the α3β3γ2L $GABA_AR$. **A**: Various views of the α1β3γ2L model docked into the cryo-EM density map for α3β3γ2L. The α3, β3 and γ2L subunits are indicated in red, blue and yellow. The resolved portion of the megabody is indicated in beige. Density not accounted for by the protein is indicated in orange, presumably corresponding to picrotoxin (in the pore) and N-linked glycans (see also Figure 5.5A). **B**: Density for individual subunits (α3-A, β3-B, γ2L-C, α3-D, and β3-E), as well as the nanobody portion of the megabody (α3β3mb173).

residues involved (Figure 5.14A, B), the CDR binding loops could be built, although caution is warranted when interpreting this model. An inspection of the potential $GABA_AR$-megabody interface in the model reveals a possible interaction between loop 3 of the α3 subunit with the CDR1 and/or CDR2 loops, and between loop 1 of the β3 subunit with the CDR3 loop. Some residues on these loops are illustrated in Figure 5.14C-E; however, the involvement of these residues in binding cannot yet be stated with certainty. Nevertheless, the overall location of the nanobody binding site above the GABA binding site is clear.

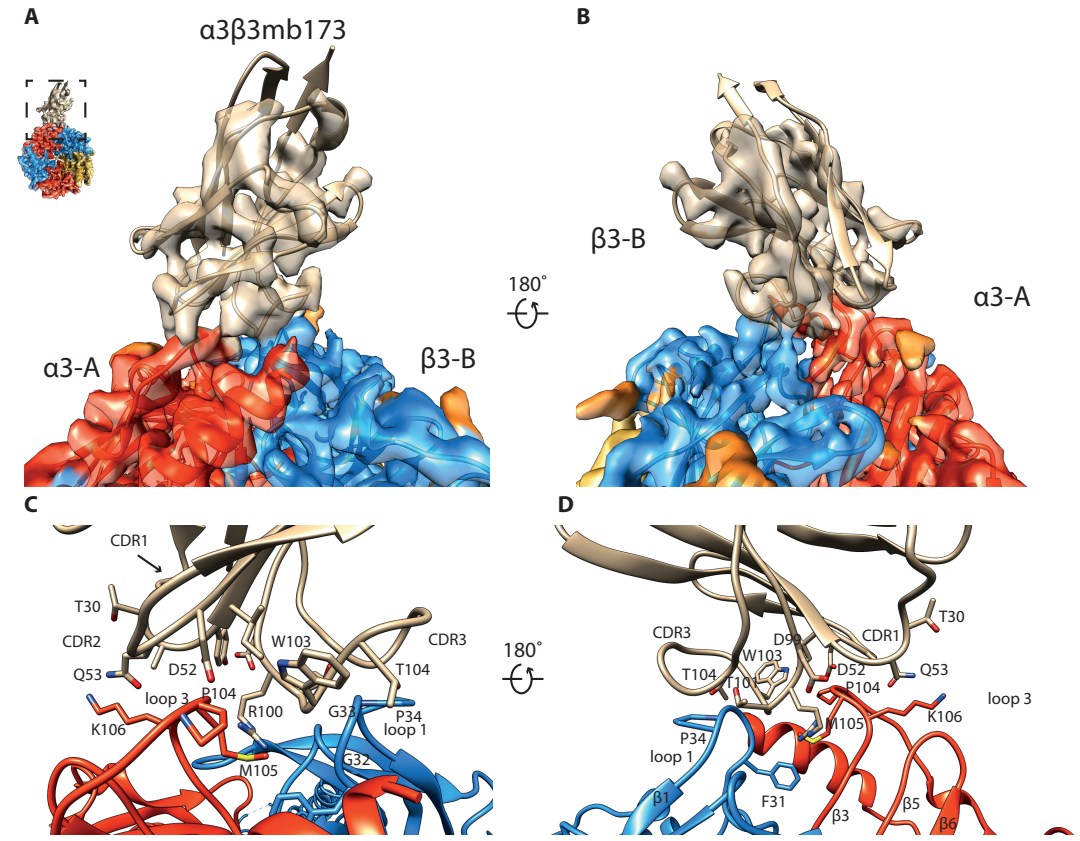

E

Loop 3

α1	74	RLKFKGPMTVL	84
α2	73	RLKFKGPMNIL	83
α3	98	RLKFDGPMKIL	108
α4	72	RLKYDGPIEIL	82
α5	77	RLRFKGPMQRL	87
α6	72	RLKFGGPTEIL	82

Loop 1

β1	27	LRPDFGGPPVDV	38
β2	27	LRPDFGGPPVAV	38
β3	27	LRPDFGGPPVCV	38

CDR1

α3β3nb173	27	RTLSSSAVGW	36
α1β3nb138	27	RTFTTYIMAW	36

CDR2

α3β3nb173	51	ISYSGGYTSY	60
α1β3nb138	51	MD-QGRIQYY	59

CDR3

α3β3nb173	94	YYCAVDRTGWTTRI-GGYDYWGQ	115
α1β3nb138	93	YYCAAGAGFWGLRTASSYHYWGQ	115

Figure 5.14: Possible α3β3mb173-GABA$_A$R interface. A, B: Top (**A**) and bottom (**B**) views of the nanobody-GABA$_A$R interface in the cryo-EM density map. **C, D**: Top (**A**) and bottom (**B**) views of a possible model of the nanobody-GABA$_A$R interface. Individual residues are shown only to indicate a possible interface; the density is too low-resolution to unambiguously identify the amino acids that constitute the interface. The interaction of α3 loop 3 with the nanobody CRD1/2 loops and β3 loop 1 with the nanobody CDR3 loop appears to be likely. **C**: Sequence alignment of the likely interface: loops 1 and 3 for the human β and α subunits, respectively; and the CDR loops for α3β3nb173 and α1β3nb138.

5.6 Discussion

This chapter described efforts to investigate the structure of a $GABA_AR$-nanobody complex by single-particle cryo-EM. After exploring various sample and grid types, four main data collections were carried out: for FLAG-purified α3β3γ2L $GABA_AR$ in nanodiscs in complex with GABA and α3β3mb173, for 1D4-purified α3β3γ2L $GABA_AR$ in nanodiscs in complex with GABA and α3β3mb173, for 1D4-purified α3β3γ2L $GABA_AR$ in nanodiscs in complex with GABA, picrotoxin and α3β3mb173, and for 1D4-purified α3β3γ2L $GABA_AR$ in amphipols in complex with GABA, picrotoxin and α3β3mb173. A combination of the latter two datasets yielded the best map, with a nominal resolution of 3.8 Å. This work revealed the binding site for the megabody, at the top of the ECD at the β+/α- interface.

5.6.1 Grid optimisation

The first task in this work was to find conditions under which useful cryo-EM grids could be made. A main concern for this work is preferential orientation, which is often caused by adsorption of particles to the air-water interface [321]. This has been a concern in previous work with the $GABA_AR$, typically manifesting as a predominant 'top' view of the ECD [296]. This was the reason for inclusion of a megabody in all samples, in the hope that the complex would have a significantly altered interaction with the air-water interface that would prevent preferential orientation. However, when reconstituted into amphipols, $GABA_ARs$ appeared to be preferentially oriented when in complex with α3β3mb173 or α3β3mb183 (5.2A, B). The use of graphene oxide as a support has been suggested to support the adherence of biological samples, keeping them away from the air-water interface [250], and this approach has been used for $GABA_ARs$ [38]. However, this approach did not appear to help in the case of $GABA_ARs$ in amphipols, at least in initial trials (5.2C).

However, deglycosylation of $GABA_ARs$ with EndoF1 did seem to allow the protein to orient more randomly in vitrified ice. The reason for this is unclear. It is possible that the cleavage of these mannose moieties alters the nature of the interaction between the $GABA_AR$ and the air-water interface to prevent adherence. Alternatively, since the deglycosylation reaction occurred just prior to application of the protein to grids, the cleaved glycans were still present in the sample. If these do adhere to the air-water interface

themselves, it could be that they prevent the protein from adhering, if present in high enough concentrations to occupy a large portion of this interface. Although not done here, these two possibilities could be distinguished by using SEC to separate the protein from the cleaved glycans.

Another approach to improving the distribution of observed orientations in ice that seemed to be successful was reconstitution of $GABA_ARs$ into nanodiscs. Again, it is unclear why this worked, but given that the only difference between the amphipol sample with α3β3mb173 and the nanodisc sample with the same megabody is the presence of MSP2N2 or A8-35, it is likely that this accounts for the difference. It could be that MSP2N2 itself interacts with the air-water interface (whereas A8-35 does not), skewing the distribution of orientations observed to include some side-on views of the receptor.

After obtaining a workable solution, other approaches to improving particle distribution such as the use of alternative supports, smaller holes, cross-linking or surfactants [328] were not explored. The possibility remains that these may further improve the quality of cryo-EM grids.

5.6.2 Datasets collected

After optimisation of cryo-EM grids, four different samples were used for larger data collections, all on a Titan Krios with a VPP, and the Falcon III detector operated in counting mode. For a one-day collection, around 300-400 movies were obtained (for the first two datasets), and for a three-day collection, around 1000-1200 movies were obtained (for the second two datasets).

Since the $GABA_AR$ is relatively small compared with other proteins investigated using cryo-EM, a phase plate was used to increase the signal-to-noise ratio [268]. A small defocus was applied (-500 nm to -700 nm), since this does not require as accurate focusing as the in-focus approach, and alleviates the limit of spherical aberration on achievable resolution [268]. In three of the datasets the VPP performed as expected, with an increase in phase shift evident for each new position, although in the fourth (α3β3γ2L $GABA_AR$ in amphipols in complex with α3β3, GABA and picrotoxin), the phase shift was lower than expected. It is unclear why this was the case, but the lower phase shifts were evident in the

aligned micrographs, which had lower contrast compared with the previous datasets. This made particle picking difficult, but the data could still be processed to give a reconstruction with a resolution of 4.2 Å.

The first dataset collected was the FLAG-purified α3β3γ2L $GABA_AR$ reconstituted into nanodiscs, in complex with α3β3mb173 and GABA. As noted in Chapter 4, this sample is likely to be composed mainly of αβ heteromers, rather than αβγ heteromers, due to the co-purification of these two receptor types using the FLAG-tag at the α3 N-terminus. Thus, the sample is likely to be somewhat heterogenous. This is evident when identifying individual subunits in the receptor based on the pattern of N-linked glycosylation: although two subunits appear to be α3 and two β3, the identity of the fifth subunit is unclear (compare Figure 5.5C with Figure 5.13). This is likely due to heterogeneity in the sample, which could also be a limiting factor on resolution. This factor, combined with the smaller size of this dataset, could explain the lower resolution of the final reconstruction obtained (6.6 Å) for this data, compared with the datasets collected for $GABA_AR$ in the presence of picrotoxin. Although approaches exist for 'computational' purification of single particle data, mainly through classification [255], this requires more data than was available, or at least a larger proportion of 'good' particles.

Another consideration is the representation of particle orientations; if particular views are under- or over-represented, anisotropy in the reconstruction can result. The reconstructed map looks somewhat streaky (clearest in Figure 5.4C). The orientational distribution does indeed seem to lack data for particular orientations (Figure 5.4D), which was likely a further limiting factor on map quality.

The second dataset collected was similar to the first, but $GABA_AR$ was purified using 1D4 affinity chromatography, rather than FLAG. This should have resulted in the enrichment of only γ-containing $GABA_ARs$, addressing the concerns about sample heterogeneity in the first dataset. However, this sample seemed also to be heterogenous, since not all particles in the aligned micrographs appeared to be identical (e.g. Figure 5.7A). Furthermore, the size of the nanodisc appeared to be somewhat variable, with different sizes evident in 2D classes, leading to a reconstruction with an oval-shaped density around

the TMD. This final reconstruction was also limited in resolution, with the FSC dropping below 0.143 at 13 Å.

In a further attempt to improve sample quality, α3β3γ2L was purified in the presence of 1 mM picrotoxin. This drug binds deep in the pore and stabilises the closed state [48], [163], and was included in the hope that its presence would rigidify the receptor. A comparison of recent cryo-EM structures of the α1β32L GABA$_A$R in complex with either picrotoxin and α1β3mb138, or GABA, picrotoxin and α1β3mb138, indicated that binding of GABA in the presence of picrotoxin can induce an open-like state of the ECD, despite the channel being closed at the level of the TMD [41]. This GABA-induced open conformation in the ECD is also likely to be stabilised in the α3β3γ2L by the megabody α3β3mb173.

Furthermore, since GABA$_A$Rs appeared to be heterogenous when reconstituted into nanodiscs in negative stain (see Chapter 4), A8-35 was used instead. Despite the low phase shifts for this dataset (Figure 5.10), after classification a map with a nominal resolution of 4.2 Å was obtained. This was a larger dataset than the previous two, and represents a substantial improvement, likely to be due to a combination of a better sample and the use of more data.

Similarly, the best resolution map was obtained from the same sample, but reconstituted into nanodiscs rather than amphipols. One aspect that is not clear from these data is the best system for replacing detergent. The best resolution map was obtained from GABA$_A$R reconstituted into nanodiscs, despite amphipols looking more promising in screening by negative stain EM and FSEC (Chapter 4). Previous work has also indicated that reconstitution into nanodiscs may be preferable to amphipols; for example, the a map of TRPV1 with a resolution of 2.9 Å, compared to 3.8 Å for amphipol-stabilised protein but lipids were not used during reconstitution in this case [329]. It could be that there is greater variability in the nanodisc reconstitution, such that there is some good quality protein, and some poorer quality protein. During classification, the better particles were selected, which resulted in a higher resolution final reconstruction. There could perhaps be further room for improvement in the reconstitution process. Another option for future work is to explore other methods for replacing detergent, such as Salipro, SMALPs or peptidiscs [317], [318], [330].

5.6.3 Data processing strategies

A variety of data processing strategies were used for these datasets. For preprocessing, MotionCor2, gctf, RELION-3, Warp, crYOLO and cryoSPARC (v2) were all used [275], [277], [278], [280], [281], [320]. Only the strategy that resulted in the best reconstruction is reported here, which differed between datasets. Generally, particles extracted in RELION-3 (or in one case, Warp), were input into cryoSPARC for classification and 3D refinement. Although processing in RELION-3 was also attempted for all datasets, generally the results were of lower resolution, with fewer features visible in the map, compared with non-uniform refinement in cryoSPARC. Therefore, only the maps from cryoSPARC are presented here. At the time of writing, the algorithm used by non-uniform refinement has not been described publicly, so it is difficult to assess the reason for this difference in maps produced from different software packages.

The general strategy pursued during cryo-EM data processing was to autopick as much as possible, and then perform classification to find the best subset of particles. For each dataset, a wide variety of classifications were conducted, and only the best scheme is illustrated. In general, the majority of particles were discarded during classification: for example, for the dataset collected of α3β3γ2L $GABA_AR$ in nanodiscs, 1D4 purification, in complex with α3β3mb173, GABA and picrotoxin, 135316 particles were picked but only 20563 were used for the final reconstruction. The large number of particles lost during classification could be indicative of an interaction with the air-water interface, which can have a dramatic detrimental effect on the structural integrity of proteins exposed to it [254], [321]. There is also likely to be contribution of the method of preparation to sample heterogeneity (see Chapter 4).

After separate refinement of the data collected for α3β3γ2L $GABA_ARs$ in amphipols or nanodiscs, in complex with α3β3mb173, GABA and picrotoxin, these data were combined to give a higher resolution map. This approach has been used in the past, for example to solve the structure of the mRNA 3'-end processing machinery to 3.5 Å from several datasets that independently yielded reconstructions to ~4 Å [331]. Here, combining the two datasets gave only a slight improvement in resolution, from 3.9 Å resolution for the best map from the nanodisc dataset, to 3.8 Å. The reason that only a small increase was

achieved could be that one dataset contributed most of the particles, and indeed this is likely to be the case since the final reconstruction resembles the nanodisc reconstruction more than the amphipol one.

5.6.4 Structure of the α3β3γ2L $GABA_AR$, in complex with α3β3γ2L, GABA and picrotoxin

This map from the combined dataset shows features typical of $GABA_ARs$, and indeed pLIGCs. Five-fold pesudosymmetry of the five subunits about the central pore axis is evident, and the TMD and ECD are clearly distinguishable. Unlike recent structures of heteromeric $GABA_ARs$ in detergent [38], [39], but like those in nanodiscs [41], [42], the subunits appear to be symmetrically arranged around the pore axis in the TMD. The conformation of the receptor appears to be similar to the α1β3γ2 $GABA_AR$ in complex with α1β3mb138, GABA and picrotoxin [41]. In particular, loop C appears to be closed over the agonist binding site, which is presumably occupied by GABA, although this could not be directly observed at the current resolution. The TMD appears to be in a closed state, presumably induced by picrotoxin, as observed for the α1β3γ2 $GABA_AR$[41].

Arguably the most novel finding from this work is the observation that α3β3mb173 binds at a site that is, to the best of my knowlege, previously undescribed as a modulatory site for the $GABA_AR$(see also Chapter 3). This site is located above the GABA binding site, at the top of the β+/α- interface. The density in the map is not well-resolved enough to identify the precise residues involved in binding, the site appears to be formed by loop 3 from the α3 subunit and loop 1 from the β3 subunit. Although no other ligands at this site have been described for the $GABA_AR$, recently a ligand at an analogous site in the GlyR was shown to be a positive modulator [36]. This molecule, AM-3607, occupies a homologous site between loop 1 and loop 3 at the top of the interface between adjacent subunits in a homomeric α3 $GABA_AR$. A comparison between the binding sites for these two modulators, α3β3nb173 and AM-3607, would be facilitated by the identification of the interface between the $GABA_AR$ and α3β3nb173 in a higher-resolution map but these two positive modulators would appear to bind to the same site [36] (Figure 5.15).

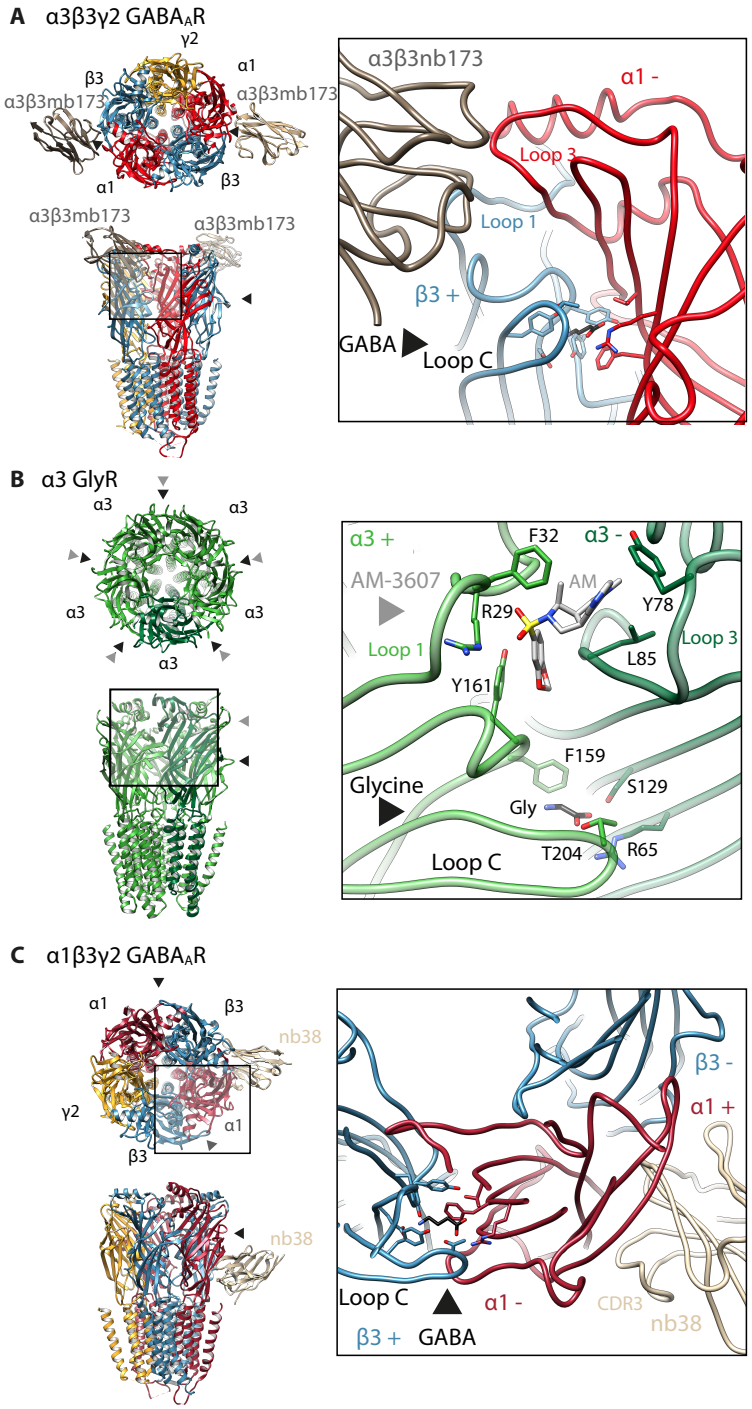

Figure 5.15: Relative positions of agonist and modulatory sites at GABA$_A$R and GlyRs, illustrated in top (top left) and side (bottom left) views, as well as a close up of the relative positioning of the sites (right). A: Positions of the two bound megabodies (α3β3mb173, beige) and GABA sites (black arrows) in the α3β3γ2L GABA$_A$R. The megabody binds at the same interface (β+/α-), above the GABA site and between loops 1 and 3. **B**: Position of the agonist (black arrows) and AM-3607 (grey arrows) sites in the α3 homomeric GlyR (PDB: 5TIO). AM-3607 binds in a similar manner to α3β3mb173, between loops 1 and 3, and above the agonist site. **C**: Position of the agonist (black arrows) and nb38 (beige) binding sites in the α1β3γ2 GABA$_A$R (PDB: 5HUP). Although also a positive modulator, nb38 binds at a different interface (α+/β-) to α3β3mb173.

Despite the necessity for higher-resolution maps to visualise the megabody-$GABA_AR$ interface more clearly, it is clear from the findings here that this is a modulatory site. This is consistent with a recent comparison of the α1β3γ2L $GABA_AR$ in complex with GABA and picrotoxin, or GABA only, which indicated rearrangements of this region are important for activation of the channel [41]. This indicated that binding of GABA induces rearrangement of a phenylalanine side chain (α1Phe15) and the formation of new salt bridges between the side chains of α1Arg85 and β3Asp163 that cause the more intimate coupling of the α1 and β3 interfaces. The resulting rotation of these subunits is proposed to be then transmitted to their neighbours, causing a concerted rotation of the whole ECD. It is likely that the megabody (or nanobody) can also promote these rearrangements, binding the β and α subunits together to facilitate activation.

The number of occupied megabody sites varied between datasets, with two being observed in three datasets, but only one megabody visible in the dataset for α3β3γ2L $GABA_AR$ in the presence of GABA and picrotoxin. The reason for this difference is likely to be the lower concentration of megabody added for the latter sample. Interestingly, although it would appear that megabody can bind at both β+/α- interfaces in the heteromeric receptor, the preferential presence of megabody at one interface suggests that these binding sites are not identical. This is consistent with both functional work with concatemeric receptors, which found that one GABA site has approximately three-fold higher affinity compared with the other [68], and structural observations which found that the motions induced upon GABA binding are not identical for each interface [41]. Since each GABA-binding interface has different neighbours, this is, upon reflection, not too surprising.

Despite these findings, a precise identification of the α3β3mb173 binding site is left to future work. A clearer view of the binding site would be facilitated by improving the resolution of the map. This could likely be achieved by either collecting more data, or further improving the sample, perhaps through the use of alternative replacements for detergent, or by avoiding detergent solubilisation altogether. A higher resolution model for the megabody would also be of significant utility to clarify the interface, and to give greater confidence in the placement of the CDR loops in the density. Future work could also include mutations to the binding site, both on the $GABA_AR$ side and the

nanobody/megabody side, coupled with SPR/BLI and electrophysiology, to functionally validate the involvement of residues at the interface.

6
General discussion

The aim of the work described in this thesis was to investigate the structural basis for modulation of the $GABA_AR$. This receptor is the main mediator of fast ionotropic neurotrainsmission in the brain, and is crucial for maintaining the excitatory-inhibitory balance that underlies normal function of the nervous system. This receptor, and in particular α2- and α3-containing receptors are also implicated in several pathological states, including pain and anxiety [147], [169].

As mentioned at the end of Chapter 1, prior to work described in Chapters 3, 4 and 5, the neurosteroid binding site of a chimeric $GABA_AR$ was investigated (Appendix F). This work, together with another study published at the same time [332], revealed the allosteric site for the neurosteroid pregnanolone, an important endogenous modulator of $GABA_ARs$. The binding site identified in a crystal structure of a chimeric receptor was then investigated my making mutations to the receptor, and pregnanolone potentiation was found to be knocked out by mutations to this site.

Nanobodies against $GABA_ARs$ were then investigated (Chapter 3). Previous work with nanobodies against the α1β3 $GABA_AR$ had indicated that these are tight binders with nanomolar affinity, and α1-specific nanobodies can act as positive modulators of the channel [40], [296]. These findings were replicated here, with α1β3nb138 shown to be a potent and selective postive allosteric modulator of the α1β3γ2L receptor.

Then, more nanobodies were raised against purified α2β3 and α3β3 $GABA_A$Rs, in collaboration with Els Pardon and Jan Stayert, using methods developed by this group [214]. These were screened by BLI and electrophysiology for affinity and functional effects. Some positive modulators were identified, particularly α2β3nb095, α2β3nb148, α3β3nb172, α3β3nb173, and α3β3nb183. Given that nanobodies tend to recognise structural epitopes [293], and that α1β3nb138 was found to be selective, it is likely that these nanobodies might also be selective for α2- or α3-containing $GABA_A$Rs. This remains to be determined, but if true this would make these nanobodies interesting prospects as research tools for investigating the role of particular types of $GABA_A$Rs in the brain, perhaps at the circuit level, or in rodent models of behaviour. Given the role of α2- and α3-containing $GABA_A$Rs in pathological processes such as pain and anxiety, these nanobodies could also potentially be used a drugs, provided a suitable mechanism for their delivery into the brain is developed.

In the search for binders to αβγ $GABA_A$Rs, nanobodies derived from heavy-chain antibodies were used, rather than traditional antibodies. Derivatives of anti-$GABA_A$R antibodies, such as the antigen-binding fragment (Fab), have also been used in recent structural studies of the $GABA_A$R [38], [39], whereas the use of single-chain fusion of heavy and light variable fragments (scFv) appears less common. Furthermore, although nanobodies have been shown to have functional effects on their targets, and in particular can positively modulate $GABA_A$Rs [40] (see Chapter 3), the functional effects of these Fabs have not been examined [38], [39]. It would be of interest to compare the structural and correlated functional effects of these Fabs, in order to compare the kinds of conformational changes they might cause with those caused by nanobodies. Is is generally believed that nanobodies access different kinds of epitopes compared to antibodies because of their small size [333], and this tendency might also correlate with a higher likelihood of inducing functional effects. A comparison of this property of nanobodies and antibody fragments could be one future direction for this work.

Next, methods of expressing and purifying full-length heteromeric $GABA_A$Rs were developed (Chapter 4). Several expression methods were tested, with cell lines created by transduction with recombinant lentiviruses found to be the best method. This is not

surprising, since exposure of a high viral titre to cells is likely to result in many copies of the transgene becoming integrated into the host cell genome [334]. Coupled with the use of the strong CMV promoter, [221] these cell lines had much higher levels of expression compared to transient transfection of HEK293S GnTI$^-$ cells in suspension, or BacMam. Although not performed here, it could be advantageous to isolate clones of single cells, since the polyclonal nature of these cell lines makes them heterogeneous. Higher expression could potentially be achieved by isolating clones with higher expression than the average level present in all cells; indeed this approach has previously been shown to result in high-level expression functional of αβγGABA$_A$Rs [307]. The approach taken here represents a trade-off between time taken to establish cell lines and expression level.

Finally, cryo-EM was used to investigate the structure of a α3β3γ2L in complex with a megabody version of one of these newly-discovered potentiating nanobodies, α3β3nb173 (Chapter 5). After optimisation of grids and the collection of several datasets, the binding site for this nanobody was identified: at the β+/α- interface, at the top of the ECD. Although precise residues at the GABA$_A$R-nanobody interface could not be identified, it is likely that the CDR loops of the nanobody interact with loop 3 from the α3 subunit and loop 1 from the β3 subunit. This is a novel allosteric site for the GABA$_A$R, although recently a positive modulatory site was found in the homomeric α3 GlyR in a similar region [36]. Further characterisation of this site on the GABA$_A$R is necessary to fully understand the mechanism of potentiation by α3β3nb173. In particular, electrophysiology with mutated GABA$_A$Rs and nanobodies could be used to investigate potential residues involved on both sides of the interface.

Since this structural work focused on the interaction of α3β3nb173 with the α3β3γ2L GABA$_A$R. The binding site for the other identified modulatory nanobodies is left for future work. Furthermore, since methods to express and purify the full-length heteromeric GABA$_A$R have now been developed, the binding sites of other drugs, such as the new generation of more α2- and α3-selective benzodiazepines could be interrogated. Given the primary interest in these receptors as drug targets, these findings could be of great importance for the development of novel analgesics and anxiolytics.

Appendices

A

Expression vectors used for cloning

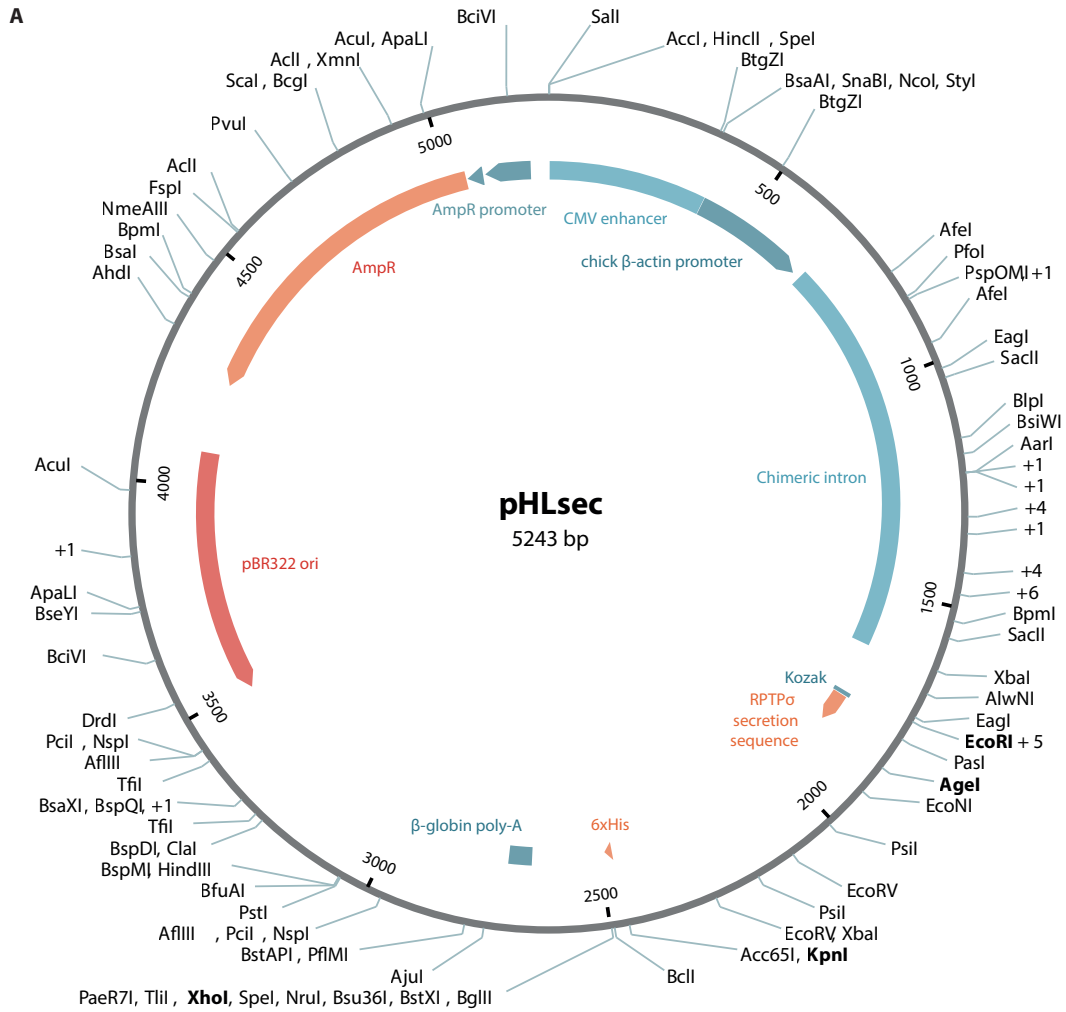

B

Multiple cloning site:

EcoRI Kozak *M* G I L P S P G

GAATTCAAGCTTGCCACC*ATG*GGGATCCTTCCCAGCCCTGGG

M P A L L S L V S L L S V L

ATGCCTGCGCTGCTCTCCCTCGTGAGCCTTCTCTCCGTGCTG

L M G C V A E **T G**

CTGATGGGTTGCGTAGCTGAA**ACCGGT**....insert.....

G **T K** H H H H H H * * **XhoI**

GGT**ACCAAG**CACCACCATCACCATCAC*TAATGA*TCA**CTCGAG**

Figure A.1: Features of the pHLsec vector. A: A vector map showing the main features: ampicillin resistance gene, origin of replication, and expression casette consisting of the CAG promoter, multiple cloning site (restriction sites in bold), 6xHis tag and β-globin polyA. The CAG promoter is composed of the cytomegalovirus early enhancer element, the promoter, first exon and first intron of the chicken β-actin gene, and the splice acceptor of the rabbit beta-globin gene. **B:** Detailed view of the multiple cloning site, with restriction sites in bold, Kozak sequence in red, secretion sequence in blue, hexahistidine tag in yellow, and start and stop codons in italics. Vector information from addgene (plasmid #99845), figure adapted from [219]

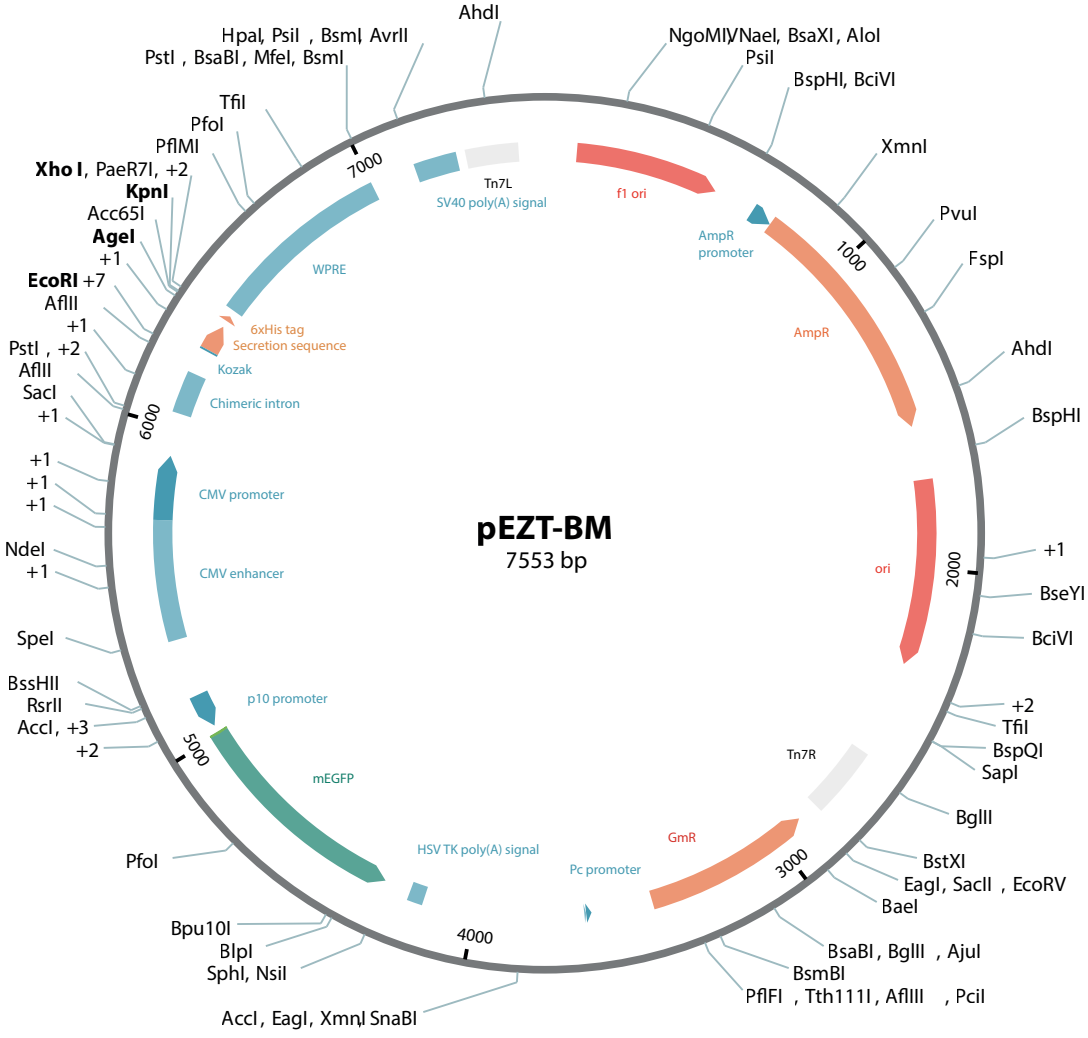

Figure A.2: Features of the pEZT-BM vector [220]. A vector map of pEZT-BM showing the main features: ampicillin (AmpR) and gramicidin (GmR) resistance genes, origins of replication (ori, f1 ori), mammalian expression casette consisting of the CMV promoter, multiple cloning site from pHLsec (restriction sites in bold, see also Figure A.1B), 6xHis tag, WPRE and SV40 poly(A) signal, insect expression casette containing p10 promoter, mEGFP and HSVpoly(A) signal, as well as the transposition elements Tn7L and Tn7R.

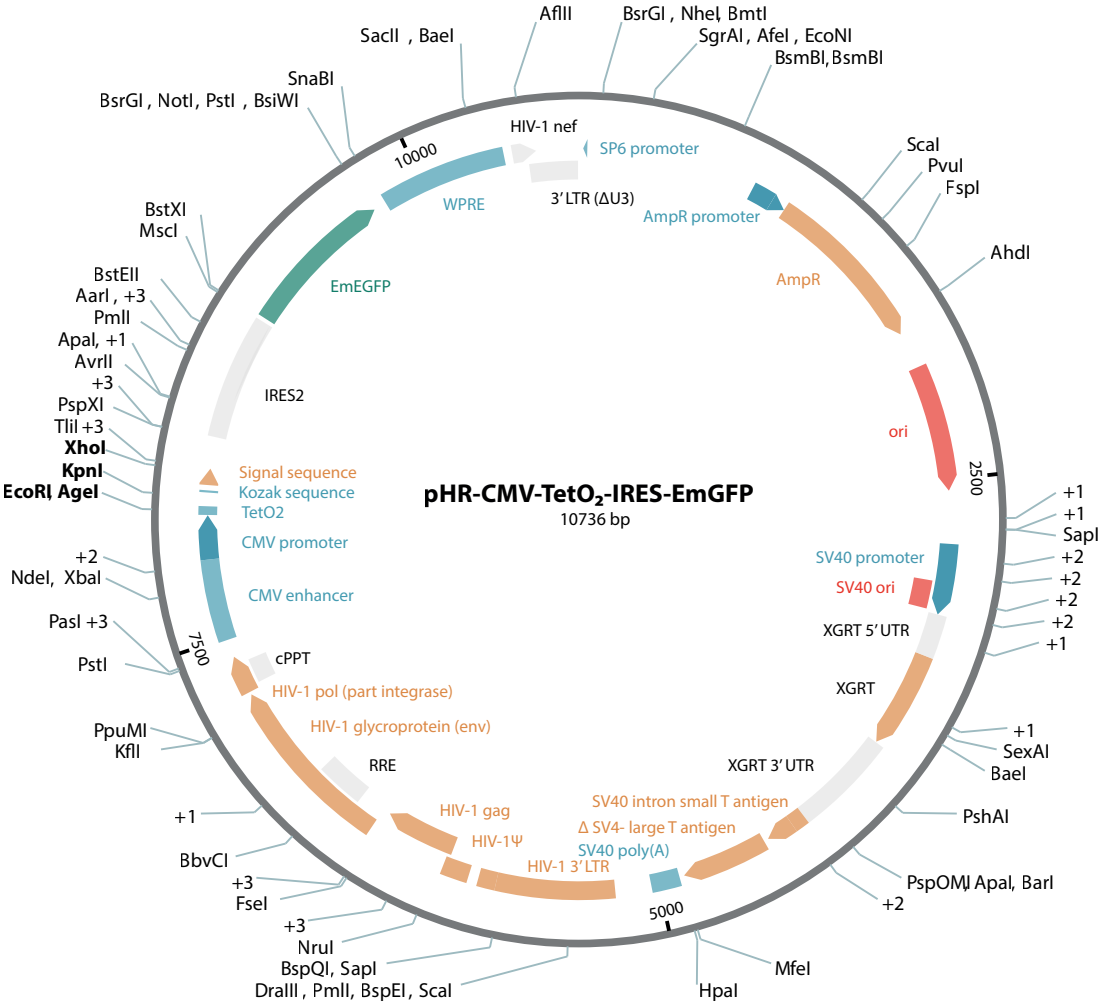

Figure A.3: Features of the pHR-CMV-TetO$_2$-IRES-EmGFP vector. A vector map of pHR showing the main features: ampicillin (AmpR) resistance genes, origins of replication (ori), mammalian expression casette consisting of the CMV promoter, multiple cloning site from pHLsec (restriction sites in bold, see also Figure A.1B), IRES, EmGFP, WPRE, as well as elements necessary for lentiviral packaging. Versions of this vector where the EmEGFP was replaced by another fluorescent protein, or the IRES-FP sequence was omitted, were also used.

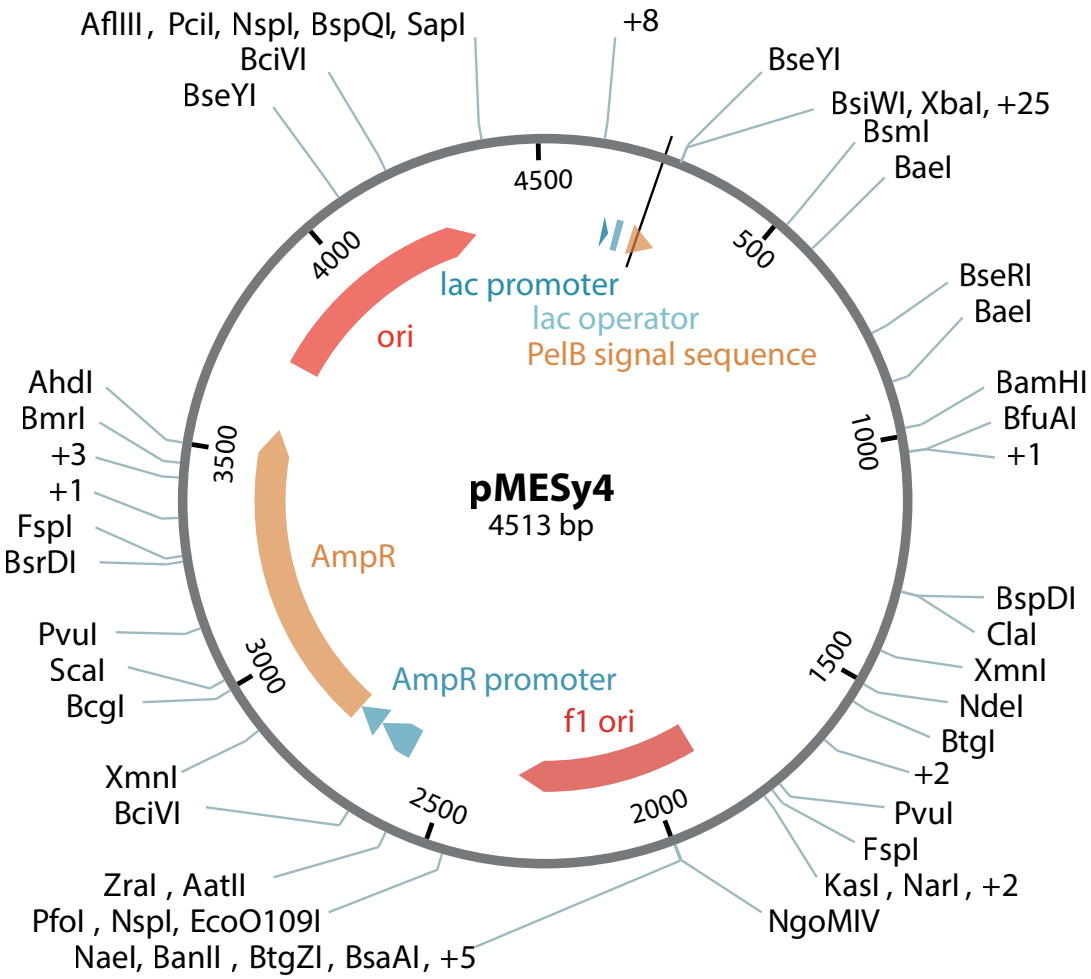

Figure A.4: Features of the pMESy4 vector. A vector map of pMESy4 showing the main features: ampicillin (AmpR) resistance genes, origins of replication (ori, f1 ori), bacterial expression casette consisting of the lac promoter, lac operator and PelB leader sequence for targeting to the periplasmic space.

B
Constructs

A list of the constructs used in this work is given in Table B.1, and the cloning of each construct is described in Table B.2. A list of the olignucleotides used for cloning can be found in Appendix C. For a list of the boundaries for $GABA_AR$ subunit constructs, see Table 2.1.

Table B.1: Constructs used in this work

Protein	Name	Vector	5' Features	Insert	3' features
α constructs					
GABR α1	pHLsec-α1	pHLsec	EcoRI-kozak-SS-AgeI	α1FL	dblstp-XhoI
GABR α2	pHLsec-α2-1D4	pHLsec	EcoRI-kozak-SS-AgeI	α2FL	KpnI-1D4-dblstp-XhoI
GABR α2	pHLsec-α2	pHLsec	EcoRI-kozak-SS-AgeI	α2FL	KpnI-dblstp-XhoI
GABR α2	pHLsec-α2glvi-1D4	pHLsec	EcoRI-kozak-SS-AgeI	α2glvi	KpnI-1D4-dblstp-XhoI
GABR α2	pEZT-α2	pEZT-BM	EcoRI-kozak-SS-AgeI	α2FL	KpnI-dblstp-XhoI
GABR α2	pHR-FLAG-α2	pHR	TetO2-EcoRI-kozak-SS-FLAG-AgeI	α2FL	KpnI-dblstp-XhoI
GABR α2	pHR-FLAG-α2-IRES-mRuby2	pHR	TetO2-EcoRI-kozak-SS-FLAG-AgeI	α2FL	KpnI-dblstp-XhoI-IRES-mRuby2
GABR α3	pHLsec-α3-1D4	pHLsec	EcoRI-kozak-SS-AgeI	α3FL	KpnI-1D4-dblstp-XhoI
GABR α3	pHLsec-α3	pHLsec	EcoRI-kozak-SS-AgeI	α3FL	KpnI-dblstp-XhoI
GABR α3	pHLsec-α3glvi-1D4	pHLsec	EcoRI-kozak-SS-AgeI	α3glvi	KpnI-1D4-dblstp-XhoI
GABR α3	pEZT-α3	pEZT-BM	EcoRI-kozak-SS-AgeI	α3FL	KpnI-dblstp-XhoI
GABR α3	pHR-FLAG-α3-IRES-mRuby2	pHR	TetO2-EcoRI-kozak-SS-FLAG-AgeI	α3FL	KpnI-dblstp-XhoI-IRES-mRuby2
GABR α3	pEZT-FLAG-α3	pHR	TetO2-EcoRI-kozak-SS-FLAG-AgeI	α3FL	KpnI-dblstp-XhoI
GABR α4	pHLsec-α4-1D4	pHLsec	EcoRI-kozak-SS-AgeI	α4FL	KpnI-1D4-dblstp-XhoI
GABR α5	pHLsec-α5-1D4	pHLsec	EcoRI-kozak-SS-AgeI	α5FL	KpnI-1D4-dblstp-XhoI
GABR α6	pHLsec-α6-1D4	pHLsec	EcoRI-kozak-SS-AgeI	α6FL	KpnI-1D4-dblstp-XhoI
β constructs					
GABR β3	pHLsec-β3	pHLsec	EcoRI-kozak-SS-AgeI	β3FL (KpnI site after M3-4 loop)	dblstp-XhoI
GABR β3	pHLsec-β3glvi	pHLsec	EcoRI-kozak-SS-AgeI	β3glvi	dblstp-XhoI

Table B.1 continued from previous page

Protein	Name	Vector	5' Features	Insert	3' features
GABR β3	pHLsec-β3glvi-avi	pHLsec	EcoRI-kozak-SS-AgeI	β3glvi	KpnI-(GGS)2-avi-dblstp-XhoI
GABR β3	pHLsec-β3glvi-1D4	pHLsec	EcoRI-kozak-SS-AgeI	β3glvi	KpnI-1D4-dblstp-XhoI
GABR β3	pHLsec-mV-β3-1D4	pHLsec	EcoRI-kozak-SS-6xHis-mV-AgeI	β3FL (KpnI site after M3-4 loop)	KpnI-1D4-dblstp-XhoI
GABR β3	pHLsec-mV-β3glvi-1D4	pHLsec	EcoRI-kozak-SS-6xHis-mV-AgeI	β3glvi	KpnI-1D4-dblstp-XhoI
GABR β3	pEZT-β3	pEZT-BM	EcoRI-kozak-SS-AgeI	β3FL (KpnI site after M3-4 loop)	KpnI-dblstp-XhoI
GABR β3	pHR-mV-β3-1D4	pHR	TetO2-EcoRI-kozak-SS-6xHis-mV-AgeI	β3FL (KpnI site after M3-4 loop)	KpnI-1D4-dblstp-XhoI
GABR β3	pEZT-mV-β3-1D4	pEZT-BM	TetO2-EcoRI-kozak-SS-6xHis-mV-AgeI	β3FL (KpnI site after M3-4 loop)	KpnI-1D4-dblstp-XhoI
GABR β3	pHR-HA-β3	pHR	TetO2-EcoRI-kozak-SS-HA-AgeI	β3FL (KpnI site after M3-4 loop)	KpnI-dblstp-XhoI
GABR β3	pHR-HA-β3-IRES-mTurquoise2	pHR	TetO2-EcoRI-kozak-SS-HA-AgeI	β3FL (KpnI site after M3-4 loop)	KpnI-dblstp-XhoI-IRES-mTurquoise2
γ constructs					
GABR γ2	pHLsec-SBP-γ2L-1D4	pHLsec	EcoRI-kozak-SS-SBP-linker(DYDIPTT)-TEV-AgeI	γ2L_FL	KpnI-1D4-dblstp-XhoI
GABR γ2	pHLsec-mEGFP-γ2L-1D4	pHLsec	EcoRI-kozak-SS-mEGFP	γ2L_FL	
GABR γ2	pEZT-mEGFP-γ2-1D4	pEZT-BM	EcoRI-kozak-SS-mEGFP	γ2L_FL	KpnI-1D4-dblstp-XhoI
GABR γ2	pHLsec-mEGFP-TEV-γ2L-1D4	pHLsec	TetO2-EcoRI-kozak-SS-mEGFP-TEV-AgeI	γ2L_FL	KpnI-1D4-dblstp-XhoI
GABR γ2	pHR-mEGFP-TEV-γ2-3x(GGS)-1D4	pHR	TetO2-EcoRI-kozak-SS-mEGFP-TEV-AgeI	γ2L_FL	KpnI-3x(GGS)-1D4-dblstp-XhoI

Table B.1 continued from previous page

Protein	Name	Vector	5' Features	Insert	3' features
GABR γ2	pHR-mEGFP-TEV-γ2-3x(GGS)-1D4-IRES-EmGFP	pHR	TetO2-EcoRI-kozak-SS-mEGFP-TEV-AgeI	γ2L_FL	KpnI-3x(GGS)-1D4-dblstp-XhoI-IRES-EmGFP

Table B.2: Cloning methods for constructs

Name	Cloning method
α constructs	
pHLsec-α1	Provided by Paul Miller
pHLsec-α2-1D4	Synthetic gene with C-terminl KpnI-1D4-double stop-XhoI sequence inserted by restriction and ligation between AgeI and XhoI sites
pHLsec-α2	PCR of α2 from pHLsec-α2-1D4 using primers 1 and 9, digestion with EcoRI and XhoI, ligation into pHLsec
pHLsec-α2glvi-1D4	Provided by Paul Miller
pEZT-α2	Digestion of pHLsec-α2 with EcoRI and XhoI, and ligation into pEZT-BM (digested with the same enzymes)
pHR-FLAG-α2	Addition of FLAG tag to α2 by overlap PCR using primers 1, 2, 14 and 15, digestion with EcoRI and XhoI, ligation into pHR (digested with the same enzymes)
pHR-FLAG-α2-IRES-mRuby2	Digestion of pHR-FLAG-α2 with EcoRI and XhoI, and ligation into pHR-IRES-mRuby2
pHLsec-α3-1D4	Synthetic gene with C-terminl KpnI-1D4-double stop-XhoI sequence inserted by restriction and ligation between AgeI and XhoI sites
pHLsec-α3	PCR of α3 from pHLsec-α2-1D4 using primers 1 and 10, digestion with EcoRI and XhoI, ligation into pHLsec
pHLsec-α3glvi-1D4	Provided by Paul Miller
pEZT-α3	Digestion of pHLsec-α3 with EcoRI and XhoI, and ligation into pEZT-BM (digested with the same enzymes)
pHR-FLAG-α3-IRES-mRuby2	Digestion of pHR-FLAG-α3 with EcoRI and XhoI, and ligation into pHR-IRES-mRuby2
pEZT-FLAG-α3	Addition of FLAG tag to α3 by overlap PCR using primers 1, 2, 16 and 17, digestion with EcoRI and XhoI, ligation into pHR (digested with the same enzymes)
pHLsec-α4-1D4	Synthetic gene with C-terminl KpnI-1D4-double stop-XhoI sequence inserted by restriction and ligation between AgeI and XhoI sites
pHLsec-α5-1D4	Synthetic gene with C-terminl KpnI-1D4-double stop-XhoI sequence inserted by restriction and ligation between AgeI and XhoI sites
pHLsec-α6-1D4	Synthetic gene with C-terminl KpnI-1D4-double stop-XhoI sequence inserted by restriction and ligation between AgeI and XhoI sites
β constructs	
pHLsec-β3	Provided by Paul Miller
pHLsec-β3glvi	Provided by Paul Miller

Table B.2 continued from previous page

Name	Cloning method
pHLsec-β3glvi-avi	Provided by Paul Miller
pHLsec-β3glvi-1D4	Provided by Paul Miller
pHLsec-mV-β3-1D4	Provided by Paul Miller
pHLsec-mV-β3glvi-1D4	Created by digestion of pHLsec-β3glvi-1D4 with AgeI and XhoI, and ligation of the β3glvi-1D4 fragment into pHLsec-mV (from pHLsec-mV-β3-1D4, digested with the same enzymes)
pEZT-β3	Digestion of pHLsec-β3 with EcoRI and XhoI, and ligation into pEZT-BM (digested with the same enzymes)
pHR-mV-β3-1D4	Digestion of pHLsec-mV-β3-1D4 with EcoRI and XhoI, and ligation into pHR (digested with the same enzymes)
pEZT-mV-β3-1D4	Digestion of pHLsec-mV-β3-1D4 with EcoRI and XhoI, and ligation into pEZT-BM (digested with the same enzymes)
pHR-HA-β3	Addition of HA tag to β3 by overlap PCR using primers 1, 2, 18 and 19, digestion with EcoRI and XhoI, ligation into pHR (digested with the same enzymes)
pHR-HA-β3-IRES-mTurquoise2	Digestion of pHR-HA-β3 with EcoRI and XhoI, and ligation into pHR-IRES-mTurquoise2
γ constructs	
pHLsec-SBP-γ2L-1D4	Provided by Paul Miller
pHLsec-mEGFP-γ2L-1D4	Overlap PCR to join mEGFP (primers 11 and 12, cDNA provided by Holly Sun) and γ2L_FL (primers 13 and 2, cDNA provided by Duncan Laverty, digestion with EcoRI and XhoI, ligation into pHLsec
pEZT-mEGFP-γ2-1D4	Digestion of pHLsec-mEGFP-γ2L-1D4 with EcoRI and XhoI, and ligation into pEZT-BM (digested with the same enzymes)
pHLsec-mEGFP-TEV-γ2L-1D4	PCR of mEGFP-TEV-AgeI fragment with primers 1 and 20, digest with EcoRI and AgeI, and ligation into pHLsec-SBP-γ2L-1D4 (digested with the same primers)
pHR-mEGFP-TEV-γ2-3x(GGS)-1D4	Addition of 3x(GGS) between g2L and 1D4 by overlap PCR using primers 1, 2, 16 and 17 (with template pHLsec-mEGFP-TEV-γ2L-1D4) , digestion with EcoRI and XhoI, ligation into pHR (digested with the same enzymes)
pHR-mEGFP-TEV-γ2-3x(GGS)-1D4-IRES-EmGFP	Digestion of pHR-mEGFP-TEV-γ2-3x(GGS)-1D4 with EcoRI and XhoI, and ligation into pHR-IRES-EmGFP

C
Oligonucleotide primers

Oligonucleotide primers used in this work can be found in Table C.1

Table C.1: Oligonucleotide primers used in this work

No.	Name	Use	Target	Sequence (5' ->3')
1	pHLsec F	Sequencing pHLsec	pHLsec 5' UTR	GCTCTAGAGCCTCTGCTAACC
2	pHLsec R	Sequencing pHLsec	pHLsec 3' UTR	CACCAGCCACCACCTTCTGAT
3	pMESy4 F	Sequencing pMESy4	pMESy4 5' UTR	CGATAAGCTTAAGGAGACAGTACATATG
4	pMESy4 R	Sequencing pMESy4	pMESy4 3' UTR	TTTTGTCGTCTTTCCAGACG
5	pEZT-BM F	Sequencing pEZT-BM, pHR	CMV promoter	CAACGGGACTTTCCAAAATG
6	pEZT-BM R	Sequencing pEZT-BM, pHR	WPRE	ATACCAGTCAATCTTTCAC
7	pHR R	Sequencing pHR	IRES	CCCTCACATTGCCAAAAGACGG
8	mEGFP_ct F	Sequencing mEGFP fusions	mEGFP C-terminal	CCAATGAGAAGCGTGACC
9	ha2_remove1D4 R	Removing 1D4 tag from α2	hGABRα2 FL synth	AGTCTCGAGTCATCAGGTACCGGGGGACACTCC
10	ha3_remove1D4 R	Removing 1D4 tag from α3	hGABRα3 FL synth	TAGTCTCGAGTCATCAGGTACCCTGC
11	mGFP F	Creating mGFP-hγ2L	mEGFP	GCCGAATTCGCCACCATGG
12	mGFP_hg2_join R	Creating mGFP-hγ2L	mEGFP	TAGTCATCATCTGACTTTTGTTTATACAGCTCGTCCATGC
13	mGFP_hg2_join F	Creating mGFP-hγ2L	hGABR γ2	GCATGGACGAGCTGTATAAACAAAAGTCAGATGATGACTATGA
14	FLAGa2_F	Adding FLAG tag to α2	hGABR α2	ctgatgggttgcgtagctgaaGACTACAAGGACGATGACGATAAGACCGG TAACATCCAGGAAGATGAG
15	FLAGa2_R	Adding FLAG tag to α2	hGABR α2	CTCATCTTCCTGGATGTTACCGGTCTTATCGTCATCGTCCTTGT AGTCttcagctacgcaacccatcag
16	FLAGa3_F	Adding FLAG tag to α3	hGABR α3	ctgatgggttgcgtagctgaaGACTACAAGGACGATGACGATAAGACCGGT CAAGGCGAGAGC
17	FLAGa3_R	Adding FLAG tag to α3	hGABR α3	GCTCTCGCCTTGACCGGTCTTATCGTCATCGTCCTTGTAGTCttcag ctacgcaacccatcag
18	HA_b3_F	Adding HA tag to β3	hGABR β3	ctgatgggttgcgtagctgaaTACCCATACGATGTTCCAGATTACGCTACCG GTCAAAGCGTGAACG
19	HA_b3_R	Adding HA tag to β3	hGABR β3	CGTTCACGCTTTGACCGGTAGCGTAATCTGGAACATCGTATGG GTAttcagctacgcaacccatcag

Table C.1: Oligonucleotide primers used in this work

No.	Name	Use	Target	Sequence (5' ->3')
20	mEGFP_TEV_ageI_R	Adding TEV site between mEGFP and γ2L	mEGFP-γ2L	GTTACCGGTACTACCGCCGCCCTGAAAATACAAGTTTTCAGACC CCCCTTTATACAGCTCGTCCATGCCAAGT
21	KpnI_GGS3_1D4_F	Adding 3GGS linker between γ2L and 1D4	γ2L-1D4	GTTTACTGGGTCTCCTATCTTTATCTGGGTACCGGTACCGG GGGGTCTGGTGGTTCCGGTGGCTCTACCGAGACATCTCAGGTGG
22	KpnI_GGS3_1D4_R	Adding 3GGS linker between γ2L and 1D4	γ2L-1D4	CCACCTGAGATGTCTCGGTAGAGCCACCGGAACCACCAGACCCC CCGGTACCGGTACCCAGATAAAGATAGGAGACCCAGTAAAC

D

MATLAB scripts used for data analysis and presentation

Contents

D.1 FSEC data analysis 190
D.2 BLI data analysis 197
D.3 Electrophysiology data analysis 211

D.1 FSEC data analysis

A simple function import_shimadzu was written to extract the relevant data for each channel from the .txt files that are exported by the LabSolutions software. This function takes as input a path to a folder where the .txt files are located, and outputs a data structure containing the data for each channel. This function is given below:

```
%load and plot Shimadzu files
function data = import_shimadzu(folder)
%put path to folder of files here - must contain .txt files!

%change directory and get all .txt files in this folder
oldfolder = pwd;
cd(folder)
filelist = dir('*.txt');
pathlist = cell(size({filelist.name}));
```

```
pathlist(:) = {strcat(folder, '/')};
pathlist = strcat(pathlist, {filelist.name})';
%change back to original directory
cd(oldfolder)

rawdata = cell(size(pathlist));
%import all data
delimiter = '\t';
formatSpec = '%s%s%s%s%s%s%s%s%s%s%s%s%s%s%s%s%s%s%s%s%s%s%[^\n\r]';
for i = 1:length(pathlist)
    fileID = fopen(pathlist{i},'r');
    dataArray = textscan(fileID, formatSpec, 'Delimiter', delimiter,
        'EmptyValue' ,NaN, 'ReturnOnError', false);
    fclose(fileID);
    rawdata{i} = [dataArray{1:end-1}];
end

%find number of detectors, number of channels and data for each detector
detectors = cell(size(pathlist));
for i = 1:length(pathlist)
    temp = find(strcmp(rawdata{i,1}, ['Detector Name']));
    temp2 = find(~cellfun(@isempty,rawdata{i,1}(temp,2:end)));
    %find name of sample
    temp3 = find(strcmp(rawdata{i,1}, ['Sample Name']));
    detectors{i,2} = rawdata{i,1}{temp3, 2};
    detectors{i,1} = rawdata{i,1}(temp:temp+1,temp2+1);
    %find info about each detector
    for j = 1:length(detectors{i,1})
        searchCh = detectors{i,1}(1,j);
        noCh = str2num(detectors{i,1}{2,j});
        for k = 1:noCh
            detNam = ['A', 'B', 'C', 'D', 'E'];
            detectors{i,1}{k+2 ,j} = cell(2,1);
            %find wavelength for UV, put in 'detector' cell array
            if strcmp(searchCh, 'UV')
                ind = find(strcmp(rawdata{i,1}, {sprintf('[LC
                    Chromatogram(Detector %s-Ch%d)]', detNam(j), k)}));
                detectors{i,1}{k+2,j}{1,1} = rawdata{i,1}(ind+7,2);
                %add data to 'detectors' cell array
                datastart = ind+9;
                %need to find the end of this particular dataset
                dataend = ind+10;
                endsearch = 0;
                while not(endsearch)
                    [a, status] = str2num(rawdata{i,1}{dataend,1});
                    if status
                        dataend = dataend+1;
                    else
```

```
                    endsearch = 1;
                end
            end
            dataend = dataend-1;
            detectors{i,1}{k+2,j}{2,1} =
                str2double(rawdata{i,1}(datastart:dataend,1:2));
        %find excitation and emission wavelengths for FL, put in
        %'detector' cell array
        elseif strcmp(searchCh, 'FL')
            ind = find(strcmp(rawdata{i,1}, {sprintf('[LC
                Chromatogram(Detector %s-Ch%d)]', detNam(j), k)}));
            detectors{i,1}{k+2, j} = [rawdata{i,1}(ind+7,2)
                rawdata{i,1}(ind+8,2)];
            %add data to 'detectors' cell array
            datastart = ind+10;
            %need to find the end of this particular dataset
            dataend = ind+11;
            endsearch = 0;
            while not(endsearch)
                [a, status] = str2num(rawdata{i,1}{dataend,1});
                if status
                    dataend = dataend+1;
                else
                    endsearch = 1;
                end

            end
            dataend = dataend-1;
            detectors{i,1}{k+2,j}{2,1} =
                str2double(rawdata{i,1}(datastart:dataend,1:2));
        end

    end
end
%can delete second row from each cell arary in 'detectors' cell array
%beacuse it's now redundant
detectors{i,1}(2,:) = [] ;
end
data = detectors;
```

D.1.1 plot_data.m

In order to efficiently plot the data after its import to Matlab, other scripts (plot_data.m) were written that call import_shimadzu and the desired data. One example is as follows:

```
folder =
    '/Users/sscott/Documents/University/Oxford/DPhil/Aricescu_lab/...
Labbook/FL heteromers/Shimadzu/180619-Fa3Hb3GFPg2L1D4_1D4_apols_EndoF';

data = import_shimadzu(folder);

%zero data - delete average of signal at 5-10 minutes


for i = 1:length(data)
    for j = 2:3
        for k = 1:2
            curr = data{i,1}{j,k}{2,1};
            bl_times = find(curr(:,1) > 5 & curr(:,1) < 10);
            bl = mean(curr(bl_times, 2));
            curr(:,2) = curr(:,2)-bl;
            data{i,1}{j,k}{2,1} = curr;
        end
    end
end

%plot all samples - GFP FL
figure(1)
clf
toplot = [1:length(data)];
hold on
for i = 1:length(data)
    plot(data{i,1}{3,1}{2,1}(:,1), data{i,1}{2,2}{2,1}(:,2))
end
xlabel('Time (min)')
ylabel(' Ex 488nm Em 525nm (GFP) Fluo (AU)')
legend('pre Endo F1', 'after Endo F1')
set(gca,'FontSize',18)
set(findall(gca, 'Type', 'Line'),'LineWidth',2);

saveas(gcf, strcat(folder, '/all_GFP.png'))

%plot all disc preps (trp)
figure(2)
clf
hold on
toplot = [1:length(data)];
for i = toplot
    plot(data{i,1}{3,2}{2,1}(:,1), data{i,1}{3,2}{2,1}(:,2))
end
xlabel('Time (min)')
ylabel(' Ex 295nm Em 350nm (trp) Fluo (AU)')
legend('pre Endo F1', 'after Endo F1')
```

```
set(gca,'FontSize',18)
set(findall(gca, 'Type', 'Line'),'LineWidth',2);


saveas(gcf, strcat(folder, '/all_trp.png'))


%plot trp and GFP for each sample
for j = 1:length(data)
    figure
    clf
    hold on
    toplot = j;
    for i = toplot
        plot(data{i,1}{3,2}{2,1}(:,1), data{i,1}{3,2}{2,1}(:,2))
        plot(data{i,1}{3,1}{2,1}(:,1), data{i,1}{2,2}{2,1}(:,2))
    end
    xlabel('Time (min)')
    ylabel('  Fluo (AU)')
    title(data{j,2})
    legend({'TRP fluo', 'GFP fluo'})
    set(gca,'FontSize',18)
    set(findall(gca, 'Type', 'Line'),'LineWidth',2);


    saveas(gcf, strcat(folder,'/', data{j,2}, '.png'))
end
```

D.1.2 analyse_lysates.m

For analysis of lysate FSEC to optimise $GABA_A$Rexpression conditions (Chapter 4), another script, analyse_lysates.m was written. This not only plots each Shimadzu run as for import_shimadzu.m, but also uses Matlab's findpeaks function in the Signal Processing toolbox to find local maxima in the chromatogram. For ease of further analysis, the search is restricted to the region around 25 minutes, when the $GABA_AR$ peak is expected.

```
%%% analyse lysate data from the shimadzu
%lenti stable cells: mV-b3-1D4


clear all

folder =
    '/Users/Suzanne/Documents/University/Oxford/DPhil/Aricescu_lab/...
Labbook/FL heteromers/Shimadzu/180207_mVb31D4_lenti_bacmam';
```

```
data = import_shimadzu(folder);



%row 29 looks to be repeat of row 28
data(29,:) = [];
%row 76 is incomplete repeat of row 75
data(76,:) = [];


% %plot data to check all is ok
%
% for i = 1:length(data)
%            clf
%        figure(1)
%        hold on
%        plot(data{i,1}{2,2}{2,1}(:,1),data{i,1}{2,2}{2,1}(:,2) )
%    title(data{i,2})
%    waitforbuttonpress
% end

%subtract sloping baseline - average of 5-10 and 50-55 minutes

%set parameters for baseline
bl1 = [10 14];
bl2 = [50 55];
bl_ind = [(find(data{1,1}{2,2}{2,1}(:,1)>bl1(1) &
    data{1,1}{2,2}{2,1}(:,1) <bl1(2)))'
    (find(data{1,1}{2,2}{2,1}(:,1)>bl2(1) & data{1,1}{2,2}{2,1}(:,1)
    <bl2(2)))']';

%need to check that all the runs are the correct length - ie they contain
%data for the times at which the baseline will be done
nobl = [];
for i = 1:length(data)
    if sum(data{i,1}{2,2}{2,1}(:,1)>bl2(1) & data{i,1}{2,2}{2,1}(:,1)
        <bl2(2)) == 0
        nobl = [nobl i];
    end
end

%subtract sloping baseline
baselines = setxor(1:length(data), nobl)'; %%want all runs that didn't
    get excluded above
for i  = baselines
     x = data{i,1}{2,2}{2,1}(bl_ind,1);
     X = [ones(length(x),1) x];
```

```
     y = data{i,1}{2,2}{2,1}(bl_ind,2);
     b = X\y;
     bl = ([ones(length(data{i,1}{2,2}{2,1}(:,1)),1)
         data{i,1}{2,2}{2,1}(:,1)]*b);
    %    plot all data to check
     clf
     hold on
     plot(data{i,1}{2,2}{2,1}(:,1), data{i,1}{2,2}{2,1}(:,2))
     plot(data{i,1}{2,2}{2,1}(:,1), bl)
     plot(data{i,1}{2,2}{2,1}(:,1), data{i,1}{2,2}{2,1}(:,2)-bl)
     title(data{i,2})
    %      waitforbuttonpress
     data{i,1}{2,2}{2,1}(:,2) = data{i,1}{2,2}{2,1}(:,2) - bl;
end

%filter data a bit - moving average filter, n=6 samples (note this will
%give delay of (n-1)/2 samples - account for this manually)

nfilt = 20;
coeffFilt = ones(1, nfilt)/nfilt;

for i = 1:length(data)
    withFilt = filter(coeffFilt, 1, data{i,1}{2,2}{2,1}(:,2));
    oneSamp = (data{i,1}{2,2}{2,1}(end,1)-data{i,1}{2,2}{2,1}(1,1))/...
    length(data{i,1}{2,2}{2,1}(:,1));
    clf
     hold on

%      plot(data{i,1}{2,2}{2,1}(:,1), data{i,1}{2,2}{2,1}(:,2))
%      plot(data{i,1}{2,2}{2,1}(:,1), withFilt)
%      waitforbuttonpress
    data{i,1}{2,2}{2,1}(:,2) = withFilt;
end


%find local maima around 25 minutes

%set time to search within
searchtimes = [22.5 25.5];
%initialize arracys to store data
pks = cell(length(data),1);
locs = cell(length(data),1);
widths = cell(length(data),1);
proms = cell(length(data),1);
minprom = 400;

for i = 1:length(data)
    %extract data to search
```

```
    searchind = [(find(data{i,1}{2,2}{2,1}(:,1)>searchtimes(1) &
        data{i,1}{2,2}{2,1}(:,1) <searchtimes(2)))' ]';
    searchx = data{i,1}{2,2}{2,1}(searchind,1);
    searchy = data{i,1}{2,2}{2,1}(searchind,2);
    [pks{i}, locs{i}, widths{i}, proms{i}] = findpeaks(searchy, searchx,
        'MinPeakProminence', minprom, 'Annotate', 'extents');

    clf
    hold on
    plot(data{i,1}{2,2}{2,1}(:,1), data{i,1}{2,2}{2,1}(:,2))
    plot(locs{i}, pks{i}, 'o')
    title(data{i,2})
    xlabel('Time (min)')
    ylabel('mVenus fluorsence, (Ex 515 Em 528)')
    %waitforbuttonpress
    saveas(gcf, strcat(folder, '/', data{i,2}, '_g.png'))

    if length(pks{i}) == 0
        sprintf('No peaks found for sample %s (row %f)', data{i,2}, i)
        pks{i} = nan;
    elseif length(pks{i}) >1
        sprintf('More than one peak found for sample %s (row %f)',
            data{i,2}, i)
        [temp choose] = max(pks{i});
        pks{i} = pks{i}(choose);
        locs{i} = locs{i}(choose);
        widths{i} = widths{i}(choose);
        proms{i} = proms{i}(choose);
    end
end


%note this will only work if one peak is found for each run
out = table(data(:,2),cell2mat(pks), cell2mat(locs), cell2mat(proms),
    'VariableNames', {'Condition', 'PeakHeight', 'TimeofPeak',
    'PeakProms'});

writetable(out, strcat(folder, '/_analysed.xls'))
```

D.2 BLI data analysis

D.2.1 SCK_fit

In order to analyse data, the function SCK_fit was written in MATLAB. This script takes as input the parameters of the data collections (number of concentrations, time of exposure

to each concentration, time for dissociation step, etc) and attempts to find the parameters that best fit the data. It assumes a 1:1 binding model uses MATLAB's curve fitting toolbox (function 'fit', after first declaring a 'fitobj') to optimize the parameters of the inputs to the functions 'SCK_sim_fit_preset_R0' and 'SCK_sim_fit_drift_preset_R0'. These functions simulate SCK data given a particular k_a, k_d and set of analyte concentrations and times, and are also given below the main function.

```
%this function fits single cycle kintics data to determine Kd

%INPUTS:
%   T and R are a vector of times and responses that define the
    sensorgram,
%   n_inj is the number of analyte injections,
%   inj_length is the length of each injection,
%   diss_length is the time of the dissociations between injections,
%   end_diss_length is the length of the long dissocation at the end,
%   high_conc is the highest concentration used in the dilution series
%   diln is the dilution series factor (ie 3 for 1/3 dilutions)

%OUTPUTS


function out = SCK_fit(T, R, n_inj, inj_length, diss_length,
    end_diss_length, high_conc, diln)

%calculate sampling frequency
freq = 1/(T(2)-T(1));

%calculate injection times
t_injs = zeros(1,n_inj);
for i = 1:n_inj
    t_injs(i) = (i-1)*(inj_length+diss_length);
end
t_diss = zeros(1, n_inj);
for i = 1:n_inj
    t_diss(i) = t_injs(i)+inj_length;
end

%pick guesses for constants
ka_init = 1e3;
kd_init = 1e-2;
Rmax_init = max(R)+0.1;
offset = 0;
R0_init = Rmax_init*[0 0.01 0.01 0.1 0.5];
```

```
R02_start = Rmax_init*0.01;
R03_start = Rmax_init*0.01;
R04_start = Rmax_init*0.1;
R05_start = Rmax_init*0.5;

R01_end = Rmax_init*0.01;
R02_end = Rmax_init*0.01;
R03_end = Rmax_init*0.1;
R04_end = Rmax_init*0.5;
R05_end = Rmax_init;

offset = 0;

%average over first t_av second(s) of each injection
t_av = 5;

for i = 1:n_inj
    if i == 1
        R01 = mean(R(t_injs(i) < T & T < (t_injs(i)+t_av)));
        R02 = mean(R(t_diss(i) < T & T < (t_diss(i)+t_av)));
    elseif i == 2
        R03 = mean(R(t_injs(i) < T & T < (t_injs(i)+t_av)));
        R04 = mean(R(t_diss(i) < T & T < (t_diss(i)+t_av)));
    elseif i == 3
        R05 = mean(R(t_injs(i) < T & T < (t_injs(i)+t_av)));
        R06 = mean(R(t_diss(i) < T & T < (t_diss(i)+t_av)));
    elseif i == 4
        R07 = mean(R(t_injs(i) < T & T < (t_injs(i)+t_av)));
        R08 = mean(R(t_diss(i) < T & T < (t_diss(i)+t_av)));
    elseif i == 5
        R09 = mean(R(t_injs(i) < T & T < (t_injs(i)+t_av)));
        R010 = mean(R(t_diss(i) < T & T < (t_diss(i)+t_av)));
    end
end

%generate initial guesses for fit parameters
guess1 = [ka_init, kd_init, Rmax_init, R02_start, R03_start, R04_start,
    R05_start, R01_end, R02_end, R03_end, R04_end, R05_end];
lb1 = zeros(size(guess1));
ub1 = [Inf Inf Inf Inf Inf Inf Inf Inf Inf Inf Inf Inf];

guess2 = [ka_init, kd_init, Rmax_init];
lb2 = [0 0 0];
ub2 = [Inf Inf Inf];

ftobj2 = fittype(@(ka, kd, Rmax,R01, R02, R03, R04, R05, R06, R07, R08,
    R09, R010, n_inj, inj_length, diss_length, end_diss_length,
    high_conc, diln, x)...
```

```
    SCK_sim_fit_preset_R0(x, ka, kd, Rmax, R01, R02, R03, R04, R05, R06,
        R07, R08, R09, R010, n_inj, inj_length, diss_length,
        end_diss_length, high_conc, diln),...
 'problem', { 'R01', 'R02', 'R03', 'R04', 'R05', 'R06', 'R07', 'R08',
    'R09', 'R010', 'n_inj', 'inj_length', 'diss_length',
    'end_diss_length', 'high_conc', 'diln'});

[fit2, gof2] = fit(T, R, ftobj2, 'startpoint', guess2, 'problem', {R01,
    R02, R03, R04, R05, R06, R07, R08, R09, R010, n_inj, inj_length,
    diss_length, end_diss_length, high_conc, diln}, 'Lower', lb2,
    'Upper', ub2);

ftobj3 = fittype(@(ka, kd, Rmax, drift, R01, R02, R03, R04, R05, R06,
    R07, R08, R09, R010, n_inj, inj_length, diss_length,
    end_diss_length, high_conc, diln, x)...
    SCK_sim_fit_drift_preset_R0(x, ka, kd, Rmax, drift, R01, R02, R03,
        R04, R05, R06, R07, R08, R09, R010, n_inj, inj_length,
        diss_length, end_diss_length, high_conc, diln),...
 'problem', { 'R01', 'R02', 'R03', 'R04', 'R05', 'R06', 'R07', 'R08',
    'R09', 'R010', 'n_inj', 'inj_length', 'diss_length',
    'end_diss_length', 'high_conc', 'diln'});

%use output from second fit and add linear drift term
guess3 = [fit2.ka, fit2.kd, fit2.Rmax, 0];

[fit3, gof3] = fit(T, R, ftobj3, 'startpoint', guess3, 'problem', {R01,
    R02, R03, R04, R05, R06, R07, R08, R09, R010, n_inj, inj_length,
    diss_length, end_diss_length, high_conc, diln}, 'Lower', lb2,
    'Upper', ub2);



    out.fit = fit3;
    out.gof = gof3;
    disp('using fit 3')

end
```

D.2.2 SCK_sim_fit_preset_R0

The function SCK_sim_fit_preset_R0 is given below. Along with the obvious parameters, this function also takes as input R0, which is an array of the signal at the start and end of each association or dissociation step. During data processing it was found that without this, the function often converged to the wrong solution due to a large parameter space.

```
%generate example single cycle kinetics data
%example inputs
% n_inj = 5;
% inj_length = 140;
% diss_length = 60;
% end_diss_length = 900;
% diln = 2;
% high_conc = 40e-9;
% ka = 4.231e5;
% kd = 1.385e-3;
% Rmax = 7;
%R0 is cell array of numbers that define starting points of each
%association/dissociation step


function y = SCK_sim_fit_preset_R0(x, ka, kd, Rmax, R01, R02, R03, R04,
    R05 ,R06, R07, R08, R09, R010, n_inj, inj_length, diss_length,
    end_diss_length, high_conc, diln)

% %find total length of experiment
% len = (inj_length + diss_length)*(n_inj-1) + inj_length +
    end_diss_length;
%
% x = [0:1/freq:len];

y = zeros(size(x));

%in case this input isn't an integer
if not(isinteger(n_inj))
    n_inj = round(n_inj);
%     warning('Rounded n_inj to nearest integer')
end

% n_inj = 5;

%times of injections etc (in seconds)
t_injs = zeros(1,n_inj);
for i = 1:n_inj
    t_injs(i) = (i-1)*(inj_length+diss_length);
end

conc = zeros(size(t_injs));
count = 0;
for i = length(t_injs):-1:1
    conc(i) = high_conc/diln^count;
    count = count+1;
end
```

```
%calculate frequency
period = (x(end)-x(1))/length(x);
frequ = 1/period;

%Calculate using differential rate law form (y)
dRdt = zeros(size(x));
y = zeros(size(x));


%loop over injections
for i = 1:length(conc)
    t_inj = find(x>= (i-1)*(inj_length+diss_length) &
        x<=(i*(inj_length+diss_length)-diss_length));
    t_diss = find(x>=(i*(inj_length+diss_length)-diss_length) &
        x<=(i*(inj_length+diss_length)));
    %injections - differential rate law
    for j = t_inj(1):t_inj(end)
        dRdt(j) = ka*conc(i)*(Rmax-y(j))-kd*y(j);
        y(j+1) = y(j)+dRdt(j)*1/frequ;
        if j == t_inj(1)
            %this bit is really ugly but I can't work out how to feed
            %vectors or cell arrays into fittype, so I'm stuck with it
            if i == 1 & (j+1) <= length(y)
                y(j+1) = R01;
            elseif i == 2
                y(j+1) = R03;
            elseif i == 3
                y(j+1) = R05;
            elseif i == 4
                y(j+1) = R07;
            elseif i == 5
                y(j+1) = R09;
            end

        end

    end
    %short dissociations - differential rate law
    for j = t_diss(1):t_diss(end)
        if (j+1) <= length(y)
            dRdt(j) = -kd*y(j);
            y(j+1) = y(j)+dRdt(j)*1/frequ;
            if j == t_diss(1) & (j+1) <= length(y)
                if i == 1
                    y(j+1) = R02;
                elseif i == 2
```

```
                y(j+1) = R04;
            elseif i == 3
                y(j+1) = R06;
            elseif i == 4
                y(j+1) = R08;
            elseif i == 5
                y(j+1) = R010;
            end
        end
    end

    end
end

%long dissociation - differential rate law
t_diss = find(x>(n_inj*(inj_length+diss_length)));
if not(isempty(t_diss))
    for j = t_diss(1):t_diss(end-1)
        if (j+1) <= length(y)
            dRdt(j) = -kd*y(j);
            y(j+1) = y(j)+dRdt(j)*1/frequ;
        end
    end
end

end
```

D.2.3 SCK_sim_fit_drift_preset_R0

A drift term was also added to the model of the data, which allowed for a linear drift in the signal. This is encapsulated in the function SCK_sim_fit_drift_preset_R0

```
%generate example single cycle kinetics data
%example inputs
% n_inj = 5;
% inj_length = 140;
% diss_length = 60;
% end_diss_length = 900;
% diln = 2;
% high_conc = 40e-9;
% ka = 4.231e5;
% kd = 1.385e-3;
% Rmax = 7;
%R0 is cell array of numbers that define starting points of each
%association/dissociation step
```

```
function y = SCK_sim_fit_drift_preset_R0(x, ka, kd, Rmax, drift, R01,
    R02, R03, R04, R05 ,R06, R07, R08, R09, R010, n_inj, inj_length,
    diss_length, end_diss_length, high_conc, diln)

% %find total length of experiment
% len = (inj_length + diss_length)*(n_inj-1) + inj_length +
    end_diss_length;
%
% x = [0:1/freq:len];

y = zeros(size(x));

%in case this input isn't an integer
if not(isinteger(n_inj))
    n_inj = round(n_inj);
%     warning('Rounded n_inj to nearest integer')
end

% n_inj = 5;

%times of injections etc (in seconds)
t_injs = zeros(1,n_inj);
for i = 1:n_inj
    t_injs(i) = (i-1)*(inj_length+diss_length);
end

conc = zeros(size(t_injs));
count = 0;
for i = length(t_injs):-1:1
    conc(i) = high_conc/diln^count;
    count = count+1;
end


%calculate frequency
period = (x(end)-x(1))/length(x);
frequ = 1/period;

%Calculate using differential rate law form (y)
dRdt = zeros(size(x));
y = zeros(size(x));

%add linear drift
offset = drift*x;
y = y+offset;
%adjust R0 inputs
```

```
%loop over injections
for i = 1:length(conc)
    t_inj = find(x>= (i-1)*(inj_length+diss_length) &
        x<=(i*(inj_length+diss_length)-diss_length));
    t_diss = find(x>=(i*(inj_length+diss_length)-diss_length) &
        x<=(i*(inj_length+diss_length)));
    %injections - differential rate law
    for j = t_inj(1):t_inj(end)
        dRdt(j) = ka*conc(i)*(Rmax-y(j))-kd*y(j);
        y(j+1) = y(j)+dRdt(j)*1/frequ;
        if j == t_inj(1)
            %this bit is really ugly but I can't work out how to feed
            %vectors or cell arrays into fittype, so I'm stuck with it
            if i == 1 & (j+1) <= length(y)
                y(j+1) = R01+drift*x(j+1);
            elseif i == 2
                y(j+1) = R03+drift*x(j+1);
            elseif i == 3
                y(j+1) = R05+drift*x(j+1);
            elseif i == 4
                y(j+1) = R07+drift*x(j+1);
            elseif i == 5
                y(j+1) = R09+drift*x(j+1);
            end

        end

    end
    %short dissociations - differential rate law
    for j = t_diss(1):t_diss(end)
        if (j+1) <= length(y)
            dRdt(j) = -kd*y(j);
            y(j+1) = y(j)+dRdt(j)*1/frequ;
            if j == t_diss(1) & (j+1) <= length(y)
                if i == 1
                    y(j+1) = R02+drift*x(j+1);
                elseif i == 2
                    y(j+1) = R04+drift*x(j+1);
                elseif i == 3
                    y(j+1) = R06+drift*x(j+1);
                elseif i == 4
                    y(j+1) = R08+drift*x(j+1);
                elseif i == 5
                    y(j+1) = R010+drift*x(j+1);
                end
```

```
            end
        end

    end
end

%long dissociation - differential rate law
t_diss = find(x>(n_inj*(inj_length+diss_length)));
if not(isempty(t_diss))
    for j = t_diss(1):t_diss(end-1)
        if (j+1) <= length(y)
            dRdt(j) = -kd*y(j);
            y(j+1) = y(j)+dRdt(j)*1/frequ;
        end
    end
end



end
```

D.2.4 import_octet.m

The function SCK_fit can only analyse one experiment at a time. In order to process data in batches, a script 'import_octet.m' was written to loop over all experiments in a number of listed files. One example is as follows:

```
%ideas to improve fit: filter the data??? add (linear?) drift term to
    fit?


%preallocate cell arrays to hold metadata

n_files = 12; %put number of files here
file = cell(1,n_files);
NB_names = cell(1,n_files);
% datastart = cell(1,n_files);
data = cell(1,n_files);
keep = cell(1,n_files);
bl = cell(1, n_files);

%parameters of experiment
n_inj =5; %number of concentations of nanobodies
inj_length = 180; %length of time in nanobodies
diss_length = 20; %dissociation time between nanobodies
```

```
end_diss_length = 600; %length of end dissociation step
high_conc = 1e-6; %highest concentration
diln = 10; %dilution factor

%file paths - add or delete as necessary, number needs to match n_files
    above
file{1} =
    '/Users/sscott/Documents/University/Oxford/DPhil/Aricescu_lab/Labbook/a3b3
    nanobodies/Octet/170405-170406/170406_Experiment_2_a3NBs_apo_153_168/...
RawData0.csv';
file{2} =
    '/Users/sscott/Documents/University/Oxford/DPhil/Aricescu_lab/Labbook/a3b3
    nanobodies/Octet/170405-170406/170406_Experiment_3_a3NBs_apo_169_184...
/RawData0.csv';
file{3} =
    '/Users/sscott/Documents/University/Oxford/DPhil/Aricescu_lab/Labbook/a3b3
    nanobodies/Octet/170405-170406/170406_Experiment_6_a3NBs_apo_201-206...
_GABA153-162/RawData0.csv';
file{4} =
    '/Users/sscott/Documents/University/Oxford/DPhil/Aricescu_lab/Labbook/a3b3
    nanobodies/Octet/170405-170406/170406_Experiment_7_a3NBs_GABA_163_178...
/RawData0.csv';
file{5} =
    '/Users/sscott/Documents/University/Oxford/DPhil/Aricescu_lab/Labbook/a3b3
    nanobodies/Octet/170405-170406/170406_Experiment_8_a3NBs_GABA_179_193...
_apo157/RawData0.csv';
file{6} =
    '/Users/sscott/Documents/University/Oxford/DPhil/Aricescu_lab/Labbook/a3b3
    nanobodies/Octet/170405-170406/170406_Experiment_10_a3NBs_GABA156_194-...
206_apo171_201/RawData0.csv';
file{7} =
    '/Users/sscott/Documents/University/Oxford/DPhil/Aricescu_lab/Labbook/a3b3
    nanobodies/Octet/170405-170406/170406_Experiment_13_a3NBs_gabazine183...
-198/RawData0.csv';
file{8} =
    '/Users/sscott/Documents/University/Oxford/DPhil/Aricescu_lab/Labbook/a3b3
    nanobodies/Octet/170405-170406/170406_Experiment_14_a3NBs_gabazine156_...
199-206_GABA_194_196/RawData0.csv';
file{9} =
    '/Users/sscott/Documents/University/Oxford/DPhil/Aricescu_lab/Labbook/a3b3
    nanobodies/Octet/170405-170406/170406_Experiment_16_a3NBs_gabazine167_...
1482-repeat/RawData0.csv';
file{10} =
    '/Users/sscott/Documents/University/Oxford/DPhil/Aricescu_lab/Labbook/a3b3
    nanobodies/Octet/170405-170406/170406_Experiment_17_a3NBs_GABA187-188_...
gabazine153_166-repeat/RawData0.csv';
file{11} =
    '/Users/sscott/Documents/University/Oxford/DPhil/Aricescu_lab/Labbook/a3b3
```

```
    nanobodies/Octet/170405-170406/170406_Experiment_18_a3NBs_apo185_200-...
repeat/RawData0.csv';
file{12} =
    '/Users/sscott/Documents/University/Oxford/DPhil/Aricescu_lab/Labbook/...
a3b3
    nanobodies/Octet/170405-170406/170406_Experiment_19_a3NBs_apo188_196-...
199_GABA194_gabazine_160_199/RawData0.csv';

%define nanobody names - names of nanobodies in each file
NB_names{1} = {'NB154', 'NB155', 'NB156', 'NB157', 'NB158', 'NB159',
    'NB160', 'NB162','NB167', 'NB168', 'NB169', 'NB153', 'NB161',
    'NB163', 'NB164', 'NB165'};
NB_names{2} = {'NB170', 'NB173', 'NB171_discard', 'NB174', 'NB175',
    'NB176', 'NB177', 'NB178','NB179', 'NB180', 'NB181', 'NB182',
    'NB183', 'NB184', 'NB169', 'NB172'};
NB_names{3} = {'NB201_discard', 'NB203', 'NB202', 'NB204', 'NB205',
    'NB206', 'NB154_GABA', 'NB155_GABA','NB156_GABA_discard',
    'NB157_GABA', 'NB158_GABA', 'NB159_GABA', 'NB160_GABA',
    'NB162_GABA', 'NB153_GABA', 'NB161_GABA'};
NB_names{4} = {'NB167_GABA', 'NB168_GABA', 'NB170_GABA', 'NB171_GABA',
    'NB173_GABA', 'NB174_GABA', 'NB175_GABA', 'NB176_GABA','NB177_GABA',
    'NB178_GABA', 'NB163_GABA', 'NB164_GABA', 'NB165_GABA',
    'NB166_GABA', 'NB169_GABA', 'NB172_GABA'};
NB_names{5} = {'NB179_GABA', 'NB180_GABA', 'NB181_GABA', 'NB182_GABA',
    'NB183_GABA', 'NB184_GABA', 'NB185_GABA',
    'NB186_GABA','NB187_GABA_discard', 'NB188_GABA_discard',
    'NB189_GABA', 'NB190_GABA', 'NB191_GABA', 'NB192_GABA',
    'NB193_GABA', 'NB157_repeat'};
NB_names{6} = {'NB194_GABA_discard', 'NB196_GABA_discard', 'NB197_GABA',
    'NB198_GABA', 'NB199_GABA', 'NB200_GABA', 'NB201_GABA',
    'NB203_GABA','NB195_GABA', 'NB202_GABA', 'NB204_GABA', 'NB205_GABA',
    'NB206_GABA', 'NB171', 'NB201', 'NB156_GABA'};
NB_names{7} = {'NB183_gabazine', 'NB184_gabazine', 'NB185_gabazine',
    'NB186_gabazine', 'NB187_gabazine', 'NB188_gabazine',
    'NB189_gabazine', 'NB190_gabazine','N191_gabazine',
    'NB192_gabazine', 'NB193_gabazine', 'NB194_gabazine',
    'NB196_gabazine', 'NB197_gabazine', 'NB198_gabazine',
    'NB195_gabazine'};
NB_names{8} = {'NB199_gabazine', 'NB200_gabazine', 'NB201_gabazine',
    'NB203_gabazine', 'NB202_gabazine', 'NB204_gabazine',
    'NB205_gabazine', 'NB206_gabazine','NB194_GABA', 'NB196_GABA',
    'NB156_gabazine'};
NB_names{9} = {'NB167_gabazine', 'NB168_gabazine', 'NB170_gabazine',
    'NB171_gabazine', 'NB173_gabazine', 'NB174_gabazine',
    'NB175_gabazine', 'NB176_gabazine','NB177_gabazine',
    'NB178_gabazine', 'NB179_gabazine', 'NB180_gabazine',
    'NB181_gabazine', 'NB182_gabazine', 'NB169_gabazine',
    'NB172_gabazine'};
```

```
NB_names{10} = {'NB187_GABA', 'NB188_GABA', 'NB154_gabazine',
    'NB155_gabazine', 'NB156_gabazine', 'NB157_gabazine',
    'NB158_gabazine', 'NB159_gabazine','NB160_gabazine',
    'NB162_gabazine', 'NB153_gabazine', 'NB161_gabazine',
    'NB163_gabazine', 'NB164_gabazine', 'NB165_gabazine',
    'NB166_gabazine'};
NB_names{11} = {'NB185_discard', 'NB186', 'NB187', 'NB188_discard',
    'NB189', 'NB190', 'NB191', 'NB192','NB193', 'NB194', 'NB196',
    'NB197', 'NB198', 'NB199', 'NB200', 'NB195'};
NB_names{12} = {'NB194_GABA', 'NB199_gabazine', 'NB160_gabazine',
    'NB188', 'NB196', 'NB197', 'NB198', 'NB199'};

%time that the acutal recording started (to skip baselines and loading
    steps)
datastart = num2cell(ones(1,n_files)*600);


%structure fits will store all the fits
fits = struct;
%preallocate cell arrays and vectors to create table
number_NBs = 0;
for i = 1:length(data)
    number_NBs = number_NBs + length(NB_names{i});
end
table_date = zeros(1, number_NBs);
table_plate = zeros(1, number_NBs);
table_NB = cell(1, number_NBs);
table_ka = zeros(1, number_NBs);
table_ka_top = zeros(1, number_NBs);
table_ka_bottom = zeros(1, number_NBs);
table_kd = zeros(1, number_NBs);
table_kd_top = zeros(1, number_NBs);
table_kd_bottom = zeros(1, number_NBs);
table_Rmax = zeros(1, number_NBs);
table_Rmax_top = zeros(1, number_NBs);
table_Rmax_bottom = zeros(1, number_NBs);
table_Kd = zeros(1, number_NBs);
table_Kd_top = zeros(1, number_NBs);
table_Kd_bottom = zeros(1, number_NBs);
table_Rsquared = zeros(1, number_NBs);
table_path = cell(1, number_NBs);
prompt = 'Input a comment about the fit: ';

count = 1;
for i = 1:length(data);
    data{i} = csvread(file{i}, 2, 0); %import data from csv file
    %delete data before datastart
    keep{i} = find(data{i}(:,1)>datastart{i});
```

```
    data{i} = data{i}(keep{i}, :);
    %baseline data
    bl{i} = data{i}(1,:);
    for j = 1:size(data{i}, 1)
        data{i}(j,:) = data{i}(j,:) - bl{i};
    end
%     %plot imported data
    clf
    hold on
    for j = 1:length(NB_names{i})
        plot(data{i}(:,j*2-1), data{i}(:,j*2))
    end
    legend(NB_names{i})
    xlabel('Time (s)')
    ylabel('Thickness (nm)')
%     waitforbuttonpress
    for j = 1:length(NB_names{i})
    %extract times and signals to fit
    X = round(data{i}(:,2*j-1), 4);
    Y = data{i}(:,2*j);
    %fit data using SCK_fit
    fits.(NB_names{i}{j}) = SCK_fit(X, Y, n_inj, inj_length,
        diss_length, end_diss_length, high_conc, diln);
        %plot data and fit
        clf
        plot(fits.(NB_names{i}{j}).fit, X, Y)
        xlabel('Time (s)')
        ylabel('Response (nm)')
        title(sprintf('%s, Kd = %fnM, R2 = %f', NB_names{i}{j},
            fits.(NB_names{i}{j}).fit.kd/fits.(NB_names{i}{j}).fit.ka*1e9,
            fits.(NB_names{i}{j}).gof.rsquare))
         ylim([-0.05 0.4])
         set(findall(gca, 'Type', 'Line'),'LineWidth',2);
        saveas(gcf, strcat(file{i}(1:end-4),NB_names{i}{j}, '.svg'))
%         waitforbuttonpress
%     table_comment{count} = input(prompt, 's');
     table_comment{count} = 'N/A';
    table_date(count) = dat(i);
    table_plate(count) = plate(i);
    table_NB{count} = NB_names{i}{j};
    table_ka(count) = fits.(NB_names{i}{j}).fit.ka;
    table_ka_bottom(count) = temp(1,1);
    table_ka_top(count) = temp(2,1);
    table_kd(count) = fits.(NB_names{i}{j}).fit.kd;
    table_kd_bottom(count) = temp(1,2);
    table_kd_top(count) = temp(2,2);
    table_Rmax(count) = fits.(NB_names{i}{j}).fit.Rmax;
    table_Rmax_bottom(count) = temp(1,3);
```

```
    table_Rmax_top(count) = temp(2,3);
    table_Rsquared(count) = fits.(NB_names{i}{j}).gof.rsquare;
    table_Kd(count) =
        fits.(NB_names{i}{j}).fit.kd/fits.(NB_names{i}{j}).fit.ka*1e9;
    table_Kd_bottom(count) = temp(2,2)/temp(1,1)*1e9;
    table_Kd_top(count) = temp(1,2)/temp(2,1)*1e9;
    count = count+1;
    end
end

fitted = table(table_NB', table_ka', table_kd', table_Rmax', table_Kd',
    table_Rsquared', table_comment', 'VariableNames', {'NB', 'ka', 'kd',
    'Rmax', 'Kd_in_nM', 'Rsquared', 'Comment'});
writetable(fitted, strcat(file{1}(1:end-4), 'CI.xlsx'));
```

D.3 Electrophysiology data analysis

D.3.1 load_ionflux

Ionflux data were imported into MATLAB with the function 'load_ionflux'. This takes as input three files that are exported from the Ionflux software. The first is the exported current data ('sweeps_file' in the function), exported from the data analysis software as a .csv file. The second and third are the exported compound addition times (the times at which compounds, C1-8 in the nomenclature of the program) and the exported compound plate (the information about which drugs and drug concentrations correspond to the compounds C1-8).

```
%this function loads ionflux data
%
%
%   inputs
%         sweeps_file: path to a .csv file containing current data
%         comp_add_file: path to a .xlsx file exported from ionflux
    software containing
%           compound addition times
%         comp_file: path to a .xlsx file with compounds in each well
%   optional inputs
%         'half' - input this if run is in half plate configuration
%         (default is full plate)
%         'plotComp' - input this to plot the compound application times
%         'plotSweeps' - browse sweeps
```

```
%        'lnBaseline' - checks baseline doesn't deviate by more than
    100% and then
%         subtracts baseline from data ('leak subtraction')
%        'slBaseline' - checks baseline dosen't deviate by more than 100%
%        and then subtracts sloping baseline'
%        'dontChoose' - use all traces, don't plot each and choose which
%        ones to use
%
%
%
function data = load_ionflux(sweeps_file, comp_add_file, comp_file,
    varargin)

%default values
half = 0;
plot_comp = 0;
plot_sweeps = 0;
bl = 0;
bl_slope = 0;
choose = 1;
%define period of trace over which to average for baseline
bl_t = [0.7 1];
bl_sloping = [0.7 1 19.5 20];
%tol is the tolerance for baseline deviation
tol = 2;

i = 1;
while i<= length(varargin)
    if not(isempty(varargin{i}))
        if strcmp(varargin{i}, 'half')
            half = 1;
        elseif strcmp(varargin{i}, 'plotComp')
            plot_comp = 1;
        elseif strcmp(varargin{i}, 'plotSweeps')
            plot_sweeps = 1;
        elseif strcmp(varargin{i}, 'lnBaseline')
            bl = 1;
            bl_slope = 0;
        elseif strcmp(varargin{i}, 'slBaseline')
            bl = 1;
            bl_slope = 1;
        elseif strcmp(varargin{i}, 'dontChoose')
            choose = 0;
        end
    end
    i = i+1;
end
```

```
%nubmer of repeats for each drug applcation
if half
    rep = 8;
else
    rep = 16;
end

data = struct;


%load compound names and concentrations
[dummy, dumm2, data.comp] = xlsread(comp_file, 'A7:G14');

%load compound additions
[dummy, dummy2, data.add] = xlsread(comp_add_file);
    %replace 'C' labels with drug name and concentration
    plotComps = zeros(size(data.add,1));
spc = ' ';
for i = 1:size(data.add, 1)
    if strcmp(data.add(i,1), 'C1')
        data.add{i,1} = [num2str(data.comp{1,5}) 'uM' spc
            (data.comp{1,4}) spc num2str(data.comp{1,7}) 'uM' spc
            (data.comp{1,6})];
        plotComps(i) = 1;
    elseif strcmp(data.add(i,1), 'C2')
        data.add{i,1} = [num2str(data.comp{2,5}) 'uM' spc
            (data.comp{2,4}) spc num2str(data.comp{2,7}) 'uM' spc
            (data.comp{2,6})];
        plotComps(i) = 2;
    elseif strcmp(data.add(i,1), 'C3')
        data.add{i,1} = [num2str(data.comp{3,5}) 'uM' spc
            (data.comp{3,4}) spc num2str(data.comp{3,7}) 'uM' spc
            (data.comp{3,6})];
        plotComps(i) = 3;
    elseif strcmp(data.add(i,1), 'C4')
        data.add{i,1} = [num2str(data.comp{4,5}) 'uM' spc
            (data.comp{4,4}) spc num2str(data.comp{4,7}) 'uM' spc
            (data.comp{4,6})];
        plotComps(i) = 4;
    elseif strcmp(data.add(i,1), 'C5')
        data.add{i,1} = [num2str(data.comp{5,5}) 'uM' spc
            (data.comp{5,4}) spc num2str(data.comp{5,7}) 'uM' spc
            (data.comp{5,6})];
        plotComps(i) = 5;
    elseif strcmp(data.add(i,1), 'C6')
        data.add{i,1} = [num2str(data.comp{6,5}) 'uM' spc
            (data.comp{6,4}) spc num2str(data.comp{6,7}) 'uM' spc
            (data.comp{6,6})];
```

```
        plotComps(i) = 6;
    elseif strcmp(data.add(i,1), 'C7')
        data.add{i,1} = [num2str(data.comp{7,5}) 'uM' spc
            (data.comp{7,4}) spc num2str(data.comp{7,7}) 'uM' spc
            (data.comp{7,6})];
        plotComps(i) = 7;
    elseif strcmp(data.add(i,1), 'C8')
        data.add{i,1} = [num2str(data.comp{8,5}) 'uM' spc
            (data.comp{8,4}) spc num2str(data.comp{8,7}) 'uM' spc
            (data.comp{8,6})];
        plotComps(i) = 8;
    else
        warning('Check compound table labels')
    end
end

%load sweeps from csv file
data.sweeps = csvread(sweeps_file, 1, 0);
    %first column is time, make seperate column
data.t = data.sweeps(:,1);
    %delete time from sweeps
data.sweeps(:,1) = [];

%find number of sweeps
data.no_sweeps = size(data.sweeps,2)/rep;

%check if have already chosen sweeps to include
while not(exist('chosen'))
    if exist(strcat(sweeps_file(1:end-4), '_excluded.mat'), 'file') == 2
        reply = input('Would you like to choose sweeps to be included
            again? [yes/no]\n', 's');
        if strcmp('no', reply)
            chosen = 1;
        elseif strcmp('yes', reply)
            chosen = 0;
        else
            disp('Not recgonised, please try again')
        end
    else
        chosen = 0;
    end
end
if choose && not(chosen)

end
if bl
    %subtract baseline from data
    bl_ind = find(data.t>bl_t(1) & data.t <bl_t(2));
```

```
bl = mean(data.sweeps(bl_ind, :));
%check that baseline doesn't diverge by more than 100%
check = [0:data.no_sweeps-1]*rep;
exc = [];
for i = 1:rep
    ind = check+i;
    temp = bl(ind);
    temp = temp/temp(1);
    if any(temp>tol) || any(temp<(1/tol))
        exc = [exc ind];
        fprintf('Sweep %d has been excluded because the baseline
            diverges by more than 100 per cent\n', i)
    end
end
data.sweeps(:, exc) = NaN;
bl(exc) = NaN;

%subtract sloping baseline based on start and end of tract
if bl_slope
    bl_ind = [(find(data.t>bl_sloping(1) & data.t <bl_sloping(2)))'
        (find(data.t>bl_sloping(3) & data.t <bl_sloping(4)))']';
    for i = 1:size(data.sweeps,2)
         x = data.t(bl_ind);
         X = [ones(length(x),1) x];
         y = data.sweeps(bl_ind, i);
         b = X\y;
         bl = ([ones(length(data.t),1) data.t]*b);
         data.sweeps(:,i) = data.sweeps(:,i) - bl;
    end
    if choose && not(chosen)
        i = 1;
        while i <= rep
           check = [0:data.no_sweeps-1]*rep+i;
           %plot all sweeps from one cell/ensemble
               figure(1)
               clf
               plot(data.t, data.sweeps(:,check))
               a = input(sprintf('Ensemble %d of %d; Press a to
                   include all, e to exclude all, or c to choose some
                   sweeps: ', i, rep), 's');
               drawnow
               commandwindow
               %include all sweeps
               if strcmp('a', a)
                %exclude all sweeps
               elseif strcmp('e', a)
                   data.sweeps(:,check) = NaN;
                %choose some to include and some to exclude
```

```
                elseif strcmp('c', a)
                    disp('Press any button to include, or click to
                        exclude')
                    for j = check
                        figure(1)
                        clf
                        plot(data.t, data.sweeps(:,j))
                        a = waitforbuttonpress;
                         if not(a)
                             data.sweeps(:,j) = NaN;
                         end
                    end
                    %check the input was one of the three options,
                    %otherwise
                else
                    disp('Did not recgonise input, please try again')
                    i = i-1;
                end
                i = i+1;
            end
        end



% %             if choose && not(chosen)
% %                 figure(1)
% %                 clf
% %                 subplot(2,1,1)
% %                 plot(data.t, data.sweeps(:,i), 'r')
% %                 subplot(2,1,2)
% %                 plot(data.t, data.sweeps(:,i) - bl, 'b')
% %                 a = waitforbuttonpress;
% %                    if not(a)
% %                        data.sweeps(:,i) = NaN(size(data.sweeps(:,i)));
% %                    end
% %             end
% %             data.sweeps(:,i) = data.sweeps(:,i) - bl;
%           end

%
%       end
    %subtract constant baseline
    else
        disp('Press any key to include or click to exclude')
        bl_ind = find(data.t>bl_t(1) & data.t <bl_t(2));
        bl = mean(data.sweeps(bl_ind, :));
        for i = 1:size(data.sweeps ,1)
            data.sweeps(i,:) = data.sweeps(i,:) - bl;
```

```
        end
        if choose && not(chosen)
            %plot all sweeps to decide which ones to keep - plot all drug
                applicaitons
            %for one ensemble of cell, and then repeat for all ensenbles
                of cells
            for i = 1:rep
               check = [0:data.no_sweeps-1]*rep+i;
               for i = 1:length(check)
                   figure(1)
                   clf
                   plot(data.t, data.sweeps(:,check(i)))
                   a = waitforbuttonpress;
                   if not(a)
                        data.sweeps(:,check(i)) =
                            NaN(size(data.sweeps(:,i)));
                   end
               end
            end
        end

end

%save choices of included files
if not(chosen) && choose
    data.excluded = isnan(data.sweeps(1,:));
    save(strcat(sweeps_file(1:end-4), '_excluded.mat'), '-struct',
        'data', 'excluded')
elseif choose && chosen
    temp = load(strcat(sweeps_file(1:end-4), '_excluded.mat'));
    data.excluded = temp.excluded;
    for i = 1:length(data.excluded)
        if data.excluded(i)
            data.sweeps(:,i) = nan(size(data.sweeps(:,i)));
        end
    end
end

    %rearrange sweeps by repeats of same drug
    data.divsweeps = cell(2, size(data.sweeps,2)/rep);
for i = 1:size(data.sweeps,2)/rep
    data.divsweeps{1,i} = data.sweeps(:, (1+rep*(i-1)):rep*i);
    starttime = (i-1)*20+1;
    endtime = (i)*20;
    %add drug information for each sweep
    drug_ind = find(cell2mat(data.add(:,2)) >= starttime &
        cell2mat(data.add(:,2)) <= endtime);
    data.divsweeps{2,i} = data.add(drug_ind,1);
```

```
    %if only half a plate, pad the divsweeps matricies with 8 columns of
    %NaN
    if half
        data.divsweeps{1,i} = [data.divsweeps{1,i}
            NaN(size(data.divsweeps{1,i}))];
    end
end



%plot compound additions
if plot_comp
    plotTimes = cell2mat(data.add(:, 2:3));
    figure
    clf
    hold on
    %plot compound additions
    for i = 1:length(plotTimes)
        plot([plotTimes(i,1) plotTimes(i,1)+plotTimes(i,2)],
            [plotComps(i) plotComps(i)], 'LineWidth', 3)
    end
    %plot sweep divisions
    for i = 1:ceil(max(cell2mat(data.add(:,2)))/20)
        plot([i*20 i*20], [1 8], 'k.:', 'LineWidth', 0.2)
    end
    %change y axis numbers to labels
    set(gca, 'YTickLabel', unique(data.add(:,1), 'stable'))
    axis tight
end

%plot sweeps
no_sweeps = size(data.sweeps,2)/rep;
if plot_sweeps
   cont = 1;
   curr = 1;
   while cont

       figure(1)
       clf
       subplot(2,1,2)
       %plot current sweep
       plot(data.t, data.divsweeps{1,curr})
       title(['Sweep' num2str(curr)])
       xlabel('Time (s)')
       ylabel('Current (nA)')
       legend(strread(num2str(1:16),'%s'), 'Location', 'bestoutside')
       subplot(2,1,1)
       hold on
```

```
        %plot drugs applied
        ind = find(cell2mat(data.add(:,2)) > (curr-1.5)*20 &
            cell2mat(data.add(:,2)) < (curr*20));
        times = cell2mat(data.add(ind, 2:3));
        if not(isempty(times))
            for i = 1:size(times,1)
                 plot([times(i,1)-((curr-1)*20)
                     times(i,1)+times(i,2)-((curr-1)*20)], [i i])
            end
            legend(data.add(ind, 1), 'Location', 'bestoutside')
%           set(gca, 'Ytick', 1:size(times,1))
%           set(gca, 'YTickLabel', data.add(ind, 1))
            xlim([0 20])
        end

        drawnow
        commandwindow

        x = input('Input f to go forwards, b to go backwards, input the
            number of the sweep you would like to go to, or press e to
            exit:\n', 's');
        %to go forwards
        if strcmp(x, 'f')
            if curr+1 <= no_sweeps
            curr = curr+1;
            else
                sprintf('Already on the last trace!')
            end
            %to go backwards
        elseif strcmp(x, 'b')
            if curr - 1 > 0
                curr = curr-1;
            else
                sprintf('Already on the first trace!')
            end
            %to go to custom trace
        elseif not(isempty(str2num(x)))
            if sum(str2num(x) == [1:no_sweeps])
                curr = str2num(x);
            end
            %to end
        elseif strcmp(x, 'e')
            cont = 0;
        else
            sprintf('Did not recgonize input, please try again')
        end
    end
end
```

```
end
```

D.3.2 analyze_ionflux_screen.m

Dose-response data were analysed with a series of scripts based on analyze_ionflux_screen.m. The example given below was used to analyse the entire Ionflux nanobody screen for positive modulation. In this version, the files for each Ionflux plate, and the details of where currents should be measured, are defined. The script then imports all files, and then loops over each file to measure the current at the defined time points. It also plots graphs of currents for each nanobody, and for each drug application, and saves in Scalable Vector Graphics (svg) format. During this loop it creates an array in which each row corresponds to a particular time point at which the current should be measured, and each column corresponds to one ensemble of cells (i.e. one trap, with two traps per nanobody in each pattern, see Figure 2.3). Next, the current data is normalised to an I_{max} current, and then various rows are divided by others to calculate the fold-change in current for each nanobody dose (relative to an EC_{10} GABA dose without nanobody), as well as numbers of measurements and standard deviations. Finally, this data as well as the current data, and normalised current data, are saved each saved to a sheet in a Microsoft Excel file.

```
%analyse a2 and a3 screening ionflux data


%%define parameters of analysis
%define sweeps to use - for multiple measurements per sweep add the sweep
%more than once
sweeps = [3 4 5 7 9 11 12 12 12 12 14 16];
%define times within each sweep to measure current
measureTime = {[2.5 3] [3.5 5.5] [3 7] [3 7] [3 7] [3 5.5] [3 5] [6.6 7]
    [11 11.5] [14 15] [2.5 3.5] [2.5 3.5]};
%check sweeps and measure are the same size
if size(measureTime,2) ~= size(sweeps,2)
    error('measure and sweeps are not the same size')
end
```

```
%define whether to measure min or mean for each measurement
%min = average of data within +/- averageTime s of the minimum point
    found in
%average = mean of data within time points
whatToMeasure = {'min' 'min' 'min' 'min' 'min' 'min' 'min' 'average'
    'average' 'min' 'min' 'min'};

averageTime = 0.05;

%construct table that gives details of what was measured
measurementNumber = 1:length(sweeps);
measureLength = cell(size(whatToMeasure));
for i = 1:length(measureLength)
    if strcmp(whatToMeasure{i}, 'min')
        measureLength{i} = averageTime;
    elseif strcmp(whatToMeasure{i}, 'average')
        measureLength{i} = measureTime{i}(2)-measureTime{i}(1);
    end
end
%construct table
varNames = {'measurementNumber', 'sweeps', 'measureTime',
    'whatToMeasure', 'measureLength'};
measurementDetails = table(measurementNumber', sweeps', measureTime',
    whatToMeasure', measureLength', 'VariableNames',varNames);

%parse whatToMeasure to check all entries are allowed
for i = 1:length(whatToMeasure)
    if not(strcmp(whatToMeasure{i}, 'min') || strcmp(whatToMeasure{i},
        'average'))
        error('Check whatToMeasure contains allowed values, wrong value
            at position %d', i);
    end
end

%check whatToMeasure and measure are the same size
if size(measureTime,2) ~= size(whatToMeasure,2)
    error('measure and whatToMeasure are not the same size')
end
```

```
%%define datasets to analyse
%put number of datasets here
files = 11;
%preallocate cell arrays to store file locaitons for each dataset
data_files = cell(files,1);
```

```
CA_files = cell(files,1);
comp_files = cell(files,1);
first_row = ones(files,1)*7;
pattern_names = cell(files,1);
plate_type = cell(files,1);
raw_data = cell(files,1);

%import a2 data
%import time series data
data_files{1} =
    '/Users/sscott/Documents/University/Oxford/DPhil/Aricescu_lab/...
Labbook/a2b3nanobodies/Ionflux/170502-a2NBs_a3NBs_screen/170509-a2a3NBs/...
170509_1357_170411b gf06_170509-a2b3g2-a2NBs95_99_100_148__data.csv';
data_files{2} =
    '/Users/sscott/Documents/University/Oxford/DPhil/Aricescu_lab/Labbook/...
a2b3
    nanobodies/Ionflux/170502-a2NBs_a3NBs_screen/170502-a2NBs_screen2/...
170502_1858_170411c gd06_170502-a2NBs_99_121__data.csv';
data_files{3} =
    '/Users/sscott/Documents/University/Oxford/DPhil/Aricescu_lab/Labbook/...
a2b3
    nanobodies/Ionflux/170502-a2NBs_a3NBs_screen/170502-a2NBs_screen2/...
170502_1911_160606a gd04_170502-a2b3g2_a2125_150__data.csv';
data_files{4} =
    '/Users/sscott/Documents/University/Oxford/DPhil/Aricescu_lab/Labbook/...
a2b3
    nanobodies/Ionflux/170502-a2NBs_a3NBs_screen/170502-a2NBs_screen2/...
170505_1212_170413c gf06_170505-a2b3g2-NBs95to116__data.csv';
data_files{5} =
    '/Users/sscott/Documents/University/Oxford/DPhil/Aricescu_lab/Labbook/...
a2b3
    nanobodies/Ionflux/170502-a2NBs_a3NBs_screen/170502-a2NBs_screen2/...
170505_1230_170413b gd06_170505-a2b3g2-NBs117to132__data.csv';
data_files{6} =
    '/Users/sscott/Documents/University/Oxford/DPhil/Aricescu_lab/Labbook/...
a2b3
    nanobodies/Ionflux/170502-a2NBs_a3NBs_screen/170502-a2NBs_screen2/...
170505_1331_170413c gd06_170505-a2b3g2-a2NBs133to149__data.csv';
data_files{7} =
    '/Users/sscott/Documents/University/Oxford/DPhil/Aricescu_lab/Labbook/...
a3b3 nanobodies/Ionflux/170502-a2NBs_a3NBs_screen/170425-a3NBs_screen/...
170426_1234_161117d gd03_170426-a3Nbs160-172_a3b3g2__data.csv';
data_files{8} =
    '/Users/sscott/Documents/University/Oxford/DPhil/Aricescu_lab/Labbook/...
a3b3 nanobodies/Ionflux/170502-a2NBs_a3NBs_screen/170425-a3NBs_screen/...
170426_1251_160531b gd04_170426-a3NBs173-186_a3b3g2__data.csv';
data_files{9} =
    '/Users/sscott/Documents/University/Oxford/DPhil/Aricescu_lab/Labbook/...
```

```
a3b3 nanobodies/Ionflux/170502-a2NBs_a3NBs_screen/170425-a3NBs_screen/...
170426_1423_160606a gd04_170426-a3Nbs153-158_a3b3g2FL__data.csv';
data_files{10} =
    '/Users/sscott/Documents/University/Oxford/DPhil/Aricescu_lab/Labbook/...
a3b3 nanobodies/Ionflux/170502-a2NBs_a3NBs_screen/170425-a3NBs_screen/...
170426_1445_160604d gf06_170426-a3Nbs187-206_a3b3g2__data.csv';
data_files{11} =
    '/Users/sscott/Documents/University/Oxford/DPhil/Aricescu_lab/Labbook/...
a3b3 nanobodies/Ionflux/170502-a2NBs_a3NBs_screen/170509-a2a3NBs/...
170509_1451_170411b gd06_170509-a3b3g2-160to190__data.csv';

%import compound additions (will all be the same drug names for each
%pattern)
CA_files{1} =
    '/Users/sscott/Documents/University/Oxford/DPhil/Aricescu_lab/Labbook/...
a2b3 nanobodies/Ionflux/170502-a2NBs_a3NBs_screen/170509-a2a3NBs/...
170509_1357_170411b gf06_170509-a2b3g2-a2NBs95_99_100_148__CA.xlsx';
CA_files{2} =
    '/Users/sscott/Documents/University/Oxford/DPhil/Aricescu_lab/Labbook/...
a2b3
    nanobodies/Ionflux/170502-a2NBs_a3NBs_screen/170502-a2NBs_screen2/...
170502_1858_170411c gd06_170502-a3NBs_99_121__CA.xlsx';
CA_files{3} =
    '/Users/sscott/Documents/University/Oxford/DPhil/Aricescu_lab/Labbook/...
a2b3
    nanobodies/Ionflux/170502-a2NBs_a3NBs_screen/170502-a2NBs_screen2/...
170502_1911_160606a gd04_170502-a2b3g2_a2125_150__CA.xlsx';
CA_files{4} =
    '/Users/sscott/Documents/University/Oxford/DPhil/Aricescu_lab/Labbook/...
a2b3
    nanobodies/Ionflux/170502-a2NBs_a3NBs_screen/170502-a2NBs_screen2/...
170505_1212_170413c gf06_170505-a2b3g2-NBs95to116__CA.xlsx';
CA_files{5} =
    '/Users/sscott/Documents/University/Oxford/DPhil/Aricescu_lab/Labbook/...
a2b3
    nanobodies/Ionflux/170502-a2NBs_a3NBs_screen/170502-a2NBs_screen2/...
170505_1230_170413b gd06_170505-a2b3g2-NBs117to132__CA.xlsx';
CA_files{6} =
    '/Users/sscott/Documents/University/Oxford/DPhil/Aricescu_lab/Labbook/...
a2b3
    nanobodies/Ionflux/170502-a2NBs_a3NBs_screen/170502-a2NBs_screen2/...
170505_1331_170413c gd06_170505-a2b3g2-a2NBs133to149__CA.xlsx';
CA_files{7} =
    '/Users/sscott/Documents/University/Oxford/DPhil/Aricescu_lab/Labbook/...
a3b3 nanobodies/Ionflux/170502-a2NBs_a3NBs_screen/170425-a3NBs_screen/...
170426_1234_161117d gd03_170426-a3Nbs160-172_a3b3g2__CA.xlsx';
CA_files{8} =
    '/Users/sscott/Documents/University/Oxford/DPhil/Aricescu_lab/Labbook/...
```

```
a3b3 nanobodies/Ionflux/170502-a2NBs_a3NBs_screen/170425-a3NBs_screen/...
170426_1251_160531b gd04_170426-a3NBs173-186_a3b3g2__CA.xlsx';
CA_files{9} =
    '/Users/sscott/Documents/University/Oxford/DPhil/Aricescu_lab/Labbook/...
a3b3 nanobodies/Ionflux/170502-a2NBs_a3NBs_screen/170425-a3NBs_screen/...
170426_1423_160606a gd04_170426-a3Nbs153-158_a3b3g2FL__CA.xlsx';
CA_files{10} =
    '/Users/sscott/Documents/University/Oxford/DPhil/Aricescu_lab/Labbook/...
a3b3 nanobodies/Ionflux/170502-a2NBs_a3NBs_screen/170425-a3NBs_screen/...
170426_1423_160606a gd04_170426-a3Nbs153-158_a3b3g2FL__CA.xlsx';
CA_files{11} =
    '/Users/sscott/Documents/University/Oxford/DPhil/Aricescu_lab/Labbook/...
a3b3 nanobodies/Ionflux/170502-a2NBs_a3NBs_screen/170509-a2a3NBs/...
170509_1451_170411b gd06_170509-a3b3g2-160to190__CA.xlsx';

%import compound defintion table
comp_files{1} =
    '/Users/sscott/Documents/University/Oxford/DPhil/Aricescu_lab/Labbook/...
a2b3 nanobodies/Ionflux/170502-a2NBs_a3NBs_screen/170509-a2a3NBs/...
170509_1357_170411b gf06_170509-a2b3g2-a2NBs95_99_100_148__comp.xlsx';
comp_files{2} =
    '/Users/sscott/Documents/University/Oxford/DPhil/Aricescu_lab/Labbook/...
a2b3
    nanobodies/Ionflux/170502-a2NBs_a3NBs_screen/170502-a2NBs_screen2/...
170502_1858_170411c gd06_170502-a3NBs_99_121__comp.xlsx';
comp_files{3} =
    '/Users/sscott/Documents/University/Oxford/DPhil/Aricescu_lab/Labbook/..
a2b3
    nanobodies/Ionflux/170502-a2NBs_a3NBs_screen/170502-a2NBs_screen2/...
170502_1911_160606a gd04_170502-a2b3g2_a2125_150__comp.xlsx';
comp_files{4} =
    '/Users/sscott/Documents/University/Oxford/DPhil/Aricescu_lab/Labbook/...
a2b3
    nanobodies/Ionflux/170502-a2NBs_a3NBs_screen/170502-a2NBs_screen2/...
170505_1212_170413c gf06_170505-a2b3g2-NBs95to116__comp.xlsx';
comp_files{5} =
    '/Users/sscott/Documents/University/Oxford/DPhil/Aricescu_lab/Labbook/...
a2b3
    nanobodies/Ionflux/170502-a2NBs_a3NBs_screen/170502-a2NBs_screen2/...
170505_1230_170413b gd06_170505-a2b3g2-NBs117to132__comp.xlsx';
comp_files{6} =
    '/Users/sscott/Documents/University/Oxford/DPhil/Aricescu_lab/Labbook/...
a2b3
    nanobodies/Ionflux/170502-a2NBs_a3NBs_screen/170502-a2NBs_screen2/...
170505_1331_170413c gd06_170505-a2b3g2-a2NBs133to149__COMP.xlsx';
comp_files{7} =
    '/Users/sscott/Documents/University/Oxford/DPhil/Aricescu_lab/Labbook/...
a3b3 nanobodies/Ionflux/170502-a2NBs_a3NBs_screen/170425-a3NBs_screen/...
```

```
170426_1234_161117d gd03_170426-a3Nbs160-172_a3b3g2__comp.xlsx';
comp_files{8} =
    '/Users/sscott/Documents/University/Oxford/DPhil/Aricescu_lab/Labbook/...
a3b3 nanobodies/Ionflux/170502-a2NBs_a3NBs_screen/170425-a3NBs_screen/...
170426_1251_160531b gd04_170426-a3NBs173-186_a3b3g2__comp.xlsx';
comp_files{9} =
    '/Users/sscott/Documents/University/Oxford/DPhil/Aricescu_lab/Labbook/...
a3b3 nanobodies/Ionflux/170502-a2NBs_a3NBs_screen/170425-a3NBs_screen/...
170426_1423_160606a gd04_170426-a3Nbs153-158_a3b3g2FL__comp.xlsx';
comp_files{10} =
    '/Users/sscott/Documents/University/Oxford/DPhil/Aricescu_lab/Labbook/...
a3b3 nanobodies/Ionflux/170502-a2NBs_a3NBs_screen/170425-a3NBs_screen/...
170426_1445_160604d gf06_170426-a3Nbs187-206_a3b3g2__comp.xlsx';
comp_files{11} =
    '/Users/sscott/Documents/University/Oxford/DPhil/Aricescu_lab/Labbook/...
a3b3 nanobodies/Ionflux/170502-a2NBs_a3NBs_screen/170509-a2a3NBs/...
170509_1451_170411b gd06_170509-a3b3g2-160to190__comp.xlsx';

%define first row for load_ionflux to read in compound table - default
    for
%load_ionflux is 7, but for some files this is 2
first_row(1) = 2;
first_row(2) = 2;
first_row(3) = 2;
first_row(4) = 2;
first_row(5) = 2;
first_row(6) = 2;
first_row(7) = 2;
first_row(8) = 2;
first_row(9) = 2;
first_row(10) = 2;
first_row(11) = 2;

%also need to define the nanobodies in each pattern in the plates,
    because
%the load_ionflux script only looks at the first pattern and assumes that
%everything is the same

pattern_names{1} = {'nb095_1', 'nb095_2', 'nb099_1', 'nb099_2',
    'nb100_1', 'nb100_2', 'nb148_1', 'nb148_2'};
pattern_names{2} = {'nb099', 'nb101', 'nb105', 'nb110', 'nb111',
    'nb112', 'nb120', 'nb121'};
pattern_names{3} = {'nb125', 'nb128', 'nb145', 'nb150'};
pattern_names{4} = {'nb095', 'nb102', 'nb103', 'nb106', 'nb108',
    'nb113', 'nb114', 'nb116'};
pattern_names{5} = {'nb117', 'nb118', 'nb119', 'nb122', 'nb123',
    'nb130', 'nb131', 'nb132'};
pattern_names{6} = {'nb133', 'nb134', 'nb136', 'nb142', 'nb144',
```

```
    'nb146', 'nb147', 'nb149'};
pattern_names{7} = {'nb160', 'nb161', 'nb170', 'nb172'};
pattern_names{8} = {'nb173', 'nb175', 'nb176', 'nb177', 'nb181',
    'nb183', 'nb184', 'nb186'};
pattern_names{9} = {'nb153', 'nb154', 'nb157', 'nb158'};
pattern_names{10} = {'nb187', 'nb188', 'nb189', 'nb190', 'nb191',
    'nb196', 'nb197', 'nb206'};
pattern_names{11} = {'nb160_2', 'nb172_2', 'nb173_1', 'nb173_2',
    'nb183_1', 'nb183_2', 'nb190_1', 'nb190_2'};


%add T1 and T2 to all NB names
for i = 1:files
    temp = cell(1, size(pattern_names{i},2)*2);
    for j = 1:size(pattern_names{i},2)
        temp{2*j-1} = strcat(pattern_names{i}{j}, '_T1');
        temp{2*j} = strcat(pattern_names{i}{j}, '_T2');
    end
    pattern_names{i} = temp;
end

%full or half plate?
plate_type{1} = 'full';
plate_type{2} = 'full';
plate_type{3} = 'half';
plate_type{4} = 'full';
plate_type{5} = 'full';
plate_type{6} = 'full';
plate_type{7} = 'half';
plate_type{8} = 'full';
plate_type{9} = 'half';
plate_type{10} = 'full';
plate_type{11} = 'full';



%import data: loop over all datasets
for i = 1:files
    sprintf('Importing dataset %d file %s', i, data_files{i})
    %uncomment this line to use all sweeps in all files
    %raw_data{i} = load_ionflux2(data_files{i}, CA_files{i},
        comp_files{i}, 'lnBaseline', 'dontChoose', 'firstRow',
        first_row(i), plate_type{i});
    %uncomment this line to do choosing for all files
    raw_data{i} = load_ionflux3(data_files{i}, CA_files{i},
        comp_files{i}, 'lnBaseline', 'firstRow', first_row(i),
        plate_type{i});
    %need to clean up excess nans from half plates
```

```
    if strcmp(plate_type{i}, 'half')
        for j = 1:size(raw_data{i}.divsweeps, 2)
            raw_data{i}.divsweeps{1,j}(:,9:end) = [];
        end
    end
end

%%do analysis: extract currents at relevant times

data_out = []; %data_out will store all measurements from all datasets
drugs = cell(length(sweeps),1);
%measure currents as defined by sweeps, measure and whatToMeasure above
for i = 1:length(raw_data)
    measurements = zeros(length(measureTime),length(pattern_names{i}));
        %will store data for this dataset
    for j = 1:length(sweeps)
        %take a snippet of the data over which to analyse
        snippet_t = raw_data{i}.t(intersect(find(raw_data{i}.t >
            measureTime{j}(1)), find(raw_data{i}.t < measureTime{j}(2))));
        snippet_Is =
            raw_data{i}.divsweeps{1,sweeps(j)}(intersect(find(raw_data{i}.t
            > measureTime{j}(1)), find(raw_data{i}.t <
            measureTime{j}(2))),:);


        %make mesurements
        if strcmp(whatToMeasure{j}, 'average') %if just averaging over
            whole time period
            measurements(j,:) = mean(snippet_Is); %take mean

            %plot sweeps and snippets to check all is ok
            clf
            hold on
            plot(snippet_t, snippet_Is, 'LineWidth',3);
            plot(raw_data{i}.t, raw_data{i}.divsweeps{1,sweeps(j)})
            legend(pattern_names{i}, 'Location', 'eastoutside')
            drugs{j} =
                strcat(raw_data{i}.divsweeps{2,sweeps(j)}{1:end-1,1}, '
                ');
            title(sprintf("dataset %d, sweep %d, %s ", i, sweeps(j),
                drugs{j}))
            xlabel('Time (s)')
            ylabel('Current (pA)')
            saveas(gcf,
                strcat(data_files{i}(1:end-4),sprintf('_point_%d', j)),
                'svg')
%             drugs{j} = workingTitle;
%             waitforbuttonpress
```

```
        elseif strcmp(whatToMeasure{j}, 'min') %if taking minimum +/-
            averageTime

            [mins, minlocs] = min(snippet_Is); %find minima
            for ind = 1:length(minlocs) %loop over each sweep in file
                %check that adding +/- averageTime won't result in
                    indexing
                %outside snippet_t
                startTime = snippet_t(minlocs(ind))- averageTime;
                endTime = snippet_t(minlocs(ind))+ averageTime;
                if (endTime > snippet_t(end)) %if end time is greater
                    than end of snippet
                    endTime = snippet_t(end);
                elseif startTime < snippet_t(1) %if start time is less
                    than start of snippet
                    startTime = snippet_t(1);
                end
                %make measurements
                toMeasureTime = snippet_t(intersect(find(snippet_t >
                    startTime), find(snippet_t < endTime)));
                toMeasureI = snippet_Is(intersect(find(snippet_t >
                    startTime), find(snippet_t < endTime)), ind);
                measurements(j,ind) = mean(toMeasureI);
            end
            %plot to check all is OK
            clf
            hold on
            plot(snippet_t, snippet_Is, 'LineWidth',3);
            plot(raw_data{i}.t, raw_data{i}.divsweeps{1,sweeps(j)})
            plot(snippet_t(minlocs), measurements(j,:), 'o')
            legend(pattern_names{i}, 'Location', 'eastoutside')
            drugs{j} =
                strcat(raw_data{i}.divsweeps{2,sweeps(j)}{1:end-1,1}, '
                ');
            title(sprintf("dataset %d, sweep %d, %s ", i, sweeps(j),
                drugs{j}))
            xlabel('Time (s)')
            ylabel('Current (pA)')
            saveas(gcf,
                strcat(data_files{i}(1:end-4),sprintf('_point_%d', j)),
                'svg')
%             drugs{j} = workingTitle;
%            waitforbuttonpress
        end
    end

    %%optional - plot each pattern in each plate. Comment out to not do.
```

```
    %%Useful for making figures?
    [sweepsToPlot ia ic] = unique(sweeps);
    for j = 1:length(pattern_names{i})
        clf
        hold on
        for k = sweepsToPlot
            plot(raw_data{i}.t, raw_data{i}.divsweeps{1,k}(:,j),
                'LineWidth', 2) %plot only analysed sweeps, and each
                sweep only once
        end
        legend(drugs(ia), 'Location', 'southoutside')
        title(pattern_names{i}{j})
        xlabel('Time (s)')
        ylabel('Current (pA)')
        saveas(gcf, strcat(data_files{1}(1:end-4),
            '_',pattern_names{i}{j}), 'svg')
    end


    %construct table of data for this plate
    data_table = array2table(measurements);
    data_table.Properties.VariableNames = pattern_names{i};
    table_out = [measurementDetails drugs data_table];
    %save data for this plate
    writetable(table_out, strcat(data_files{i}(1:end-4),
        'analysed.xlsx'));
    %incorporate into table with data from whole screen
    data_out = [data_out data_table];
end



%append measurement details to whole screen
fulldata = [measurementDetails drugs data_out];

%sort to bring same nanobodies together
dataAnalysed =
    dataAnalysed(:,sort(dataAnalysed.Properties.VariableNames));

%save whole dataset as xls file
writetable(fulldata, strcat(data_files{1}(1:end-4), '_analysed.xlsx'),
    'Sheet',3);

%%%%NOTE: THE ABOVE SHOULD WORK FOR ANY IONFLUX PROTOCOL, FOR THE DEFINED
%%%%MEASUREMENT TIMES, ASSUMING EACH PATTERN SHOULD BE ANALYSED
    SEPERATELY.
%%%%PROCESSING SPECIFIC TO THIS PROTOCOL BEGINS HERE
```

```
%check number of measurements
numMeasurements = size(fulldata, 1);
%check total number of patterns
numPatterns = size(fulldata, 2);

%%construct new table with I/Imax
%start with unnormalised data
dataNorm = data_out;
%define Imax measurmentNumber (ie row in which Imax is)
Imax = 1;

%divide all other rows by Imax row
for i = 1:numMeasurements
    dataNorm{i,:} = dataNorm{i,:}./data_out{Imax,:};
end

dataNormFull = [measurementDetails drugs dataNorm];

%sort to bring same nanobodies together
dataAnalysed =
    dataAnalysed(:,sort(dataAnalysed.Properties.VariableNames));

%write to same xls file
writetable(dataNormFull, strcat(data_files{1}(1:end-4),
    '_analysed.xlsx'), 'Sheet',2);

%%construct a third table with nanobody rows divided by the nearest
%first need column names from above tables for later
columnNames = dataNorm.Properties.VariableNames;

%%hard-coded variables for this section:
%rows in which GABA doses are
firstLowGABARow = 2;
secondLowGABARow = 3;
thirdLowGABARow = 6;
fourthLowGABARow = 7;
%rows in which nb doses are
nbDose1Row = 4;
nbDose2Row = 5;
nbDose3Row = 8;
nbDose4Row = 9;
nbDose5Row = 10;
%rows in a new table that contain current (I/Imax or Inb/IEC10) data.
    When combining
%nanobodies later these are to be averaged over (rather than summed,
    which
%is what happens for the rest of the rows which contain n numbers)
```

```
rowsToAverage = [1 2 3 4 5 7 9 12 15 18 21];
%rows which contain n numbers - need to sum these
rowsToSum = [6 8 10 13 16 19 22];
%rows which will contain duplicate current (I/Imax to Inb/IEC10) data
rowsToStd = [11 14 17 20 23];

%extract relevant rows from dataNorm
firstLowGABA = dataNorm(firstLowGABARow, :);
secondLowGABA = dataNorm(secondLowGABARow, :);
thirdLowGABA = dataNorm(thirdLowGABARow, :);
fourthLowGABA = dataNorm(fourthLowGABARow, :);
nbDose1 = dataNorm(nbDose1Row, :);
nbDose2 = dataNorm(nbDose2Row, :);
nbDose3 = dataNorm(nbDose3Row, :);
nbDose4 = dataNorm(nbDose4Row, :);
nbDose5 = dataNorm(nbDose5Row, :);

%get average of first two low gaba applications, and n number for each
avFirstTwoLowGABA =
    array2table(nanmean([firstLowGABA{:,:};secondLowGABA{:,:}]),
    'VariableNames',columnNames);
nForFirstTwoLowGABA =
    array2table(sum(~isnan([firstLowGABA{:,:};secondLowGABA{:,:}]),1),
    'VariableNames',columnNames);

%get average of all low gaba applications, and n number for each
avAllLowGABA =
    array2table(nanmean([firstLowGABA{:,:};secondLowGABA{:,:};...
thirdLowGABA{:,:};fourthLowGABA{:,:}]), 'VariableNames',columnNames);
nForAllLowGABA =
    array2table(sum(~isnan([firstLowGABA{:,:};secondLowGABA{:,:};...
thirdLowGABA{:,:};fourthLowGABA{:,:}]),1), 'VariableNames',columnNames);

%to find potentiation for each nanobody dose, divide by relevant
    GABA-only
%dose
potentNbDose1 = array2table(nbDose1{:,:}./avFirstTwoLowGABA{:,:},
    'VariableNames',columnNames);
potentNbDose2 = array2table(nbDose2{:,:}./avFirstTwoLowGABA{:,:},
    'VariableNames',columnNames);
potentNbDose3 = array2table(nbDose3{:,:}./fourthLowGABA{:,:},
    'VariableNames',columnNames);
potentNbDose4 = array2table(nbDose4{:,:}./fourthLowGABA{:,:},
    'VariableNames',columnNames);
potentNbDose5 = array2table(nbDose5{:,:}./fourthLowGABA{:,:},
    'VariableNames',columnNames);

%these n-numbers are not useful right now but will become more relvant
```

```
    when
%combining columns belonging to the same nanobody
nForPotentNbDose1 = array2table(sum(~isnan(potentNbDose1{:,:}),1),
    'VariableNames',columnNames);
nForPotentNbDose2 = array2table(sum(~isnan(potentNbDose2{:,:}),1),
    'VariableNames',columnNames);
nForPotentNbDose3 = array2table(sum(~isnan(potentNbDose3{:,:}),1),
    'VariableNames',columnNames);
nForPotentNbDose4 = array2table(sum(~isnan(potentNbDose4{:,:}),1),
    'VariableNames',columnNames);
nForPotentNbDose5 = array2table(sum(~isnan(potentNbDose5{:,:}),1),
    'VariableNames',columnNames);

%%construct new table of results
%new table
dataAnalysed = [firstLowGABA; secondLowGABA; thirdLowGABA;
    fourthLowGABA; avFirstTwoLowGABA; nForFirstTwoLowGABA; avAllLowGABA;
    nForAllLowGABA; potentNbDose1; nForPotentNbDose1; potentNbDose1;
    potentNbDose2; nForPotentNbDose2; potentNbDose2; potentNbDose3;
    nForPotentNbDose3; potentNbDose3; potentNbDose4; nForPotentNbDose4;
    potentNbDose4; potentNbDose5; nForPotentNbDose5; potentNbDose5];

%each column represents one trap, and plates always have two traps per
%pattern. average across the traps for each pattern, and add n numbers
    for
%relevant rows. also average across nanobody repeats from different
%patterns

%sort to bring same nanobodies together
dataAnalysed =
    dataAnalysed(:,sort(dataAnalysed.Properties.VariableNames));
%get column numbers where unique nanobodies are: note this only works
    after
%sorting! and assumes all nanobody names are in the format nbxxx where
    xxx
%is a three digit number
%first unique nanobody
%this works but may be better way of doing it using the unique function
uniqueNbsNames = unique({dataAnalysed.Properties.VariableNames{1}(1:5)});
uniqueNbsLocs = 1;
uniqueNbsNames = {dataAnalysed.Properties.VariableNames{1}(1:5)};
currNb = dataAnalysed.Properties.VariableNames{1}(1:5);
for i = 1:size(dataAnalysed,2)
    if ~strcmp(dataAnalysed.Properties.VariableNames{i}(1:5), currNb)
        %if not the same as current nanobody (ie if unique)
        uniqueNbsLocs = [uniqueNbsLocs i]; %add to list of indices of
            unique nanobodies
        uniqueNbsNames = [uniqueNbsNames
```

```
            dataAnalysed.Properties.VariableNames{i}(1:5)];
        currNb = dataAnalysed.Properties.VariableNames{i}(1:5);
    end
end

%average/sum/do standard deviation for same nanobodies and combine
uniqueNbsLocs = [uniqueNbsLocs size(dataAnalysed,2)+1]; %need to add
    this to find last nanobody
tempArray = zeros(size(dataAnalysed,1), length(uniqueNbsNames));
for i = 1:size(dataAnalysed,1)
    for j = 1:length(uniqueNbsLocs)-1
        toCombine = uniqueNbsLocs(j):(uniqueNbsLocs(j+1)-1); %combine
            same nanobodies in these columns
        if sum(i == rowsToAverage) %if to average
            tempArray(i,j) = nanmean(dataAnalysed{i,toCombine});
        elseif sum(i == rowsToSum) %if not to aveage, must be to sum
            tempArray(i,j) = nansum(dataAnalysed{i,toCombine});
        elseif sum(i == rowsToStd)
            tempArray(i,j) = nanstd(dataAnalysed{i,toCombine});
        end
    end
end
dataAnalysed = array2table(tempArray, 'VariableNames', uniqueNbsNames);
%row labels for new table
rowNames = {'firstLowGABA', 'secondLowGABA', 'thirdLowGABA',
    'fourthLowGABA','avFirstTwoLowGABA', 'nForFirstTwoLowGABA',
    'avAllLowGABA', 'nForAllLowGABA', 'potentNbDose1',
    'nForPotentNbDose1', 'stdForPotentNbDose1' , 'potentNbDose2',
    'nForPotentNbDose2', 'stdForPotentNbDose2', 'potentNbDose3',
    'nForPotentNbDose3', 'stdForPotentNbDose3', 'potentNbDose4',
    'nForPotentNbDose4', 'stdForPotentNbDose4' , 'potentNbDose5',
    'nForPotentNbDose5', 'stdForPotentNbDose5'};
dataAnalysed.Properties.RowNames = rowNames;


%save whole dataset as xls file
writetable(dataAnalysed, strcat(data_files{1}(1:end-4),
    '_analysed.xlsx'), 'Sheet',1, 'WriteRowNames',true);

clearvars -except raw_data data_out fulldata dataAnalysed
    measurementDetails drugs
```

E

Supplementary data

Table E.1: α2β3 $GABA_AR$ nanobody selection conditions (Data provided by Nele Buys, Els Pardon and Jan Steyaert)

α2β3nb	Family	Occurence	Selection conditions			
			GABA		Gabazine	
			Solid phase coated	NeutrAvidin captured	Solid phase coated	NeutrAvidin captured
088 089 090 092	1	13	x	x	x	x
093 094 095	2	10	x	x	x	x
096 097 098	3	6	x	x	x	
099 100 101	4	6	x	x		x
102 103 104 105 117	5	15	x		x	x

Table E.1 continued from previous page

α2β3nb	Family	Occurence	Selection conditions			
			GABA		Gabazine	
			Solid phase coated	NeutrAvidin captured	Solid phase coated	NeutrAvidin captured
106	6	3		x	x	x
107 108	7	9	x	x		
109	8	3	x	x		
110	9	2	x	x		
111 112	10	2	x		x	
113	11	2	x			x
114	12	2		x	x	
115	13	2		x	x	
116	14	3			x	x
118	15	2			x	x
119	16	2	x			
120 121	17	2	x			
122	18	1	x			
123	19	1	x			
124	20	1	x			
125	21	1	x			
126	22	1	x			
127	23	1	x			
128	24	1	x			
129	25	1	x			
130	26	1		x		
131	27	1		x		
132	28	1		x		
133	29	1		x		
134	30	1		x		

Table E.1 continued from previous page

α2β3nb	Family	Occurence	Selection conditions			
			GABA		Gabazine	
			Solid phase coated	NeutrAvidin captured	Solid phase coated	NeutrAvidin captured
135	31	1		x		
136	32	2			x	
137	33	2			x	
138	34	1			x	
139	35	1			x	
140	36	1			x	
141	37	1			x	
142	38	1			x	
143	39	1			x	
144	40	1			x	
145	41	1			x	
146	42	1			x	
147	43	1			x	x
148	44	1				x
149	45	1				x
150	46	1				x
151	47	1				x
152	48	1				x

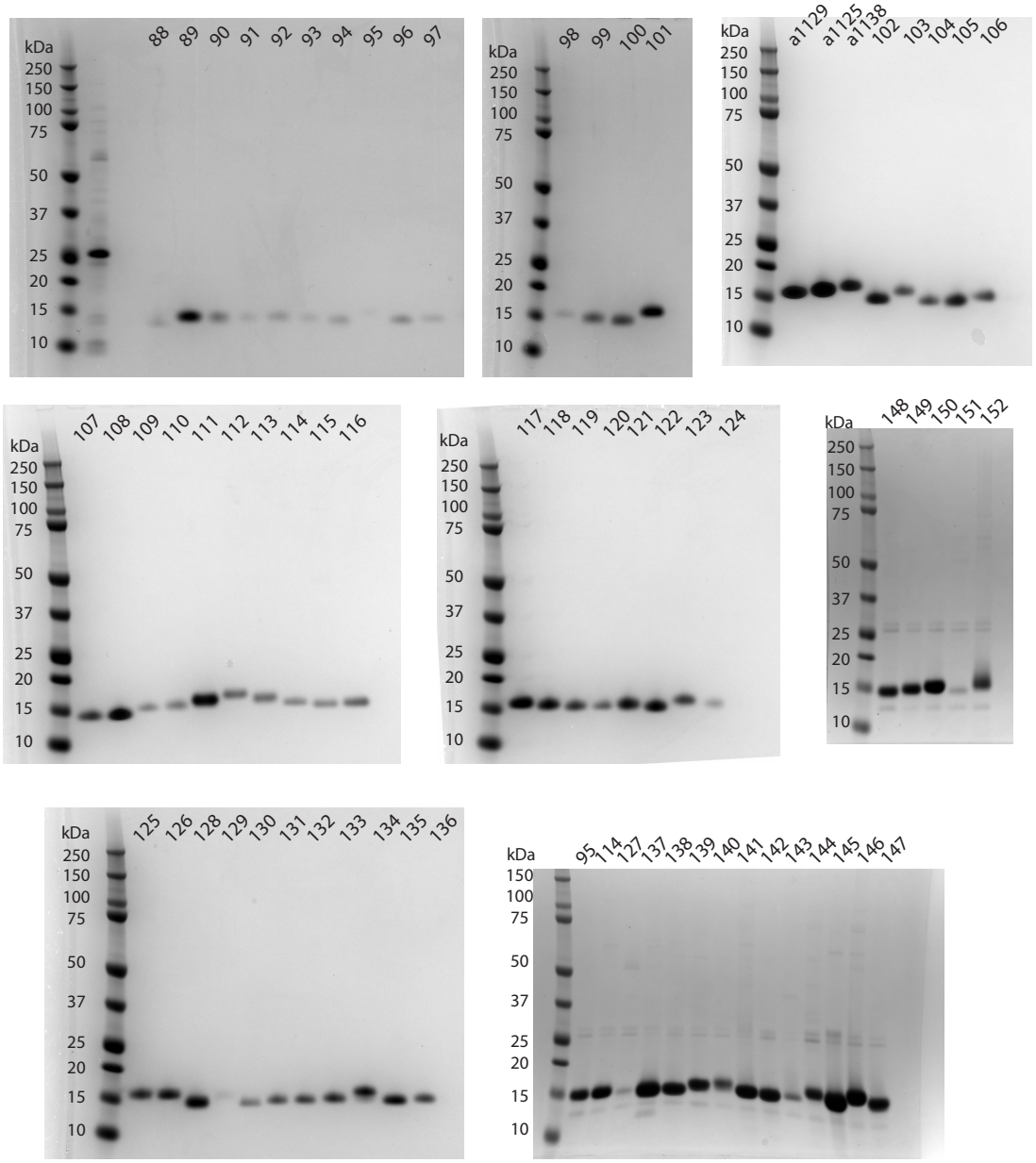

Figure E.1: Full SDS-PAGE gels for purification of α1β3 and α2β3 nanobodies. Nanobodies are against α2β3 unless specified. See also Figure 3.6

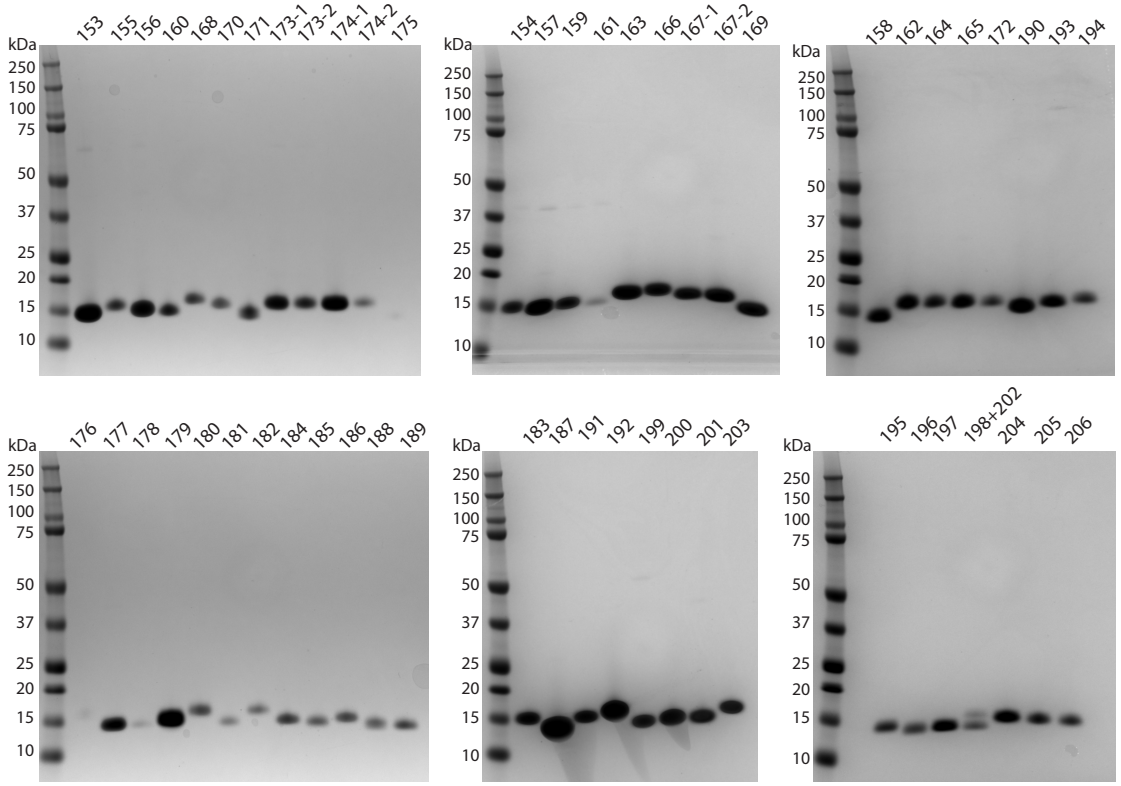

Figure E.2: Full SDS-PAGE gels for purification of α3β3 nanobodies. See also Figure 3.7

Table E.2: α3β3 $GABA_AR$ nanobody selection conditions (Data provided by Nele Buys, Els Pardon and Jan Steyaert)

α3β3nb	Family	Occurence	Selection conditions			
			GABA		Gabazine	
			Solid phase coated	NeutrAvidin captured	Solid phase coated	NeutrAvidin captured
153 154 155 156 157 158 159 160 161 162	1	34	x	x	x	x
163 164 165 166	2	16	x	x	x	x
167 168	3	8	x	x	x	x
169	4	6	x	x	x	x
170	5	4	x	x	x	x
171	6	4	x	x		x
172	7	2	x	x		
173 174	8	5	x		x	
175	9	4	x			x
176	10	3		x		x
177 178	11	2		x		x
179	12	2			x	x
180	13	2	x			
181	14	2	x			
182	15	1	x			
183	16	1	x			

Table E.2 continued from previous page

α3β3nb	Family	Occurence	Selection conditions			
			GABA		Gabazine	
			Solid phase coated	NeutrAvidin captured	Solid phase coated	NeutrAvidin captured
184	17	1	x			
185	18	2		x		
186 187	19	2		x		
188	20	1		x		
189	21	1		x		
190	22	3			x	
191	23	2			x	
192	24	1			x	
193	25	1			x	
194	26	1			x	
195	27	1			x	
196	28	1			x	
197	29	1			x	
198	30	1			x	
199	31	1			x	
200	32	1			x	
201	33	1				x
202	34	1				x
203	35	1				x
204	36	1				x
205	37	1				x
206	38	1				x

Table E.3: Investigating α2β3nb-GABA$_A$R binding by kinetic titration using BLI: results of fits from MATLAB

α2β3nb	k_a (M^{-1} s^{-1}) [95% CI]	k_d (s^{-1}) [95% CI]	R_{max} (nm) [95% CI]	K_D (nM) [95% CI]	R^2
088	$6.13x10^4$ [$6.00x10^4$-$6.26x10^4$]	$5.17x10^{-3}$ [$5.12x10^{-3}$-$5.22x10^{-3}$]	0.124 [0.124-0.125]	84.4 [82.3-86.4]	0.955
090	$1.80x10^4$ [$1.77x10^4$-$1.82x10^4$]	$2.30x10^{-3}$ [$2.29x10^{-3}$-$2.31x10^{-3}$]	0.155 [0.155-0.156]	128 [126-130]	0.995
091	$4.37x10^4$ [$4.25x10^4$-$4.48x10^4$]	$1.42x10^{-2}$ [$1.40x10^{-2}$-$1.44x10^{-2}$]	0.134 [0.133-0.136]	325 [315-335]	0.963
093	$4.56x10^4$ [$4.52x10^4$-$4.60x10^4$]	$3.62x10^{-4}$ [$3.58x10^{-4}$-$3.67x10^{-4}$]	0.236 [0.236-0.237]	7.95 [7.82-8.07]	0.997
094	$1.11x10^4$ [$1.08x10^4$-$1.15x10^4$]	$5.19x10^{-3}$ [$5.16x10^{-3}$-$5.21x10^{-3}$]	0.143 [0.141-0.145]	466 [452-480]	0.988
095	$4.09x10^4$ [$4.03x10^4$-$4.14x10^4$]	$2.00x10^{-3}$ [$1.99x10^{-3}$-$2.01x10^{-3}$]	0.198 [0.197-0.198]	49.0 [48.3-49.7]	0.988
099	$8.77x10^4$ [$8.60x10^4$-$8.94x10^4$]	$7.65x10^{-3}$ [$7.56x10^{-3}$-$7.73x10^{-3}$]	0.218 [0.217-0.220]	87.2 [85.3-89.1]	0.958
100	$6.74x10^4$ [$6.59x10^4$-$6.88x10^4$]	$2.43x10^{-3}$ [$2.40x10^{-3}$-$2.47x10^{-3}$]	0.195 [0.194-0.197]	36.1 [35.2-37.1]	0.932
101	$1.07x10^5$ [$1.06x10^5$-$1.09x10^5$]	$2.76x10^{-3}$ [$2.74x10^{-3}$-$2.77x10^{-3}$]	0.243 [0.243-0.244]	25.7 [25.3-26.0]	0.984
102	$7.58x10^4$ [$7.49x10^4$-$7.67x10^4$]	$3.88x10^{-3}$ [$3.85x10^{-3}$-$3.90x10^{-3}$]	0.275 [0.275-0.276]	51.2 [50.5-51.9]	0.984
103	$7.11x10^4$ [$7.05x10^4$-$7.18x10^4$]	$2.18x10^{-3}$ [$2.17x10^{-3}$-$2.19x10^{-3}$]	0.281 [0.280-0.281]	30.6 [30.3-30.9]	0.992
106	$7.50x10^4$ [$7.44x10^4$-$7.56x10^4$]	$1.64x10^{-3}$ [$1.64x10^{-3}$-$1.65x10^{-3}$]	0.265 [0.265-0.266]	21.9 [21.7-22.1]	0.995
109	$4.75x10^4$ [$4.69x10^4$-$4.82x10^4$]	$2.49x10^{-3}$ [$2.48x10^{-3}$-$2.50x10^{-3}$]	0.137 [0.137-0.138]	52.4 [51.7-53.2]	0.989
111	$9.76x10^4$ [$9.71x10^4$-$9.81x10^4$]	$5.60x10^{-5}$ [$5.34x10^{-5}$-$5.87x10^{-5}$]	0.249 [0.249-0.249]	0.57 [0.55-0.60]	0.999
112	$1.83x10^5$ [$1.82x10^5$-$1.85x10^5$]	$1.17x10^{-4}$ [$1.14x10^{-4}$-$1.20x10^{-4}$]	0.258 [0.258-0.258]	0.64 [0.62-0.65]	0.999
114	$2.00x10^5$ [$1.99x10^5$-$2.02x10^5$]	$2.57x10^{-3}$ [$2.56x10^{-3}$-$2.59x10^{-3}$]	0.232 [0.232-0.233]	12.8 [12.7-13.0]	0.992
115	$1.70x10^4$ [$1.68x10^4$-$1.72x10^4$]	$5.93x10^{-3}$ [$5.91x10^{-3}$-$5.95x10^{-3}$]	0.277 [0.276-0.279]	348 [344-353]	0.995
116	$2.13x10^5$ [$2.11x10^5$-$2.15x10^5$]	$2.11x10^{-3}$ [$2.10x10^{-3}$-$2.11x10^{-3}$]	0.208 [0.207-0.208]	9.88 [9.78-9.98]	0.995
117	$2.97x10^5$ [$2.95x10^5$-$3.00x10^5$]	$3.09x10^{-3}$ [$3.07x10^{-3}$-$3.10x10^{-3}$]	0.218 [0.217-0.218]	10.4 [10.3-10.5]	0.993
118	$1.29x10^5$ [$1.28x10^5$-$1.30x10^5$]	$1.24x10^{-3}$ [$1.24x10^{-3}$-$1.25x10^{-3}$]	0.254 [0.254-0.255]	9.64 [9.54-9.74]	0.995
119	$5.47x10^4$ [$5.41x10^4$-$5.53x10^4$]	$1.73x10^{-4}$ [$1.69x10^{-4}$-$1.78x10^{-4}$]	0.213 [0.213-0.214]	3.17 [3.08-3.26]	0.996

Table E.3 continued from previous page

α2β3nb	k_a ($M^{-1}\,s^{-1}$) [95% CI]	k_d (s^{-1}) [95% CI]	R_{max} (nm) [95% CI]	K_D (nM) [95% CI]	R^2
124	$4.57x10^4$ [$4.48x10^4$-$4.65x10^4$]	$3.22x10^{-3}$ [$3.19x10^{-3}$-$3.25x10^{-3}$]	0.211 [0.210-0.212]	70.5 [69.1-71.9]	0.972
125	$1.02x10^4$ [$1.00x10^4$-$1.04x10^4$]	$1.11x10^{-3}$ [$1.10x10^{-3}$-$1.11x10^{-3}$]	0.183 [0.182-0.185]	108 [106-110]	0.996
128	$5.78x10^4$ [$5.62x10^4$-$5.94x10^4$]	$4.96x10^{-3}$ [$4.89x10^{-3}$-$5.03x10^{-3}$]	0.223 [0.222-0.225]	85.8 [83.1-88.4]	0.914
129	$9.42x10^3$ [$9.04x10^3$-$9.79x10^3$]	$1.19x10^{-3}$ [$1.18x10^{-3}$-$1.21x10^{-3}$]	0.124 [0.122-0.127]	127 [122-132]	0.985
130	$6.59x10^4$ [$6.46x10^4$-$6.73x10^4$]	$4.02x10^{-3}$ [$3.97x10^{-3}$-$4.06x10^{-3}$]	0.278 [0.277-0.280]	61.0 [59.6-62.4]	0.948
131	$1.01x10^5$ [$9.96x10^4$-$1.01x10^5$]	$3.01x10^{-5}$ [$2.55x10^{-5}$-$3.47x10^{-5}$]	0.299 [0.299-0.300]	0.30 [0.25-0.34]	0.996
132	$1.20x10^4$ [$1.18x10^4$-$1.21x10^4$]	$1.69x10^{-4}$ [$1.65x10^{-4}$-$1.73x10^{-4}$]	0.205 [0.204-0.206]	14.1 [13.7-14.5]	0.998
137	$1.68x10^5$ [$1.67x10^5$-$1.70x10^5$]	$3.68x10^{-3}$ [$3.66x10^{-3}$-$3.70x10^{-3}$]	0.252 [0.252-0.253]	21.8 [21.6-22.0]	0.994
139	$1.01x10^5$ [$9.93x10^4$-$1.03x10^5$]	$3.26x10^{-3}$ [$3.23x10^{-3}$-$3.30x10^{-3}$]	0.181 [0.180-0.182]	32.3 [31.6-32.9]	0.973
140	$1.64x10^4$ [$1.59x10^4$-$1.69x10^4$]	$3.95x10^{-4}$ [$3.87x10^{-4}$-$4.03x10^{-4}$]	0.232 [0.230-0.234]	24.1 [23.2-24.9]	0.987
144	$3.58x10^4$ [$3.50x10^4$-$3.66x10^4$]	$1.06x10^{-4}$ [$9.81x10^{-5}$-$1.14x10^{-4}$]	0.157 [0.156-0.158]	2.96 [2.73-3.19]	0.992
146	$1.96x10^5$ [$1.93x10^5$-$2.00x10^5$]	$4.30x10^{-4}$ [$4.18x10^{-4}$-$4.41x10^{-4}$]	0.206 [0.205-0.207]	2.19 [2.12-2.26]	0.987
150	$3.45x10^4$ [$3.43x10^4$-$3.47x10^4$]	$1.98x10^{-4}$ [$1.95x10^{-4}$-$2.01x10^{-4}$]	0.257 [0.256-0.257]	5.74 [5.65-5.83]	0.999
152	$2.83x10^5$ [$2.80x10^5$-$2.86x10^5$]	$1.28x10^{-3}$ [$1.27x10^{-3}$-$1.29x10^{-3}$]	0.238 [0.237-0.238]	4.51 [4.45-4.57]	0.992
		Poor fits			
089	$3.60x10^4$ [$3.40x10^4$-$3.79x10^4$]	$8.61x10^{-3}$ [$8.47x10^{-3}$-$8.74x10^{-3}$]	0.071 [0.070-0.072]	239 [226-253]	0.920
092	$1.76x10^5$ [$1.62x10^5$-$1.89x10^5$]	$2.74x10^{-2}$ [$2.57x10^{-2}$-$2.90x10^{-2}$]	0.054 [0.053-0.055]	156 [141-171]	0.750
096	$1.60x10^2$ [(-1.73-2.05)$x10^3$]	$1.66x10^{-2}$ [$1.58x10^{-2}$-$1.73x10^{-2}$]	6.133 [-65.780-78.045]	$1.03x10^5$ [(-1.11-1.32)$x10^6$]	0.668
097	$3.69x10^1$ [(-1.12-1.20)$x10^3$]	$2.67x10^{-3}$ [$2.62x10^{-3}$-$2.71x10^{-3}$]	5.670 [-172.080-183.419]	$7.22x10^4$ [(-2.20-2.34)$x10^6$]	0.807
098	$4.12x10^1$ [(-1.03-1.11)$x10^3$]	$6.34x10^{-3}$ [$6.21x10^{-3}$-$6.47x10^{-3}$]	6.032 [-150.719-162.782]	$1.54x10^5$ [(-3.85-4.15)$x10^6$]	0.812
105	$3.86x10^2$ [(-1.29-2.06)$x10^3$]	$1.72x10^{-2}$ [$1.65x10^{-2}$-$1.79x10^{-2}$]	1.188 [-3.904-6.281]	$4.47x10^4$ [(-1.49-2.38)$x10^5$]	0.755
107	$1.08x10^2$ [(-8.85-9.06)$x10^3$]	$3.67x10^{-2}$ [$3.00x10^{-2}$-$4.34x10^{-2}$]	4.955 [-406.705-416.615]	$3.41x10^5$ [(-2.80-2.87)$x10^7$]	-0.479

Table E.3 continued from previous page

α2β3nb	k_a ($M^{-1}\,s^{-1}$) [95% CI]	k_d (s^{-1}) [95% CI]	R_{max} (nm) [95% CI]	K_D (nM) [95% CI]	R^2
108	6.32x10^{4} [6.01x10^{4}-6.63x10^{4}]	1.92E-12 [ND]	0.000 [ND]	0.00 [ND]	0.556
110	1.69x10^{5} [1.66x10^{5}-1.73x10^{5}]	6.61x10^{-3} [6.52x10^{-3}-6.70x10^{-3}]	0.055 [0.055-0.056]	39.1 [38.1-40.1]	0.958
113	8.24x10^{6} [7.40x10^{6}-9.07x10^{6}]	2.53x10^{-2} [2.39x10^{-2}-2.67x10^{-2}]	0.014 [0.014-0.014]	3.07 [2.72-3.43]	0.750
120	5.57x10^{4} [5.28x10^{4}-5.85x10^{4}]	3.60E-10 [ND]	0.004 [0.003-0.004]	0.00 [ND]	0.675
121	1.18x10^{5} [1.08x10^{5}-1.27x10^{5}]	1.10E-13 [ND]	0.000 [ND]	0.00 [ND]	0.676
122	3.14x10^{-8} [(-1.83-1.83)x10^{3}]	2.23E-14 [ND]	0.000 [ND]	711 [ND]	0.413
123	8.72x10^{3} [7.87x10^{3}-9.56x10^{3}]	8.96E-10 [ND]	0.000 [ND]	0.00 [ND]	0.643
126	2.54x10^{4} [2.44x10^{4}-2.64x10^{4}]	3.12x10^{-3} [3.07x10^{-3}-3.18x10^{-3}]	0.094 [0.093-0.095]	123 [118-128]	0.912
127	3.03x10^{-7} [(-3.68-3.68)x10^{2}]	1.26x10^{-3} [1.18x10^{-3}-1.33x10^{-3}]	0.000 [ND]	4.15x10^{12} [(-5.05-5.05)x10^{21}]	-1.139
133	3.23x10^{3} [(-6.72-7.12)x10^{3}]	2.22E-14 [ND]	0.000 [-0.049-0.049]	0.00 [ND]	0.524
134	1.61x10^{4} [1.43x10^{4}-1.80x10^{4}]	5.61x10^{-4} [5.40x10^{-4}-5.83x10^{-4}]	0.003 [0.003-0.004]	34.8 [30.6-39.0]	0.956
135	3.90x10^{4} [3.79x10^{4}-4.00x10^{4}]	6.84x10^{-4} [6.73x10^{-4}-6.96x10^{-4}]	0.052 [0.052-0.052]	17.6 [17.0-18.1]	0.978
136	7.61x10^{4} [7.41x10^{4}-7.81x10^{4}]	7.14x10^{-4} [6.99x10^{-4}-7.28x10^{-4}]	0.074 [0.073-0.074]	9.38 [9.07-9.69]	0.967
138	7.64x10^{4} [7.39x10^{4}-7.89x10^{4}]	1.06E-11 [ND]	0.040 [0.038-0.042]	0.00 [ND]	0.605
141	1.18x10^{5} [1.02x10^{5}-1.34x10^{5}]	8.60x10^{-2} [7.61x10^{-2}-9.59x10^{-2}]	0.309 [0.294-0.324]	728 [599-856]	0.845
142	6.29x10^{1} [(-2.06-2.18)x10^{3}]	4.47x10^{-4} [4.23x10^{-4}-4.72x10^{-4}]	0.187 [-5.750-6.124]	7.12x10^{3} [(-2.33-2.47)x10^{5}]	0.940
143	1.50x10^{1} [(-2.57-2.60)x10^{3}]	2.46E-14 [ND]	2.398 [-429.801-434.597]	0.00 [ND]	0.704
145	5.85x10^{4} [5.63x10^{4}-6.06x10^{4}]	1.15x10^{-3} [1.14x10^{-3}-1.17x10^{-3}]	0.078 [0.077-0.079]	19.7 [18.9-20.4]	0.979
147	8.15x10^{0} [(-5.57-5.59)x10^{3}]	5.00E-10 [ND]	0.898 [-660.909-662.705]	0.06 [ND]	0.814
148	1.43x10^{5} [1.39x10^{5}-1.46x10^{5}]	2.50x10^{-3} [2.48x10^{-3}-2.52x10^{-3}]	0.070 [0.070-0.070]	17.5 [17.1-17.9]	0.979
149	1.72x10^{4} [1.65x10^{4}-1.78x10^{4}]	2.05x10^{-3} [2.03x10^{-3}-2.06x10^{-3}]	0.089 [0.087-0.091]	119 [115-124]	0.983
151	2.66E-12 [ND]	8.11x10^{-4} [7.45x10^{-4}-8.77x10^{-4}]	0.000 [ND]	3.05x10^{17} [ND]	0.044

Table E.4: Investigating α3β3nb-GABA$_A$R binding by kinetic titration using BLI: results of fits from MATLAB

α3β3nb	k_a (M^{-1} s^{-1}) [95% CI]	k_d (s^{-1}) [95% CI]	R_{max} (nm) [95% CI]	K_D (nM) [95% CI]	R^2
153	7.82x10^5 [(7.78-7.86)x10^5]	5.59x10^{-5} [(5.22-5.95)x10^{-5}]	0.283 [0.283-0.283]	0.07 [0.07-0.08]	0.998
156	7.50x10^5 [(7.44-7.56)x10^5]	1.12x10^{-3} [(1.11-1.13)x10^{-3}]	0.288 [0.288-0.288]	1.49 [1.48-1.51]	0.993
157	8.89x10^5 [(8.83-8.95)x10^5]	3.41x10^{-4} [(3.36-3.46)x10^{-4}]	0.297 [0.296-0.297]	0.38 [0.38-0.39]	0.996
158	2.86x10^5 [(2.83-2.89)x10^5]	1.90x10^{-3} [(1.89-1.92)x10^{-3}]	0.267 [0.266-0.267]	6.66 [6.58-6.75]	0.991
159	6.51x10^5 [(6.43-6.60)x10^5]	1.29x10^{-3} [(1.28-1.30)x10^{-3}]	0.300 [0.299-0.301]	1.98 [1.95-2.01]	0.983
160	3.07x10^5 [(3.00-3.15)x10^5]	1.48x10^{-2} [(1.45-1.51)x10^{-2}]	0.302 [0.300-0.303]	48.2 [46.7-49.7]	0.953
161	2.32x10^5 [(2.30-2.33)x10^5]	1.27x10^{-3} [(1.26-1.27)x10^{-3}]	0.250 [0.250-0.251]	5.47 [5.42-5.52]	0.997
167	4.70x10^5 [(4.62-4.79)x10^5]	9.89x10^{-3} [(9.72-1.01)x10^{-2}]	0.293 [0.292-0.294]	21.0 [20.5-21.5]	0.974
168	6.66x10^5 [(6.58-6.74)x10^5]	1.15x10^{-3} [(1.14-1.17)x10^{-3}]	0.301 [0.300-0.301]	1.73 [1.70-1.77]	0.982
169	1.61x10^5 [(1.48-1.74)x10^5]	8.06x10^{-2} [(7.53-8.59)x10^{-2}]	0.301 [0.295-0.307]	502 [450-554]	0.903
170	3.77x10^5 [(3.73-3.82)x10^5]	3.25x10^{-3} [(3.22-3.27)x10^{-3}]	0.260 [0.260-0.261]	8.60 [8.48-8.72]	0.988
171	2.43x10^5 [(2.37-2.50)x10^5]	3.24x10^{-2} [(3.16-3.32)x10^{-2}]	0.353 [0.351-0.355]	133 [128-138]	0.964
173	1.20x10^5 [(1.19-1.22)x10^5]	6.66x10^{-3} [(6.61-6.72)x10^{-3}]	0.311 [0.309-0.312]	55.4 [54.5-56.3]	0.978
174	1.67x10^3 [(4.22-2.92)x10^3]	7.42x10^{-4} [(7.12-7.72)x10^{-4}]	0.124 [0.047-0.201]	444 [112-776]	0.931
175	5.35x10^5 [(5.29-5.42)x10^5]	1.22x10^{-3} [(1.20-1.23)x10^{-3}]	0.275 [0.274-0.275]	2.27 [2.24-2.31]	0.984
176	1.19x10^5 [(1.18-1.21)x10^5]	1.88x10^{-3} [(1.87-1.90)x10^{-3}]	0.295 [0.294-0.296]	15.8 [15.5-16.0]	0.984
177	4.74x10^5 [(4.68-4.81)x10^5]	1.05x10^{-3} [(1.04-1.06)x10^{-3}]	0.323 [0.322-0.324]	2.21 [2.17-2.25]	0.982
178	1.53x10^5 [(1.52-1.54)x10^5]	2.51x10^{-4} [(2.47-2.55)x10^{-4}]	0.335 [0.334-0.335]	1.64 [1.61-1.67]	0.998
179	1.36x10^5 [(1.34-1.39)x10^5]	5.49x10^{-2} [(5.42-5.56)x10^{-2}]	0.300 [0.299-0.302]	403 [394-411]	0.993
180	3.51x10^5 [(3.42-3.59)x10^5]	2.37x10^{-2} [(2.32-2.42)x10^{-2}]	0.313 [0.312-0.315]	67.6 [65.4-69.9]	0.960
181	4.67x10^5 [(4.58-4.77)x10^5]	2.16x10^{-3} [(2.13-2.20)x10^{-3}]	0.254 [0.253-0.255]	4.62 [4.51-4.74]	0.953

Table E.4 continued from previous page

α3β3nb	k_a (M^{-1} s^{-1}) [95% CI]	k_d (s^{-1}) [95% CI]	R_{max} (nm) [95% CI]	K_D (nM) [95% CI]	R^2
184	4.10x10^5 [(4.07-4.14)x10^5]	3.54x10^{-4} [(3.49-3.59)x10^{-4}]	0.304 [0.304-0.305]	0.86 [0.85-0.88]	0.997
186	2.32x10^5 [(2.27-2.37)x10^5]	4.64x10^{-2} [(4.55-4.73)x10^{-2}]	0.288 [0.287-0.289]	200 [194-206]	0.981
187	3.90x10^5 [(3.81-3.98)x10^5]	5.40x10^{-3} [(5.32-5.48)x10^{-3}]	0.281 [0.280-0.282]	13.9 [13.5-14.2]	0.954
189	5.33x10^5 [(5.30-5.37)x10^5]	2.61x10^{-4} [(2.56-2.66)x10^{-4}]	0.300 [0.300-0.300]	0.49 [0.48-0.50]	0.997
190	2.88x10^5 [(2.81-2.95)x10^5]	6.26x10^{-3} [(6.15-6.37)x10^{-3}]	0.301 [0.300-0.303]	21.7 [21.1-22.4]	0.936
191	3.53x10^5 [(3.47-3.58)x10^5]	1.60x10^{-3} [(1.58-1.62)x10^{-3}]	0.305 [0.304-0.306]	4.53 [4.45-4.62]	0.978
197	3.01x10^6 [(2.95-3.08)x10^6]	4.81x10^{-3} [(4.73-4.88)x10^{-3}]	0.377 [0.376-0.378]	1.59 [1.55-1.64]	0.980
198	4.82x10^6 [(4.57-5.07)x10^6]	8.06x10^{-3} [(7.77-8.36)x10^{-3}]	0.323 [0.321-0.324]	1.67 [1.57-1.78]	0.929
201	4.37x10^4 [(4.26-4.48)x10^4]	1.47x10^{-3} [(1.43-1.52)x10^{-3}]	0.144 [0.143-0.145]	33.7 [32.4-35.0]	0.905
202	1.14x10^5 [(1.10-1.17)x10^5]	7.34x10^{-2} [(7.19-7.49)x10^{-2}]	0.336 [0.333-0.339]	646 [623-669]	0.987
205	3.05x10^5 [(3.02-3.09)x10^5]	1.57x10^{-3} [(1.55-1.58)x10^{-3}]	0.328 [0.327-0.328]	5.13 [5.06-5.20]	0.990
206	1.34x10^5 [(1.31-1.37)x10^5]	7.74x10^{-3} [(7.60-7.87)x10^{-3}]	0.412 [0.410-0.415]	57.9 [56.2-59.5]	0.943
			Poor fits		
154	1.43x10^6 [(1.40-1.47)x10^6]	7.98x10^{-4} [(7.77-8.18)x10^{-4}]	0.408 [0.407-0.410]	0.56 [0.54-0.58]	0.891
155	4.10x10^4 [(3.82-4.37)x10^4]	2.23x10^{-14} [ND]	0.000 [-0.001-0.001]	5.44x10^{-10} [ND]	-0.138
162	3.72x10^1 [(-3.21-3.29)x10^3]	2.25x10^{-14} [ND]	0.508 [-43.839-44.855]	6.07x10^{-7} [ND]	0.853
163	8.69x10^{-11} [ND]	1.77x10^{-3} [(1.70-1.85)x10^{-3}]	0.000 [ND]	2.04x10^{16} [ND]	-0.368
164	1.15x10^1 [(-2.15-2.17)x10^3]	9.43x10^{-12} [ND]	0.227 [-46.472-46.926]	8.17x10^{-4} [ND]	0.585
165	5.62x10^{-6} [(-2.76-2.76)x10^3]	2.24x10^{-3} [(2.15-2.32)x10^{-3}]	0.000 [ND]	3.97x10^{11} [-2x10^{20}-2x10^{20}]	-0.195
166	3.27x10^{-7} [(-5.99-5.99)x10^2]	1.79x10^{-3} [(1.70-1.88)x10^{-3}]	0.000 [ND]	5.47x10^{12} [-1x10^{22}-1x10^{22}]	0.030
172	1.17x10^4 [(6.91-1.65)x10^4]	6.22x10^{-2} [(5.87-6.56)x10^{-2}]	1.102 [0.707-1.497]	5.32x10^3 [(3.13-7.52)x10^3]	0.892
182	3.51x10^4 [(3.40-3.62)x10^4]	1.15x10^{-4} [(5.14-1.78)x10^{-4}]	0.105 [0.104-0.106]	3.27 [1.46-5.09]	0.857

Table E.4 continued from previous page

α3β3nb	k_a ($M^{-1}\,s^{-1}$) [95% CI]	k_d (s^{-1}) [95% CI]	R_{max} (nm) [95% CI]	K_D (nM) [95% CI]	R^2
183	$9.10x10^4$ [$(8.84\text{-}9.35)x10^4$]	$2.72x10^{-3}$ [$(2.63\text{-}2.81)x10^{-3}$]	0.310 [0.307-0.312]	29.9 [28.6-31.2]	0.865
188	$1.39x10^4$ [$(-3.24\text{-}3.11)x10^4$]	$6.83x10^{-3}$ [$(6.40\text{-}7.26)x10^{-3}$]	0.147 [0.086-0.208]	491 [-115-1096]	0.507
192	$5.80x10^0$ [$(-6.48\text{-}6.49)x10^3$]	$5.13x10^{-4}$ [$(4.64\text{-}5.62)x10^{-4}$]	1.340 [$(-1.50\text{-}1.50)x10^3$]	$8.85x10^4$ [$(-9.89\text{-}9.91)x10^7$]	0.809
193	$9.57x10^3$ [$(9.26\text{-}9.88)x10^3$]	$1.84x10^{-4}$ [$(9.53\text{-}2.74)x10^{-4}$]	0.000 [ND]	19.3 [9.94-28.61]	-1.209
194	$1.92x10^4$ [$(1.74\text{-}2.11)x10^4$]	$1.61x10^{-3}$ [$(1.48\text{-}1.73)x10^{-3}$]	0.006 [0.005-0.007]	83.5 [73.1-93.9]	0.682
195	$4.34x10^3$ [$(2.19\text{-}6.48)x10^3$]	$2.34x10^{-14}$ [ND]	0.000 [-0.015-0.015]	$5.40x10^{-9}$ [ND]	0.661
196	$9.45x10^4$ [$(9.10\text{-}9.80)x10^4$]	$4.05x10^{-11}$ [ND]	0.213 [0.209-0.217]	$4.29x10^{-7}$ [ND]	0.774
199	$3.51x10^6$ [$(2.87\text{-}4.14)x10^6$]	$4.00x10^{-2}$ [$(3.29\text{-}4.71)x10^{-2}$]	0.252 [0.248-0.257]	11.4 [8.53-14.30]	0.684
203	$9.29x10^1$ [$(-4.70\text{-}4.88)x10^3$]	$2.20x10^{-11}$ [ND]	0.564 [-29.190-30.318]	$2.37x10^{-4}$ [ND]	0.724
204	$2.28x10^3$ [$(8.92\text{-}3.67)x10^3$]	$9.34x10^{-3}$ [$(9.05\text{-}9.62)x10^{-3}$]	0.233 [0.108-0.359]	$4.09x10^3$ [$(1.59\text{-}6.58)x10^3$]	0.848

Table E.5: Investigating α2β3nb-$GABA_AR$ binding in the presence of 1 mM GABA by kinetic titration using BLI: results of fits from MATLAB

α2β3nb	k_a (M^{-1} s^{-1}) [95% CI]	k_d (s^{-1}) [95% CI]	R_{max} (nm) [95% CI]	K_D (nM) [95% CI]	R^2
088	$2.70x10^4$ [(2.66-2.74)$x10^4$]	$8.06x10^{-4}$ [(7.97-8.14)$x10^{-4}$]	0.267 [0.266-0.268]	29.8 [29.3-30.4]	0.992
089	$1.47x10^4$ [(1.44-1.51)$x10^4$]	$1.39x10^{-3}$ [(1.38-1.40)$x10^{-3}$]	0.234 [0.232-0.236]	94.0 [91.9-96.1]	0.990
090	$2.41x10^4$ [(2.38-2.44)$x10^4$]	$4.04x10^{-4}$ [(3.98-4.10)$x10^{-4}$]	0.295 [0.294-0.296]	16.8 [16.4-17.1]	0.995
091	$5.34x10^4$ [(5.30-5.38)$x10^4$]	$9.79x10^{-4}$ [(9.73-9.86)$x10^{-4}$]	0.281 [0.280-0.281]	18.3 [18.1-18.5]	0.995
092	$4.95x10^4$ [(4.91-4.99)$x10^4$]	$1.39x10^{-3}$ [(1.38-1.39)$x10^{-3}$]	0.281 [0.280-0.282]	28.0 [27.8-28.3]	0.996
094	$1.78x10^4$ [(1.77-1.80)$x10^4$]	$4.35x10^{-4}$ [(4.32-4.38)$x10^{-4}$]	0.329 [0.328-0.329]	24.4 [24.1-24.7]	0.998
096	$2.18x10^5$ [(2.17-2.20)$x10^5$]	$1.04x10^{-4}$ [(1.00-1.09)$x10^{-4}$]	0.197 [0.197-0.197]	0.48 [0.46-0.50]	0.997
097	$3.92x10^4$ [(3.89-3.96)$x10^4$]	$7.20x10^{-4}$ [(7.14-7.27)$x10^{-4}$]	0.329 [0.328-0.330]	18.4 [18.1-18.6]	0.994
098	$8.59x10^3$ [(8.39-8.79)$x10^3$]	$3.42x10^{-4}$ [(3.38-3.46)$x10^{-4}$]	0.331 [0.327-0.335]	39.8 [38.7-40.9]	0.997
099	$2.14x10^5$ [(2.13-2.15)$x10^5$]	$6.46x10^{-4}$ [(6.42-6.51)$x10^{-4}$]	0.281 [0.281-0.281]	3.02 [2.99-3.05]	0.997
100	$1.49x10^5$ [(1.48-1.51)$x10^5$]	$6.14x10^{-4}$ [(6.07-6.22)$x10^{-4}$]	0.248 [0.248-0.249]	4.12 [4.06-4.18]	0.993
101	$1.27x10^5$ [(1.26-1.29)$x10^5$]	$3.50x10^{-4}$ [(3.44-3.56)$x10^{-4}$]	0.244 [0.243-0.244]	2.75 [2.69-2.80]	0.995
102	$6.55x10^4$ [(6.49-6.62)$x10^4$]	$4.19x10^{-3}$ [(4.16-4.21)$x10^{-3}$]	0.314 [0.313-0.315]	63.9 [63.2-64.6]	0.989
103	$6.83x10^4$ [(6.78-6.89)$x10^4$]	$2.71x10^{-3}$ [(2.70-2.72)$x10^{-3}$]	0.315 [0.314-0.316]	39.6 [39.3-40.0]	0.992
105	$1.26x10^5$ [(1.24-1.27)$x10^5$]	$3.64x10^{-3}$ [(3.62-3.66)$x10^{-3}$]	0.258 [0.258-0.259]	29.0 [28.7-29.3]	0.990
106	$9.03x10^4$ [(8.94-9.11)$x10^4$]	$1.69x10^{-3}$ [(1.68-1.70)$x10^{-3}$]	0.280 [0.280-0.281]	18.7 [18.5-18.9]	0.993
107	$5.10x10^4$ [(5.05-5.14)$x10^4$]	$2.30x10^{-3}$ [(2.29-2.31)$x10^{-3}$]	0.321 [0.321-0.322]	45.1 [44.6-45.5]	0.993
108	$3.69x10^4$ [(3.64-3.73)$x10^4$]	$4.34x10^{-3}$ [(4.32-4.37)$x10^{-3}$]	0.281 [0.280-0.282]	118 [116-119]	0.989
110	$1.06x10^5$ [(1.05-1.06)$x10^5$]	$1.03x10^{-3}$ [(1.03-1.04)$x10^{-3}$]	0.301 [0.300-0.301]	9.76 [9.67-9.85]	0.996
111	$7.53x10^4$ [(7.48-7.59)$x10^4$]	$3.90x10^{-4}$ [(3.85-3.94)$x10^{-4}$]	0.353 [0.353-0.354]	5.17 [5.10-5.25]	0.997
112	$1.21x10^5$ [(1.21-1.22)$x10^5$]	$4.62x10^{-4}$ [(4.58-4.67)$x10^{-4}$]	0.317 [0.317-0.318]	3.81 [3.77-3.85]	0.997

Table E.5 continued from previous page

α2β3nb	k_a (M^{-1} s^{-1}) [95% CI]	k_d (s^{-1}) [95% CI]	R_{max} (nm) [95% CI]	K_D (nM) [95% CI]	R^2
113	$8.54x10^4$ [(8.49-8.60)x10^4]	$1.09x10^{-3}$ [(1.09-1.10)x10^{-3}]	0.295 [0.294-0.295]	12.8 [12.7-12.9]	0.996
114	$1.06x10^4$ [(1.03-1.08)x10^4]	$2.30x10^{-3}$ [(2.29-2.31)x10^{-3}]	0.400 [0.395-0.404]	218 [214-223]	0.993
115	$7.98x10^3$ [(7.51-8.45)x10^3]	$1.07x10^{-2}$ [(1.06-1.08)x10^{-2}]	0.565 [0.541-0.589]	1343 [1263-1423]	0.978
116	$1.14x10^5$ [(1.13-1.14)x10^5]	$1.38x10^{-3}$ [(1.37-1.39)x10^{-3}]	0.334 [0.333-0.334]	12.2 [12.0-12.3]	0.996
117	$1.93x10^5$ [(1.91-1.95)x10^5]	$3.46x10^{-3}$ [(3.44-3.48)x10^{-3}]	0.306 [0.306-0.307]	17.9 [17.7-18.1]	0.993
118	$8.68x10^4$ [(8.62-8.74)x10^4]	$1.89x10^{-3}$ [(1.88-1.90)x10^{-3}]	0.342 [0.341-0.342]	21.8 [21.6-22.0]	0.995
119	$7.56x10^4$ [(7.52-7.60)x10^4]	$5.49x10^{-4}$ [(5.45-5.52)x10^{-4}]	0.318 [0.317-0.318]	7.26 [7.19-7.32]	0.998
120	$1.18x10^5$ [(1.17-1.19)x10^5]	$2.47x10^{-3}$ [(2.46-2.48)x10^{-3}]	0.309 [0.308-0.309]	20.9 [20.7-21.1]	0.992
121	$1.08x10^5$ [(1.07-1.09)x10^5]	$1.76x10^{-3}$ [(1.75-1.76)x10^{-3}]	0.250 [0.250-0.251]	16.2 [16.1-16.4]	0.996
122	$2.64x10^4$ [(2.62-2.67)x10^4]	$1.44x10^{-3}$ [(1.43-1.44)x10^{-3}]	0.293 [0.292-0.293]	54.3 [53.8-54.9]	0.996
123	$1.49x10^5$ [(1.48-1.51)x10^5]	$1.56x10^{-3}$ [(1.54-1.57)x10^{-3}]	0.294 [0.294-0.295]	10.4 [10.3-10.6]	0.989
124	$1.23x10^4$ [(1.21-1.24)x10^4]	$5.87x10^{-4}$ [(5.83-5.90)x10^{-4}]	0.314 [0.313-0.316]	47.9 [47.2-48.5]	0.998
125	$8.93x10^4$ [(8.89-8.97)x10^4]	$5.31x10^{-4}$ [(5.28-5.33)x10^{-4}]	0.343 [0.342-0.343]	5.94 [5.90-5.98]	0.999
126	$9.56x10^4$ [(9.45-9.68)x10^4]	$1.42x10^{-2}$ [(1.41-1.43)x10^{-2}]	0.298 [0.297-0.299]	149 [146-151]	0.989
128	$5.17x10^4$ [(5.14-5.20)x10^4]	$4.58x10^{-4}$ [(4.53-4.63)x10^{-4}]	0.220 [0.219-0.220]	8.85 [8.75-8.96]	0.997
129	$8.66x10^4$ [(8.61-8.72)x10^4]	$7.02x10^{-3}$ [(6.99-7.04)x10^{-3}]	0.304 [0.304-0.305]	81.0 [80.4-81.6]	0.996
130	$4.41x10^4$ [(4.38-4.45)x10^4]	$5.61x10^{-4}$ [(5.55-5.66)x10^{-4}]	0.268 [0.267-0.268]	12.7 [12.5-12.9]	0.996
131	$2.09x10^4$ [(2.07-2.11)x10^4]	$1.42x10^{-3}$ [(1.42-1.43)x10^{-3}]	0.248 [0.247-0.248]	67.9 [67.2-68.6]	0.997
132	$3.70x10^4$ [(3.66-3.75)x10^4]	$3.02x10^{-3}$ [(3.00-3.03)x10^{-3}]	0.293 [0.292-0.294]	81.4 [80.4-82.4]	0.991
133	$8.61x10^4$ [(8.54-8.69)x10^4]	$3.14x10^{-3}$ [(3.13-3.16)x10^{-3}]	0.279 [0.278-0.280]	36.5 [36.2-36.9]	0.992
134	$9.74x10^4$ [(9.65-9.82)x10^4]	$2.35x10^{-3}$ [(2.33-2.36)x10^{-3}]	0.261 [0.261-0.262]	24.1 [23.9-24.3]	0.993
136	$1.31x10^5$ [(1.30-1.32)x10^5]	$7.25x10^{-3}$ [(7.21-7.29)x10^{-3}]	0.297 [0.296-0.298]	55.2 [54.6-55.8]	0.992

Table E.5 continued from previous page

α2β3nb	k_a (M^{-1} s^{-1}) [95% CI]	k_d (s^{-1}) [95% CI]	R_{max} (nm) [95% CI]	K_D (nM) [95% CI]	R^2
142	$3.47x10^4$ [(3.39-3.55)x10^4]	$1.26x10^{-3}$ [(1.25-1.28)x10^{-3}]	0.250 [0.249-0.251]	36.4 [35.4-37.4]	0.961
144	$4.70x10^4$ [(4.68-4.72)x10^4]	$3.84x10^{-4}$ [(3.82-3.87)x10^{-4}]	0.294 [0.294-0.294]	8.18 [8.11-8.24]	0.999
145	$7.96x10^4$ [(7.91-8.00)x10^4]	$7.00x10^{-4}$ [(6.97-7.04)x10^{-4}]	0.304 [0.304-0.305]	8.80 [8.74-8.87]	0.998
146	$2.42x10^5$ [(2.39-2.44)x10^5]	$3.26x10^{-4}$ [(3.22-3.31)x10^{-4}]	0.318 [0.317-0.318]	1.35 [1.33-1.37]	0.997
147	$9.36x10^4$ [(9.30-9.42)x10^4]	$3.20x10^{-4}$ [(3.16-3.24)x10^{-4}]	0.294 [0.294-0.295]	3.42 [3.37-3.46]	0.998
148	$8.13x10^4$ [(8.08-8.18)x10^4]	$1.57x10^{-4}$ [(1.54-1.61)x10^{-4}]	0.302 [0.302-0.303]	1.94 [1.89-1.98]	0.998
149	$4.67x10^4$ [(4.59-4.74)x10^4]	$1.90x10^{-3}$ [(1.88-1.91)x10^{-3}]	0.312 [0.311-0.313]	40.6 [40.0-41.3]	0.982
150	$8.74x10^4$ [(8.70-8.79)x10^4]	$3.01x10^{-5}$ [(2.76-3.26)x10^{-5}]	0.292 [0.292-0.293]	0.34 [0.32-0.37]	0.999
		Poor fits			
093	$5.30x10^{-7}$ [(-3.65-3.65)x10^2]	$2.99x10^{-4}$ [(2.32-3.65)x10^{-4}]	0.000 [ND]	$5.64x10^{11}$ [(-3.89-3.89)x10^{20}]	0.258
095	$1.35x10^6$ [(1.07-1.63)x10^6]	$9.10x10^{-4}$ [(7.54-1.07)x10^{-3}]	0.000 [ND]	0.67 [0.49-0.85]	0.102
104	$3.12x10^3$ [(7.90-5.46)x10^3]	$4.03x10^{-14}$ [ND]	0.000 [-0.020-0.020]	0.00 [ND]	0.597
109	$2.64x10^2$ [(-9.30-9.83)x10^3]	$1.15x10^{-3}$ [(1.10-1.20)x10^{-3}]	0.048 [-1.533-1.629]	$4.36x10^3$ [(-1.54-1.62)x10^5]	0.704
127	$1.17x10^{-4}$ [(-2.02-2.02)x10^2]	$7.97x10^{-11}$ [ND]	0.000 [ND]	684 [ND]	0.804
135	$7.34x10^2$ [(-4.34-1.90)x10^3]	$6.12x10^{-3}$ [(6.01-6.23)x10^{-3}]	0.362 [-0.193-0.917]	$8.34x10^3$ [(-4.93-2.16)x10^4]	0.817
137	$1.20x10^2$ [(-9.53-9.77)x10^3]	$4.61x10^{-4}$ [(4.01-5.20)x10^{-4}]	0.006 [-0.325-0.338]	$3.82x10^3$ [(-3.03-3.10)x10^5]	0.740
138	$1.18x10^3$ [(-1.11-3.48)x10^3]	$8.75x10^{-3}$ [(7.19-1.03)x10^{-2}]	0.114 [-0.079-0.307]	$7.39x10^3$ [(-6.99-2.18)x10^4]	0.536
139	$2.37x10^4$ [(2.03-2.72)x10^4]	$2.22x10^{-12}$ [ND]	0.000 [ND]	0.00 [ND]	0.648
140	$6.90x10^4$ [(6.03-7.76)x10^4]	$2.22x10^{-14}$ [ND]	0.024 [0.024-0.025]	0.00 [ND]	0.828
141	$3.00x10^2$ [(-8.19-8.79)x10^3]	$2.28x10^{-4}$ [(1.29-3.28)x10^{-4}]	0.035 [-1.428-1.499]	762 [(-2.08-2.23)x10^4]	0.809
143	$4.33x10^{-10}$ [ND]	$1.02x10^{-10}$ [ND]	0.000 [ND]	$2.36x10^8$ [ND]	0.708
151	$5.70x10^2$ [(-4.63-5.77)x10^3]	$1.11x10^{-3}$ [(1.06-1.17)x10^{-3}]	0.000 [-1.622-1.622]	$1.96x10^3$ [(-1.59-1.98)x10^4]	0.994

Table E.5 continued from previous page

α2β3nb	k_a (M^{-1} s^{-1}) [95% CI]	k_d (s^{-1}) [95% CI]	R_{max} (nm) [95% CI]	K_D (nM) [95% CI]	R^2
152	$3.56x10^3$ [$(2.90\text{-}4.21)x10^3$]	$1.52x10^{-3}$ [$(1.45\text{-}1.59)x10^{-3}$]	0.000 [ND]	427 [346.56-507.99]	0.768

Table E.6: Investigating α3β3nb-$GABA_AR$ binding in the presence of 1 mM GABA by kinetic titration using BLI: results of fits from MATLAB

α3β3nb	k_a ($M^{-1}\,s^{-1}$) [95% CI]	k_d (s^{-1}) [95% CI]	R_{max} (nm) [95% CI]	K_D (nM) [95% CI]	R^2
154	$8.07x10^5$ [(7.95-8.19)$x10^5$]	$7.86x10^{-4}$ [(7.73-7.99)$x10^{-4}$]	0.342 [0.341-0.343]	0.97 [0.95-1.00]	0.977
156	$2.00x10^5$ [(1.97-2.04)$x10^5$]	$5.52x10^{-4}$ [(5.33-5.70)$x10^{-4}$]	0.334 [0.333-0.336]	2.75 [2.65-2.86]	0.971
157	$7.57x10^5$ [(7.52-7.63)$x10^5$]	$7.20x10^{-5}$ [(6.71-7.69)$x10^{-5}$]	0.323 [0.323-0.323]	0.10 [0.09-0.10]	0.996
158	$3.13x10^5$ [(3.10-3.17)$x10^5$]	$8.73x10^{-4}$ [(8.65-8.81)$x10^{-4}$]	0.309 [0.308-0.309]	2.79 [2.75-2.83]	0.992
159	$5.52x10^5$ [(5.45-5.59)$x10^5$]	$7.09x10^{-4}$ [(6.98-7.19)$x10^{-4}$]	0.325 [0.324-0.325]	1.28 [1.26-1.31]	0.984
160	$3.09x10^5$ [(3.01-3.17)$x10^5$]	$1.59x10^{-3}$ [(1.54-1.64)$x10^{-3}$]	0.308 [0.307-0.310]	5.16 [4.95-5.38]	0.908
161	$2.56x10^5$ [(2.54-2.58)$x10^5$]	$7.66x10^{-4}$ [(7.61-7.71)$x10^{-4}$]	0.294 [0.294-0.295]	2.99 [2.96-3.02]	0.997
167	$3.72x10^5$ [(3.67-3.78)$x10^5$]	$3.48x10^{-2}$ [(3.44-3.53)$x10^{-2}$]	0.248 [0.248-0.249]	93.57 [91.75-95.40]	0.990
168	$7.20x10^5$ [(7.10-7.31)$x10^5$]	$2.23x10^{-3}$ [(2.20-2.26)$x10^{-3}$]	0.283 [0.282-0.284]	3.09 [3.03-3.15]	0.970
169	$1.17x10^5$ [(1.09-1.24)$x10^5$]	$6.64x10^{-2}$ [(6.32-6.96)$x10^{-2}$]	0.325 [0.319-0.331]	570 [525-615]	0.933
170	$3.34x10^5$ [(3.29-3.40)$x10^5$]	$2.15x10^{-3}$ [(2.13-2.17)$x10^{-3}$]	0.299 [0.298-0.300]	6.43 [6.31-6.55]	0.978
171	$2.77x10^5$ [(2.69-2.85)$x10^5$]	$2.87x10^{-2}$ [(2.79-2.94)$x10^{-2}$]	0.326 [0.324-0.328]	104 [100-108]	0.950
172	$1.54x10^5$ [(1.49-1.59)$x10^5$]	$4.67x10^{-2}$ [(4.54-4.80)$x10^{-2}$]	0.329 [0.326-0.331]	303 [290-317]	0.967
173	$4.26x10^5$ [(4.18-4.34)$x10^5$]	$1.99x10^{-3}$ [(1.96-2.01)$x10^{-3}$]	0.306 [0.305-0.307]	4.66 [4.56-4.77]	0.966
174	$1.79x10^4$ [(1.72-1.86)$x10^4$]	$8.03x10^{-4}$ [(7.75-8.30)$x10^{-4}$]	0.120 [0.118-0.121]	44.84 [42.45-47.23]	0.940
175	$4.82x10^5$ [(4.75-4.89)$x10^5$]	$1.03x10^{-3}$ [(1.02-1.04)$x10^{-3}$]	0.275 [0.274-0.275]	2.13 [2.09-2.18]	0.979
176	$1.59x10^5$ [(1.57-1.62)$x10^5$]	$8.15x10^{-4}$ [(8.04-8.25)$x10^{-4}$]	0.265 [0.264-0.266]	5.11 [5.01-5.22]	0.986
177	$6.87x10^5$ [(6.75-6.99)$x10^5$]	$1.36x10^{-3}$ [(1.35-1.38)$x10^{-3}$]	0.292 [0.291-0.292]	1.98 [1.94-2.02]	0.970
178	$1.35x10^5$ [(1.34-1.36)$x10^5$]	$5.69x10^{-4}$ [(5.65-5.73)$x10^{-4}$]	0.308 [0.307-0.308]	4.22 [4.18-4.26]	0.998
179	$9.56x10^4$ [(9.29-9.82)$x10^4$]	$4.00x10^{-2}$ [(3.93-4.07)$x10^{-2}$]	0.315 [0.312-0.318]	418 [405-432]	0.974
180	$1.06x10^5$ [(1.01-1.11)$x10^5$]	$4.31x10^{-2}$ [(4.15-4.46)$x10^{-2}$]	0.396 [0.391-0.402]	407 [382-431]	0.938

Table E.6 continued from previous page

α3β3nb	k_a (M^{-1} s^{-1}) [95% CI]	k_d (s^{-1}) [95% CI]	R_{max} (nm) [95% CI]	K_D (nM) [95% CI]	R^2
181	$4.75x10^5$ [$(4.64\text{-}4.86)x10^5$]	$1.77x10^{-3}$ [$(1.74\text{-}1.80)x10^{-3}$]	0.269 [0.268-0.270]	3.73 [3.62-3.83]	0.939
183	$1.79x10^5$ [$(1.74\text{-}1.83)x10^5$]	$1.95x10^{-3}$ [$(1.90\text{-}2.01)x10^{-3}$]	0.343 [0.341-0.346]	10.94 [10.52-11.36]	0.903
184	$4.57x10^5$ [$(4.52\text{-}4.62)x10^5$]	$2.86x10^{-4}$ [$(2.79\text{-}2.93)x10^{-4}$]	0.338 [0.337-0.338]	0.63 [0.61-0.64]	0.992
187	$7.68x10^5$ [$(7.50\text{-}7.85)x10^5$]	$5.65x10^{-3}$ [$(5.56\text{-}5.75)x10^{-3}$]	0.279 [0.278-0.280]	7.37 [7.16-7.57]	0.940
188	$1.07x10^5$ [$(1.05\text{-}1.08)x10^5$]	$4.27x10^{-3}$ [$(4.23\text{-}4.31)x10^{-3}$]	0.200 [0.199-0.201]	40.08 [39.28-40.89]	0.963
190	$3.43x10^5$ [$(3.34\text{-}3.53)x10^5$]	$2.02x10^{-3}$ [$(1.97\text{-}2.08)x10^{-3}$]	0.295 [0.293-0.297]	5.90 [5.66-6.13]	0.902
191	$4.74x10^5$ [$(4.67\text{-}4.82)x10^5$]	$8.58x10^{-4}$ [$(8.43\text{-}8.73)x10^{-4}$]	0.321 [0.320-0.322]	1.81 [1.77-1.85]	0.975
196	$7.54x10^4$ [$(7.32\text{-}7.76)x10^4$]	$2.09x10^{-2}$ [$(2.05\text{-}2.13)x10^{-2}$]	0.281 [0.278-0.283]	277 [268-287]	0.951
197	$1.02x10^6$ [$(1.00\text{-}1.03)x10^6$]	$1.38x10^{-3}$ [$(1.36\text{-}1.40)x10^{-3}$]	0.262 [0.261-0.263]	1.36 [1.33-1.39]	0.968
198	$4.65x10^5$ [$(4.52\text{-}4.77)x10^5$]	$5.85x10^{-3}$ [$(5.73\text{-}5.96)x10^{-3}$]	0.304 [0.302-0.306]	12.59 [12.16-13.01]	0.928
199	$8.30x10^3$ [$(7.20\text{-}9.40)x10^3$]	$1.44x10^{-2}$ [$(1.41\text{-}1.46)x10^{-2}$]	0.853 [0.773-0.933]	1729 [1497-1961]	0.944
205	$1.41x10^4$ [$(1.35\text{-}1.47)x10^4$]	$1.46x10^{-3}$ [$(1.44\text{-}1.49)x10^{-3}$]	0.373 [0.368-0.379]	104 [99-108]	0.967
206	$1.66x10^5$ [$(1.63\text{-}1.70)x10^5$]	$1.48x10^{-2}$ [$(1.45\text{-}1.51)x10^{-2}$]	0.394 [0.392-0.396]	89.09 [86.55-91.62]	0.966
			Poor fits		
153	$6.66x10^5$ [$(6.61\text{-}6.72)x10^5$]	$5.33x10^{-13}$ [ND]	0.345 [0.344-0.345]	$8.00329x10^{-10}$ [ND]	0.996
155	$2.18x10^4$ [$(1.95\text{-}2.42)x10^4$]	$2.13x10^{-10}$ [ND]	0.053 [0.053-0.054]	$9.76484x10^{-6}$ [ND]	0.937
162	$1.82x10^5$ [$(1.58\text{-}2.06)x10^5$]	$2.34x10^{-14}$ [ND]	0.027 [0.026-0.027]	$1.28694x10^{-10}$ [ND]	0.841
163	$3.73x10^{-10}$ [ND]	$1.16x10^{-3}$ [$(9.65\text{-}1.36)x10^{-3}$]	$1.44x10^{-12}$ [ND]	$3.11x10^{15}$ [ND]	0.566
164	$8.44x10^{-8}$ [$(-6.72\text{-}6.72)x10^2$]	$9.77x10^{-11}$ [ND]	$2.00x10^{-10}$ [ND]	$1.16x10^6$ [ND]	0.498
165	$2.51x10^{-5}$ [$(-1.21\text{-}1.21)x10^3$]	$7.87x10^{-3}$ [$(7.03\text{-}8.71)x10^{-3}$]	$1.81x10^{-11}$ [ND]	$3.13x10^{11}$ [$(-1.50\text{-}1.50)x10^{19}$]	0.234
166	$2.36x10^{-4}$ [$(-1.25\text{-}1.25)x10^4$]	$9.90x10^{-3}$ [$(7.21\text{-}1.26)x10^{-2}$]	$4.14x10^{-8}$ [$(-4.09\text{-}4.09)x10^5$]	$4.19x10^{10}$ [$(-2.22\text{-}2.22)x10^{18}$]	0.013
182	$4.21x10^4$ [$(4.07\text{-}4.36)x10^4$]	$3.63x10^{-3}$ [$(3.55\text{-}3.72)x10^{-3}$]	0.266 [0.263-0.269]	86.22 [82.62-89.82]	0.855

Table E.6 continued from previous page

α3β3nb	k_a (M^{-1} s^{-1}) [95% CI]	k_d (s^{-1}) [95% CI]	R_{max} (nm) [95% CI]	K_D (nM) [95% CI]	R^2
185	$4.77x10^4$ [(4.57-4.96)$x10^4$]	$2.98x10^{-11}$ [ND]	0.105 [0.104-0.105]	$6.24795x10^{-7}$ [ND]	0.946
186	$7.99x10^4$ [(7.74-8.23)$x10^4$]	$1.71x10^{-3}$ [(1.65-1.77)$x10^{-3}$]	0.298 [0.295-0.300]	21.42 [20.40-22.45]	0.832
189	$8.58x10^5$ [(8.51-8.64)$x10^5$]	$5.62x10^{-11}$ [ND]	0.315 [0.315-0.316]	$6.55537x10^{-8}$ [ND]	0.996
192	$1.72x10^5$ [(1.42-2.02)$x10^5$]	$2.34x10^{-14}$ [ND]	0.046 [0.046-0.047]	$1.35825x10^{-10}$ [ND]	0.808
193	$9.91x10^4$ [(8.10-1.17)$x10^5$]	$2.34x10^{-14}$ [ND]	0.056 [0.056-0.057]	$2.35787x10^{-10}$ [ND]	0.864
194	$2.48x10^4$ [(2.26-2.70)$x10^4$]	$3.26x10^{-14}$ [ND]	0.000 [-0.001-0.001]	$1.31516x10^{-9}$ [ND]	0.932
195	$2.07x10^2$ [(-5.62-6.03)$x10^3$]	$1.14x10^{-12}$ [ND]	0.266 [-8.418-8.950]	$5.53587x10^{-6}$ [ND]	0.256
200	$1.94x10^2$ [(-1.77-2.16)$x10^3$]	$1.93x10^{-2}$ [(1.85-2.02)$x10^{-2}$]	21 [-192-235]	$9.96x10^4$ [(-9.07-1.11)$x10^6$]	0.852
201	$4.30x10^4$ [(4.16-4.43)$x10^4$]	$1.55x10^{-3}$ [(1.50-1.60)$x10^{-3}$]	0.104 [0.103-0.105]	36.02 [34.42-37.62]	0.885
202	$2.51x10^4$ [(2.02-3.01)$x10^4$]	$2.18x10^{-2}$ [(1.95-2.40)$x10^{-2}$]	0.315 [0.274-0.355]	865 [674-1057]	0.574
203	$2.19x10^4$ [(1.99-2.38)$x10^4$]	$2.01x10^{-4}$ [(1.62-2.39)$x10^{-4}$]	0.030 [0.029-0.031]	9.18 [7.25-11.11]	0.834
204	$4.27x10^4$ [(4.08-4.45)$x10^4$]	$2.37x10^{-14}$ [ND]	0.001 [0.000-0.002]	$5.555x10^{-10}$ [ND]	0.611

Table E.7: Investigating α2β3nb-$GABA_AR$ binding in the presence of 10 μM gabazine by kinetic titration using BLI: results of fits from MATLAB

α2β3nb	k_a (M^{-1} s^{-1}) [95% CI]	k_d (s^{-1}) [95% CI]	R_{max} (nm) [95% CI]	K_D (nM) [95% CI]	R^2
093	$8.95x10^4$ [(8.71-9.19)$x10^4$]	$2.37x10^{-2}$ [(2.33-2.42)$x10^{-2}$]	0.130 [0.129-0.132]	265 [256-274]	0.962
097	$9.54x10^3$ [(7.72-1.14)$x10^4$]	$4.18x10^{-4}$ [(3.61-4.76)$x10^{-4}$]	0.224 [0.211-0.237]	43.9 [33.6-54.2]	0.978
102	$5.54x10^4$ [(5.43-5.65)$x10^4$]	$9.46x10^{-3}$ [(9.34-9.57)$x10^{-3}$]	0.244 [0.243-0.246]	171 [167-175]	0.974
103	$5.98x10^4$ [(5.92-6.04)$x10^4$]	$2.75x10^{-3}$ [(2.74-2.77)$x10^{-3}$]	0.247 [0.246-0.247]	46.0 [45.5-46.6]	0.989
104	$1.37x10^5$ [(1.36-1.39)$x10^5$]	$1.69x10^{-3}$ [(1.68-1.70)$x10^{-3}$]	0.290 [0.289-0.290]	12.3 [12.2-12.5]	0.993
106	$6.04x10^4$ [(5.89-6.19)$x10^4$]	$4.94x10^{-3}$ [(4.87-5.02)$x10^{-3}$]	0.186 [0.184-0.187]	81.9 [79.5-84.2]	0.929
108	$5.18x10^3$ [(4.48-5.88)$x10^3$]	$3.86x10^{-3}$ [(3.79-3.93)$x10^{-3}$]	0.105 [0.096-0.114]	745 [643-848]	0.923
110	$1.56x10^4$ [(1.49-1.63)$x10^4$]	$4.22x10^{-3}$ [(4.13-4.31)$x10^{-3}$]	0.165 [0.162-0.168]	271 [258-285]	0.945
111	$5.38x10^4$ [(5.33-5.42)$x10^4$]	$7.45x10^{-4}$ [(7.38-7.51)$x10^{-4}$]	0.284 [0.284-0.285]	13.9 [13.7-14.0]	0.994
112	$1.09x10^5$ [(1.07-1.10)$x10^5$]	$6.15x10^{-4}$ [(6.08-6.23)$x10^{-4}$]	0.285 [0.284-0.286]	5.67 [5.58-5.76]	0.992
114	$5.24x10^4$ [(5.20-5.28)$x10^4$]	$4.35x10^{-3}$ [(4.33-4.36)$x10^{-3}$]	0.243 [0.242-0.243]	83.0 [82.3-83.6]	0.995
115	$8.48x10^3$ [(8.25-8.70)$x10^3$]	$5.26x10^{-3}$ [(5.24-5.29)$x10^{-3}$]	0.392 [0.385-0.398]	621 [604-638]	0.992
116	$1.28x10^5$ [(1.26-1.30)$x10^5$]	$3.35x10^{-3}$ [(3.33-3.37)$x10^{-3}$]	0.242 [0.241-0.243]	26.1 [25.8-26.5]	0.988
117	$1.67x10^5$ [(1.64-1.69)$x10^5$]	$3.95x10^{-3}$ [(3.92-3.98)$x10^{-3}$]	0.258 [0.257-0.259]	23.7 [23.3-24.1]	0.982
118	$6.03x10^4$ [(5.99-6.08)$x10^4$]	$2.01x10^{-3}$ [(2.00-2.02)$x10^{-3}$]	0.292 [0.291-0.292]	33.3 [33.1-33.6]	0.994
119	$3.20x10^4$ [(3.14-3.26)$x10^4$]	$2.55x10^{-3}$ [(2.53-2.56)$x10^{-3}$]	0.241 [0.240-0.242]	79.5 [77.9-81.1]	0.977
124	$1.73x10^4$ [(1.70-1.75)$x10^4$]	$9.00x10^{-4}$ [(8.94-9.07)$x10^{-4}$]	0.200 [0.199-0.201]	52.1 [51.3-53.0]	0.995
125	$4.32x10^4$ [(4.27-4.37)$x10^4$]	$1.29x10^{-4}$ [(1.24-1.35)$x10^{-4}$]	0.305 [0.304-0.305]	3.00 [2.86-3.14]	0.994
126	$8.99x10^4$ [(8.86-9.11)$x10^4$]	$8.71x10^{-3}$ [(8.63-8.78)$x10^{-3}$]	0.268 [0.267-0.269]	96.9 [95.3-98.5]	0.982
129	$1.21x10^4$ [(1.09-1.34)$x10^4$]	$2.76x10^{-2}$ [(2.70-2.81)$x10^{-2}$]	0.506 [0.464-0.547]	2272 [2029-2515]	0.959
131	$1.12x10^4$ [(1.10-1.15)$x10^4$]	$1.89x10^{-3}$ [(1.87-1.90)$x10^{-3}$]	0.176 [0.174-0.179]	168 [164-172]	0.989

Table E.7 continued from previous page

α2β3nb	k_a (M^{-1} s^{-1}) [95% CI]	k_d (s^{-1}) [95% CI]	R_{max} (nm) [95% CI]	K_D (nM) [95% CI]	R^2
132	5.04x10^4 [(4.82-5.25)x10^4]	9.82x10^{-4} [(9.57-1.01)x10^{-3}]	0.141 [0.140-0.142]	19.5 [18.5-20.5]	0.927
134	3.27x10^3 [(2.62-3.91)x10^3]	2.31x10^{-3} [(2.29-2.34)x10^{-3}]	0.190 [0.166-0.215]	708 [568-849]	0.937
136	6.41x10^4 [(6.34-6.49)x10^4]	5.68x10^{-3} [(5.65-5.72)x10^{-3}]	0.268 [0.267-0.269]	88.6 [87.5-89.8]	0.987
137	1.52x10^4 [(1.45-1.59)x10^4]	2.10x10^{-3} [(2.07-2.13)x10^{-3}]	0.402 [0.395-0.410]	139 [132-146]	0.944
139	7.76x10^4 [(7.64-7.88)x10^4]	1.67x10^{-3} [(1.65-1.69)x10^{-3}]	0.204 [0.203-0.205]	21.5 [21.1-22.0]	0.970
141	4.70x10^5 [(4.54-4.87)x10^5]	6.76x10^{-2} [(6.54-6.99)x10^{-2}]	0.221 [0.220-0.222]	144 [137-151]	0.974
144	5.43x10^4 [(5.33-5.53)x10^4]	1.67x10^{-3} [(1.66-1.68)x10^{-3}]	0.261 [0.260-0.262]	30.7 [30.1-31.3]	0.981
145	1.89x10^5 [(1.87-1.91)x10^5]	8.63x10^{-4} [(8.58-8.69)x10^{-4}]	0.300 [0.299-0.300]	4.58 [4.52-4.63]	0.995
146	5.60x10^5 [(5.56-5.64)x10^5]	2.76x10^{-4} [(2.72-2.80)x10^{-4}]	0.331 [0.331-0.331]	0.49 [0.48-0.50]	0.997
147	8.91x10^4 [(8.86-8.97)x10^4]	7.42x10^{-4} [(7.37-7.46)x10^{-4}]	0.280 [0.279-0.280]	8.32 [8.25-8.39]	0.997
148	5.19x10^4 [(5.05-5.32)x10^4]	1.32x10^{-3} [(1.29-1.35)x10^{-3}]	0.116 [0.115-0.117]	25.5 [24.6-26.4]	0.918
149	5.80x10^4 [(5.62-5.97)x10^4]	1.55x10^{-3} [(1.52-1.57)x10^{-3}]	0.121 [0.120-0.123]	26.7 [25.8-27.6]	0.915
150	4.39x10^4 [(4.33-4.45)x10^4]	1.23x10^{-3} [(1.22-1.24)x10^{-3}]	0.301 [0.300-0.302]	28.0 [27.6-28.4]	0.990
151	9.22x10^4 [(8.81-9.63)x10^4]	1.84x10^{-4} [(1.70-1.97)x10^{-4}]	0.138 [0.137-0.139]	1.99 [1.82-2.17]	0.968
152	4.89x10^5 [(4.82-4.97)x10^5]	1.42x10^{-3} [(1.41-1.44)x10^{-3}]	0.324 [0.323-0.325]	2.91 [2.86-2.96]	0.981
		Poor fits			
088	3.68x10^4 [(3.44-3.92)x10^4]	2.23x10^{-14} [ND]	0.000 [-0.001-0.001]	0.00 [ND]	0.286
089	6.82x10^4 [(6.47-7.16)x10^4]	2.22x10^{-14} [ND]	0.000 [-0.001-0.001]	0.00 [ND]	0.225
090	2.08x10^4 [(1.92-2.24)x10^4]	3.01x10^{-3} [(2.81-3.21)x10^{-3}]	0.041 [0.039-0.044]	145 [130-159]	0.580
091	5.02x10^4 [(4.76-5.27)x10^4]	2.24x10^{-14} [ND]	0.000 [-0.001-0.001]	0.00 [ND]	0.307
092	6.21x10^4 [(5.96-6.46)x10^4]	6.29x10^{-11} [ND]	0.012 [0.011-0.013]	0.00 [ND]	0.460
093	1.95x10^4 [(1.82-2.08)x10^4]	5.80x10^{-3} [(5.66-5.94)x10^{-3}]	0.157 [0.152-0.162]	298 [277-318]	0.799

Table E.7 continued from previous page

α2β3nb	k_a (M^{-1} s^{-1}) [95% CI]	k_d (s^{-1}) [95% CI]	R_{max} (nm) [95% CI]	K_D (nM) [95% CI]	R^2
094	3.19x10^{4} [(3.05-3.32)x10^{4}]	1.18x10^{-10} [ND]	0.017 [0.016-0.018]	0.00 [ND]	0.703
095	2.24x10^{4} [(2.15-2.32)x10^{4}]	1.65x10^{-3} [(1.61-1.68)x10^{-3}]	0.087 [0.086-0.088]	73.7 [70.6-76.9]	0.896
096	1.97x10^{2} [(-2.00-2.39)x10^{3}]	3.05x10^{-3} [(2.91-3.20)x10^{-3}]	0.593 [-6.084-7.270]	1.55x10^{4} [(-1.57-1.88)x10^{5}]	0.655
098	9.14x10^{2} [(-1.15-2.98)x10^{3}]	2.09x10^{-5} [(-6.49-1.07)x10^{-4}]	0.137 [-0.248-0.522]	22.9 [-84.4-130.2]	0.844
099	5.55x10^{4} [(5.16-5.95)x10^{4}]	8.48x10^{-3} [(8.19-8.77)x10^{-3}]	0.067 [0.066-0.068]	153 [141-165]	0.805
100	5.64x10^{3} [(3.16-8.12)x10^{3}]	4.42x10^{-14} [ND]	0.000 [-0.012-0.012]	0.00 [ND]	0.588
101	5.59x10^{4} [(5.37-5.81)x10^{4}]	1.79x10^{-10} [ND]	0.028 [0.027-0.030]	0.00 [ND]	0.557
105	4.30x10^{2} [(-2.56-3.42)x10^{3}]	1.68x10^{-9} [ND]	0.079 [-0.556-0.713]	0.00 [ND]	0.419
107	1.67x10^{4} [(1.60-1.74)x10^{4}]	2.22x10^{-3} [(2.18-2.25)x10^{-3}]	0.080 [0.079-0.081]	133 [126-139]	0.913
109	1.15x10^{3} [(4.08-1.88)x10^{3}]	2.62x10^{-3} [(2.58-2.66)x10^{-3}]	0.165 [0.057-0.273]	2.29x10^{3} [(8.14-3.76)x10^{3}]	0.880
113	7.64x10^{4} [(7.16-8.11)x10^{4}]	5.14x10^{-3} [(4.75-5.52)x10^{-3}]	0.037 [0.036-0.038]	67.3 [60.7-73.8]	0.699
120	5.26x10^{1} [(-1.19-1.30)x10^{3}]	8.04x10^{-3} [(7.83-8.25)x10^{-3}]	6.360 [-143.631-156.351]	1.53x10^{5} [(-3.47-3.77)x10^{6}]	0.883
121	3.69x10^{1} [(-1.96-2.03)x10^{3}]	3.32x10^{-3} [(2.99-3.66)x10^{-3}]	3.699 [-196.256-203.654]	9.02x10^{4} [(-4.79-4.97)x10^{6}]	0.663
122	4.53x10^{2} [(2.43-6.64)x10^{2}]	1.78x10^{-3} [(1.57-2.00)x10^{-3}]	0.000 [ND]	3.94x10^{3} [(2.05-5.83)x10^{3}]	0.997
123	1.99x10^{4} [(1.93-2.06)x10^{4}]	1.05x10^{-3} [(1.02-1.08)x10^{-3}]	0.073 [0.072-0.073]	52.7 [50.5-55.0]	0.934
127	3.27x10^{-9} [ND]	1.12x10^{-2} [(1.03-1.22)x10^{-2}]	0.000 [ND]	3.43x10^{15} [ND]	0.108
128	2.32x10^{2} [(-2.39-2.86)x10^{3}]	1.05x10^{-12} [ND]	0.278 [-3.048-3.604]	0.00 [ND]	0.777
130	7.33x10^{1} [(-1.74-1.89)x10^{3}]	1.14x10^{-2} [(1.09-1.19)x10^{-2}]	7.292 [-172.310-186.895]	1.56x10^{5} [(-3.70-4.02)x10^{6}]	0.843
133	9.08x10^{3} [(8.20-9.97)x10^{3}]	1.25x10^{-3} [(1.22-1.28)x10^{-3}]	0.058 [0.056-0.059]	138 [124-151]	0.914
135	2.67x10^{4} [(2.54-2.81)x10^{4}]	1.88x10^{-3} [(1.84-1.92)x10^{-3}]	0.048 [0.048-0.049]	70.2 [66.4-74.0]	0.869
138	2.42x10^{4} [(2.35-2.49)x10^{4}]	7.89x10^{-4} [(7.72-8.06)x10^{-4}]	0.063 [0.062-0.063]	32.6 [31.5-33.8]	0.968
140	4.16x10^{4} [(4.06-4.25)x10^{4}]	7.75x10^{-4} [(7.47-8.03)x10^{-4}]	0.060 [0.059-0.060]	18.6 [17.8-19.4]	0.954

Table E.7 continued from previous page

α2β3nb	k_a ($M^{-1}\,s^{-1}$) [95% CI]	k_d (s^{-1}) [95% CI]	R_{max} (nm) [95% CI]	K_D (nM) [95% CI]	R^2
142	$1.01x10^4$ $[(9.46\text{-}1.08)x10^4]$	$8.69x10^{-9}$ [ND]	0.087 [0.084-0.089]	0.00 [ND]	0.966
143	$5.32x10^6$ $[(4.40\text{-}6.23)x10^6]$	$2.17x10^{-3}$ $[(2.07\text{-}2.27)x10^{-3}]$	0.020 [0.020-0.020]	0.41 [0.34-0.48]	0.181

Table E.8: Investigating α3β3nb-$GABA_AR$ binding in the presence of 10 μM gabazine by kinetic titration using BLI: results of fits from MATLAB

α3β3nb	k_a (M^{-1} s^{-1}) [95% CI]	k_d (s^{-1}) [95% CI]	R_{max} (nm) [95% CI]	K_D (nM) [95% CI]	R^2
156	$6.57x10^5$ [(6.51-6.64)$x10^5$]	$7.37x10^{-4}$ [(7.28-7.47)$x10^{-4}$]	0.299 [0.298-0.299]	1.12 [1.10-1.14]	0.989
156	$4.76x10^5$ [(4.72-4.81)$x10^5$]	$9.06x10^{-4}$ [(8.98-9.15)$x10^{-4}$]	0.314 [0.314-0.315]	1.90 [1.88-1.93]	0.992
157	$2.50x10^5$ [(2.46-2.54)$x10^5$]	$1.04x10^{-4}$ [(9.55-1.12)$x10^{-4}$]	0.337 [0.336-0.338]	0.42 [0.38-0.45]	0.987
158	$2.58x10^5$ [(2.54-2.62)$x10^5$]	$9.54x10^{-4}$ [(9.43-9.65)$x10^{-4}$]	0.308 [0.308-0.309]	3.70 [3.63-3.76]	0.987
159	$2.77x10^5$ [(2.72-2.82)$x10^5$]	$9.46x10^{-4}$ [(9.29-9.63)$x10^{-4}$]	0.325 [0.323-0.326]	3.42 [3.33-3.51]	0.973
160	$4.33x10^6$ [(4.03-4.63)$x10^6$]	$3.68x10^{-2}$ [(3.43-3.92)$x10^{-2}$]	0.323 [0.321-0.325]	8.49 [7.68-9.31]	0.936
161	$1.73x10^5$ [(1.71-1.75)$x10^5$]	$1.15x10^{-3}$ [(1.15-1.16)$x10^{-3}$]	0.256 [0.256-0.257]	6.67 [6.58-6.76]	0.993
167	$3.89x10^5$ [(3.77-4.01)$x10^5$]	$1.67x10^{-2}$ [(1.63-1.71)$x10^{-2}$]	0.252 [0.251-0.254]	43 [41-45]	0.933
168	$4.21x10^5$ [(4.10-4.33)$x10^5$]	$1.42x10^{-3}$ [(1.39-1.45)$x10^{-3}$]	0.278 [0.276-0.279]	3.36 [3.25-3.48]	0.928
169	$2.15x10^5$ [(2.06-2.24)$x10^5$]	$1.06x10^{-1}$ [(1.02-1.10)$x10^{-1}$]	0.281 [0.278-0.284]	492 [464-519]	0.978
170	$2.51x10^5$ [(2.46-2.55)$x10^5$]	$2.25x10^{-3}$ [(2.23-2.27)$x10^{-3}$]	0.281 [0.280-0.282]	8.97 [8.78-9.16]	0.972
171	$2.16x10^5$ [(2.07-2.25)$x10^5$]	$4.07x10^{-2}$ [(3.91-4.23)$x10^{-2}$]	0.322 [0.319-0.325]	188 [177-199]	0.924
175	$5.99x10^5$ [(5.88-6.09)$x10^5$]	$1.30x10^{-3}$ [(1.28-1.32)$x10^{-3}$]	0.270 [0.269-0.271]	2.17 [2.12-2.22]	0.967
176	$7.06x10^4$ [(6.90-7.21)$x10^4$]	$3.75x10^{-3}$ [(3.70-3.80)$x10^{-3}$]	0.292 [0.290-0.293]	53 [52-54]	0.942
177	$2.17x10^5$ [(2.12-2.21)$x10^5$]	$1.62x10^{-3}$ [(1.60-1.64)$x10^{-3}$]	0.293 [0.291-0.294]	7.47 [7.30-7.65]	0.965
179	$9.26x10^4$ [(8.81-9.72)$x10^4$]	$5.87x10^{-2}$ [(5.68-6.06)$x10^{-2}$]	0.346 [0.339-0.352]	634 [597-671]	0.950
181	$2.23x10^4$ [(2.15-2.32)$x10^4$]	$2.58x10^{-3}$ [(2.54-2.63)$x10^{-3}$]	0.327 [0.323-0.330]	116 [111-121]	0.929
189	$8.30x10^5$ [(8.24-8.36)$x10^5$]	$1.74x10^{-4}$ [(1.69-1.79)$x10^{-4}$]	0.341 [0.341-0.341]	0.21 [0.20-0.22]	0.995
191	$4.87x10^5$ [(4.78-4.96)$x10^5$]	$2.71x10^{-3}$ [(2.67-2.74)$x10^{-3}$]	0.293 [0.292-0.294]	5.55 [5.43-5.68]	0.960
195	$1.93x10^3$ [(7.26-3.13)$x10^3$]	$1.74x10^{-4}$ [(1.53-1.96)$x10^{-4}$]	0.112 [0.061-0.162]	90 [33-148]	0.936
197	$4.39x10^5$ [(4.32-4.47)$x10^5$]	$1.04x10^{-3}$ [(1.03-1.06)$x10^{-3}$]	0.302 [0.301-0.303]	2.38 [2.32-2.43]	0.973

Table E.8 continued from previous page

α3β3nb	k_a (M^{-1} s^{-1}) [95% CI]	k_d (s^{-1}) [95% CI]	R_{max} (nm) [95% CI]	K_D (nM) [95% CI]	R^2
199	1.72x10^{5} [(1.69-1.74)x10^{5}]	1.63x10^{-2} [(1.61-1.64)x10^{-2}]	0.299 [0.298-0.300]	95 [93-96]	0.985
200	3.07x10^{4} [(2.96-3.18)x10^{4}]	5.97x10^{-3} [(5.81-6.13)x10^{-3}]	0.120 [0.119-0.122]	194 [186-203]	0.916
206	3.99x10^{5} [(3.90-4.07)x10^{5}]	1.27x10^{-3} [(1.26-1.29)x10^{-3}]	0.285 [0.284-0.286]	3.19 [3.11-3.27]	0.967
			Poor fits		
153	4.22x10^{5} [(4.19-4.24)x10^{5}]	7.32x10^{-9} [ND]	0.283 [0.283-0.284]	1.7355x10^{-5} [ND]	0.997
154	4.01x10^{2} [(-2.28-3.08)x10^{3}]	2.32x10^{-14} [ND]	0.064 [-0.258-0.386]	5.7947x10^{-8} [ND]	0.829
155	1.34x10^{4} [(1.13-1.54)x10^{4}]	4.39x10^{-14} [ND]	0.069 [0.067-0.070]	3.28088x10^{-9} [ND]	0.885
162	1.23x10^{4} [(1.04-1.41)x10^{4}]	3.62x10^{-14} [ND]	0.009 [0.008-0.010]	2.95477x10^{-9} [ND]	0.821
163	3.32x10^{4} [(2.79-3.84)x10^{4}]	3.38x10^{-3} [(3.13-3.63)x10^{-3}]	0.000 [ND]	102 [84-120]	0.418
164	7.16x10^{3} [(4.50-9.82)x10^{3}]	2.62x10^{-14} [ND]	0.001 [-0.006-0.007]	3.66195x10^{-9} [ND]	0.729
165	1.23x10^{4} [(1.19-1.27)x10^{4}]	1.52x10^{-11} [ND]	0.000 [ND]	1.23688x10^{-6} [ND]	0.643
166	1.46x10^{4} [(1.35-1.58)x10^{4}]	4.31x10^{-4} [(3.78-4.84)x10^{-4}]	0.032 [0.031-0.032]	29 [25-34]	0.896
172	1.85x10^{2} [(-1.54-1.91)x10^{3}]	3.27x10^{-3} [(3.00-3.54)x10^{-3}]	2 [-12-15]	1.77x10^{4} [(-1.47-1.83)x10^{5}]	0.764
173	5.26x10^{4} [(5.09-5.42)x10^{4}]	6.58x10^{-3} [(6.43-6.74)x10^{-3}]	0.313 [0.310-0.316]	125 [120-130]	0.898
174	1.90x10^{4} [(1.82-1.98)x10^{4}]	1.31x10^{-11} [ND]	0.067 [0.067-0.068]	6.92041x10^{-7} [ND]	0.974
178	1.03x10^{5} [(1.01-1.04)x10^{5}]	2.34x10^{-14} [ND]	0.290 [0.289-0.291]	2.27907x10^{-10} [ND]	0.990
180	6.96x10^{4} [(6.76-7.16)x10^{4}]	2.15x10^{-3} [(2.05-2.24)x10^{-3}]	0.272 [0.269-0.274]	31 [29-33]	0.879
182	3.93x10^{3} [(1.59-6.26)x10^{3}]	2.37x10^{-14} [ND]	0.000 [-0.031-0.031]	6.02534x10^{-9} [ND]	0.698
183	6.16x10^{4} [(5.83-6.50)x10^{4}]	2.31x10^{-2} [(2.22-2.41)x10^{-2}]	0.270 [0.265-0.274]	375 [349-401]	0.889
184	6.49x10^{5} [(6.32-6.66)x10^{5}]	3.78x10^{-4} [(3.61-3.95)x10^{-4}]	0.440 [0.438-0.441]	0.58 [0.55-0.61]	0.894
185	1.35x10^{6} [(1.30-1.39)x10^{6}]	1.10x10^{-10} [ND]	0.065 [0.064-0.065]	8.1472x10^{-8} [ND]	0.806
186	1.10x10^{5} [(1.05-1.14)x10^{5}]	1.79x10^{-2} [(1.73-1.85)x10^{-2}]	0.320 [0.316-0.323]	163 [155-172]	0.864

Table E.8 continued from previous page

α3β3nb	k_a ($M^{-1}\,s^{-1}$) [95% CI]	k_d (s^{-1}) [95% CI]	R_{max} (nm) [95% CI]	K_D (nM) [95% CI]	R^2
187	$2.46x10^5$ [$(2.39\text{-}2.54)x10^5$]	$3.97x10^{-3}$ [$(3.90\text{-}4.05)x10^{-3}$]	0.338 [0.336-0.341]	16 [16-17]	0.897
188	$5.25x10^4$ [$(5.07\text{-}5.43)x10^4$]	$3.50x10^{-3}$ [$(3.44\text{-}3.57)x10^{-3}$]	0.215 [0.213-0.217]	67 [64-69]	0.837
190	$3.22x10^5$ [$(3.13\text{-}3.32)x10^5$]	$2.26x10^{-3}$ [$(2.20\text{-}2.32)x10^{-3}$]	0.298 [0.297-0.300]	7.02 [6.74-7.30]	0.884
192	$3.63x10^4$ [$(3.42\text{-}3.83)x10^4$]	$8.39x10^{-4}$ [$(7.94\text{-}8.84)x10^{-4}$]	0.021 [0.021-0.021]	23 [21-25]	0.844
193	$1.43x10^3$ [$(-2.77\text{-}3.13)x10^3$]	$2.89x10^{-12}$ [ND]	0.089 [0.022-0.155]	$2.02596x10^{-6}$ [ND]	0.895
194	$1.85x10^4$ [$(1.51\text{-}2.20)x10^4$]	$2.43x10^{-14}$ [ND]	0.031 [0.030-0.032]	$1.31314x10^{-9}$ [ND]	0.856
196	$6.85x10^4$ [$(6.66\text{-}7.04)x10^4$]	$2.10x10^{-3}$ [$(2.05\text{-}2.16)x10^{-3}$]	0.273 [0.271-0.276]	31 [30-32]	0.858
198	$1.55x10^5$ [$(1.50\text{-}1.59)x10^5$]	$3.85x10^{-3}$ [$(3.76\text{-}3.94)x10^{-3}$]	0.340 [0.338-0.343]	25 [24-26]	0.893
201	$2.69x10^4$ [$(2.58\text{-}2.81)x10^4$]	$5.91x10^{-3}$ [$(5.81\text{-}6.02)x10^{-3}$]	0.087 [0.086-0.089]	220 [210-230]	0.903
202	$8.59x10^4$ [$(8.13\text{-}9.06)x10^4$]	$2.44x10^{-2}$ [$(2.33\text{-}2.55)x10^{-2}$]	0.260 [0.256-0.264]	284 [264-304]	0.848
203	$5.91x10^3$ [$(5.02\text{-}6.81)x10^3$]	$2.74x10^{-14}$ [ND]	0.065 [0.060-0.069]	$4.63977x10^{-9}$ [ND]	0.947
204	$1.74x10^4$ [$(1.63\text{-}1.85)x10^4$]	$2.75x10^{-11}$ [ND]	0.061 [0.060-0.061]	$1.58219x10^{-6}$ [ND]	0.901
205	$1.18x10^5$ [$(1.15\text{-}1.22)x10^5$]	$4.26x10^{-3}$ [$(4.16\text{-}4.36)x10^{-3}$]	0.399 [0.396-0.402]	36 [35-37]	0.877

Table E.9: Results of ionflux screen for positive modulation: fold-change from EC_{10} GABA dose (FC), standard deviation (SD) and number of recordings for each (n)

nb	100 nM nb			300 uM nb			1 uM nb			3 uM nb			10 uM nb		
	FC	SD	n	FC	SD	n	FC	SD	n	FC	SD	n	FC	SD	n
095	0.95	0.07	6	0.73	0.12	6	1.01	0.43	6	1.67	0.18	6	2.26	0.44	6
099	0.92	0.09	6	0.95	0.11	6	0.75	0.15	6	0.83	0.34	6	1.15	0.18	6
100	1.02	0.16	4	1.23	0.34	4	0.98	0.12	4	1.22	0.19	4	1.49	0.23	4
102	0.86	0.01	2	0.78	0.04	2	0.70	0.01	2	0.54	0.02	2	0.56	0.05	2
103	0.86	0.06	2	0.78	0.02	2	0.73	0.05	2	0.62	0.08	2	0.61	0.12	2
106	0.84	0.06	2	0.82	0.00	2	0.76	0.08	2	0.67	0.06	2	0.69	0.05	2
108	0.87	0.04	2	0.87	0.13	2	0.70	0.01	2	0.74	0.09	2	0.90	0.10	2
111	0.94	0.01	2	ND	ND	ND	-0.80	ND	1	1.43	ND	1	1.55	ND	1
112	0.88	ND	1	ND	ND	ND	0.65	0.05	2	0.72	0.30	2	0.77	0.38	2
113	0.89	0.02	2	1.32	0.15	2	0.76	0.09	2	0.98	0.15	2	1.35	0.34	2
114	0.85	0.09	2	0.81	0.11	2	0.67	0.04	2	0.73	0.09	2	0.86	0.11	2
116	0.87	0.06	2	0.80	0.01	2	0.74	0.02	2	0.84	0.08	2	0.97	0.09	2
117	0.91	ND	1	0.83	0.05	2	0.71	0.08	2	0.71	0.16	2	0.84	0.02	2
118	0.86	ND	1	0.86	0.10	2	0.79	ND	1	0.65	ND	1	0.87	ND	1
119	0.83	ND	1	0.96	ND	1	0.73	0.20	2	0.60	0.39	2	0.51	0.45	2
120	0.90	0.07	2	0.78	0.06	2	0.97	0.37	2	0.50	0.04	2	0.49	0.00	2
121	0.91	0.01	2	0.79	ND	1	0.58	0.12	2	0.62	0.22	2	0.82	0.23	2
122	0.96	0.10	2	0.87	0.07	2	0.84	ND	1	0.90	ND	1	1.04	ND	1
123	1.01	0.03	2	0.89	0.03	2	0.70	0.07	2	0.73	0.11	2	1.00	0.12	2
125	1.32	ND	1	1.05	ND	1	0.90	ND	1	0.75	ND	1	0.90	ND	1
130	0.86	0.03	2	0.78	0.05	2	0.62	0.09	2	0.51	0.07	2	0.59	0.07	2
131	0.91	0.02	2	0.87	0.00	2	0.72	0.12	2	0.62	0.07	2	0.61	0.08	2
132	0.84	0.16	2	0.85	0.02	2	0.71	0.02	2	0.67	0.06	2	0.69	0.12	2
133	0.87	0.01	2	0.75	0.11	2	0.75	0.08	2	0.71	0.01	2	0.96	0.02	2
134	1.12	0.12	2	0.80	0.17	2	0.89	ND	1	0.97	ND	1	1.32	ND	1
136	0.92	0.13	2	0.96	0.14	2	0.73	0.10	2	0.78	0.12	2	0.94	0.10	2
142	0.83	0.03	2	0.78	0.11	2	0.73	ND	1	0.55	ND	1	0.30	ND	1
144	0.94	0.04	2	0.92	0.02	2	0.79	0.13	2	0.66	0.11	2	0.55	0.13	2
145	0.82	ND	1	0.85	ND	1	0.86	0.23	2	-0.27	1.46	2	-0.57	2.16	2
146	0.89	0.11	2	0.91	0.24	2	0.72	ND	1	0.78	ND	1	0.89	ND	1
148	0.96	0.08	4	0.84	0.15	4	0.91	0.05	4	1.89	0.25	4	2.64	0.71	4
149	ND	ND	ND	ND	ND	ND	1.96	1.07	2	1.42	0.38	2	1.37	0.23	2
150	ND	ND	ND	0.90	ND	1	1.47	ND	1	1.94	ND	1	2.28	ND	1
154	ND	ND	ND	ND	ND	ND	1.33	0.10	2	1.37	0.11	2	1.65	0.05	2
161	1.49	0.22	2	0.95	0.05	2	1.14	0.04	2	1.11	0.16	2	1.22	0.11	2
170	1.00	0.00	1	0.91	0.00	1	1.79	0.35	2	1.44	0.10	2	2.06	0.44	2
172	1.09	0.09	4	1.24	0.55	4	1.30	0.31	4	2.14	0.68	4	3.15	1.18	4
173	2.66	0.15	3	2.13	0.35	3	2.37	0.94	5	3.99	1.69	5	3.26	1.30	5
175	1.05	ND	1	1.02	ND	1	1.22	ND	1	1.06	ND	1	0.76	ND	1
176	1.25	ND	1	1.02	ND	1	1.46	0.17	2	1.53	0.15	2	1.56	0.25	2
177	0.94	0.07	2	0.92	0.12	2	1.14	0.05	2	1.24	0.18	2	1.28	0.31	2

Table E.9 continued from previous page

nb	100 nM nb			300 uM nb			1 uM nb			3 uM nb			10 uM nb		
	FC	SD	n	FC	SD	n	FC	SD	n	FC	SD	n	FC	SD	n
183	1.26	0.28	6	2.83	2.44	6	1.90	0.45	6	3.19	0.98	6	4.29	1.50	6
184	1.41	0.00	1	1.43	0.00	1	1.20	0.05	2	1.50	0.05	2	1.41	0.02	2
186	1.12	0.37	2	1.37	0.34	2	1.27	0.01	2	1.24	0.06	2	1.22	0.25	2
189	1.28	0.00	1	1.09	0.35	2	1.15	0.08	2	1.22	0.33	2	1.27	0.45	2
190	1.16	0.32	5	1.14	0.38	5	1.21	0.36	5	1.75	0.71	5	1.77	0.32	5
191	1.22	0.16	2	0.82	0.01	2	1.09	ND	1	1.67	ND	1	1.92	ND	1
197	1.08	ND	1	1.16	ND	1	1.05	ND	1	1.46	ND	1	1.40	ND	1
206	0.99	ND	1	ND	ND	ND	1.12	0.03	2	1.33	0.03	2	1.41	0.11	2
							Poor data								
101	1.01	ND	1	0.08	0.00	2	ND	ND	ND	ND	ND	ND	ND	ND	ND
105	4.89	ND	1	ND	ND	0	ND	ND	ND	ND	ND	ND	ND	ND	ND
110	ND	ND	0	ND	ND	0	ND	ND	ND	ND	ND	ND	ND	ND	ND
128	ND	ND	0	ND	ND	0	ND	ND	ND	ND	ND	ND	ND	ND	ND
147	1.03	0.16	2	ND	ND	0	ND	ND	ND	ND	ND	ND	ND	ND	ND
153	ND	ND	0	ND	ND	0	ND	ND	ND	ND	ND	ND	ND	ND	ND
157	ND	ND	0	ND	ND	0	ND	ND	ND	ND	ND	ND	ND	ND	ND
158	ND	ND	0	ND	ND	0	ND	ND	ND	ND	ND	ND	ND	ND	ND
160	1.22	0.48	2	1.33	ND	1	ND	ND	ND	ND	ND	ND	ND	ND	ND
181	1.03	0.04	2	1.03	0.01	2	ND	ND	ND	ND	ND	ND	ND	ND	ND
187	1.05	0.00	1	1.24	0.19	2	ND	ND	ND	ND	ND	ND	ND	ND	ND
188	0.70	0.00	1	1.44	ND	1	ND	ND	ND	ND	ND	ND	ND	ND	ND
196	ND	ND	0	ND	ND	0	ND	ND	ND	ND	ND	ND	ND	ND	ND

Table E.10: Lysate FSEC results comparing mV-β3-1D4 expression using BacMam and a stable cell line in various conditions

Rank	Expression system	VPA (mM)	Sodium butyrate (mM)	Temperature (°C)	Time (hours)	MOI	Doxycycline concentration (mg ml^{-1})	Peak Height (AU)	Elution time (min)
91	Stable	0	0	30	24	-	0	5.34E+03	23.6
33	Stable	0	0	30	24	-	5	9.34E+04	23.8
34	Stable	0	0	30	24	-	10	9.08E+04	23.8
61	Stable	0	0	30	48	-	0	9.28E+03	23.9
14	Stable	0	0	30	48	-	5	1.77E+05	23.8
15	Stable	0	0	30	48	-	10	1.74E+05	23.8
64	Stable	0	0	30	72	-	0	9.08E+03	23.8
9	Stable	0	0	30	72	-	5	2.01E+05	23.8
6	Stable	0	0	30	72	-	10	2.16E+05	23.8
78	Stable	0	0	37	24	-	0	6.58E+03	23.8
7	Stable	0	0	37	24	-	5	2.08E+05	23.8
11	Stable	0	0	37	24	-	10	1.89E+05	23.8
58	Stable	0	0	37	48	-	0	9.53E+03	23.8
2	Stable	0	0	37	48	-	5	2.56E+05	23.7
3	Stable	0	0	37	48	-	10	2.41E+05	23.8
50	Stable	0	0	37	72	-	0	1.25E+04	23.6
1	Stable	0	0	37	72	-	5	2.58E+05	23.7
12	Stable	0	0	37	72	-	10	1.88E+05	23.8
71	Stable	0	5	30	24	-	0	7.46E+03	24.0
31	Stable	0	5	30	24	-	5	1.31E+05	23.8
37	Stable	0	5	30	24	-	10	6.09E+04	23.8
57	Stable	0	5	30	48	-	0	9.81E+03	23.9
10	Stable	0	5	30	48	-	5	2.01E+05	23.8
8	Stable	0	5	30	48	-	10	2.01E+05	23.7
65	Stable	0	5	30	72	-	0	9.07E+03	24.1
5	Stable	0	5	30	72	-	5	2.17E+05	23.8
4	Stable	0	5	30	72	-	10	2.26E+05	23.8
92	Stable	0	5	37	24	-	0	5.28E+03	24.0
17	Stable	0	5	37	24	-	5	1.71E+05	23.8
18	Stable	0	5	37	24	-	10	1.71E+05	23.8
80	Stable	0	5	37	48	-	0	6.50E+03	23.7
20	Stable	0	5	37	48	-	5	1.69E+05	23.8
13	Stable	0	5	37	48	-	10	1.82E+05	23.7
83	Stable	0	5	37	72	-	0	6.00E+03	23.9
27	Stable	0	5	37	72	-	5	1.46E+05	23.8
30	Stable	0	5	37	72	-	10	1.35E+05	23.8
84	Stable	5	0	30	24	-	0	5.97E+03	23.8
35	Stable	5	0	30	24	-	5	8.05E+04	23.8
25	Stable	5	0	30	24	-	10	1.55E+05	23.9
70	Stable	5	0	30	48	-	0	7.89E+03	23.8
29	Stable	5	0	30	48	-	5	1.36E+05	23.8
32	Stable	5	0	30	48	-	10	1.23E+05	23.8

Table E.10 continued from previous page

Rank	Expression system	VPA (mM)	Sodium butyrate (mM)	Temperature (°C)	Time (hours)	MOI	Doxycycline concentration (mg ml^{-1})	Peak Height (AU)	Elution time (min)
74	Stable	5	0	30	72	-	0	7.06E+03	23.8
24	Stable	5	0	30	72	-	5	1.59E+05	23.8
28	Stable	5	0	30	72	-	10	1.42E+05	23.8
96	Stable	5	0	37	24	-	0	5.18E+03	24.1
22	Stable	5	0	37	24	-	5	1.68E+05	23.8
19	Stable	5	0	37	24	-	10	1.71E+05	23.8
99	Stable	5	0	37	48	-	0	5.01E+03	23.6
21	Stable	5	0	37	48	-	5	1.68E+05	23.8
16	Stable	5	0	37	48	-	10	1.74E+05	23.8
90	Stable	5	0	37	72	-	0	5.40E+03	23.4
23	Stable	5	0	37	72	-	5	1.60E+05	23.8
26	Stable	5	0	37	72	-	10	1.50E+05	23.8
114	BacMam	0	0	30	24	0	-	4.15E+03	24.0
117	BacMam	0	0	30	24	1	-	3.96E+03	23.8
120	BacMam	0	0	30	24	4	-	3.73E+03	24.1
123	BacMam	0	0	30	24	10	-	3.58E+03	24.2
125	BacMam	0	0	30	48	0	-	3.47E+03	24.0
102	BacMam	0	0	30	48	1	-	4.83E+03	24.0
94	BacMam	0	0	30	48	4	-	5.24E+03	24.1
81	BacMam	0	0	30	48	10	-	6.46E+03	24.1
118	BacMam	0	0	30	72	0	-	3.83E+03	25.0
108	BacMam	0	0	30	72	1	-	4.33E+03	24.0
106	BacMam	0	0	30	72	4	-	4.47E+03	23.9
93	BacMam	0	0	30	72	10	-	5.25E+03	23.6
82	BacMam	0	0	37	24	0	-	6.04E+03	23.9
101	BacMam	0	0	37	24	1	-	4.96E+03	24.2
89	BacMam	0	0	37	24	4	-	5.45E+03	23.8
72	BacMam	0	0	37	24	10	-	7.26E+03	23.8
88	BacMam	0	0	37	48	0	-	5.54E+03	23.7
79	BacMam	0	0	37	48	1	-	6.57E+03	24.4
68	BacMam	0	0	37	48	4	-	8.34E+03	23.9
59	BacMam	0	0	37	48	10	-	9.42E+03	24.0
87	BacMam	0	0	37	72	0	-	5.61E+03	23.9
76	BacMam	0	0	37	72	1	-	6.88E+03	23.9
75	BacMam	0	0	37	72	4	-	6.97E+03	23.9
62	BacMam	0	0	37	72	10	-	9.22E+03	24.0
107	BacMam	0	5	30	24	0	-	4.45E+03	24.1
113	BacMam	0	5	30	24	1	-	4.16E+03	23.9
52	BacMam	0	5	30	24	4	-	1.23E+04	24.2
69	BacMam	0	5	30	24	10	-	8.04E+03	24.0
109	BacMam	0	5	30	48	0	-	4.33E+03	24.3
73	BacMam	0	5	30	48	1	-	7.17E+03	24.0
43	BacMam	0	5	30	48	4	-	1.99E+04	23.9
41	BacMam	0	5	30	48	10	-	3.34E+04	23.9

Table E.10 continued from previous page

Rank	Expression system	VPA (mM)	Sodium butyrate (mM)	Temperature (°C)	Time (hours)	MOI	Doxycycline concentration (mg ml^{-1})	Peak Height (AU)	Elution time (min)
124	BacMam	0	5	30	72	0	-	3.56E+03	24.0
51	BacMam	0	5	30	72	1	-	1.23E+04	24.0
39	BacMam	0	5	30	72	4	-	3.52E+04	23.9
36	BacMam	0	5	30	72	10	-	6.13E+04	23.9
105	BacMam	0	5	37	24	0	-	4.74E+03	23.7
67	BacMam	0	5	37	24	1	-	8.46E+03	23.8
48	BacMam	0	5	37	24	4	-	1.48E+04	23.7
40	BacMam	0	5	37	24	10	-	3.39E+04	23.6
115	BacMam	0	5	37	48	0	-	4.09E+03	23.9
66	BacMam	0	5	37	48	1	-	9.00E+03	23.8
44	BacMam	0	5	37	48	4	-	1.87E+04	23.9
38	BacMam	0	5	37	48	10	-	3.80E+04	23.9
98	BacMam	0	5	37	72	0	-	5.02E+03	24.2
55	BacMam	0	5	37	72	1	-	9.92E+03	23.7
47	BacMam	0	5	37	72	4	-	1.57E+04	23.9
42	BacMam	0	5	37	72	10	-	2.73E+04	23.9
126	BacMam	5	0	30	24	0	-	2.98E+03	23.7
116	BacMam	5	0	30	24	1	-	4.08E+03	24.2
121	BacMam	5	0	30	24	4	-	3.73E+03	23.7
104	BacMam	5	0	30	24	10	-	4.74E+03	23.7
119	BacMam	5	0	30	48	0	-	3.73E+03	24.9
112	BacMam	5	0	30	48	1	-	4.24E+03	24.2
97	BacMam	5	0	30	48	4	-	5.08E+03	24.0
63	BacMam	5	0	30	48	10	-	9.12E+03	23.8
122	BacMam	5	0	30	72	0	-	3.59E+03	24.3
95	BacMam	5	0	30	72	1	-	5.23E+03	24.0
77	BacMam	5	0	30	72	4	-	6.68E+03	24.0
49	BacMam	5	0	30	72	10	-	1.44E+04	24.0
111	BacMam	5	0	37	24	0	-	4.29E+03	24.3
100	BacMam	5	0	37	24	1	-	4.99E+03	23.8
60	BacMam	5	0	37	24	4	-	9.40E+03	23.5
45	BacMam	5	0	37	24	10	-	1.67E+04	23.7
110	BacMam	5	0	37	48	0	-	4.30E+03	23.8
85	BacMam	5	0	37	48	1	-	5.88E+03	24.0
53	BacMam	5	0	37	48	4	-	1.11E+04	24.0
46	BacMam	5	0	37	48	10	-	1.66E+04	23.9
103	BacMam	5	0	37	72	0	-	4.79E+03	23.9
86	BacMam	5	0	37	72	1	-	5.85E+03	23.7
54	BacMam	5	0	37	72	4	-	1.00E+04	23.9
56	BacMam	5	0	37	72	10	-	9.91E+03	23.8

Table E.11: Optimisation of expression conditions for cell lines expressing heteromeric $GABA_A$Rs, ranked by peak height

Time (h)	VPA (mM)	Sodium butyrate (mM)	Doxycycline (ug/ml)	Peak height (AU)	Peak time (min)
FLAG-α2/β3/mEGFP-TEV-γ2L-1D4					
48	-	-	5	$7.64x10^3$	24.5
48	-	-	10	$7.08x10^3$	24.6
48	-	5	10	$6.13x10^3$	24.6
24	5	-	5	$6.08x10^3$	24.7
48	5	-	10	$5.89x10^3$	24.6
24	5	-	10	$5.87x10^3$	24.6
48	5	-	5	$5.75x10^3$	24.5
48	-	5	5	$5.56x10^3$	24.2
24	-	5	5	$5.52x10^3$	24.6
24	-	5	10	$4.69x10^3$	24.7
48	-	-	10	$3.81x10^3$	24.6
48	-	-	5	$3.66x10^3$	24.5
24	-	-	5	$3.29x10^3$	24.7
24	-	-	10	$3.28x10^3$	24.7
24	-	-	5	$2.75x10^3$	24.5
24	-	-	10	$2.59x10^3$	24.6
24	5	-	10	$2.33x10^3$	24.5
24	-	5	5	$2.06x10^3$	24.5
24	5	-	5	$1.97x10^3$	24.4
24	-	5	10	$1.93x10^3$	24.4
48	5	-	10	$1.24x10^3$	24.4
48	-	5	5	$1.20x10^3$	24.2
48	-	5	10	$1.17x10^3$	24.1
48	5	-	5	$1.09x10^3$	24.5
FLAG-α3/β3/mEGFP-TEV-γ2L-1D4					
48	-	-	5	$8.05x10^3$	24.5
48	5	-	10	$7.96x10^3$	24.5
48	-	-	10	$7.86x10^3$	24.5
48	-	5	5	$7.21x10^3$	24.5
48	5	-	5	$7.10x10^3$	24.5
24	5	-	5	$6.92x10^3$	24.3
48	-	5	10	$6.77x10^3$	24.4
24	-	5	5	$6.60x10^3$	24.5
24	5	-	10	$5.64x10^3$	24.4
24	-	5	10	$4.84x10^3$	24.4
24	-	-	5	$4.45x10^3$	24.4
48	-	-	5	$4.13x10^3$	24.3

Table E.11 continued from previous page

Time (h)	VPA (mM)	Sodium butyrate (mM)	Doxycycline (ug/ml)	Peak height (AU)	Peak time (min)
48	-	-	10	$3.82x10^3$	24.5
24	-	-	10	$3.04x10^3$	24.6
24	5	-	5	$2.60x10^3$	24.5
24	-	-	5	$2.57x10^3$	24.4
24	5	-	10	$2.44x10^3$	24.9
24	-	-	10	$2.32x10^3$	24.5
24	-	5	5	$1.87x10^3$	24.3
24	-	5	10	$1.83x10^3$	24.4
48	-	5	10	$1.64x10^3$	24.5
48	-	5	5	$1.36x10^3$	24.6
48	5	-	10	$1.29x10^3$	24.7
48	5	-	5	$1.19x10^3$	24.3

F
Published work

This appendix contains publications that were accepted during the course of this work, but not included in the main text.

The first was an investigation of the location of the neurosteroid binding site on the $GABA_AR$. In this investigation, we crystallised a homomeric $GABA_AR$, in which each subunit was a chimera of the β3 extracellular domain and the α5 transmembrane domain. The rationale for this chimera was that nanobodies were available that bound the β3 extracellular domain, which were believed act as crystallisation chaperones, whereas neurosteroid binding was likely to occur in the transmembrane domain of a homomer composed of α subunits. This chimera was created as part of a larger programme of work before my involvement in the project by Dr Paul Miller, who characterised these homomeric receptors and neurosteroid binding at them using a thermostability assay. My contribution to this work was expression, purification and crystallisation of this chimera, both in the presence of neurosteroids, as well as performing patch-clamp electrophysiology (Ionflux) to functionally characterise neurosteroid binding at the the chimeric $GABA_AR$, as well as point-mutated receptors. The work with the crystal structure of a neurosteroid-bound receptor occurred before the beginning of this DPhil course, with a preliminary structure presented in my MSc dissertation. However, since then the structure has been refined, and the work completed with the apo structure and the functional characterisation.

The second publication is a description of a protocol for the use of lentiviruses to create stable cell lines for protein expression. My contribution to this work was a comparison of this method with the BacMam method of protein expression by exploring the expression of the mVenus-β3-1D4 construct using both methods. This data is also presented in Section 4.4 of this thesis. I screened a number of expression conditions using lysate FSEC, and analysed the data using a Matlab script (detailed in Appendix D). I also provided this construct to Dr Jonathan Elegheert for further work (fluorescence microscopy and FACS).

ARTICLES

Structural basis for $GABA_A$ receptor potentiation by neurosteroids

Paul S Miller[1,5], Suzanne Scott[1,2,5], Simonas Masiulis[1,2], Luigi De Colibus[1], Els Pardon[3,4], Jan Steyaert[3,4] & A Radu Aricescu[1,2]

© 2017 Nature America, Inc., part of Springer Nature. All rights reserved.

Type A γ-aminobutyric acid receptors ($GABA_A$Rs) are the principal mediators of inhibitory neurotransmission in the human brain. Endogenous neurosteroids interact with $GABA_A$Rs to regulate acute and chronic anxiety and are potent sedative, analgesic, anticonvulsant and anesthetic agents. Their mode of binding and mechanism of receptor potentiation, however, remain unknown. Here we report crystal structures of a chimeric $GABA_A$R construct in apo and pregnanolone-bound states. The neurosteroid-binding site is mechanically coupled to the helices lining the ion channel pore and modulates the desensitization-gate conformation. We demonstrate that the equivalent site is responsible for physiological, heteromeric $GABA_A$R potentiation and explain the contrasting modulatory properties of 3α versus 3β neurosteroid epimers. These results illustrate how peripheral lipid ligands can regulate the desensitization gate of $GABA_A$Rs, a process of broad relevance to pentameric ligand-gated ion channels.

$GABA_A$Rs are pentameric ligand-gated ion channels (pLGICs)[1]. Binding of the neurotransmitter GABA to the extracellular domain (ECD) opens an intrinsic pore surrounded by a ring of five M2 transmembrane domain (TMD) helices, one from each subunit, to permit the passage of negatively charged chloride ions[2]. The pore-opening event is subject to modulation by endogenous ligands such as Zn^{2+} and neurosteroids, including pregnanolone and its 5α epimer allopregnanolone[3]. Through their modulation of $GABA_A$Rs, neurosteroids are key regulators of the stress response and anxiety[4–6]. During the ovarian cycle, fluctuations in neurosteroid levels impact the $GABA_A$R inhibitory drive affecting neuronal excitability, thereby raising susceptibility to seizure and anxiety[7]. Changes to $GABA_A$R subunit expression levels in the dentate gyrus due to fluctuating neurosteroid concentrations are linked to postpartum depression following pregnancy[8]. Most $GABA_A$Rs in the human brain are heteromers, typically comprising two α subunits (α1–6), two β subunits (β1–3) and one γ (γ1–3) or δ subunit, out of 19 possible types[9]. The only $GABA_A$R structure solved to date, the β3 homopentamer crystallized in an agonist-bound desensitized conformation, offers the best available guide to a physiological receptor[10]. However, the other principal components of $GABA_A$Rs, the α subunits, are the components that convey neurosteroid potentiation through a key glutamine residue within the M1 helices[3,11]. In the absence of structural information, it is impossible to understand how neurosteroids modulate GABAergic neurotransmission in mechanistic terms. To address this limitation, we sought to express, characterize and solve structures of apo and neurosteroid-bound $GABA_A$R constructs containing α-subunit TMDs.

RESULTS

Neurosteroid potentiation of a β3–α5 chimeric $GABA_A$R

Heteromeric $GABA_A$Rs have, thus far, proved intransigent to structural determination, and α subunits expressed alone do not form homopentameric assemblies. To overcome these limitations, we generated a chimeric human receptor by fusing the α5-subunit TMD to the β3-subunit ECD. $GABA_A$R-β3 homopentamers are gated by the natural agonist histamine[10,12] (rather than GABA), and the chimera, referred to as $\alpha5_{TMD}$, was also activated and then desensitized by histamine during whole-cell patch-clamp recordings from transfected HEK-293T cells (**Fig. 1a**). As reported for $GABA_A$R-β3 (ref. 12), $\alpha5_{TMD}$ channels also mediate a picrotoxin-sensitive leak current (I_{PTX}) caused by spontaneous (agonist-independent) gating, which accounts for 67 ± 3% (n = 8 measurements) of the total current ($I_{histamineMAX}$ + I_{PTX}) (**Fig. 1b**). Thus, $\alpha5_{TMD}$ assembles into a functional gating unit. To measure pregnanolone potentiation of submaximal histamine responses, it was necessary to reduce the high level of spontaneous activity in $\alpha5_{TMD}$, because neurosteroids potentiate low-efficacy activated states, as observed in heteromeric $GABA_A$Rs[13]. To achieve this state, we introduced a point mutation, T287K, into the M2–M3 loop, which is critical for receptor gating (identified from screening residue swaps between the α5 and β3 subunits; see alignment in **Fig. 1c**), thereby reducing spontaneous gating from 67 ± 3% to 21 ± 3% (n = 16). On this background, pregnanolone strongly potentiated submaximal ($EC_{10–15}$) histamine doses by 325 ± 104%, n = 6 (EC_{50} = 1.3 ± 0.1 μM, n = 6) (**Fig. 1d,e**). Notably, this effect was ablated by leucine substitution of the key M1 glutamine (α5 Gln245) previously identified to be essential for neurosteroid potentiation in heteromeric

[1]Division of Structural Biology, Wellcome Trust Centre for Human Genetics, University of Oxford, Oxford, UK. [2]Neurobiology Division, MRC Laboratory of Molecular Biology, Cambridge, UK. [3]Structural Biology Brussels, Vrije Universiteit Brussel (VUB), Brussels, Belgium. [4]VIB-VUB Center for Structural Biology, VIB, Brussels, Belgium. [5]These authors contributed equally to this work. Correspondence should be addressed to A.R.A. (radu@mrc-lmb.cam.ac.uk) or P.S.M. (paul@strubi.ox.ac.uk).

Received 5 January; accepted 13 September; published online 9 October 2017; doi:10.1038/nsmb.3484

© 2017 Nature America, Inc., part of Springer Nature. All rights reserved.

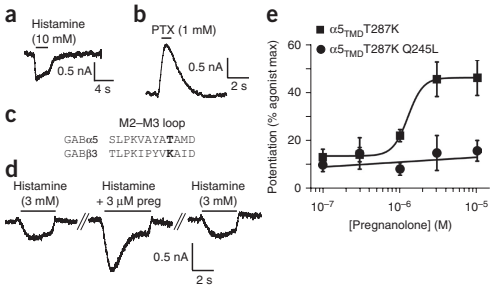

Figure 1 $\alpha5_{TMD}$ forms a functional gating unit potentiated by pregnanolone at the Gln245 site. (**a**) HEK-293T whole-cell patch-clamp recording of the agonist histamine activating an inward current through $\alpha5_{TMD}$ that subsequently desensitizes. (**b**) The classical $GABA_AR$ channel blocker picrotoxin blocks a spontaneous inward leak current generated by $\alpha5_{TMD}$. (**c**) Sequence alignment of the M2–M3 loop from $GABA_AR$ α5 and β3 subunits, with T287K substitution bolded. (**d**) Raw whole-cell patch-clamp EC_{10} histamine responses from HEK cells transfected with $\alpha5_{TMD}$T287K, before and after coapplication with 3 μM pregnanolone (preg). (**e**) Pregnanolone dose–response curve for potentiation of histamine $EC_{10–15}$ responses in $\alpha5_{TMD}$T287K and the ablation of potentiation upon introduction of a Q245L mutation in the M1 helix. Each data point represents mean ± s.e.m. of $n = 6$ experiments, with each measurement from different cells. Source data for **e** are available online.

Table 1 Crystallographic data collection and refinement statistics

	Pregnanolone-bound $\alpha5_{TMD}$ (PDB 5O8F)	Apo $\alpha5_{TMD}$	
		Uncorrected	Anisotropy corrected (PDB 5OJM)
Data collection			
Space group	*I*23	*C*2	
Cell dimensions			
a, *b*, *c* (Å)	290.1, 290.1, 290.1	177.3, 139.9, 191.5	
α, β, γ (°)	90.0, 90.0, 90.0	90.0, 102.2, 90.0	
Resolution (Å)	205.13–3.15 (3.31–3.15)[a]	187.14–3.28 (3.42–3.28)	
R_{merge}	0.728 (3.107)	0.352 (2.807)	–
R_{meas}	0.741 (3.169)	0.371 (2.960)	–
R_{pim}	0.135 (0.621)	0.117 (0.936)	–
$I/\sigma(I)$	7.55 (1.26)	7.85 (1.08)	–
$CC_{1/2}$	0.988 (0.215)	0.998 (0.395)	–
Completeness (%)	99.94 (100.00)	99.78 (99.71)	–
Redundancy	30.4 (25.6)	10.0 (9.9)	–
Refinement			
Resolution (Å)	49.75–3.19 (3.31–3.19)	48.88–3.30 (3.42–3.30)	48.88–3.30 (3.42–3.30)
No. reflections	66,647 (6,629)	68,726 (6,866)	50,816 (473)
R_{work} / R_{free}	0.232 / 0.244 (0.360 / 0.367)	0.255 / 0.282 (0.389 / 0.395)	0.236 / 0.256 (0.244 / 0.261)
No. atoms			
Protein	18,217	–	18,141
N-linked glycans	485	–	397
Pregnanolone	115	–	–
B factors (Å^2)			
Protein	72.1	–	71.3
N-linked glycans	90.7	–	99.1
Pregnanolone	59.6	–	–
R.m.s. deviations			
Bond lengths (Å)	0.008	–	0.009
Bond angles (°)	1.22	–	0.71

One crystal was used per structure. [a]Values in parentheses are for the highest-resolution shell.

αβγ/δ $GABA_ARs$ (**Fig. 1e**). Furthermore, purified $\alpha5_{TMD}$ in detergent was thermostabilized by the addition of pregnanolone (EC_{50} = 5.5 ± 0.3 μM, $n = 3$), and this thermostabilization was strongly attenuated by Q245L or Q245W mutations (tryptophan is the equivalent residue in β1–3 subunits) (EC_{50} > 30 μM, $n = 3$, in both cases) (**Supplementary Fig. 1**). Thus, whether in cell membranes or in detergent, $\alpha5_{TMD}$ houses a neurosteroid-potentiation site that requires the same key M1 glutamine to function as reported for heteromeric $GABA_ARs$.

The $\alpha5_{TMD}$ crystal structure

We next crystallized and determined the X-ray structures of $\alpha5_{TMD}$ in the absence and presence of pregnanolone to 3.3- and 3.2-Å resolution, respectively (**Table 1**, **Fig. 2a–d**, and **Supplementary Video 1**). In each case, $\alpha5_{TMD}$ was bound to a nanobody (Nb25) raised against the β3 ECD, which facilitated crystallization (**Supplementary Fig. 2a**). $\alpha5_{TMD}$ retains the hallmark architecture of all eukaryotic pLGICs characterized to date, including nicotinic acetylcholine, serotonin type 3, glycine and GluCl receptors[1,14–21]. Each subunit comprises an N-terminal β3 ECD folded into a twisted β-sandwich followed by an α5 four-helical-bundle TMD (**Fig. 2a**,**b**). The principal face (P) of each subunit intercalates with the complementary face (C) of its neighbor to form a ring of five subunits surrounding a central vestibule at the ECD level, which flows into a five-fold pseudosymmetric pore in the TMD region. Each Nb25 straddles the neurotransmitter-binding site located under loop C between adjacent subunits (**Supplementary Fig. 2a–d**). The ECDs of the apo and pregnanolone-bound $\alpha5_{TMD}$ structures are very similar (r.m.s. deviation in the 0.16–0.21-Å range between different chains, over 204 equivalent Cα positions). Both structures adopt the same overall activated conformation as the agonist-bound $GABA_AR$-β3 (ref. 10), exhibiting a closed loop C that contrasts with the antagonist-bound open loop C in glycine receptors[16,17] (**Supplementary Fig. 2c**,**e**,**f**). When applied to $\alpha5_{TMD}$ T287K–transfected HEK-293T cells in whole-cell patch-clamp recordings, Nb25 alone did not induce responses. Moreover, Nb25 did not affect maximal potentiation in the presence of 10 μM pregnanolone, the concentration used in crystallization experiments (**Supplementary Fig. 2g**). However, the activated state adopted by $\alpha5_{TMD}$ ECDs in crystal structures in the absence of agonist is consistent with the strong propensity of this construct to be spontaneously active in a cellular context (**Fig. 1b**).

Neurosteroid-binding modes

Surrounding the TMD pentamer of the pregnanolone-bound structure, but not the apo structure, five large peaks were observed in the $F_o - F_c$ omit electron density map. Each occupies a hydrophobic cavity at the interface between the principal M3 and complementary M1 helices of adjacent subunits (**Supplementary Fig. 3**). These densities were accounted for by pregnanolone molecules with half-chair geometry due to a *cis* junction between the A and B rings (**Fig. 2c**,**d**). The hydrophobic cavities contain the critical Gln245 residue, whose ε-oxygen contributes a putative hydrogen bond from the top of the

© 2017 Nature America, Inc., part of Springer Nature. All rights reserved.

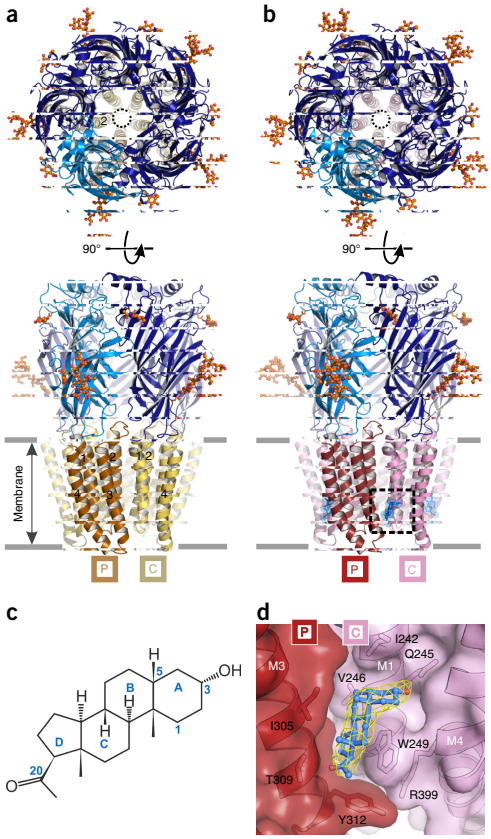

Figure 2 Architecture of $GABA_AR$ $\alpha5_{TMD}$. Top-down (top) and side-on (bottom) views of the $\alpha5_{TMD}$ pentamer in apo (**a**) and pregnanolone-bound (**b**) forms. Subunits each comprise the β3 extracellular domain (dark and light blue) and α5 TMD (α-helices M1–M4 shown in beige and yellow or red and pink). In top-down views, the pore is indicated by a black circle lined by five M2 helices (one per subunit). Side-on views highlight the helical organization (M1–M4, numbered 1–4 per subunit, where visible) in **a**, and the presence of pregnanolone in **b** (blue stick and space-fill, inside dashed box). N-linked glycans are shown as spheres colored by atom type (carbon atoms in orange, oxygen atoms in red). The principal (P) and complementary (C) subunits for the visible intersubunit interface are indicated. (**c**) Structural formula of pregnanolone with rings labeled A–D. Carbon atoms mentioned in the text are numbered. (**d**) Close-up of pregnanolone ('ball-and-stick' representation) bound to $\alpha5_{TMD}$ (cartoon and surface representation). The $2F_o - F_c$ electron density map surrounding the ligand is contoured at 1.3 σ (yellow mesh).

site to anchor the pregnanolone A ring 3α-hydroxyl (**Fig. 3a**). The neurosteroid A ring is positioned flat beneath the M1 Ile242 side chain, perpendicular to and above the indole rings of M1 Trp249 (**Fig. 3a**). The B–D rings angle downward, sandwiched between the side chains of M3 Ile305 and M1 Trp249. Tryptophan residues are highly prevalent in protein steroid-binding sites[22], and the stacking interaction observed is consistent with observations from a previous study that showed that an aliphatic leucine substitution of this M1 tryptophan ablated potentiation in $GABA_AR$ heteromers[11]. Pregnanolone B–D rings also make side-on van der Waals contacts with M1 Val246, which demarcates the deepest point of the pocket. Polar interactions anchor the neurosteroid at both ends. The D-ring C20 ketone anchors the bottom end of the ligand by acting as a hydrogen bond acceptor for the M3 Thr309 hydroxyl. Mutation of each of these residues individually, Q245S, V246A, W249L, I305A and T309A, all reduced sensitivity to pregnanolone potentiation of histamine responses on the T287K background by between three- and ten-fold, with W249L reducing sensitivity the most (from 0.8 ± 0.2 μM, n = 4 to > 10 μM, n = 8) and T309A reducing sensitivity the least (to 2.2 ± 0.3 μM, n = 3) (**Supplementary Fig. 4a**). Structural alignment of the β3 TMD pentamer[10] over the α5 TMD pentamer and subsequent examination of α–β interfaces revealed that pregnanolone is well accommodated in the heteromer site at the β_P–α_C interface that contains the highly conserved α-subunit M1 glutamine (Gln245 in $\alpha5_{TMD}$, **Fig. 3b**). However, at the α_P–β_C interface, the equivalent M1 position is occupied by β3 Trp237, thus removing the potential for 3α-hydroxyl coordination, clashing with pregnanolone and closing the top of the pocket (**Fig. 3c**,**d**). Although no structure for the γ subunit is currently available, sequence alignment reveals an M1 tryptophan in place of M1 glutamine, suggesting that the α_P–γ_C pocket would be similarly occluded. Thus, $\alpha5_{TMD}$ possesses a neurosteroid-binding site that correctly predicts: (i) an involvement for the key M1 glutamine and tryptophan residues in heteromeric $GABA_ARs$[3,11] and (ii) that receptor potentiation by neurosteroids only occurs via the β_P–α_C interface[23] (**Fig. 3b** versus **3c**).

A previous mutagenesis study, guided by homology modeling, had placed the α-subunit M1 glutamine close to M4 residues to create an intrasubunit pocket[3], rather than the intersubunit pocket described here. In $\alpha5_{TMD}$, the equivalent M4 residues Asn410 and Tyr413 are located outside the neurosteroid-binding site and are incompatible with ligand coordination by Gln245 (**Supplementary Fig. 4b**,**c**). Therefore, the previously reported effects of mutations to these residues on neurosteroid binding were, most likely, indirect. Moreover, (3α,5β)-6-azipregnanolone photolabels β3 homopentameric $GABA_ARs$ at Phe301 (ref. 24), the residue equivalent to $\alpha5_{TMD}$ M3 Thr309 (**Fig. 3a**,**b**), consistent with the intersubunit site we identified. To functionally validate whether the neurosteroid-binding site observed crystallographically is equivalent to an intersubunit potentiation site in the heteromeric α1β3γ2 $GABA_AR$, we introduced mutations into the β-subunit face that opposes the key heteromer α-subunit M1 glutamine and tryptophan residues[11]. We compared the sensitivity to pregnanolone potentiation of wild-type $GABA_AR$ heteromers to those of heteromers containing β3 subunits with alanine substitutions at either M3 Leu297 (corresponding to $\alpha5_{TMD}$ Ile305) or M3 Phe301 (corresponding to $\alpha5_{TMD}$ Thr309) in whole-cell patch-clamp recordings from transfected HEK-293T cells (**Fig. 3e**). Both α1β3L297Aγ2 and α1β3F301Aγ2 $GABA_ARs$ retained wild-type-level sensitivity to the neurotransmitter GABA (wild-type (WT) EC_{50} = 3.0 ± 1 μM, n = 8; L297A EC_{50} = 5.0 ± 2 μM, n = 3; F301A EC_{50} = 4.2 ± 2 μM, n = 3). However, α1β3L297Aγ2 $GABA_ARs$ were less sensitive to potentiation by both pregnanolone and its 5α epimer allopregnanolone (a *trans* isomer with a 'flat' geometry) by ten-fold and five-fold, respectively (pregnanolone WT EC_{50} = 240 ± 20 nM, n = 13; L297A EC_{50} = 2500 ± 200 nM, n = 11; allopregnanolone WT EC_{50} = 280 ± 40 nM, n = 5; L297A EC_{50} = 1,600 ± 200 nM, n = 9) (**Fig. 3e**,**f**). In contrast, α1β3F301Aγ2 $GABA_ARs$ retained wild-type-level sensitivity to both pregnanolone and allopregnanolone potentiation (pregnanolone EC_{50}

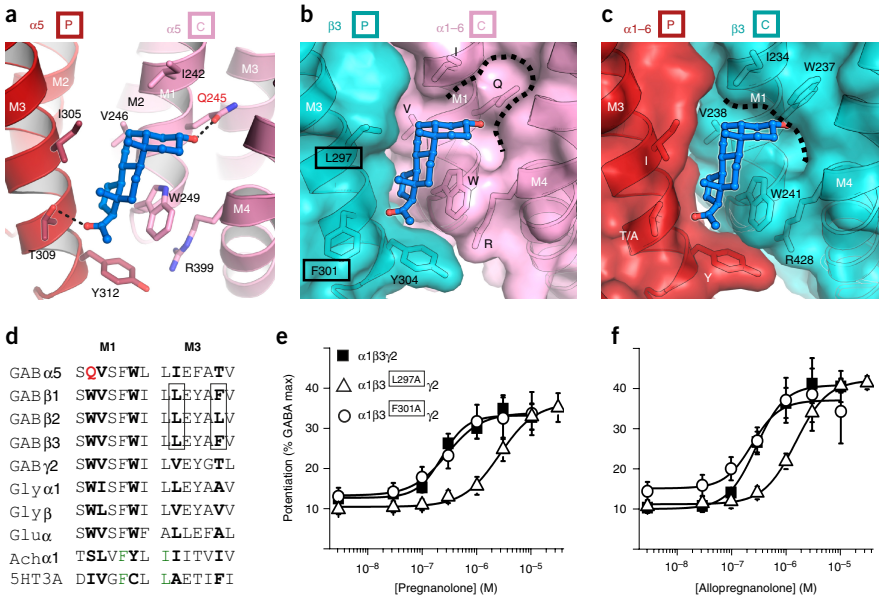

Figure 3 The neurosteroid potentiation site. (**a**) Pregnanolone (ball-and-stick representation; carbon atoms in blue, oxygen atoms in red) bound to an intersubunit site between M3 residues on the P face of one subunit and M1 residues on the C face of the next. Putative hydrogen bonds between the pregnanolone 3α-hydroxyl and the Gln245 amide (2.4 Å) and the C20 ketone and Thr309 hydroxyl (3.0 Å) are indicated by dashed lines. (**b**,**c**) Modeled heteromeric β_P–α_C (**b**) and α_P–β_C interfaces (**c**) in cartoon and surface representation, in which the relevant $\alpha5_{TMD}$ face is substituted by the equivalent β3 subunit structure (PDB 4COF). Note that the α5 residues in these two panels are labeled by letters only, without numbers, to reflect their conservation across the α subunits (α1–6) within this site. Pregnanolone is well accommodated in the heteromeric β_P–α_C site (**b**) but not in the α_C–β_P site (**c**) owing to the replacement of the α-subunit M1 glutamine with the β3 M1 Trp237, which closes the top of the pocket (dashed line). (**d**) Sequence alignment of the M1 and M3 motifs containing the neurosteroid-binding-site residues (bold) in the $GABA_AR$ α5 subunit and equivalent regions in other human pLGIC superfamily members. M1 Gln245, unique to $GABA_AR$ α subunits, is highlighted in red. $GABA_AR$ β-subunit residues contributed from the complementary face in heteromeric receptors are boxed. (**e**) Pregnanolone and (**f**) allopregnanolone dose–response curves for potentiation of GABA $EC_{10–15}$ responses. Alanine substitution of the β3 principal-face residue Leu297, but not Phe301, reduces neurosteroid sensitivity. These residues are highlighted by black boxes in **b**. Each data point represents mean ± s.e.m. Pregnanolone EC_{50}: WT, $n = 13$; L297A, $n = 11$; F301A, $n = 8$. Allopregnanolone EC_{50}: WT, $n = 5$; L297A, $n = 9$; F301A, $n = 4$. Each measurement is from different cells. Source data for **e** and **f** are available online.

= 280 ± 40 nM, $n = 8$; allopregnanolone EC_{50} = 260 ± 60 nM, $n = 4$). This finding is consistent with Phe301 having a more distal location on the border of the pocket, as well as with its lack of conservation between human β-subunit subtypes at this position and the fact that the β-subunit subtype does not impact neurosteroid potentiation[25]. However, the strong impact of the β3 L297A mutation confirms that the intersubunit location of the neurosteroid site observed in $\alpha5_{TMD}$ is retained in α1β3γ2 heteromeric $GABA_AR$s.

To explore the $\alpha5_{TMD}$ neurosteroid-binding mechanism further, we performed *in silico* analyses using the quantum mechanics polarized ligand docking (QMPLD)[26] algorithm implemented in the Schrödinger suite (http://www.schrodinger.com). The binding mode observed upon pregnanolone docking into the $\alpha5_{TMD}$ neurosteroid pocket was in agreement with the crystal structure (r.m.s. deviation of 1.7 Å, calculated by VMD over all pregnanolone atoms) (**Fig. 4a** and **Supplementary Fig. 5a**). Van der Waals contacts were predicted to be the predominant driving force of interaction (binding energy of −36.6 kcal mol^{-1}), consistent with other steroid-binding site analyses[27]. The electrostatic contribution was only −1.2 kcal mol^{-1}. Despite an elongated flat geometry rather than half-chair geometry, allopregnanolone was also well accommodated into the site (**Fig. 4b**), with a similar binding energy (E_{vdw} = −35.4 kcal mol^{-1}; E_{coul} = −1.4 kcal mol^{-1}). Moreover, pregnanolone and allopregnanolone similarly potentiated the $\alpha5_{TMD}$T287K histamine responses (**Supplementary Fig. 5b**). Allopregnanolone retained the same binding mode for its 3α-hydroxyl, positioned equidistantly between the M1 Gln245 εO and the Trp249 εN (3.5 Å for pregnanolone; 3.6 Å for allopregnanolone). Owing to its elongated flat geometry, binding imposed a 1.2-Å downward translation on the allopregnanolone B–D rings. In contrast to pregnanolone, its 3β epimer epipregnanolone is a weak potentiator of $GABA_AR$ heteromers[28]. Epipregnanolone has been shown to noncompetitively antagonize pregnanolone potentiation, thus raising the hypothesis that it acts through an alternative site[28]. However, our epipregnanolone docking in the $\alpha5_{TMD}$ neurosteroid pocket led to similar binding energy estimates (E_{vdw} = −35.5 kcal mol^{-1}; E_{coul} = −1.8 kcal mol^{-1}), suggesting that it can bind the same site as pregnanolone and allopregnanolone. These alternative scenarios can be reconciled if epipregnanolone binding to one $GABA_A$ heteromer site allosterically prevents potentiation by pregnanolone bound at the other. However, the possibility also remains that $GABA_AR$ heteromers contain

© 2017 Nature America, Inc., part of Springer Nature. All rights reserved.

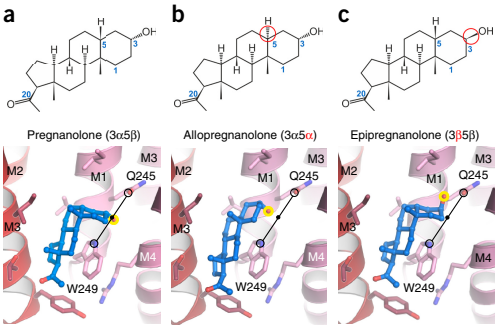

Figure 4 Computational docking of pregnanolone and related neurosteroids. Structural formulae and $\alpha5_{TMD}$ structures showing binding modes of computationally docked pregnanolone (**a**), allopregnanolone (**b**) and epipregnanolone (**c**). Stereoisomeric differences from pregnanolone are indicated in formulae by red circles. In the 3D models, the critical C3 hydroxyl group is highlighted by a yellow circle. Potentiators possess a 3α-hydroxyl, which is docked equidistantly between the Gln245 εO and Trp249 εN (3.5 Å for pregnanolone; 3.6 Å for allopregnanolone; indicated by a solid black line) regardless of whether the rings assume a half-chair or flat geometry. The C3 hydroxyl of 3β pregnanolone can only share a putative hydrogen bond with the Gln245 amide (2.8-Å distance).

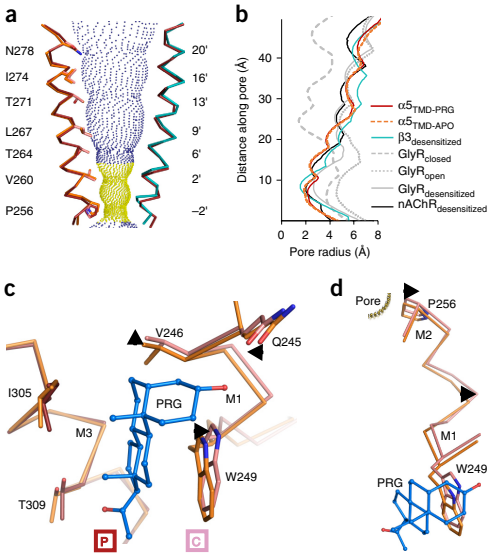

Figure 5 Pore conformation and neurosteroid-induced motions in $\alpha5_{TMD}$. (**a**) View of two opposing pore-lining M2 helices, the other three being removed for clarity. The pregnanolone-bound $\alpha5_{TMD}$ state (red) is shown on both sides. For comparison, overlays of the $\alpha5_{TMD}$ apo state (left, orange) and of $GABA_AR$-β3 (right, teal) M2 helices are shown. Blue and yellow spheres define pregnanolone-bound $\alpha5_{TMD}$ pore radii greater than or less than 3.2 Å, respectively (the radius of a hydrated Cl^- ion). (**b**) A plot of pore radii for $\alpha5_{TMD}$ structures compared to $GABA_AR$-β3 in the desensitized state (PDB 4COF), the glycine receptor in the resting closed, open and desensitized states (PDB 5JAD, PDB 5JAE and PDB 5JAF) and α4β2 nAChR (PDB 5KXI). (**c**) Superposition of apo (orange) versus pregnanolone-bound (red) $\alpha5_{TMD}$ principal faces reveals pregnanolone-induced motions on the complementary face (pink) of the neurosteroid pocket (indicated by black arrowheads). (**d**) The same superposition as in **c**, zoomed in on the pregnanolone-induced motions along the M1–M2 linker of a complementary face subunit, which impact the Pro256 desensitization gate.

additional, nonoverlapping sites that bind epipregnanolone and mediate noncompetitive inhibition. Notably, our docking studies reveal that the 3α-hydroxyl group of epipregnanolone points 'upward' rather than 'downward', thereby losing potential coordination with the Trp249 εN, although potential coordination with Gln245 εO is retained (**Fig. 4c**). We propose that the positioning of the 3α-hydroxyl between the Gln245 and Trp249 side chains is a contributing factor in determining whether transduction is potentiating or inhibitory in $GABA_AR$ heteromers. In contrast to its very weak potentiation on $GABA_AR$ heteromers, epipregnanolone triggers significant $\alpha5_{TMD}$T287K potentiation (**Supplementary Fig. 5b**). This might be due to its cumulative action through the five neurosteroid-binding sites present in $\alpha5_{TMD}$T287K, as opposed to that through only two equivalent sites in $GABA_AR$ heteromers, thus resulting in a stronger effect. Nevertheless, in these circumstances, the proposal that an 'upward' position of the 3α-hydroxyl reduces neurosteroid potentiation cannot be validated in the $\alpha5_{TMD}$T287K chimera.

Impact of neurosteroid binding on TMD conformation

To examine the impact of pregnanolone binding on the pore conformation, we next compared the TMD regions of the apo and pregnanolone-bound $\alpha5_{TMD}$ structures. Individual subunit TMDs closely superimpose (r.m.s. deviation in the 0.43–0.55-Å range between different chains over 123 equivalent Cα positions), adopting pore conformations similar to that of the desensitized $GABA_AR$-β3 homopentamer[10] (**Fig. 5a**), rather than to the open, desensitized (or partly open) and closed conformations of the related glycine receptor (GlyR)[16,17] (**Fig. 5b**). In both apo and pregnanolone-bound states, the five M2 helices lining the pore, taper inward to a constriction at the intracellular end. The side chains of Val260 and Pro256, occupying the 2′ and −2′ positions (pLGIC pore numbering convention), demarcate a hydrophobic desensitization gate (**Fig. 5a**). However, whereas the pore diameter at 2′ valine appears to be state independent (4.8 Å), pregnanolone binding leads to pore enlargement, from 3.7-Å to 4.3-Å diameter, at −2 proline (**Fig. 5b** and **Supplementary Video 2**). This contrasts with the $GABA_AR$-β3 homopentamer, in which the desensitization gate comprises only a single ring at −2′ (Ala248) with a 3.1-Å diameter (**Supplementary Fig. 6**), but is reminiscent of the cation-conducting α4β2 nicotinic acetylcholine receptor (nAChR) in which two rings of residues at 2′ and −1′ form a similar, albeit negatively charged, gate[21] (**Fig. 5b**). Although the $\alpha5_{TMD}$ pore in both states is theoretically wide enough to conduct dehydrated Cl^- ions (Pauling radius 1.8 Å), the gate contains no polar groups to substitute for the hydration shell and is highly likely to impede conductance[29].

The increased −2′ proline-ring diameter is the result of neurosteroid pocket expansion, required to accommodate pregnanolone (**Fig. 5c**,**d** and **Supplementary Video 2**). Neurosteroid binding displaces the complementary face away from the principal face, in particular at M1 Val246 (Cα displaced 0.9 Å) and Trp249 (Cα displaced 0.7 Å). Contrasting with this expansion, the polar interaction from the 3α-hydroxyl draws the side chain of Gln245 into the pocket by 0.6 Å and down toward the Trp249 εN by 0.7 Å (measurements

© 2017 Nature America, Inc., part of Springer Nature. All rights reserved.

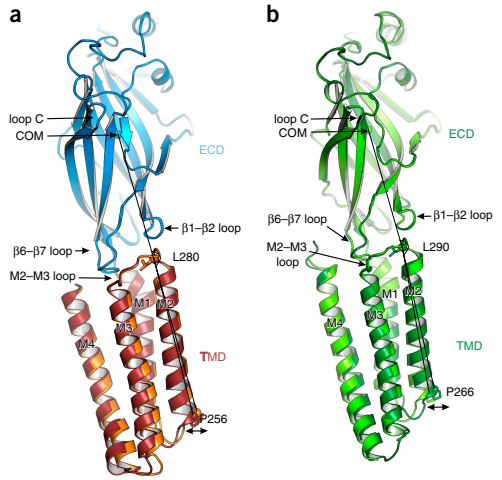

Figure 6 TMD motions relative to the ECD. (**a**) Side-on view of a single subunit (B chains), from apo $\alpha5_{TMD}$ (orange TMD) and pregnanolone-bound $\alpha5_{TMD}$ (red TMD), superposed by their ECDs (blue). The ECD conformations are very similar (r.m.s. deviation of 0.19 Å over 204 equivalent Cα positions). However, the lower half of the pregnanolone-bound TMD flexes such that the desensitization gate at Pro256 swings outward from the pore (indicated by double-headed arrow). The angles measured between the ECD center of mass (COM) and the Cα atoms of Leu280 at the top of M2 and Pro256 at the bottom of M2 are 162.5° (apo $\alpha5_{TMD}$) and 164.4° (pregnanolone-bound $\alpha5_{TMD}$), respectively, and thus, a 1.9° swing. (**b**) Equivalent view and superposition between open GlyR (light green, PDB 3JAE) and desensitized (or partially open) GlyR (dark green, PDB 3JAF). The narrowest pore diameter is at –2′ (Pro266) position in both cases (8.8 Å and 5 Å, respectively). The GlyR ECD conformations are also very similar (r.m.s. deviation of 0.31 Å over 210 equivalent Cα positions in B chains). As observed in $\alpha5_{TMD}$, relative to the superimposed ECDs, the lower half of the GlyR TMD flexes such that the desensitization gate at Pro266 is displaced outward from the pore to expand and open the channel. The angles measured between the ECD COM and the Cα atoms of Leu290 at the top of M2 and Pro266 at the bottom of M2 are 161.4° (desensitized GlyR) and 164.1° (open GlyR), respectively, and thus, a 2.7° swing.

corresponding to Gln245 εO in both cases). The resultant torque from this rearrangement at the base of the M1 helix, which twists sideways and outward, drives the translation of the M1–M2 intracellular linker (**Fig. 5d** and **Supplementary Video 2**; mean Cα displacement of Leu250, Asn251, Arg252, Glu253, Ser254, Val255 is 0.95 Å), which is not involved in crystal packing (**Supplementary Fig. 7**).

Aside from pore dilation, which partly relieves its hydrophobic constriction, pregnanolone binding has longer-range effects that extend upward through the TMD helical bundles and destabilize their desensitized-state arrangement. Notably, straightening of the M2 helices drives their extracellular ends and the contiguous M2–M3 loop (a key component of the TMD–ECD interface) inward (**Supplementary Video 3**). This shift leads to an overall straightening of the subunits, with the ECD and TMD undergoing a rocking motion about their shared interface as $\alpha5_{TMD}$ switches between apo and pregnanolone-bound states (**Fig. 6a** and **Supplementary Video 3**). The type and magnitude of motions observed here are consistent with those previously proposed to support transitions between gating states in the heteromeric *Torpedo* nAChR, studied within a membrane environment[30], as well as in the detergent-solubilized homopentameric zebrafish α1 GlyR[16] (**Fig. 6b**) and *Caenorhabditis elegans* GluClα receptor[19], suggesting that all these constructs operate in the same allosteric framework, which is broadly applicable to pLGICs[1].

The observed outward pull on the desensitization gate in response to binding pregnanolone and the impact of structure-guided mutagenesis offer a molecular mechanism by which neurosteroids support pore opening in heteromeric receptors. Consistent with this model, the M1–M2 linker controls desensitization in heteromeric $GABA_ARs$[31]. Expansion of the TMD intersubunit space as a mechanism of potentiation has previously been described for the antiparasitic agent ivermectin binding to the related *C. elegans* receptor GluCl (refs. 18,19). However, ivermectin binds GluCl to a pocket higher up the TMD that is not observed in $GABA_ARs$ and penetrates deeper between the subunits (**Supplementary Fig. 8a**,**b**).

DISCUSSION

Here, we present structures of the homomeric $GABA_AR$ construct $\alpha5_{TMD}$ in apo form and bound to a potentiation site by the endogenous neurosteroid pregnanolone. The binding site for neurosteroids corresponds to the site in heteromeric αβγ/δ $GABA_ARs$, which constitute the vast majority of physiological $GABA_ARs$[9]. These structures reveal the mode of neurosteroid binding and the motions induced in response to binding. Pregnanolone binds at the intersubunit interface between the M3 helix on the principal face and the M1 helix on the complementary face. Consistent with the high hydrophobicity of neurosteroids, binding is driven by interactions with hydrophobic residues (−36.6 kcal mol^{-1} of the total −37.8 kcal mol^{-1} binding energy), in particular by a stacking interaction between the pregnanolone B–D rings and the α5 M1 Trp249. The critical M1 Gln245 residue forms a putative hydrogen bond via its ε-oxygen to the pregnanolone A ring 3α-hydroxyl. Expansion of Trp249 away from M3 to accommodate pregnanolone within the site, combined with attraction of Gln245 toward pregnanolone stacked on Trp249 imparts torque on the lower segment of M1, which triggers a sideways motion on the M1–M2 linker and withdraws M2 at the −2 ring to expand the desensitization gate. The structure of the $\alpha5_{TMD}$ homopentamer potentiation site, compared with that of $GABA_AR$-β3 (ref. 10), also explains why in heteromeric $GABA_ARs$ neurosteroids are well accommodated at the two β_P–α_C interfaces (**Fig. 3a**–**c**) but not at the two α_P–β_C interfaces[23]. In the latter, the key α_C M1 Gln245 is replaced by β_C Trp237, which occludes the site and sterically clashes with the neurosteroid.

In a physiological context, extrasynaptic $GABA_ARs$ are key targets for endogenous neurosteroids[32]. In particular, neurosteroids increase tonic inhibition by promoting the opening of $GABA_ARs$ that are only partially occupied by the low ambient concentrations of GABA present in the extrasynaptic regions[32]. The structural framework provided by $\alpha5_{TMD}$ in a desensitized state, bound by pregnanolone, reveals that the molecular basis of this physiological process can be accounted for by the neurosteroid drawing the equilibrium away from the closed resting state toward open and desensitized states. The degree by which neurosteroid binding supports the open state versus the desensitized state probably depends on the surrounding lipid environment. Neurosteroids potentiated the open state of $\alpha5_{TMD}$ in whole-cell patch-clamp recordings in HEK cells, within a membrane environment, but was bound to desensitized $\alpha5_{TMD}$ in detergent micelles in the crystal structure. The $\alpha5_{TMD}$ structure also reveals the exposed location of the neurosteroid site on the outer face of the TMD, meaning that pregnanolone will bridge interactions

© 2017 Nature America, Inc., part of Springer Nature. All rights reserved.

between the $GABA_AR$ and the lipid bilayer. Thus, it is not surprising that the broader lipidic context of the protein will affect the extent to which neurosteroid binding expands the desensitization gate and so potentiates the open state.

Overall, this study provides key insights into the mechanical coupling between peripheral lipid-binding sites and the channel desensitization gate and illustrates a novel form of modulation within the pLGIC superfamily.

METHODS

Methods, including statements of data availability and any associated accession codes and references, are available in the online version of the paper.

Note: Any Supplementary Information and Source Data files are available in the online version of the paper.

ACKNOWLEDGMENTS

We thank staff at Diamond Light Source beamlines I03 and I04 for assistance at the synchrotron, K. Harlos and T. Walter for technical support with crystallization, J. Kammonen and staff at Pfizer for very kind time and assistance with electrophysiology, E. Beke for technical assistance during nanobody discovery, Y. Zhao for technical support with tissue culture, members of STRUBI for helpful discussions and G. Sutton and T. Malinauskas for feedback regarding the manuscript. This work was supported by the UK Biotechnology and Biological Sciences Research Council grant BB/M024709/1 (A.R.A. and P.S.M.), the UK Medical Research Council grants MR/L009609/1 and MC_UP_1201/15 (A.R.A.), the Human Frontier Science Program grant RGP0065/2014 (A.R.A.) and the Wellcome Trust studentships 105247/Z/14/Z (S.S.) and 084655/Z/08/Z (S.M.). We also thank INSTRUCT, part of the European Strategy Forum on Research Infrastructures and the Research Foundation-Flanders (FWO) for their nanobody discovery support. Further support from the Wellcome Trust Core Award 090532/Z/09/Z is acknowledged.

AUTHOR CONTRIBUTIONS

Experimental work was performed by P.S.M. and S.S. (protein expression, purification, crystallization, electrophysiology), S.M. (protein expression, purification), L.D.C. (docking experiments), E.P. and J.S. (nanobody generation) and A.R.A. (crystallography). The manuscript was written by P.S.M. and A.R.A. with input from all coauthors.

COMPETING FINANCIAL INTERESTS

The authors declare no competing financial interests.

Reprints and permissions information is available online at http://www.nature.com/reprints/index.html. Publisher's note: Springer Nature remains neutral with regard to jurisdictional claims in published maps and institutional affiliations.

1. Nemecz, Á., Prevost, M.S., Menny, A. & Corringer, P.J. Emerging molecular mechanisms of signal transduction in pentameric ligand-gated ion channels. *Neuron* **90**, 452–470 (2016).
2. Miller, P.S. & Smart, T.G. Binding, activation and modulation of Cys-loop receptors. *Trends Pharmacol. Sci.* **31**, 161–174 (2010).
3. Hosie, A.M., Wilkins, M.E., da Silva, H.M. & Smart, T.G. Endogenous neurosteroids regulate GABAA receptors through two discrete transmembrane sites. *Nature* **444**, 486–489 (2006).
4. Majewska, M.D., Harrison, N.L., Schwartz, R.D., Barker, J.L. & Paul, S.M. Steroid hormone metabolites are barbiturate-like modulators of the GABA receptor. *Science* **232**, 1004–1007 (1986).
5. Sarkar, J., Wakefield, S., MacKenzie, G., Moss, S.J. & Maguire, J. Neurosteroidogenesis is required for the physiological response to stress: role of neurosteroid-sensitive GABAA receptors. *J. Neurosci.* **31**, 18198–18210 (2011).
6. Gunn, B.G., Brown, A.R., Lambert, J.J. & Belelli, D. Neurosteroids and GABA(A) Receptor Interactions: A Focus on Stress. *Front. Neurosci.* **5**, 131 (2011).
7. Maguire, J.L., Stell, B.M., Rafizadeh, M. & Mody, I. Ovarian cycle-linked changes in GABA(A) receptors mediating tonic inhibition alter seizure susceptibility and anxiety. *Nat. Neurosci.* **8**, 797–804 (2005).
8. Maguire, J. & Mody, I. GABA(A)R plasticity during pregnancy: relevance to postpartum depression. *Neuron* **59**, 207–213 (2008).
9. Sigel, E. & Steinmann, M.E. Structure, function, and modulation of GABA(A) receptors. *J. Biol. Chem.* **287**, 40224–40231 (2012).
10. Miller, P.S. & Aricescu, A.R. Crystal structure of a human GABAA receptor. *Nature* **512**, 270–275 (2014).
11. Akk, G. *et al.* Mutations of the GABA-A receptor alpha1 subunit M1 domain reveal unexpected complexity for modulation by neuroactive steroids. *Mol. Pharmacol.* **74**, 614–627 (2008).
12. Saras, A. *et al.* Histamine action on vertebrate GABAA receptors: direct channel gating and potentiation of GABA responses. *J. Biol. Chem.* **283**, 10470–10475 (2008).
13. Bianchi, M.T. & Macdonald, R.L. Neurosteroids shift partial agonist activation of GABA(A) receptor channels from low- to high-efficacy gating patterns. *J. Neurosci.* **23**, 10934–10943 (2003).
14. Hassaine, G. *et al.* X-ray structure of the mouse serotonin 5-HT3 receptor. *Nature* **512**, 276–281 (2014).
15. Miyazawa, A., Fujiyoshi, Y. & Unwin, N. Structure and gating mechanism of the acetylcholine receptor pore. *Nature* **423**, 949–955 (2003).
16. Du, J., Lü, W., Wu, S., Cheng, Y. & Gouaux, E. Glycine receptor mechanism elucidated by electron cryo-microscopy. *Nature* **526**, 224–229 (2015).
17. Huang, X., Chen, H., Michelsen, K., Schneider, S. & Shaffer, P.L. Crystal structure of human glycine receptor-α3 bound to antagonist strychnine. *Nature* **526**, 277–280 (2015).
18. Althoff, T., Hibbs, R.E., Banerjee, S. & Gouaux, E. X-ray structures of GluCl in apo states reveal a gating mechanism of Cys-loop receptors. *Nature* **512**, 333–337 (2014).
19. Hibbs, R.E. & Gouaux, E. Principles of activation and permeation in an anion-selective Cys-loop receptor. *Nature* **474**, 54–60 (2011).
20. Unwin, N. Refined structure of the nicotinic acetylcholine receptor at 4A resolution. *J. Mol. Biol.* **346**, 967–989 (2005).
21. Morales-Perez, C.L., Noviello, C.M. & Hibbs, R.E. X-ray structure of the human α4β2 nicotinic receptor. *Nature* **538**, 411–415 (2016).
22. Hori-Tanaka, Y., Yura, K., Takai-Igarashi, T. & Tanaka, H. Structural classification of steroid-binding sites on proteins by coarse-grained atomic environment and its correlation with their biological function. *Steroids* **96**, 81–88 (2015).
23. Bracamontes, J.R., Li, P., Akk, G. & Steinbach, J.H. A neurosteroid potentiation site can be moved among GABAA receptor subunits. *J. Physiol. (Lond.)* **590**, 5739–5747 (2012).
24. Chen, Z.W. *et al.* Neurosteroid analog photolabeling of a site in the third transmembrane domain of the β3 subunit of the GABA(A) receptor. *Mol. Pharmacol.* **82**, 408–419 (2012).
25. Belelli, D., Casula, A., Ling, A. & Lambert, J.J. The influence of subunit composition on the interaction of neurosteroids with GABA(A) receptors. *Neuropharmacology* **43**, 651–661 (2002).
26. Cho, A.E., Guallar, V., Berne, B.J. & Friesner, R. Importance of accurate charges in molecular docking: quantum mechanical/molecular mechanical (QM/MM) approach. *J. Comput. Chem.* **26**, 915–931 (2005).
27. Eick, G.N. & Thornton, J.W. Evolution of steroid receptors from an estrogen-sensitive ancestral receptor. *Mol. Cell. Endocrinol.* **334**, 31–38 (2011).
28. Wang, M. *et al.* 3beta-hydroxypregnane steroids are pregnenolone sulfate-like GABA(A) receptor antagonists. *J. Neurosci.* **22**, 3366–3375 (2002).
29. Aryal, P., Sansom, M.S. & Tucker, S.J. Hydrophobic gating in ion channels. *J. Mol. Biol.* **427**, 121–130 (2015).
30. Unwin, N. & Fujiyoshi, Y. Gating movement of acetylcholine receptor caught by plunge-freezing. *J. Mol. Biol.* **422**, 617–634 (2012).
31. Gielen, M., Thomas, P. & Smart, T.G. The desensitization gate of inhibitory Cys-loop receptors. *Nat. Commun.* **6**, 6829 (2015).
32. Brickley, S.G. & Mody, I. Extrasynaptic GABA(A) receptors: their function in the CNS and implications for disease. *Neuron* **73**, 23–34 (2012).

© 2017 Nature America, Inc., part of Springer Nature. All rights reserved.

© 2017 Nature America, Inc., part of Springer Nature. All rights reserved.

ONLINE METHODS

Construct design. The $\alpha5_{TMD}$ construct was designed by fusing the ECD of the human $GABA_AR$ β3 subunit (mature polypeptide numbering 1–217, QSVN…LKRN; Uniprot P28472) to the TMD of the human $GABA_AR$ α5 subunit (mature polypeptide numbering 226–431, IGYF…GAASPK; Uniprot P31644). The α5 intracellular M3–M4 loop amino acids 316–392 (RGWA…NSIS) were substituted by the SQPARAA sequence[10,33] to enhance the recombinant protein yield and facilitate crystallization. This construct was cloned into the pHLsec vector[34] between the N-terminal secretion signal sequence and a the C-terminal 1D4 purification tag derived from bovine rhodopsin (TETSQVAPA), which is recognized by the Rho-1D4 monoclonal antibody (University of British Columbia)[35,36]. Point mutations were introduced to constructs by overlap PCR of whole-construct cDNAs and subsequent ligation into the pHLsec vector[34].

Large-scale expression and purification of $\alpha5_{TMD}$. 20-L batches of HEK293S-GnTI$^-$ cells (ATCC Cat# CRL-3022, RRID: CVCL_A785), which yield proteins with truncated N-linked glycans, $Man_5GlcNAc_2$ (refs. 37,38), were grown in suspension to densities of 2×10^6 cells ml^{-1} in Protein Expression Media (PEM, Invitrogen) supplemented with L-glutamine, nonessential amino acids (Gibco) and 1% fetal calf serum (Sigma-Aldrich) in 200-ml volumes, each in empty 600-ml DMEM bottles (Gibco) with lids loose, shaking at 130 r.p.m., 37 °C, 8% CO_2. For transient transfection, cells from 1 L of culture were collected by centrifugation (200*g* for 5 min) and resuspended in 150 ml Freestyle medium (Invitrogen) containing 3 mg PEI Max (Polysciences) and 1 mg plasmid DNA, and then incubated for 4 h in a 2-L conical flask with shaking at 160 r.p.m. Subsequently, culture media were topped up to 1 L with PEM containing 1 mM valproic acid and returned to empty DMEM bottles. Typically, 40–70% transfection efficiencies were achieved, as assessed using control transfections with a monoVenus-expressing plasmid[39,40]. 72 h post-transfection cell pellets were collected, snap frozen in liquid N_2 and stored at −80 °C.

Cell pellets (~200 g) were solubilized in 600 ml buffer containing 20 mM HEPES, pH 7.2, 300 mM NaCl, 1.5% (w/v) dodecyl 1-thio-β-maltoside (DDTM, Anatrace), 1% (v/v) mammalian protease inhibitor cocktail (Sigma-Aldrich, cat. P8340) for 2 h at 4 °C. Insoluble material was removed by centrifugation (10,000*g*, 15 min). The supernatant was diluted two-fold in a buffer containing 20 mM HEPES, pH 7.2, and 300 mM NaCl and incubated for 2 h at 4 °C with 10 ml CNBr-activated Sepharose beads (GE Healthcare) precoated with 50 mg Rho-1D4 antibody (3.3 g dry powdered beads expand during antibody coupling to approximately 10 ml). Affinity-bound samples were washed slowly by gravity flow over 2 h at 4 °C with 200 ml of buffer containing 20 mM HEPES, pH 7.2, 300 mM NaCl and 0.1% (w/v) DDTM (approximately 20× CMC) and then 200 ml of buffer containing 20 mM HEPES, pH 7.2, 300 mM NaCl and 0.01% (w/v) DDTM. $\alpha5_{TMD}$ was eluted overnight in 15 ml of buffer containing 15 mM HEPES, pH 7.2, 225 mM NaCl, 0.007% (w/v) DDTM and 500 μM TETSQVAPA peptide (Genscript). The eluate was centrifuged (30,000*g*, 15 min) and the supernatant was concentrated by ultrafiltration to 1–2 ml at 1–5 mg/ml using 100-kDa-cutoff membranes (Millipore). The concentrated sample was centrifuged (30,000*g*, 15 min) and the supernatant was aliquoted in 0.5–1.5 mg protein per 0.7 ml aliquots and either snap frozen for storage at −80 °C or gel filtrated as appropriate. A single aliquot was loaded onto a Superose 6 10/300 Increase gel filtration column (GE Healthcare) equilibrated in 10 mM HEPES, pH 7.2, 150 mM NaCl and 0.007% (w/v) DDTM. The nanobody Nb25, expressed and purified as described below, was added to $\alpha5_{TMD}$ at ten-fold molar excess and the complex was concentrated by ultrafiltration to 4 mg/ml, using a 100-kDa-cutoff membranes (Millipore) for crystallization trials. Typical final yields were 0.2 mg $\alpha5_{TMD}$ per liter of cells grown in suspension (10*g* cell pellet). For the production of neurosteroid-bound $\alpha5_{TMD}$, the gel filtration buffer described above was supplemented with pregnanolone, 30 μM final concentration.

Large-scale expression and purification of heteromeric $\alpha1\beta3$ $GABA_ARs$ for generation of nanobody libraries. Human $GABA_AR$ α1 and β3 subunits wild-type mature protein sequences were used (α1 Uniprot P14867 entry Gln28 is Gln1 1–429 QPSL…PTPHQ; β3 Uniprot P28472 isoform 1 entry Gln26 is Gln1 1–448 QVSN…LYYVN), except that the intracellular loop between transmembrane helices 3 and 4 (M3–M4) was substituted for α1 from Arg313 to Ser390, and the linker sequence SQPARAA was substituted for β3 from Gly308 to Asn421to increase expression[10]. These constructs were cloned into the pHLsec vector[34] between the N-terminal secretion signal sequence either a double stop codon (for β3) or a C-terminal 1D4 purification tag (for α1). The expression and purification procedure was as described for $\alpha5_{TMD}$ but with the following differences: plasmids encoding the α1 and β3 subunits were cotransfected in a 1:1 ratio, the detergent used for solubilization was decyl maltose neopentyl glycol (DMNG, Anatrace) supplemented with cholesterol hemisuccinate (CHS, Anatrace) at a 10:1 molar ratio, the 15-ml eluted samples were loaded in 5-ml batches onto a Superdex 200 16/600 column (GE Healthcare) equilibrated in 10 mM HEPES, pH 7.2, 150 mM NaCl, 0.007% (w/v) DMNG10:1CHS and 50 μM GABA. Peak fraction concentrations were typically 0.1 mg/ml and were further concentrated by ultrafiltration to 1 mg/ml using 100-kDa-cutoff membranes (Millipore), aliquoted and snap frozen at −80 °C. The final $\alpha1\beta3$ $GABA_AR$ yield was 0.05 mg per liter of suspension culture (10*g* cell pellet).

Nanobody generation and purification. Camelid nanobodies against $\alpha1\beta3$ $GABA_ARs$ were generated using established protocols[41]. One animal was immunized six times with the recombinant 1D4-tagged human $\alpha1\beta3$ $GABA_AR$ pentamer (described above). Subsequent to library generation, nanobodies were selected by phage display in two different ways: either by passive absorption of the $GABA_A$-$\alpha1\beta3$ pentamer or by trapping the receptor using the 1D4 antibody. After two rounds of selections, 96 clones were screened and positive clones were sequenced, revealing 13 nanobody families. The nanobody Nb25, binding to the $GABA_A$ β3 subunit, was produced and purified in milligram quantities from WK6su$^-$*Escherichia coli* bacteria. Bacteria were transformed with ~200 ng of the nanobody expression plasmid pMESy4 containing the nanobody of interest and selected on Lysogeny broth (LB)-agar plates containing 2% glucose and 100 μg/ml ampicillin. 2–3 colonies were used for preparing a preculture, which was used to inoculate 0.5 L Terrific broth (TB) cultures supplemented with 0.1% glucose, 2 mM $MgCl_2$ and 100 μg/mL ampicillin. Cultures were grown at 37 °C until their OD_{600} reached 0.7, at which point Nb25 expression was induced with 1 mM IPTG. After induction, cells were grown at 28 °C overnight and harvested by centrifugation (20 min, 5,000*g*). Nanobodies were released from the bacterial periplasm by incubating cell pellets with an osmotic shock buffer containing 0.2 M Tris, pH 8.0, 0.5 mM EDTA and 0.5 M sucrose. The C-terminally His6-tagged Nb25 was purified using nickel affinity chromatography (binding buffer: 50 mM HEPES, pH 7.2, 1 M NaCl, 10 mM imidazole; elution buffer: 50 mM HEPES, pH 7.2, 0.2 M NaCl, 0.5 M imidazole) and then subjected to size-exclusion chromatography on a Superdex 75 16/600 column (GE Healthcare) in 10 mM HEPES, pH 7.2, 150 mM NaCl. Nb25 stocks were concentrated to 5–10 mg/mL, snap frozen in liquid nitrogen and stored at −80 °C.

Crystallization and X-ray data collection. The $\alpha5_{TMD}$ construct contains 15 N-linked glycosylation sites, bringing a considerable extra volume, flexibility and potential occupancy heterogeneity. Therefore, before crystallization, concentrated $\alpha5_{TMD}$ samples, with and without pregnanolone, were incubated with 0.01 mg ml^{-1} endoglycosidase F1 (ref. 42) for 2 h at room temperature. Sitting-drop vapor diffusion crystallization trials were performed in 96-well Swisssci 3-well crystallization plates (Hampton Research) at three ratios: 200 nL protein plus 100 nL reservoir, 100 nL protein plus 100 nL reservoir, 100 nL protein plus 200 nL reservoir. Drops were dispensed by a Cartesian Technologies robot[43], and plates were maintained at 6.5 °C in a Formulatrix storage and imaging system. Initial crystals grew within 1–7 d in a range of conditions[44] and diffracted up to intermediate resolution (>5 Å). Following additive-based optimization (MemAdvantage, Molecular Dimensions), pregnanolone-bound $\alpha5_{TMD}$ crystals diffracting to 3.2-Å resolution were grown in 14% poly-ethylene (PEG) 6000, 0.1 M *N*-(2-Acetamido)iminodiacetic acid (ADA), pH 5.6, 7.6 mM 4-Cyclohexyl-1-Butyl-β-D-Maltoside (CYMAL-4) and apo $\alpha5_{TMD}$ crystals diffracting to 3.3-Å resolution were grown in 14% poly-ethylene (PEG) 5000, 0.08 M magnesium acetate, 0.1 M sodium citrate, pH 5.8, 1 mM ethylene glycol tetraacetic acid (EGTA). Crystals were cryo-protected by soaking in reservoir solution supplemented with 30% ethylene glycol and were then flash frozen in liquid nitrogen. Diffraction images of 0.2° oscillation were collected at the Diamond Light Source, beamlines I03 (pregnanolone-bound $\alpha5_{TMD}$, $\lambda = 0.9763$ Å) and I04 (apo $\alpha5_{TMD}$, $\lambda = 0.9795$ Å) on Pilatus3 6M and Pilatus 6M-F detectors, respectively. X-ray data were indexed, integrated and scaled using the HKL2000 package[45] and merged using Aimless[46,47]. Data collection statistics are shown in **Table 1**.

© 2017 Nature America, Inc., part of Springer Nature. All rights reserved.

Structure determination, refinement and analysis. Pregnanolone-bound and apo $\alpha5_{TMD}$ structures were solved by molecular replacement using the human $GABA_AR$-$\beta3_{cryst}$ homopentamer[10] (PDB 4COF) and the gelsolin nanobody[48] (PDB 2X1Q) as a search model in Phaser[49]. Polypeptide chains were traced using iterative rounds of manual model building in Coot[50] and refinement in Refmac[51] and Phenix[52,53]. Automated X-ray and atomic displacement parameter (ADP) weight optimization and torsion angle noncrystallographic symmetry (NCS) restraints, were applied. The pregnanolone coordinates and geometry restraints were generated using the Grade Web Server (http://grade.globalphasing.org). Diffraction from the apo $\alpha5_{TMD}$ crystal was strongly anisotropic. Ellipsoidal truncation, with resolution limits along the reciprocal cell directions a*, b* and c* being 3.9 Å, 3.8 Å and 3.3 Å, respectively, anisotropic scaling and a negative isotropic *B*-factor correction (−49.29 $Å^2$) were performed using the UCLA–DOE Lab Diffraction Anisotropy server (https://services.mbi.ucla.edu/anisoscale/)[54]. Anisotropy correction led to improvements in the electron density map quality and facilitated model building. Both data sets (uncorrected and anisotropy-corrected) were deposited in the Protein Data Bank. The model deposited was refined against the anisotropy-corrected data set, however we also provide refinement statistics against the full (uncorrected) data set in **Table 1**.

The final models contain one $\alpha5_{TMD}$ homopentamer bound to five Nb25 nanobodies per asymmetric unit. The complete polypeptide chains could be built, with the exception of thirteen N-terminal (QSVNDPGNMSFVK) and thirteen C-terminal (NREPVIKGAASPK) $GABA_A$ residues, the final serine residue in nanobody chains L, M and N and the C-terminal purification tags, presumably disordered. Furthermore, very strong additional electron density peaks were clearly visible in the outer parts of intersubunit TMD regions in the $\alpha5_{TMD}$ maps. These could be unambiguously assigned to five pregnanolone molecules, one per intersubunit interface, based on shape, coordination and refinement statistics. The $\alpha5_{TMD}$ extracellular region is heavily glycosylated, and we observed clear electron density for 10 out of the 15 N-linked glycosylation sites, with the remaining five being located in the N-terminal disordered regions. Glycans attached to Asn149 in each chain were protected from endoglycosidase F1 cleavage owing to extensive interactions with both $\alpha5_{TMD}$ and the Nb25 nanobody molecules, underlying their important structural role[10]. Stereochemical properties of the models were assessed in Coot[50] and Molprobity[55]. Protein geometry analyses revealed no Ramachandran outliers, with 97.88% residues in favored regions, 2.12% residues in allowed regions for pregnanolone-bound $\alpha5_{TMD}$ and 96.76% residues in favored regions and 3.24% residues in allowed regions for apo $\alpha5_{TMD}$. The overall Molprobity scores are 1.24 and 1.74, respectively (100th percentile).

Structural alignments were performed in SHP[56]. Protein interfaces were analyzed using the PDBePISA web server at the European Bioinformatics Institute (http://www.ebi.ac.uk/pdbe/prot_int/pistart.html)[57] and pore dimensions were analyzed using the Coot implementation of Hole[58], with a probe radius of 1.4 Å. Structural figures were prepared with the PyMOL Molecular Graphics System, Version 1.8, Schrödinger, LLC. Molecular videos and analyses were performed with the UCSF Chimera package, developed by the Resource for Biocomputing, Visualization, and Informatics at the University of California, San Francisco (supported by NIGMS P41-GM103311) (ref. 59).

Cell preparation and electrophysiology. One day before experiments, 8 mL of DMEM was preincubated for 10 min at room temperature with 96 µL Lipofectamine2000 (Thermofisher) and 48 µg plasmid DNA, then added to a single T175 cm^2 flask containing HEK293T cells (30–50% confluency; HEK 293T, ATCC Cat# CRL-3216, RRID: CVCL_0063) and 2 mL DMEM (supplemented with 10% FCS, L-glutamine and nonessential amino acids). After 3 h, this media was removed and replaced by DMEM supplemented with 10% FCS. For $GABA_AR$ heteromers, pHLsec plasmids containing human full-length cDNA constructs were mixed in a 1:1:2 ratio (α:β:γ), supplemented with 3% plasmid encoding enhanced GFP (EGFP) to assess transfection efficiency. Specifically, the cDNA inserts used for heteromeric receptor expression were as follows: human $GABA_AR$ α1 mature protein sequence (α1 Uniprot P14867 entry Gln28 is Gln1 1-429 QPSL…PTPHQ) and human β3 mature protein sequence (β3 Uniprot P28472 entry isoform 1 Gln26 is Gln1 1-448 QVSN…LYYVN) cloned into the pHLsec vector[34] between the N-terminal secretion signal sequence and a double stop codon; human $GABA_AR$ γ2 mature protein sequence (γ2 Uniprot P18507 isoform 1 entry Gln40 is Gln1 1-428 QKSDD…SYLYL) cloned into the pHLsec vector[34] between the N-terminal secretion signal sequence followed by streptavidin-binding protein (MDEKTTGWRGGHVVEGLAGELEQLRARLE HHPQGQREP) and a C-terminal 1D4 purification tag. Transfection efficiencies were typically 50–80% (cells expressing EGFP, as estimated by fluorescence microscopy). 18–24 h later, cells were washed with PBS, incubated in 4 ml TrypLE (Gibco) for 7 min at 37 °C, suspended in 21 ml DMEM supplemented with 10% FCS and L-glutamine, centrifuged at 100*g* for 1.5 min, then suspended in 50 ml Freestyle 293 Expression Medium (Gibco) and placed in a shaking incubator (130 r.p.m., 37°C, 8% CO_2) for 30 min. 25 ml of cell suspension was then centrifuged at 100*g* for 1.5 min and suspended in 4 ml of external recording solution. This solution contained: 137 mM NaCl, 4 mM KCl, 1 mM $MgCl_2$, 1.8 mM $CaCl_2$, 10 mM HEPES and 10 mM D-Glucose, pH 7.4 (≈305 mOsm). The internal recording solution contained: 140 mM CsCl, 5 mM NaCl, 1 mM $MgCl_2$, 10 mM HEPES, 5 mM EGTA, 0.2 mM ATP, pH 7.35 (≈295 mOsm). Electrophysiological recordings were performed at room temperature using an Ionflux16 (Molecular Devices) in ensemble mode, with series resistance compensation set at 80% and cells held at −60 mV. Pregnanolone and allopregnanolone (Sigma-Aldrich) were dissolved in DMSO as 100 mM stocks before dilution in external recording solution. These neurosteroids were coapplied with $EC_{10–15}$ GABA or histamine doses to generate dose–response curves for heteromeric $GABA_ARs$ and $\alpha5_{TMD}$. Expression of heteromeric receptors as assemblies of αβγ subunits was confirmed by response to GABA, which requires coassembly of α1 and β3 subunits, and efficient inclusion of the γ2 subunit into αβγ heteromers was verified by testing for Zn^{2+} sensitivity, with heteromeric constructs exhibiting low sensitivity to Zn^{2+}, defined as less than 50% inhibition of an EC_{50} GABA response[60].

Molecular docking and binding-energy calculation. Small-molecule coordinates were generated by eLBOW and energy minimized with Ligprep in the Schrödinger suite at pH 7.0 with the OPLS_2005 force field[61]. The standard conversion procedure with full hydrogen optimization was applied with the Protein Preparation workflow to the protein structure. The neurosteroid-binding pocket between chains B and C in $\alpha5_{TMD}$ was used for the subsequent grid generation and ligand-docking procedures. The Glide Grid[62,63] (Schrödinger suite) was built using an inner box (the centroid of the pregnanolone molecule) of 10 × 10 × 10 $Å^3$ and an outer box (within which all the ligand atoms must be contained) that extended 20 Å in each direction from the inner box. Default values were used for all other parameters. The hydrogen bonds between the 3α-hydroxyl group and the 20-carbonyl group of the pregnanolone molecule, respectively, with the carbonyl group of Gln245 and hydroxyl group of Thr309 were used as positional constraints. Furthermore, the atoms C03, C20 and C06 of the pregnanolone molecule were used as additional positional constraints. For docking, the QMPLD[26] protocol (Schrödinger suite, http://www.schrodinger.com/) was used. The most reliable binding pose for each small molecule was selected on the basis of calculated van der Waals and electrostatic interactions. r.m.s. deviation values were calculated with VMD[64].

Thermostability binding experiments. Information regarding the thermostability of a detergent-solubilized protein can be determined by heating protein samples over a range of temperatures for equal time periods and then measuring the reduction in the intensity of the monodisperse SEC profile for each protein sample[65]. With increasing temperature, an increased proportion of protein is denatured, forms aggregates and is lost from the monodisperse peak when the protein is subsequently run on SEC. A measure of protein stability can then be obtained by plotting the decay in peak UV absorbance against increasing temperature, for example to obtain a 50% melting temperature (T_m). Purified $GABA_AR$ $\alpha5_{TMD}$ or $\alpha5_{TMD}$ mutants at 0.02 mg ml^{-1} (100 nM) in 150 mM NaCl, 10 mM HEPES, pH 7.2, 0.007% DDTM (w/v) were separated into 50-µl aliquots in PCR tubes and heated at a range of temperatures from 40–80 °C for 1 h. Samples were run on a high-performance liquid chromatography system with an automated micro-volume loader (Shimadzu) through a Superdex 200 Increase 3.2/300 column (GE Healthcare) maintained in 300 mM NaCl, 10 mM HEPES and 0.007% DDTM (w/v). Monodisperse peak reduction with increasing temperature was measured relative to an unheated control sample maintained at 4 °C.

Importantly, because some drugs thermostabilize when bound to detergent-solubilized protein[65], the thermostability assay offers an efficient strategy to measure protein sensitivity to drugs in the detergent-solubilized environment. Purified $GABA_AR$ $\alpha5_{TMD}$ or $\alpha5_{TMD}$ mutants were separated into PCR tubes, supplemented with pregnanolone at a range of concentrations and heated at Tm30%

 doi:10.1038/nsmb.3484

(the temperature at which the monodisperse peak was reduced by 70%) for 1 h. Afterward, samples were run on a high-performance liquid chromatography system with an automated micro-volume loader (Shimadzu) through a Superdex 200 3.2/300 column (GE Healthcare) maintained in 300 mM NaCl, 10 mM HEPES and 0.007% DDTM. Drug dose–response curves were generated by plotting UV absorbance against drug concentration.

Cell lines used. HEK293S-GnTI$^-$ cells (ATCC Cat# CRL-3022, RRID: CVCL_A785) and HEK 293T (ATCC Cat# CRL-3216, RRID: CVCL_0063) were both confirmed free from mycoplasma contamination.

Data availability. The atomic coordinates and the structure factors are available from the Protein Data Bank under accession codes PDB 5O8F (pregnanolone-bound $\alpha5_{TMD}$) and PDB 5OJM (apo $\alpha5_{TMD}$). Source data for **Figures 1e**, **3e** and **3f** are available online. A **Life Sciences Reporting Summary** for this article is available.

33. Jansen, M., Bali, M. & Akabas, M.H. Modular design of Cys-loop ligand-gated ion channels: functional 5-HT3 and GABA rho1 receptors lacking the large cytoplasmic M3M4 loop. *J. Gen. Physiol.* **131**, 137–146 (2008).
34. Aricescu, A.R., Lu, W. & Jones, E.Y. A time- and cost-efficient system for high-level protein production in mammalian cells. *Acta Crystallogr. D Biol. Crystallogr.* **62**, 1243–1250 (2006).
35. Molday, R.S. & MacKenzie, D. Monoclonal antibodies to rhodopsin: characterization, cross-reactivity, and application as structural probes. *Biochemistry* **22**, 653–660 (1983).
36. Oprian, D.D., Molday, R.S., Kaufman, R.J. & Khorana, H.G. Expression of a synthetic bovine rhodopsin gene in monkey kidney cells. *Proc. Natl. Acad. Sci. USA* **84**, 8874–8878 (1987).
37. Reeves, P.J., Callewaert, N., Contreras, R. & Khorana, H.G. Structure and function in rhodopsin: high-level expression of rhodopsin with restricted and homogeneous N-glycosylation by a tetracycline-inducible N-acetylglucosaminyltransferase I-negative HEK293S stable mammalian cell line. *Proc. Natl. Acad. Sci. USA* **99**, 13419–13424 (2002).
38. Aricescu, A.R. & Owens, R.J. Expression of recombinant glycoproteins in mammalian cells: towards an integrative approach to structural biology. *Curr. Opin. Struct. Biol.* **23**, 345–356 (2013).
39. Zacharias, D.A., Violin, J.D., Newton, A.C. & Tsien, R.Y. Partitioning of lipid-modified monomeric GFPs into membrane microdomains of live cells. *Science* **296**, 913–916 (2002).
40. Nagai, T. *et al.* A variant of yellow fluorescent protein with fast and efficient maturation for cell-biological applications. *Nat. Biotechnol.* **20**, 87–90 (2002).
41. Pardon, E. *et al.* A general protocol for the generation of Nanobodies for structural biology. *Nat. Protoc.* **9**, 674–693 (2014).
42. Chang, V.T. *et al.* Glycoprotein structural genomics: solving the glycosylation problem. *Structure* **15**, 267–273 (2007).
43. Walter, T.S. *et al.* A procedure for setting up high-throughput nanolitre crystallization experiments. Crystallization workflow for initial screening, automated storage, imaging and optimization. *Acta Crystallogr. D Biol. Crystallogr.* **61**, 651–657 (2005).
44. Parker, J.L. & Newstead, S. Current trends in α-helical membrane protein crystallization: an update. *Protein Sci.* **21**, 1358–1365 (2012).
45. Otwinowski, Z. & Minor, W. Processing of X-ray diffraction data collected in oscillation mode. *Methods Enzymol.* **276**, 307–326 (1997).
46. Winn, M.D. *et al.* Overview of the CCP4 suite and current developments. *Acta Crystallogr. D Biol. Crystallogr.* **67**, 235–242 (2011).
47. Evans, P.R. & Murshudov, G.N. How good are my data and what is the resolution? *Acta Crystallogr. D Biol. Crystallogr.* **69**, 1204–1214 (2013).
48. Van den Abbeele, A. *et al.* A llama-derived gelsolin single-domain antibody blocks gelsolin-G-actin interaction. *Cell. Mol. Life Sci.* **67**, 1519–1535 (2010).
49. McCoy, A.J. *et al.* Phaser crystallographic software. *J. Appl. Crystallogr.* **40**, 658–674 (2007).
50. Emsley, P., Lohkamp, B., Scott, W.G. & Cowtan, K. Features and development of Coot. *Acta Crystallogr. D Biol. Crystallogr.* **66**, 486–501 (2010).
51. Murshudov, G.N. *et al.* REFMAC5 for the refinement of macromolecular crystal structures. *Acta Crystallogr. D Biol. Crystallogr.* **67**, 355–367 (2011).
52. Adams, P.D. *et al.* PHENIX: a comprehensive Python-based system for macromolecular structure solution. *Acta Crystallogr. D Biol. Crystallogr.* **66**, 213–221 (2010).
53. Afonine, P.V. *et al.* Towards automated crystallographic structure refinement with phenix.refine. *Acta Crystallogr. D Biol. Crystallogr.* **68**, 352–367 (2012).
54. Strong, M. *et al.* Toward the structural genomics of complexes: crystal structure of a PE/PPE protein complex from Mycobacterium tuberculosis. *Proc. Natl. Acad. Sci. USA* **103**, 8060–8065 (2006).
55. Chen, V.B. *et al.* MolProbity: all-atom structure validation for macromolecular crystallography. *Acta Crystallogr. D Biol. Crystallogr.* **66**, 12–21 (2010).
56. Stuart, D.I., Levine, M., Muirhead, H. & Stammers, D.K. Crystal structure of cat muscle pyruvate kinase at a resolution of 2.6 A. *J. Mol. Biol.* **134**, 109–142 (1979).
57. Krissinel, E. & Henrick, K. Inference of macromolecular assemblies from crystalline state. *J. Mol. Biol.* **372**, 774–797 (2007).
58. Smart, O.S., Goodfellow, J.M. & Wallace, B.A. The pore dimensions of gramicidin A. *Biophys. J.* **65**, 2455–2460 (1993).
59. Pettersen, E.F. *et al.* UCSF Chimera–a visualization system for exploratory research and analysis. *J. Comput. Chem.* **25**, 1605–1612 (2004).
60. Hosie, A.M., Dunne, E.L., Harvey, R.J. & Smart, T.G. Zinc-mediated inhibition of GABA(A) receptors: discrete binding sites underlie subtype specificity. *Nat. Neurosci.* **6**, 362–369 (2003).
61. Banks, J.L. *et al.* Integrated modeling program, applied chemical theory (IMPACT). *J. Comput. Chem.* **26**, 1752–1780 (2005).
62. Friesner, R.A. *et al.* Glide: a new approach for rapid, accurate docking and scoring. 1. Method and assessment of docking accuracy. *J. Med. Chem.* **47**, 1739–1749 (2004).
63. Halgren, T.A. *et al.* Glide: a new approach for rapid, accurate docking and scoring. 2. Enrichment factors in database screening. *J. Med. Chem.* **47**, 1750–1759 (2004).
64. Humphrey, W., Dalke, A. & Schulten, K. VMD: visual molecular dynamics. *J. Mol. Graph.* **14**, 33–38 (1996).
65. Hattori, M., Hibbs, R.E. & Gouaux, E. A fluorescence-detection size-exclusion chromatography-based thermostability assay for membrane protein precrystallization screening. *Structure* **20**, 1293–1299 (2012).

© 2017 Nature America, Inc., part of Springer Nature. All rights reserved.

Corresponding Author: Radu Aricescu
Date: Jul 26, 2017

Life Sciences Reporting Summary

Nature Research wishes to improve the reproducibility of the work we publish. This form is published with all life science papers and is intended to promote consistency and transparency in reporting. All life sciences submissions use this form; while some list items might not apply to an individual manuscript, all fields must be completed for clarity.

For further information on the points included in this form, see Reporting Life Sciences Research. For further information on Nature Research policies, including our data availability policy, see Authors & Referees and the Editorial Policy Checklist.

Experimental design

1. Sample size

Describe how sample size was determined.

Electrophysiology experiments were performed minimally in triplicate, as described in the methods and figure legends. Crystallography experiments relied on single crystals (for both apo and neurosteroid-bound forms), however these provide sufficient internal redundancy.

2. Data exclusions

Describe any data exclusions.

Diffraction from the apo α5TMD crystal was strongly anisotropic. Ellipsoidal truncation, with resolution limits along the reciprocal cell directions a*, b* and c* being 3.9 Å, 3.8 Å and 3.3 Å respectively, anisotropic scaling and a negative isotropic B-factor correction (-49.29 Å^2) were performed using the UCLA-DOE Lab Diffraction Anisotropy server (https://services.mbi.ucla.edu/anisoscale/). Anisotropic correction led to improvements in the electron density map quality and facilitated model building. The model deposited was refined against the truncated dataset, however we have also deposited the full dataset and provide refinement statistics against it in Table 1.

3. Replication

Describe whether the experimental findings were reliably reproduced.

All functional experiments were repeated (minimal n=3) and results were consistent. Error bars etc are provided.

4. Randomization

Describe how samples/organisms/participants were allocated into experimental groups.

Samples were not randomized.

5. Blinding

Describe whether the investigators were blinded to group allocation during data collection and/or analysis.

Not applicable.

Note: all studies involving animals and/or human research participants must disclose whether blinding and randomization were used.

© 2017 Nature America, Inc., part of Springer Nature. All rights reserved.

Nature Structural & Molecular Biology: doi:10.1038/nsmb.3484

6. Statistical parameters

For all figures and tables that use statistical methods, confirm that the following items are present in relevant figure legends (or the Methods section if additional space is needed).

n/a	Confirmed	
☐	☒	The exact sample size (*n*) for each experimental group/condition, given as a discrete number and unit of measurement (animals, litters, cultures, etc.)
☐	☒	A description of how samples were collected, noting whether measurements were taken from distinct samples or whether the same sample was measured repeatedly.
☐	☒	A statement indicating how many times each experiment was replicated
☐	☒	The statistical test(s) used and whether they are one- or two-sided (note: only common tests should be described solely by name; more complex techniques should be described in the Methods section)
☒	☐	A description of any assumptions or corrections, such as an adjustment for multiple comparisons
☒	☐	The test results (e.g. *p* values) given as exact values whenever possible and with confidence intervals noted
☒	☐	A summary of the descriptive statistics, including central tendency (e.g. median, mean) and variation (e.g. standard deviation, interquartile range)
☐	☒	Clearly defined error bars

See the web collection on statistics for biologists for further resources and guidance.

Software

Policy information about availability of computer code

7. Software

Describe the software used to analyze the data in this study.	HKL2000 (X-ray data indexing, integrating, scaling); Aimless (merging); Phaser (molecular replacement); Coot (model building); Refmac, Phenix (model refinement); Grade (pregnanolone geometry restraints generation); UCLA-DOE Lab Diffraction Anisotropy server (anisotropy correction); Molprobity (model quality control); SHP (structural alignments); PDBePISA (protein interface analyses); Hole (channel pore analysis); Pymol (figure generation); UCSF Chimera (movie generation); Schrödinger suite packages (molecular docking); IonFlux Data Analyzer 4 (electrophysiology data collection and processing); OriginPro (graph generation).

For all studies, we encourage code deposition in a community repository (e.g. GitHub). Authors must make computer code available to editors and reviewers upon request. The *Nature Methods* guidance for providing algorithms and software for publication may be useful for any submission.

Materials and reagents

Policy information about availability of materials

8. Materials availability

Indicate whether there are restrictions on availability of unique materials or if these materials are only available for distribution by a for-profit company.	There is no restriction, other than customary MTA arrangements required by academic institutions.

9. Antibodies

Describe the antibodies used and how they were validated for use in the system under study (i.e. assay and species).	Rho-1D4 antibody (purchased from the University of British Columbia), for affinity protein purification (extensively used in the literature over several decades). Nanobody 25 against human beta3 GABAA receptor subunit, raised in llamas for this study. Binding confirmed by surface plasmon resonance and crystallography.

© 2017 Nature America, Inc., part of Springer Nature. All rights reserved.

Nature Structural & Molecular Biology: doi:10.1038/nsmb.3484

10. Eukaryotic cell lines

a. State the source of each eukaryotic cell line used.	HEK293S-GnTI- cells (ATCC Cat# CRL-3022, RRID: CVCL_A785), for protein production; HEK 293T (ATCC Cat# CRL-3216, RRID: CVCL_0063), for electrophysiology experiments.
b. Describe the method of cell line authentication used.	Cell lines were purchased from the ATCC.
c. Report whether the cell lines were tested for mycoplasma contamination.	Cell lines were tested and confirmed free from mycoplasma contamination.
d. If any of the cell lines used in the paper are listed in the database of commonly misidentified cell lines maintained by ICLAC, provide a scientific rationale for their use.	Not applicable.

Animals and human research participants

Policy information about studies involving animals; when reporting animal research, follow the ARRIVE guidelines

11. Description of research animals

Provide details on animals and/or animal-derived materials used in the study.	Not applicable.

Policy information about studies involving human research participants

12. Description of human research participants

Describe the covariate-relevant population characteristics of the human research participants.	Not applicable.

© 2017 Nature America, Inc., part of Springer Nature. All rights reserved.

Nature Structural & Molecular Biology: doi:10.1038/nsmb.3484

nature protocols

PROTOCOL

https://doi.org/10.1038/s41596-018-0075-9

Lentiviral transduction of mammalian cells for fast, scalable and high-level production of soluble and membrane proteins

Jonathan Elegheert[1,3,4*], Ester Behiels[1,3,4,6], Benjamin Bishop[1,6], Suzanne Scott[1,2], Rachel E. Woolley[1], Samuel C. Griffiths[1], Eamon F. X. Byrne[1,5], Veronica T. Chang[2], David I. Stuart[1], E. Yvonne Jones[1], Christian Siebold[1*], A. Radu Aricescu[1,2*]

Structural, biochemical and biophysical studies of eukaryotic soluble and membrane proteins require their production in milligram quantities. Although large-scale protein expression strategies based on transient or stable transfection of mammalian cells are well established, they are associated with high consumable costs, limited transfection efficiency or long and tedious selection of clonal cell lines. Lentiviral transduction is an efficient method for the delivery of transgenes to mammalian cells and unifies the ease of use and speed of transient transfection with the robust expression of stable cell lines. In this protocol, we describe the design and step-by-step application of a lentiviral plasmid suite, termed pHR-CMV-TetO$_2$, for the constitutive or inducible large-scale production of soluble and membrane proteins in HEK293 cell lines. Optional features include bicistronic co-expression of fluorescent marker proteins for enrichment of co-transduced cells using cell sorting and of biotin ligase for in vivo biotinylation. We demonstrate the efficacy of the method for a set of soluble proteins and for the G-protein-coupled receptor (GPCR) Smoothened (SMO). We further compare this method with baculovirus transduction of mammalian cells (BacMam), using the type-A γ-aminobutyric acid receptor (GABA$_A$R) β3 homopentamer as a test case. The protocols described here are optimized for simplicity, speed and affordability; lead to a stable polyclonal cell line and milligram-scale amounts of protein in 3–4 weeks; and routinely achieve an approximately three- to tenfold improvement in protein production yield per cell as compared to transient transduction or transfection.

Introduction

Technologies for mammalian transient or stable cell line expression have greatly facilitated the production of stabilized and correctly folded recombinant eukaryotic proteins[1]. These proteins are often large, have a multi-domain architecture, and contain numerous post-translational modifications (PTMs) such as *O*- or *N*-linked glycosylation[2]. Accordingly, such proteins are best expressed in native cell types that contain the necessary cellular machinery for protein synthesis, folding and quality control; PTMs; and correct subcellular targeting, as well as a near-native membrane and lipid environment.

Previously, we have reported protocols for efficient transient protein expression in mammalian cells using the pHLsec plasmid[3]. This plasmid and its derivatives have now been successfully used for >10 years within the Division of Structural Biology (STRUBI) at Oxford, and have been distributed to numerous other labs. During this period, limitations associated with large-scale transient protein expression in HEK293T cells have also become apparent: large-scale plasmid preparation became increasingly costly; the procedure is fairly laborious and generates considerable plastic and biological waste. The volumes of biomass and expression media typically required, and large number of plastic roller bottles often used for a given target, add up to substantial financial and environmental burdens. In our experience, large-scale transient transfection efficiencies using polyethylenimine (PEI) are typically limited to ~60–75%, meaning that approximately one-third of the total cell mass is wasted.

[1]Division of Structural Biology, Wellcome Centre for Human Genetics, University of Oxford, Oxford, UK. [2]MRC Laboratory of Molecular Biology, Cambridge Biomedical Campus, Cambridge, UK. [3]Interdisciplinary Institute for Neuroscience, University of Bordeaux, Bordeaux, France. [4]Present address: Interdisciplinary Institute for Neuroscience, CNRS UMR 5297, Bordeaux, France. [5]Present address: Department of Bioengineering, Stanford University, Stanford, CA, USA. [6]These authors contributed equally: Ester Behiels, Benjamin Bishop. *e-mails: jonathan.elegheert@u-bordeaux.fr; christian@strubi.ox.ac.uk; radu@mrc-lmb.cam.ac.uk

The generation of stably transfected cell lines overcomes many disadvantages associated with transient transfection[4]. It has, however, one important drawback; the time frame for establishing a monoclonal cell line through rigorous selection and expansion is ~8–10 weeks for each construct[4], which substantially hampers achievement of a high sample throughput.

An ideal method would combine the ease of use and speed of transient transfection with the robust expression of stable cell lines. The use of lentiviruses, belonging to the retrovirus genus, presents such a possibility. A recombinant lentivirus, containing genetic elements from HIV, is widely used for gene delivery in medical applications[5]. Lentiviruses use the host cellular machinery to amplify and package their genetic material, and the packaged transgene is delivered to the target cell via membrane fusion. Therefore, this method circumvents the need for large-scale DNA preps and laborious transfection procedures while rapidly establishing stable genome integration of the transgene with high efficiency. Although a number of laboratories have designed customized lentiviral vectors for transgene delivery[6–9], and several companies market proprietary lentiviral expression systems, the use of lentiviral transduction for large-scale protein production is not widespread in the structural biology community, perhaps owing to a lack of proof-of-principle examples and detailed protocols.

Here, we describe step-by-step procedures for large-scale expression of soluble and membrane proteins using a lentiviral system. We have constructed a plasmid suite around the transfer plasmid pHR-CMV-TetO$_2$ that is specifically designed for large-scale protein expression from HEK293 cell lines and is compatible with subcloning of cDNA inserts from the pHLsec plasmid commonly used for transient transfection[3]. Use of this lentiviral method leads to the rapid (within ~7 d) establishment of polyclonal cell lines that can be selected, expanded and adapted to a variety of protein expression setups (Fig. 1). The typical lead time for protein production of ~3–4 weeks compares well with transient expression[3]. We routinely observe an approximately three- to tenfold improvement in protein production yield per cell as compared with transient transfection.

Overview of the procedure

The procedure to transduce expression cells is straightforward; a lentivirus producer cell line (HEK293 Lenti-X) is transiently co-transfected with transfer (encoding the transgene of interest), envelope and packaging plasmids to generate lentiviral particles. The lentivirus-containing supernatant is then, normally without concentration, used to transduce the HEK293 target cell line (Fig. 1a). After genomic integration of the proviral DNA and optional enrichment using cell sorting, these cells are expanded for large-scale protein expression. The procedure can be broken down into four stages (Fig. 1b). In the first stage (Steps 1–8 and Steps 11–14), the lentivirus producer cell line is transfected, and lentiviral particles encoding the transgene(s) are collected. In the second stage (Steps 9–10 and Steps 15–21), expression cells are infected, stably transduced and expanded. In the third stage (Step 22A(i–xiii)), adherent expression cells are expanded for large-scale soluble secreted protein expression. Alternatively, in the fourth stage (Step 22B(i–xxii)), suspension expression cells are expanded for large-scale inducible membrane protein expression.

Features of the pHR-CMV-TetO$_2$ transfer plasmid

We initially developed the lentiviral transfer plasmid pHR-CMV-TetO$_2$ (Table 1) and the protocols described in this paper for high-level expression of the extracellular domain (ECD) of CD45 (protein tyrosine phosphatase receptor type C; (PTPRC)) for structural studies[10,11]. The plasmid contains the minimally necessary *cis*-acting HIV components: the 5′ and 3′ long terminal repeats (LTRs), the polypurine tract (PPT), the Rev response element (RRE) and the psi (ψ) packaging signal. The genetic elements flanked by the 5′ and 3′ LTRs will be stably integrated into the host cell genome as proviral DNA (Fig. 2 (top panel) and Supplementary Fig. 1).

The transfer plasmid is used in conjunction with a second-generation envelope plasmid (pMD2.G; Addgene plasmid no.12259) and a second-generation packaging plasmid (psPAX2; Addgene plasmid no. 12260). pMD2.G encodes the vesicular stomatitis virus G envelope protein (VSV-G), and its use ensures a pseudotyped lentiviral particle with high infectivity and broad host tropism[12]; the receptor for VSV-G is the low-density lipoprotein receptor (LDLR)[13]. psPAX2 contains the minimally necessary HIV genes required for virus production: *gag*, *pol*, *rev* and *tat*.

pHR-CMV-TetO$_2$ was derived from the second-generation pHR-SIN-CSGW lentiviral transfer plasmid[14,15]. To maximize restriction/ligation subcloning compatibility with our pHLsec plasmid for transient expression[3], we first deleted all internal *EcoRI*, *AgeI*, *KpnI*, *XhoI*, *SalI*, *XbaI*, *NotI* and *BamHI* restriction sites from the pHR-SIN-CSGW backbone, using PCR. Then we placed the pHLsec

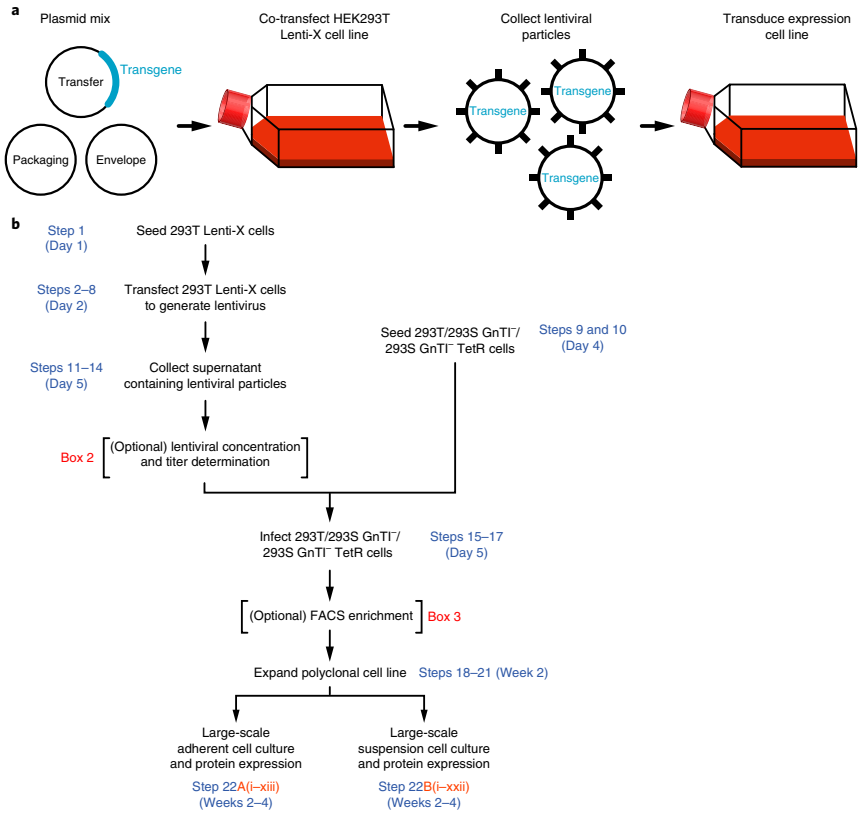

Fig. 1 | Large-scale expression of soluble or membrane proteins using lentiviral transduction. a, Graphical summary of the Procedure. **b**, Flowchart for the protocol.

multiple cloning site (MCS) after the pHR-SIN-CSGW spleen focus forming virus (SFFV) promoter. HEK293 and derived cell lines[16] are widely used for large-scale protein production for structural biology purposes (Box 1). To optimize the plasmid for protein expression in HEK293 cells, we replaced the SFFV promoter with the major immediate–early (MIE) human cytomegalovirus (CMV) enhancer and promoter[17] and two *TetO* operator sequences, all amplified from the pACMV-tetO plasmid[18], to generate pHR-CMV-$TetO_2$. The CMV promoter[19] is strongly transactivated by the adenoviral E1A protein[20] that is constitutively expressed by immortalized HEK293 cells. The pHR-CMV-$TetO_2$ plasmid retains the woodchuck hepatitis virus (WHP) post-transcriptional regulatory element (WPRE)[21] from the pHR-SIN-CSGW plasmid, leading to improved transcript stability and transgene expression (Fig. 2a and Supplementary Fig. 1).

The MCS of the pHR-CMV-$TetO_2$ plasmid is fully compatible with that of pHLsec[3], and is organized as follows: *EcoRI*–chicken RPTPσ signal sequence–*AgeI*–insert–*KpnI*–tag+stop codons–*XhoI*. Thus, by digesting pHLsec-based constructs with *EcoRI*/*AgeI* and *XhoI*, the complete expression cassette can be transferred to the pHR-CMV-$TetO_2$ backbone (Fig. 2b and Supplementary Fig. 2a,b). The chicken RPTPσ signal sequence directs targeting of the nascent protein to the secretory pathway. In the case that one wants to use the native signal sequence, in the case of intracellular proteins, or in the case of membrane proteins that do not contain a signal sequence (by relying on transmembrane domains for targeting to the secretory pathway), the chicken RPTPσ signal sequence can be removed

Table 1 | Transfer plasmids

pHR-CMV-TetO$_2$	Addgene plasmid no.	Purpose
3C-Twin-Strep	113883	Protein (co-)expression, FACS
3C-Twin-Strep_IRES-EmGFP	113884	
3C-Twin-Strep_IRES-mRuby2	113885	
3C-Twin-Strep_IRES-mTurquoise2	113886	
3C-Avi-His6	113887	Protein (co-)expression, FACS, in vivo biotinylation
3C-Avi-His6_IRES-EmGFP	113888	
3C-Avi-His6_IRES-mRuby2	113889	
3C-Avi-His6_IRES-mTurquoise2	113890	
3C-mVenus-Twin-Strep	113891	Membrane protein expression and FSEC-TS screening, FACS
EmGFP	113892	Transduction and FACS compensation controls
mVenus	113893	
mRuby2	113894	
mTurquoise2	113895	
HA-BirA	113896	HA-tagged cytosolic and ER-resident biotin ligase for in vivo biotinylation
HA-BirA-ER	113897	
3C-Avi-His6_IRES-HA-BirA-ER	113898	
pHR-CMV		
TetR-HA-NLS-P2A-BSD-Myc	113899	Generation of inducible cell lines
pHR-SFFV		
3C-Twin-Strep	113900	Alternative to CMV-TetO$_2$
pHR-CAG		
3C-Twin-Strep	113901	Alternative to CMV-TetO$_2$

by digesting the plasmid with *EcoRI*. We recommend in vivo assembly (IVA) cloning[22], which exploits recA-independent homologous recombination between a PCR amplicon and the linearized pHR-CMV-TetO$_2$ vector (Supplementary Methods), as a time- and cost-efficient alternative to regular restriction/ligation subcloning.

In the empty pHR-CMV-TetO$_2$ plasmid, the purification tag inserted between the *KpnI* and *XhoI* restriction sites is either (i) the 3C-Avi-His6 tag (pHR-CMV-TetO$_2$_3C-Avi-His6 plasmid), or (ii) the 3C-Twin-Strep tag (pHR-CMV-TetO$_2$_3C-Twin-Strep plasmid) (Table 1 and Supplementary Fig. 2a,b). The 3C-Avi-His6 tag consists of a sequential Avi-tag and His6-tag preceded by a human rhinovirus (HRV) 3C protease site. It allows purification of proteins using immobilized metal affinity chromatography (IMAC). Use of the Avi-tag for in vivo biotinylation of proteins is described in the 'Other applications of the method' section. The 3C-Twin-Strep tag consists of a sequential arrangement of two Strep-tag II sequences preceded by a HRV 3C protease site, and is used in conjunction with Strep-Tactin XT resin[23] (IBA) for one-step protein purification[24]. In both cases, the HRV 3C protease site allows removal of the purification tag by digestion with 3C protease, optionally combined with a reverse purification step.

Finally, the pHR-CMV-TetO$_2$ plasmids contain the simian vacuolating virus 40 (SV40) origin of replication (ori), as well as the SV40 large T-antigen under control of the SV40 promoter (Supplementary Fig. 1); these features allow autonomous episomal replication of the plasmid in mammalian cells to ensure maintenance of high plasmid copy numbers. The pHR-CMV-TetO$_2$ plasmids are hence also suitable for transient transfection and can be used for initial small-scale screening of expression constructs (Fig. 2c).

Extended features of the pHR-CMV-TetO$_2$ transfer plasmid suite

A limitation of the lentiviral system is that the size of the transgene to be packaged is physically constrained. Viral titers decrease semi-logarithmically with increasing insert size, with an estimated drop of ~1 log for every 2 kb of insert[25]. Measurable titers can, however, still be obtained with proviral

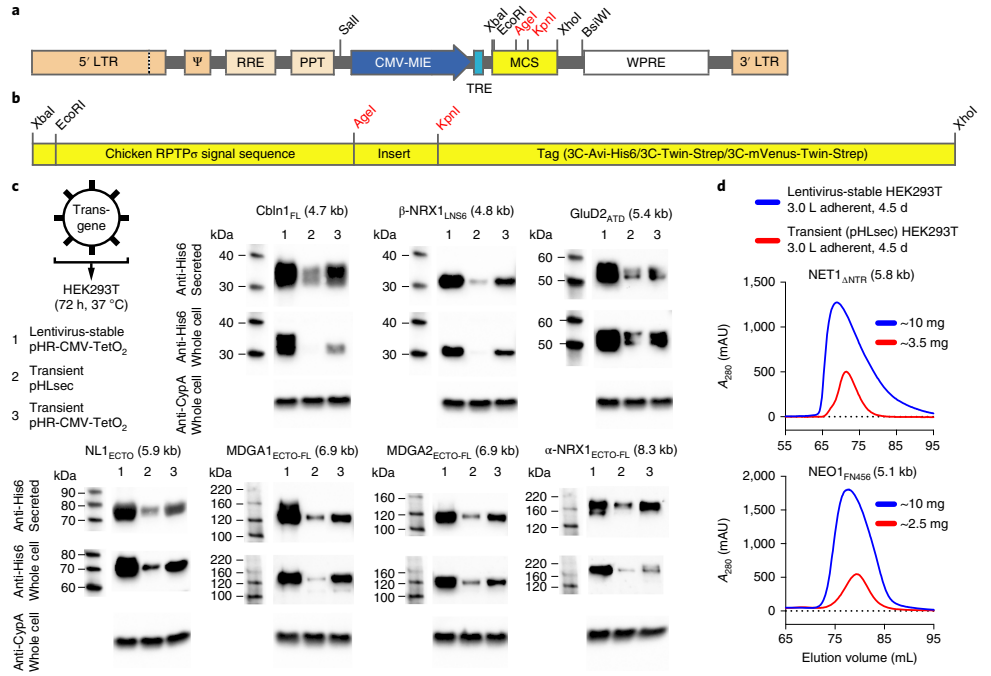

Fig. 2 | The pHR-CMV-TetO$_2$ transfer plasmid for stable lentiviral expression in HEK293 cells. a, Genetic elements between the 5′ and 3′ long terminal repeats (LTRs) are packaged in lentiviral particles and integrated into the expression cell genome as proviral DNA. Total proviral DNA size in the empty pHR-CMV-TetO$_2$ plasmid is 4.2 kb. **b**, The pHR-CMV-TetO$_2$ MCS. **c**, Non-concentrated lentiviral particles were used to infect HEK293T cells and protein was expressed for 72 h. His6-tagged proteins were detected using Western blotting (mouse anti-His6 primary antibody, 1:5,000 dilution; HRP-conjugated goat anti-mouse secondary antibody, 1:5,000 dilution; rabbit anti-cyclophilin A (CypA) primary antibody, 0.5 μg/mL; HRP-conjugated goat anti-rabbit secondary antibody, 1:5,000 dilution). Proviral DNA sizes are noted in parentheses. **d**, Comparative size-exclusion chromatograms of secreted NET1$_{\Delta NTR}$ and NEO1$_{FN456}$, showing improved secreted protein yields from lentiviral transduction (blue curves) as compared to transient transfection (red curves) of adherent HEK293T cells. ψ, psi packaging signal; CMV-MIE, major immediate-early cytomegalovirus enhancer and promoter; mAU, milliabsorbance unit; MCS, multiple cloning site; PPT, polypurine tract; RRE, Rev response element; TRE, tetracycline response element; WPRE, woodchuck hepatitis virus post-transcriptional regulatory element.

DNA sizes in excess of 18 kb[25]. We found that lentiviral titers that are obtained with (i) the HEK293 Lenti-X producer cell line, which is clonally selected to support high-level expression of viral proteins to yield higher viral titers; and (ii) proviral DNA sizes not >~8.5 kb are sufficiently high to lead to >90% transduction efficiency of HEK293 expression cells. For the pHR-CMV-TetO$_2$_3C-Avi-His6 and pHR-CMV-TetO$_2$_3C-Twin-Strep plasmids, this equates to an insert size of ~4.3 kb between the *EcoRI* and *XhoI* sites (Supplementary Fig. 1). Practically, this means that neither concentration of lentiviral titer nor selection of the polyclonal stable cell line is necessary, and that the recombinant protein–producing cell population can immediately be expanded, thereby yielding substantial time savings.

Forgoing concentration of the lentivirus-containing supernatant is time efficient, prevents any negative impact on lentiviral particle integrity and also prevents the infectious lentiviral particles from having to be taken out of the flow cabinet. Consequentially, transduction is performed at a variable multiplicity of infection (MOI; the ratio of the number of viral particles to the number of target cells) because insert size correlates strongly with viral titer and viral titer determines the MOI.

It is desirable to be able to enrich any subset of transduced cells from the total cell pool, especially when working with non-concentrated lentiviral particles encoding proviral DNA sizes >~8.5 kb, which yield lower viral titers and corresponding transduction efficiencies. Two strategies are traditionally used: antibiotic selection and enrichment by FACS. Antibiotic selection is slower, but high

Box 1 | Growth and maintenance of adherent and suspension HEK293 cells

Adherent HEK293T, HEK293S GnTI$^-$ or HEK293S GnTI$^-$ TetR cells are normally grown in DMEM/F-12/10% fetal bovine serum (FBS) medium and maintained in standard T75 (75-cm^2) or T175 (175-cm^2) flasks in a humidified incubator operated at 37 °C with 5% CO_2. Using flow cytometry, we determined that HEK293 cells reach a density of ~250,000 cells per cm^2 flask surface area upon confluency. This number is a useful reference for calculation of seeding densities of plates, flasks and bottles. It corresponds to ~2,400,000 cells in a confluent 6-well (9.6-cm^2) plate, ~6,250,000 cells in a confluent T25 flask (25 cm^2), ~18,750,000 cells in a confluent T75 flask (75 cm^2) and ~43,750,000 cells in a confluent T175 flask (175 cm^2).

Expand ('split') confluent T75 or T175 flasks containing adherent cells by removing the DMEM/F-12/10% FBS medium, washing the cells with PBS (5 or 10 mL, respectively) and incubating them with trypsin-EDTA (2 or 5 mL, respectively) for 3 min in a humidified incubator operated at 37 °C with 5% CO_2. Then gently dislodge the cells and quench the trypsin-EDTA solution using 10 or 25 mL DMEM/F-12/10% FBS medium, respectively. Pipette up and down a few times, using a sterile serological 10-mL pipette to break up any clumped cells. Finally, transfer the required number of cells (typically one-sixth of the total cell slurry) to a new T75 or T175 flask and top up the DMEM/F-12/10% FBS medium to the recommended volume (12 or 30 mL, respectively).

Large-scale adherent cultures for soluble secreted protein production are performed in expanded-surface polystyrene roller bottles (2,125 cm^2) or in HYPERFlasks (1,720 cm^2). HEK293T and HEK293S GnTI$^-$ cells are maintained in DMEM/F-12/10% FBS medium during expansion and DMEM/F-12/2% FBS medium during protein expression. HEK293S GnTI$^-$ TetR cells are grown identically, except for addition of 2 μg/mL blasticidin; this maintains the selective pressure on the pcDNA6/TR genetic elements with which the HEK293S GnTI$^-$ TetR cells are stably transfected (the cell line was originally selected using 5 μg/mL blasticidin[34], but we observe slowed cell growth at that concentration).

Suspension-adapted HEK293S GnTI$^-$ and HEK293S GnTI$^-$ TetR cells are normally grown in polycarbonate Erlenmeyer baffled flasks with a filter cap, in a shaking incubator operated at 37 °C with 8% CO_2 (note that this differs from the 5% CO_2 used for adherent cells). Cells are grown in FreeStyle 293/1% FBS medium. Although we add 1% (vol/vol) FBS to the FreeStyle 293 medium to facilitate the transfer from adherent to suspension culture (Step 22B(i–ix)), it does not, in principle, require supplementation. The flasks are shaken at 130 r.p.m., and the suspension does not exceed 40% of the flask volume (i.e., for a 2-L flask, a maximum suspension volume of 800 mL is used).

Non-suspension-adapted HEK293 cell lines such as HEK293T will require adaptation to suspension growth over a period of several weeks[60]. Indeed, full suspension adaptation of the original HEK293 cell line to yield the HEK293S cell line took ~7 months[16]. FreeStyle 293-F cells, derived from the fast-growing suspension-adapted HEK293-F cell line, are an alternative.

We prefer performing lentiviral transduction in adherent culture, because suspension-adapted HEK293S GnTI$^-$ and HEK293S GnTI$^-$ TetR expression cells adapt readily from an adherent monolayer to suspension culture (Step 22B(i–ix)), and because the method relies on direct transfer of lentivirus-containing medium from the adherent HEK293T Lenti-X producer cells to the expression cells (Steps 11–17).

We routinely do not use penicillin–streptomycin ('pen–strep') to prevent bacterial growth, relying instead on sterile technique and well-maintained tissue culture infrastructure.

Cell lines should be regularly checked to ensure that they are authentic and not infected with mycoplasma. The American Type Culture Collection (ATCC) animal cell culture guide (https://www.atcc.org/~/media/PDFs/Culture%20Guides/AnimCellCulture_Guide.ashx) contains a wealth of tips and techniques for culturing continuous cell lines.

selection pressure allows isolation of cells with high-copy-number transgene integration[7]. We opted for FACS because it is faster and because the presence of fluorescent marker proteins can have multiple downstream applications. The use of FACS to obtain high protein-expressing clonal cell lines has long precedence[26–28]. We constructed variants of the pHR-CMV-TetO$_2$ plasmid that allow co-expression of fluorescent proteins (FPs) using the following two strategies.

- The 3C-mVenus-Twin-Strep variant (Table 1) encodes mVenus (λ_{EX} = 515 nm; λ_{EM} = 528 nm) as a 3C-cleavable C-terminal fusion protein, cloned in frame as a tag between the *KpnI* and *XhoI* restriction sites (Supplementary Fig. 3). In this setup, there is a direct 1:1 stoichiometric correspondence between the target protein and the FP.
- The IRES-FP variants (Table 1; IRES-EmGFP, IRES-mRuby2 and IRES-mTurquoise2) contain an internal ribosome entry site (IRES) from the encephalomyocarditis virus (EMCV), followed by the three different FPs, to allow their expression from the same mRNA as the transgene (bicistronic expression) (Fig. 3 (top panel) and Supplementary Fig. 3). These FPs are the Emerald green fluorescent protein (EmGFP: λ_{EX} = 487 nm; λ_{EM} = 509 nm)[29], the red fluorescent protein mRuby2 (λ_{EX} = 559 nm; λ_{EM} = 600 nm)[30] and the cyan fluorescent protein mTurquoise2 (λ_{EX} = 434 nm; λ_{EM} = 474 nm)[31]. The IRES-EmGFP, IRES-mRuby2 and IRES-mTurquoise2 sequences are cloned between the *XhoI* and *BsiWI* sites, placing them downstream of the MCS and upstream of the WPRE. A consequence of this setup is that the IRES-FP elements add ~1.3 kb to the proviral DNA size and so have an impact on lentiviral titer.

To test the efficacy of the IRES-FP elements, we assembled an mRuby2-IRES-EmGFP construct (Supplementary Fig. 4a). Using quantitative fluorescence microscopy, we determined that expression

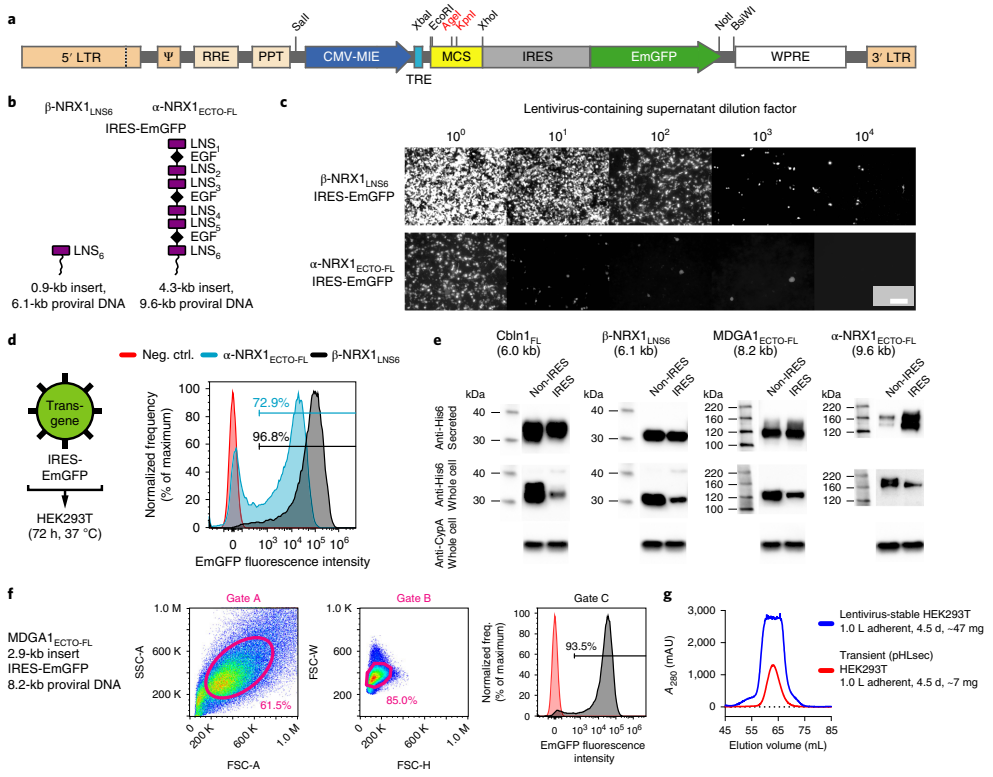

Fig. 3 | The pHR-CMV-TetO$_2$_IRES-EmGFP transfer plasmid for determination of transduction efficiency and enrichment of transduced cells using FACS. a, Schematic representation of the pHR-CMV-TetO$_2$_IRES-EmGFP proviral DNA (5.5 kb) for bicistronic expression of the transgene of interest and free cytosolic EmGFP. **b**, Schematic representation of the β-NRX1$_{LNS6}$ and α-NRX1$_{ECTO-FL}$ constructs. **c**, Endpoint dilution assay to estimate functional titer of non-concentrated lentiviral particles encoding β-NRX1$_{LNS6}$_IRES-EmGFP and α-NRX1$_{ECTO-FL}$_IRES-EmGFP. Each image was individually enhanced using ImageJ[59] to reveal all cells with fluorescence. Scale bar, 100 µm. **d**, Non-concentrated lentiviral particles were used to infect HEK293T cells and protein was expressed for 72 h. Comparison of transduction efficiency of β-NRX1$_{LNS6}$_IRES-EmGFP and α-NRX1$_{ECTO-FL}$_IRES-EmGFP. **e**, Western blot detection of His6-tagged proteins produced using the pHR-CMV-TetO$_2$_3C-Avi-His6 or pHR-CMV-TetO$_2$_3C-Avi-His6_IRES-EmGFP transfer plasmids (mouse anti-His6 primary antibody, 1:5,000 dilution; HRP-conjugated goat anti-mouse secondary antibody, 1:5,000 dilution; rabbit anti-cyclophilin A (CypA) primary antibody, 0.5 µg/mL; HRP-conjugated goat anti-rabbit secondary antibody: 1:5,000 dilution). Proviral DNA sizes are noted in parentheses. **f**, MDGA1$_{ECTO-FL}$_IRES-EmGFP: FSC-A, SSC-A, FSC-H and FSC-W, and fluorescence gates. The red curve is the negative, non-transduced control. **g**, Comparative size-exclusion chromatograms show secreted MDGA1$_{ECTO-FL}$ yields from 1.0 L (four roller bottles) of adherent HEK293T cell culture, either transiently transfected (red curve; 6.7 mg of total protein) or stably transduced using lentivirus (blue curve; 46.3 mg of total protein). Transduced cells were enriched using FACS by applying sorting gates A, B and C from **f**. FSC-A, forward scatter area; FSC-H, forward scatter height; FSC-W, forward scatter width; Neg. ctrl., negative control; SSC-A, side scatter area.

levels of EmGFP are ~30-fold lower when placed after IRES as compared to EmGFP alone, indicating that mRNA translation initiation from an IRES element is less potent than 5′ cap-dependent translation (Supplementary Fig. 4b). Importantly, however, we found that the downstream presence of IRES-EmGFP did not adversely affect fluorescence intensity levels in the red channel and that pixel values in the red and green channels correlated with a Pearson's correlation coefficient (r) of 0.89, indicating that IRES-EmGFP fluorescence can indeed be used as a qualitative and quantitative predictor of the presence and level of the protein of interest encoded by the upstream transgene (Supplementary Fig. 4c). We used flow cytometry to corroborate these results; we determined a Pearson's r of 0.85 between compensated mRuby2 and EmGFP fluorescence in 35,546 single, gated HEK293 cells expressing the mRuby2-IRES-EmGFP construct (Supplementary Fig. 4d).

Box 2 | Concentration and determination of lentiviral titer ● Timing ~4 d

Concentration and titration of the produced lentivirus allow better control over the MOI, and detailed protocols have been described previously[61]. Approaches for titration include (i) quantitative reverse transcription polymerase chain reaction (qRT-PCR) to amplify lentiviral RNA, (ii) detection of the HIV p24 capsid protein and (iii) qPCR to amplify proviral DNA. These assays are, however, time consuming and do not reflect functional viral titers when based on quantification of viral RNA or p24. Instead, we prefer to use a rapid and simple endpoint dilution assay using fluorescence, essentially as described previously for BacMam[44,45]. We recommend using EmGFP (pHR-CMV-TetO$_2$_IRES-EmGFP plasmid variant) or mVenus (pHR-CMV-TetO$_2$_3C-mVenus-Twin-Strep plasmid variant) for this purpose, as mRuby2 and mTurquoise2 are less bright, which makes it difficult to identify sparsely seeded transduced cells.

However, we do not routinely concentrate lentiviruses or determine their titer, instead preferring to place the lentivirus-containing supernatant (Steps 11–14) directly on top of the expression cells (Step 15). This approach works well for proviral DNA with a size of up to ~8.5 kb, saves time and prevents the virus-containing supernatant from exiting the laminar flow cabinet. IRES-FP fluorescence allows subsequent verification of transduction efficiency using fluorescence microscopy and flow cytometry, as well as FACS-based enrichment of subsets of cells from the total transduced cell pool.

Procedure

▲ **CRITICAL** The following titration procedure is for one 96-well black plate. It is inspired by published approaches for BacMam[44,45]. One 96-well black plate can be used to titer four lentivirus preparations simultaneously (columns 1–3, 4–6, 7–9 and 10–12); the eight dilutions (10^0 to 10^7), pipetted in triplicate, fit into rows A to H.

1 Seed each well of a 96-well black plate with ~4 × 10^4 HEK293T cells in DMEM/F-12/10% FBS medium, bringing them to ~50% confluency. It is convenient to do this the day before collection of the lentiviral particle-containing supernatant, e.g., simultaneously with Step 9.
2 Allow the cells to attach and grow overnight at 37 °C in a humidified incubator operated at 5% CO_2.
3 Filter 1 mL of lentiviral particle–containing supernatant from Step 11 through a 0.45-µm filter unit attached to a Luer-lock syringe, and into a sterile 1.5-mL tube.
4 Make dilution stocks of lentivirus from 10^0 to 10^7 in DMEM/F-12/2% FBS medium in sterile 1.5-mL tubes as follows:

Row	Dilution no.	Dilution	Medium	Lentiviral stock
A	0	10^0	–	100 µL of lentiviral stock (10^0)
B	1	10^1	900 µL	100 µL of lentiviral stock (10^0)
C	2	10^2	900 µL	100 µL of 10^1 dilution
D	3	10^3	900 µL	100 µL of 10^2 dilution
E	4	10^4	900 µL	100 µL of 10^3 dilution
F	5	10^5	900 µL	100 µL of 10^4 dilution
G	6	10^6	900 µL	100 µL of 10^5 dilution
H	7	10^7	900 µL	100 µL of 10^6 dilution

5 Remove the DMEM/F-12/10% FBS medium and replace it with 100 µL of diluted (10^0 to 10^7) virus.
6 Infect the HEK293T cells in triplicate for each virus.
7 Incubate the flask for 72 h at 37 °C in a humidified incubator operated at 5% CO_2.
8 After 72 h, count the number of fluorescent cells in the dilution that contains <10 fluorescent cells.
9 To calculate lentiviral titer, use the following equation: transduction units (TU)/mL = averaged number of fluorescent cells × dilution factor × 10. For example, when observing an averaged number of 5 fluorescent cells in dilution 5 (row F), TU/mL = 5 × 10^6. In a confluent T25 flask, which contains ~6,250,000 cells (Box 1), the application of 4 mL of this supernatant leads to a functional MOI of ~3.2 and a theoretical transduction efficiency of ~95%. Examples are shown in Fig. 3c and Supplementary Fig. 5.

To verify the inverse relation between proviral DNA size and viral titer, we performed a comparative endpoint dilution assay (Box 2) for the neuronal proteins β-NRX1$_{LNS6}$[32] and α-NRX1$_{ECTO-FL}$[33] cloned into the pHR-CMV-TetO$_2$_3C-Avi-His6_IRES-EmGFP plasmid (6.1-kb and 9.6-kb proviral DNA, respectively; Fig. 3b), and observed an ~100-fold difference in viral titer (~2 logs; Fig. 3c and Supplementary Fig. 5). Using flow cytometry, we determined a transduction efficiency of ~97% and ~73%, respectively (Fig. 3d and Supplementary Fig. 6). To boost transduction efficiency for α-NRX1$_{ECTO-FL}$, lentiviral particles would need to be concentrated before adding them to the expression cells. Alternatively, or additionally, cells expressing the EmGFP marker protein can be enriched using FACS, and then expanded (Box 3).

The pHR-CMV-TetO$_2$ plasmids are optimal for use with HEK293 cell lines

The pHR-CMV-TetO$_2$ plasmid and its variants are optimal for use with the HEK293 cell line and its derivatives[16]. We use the HEK293T, the *N*-acetylglucosaminyltransferase I-negative (GnTI$^-$)

Box 3 | FACS to enrich subpopulations of transduced cells

FACS[62–64] is a fast and convenient method of enriching transduced cell populations. The 3C-mVenus-Twin-Strep and IRES-FP plasmid variants are specifically designed for this purpose. In this box, we provide a number of pointers for optimal experimental results.

- When performing cell sorting, we pre-fill our catch tubes with complete medium.
- We find that cell viability after sorting is greatest when using suspension cells.
- For adherent cells, we recommend using soybean trypsin inhibitor (SBTI) instead of complete medium to inactivate trypsin and prevent cell clumping. We use trypsin-EDTA solution without phenol red to avoid background fluorescence.
- We pass suspension cells and trypsinized adherent cells through a 40-μm cell strainer before sorting, to ensure that cells are mostly single. This prevents clogging of the cell sorter nozzle, which is important when doing prolonged cell sorts.
- When performing multi-color FACS, fluorescence compensation is critical because of the overlap of fluorochrome emission spectra. For this reason, our pHR-CMV-$TetO_2$ suite contains plasmids for the expression of free cytosolic EmGFP, mVenus, mRuby2 and mTurquoise2. Cells expressing these fluorochromes can be used as bright positive-control samples. Non-transduced cells serve as negative-control samples. Combined, these control samples serve to properly set photomultiplier tube (PMT) detector voltages and to calculate the fluorescence compensation matrix.
- Fluorescence-minus-one (FMO) control samples are cells expressing all but one of the fluorochromes. They ensure that spread of fluorochromes into the channel of interest is properly identified and are ideal for determining accurate gating boundaries.
- Viability dyes such as propidium iodide (PI), DRAQ7, 7-AAD or TO-PRO-3 that penetrate dead and dying cells and bind their DNA can be used to design a gating strategy to remove these cells from the transduced cell population or to monitor cell viability to decide on the appropriate time for harvesting of expression cells or conditioned medium.
- When using inducible cells, FACS can be performed using either uninduced[65] or Dox-induced fluorescence. Importantly, the 405 nm laser readily excites Dox, introducing potential bias into fluorescence measurements. Therefore, we induce protein expression 24–48 h before sorting, using only 0.1 μg/mL Dox, and spin down the cells (500*g* for 5 min at room temperature (22–24 °C)) and resuspend them in Dox-free medium (without phenol red) or carrier buffer just before cell sorting. FACS compensation and FMO control samples are treated identically. Finally, we return the sorted cells to Dox-free growth medium after sorting. Representative −Dox and +Dox fluorescence of HEK293S GnTI$^-$ TetR cells expressing the membrane proteins SMO_{XTAL} and $GABA_AR$-$\beta3_{FL}$ is shown in Fig. 4c and Fig. 5c, respectively.

HEK293S[34] and the HEK293S GnTI$^-$ Tet repressor protein (TetR)[34] cell lines for high-level protein production (Box 1). The latter cell line is identical to HEK293S GnTI$^-$ but in addition stably transfected with the pcDNA6/TR vector, leading to constitutive intracellular expression of TetR. TetR binds to the tetracycline response element (TRE) that is just downstream of the CMV promoter in the pHR-CMV-$TetO_2$ plasmids (Fig. 2a and Supplementary Figs. 1 and 3), thereby repressing transcription of the transgene. In the pHR-CMV-$TetO_2$ plasmids, the TRE is composed of two repeats of the 19-bp TetO operator sequence (5′-TCCCTATCAGTGATAGAGA-3′). Transgene expression can then be induced ('de-repressed') by application of tetracycline or its more stable analog doxycycline (Dox); Dox binds TetR, thereby releasing it from the TRE[18,35].

In summary, use of the pHR-CMV-$TetO_2$ plasmids in combination with the HEK293S GnTI$^-$ TetR cell line is particularly attractive for a number of reasons when producing mammalian proteins for structural biological purposes: (i) stable expression generally yields higher amounts of protein than transient expression; (ii) the $TetO_2$–TetR system allows inducible expression, which is useful when working with toxic proteins or membrane proteins; (iii) HEK293S cells allow both suspension and adherent growth; (iv) fluorescent marker proteins allow enrichment by FACS; and (v) GnTI$^-$ ensures the presence of predominantly homogeneous high mannose-type ($Man_5GlcNAc_2$) *N*-linked glycans that are sensitive to cleavage by endoglycosidase H (EndoH) or F1 (EndoF1)[2].

Other applications of the method

Alternative promoters

The CMV-MIE promoter/enhancer is one of the strongest promoters in HEK293 cells[17]. Like other strong viral promoters, it is prone to transcriptional silencing regulated by DNA methylation after prolonged activity[36–38]. It is, however, not prominent in HEK293 cell lines within the time frame of our procedure and can be reversed by application of the DNA methyltransferase (DNMT) inhibitor 5-Aza-2′-deoxycytidine (5-aza-dC). Because the CMV-MIE promoter/enhancer may not be the best choice for any given cell type[17], we have also included pHR variants containing either the SFFV promoter (pHR-SFFV) or the CAG (CMV enhancer, chicken β-actin promoter, rabbit β-globin splice acceptor) element amplified from pHLsec[3] (pHR-CAG) (Table 1 and Supplementary Fig. 3). All

promoters/enhancers are cloned between unique *SalI* and *XbaI* restriction sites, allowing their easy replacement with any promoter of choice. Expression cassettes can be transferred between the pHR-CMV-TetO$_2$, pHR-SFFV and pHR-CAG variants (Supplementary Fig. 3).

Co-transduction of different transgenes

Co-infection of cells using separate viruses encoding different transgenes (using FP fusions or using the IRES-FP variants) is useful for the expression of heteromeric receptors or protein complexes. Co-infected cells expressing all subunits can be enriched using multi-color FACS (Box 3).

In vivo biotinylation

In vivo biotinylation is a convenient way of introducing a biotin label into a specific 15-residue acceptor sequence ('Avi-tag'; GLNDIFEAQKIEWHE in single-letter amino acid code). We have constructed the pHR-CMV-TetO$_2$_HA-BirA (5.0-kb proviral DNA size) and pHR-CMV-TetO$_2$_HA-BirA-ER (5.2-kb proviral DNA size) transfer plasmids that direct the expression of intracellular or endoplasmic reticulum (ER)-resident hemagglutinin (HA)-tagged *Escherichia coli* biotin ligase (HA-BirA and HA-BirA-ER, respectively) (Table 1). Co-transduction of target cells with lentiviruses encoding HA-BirA or HA-BirA-ER, and lentiviruses encoding the transgene of interest carrying an Avi-tag, leads to site-specific biotinylation of the transgene in the presence of D-biotin. The choice for BirA or BirA-ER is determined by the subcellular location of the Avi-tag during protein trafficking; BirA-ER is used when the Avi-tag is located in the ER lumen, and BirA is used when the Avi-tag is located in cytoplasm. We routinely use in vivo biotinylation to produce biotinylated protein ligands for biophysical analysis (e.g., surface plasmon resonance (SPR), bio-layer interferometry (BLI)) or for immunohistochemistry. Finally, we constructed the 3C-Avi-His6_IRES-HA-BirA-ER plasmid variant to allow bicistronic expression of Avi-His6-tagged transgene and HA-BirA-ER (Table 1 and Supplementary Fig. 3).

Generation of inducible cell lines

We constructed the pHR-CMV_TetR-HA-NLS-P2A-BSD-Myc transfer plasmid that leads to constitutive expression of HA-tagged TetR and c-Myc-tagged blasticidin deaminase (BSD) from a single transcript (Table 1). The plasmid can be used to make the expression cell line of choice inducible and allows blasticidin selection of the transduced cell pool. It is an alternative to the pcDNA6/TR vector (Thermo Fisher Scientific) with which the HEK293S GnTI$^-$ TetR cell line was originally constructed[34]. The 2A peptide from porcine teschovirus-1 (P2A) directs ribosomal skipping during translation and ensures that TetR and BSD occur as two separate proteins[39]. In addition, we added the SV40 nuclear localization signal (NLS) to TetR to increase its nuclear localization.

Comparison with other methods

The main advantages of our method over transient transfection[3] are that (i) no large-scale DNA preps (e.g., Mega- or Gigapreps) are necessary because a single miniprep is sufficient; (ii) no tedious large-scale transfection procedures are necessary; (iii) established cell lines can be stored in liquid nitrogen (LN_2) and re-grown when required; (iv) efficient transduction optionally preceded by lentivirus concentration and/or followed by FACS-based enrichment yields close to 100% protein-expressing cells; (v) inducible large-scale expression is greatly facilitated and (vi) protein production yields are larger.

The main advantages of our method over the establishment of a monoclonal stable cell line are simplicity and time efficiency; a polyclonal stable cell line is generated in ~7 d using our procedure, whereas establishment and selection of stably transfected monoclonal cell lines is laborious and typically takes up to 8–10 weeks[4]. Rigorous selection of monoclonal cell lines can lead to isolation of only the most potently expressing cell clones; it is of note that the use of the IRES-FP plasmid variants allows the isolation of single cells or the enrichment of subsets of cells from the total transduced cell pool using FACS (Box 3). If the user should wish so, the IRES-FP elements can readily be replaced with IRES followed by an antibiotic selection marker gene of choice, such as *ble* (zeocin resistance), *neor* (geneticin/G418 resistance), *pac* (puromycin resistance) or *bsd* (blasticidin resistance).

piggyBac (PB), a DNA transposon from the cabbage looper moth *Trichoplusia ni*, is emerging as an effective tool for the generation of inducible, stably transfected mammalian cell lines for large-scale protein production[40,41]. Like lentivirus, the *piggyBac*-based system achieves high and uniform

expression levels. Stably transfected cells must be selected with antibiotic for ~2–3 weeks before scale up to bulk cell culture.

BacMam[42,43] is the use of baculovirus to transiently deliver genes to mammalian cells. It has been widely used for both screening and large-scale expression of membrane protein constructs[44,45]. A key advantage of our method is that lentiviral transduction leads to stable transgene expression, and that successful cell lines can be stored. In addition, no dedicated infrastructure, media, cell lines or consumables to sustain working with insect cells are necessary. Moreover, the generation of lentivirus is substantially easier and faster than the production of the large quantities of P1 and P2 BacMam virus that are needed to infect large volumes of expression cells[44]. Lentivirus therefore has a much smaller laboratory footprint than BacMam. Comparative advantages of BacMam are that baculovirus requires only biosafety level 1 (BSL1) practices and that it is able to carry very large (>15 kb)[42] or multiple inserts. The latter issue can, however, be circumvented by co-infecting expression cells with multiple lentiviruses and enriching them using multi-color FACS (using the IRES-FP plasmid variants; see Box 3).

Biological safety considerations

The lentiviral expression system requires biosafety level 2 (BSL2) or 2+ (BSL2+) practices, depending on the relevant institutional and governmental biosafety guidelines. The two main safety concerns surrounding the use of lentivirus are (i) the potential for generation of replication-competent lentivirus (RCL) and (ii) the potential for oncogenesis.

The potential for generation of RCL is determined by the specific design of the plasmids. The second-generation lentiviral system described here separates transfer, envelope and packaging components of the lentivirus among three separate plasmids. Although third-generation lentiviral vectors further improve on the safety of the second generation by splitting the packaging system into two separate plasmids[46], they are more cumbersome to use and result in lower viral titers due to the requirement of one additional plasmid.

The transfer plasmid contains the sequences that will incorporate into the host cell genome, but functional viral particles cannot be produced from it without the genes encoded in the envelope and packaging plasmids. Simultaneous recombination events among the packaging, envelope and transfer plasmids that produce RCLs are very unlikely. Replication-competent retroviruses (RCRs) have, however, been reported[47]. The pHR-CMV-TetO_2 plasmids are all self-inactivating (SIN[48,49]); they have a deletion in the 3′ LTR (ΔU3) of the viral genome that is transferred into the 5′ LTR after one round of reverse transcription. This deletion abolishes transcription of the full-length proviral DNA. SIN vectors also reduce the possibility of recombination to generate RCLs.

The potential for oncogenesis is largely based on the specific insert contained within the lentiviral transfer plasmid and should be considered on a case-by-case basis.

To mitigate risks even further, we do not routinely concentrate the viral supernatant to make lentiviral stock solutions. We directly transfer the lentivirus-containing supernatant to the expression cells (Steps 11–17 in the Procedure) and use FACS to enrich transduced cell populations. This limits the time that researchers are working with viral particles that are outside of a sealed container and also prevents the viral supernatant from exiting the laminar flow cabinet.

Below is a list of risk reduction measures routinely undertaken within our laboratory:

- Only specially trained and signed-off laboratory staff are authorized to carry out Class II viral work.
- Appropriate personal protective equipment (PPE) is worn at all times: laboratory coat, safety eyewear and disposable long-cuff gloves.
- Proper decontamination of the working area is performed with 1% (wt/vol) Virkon when working with lentiviral particles, both before the work begins and after the work is completed.
- All manipulations with respect to lentiviral particle generation, packaging, harvesting and infection are carried out in a Class II microbiological safety cabinet (MSC).
- A dedicated CO_2 cell culture incubator, with affixed warning sign, is used for all lentiviral work.
- Care is taken to prevent production of aerosols that may contain viral particles during all liquid-handling steps.
- In the case of accidental spillage, surfaces and items are carefully decontaminated using 1% (wt/vol) Virkon.
- All materials exposed to viral supernatant are rinsed with 1% (wt/vol) Virkon before being disposed of into an autoclave bag. These bags are then placed in the biological waste containers for autoclaving as soon as the work is complete.

Materials

Biological materials

! CAUTION The cell lines used in your research should be regularly checked to ensure they are authentic and are not infected with mycoplasma.

- HEK293T Lenti-X cells (Takara/Clontech, cat. no. 632180)
- HEK293T cells (ATCC, cat. no. CRL-3216)
- HEK293S GnTI$^-$ cells (ATCC, cat. no. CRL-3022)
- HEK293S GnTI$^-$ TetR cells[34] (obtainable by request from the group of N. Callewaert at the VIB-UGent Center for Medical Biotechnology; nico.callewaert@ugent.vib.be). The cell line is subject to a Material Transfer Agreement (MTA). Alternatively, the cell line can be re-created by (i) stable transfection of HEK293S GnTI$^-$ cells with the pcDNA6/TR vector or (ii) lentiviral transduction of HEK293S GnTI$^-$ cells (Steps 1–17 of the Procedure) using the pHR-CMV_TetR-HA-NLS-P2A-BSD-Myc transfer plasmid (Table 1)
- FreeStyle 293-F cells (Thermo Fisher Scientific, cat. no. R79007)

Reagents

- Gibco FreeStyle 293 medium (Thermo Fisher Scientific, cat. no. 12338018)
- Gibco FBS (Thermo Fisher Scientific, cat. no. 10270)
- Gibco MEM non-essential amino acids solution (NEAA; Thermo Fisher Scientific, cat. no. 11140-035)
- Gibco L-Glutamine (L-Gln; Thermo Fisher Scientific, cat. no. 25030-024)
- Gibco PBS (calcium- and magnesium-free; Thermo Fisher Scientific, cat. no. 10010015)
- Gibco trypsin-EDTA (0.05% (wt/vol), phenol red; Thermo Fisher Scientific, cat. no. 25300054)
- Gibco trypsin-EDTA (0.05% (wt/vol), no phenol red; Thermo Fisher Scientific, cat. no. 15400054)
- Gibco DMEM/Nutrient Mixture F-12 (DMEM/F-12; with added L-Gln; Thermo Fisher Scientific, cat. no. 11320-074)
- Soybean trypsin inhibitor (SBTI; Thermo Fisher Scientific, cat. no. 17075029)
- Polyethylenimine (PEI; 25 kDa, branched; Merck, cat. no. 408727)
- Polybrene infection reagent (10 mg/mL stock = 1,000×; Merck, cat. no. TR-1003-G)
- Doxycycline hydrochloride (Dox; Merck, cat. no. D3447)
- Blasticidin S hydrochloride (Thermo Fisher Scientific, cat. no. R21001)
- Dimethyl sulfoxide (DMSO; sterile-filtered, suitable for cell culture; Merck, cat. no. D2650)
- Sodium butyrate (Merck, cat. no. 303410)
- Valproic acid (VPA; Merck, cat. no. P4543)
- Kifunensine class I α-mannosidase inhibitor (Tocris Bioscience, cat. no. 3207)
- (D-)biotin (Merck, cat. no. B4639)
- 5-Aza-2′-deoxycytidine (5-aza-dC; Merck, cat. no. A3656)
- PBS tablets (Merck, cat. no. P4417)
- RIPA lysis and extraction buffer (Thermo Fisher Scientific, cat. no. 89900)
- Benzonase nuclease (Merck, cat. no. 70746)
- QIAprep Spin Miniprep Kit (Qiagen, cat. no. 27104)
- Lenti-X concentrator (Takara/Clontech, cat. no. 631231)
- Ethanol (absolute; Merck, cat. no. 32221-M)
- Rely+On Virkon disinfectant powder (VWR, cat. no. 148-0202)
- Microsol 4 decontaminant (Anachem, cat. no. 30312915)

Antibodies

- High-sensitivity streptavidin-HRP conjugate (Pierce, cat. no. 21130)
- Mouse anti-His6 primary antibody (Takara/Clontech, cat. no. 631212)
- Mouse anti-HA primary antibody (Thermo Fisher Scientific, cat. no. 26183)
- Mouse anti-c-Myc primary antibody (Thermo Fisher Scientific, cat. no. MA1-980)
- HRP-conjugated goat anti-mouse IgG secondary antibody (Merck, cat. no. A0168)
- Rabbit anti-cyclophilin A (CypA) primary antibody (Abcam, cat. no. ab41684)
- HRP-conjugated goat anti-rabbit IgG secondary antibody (Abcam, cat. no. ab97051)

Sequencing primers

▲ CRITICAL These non-modified DNA oligos are custom orders (Merck).

- pHR-CMV and pHR-CMV-TetO$_2$ forward sequencing primer (5′-CGTCGTCGTGCTCGTTTAGTG-3′)
- pHR-SFFV forward sequencing primer (5′-GCTCACAACCCCTCACTCGG-3′)

- pHR-CAG forward sequencing primer (5′-GTGCTGGTTATTGTGCTGTCTCATC-3′)
- pHR-CMV, pHR-CMV-TetO$_2$, pHR-SFFV and pHR-CAG reverse sequencing primer (5′-CATTA AAGCAGCGTATCCACATAGC-3′)
- pHR-CMV-TetO$_2$_IRES-FP reverse sequencing primer (5′-CAAACGCACACCGGCCTTATTCCAAG-3′)
- pHR-CMV-TetO$_2$_3C-mVenus-Twin-Strep reverse sequencing primer (5′-GAACAGCTCCTCGCC CTTGCTCAC-3′)

Plasmids

▲ **CRITICAL** All transfer plasmids are available through the non-profit Addgene plasmid repository and are subject to a Uniform Biological Material Transfer Agreement (UBMTA). Addgene catalog numbers are listed in Table 1.

- Transfer plasmid: pHR-CMV-TetO$_2$/pHR-SFFV/pHR-CAG plasmids
- pMD2.G lentiviral envelope plasmid (Addgene, cat. no. 12259)
- psPAX2 lentiviral packaging plasmid (Addgene, cat. no. 12260)
- pcDNA6/TR plasmid (Thermo Fisher Scientific, cat. no. V102520)

Equipment

- Class II microbiological safety cabinet (MSC; Envair, model no. Bio 2+)
- Long-cuff nitrile gloves (StarGuard, PROTECT+ model)
- CO_2 incubator (Binder, model no. C 170)
- Shaking incubator (Infors HT, Multitron Cell model)
- Roller bottle apparatus (various capacities available; Wheaton, model no. R2P 2.0Bot)
- Roll-in incubator (Wheaton, cat. no. 753680)
- Tissue culture plate (6-well plates, flat bottom; Greiner Bio-One, cat. no. 657160)
- Tissue culture plate (T25, filter cap, 25 cm^2; Greiner Bio-One, cat. no. 690175)
- Tissue culture plate (T75, filter cap, 75 cm^2; Greiner Bio-One, cat. no. 658175)
- Tissue culture plate (T175, filter cap, 175 cm^2; Greiner Bio-One, cat. no. 660175)
- 96-Well cell culture microplate (black, clear bottom; Greiner Bio-One, cat. no. 655986)
- Sterile 30-mL Luer-lock plastic syringes (VWR, cat no. BDAM301229)
- 40-µm cell strainers (Corning, cat. no. 352340)
- Polystyrene roller bottles (2,125 cm^2; ribbed surface; Greiner Bio-One, cat. no. 681070)
- High-yielding performance flask cell culture vessel (HYPERFlask; 1,720 cm^2; Corning, cat. no. 10034)
- Syringe filter unit, polyethersulfone (PES; sterile, 0.45 µm; Merck, cat. no. SLHPM33RS)
- Polystyrene disposable standard serological pipettes (5 mL; Greiner Bio-One, cat. no. 606180)
- Polystyrene disposable standard serological pipettes (10 mL; Greiner Bio-One, cat. no. 607180)
- Polystyrene disposable standard serological pipettes (50 mL; Greiner Bio-One, cat. no. 768180)
- Bottle-top filter units (Steritop, 500 mL, sterile, 45-mm threaded; Merck, cat no. SCGPT05RE)
- Polycarbonate Erlenmeyer vented and baffled flasks (2 L; Corning, cat no. 10092591; see Equipment setup)
- Vented caps for plastic 2-L Erlenmeyer cell culture flasks (Merck, cat. no. CLS431339-24EA; see Equipment setup)
- Polycarbonate Erlenmeyer vented and baffled flasks (500 mL; Corning, cat no. 10352742; see Equipment setup)
- Vented caps for plastic 500-mL Erlenmeyer cell culture flasks (Merck, cat. no. CLS431372-50EA; see Equipment setup)
- Hemocytometer (Appleton Woods, cat. no. HC001)
- Nunc cell culture cryogenic tubes (1.8 mL; Thermo Fisher Scientific, cat. no. 377267)
- Controlled-rate freezing container (CoolCell LX; BioCision, cat. no. BCS-405G)
- Cell sorter (Sony, cat. no. SH800Z)

Reagent setup

DMEM/F-12/10% FBS

Add 50 mL of (10% (vol/vol)) FBS and 5 mL of (1% (vol/vol)) NEAA to 445 mL of DMEM/F-12. The medium can be stored at 4 °C as long as there are no visual signs of infection or contamination.

DMEM/F-12/2% FBS

Add 10 mL of (2% (vol/vol)) FBS and 5 mL of (1% (vol/vol)) NEAA to 485 mL of DMEM/F-12. The medium can be stored at 4 °C as long as there are no visual signs of infection or contamination.

DMEM/F-12/SFM (serum-free medium)
Add 5 mL of (1% (vol/vol)) NEAA to 495 mL of DMEM/F-12. The medium can be stored at 4 °C as long as there are no visual signs of infection or contamination.

FreeStyle 293/1% FBS
Add 5 mL of (1% (vol/vol)) FBS and 5 mL of (1% (vol/vol)) NEAA to 490 mL of FreeStyle 293. The medium can be stored at 4 °C as long as there are no visual signs of infection or contamination.

PEI (1 mg/mL stock)
The PEI stock solution is highly viscous and cannot be pipetted. First, pour and weigh 1–5 mL straight from the bottle into a 50-mL tube. PEI has a density of 1.030 g/mL at 25 °C. Add ultrapure water to prepare a 100-mg/mL stock solution. Rotate the tube overnight to mix. Once the solution is homogeneous, dilute it to 1 mg/mL in ultrapure water and adjust the pH to 7.0 with hydrochloric acid (HCl). Filter-sterilize, using a 0.2-μm syringe filter unit inside a biological safety cabinet. Make aliquots and store at −20 °C for up to 1 year.

Dox (10 mg/mL stock)
Dissolve 50 mg in 100% (vol/vol) ethanol to a final volume of 5 mL and filter-sterilize, using a 0.2-μm syringe filter unit inside a biological safety cabinet. Make aliquots and store at −20 °C for up to 8 weeks. ▲ **CRITICAL** Do not expose Dox to direct sunlight.

Blasticidin (2 mg/mL stock)
Dissolve 20 mg in ultrapure water to a final volume of 10 mL and filter-sterilize, using a 0.2-μm syringe filter unit. Make aliquots and store at −20 °C for up to 8 weeks. ! **CAUTION** Blasticidin is toxic. Always wear PPE: laboratory coat, safety eyewear and disposable long-cuff gloves. Weigh the powder in a chemical safety cabinet and prepare the solution inside a biological safety cabinet.

Sodium butyrate (500 mM stock)
Dissolve 1.1 g of sodium butyrate in ultrapure water to a final volume of 20 mL and filter-sterilize, using a 0.2-μm syringe filter unit inside a biological safety cabinet. Make aliquots and store at −20 °C for up to 8 weeks.

VPA (500 mM stock)
Dissolve 1.66 g of VPA in ultrapure water to a final volume of 20 mL and filter-sterilize, using a 0.2-μm syringe filter unit inside a biological safety cabinet. Make aliquots and store at −20 °C for up to 8 weeks.

Kifunensine (500 μM stock)
Dissolve 11.6 mg of kifunensine in ultrapure water to a final volume of 100 mL and filter-sterilize, using a 0.2-μm syringe filter unit inside a biological safety cabinet. Make aliquots and store at −20 °C for up to 1 year.

D-biotin (2 mM stock)
Dissolve 97.7 mg of D-biotin in 1× PBS to a final volume of 200 mL and filter-sterilize, using a 0.2-μm syringe filter unit inside a biological safety cabinet. Make aliquots and store at −20 °C for up to 1 year.

5-aza-dC (10 mM stock)
Dissolve 10 mg of 5-aza-dC in 438 μL of DMSO to obtain a 100 mM stock. Dilute 1:10 (vol/vol) in 1× PBS to obtain the final 10 mM stock. Make aliquots and store at −20 °C for up to 1 year[50]. ! **CAUTION** 5-aza-dC is toxic. Always wear PPE: laboratory coat, safety eyewear and disposable long-cuff gloves. Prepare the solution inside a biological safety cabinet. 5-aza-dC is supplied in a glass bottle or insert, ready for dissolution.

SBTI (1 mg/mL stock)
Dissolve 10 mg of SBTI in PBS to a final volume of 10 mL and filter-sterilize, using a 0.2-μm syringe filter unit inside a biological safety cabinet. 0.5 mg (= 0.5 mL) of SBTI stock solution will inhibit 0.5 mg of trypsin (or 1 mL of a 0.05% (wt/vol) trypsin solution), assuming a specific activity of 10,000 N_{α}-benzoyl-L-arginine ethyl ester (BAEE) units/mg SBTI protein. We use 1 mL of SBTI per milliliter

of a 0.05% (wt/vol) trypsin solution, yielding a 2:1 (wt/wt) SBTI/trypsin ratio. Make aliquots and store at −20 °C for up to 1 year.

Purification of plasmid DNA
Purify plasmid DNA, using a QIAprep Spin Miniprep Kit (Qiagen) according to the manufacturer's instructions. Plasmid can be stored indefinitely at −20 °C.

Growth and maintenance of adherent and suspension HEK293 cells
Culture cells as described in Box 1.

Equipment setup

Shimadzu Prominence high-performance liquid chromatography (HPLC) system.
We essentially perform established procedures for fluorescence-detection size-exclusion chromatography-based thermostability screening (FSEC-TS)[51,52].

Erlenmeyer flasks
The polycarbonate Erlenmeyer flasks for suspension cell culture can be washed, autoclaved and re-used. When the vented caps deteriorate after rounds of autoclaving, the caps can be separately purchased and replaced.

Procedure

HEK293T Lenti-X cell seeding (Day 1) ● Timing ~1 d

1 Add ~9 × 10^6 HEK293T Lenti-X cells in 12 mL of DMEM/F-12/10% FBS medium to a fresh T75 flask, bringing them to ~50% confluency. Cell culture is described in detail in Box 1.
! CAUTION Cell cultures are a potential biological hazard. Working with HEK293 cells requires BSL2 practices. Perform the work in an approved laminar flow cabinet, using sterile techniques, and comply with the appropriate institutional biosafety guidelines. This includes wearing protective clothing and eyewear, cleaning of working surfaces, and proper disposal of waste before and after performing experiments.
▲ **CRITICAL STEP** Lentivirus can be produced from regular HEK293T cells, but the HEK293 Lenti-X cell line used here has been clonally selected to yield viral titers ~30× higher than those of HEK293T cells and ~6× higher than those of HEK293FT cells, according to the manufacturer (Takara/Clontech).
▲ **CRITICAL STEP** The health of the HEK293T Lenti-X producer cell line is critical to obtaining maximal lentiviral titer for downstream transduction. Maintain it diligently and split the cells 1/6 twice a week at fixed times; we suggest Monday morning and Thursday afternoon. We do not use the cells beyond passage 20 (P20; ~10 weeks of culture) to ensure maximum viability and viral yield.
? TROUBLESHOOTING

HEK293T Lenti-X cell transfection (Day 2) ● Timing ~3 d

2 The next day, prepare the following plasmid DNA transfection mix (30 µg of total DNA; 1:1:1 (wt/wt/wt) transfer/packaging/envelope plasmid ratio) in a sterile 1.5-mL tube:
10 µg pHR-CMV-$TetO_2$ transfer plasmid variant containing the gene of interest
10 µg psPAX2 packaging plasmid
10 µg pMD2.G envelope plasmid
Top up the transfection mix with DMEM/F-12/SFM medium to a total volume of 0.25 mL and gently mix the suspension.
? TROUBLESHOOTING

3 Prepare 75 µL of PEI (1:2.5 (wt/wt) DNA:PEI ratio) in a sterile 1.5-mL tube. Top up with DMEM/F-12/SFM medium to a total volume of 0.25 mL and gently mix the suspension.

4 When both solutions are ready, add the 0.25 mL of PEI mix to the 0.25 mL of plasmid DNA transfection mix for a total of 0.5 mL in a 1.5-mL tube.
▲ **CRITICAL STEP** In our experience, both the volume in which the DNA/PEI transfection mix is prepared, and the DNA/PEI ratio, have a great effect on the transfection efficiency. We recommend adhering to the values stated in Steps 2–4.

5 Vortex the 1.5-mL tube gently for 10 s, then centrifuge it briefly at low speed (100*g*, 22–24 °C, 30 s) to collect the liquid at the bottom of the tube, and then leave it for incubation in the flow cabinet for 15–20 min.

6 The T75 flask with HEK293T Lenti-X cells is now >90% confluent (continued from Step 1); remove and discard the DMEM/F-12/10% FBS medium; wash with 10 mL of PBS and replace the medium with 11.5 mL of DMEM/F-12/2% FBS medium.

7 Add the 0.5 mL of DNA/PEI mix to the 11.5 mL of DMEM/F-12/2% FBS medium for a total of 12 mL, and gently tilt flask to cover all cells.
? TROUBLESHOOTING

8 Place the T75 flask back at 37 °C in a humidified incubator operated at 5% CO_2.
! CAUTION Lentiviral particles are a potential biological hazard and require BSL2 or BSL2+ practices, depending on the relevant institutional and governmental biosafety guidelines. Perform the work in an approved laminar flow cabinet, using sterile technique, and comply with the relevant institutional biosafety guidelines. A list of risk reduction measures can be found in the 'Biological safety considerations' section of the main text.
▲ CRITICAL STEP The transfection can also be performed in small-scale T25 format or in a T175 flask. The required amounts of plasmid DNA and PEI must be scaled with flask surface area. The T25 format allows the simultaneous screening of multiple constructs and expression conditions before scale-up, whereas using T175 flasks has the advantage that downstream scale-up is quicker. When performing transfections in T25 format, we use 10 µg of total DNA (1:1:1 (wt/wt/wt) ratio) and a total transfection mix volume of 200 µL (100 + 100 µL) is added to 4 mL of DMEM/F-12/2% FBS medium. When performing transfections in T175 format, we use 70 µg of total DNA (1:1:1 (wt/wt/wt) ratio) and a total transfection mix volume of 1.0 mL (0.5 + 0.5 mL) is added to 30 mL of DMEM/F-12/2% FBS medium. For co-transfection of different transfer plasmids, we usually divide the total amount of transfer plasmid DNA in equal parts (e.g., for a three-plasmid co-transfection in a T75 flask, we use 3.3 µg of each transfer plasmid). Transfer plasmid ratios should, however, be optimized in situations in which there is a large difference in proviral DNA size between the transfer plasmids, to ensure approximately equal viral titers for the most efficient co-transduction.

HEK293T, HEK293S GnTI$^-$ or HEK293S GnTI$^-$ TetR cell seeding (Day 4) ● Timing ~1 d

9 Add ~9 × 10^6 target cells (HEK293T, HEK293S GnTI$^-$ or HEK293S GnTI$^-$ TetR) in 12 mL of DMEM/F-12/10% FBS medium to a new T75 flask, bringing it to ~50% confluency. Incubate the flask for 24 h at 37 °C in a humidified incubator operated at 5% CO_2.

10 (Optional) In the case of HEK293S GnTI$^-$ TetR cells, add blasticidin (final concentration of 2 µg/mL from a 2-mg/mL 1,000× stock solution) to the DMEM/F-12/10% FBS medium.
▲ CRITICAL STEP The health of the HEK293 target cell lines is critical for efficient transduction and potent protein expression. Maintain them diligently and split the cells 1/6 twice a week at fixed times; we suggest Monday morning and Thursday afternoon, synchronized with the Lenti-X cells. We do not use the cells beyond passage 20 (P20; ~10 weeks of culture) to ensure maximum viability and protein yield. We do not culture the HEK293S GnTI$^-$ TetR cell line beyond passage 10 (P10; ~4–5 weeks of culture) to prevent the loss of TetR expression; TetR is under the control of a CMV promoter (pcDNA6/TR vector), which is prone to transcriptional silencing after prolonged culture. See also the 'Other applications of the method' section, 'Alternative promoters' subsection.

Collection of the lentivirus-containing medium (Day 5) ● Timing ~30 min

11 3 d after transfection, collect the 12 mL of conditioned medium from the HEK293T Lenti-X T75 flask into a sterile 50-mL tube. This contains the lentiviral particles.

12 Add 6 mL of fresh DMEM/F-12/10% FBS medium to the 50-mL tube, yielding a total of 18 mL.

13 Filter the conditioned medium through a 0.45-µm filter unit attached to a Luer-lock syringe and into a new sterile 50-mL tube.
▲ CRITICAL STEP Do not use a 0.22-µm filter unit, because this may shear the viral particles. Use only cellulose acetate or polyethersulfone (PES) (low-protein-binding) filters. Avoid the use of nitrocellulose filters; these bind lentiviral envelope proteins and destroy the virus.

14 Add 18 µL (from a 10-mg/mL 1,000× stock solution) of polybrene to the 18 mL of lentivirus-containing medium and mix gently. Polybrene (hexadimethrine bromide) is a cationic polymer that reduces charge repulsion between viral particles and the cell membrane[53]. It will promote virus–host cell fusion, leading to higher transduction efficiencies. Optional determination of lentiviral titer is described in Box 2.
? TROUBLESHOOTING

Box 4 | Long-term storage of cell lines in LN_2 ● Timing ~1 h

It is a good idea to cryopreserve the polyclonal stable HEK293 cell line, in LN_2 and in the presence of a cryoprotective agent such as DMSO directly after establishment or enrichment.

Procedure

1 Gently dislodge and resuspend the adherent cells from the T75 flask in DMEM/F-12/10% FBS medium, using a sterile serological 10-mL pipette; pipette up and down a few times to break up cell clumps. Alternatively, cells can be trypsinized.
2 Centrifuge the cells at 500*g* for 5 min at room temperature (22–24 °C), and discard the supernatant without disturbing the cell pellet.
3 Resuspend the cells in 9 mL of DMEM/F-12/10% FBS medium containing 10% (vol/vol) DMSO; this leads to a minimally recommended cell density of ~2.0 × 10^6 cells/mL.
4 Dispense aliquots of the cell suspension into cryogenic storage vials. Mix the cells frequently and gently during this process to maintain a homogeneous cell suspension.
5 Place the cryovials in an isopropanol cooling chamber and store the chamber at −80 °C overnight for controlled cooling.
6 Finally, transfer and store the cryovials in the gas phase above the LN_2.
7 To restart the cell culture, place a cryovial containing frozen cells in a 37 °C water bath for a maximum of 1 min to rapidly thaw them.
8 Slowly dilute the thawed cells using pre-warmed DMEM/F-12/10% FBS medium.
9 Plate the thawed cells at high density to optimize their recovery (e.g., use the contents of one cryovial per T75 flask).

▲ **CRITICAL STEP** The thawing procedure is stressful to cryopreserved cells; use good technique and work quickly to ensure that most of the cells survive the procedure.

Infection of the target cell line (Day 5) ● Timing ~3 d

15 The T75 flask with HEK293T, HEK293S GnTI$^-$ or HEK293S GnTI$^-$ TetR cells (continued from Steps 9 and 10) is now >90% confluent; remove and discard the DMEM/F-12/10% FBS medium; wash with 10 mL of PBS and replace the medium with the 18 mL of filtered lentivirus-containing medium (from Step 14).

? TROUBLESHOOTING

16 (Optional) In the case of HEK293S GnTI$^-$ TetR cells, add blasticidin (final concentration of 2 μg/mL from a 2-mg/mL 1,000× stock solution).
17 Place the T75 flask back at 37 °C in a humidified incubator operated at 5% CO_2. The viral particles will now infect the cells and stably integrate their genetic material into the host cell genome.

Expansion of the adherent polyclonal cell line (Day 8) ● Timing ~3 d

18 3 d after infection, the polyclonal stable cell line is established through integration of viral genetic elements into the host cell genome. If the construct is fluorescently tagged, or when using the pHR-CMV-TetO_2_IRES-FP plasmid variants, image the cells to verify and quantify cell fluorescence and transduction efficiency. Transduced cells can be enriched via FACS using FP fluorescence (Box 3). Transgene expression is repressed when using inducible HEK293S GnTI$^-$ TetR cells, meaning that either uninduced ('leaky') or induced fluorescence can be used to evaluate transduction efficiency or for FACS-based enrichment. Cryopreservation of the polyclonal stable cell line is described in Box 4.

▲ **CRITICAL STEP** A portion of the transduced cells can be split among six wells and used for a small-scale induction test, while simultaneously expanding the remainder of the cells (Steps 19–21).

19 Wash the T75 flask thoroughly, at least three times, with PBS.
20 Split the T75 flask into two new T175 flasks (each holding 30 mL of DMEM/F-12/10% FBS medium) for expansion. Place the T175 flasks back at 37 °C in a humidified incubator operated at 5% CO_2.
21 (Optional) In the case of HEK293S GnTI$^-$ TetR cells, add blasticidin (final concentration of 2 μg/mL from a 2-mg/mL 1,000 stock solution).

Protein expression in adherent or suspension cells

22 To proceed with adherent growth of the HEK293T, HEK293S GnTI$^-$ or HEK293S GnTI$^-$ TetR polyclonal cell lines in ribbed roller bottles for soluble secreted protein production, follow option A. To proceed with suspension growth of the HEK293S GnTI$^-$ TetR cell line for membrane or intracellular protein production, follow option B. Option B can also serve as a guideline when producing soluble secreted proteins from suspension-adapted cell lines such as FreeStyle 293-F.

▲ **CRITICAL** The adherent cell and suspension cell procedures describe expansion into 1.5 L (six polycarbonate roller bottles) or 1.6 L (two polycarbonate Erlenmeyer flasks), respectively. These volumes can be scaled up or down according to the protein target expression levels and desired yields.

(A) **Protein expression in adherent polyclonal cell lines (Weeks 2–4)** ● **Timing ~2–3 weeks**

(i) *Expansion of the adherent polyclonal cell line (Steps i–v).* After 3 d, split each of the two confluent T175 flasks into three new T175 flasks (each holding 30 mL of DMEM/F-12/10% FBS medium) for expansion. Place the T175 flasks back at 37 °C in a humidified incubator operated at 5% CO_2.

(ii) (Optional) In the case of HEK293S GnTI$^-$ TetR cells, add blasticidin (final concentration of 2 μg/mL from a 2-mg/mL 1,000× stock solution).

(iii) After 3 d, split each of the six T175 flasks into a new ribbed roller bottle (holding 250 mL of DMEM/F-12/10% FBS medium) for expansion.

(iv) (Optional) In the case of HEK293S GnTI$^-$ TetR cells, add blasticidin (final concentration of 2 μg/mL from a 2-mg/mL 1,000× stock solution).

(v) Place the roller bottles in a roller bottle apparatus operated at 37 °C and rotate them at 0.80 r.p.m.

(vi) *Protein expression (Steps vi–xi).* The ribbed roller bottles will be confluent after ~5 d. Remove the DMEM/F-12/10% FBS medium and replace with 250 mL of DMEM/F-12/2% FBS medium.

(vii) (Optional) In the case of HEK293S GnTI$^-$ TetR cells, add blasticidin (final concentration of 2 μg/mL from a 2-mg/mL 1,000× stock solution).

(viii) (Optional) In the case of HEK293S GnTI$^-$ TetR cells, add Dox (from the 10 mg/mL stock solution) to the desired concentration to induce protein expression.

(ix) (Optional) Add VPA or sodium butyrate to the desired concentration.

(x) (Optional) In the case of HEK293T cells, kifunensine can be added (final concentration of 5 μM from a 500-μM 100× stock solution) to inhibit class I α-mannosidases to obtain protein carrying EndoH-sensitive *N*-linked glycans[2].

(xi) Place the roller bottles in a roller bottle apparatus operated at the desired expression temperature (37 or 30 °C) and rotate them at 0.80 r.p.m.

▲ **CRITICAL STEP** The histone deacetylase inhibitors (iHDACs) VPA and sodium butyrate can enhance stable transgene expression[54]. The optimal concentrations of Dox (Step 22A (viii)) and of VPA and sodium butyrate (Step 22A(ix)), as well as the optimal expression temperature (37 or 30 °C; see Step 22A(xi)), should be first determined in small-scale culture and optimized for each target protein. The working concentration of Dox can be varied from 0.1 to 10 μg/mL, and that of VPA and sodium butyrate is usually in the 1–10 mM range[54]. The goal is to balance these expression parameters such that they lead to maximal production of secreted, correctly folded protein. Our default approach for soluble proteins is to perform expression at 37 °C, and to use 1 μg/mL Dox (in the case of HEK293S GnTI$^-$ TetR cells) and no VPA or sodium butyrate.

(xii) *Collection of expressed protein (Steps xii and xiii).* Collect the conditioned medium. The expression time depends on the cell type:

Cell type	When to collect conditioned medium
HEK293T	After 4–5 d
HEK293S GnTI$^-$	After 7–10 d
HEK293S GnTI$^-$ TetR	After 7–10 d

▲ **CRITICAL STEP** We advise monitoring cell viability throughout the protein expression and adjusting collection times accordingly, i.e., to collect sooner if a substantial proportion of cells have died. The roller bottles can, in principle, be re-fed with fresh DMEM/F-12/10% FBS medium if adherent cell death is limited. In that case, consider the addition of 5-aza-dC (final concentration of 10 μM from a 10 mM 1,000× stock solution) to counteract promoter methylation after prolonged activity.

(xiii) Centrifuge the conditioned medium (5,000*g*, 22–24 °C, 20 min) to remove cellular debris. Then, filter the conditioned medium using a Steritop bottle-top filter unit to sterilize it.

■ **PAUSE POINT** Filtered conditioned medium can be temporarily (up to 1 week) stored at 4 °C before proceeding with purification, but we recommend processing the medium quickly to avoid protein degradation.

(B) **Protein expression in polyclonal HEK293S GnTI⁻ TetR cell lines for suspension growth (Weeks 2–4)** ● **Timing ~2–3 weeks**

(i) *Expansion of the polyclonal HEK293S GnTI⁻ TetR cell line for suspension growth (Steps i–xviii).* After 3 d, pour out the DMEM/F-12/10% FBS medium of each of the two confluent T175 flasks and wash them with 10 mL of PBS.

(ii) Trypsinize the cells in each flask by adding 5 mL of trypsin-EDTA for 3 min.

(iii) Inhibit the trypsin by adding 25 mL of FreeStyle 293/1% FBS medium to each of the two T175 flasks.

(iv) Pool the cells and dispense them into one 500-mL polycarbonate Erlenmeyer baffled flask.

(v) Perform a cell count of this cell suspension; anticipated cell density is ~1.5×10^6 cells/mL.

(vi) Top up the flask with FreeStyle 293/1% FBS medium to a volume (usually ~200 mL) that corresponds to a final cell density of ~0.5×10^6 cells/mL.

(vii) Add blasticidin (final concentration of 2 μg/mL from a 2-mg/mL 1,000× stock solution).

(viii) Place the flask in a shaking incubator operated at 37 °C with 8% CO_2 and a shaking speed of 130 r.p.m.

(ix) Grow the cells until they reach a density of ~2.0×10^6 cells/mL. Monitor cell density by performing a cell count of the cell suspension.

▲ **CRITICAL STEP** For optimal cell growth, seed suspension HEK293S GnTI⁻ TetR cells at a minimum density of ~0.5×10^6 cells/mL. HEK293S GnTI⁻ TetR cells are derived from HEK293S cells, the original suspension-adapted HEK293 cell line[16]. HEK293S GnTI⁻ TetR cells adapt readily from an adherent monolayer to suspension culture[4], provided a specialized suspension growth medium with added serum (FreeStyle 293/1% FBS) is used and the cells are seeded at sufficiently high density. Anticipate a doubling time of ~24 h for HEK293S GnTI⁻ TetR cells.

(x) Transfer the 200 mL of cells to one 2-L polycarbonate Erlenmeyer baffled flask.

(xi) Top up the flask with FreeStyle 293/1% FBS medium, with added blasticidin (final concentration of 2 μg/mL from a 2-mg/mL 1,000× stock solution), to a volume of 800 mL. Starting from a cell density of ~2.0×10^6 cells/mL, the final cell density will be ~0.50×10^6 cells/mL.

(xii) Place the flask in a shaking incubator operated at 37 °C with 8% CO_2 and a shaking speed of 130 r.p.m.

(xiii) Grow the cells until they reach a density of ~2.0×10^6 cells/mL. Monitor cell density by performing a cell count of the cell suspension.

(xiv) Distribute the 800 mL of cells into two 2-L polycarbonate Erlenmeyer baffled flasks.

(xv) Top up each flask with FreeStyle 293/1% FBS medium, with added blasticidin (final concentration of 2 μg/mL from a 2-mg/mL 1,000× stock solution), to a volume of 800 mL. Starting from a cell density of ~2.0×10^6 cells/mL, the final cell density will be ~1.0×10^6 cells/mL.

(xvi) Place the flask in a shaking incubator operated at 37 °C with 8% CO_2 and a shaking speed of 130 r.p.m.

(xvii) Grow the cells until they reach a density of ~$2.0–3.0 \times 10^6$ cells/mL. Monitor cell density by performing a cell count of the cell suspension.

(xviii) (Optional) Suspension cells can be grown to a density of ~5.0×10^6 cells/mL to further increase total biomass at harvest.

(xix) *Induction of the polyclonal HEK293S GnTI⁻ TetR cell line for protein expression (Steps xix–xxi).* Add Dox (from the 10 mg/mL stock solution) to the desired concentration.

(xx) (Optional) Add VPA or sodium butyrate to the desired concentration.

(xxi) Place the flasks in a shaking incubator operated at the desired expression temperature (37 or 30 °C) with 8% CO_2 and a shaking speed of 130 r.p.m.

? TROUBLESHOOTING

(xxii) *Collection of cell pellets (Step xxii).* At the desired time of collection, centrifuge the cells for 10 min at 1,500*g* at 4 °C and discard the supernatant.

▲ **CRITICAL STEP** The iHDACs VPA and sodium butyrate can enhance stable transgene expression[54]. The optimal concentrations of Dox (Step 22B(xix)) and of VPA and

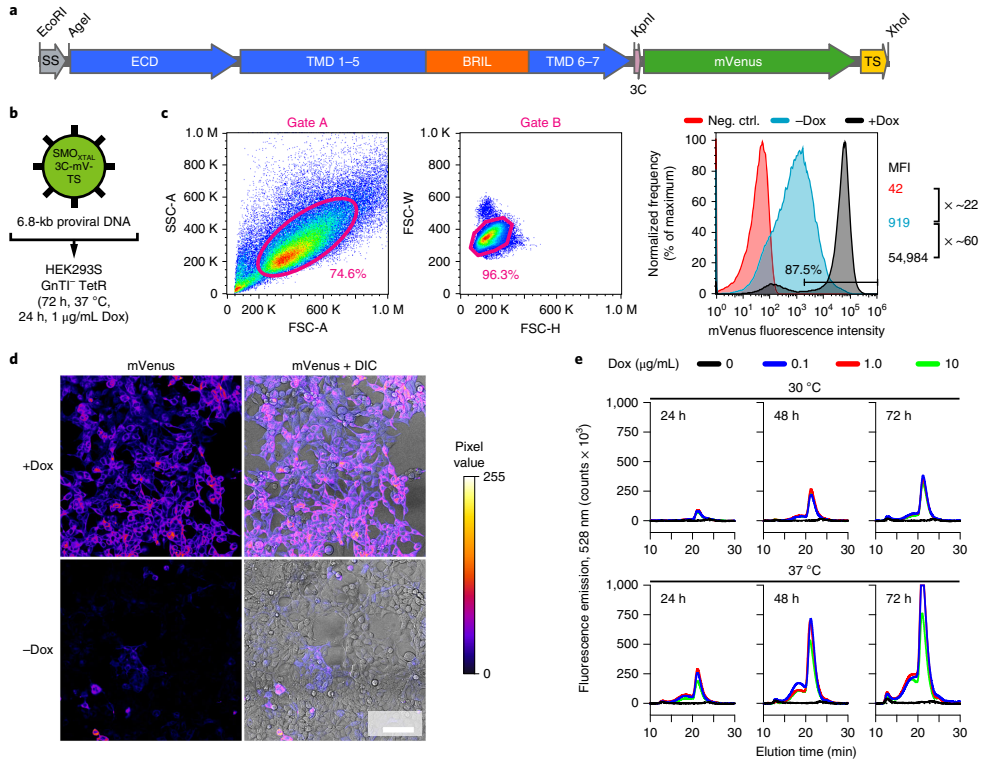

Fig. 4 | Lentiviral transduction, inducible expression and FSEC screening of the GPCR Smoothened in HEK293S GnTI⁻ TetR cells. a, The SMO_{XTAL}-3C-mVenus-Twin-Strep construct (6.8-kb proviral DNA). **b**, Non-concentrated lentiviral particles encoding SMO_{XTAL}-3C-mVenus-Twin-Strep were used to infect adherent HEK293S GnTI⁻ TetR cells. **c**, Flow cytometry analysis of non-transduced (negative control) and transduced (–Dox and +Dox, respectively) cells after trypsinization and suspension growth. Dox (1 µg/mL Dox for 24 h) was added when the suspension cell density reached ~1.0 × 10^6 cells/mL. **d**, Fluorescence microscopy imaging of transduced (+Dox and –Dox) adherent cells. Images were taken on a Leica SP8 SMD X confocal microscope. Fluorescence emission was detected using hybrid detectors operated in photon-counting mode, meaning that each incident photon gave rise to one gray value. Scale bar, 100 µm. **e**, FSEC screening of detergent-solubilized SMO_{XTAL}-3C-mVenus-Twin-Strep with varied expression temperature, collection time and Dox concentration. BRIL, thermostabilized apocytochrome b_{562}-RIL; 3C, 3C protease cleavage site; DIC, differential interference contrast; ECD, extracellular domain; MFI, median fluorescence intensity; mV, mVenus; SS, signal sequence; TMD, transmembrane domain; TS, Twin-Strep tag.

sodium butyrate (Step 22B(xx)), as well as the optimal expression temperature (37 or 30 °C[44]; see Step 22B(xxi)) and collection time (Step 22B(xxii)), should be first determined in small-scale culture and optimized for each protein. The working concentration of Dox can be varied from 0.1 to 10 µg/mL, and that of VPA and sodium butyrate is usually in the 1–10 mM range[54]. The goal is to tune these expression parameters such that they lead to maximal production of correctly folded protein. For membrane proteins, our default initial small-scale FSEC screen varies Dox concentration (at 0.0, 0.1, 1.0 and 10 µg/mL), expression temperature (37 and 30 °C) and collection time (24, 48 and 72 h), giving a total of 24 conditions (0.0 µg/mL Dox samples serve as negative controls), which takes ~24 h to run on an automated HPLC system. An example for the GPCR SMO is shown in Fig. 4e.

■ **PAUSE POINT** The cell pellets can be snap-frozen in LN_2 and stored at –80 °C indefinitely for future use.

Troubleshooting

Troubleshooting advice can be found in Table 2.

Table 2 | Troubleshooting table

Step	Problem	Possible reason	Solution
1	Mammalian cell contamination	Improper sterile technique or problem with tissue culture infrastructure	Adhere strictly to proper tissue culture technique. Ensure that all surfaces are uncluttered and cleaned with 70% (vol/vol) ethanol or 1% (wt/vol) Virkon before and after use. The use of pen-strep is not advised, as it can lead to reduced protein yields
	Low lentiviral titer	Old or badly maintained HEK293T Lenti-X cells	Start fresh HEK293T Lenti-X cell culture from a low-passage LN_2 stock
2	Low transduction efficiency	Low-quality lentivirus	Make certain that the correct packaging and envelope plasmids are used
7	Low transduction efficiency	Unsuccessful HEK293T Lenti-X cell transfection	Transfect HEK293T Lenti-X cells at the appropriate confluency, use fresh PEI or other transfection reagent, verify plasmid DNA integrity and purity. Use fluorescence to verify HEK293T Lenti-X cell transfection efficiency if the construct is fluorescently tagged
14	Low transduction efficiency	No polybrene added to viral supernatant	Ascertain the use of polybrene
15	Low transduction efficiency	Non-compatible cell line	Cell line must express the LDLR on its surface
22B(xxi)	Reduced HEK293S GnTI$^-$ TetR cell viability after induction of expression	Protein toxicity, which is mainly an issue for membrane and intracellular proteins	Screen for optimal harvesting time (e.g., limit expression time to 24 h) and expression parameters (temperature and Dox, VPA, sodium butyrate concentrations). Increase the concentration of FBS

Timing

The entire protocol, starting from the transfection of Lenti-X cells to the liter-scale collection of conditioned medium containing secreted protein, or suspension cells containing membrane or intracellular proteins, takes ~3–4 weeks. The timing for each stage of the Procedure is summarized below.

Step 1, HEK293T Lenti-X cell seeding: ~1 d

Steps 2–8, HEK293T Lenti-X cell transfection: ~3 d

Steps 9 and 10, HEK293T, HEK293S GnTI$^-$ or HEK293S GnTI$^-$ TetR cell seeding: ~1 d

Steps 11–14, collection of the lentivirus-containing medium: ~30 min

Steps 15–17, infection of the target cell line: ~3 d

Steps 18–21, expansion of the adherent polyclonal cell line: ~3 d

Step 22A(i–v), expansion of the adherent polyclonal cell line: ~8 d

Step 22A(vi–xi), protein expression: ~5–10 d

Step 22A(xii and xiii), collection of expressed protein: ~1 h

Step 22B(i–xviii), expansion of the polyclonal HEK293S GnTI$^-$ TetR cell line for suspension growth: ~14 d

Step 22B(xix–xxi), induction of the polyclonal HEK293S GnTI$^-$ TetR cell line and protein expression: ~1–3 d

Step 22B(xxii), collection of cell pellets: ~1 h

Box 2, endpoint dilution assay to determine functional lentiviral titer: ~4 d

Box 4, long-term storage of cell lines in LN_2: ~1 h

Anticipated results

The described protocols are used within our laboratories at STRUBI and the MRC-LMB to express a large number of soluble and membrane proteins varying in size, topology and oligomeric state, as well as protein complexes. The time required to identify promising constructs varies considerably on a

case-by-case basis. For soluble proteins, we identify constructs suitable for scale-up by evaluating their transient or stable expression and secretion in small-scale format using western blotting. For membrane proteins, we follow established procedures for FSEC-TS[51,52]. We emphasize the importance of exploring expression time, expression temperature and Dox concentration as variables[44]. Given the scalability of the method, polyclonal cell lines can be readily established and expanded in small-scale adherent cultures or low-volume suspension cultures, allowing the simultaneous screening of these variables before scale-up.

Examples illustrating the protocol

To illustrate the broad applicability of the method, we cloned a set of cDNA inserts into the various pHR-CMV-TetO$_2$ plasmids. These inserts code for neuronal proteins of varying sizes, folds and expression levels and have been previously successfully transiently expressed in HEK293 cells using the pHLsec plasmid. Soluble secreted proteins include 3C-Avi-His6-tagged Cbln1$_{FL}$[32], β-NRX1$_{LNS6}$[32], GluD2$_{ATD}$[32], NL1$_{ECTO}$[33], MDGA1$_{ECTO-FL}$ and MDGA2$_{ECTO-FL}$[33], and α-NRX1$_{ECTO-FL}$[33], listed in order of increasing proviral DNA and protein size.

We compared secreted and whole-cell protein levels from HEK293T cells transduced with non-concentrated lentiviral particles (pHR-CMV-TetO$_2$_3C-Avi-His6 plasmid) in T25-flask format, with levels from HEK293T cells transiently transfected with equimolar amounts of either the pHLsec or the pHR-CMV-TetO$_2$_3C-Avi-His6 plasmid, using anti-His6 western blotting. For all targets, we noted markedly increased levels of protein production and secretion from the lentivirus-transduced cells, regardless of proviral DNA size and absolute expression levels. Interestingly, we also observed higher transient expression levels using pHR-CMV-TetO$_2$ as compared with pHLsec, indicating that pHR-CMV-TetO$_2$ is very well suited to initial transient small-scale screening of expression constructs and that subcloning in pHLsec is unnecessary for this purpose (Fig. 2c). For the large-scale (12 roller bottles) production of axon guidance molecules Netrin-1 (NET1$_{ΔNTR}$) and Neogenin-1 (NEO1$_{FN456}$)[55,56], we achieved a threefold and fourfold improvement in secreted protein yield after purification, respectively, when using stable lentiviral expression as compared to transient expression using pHLsec (Fig. 2d).

We compared secreted and whole-cell protein levels from HEK293T cells transduced with non-concentrated lentiviral particles produced using the pHR-CMV-TetO$_2$_3C-Avi-His6 or pHR-CMV-TetO$_2$_3C-Avi-His6_IRES-EmGFP plasmid variant, using anti-His6 western blotting (Fig. 3e). Interestingly, although markedly lower signal was observed from the cell pellets of the IRES-EmGFP samples, the levels of secreted protein were not adversely affected. For the α-NRX1$_{ECTO-FL}$ construct, a marked increase in secreted protein levels was even observed. In summary, we prefer to use the IRES-FP plasmid variants over the non-IRES-FP plasmid variants because they lead to at least as much secreted protein while also enabling routine verification of transfection and transduction efficiency, using fluorescence microscopy or flow cytometry, as well as enrichment of the cell line using FACS. As an example, we established a polyclonal stable cell line for 3C-Avi-His6-tagged MDGA1$_{ECTO-FL}$[33] (8.2-kb proviral DNA). Using flow cytometry, we measured a transduction efficiency of ~94% (Fig. 3f). We applied this sort gate and expanded the sorted cells into four roller bottles (1 L of DMEM/F-12/2% FBS medium). From this volume, we obtained ~47 mg of purified secreted MDGA1$_{ECTO-FL}$, as compared with ~7 mg from large-scale transient transfection using pHLsec (Fig. 3g).

We further illustrate the usefulness of the method for membrane proteins using the GPCR SMO[57] and the GABA$_A$R β3 homopentamer[58]. We established polyclonal stable HEK293S GnTI$^-$ TetR cell lines for mVenus-fused SMO$_{XTAL}$ (6.8-kb proviral DNA; Fig. 4 (top and center panels)) and mVenus-fused full-length GABA$_A$R-β3 (GABA$_A$R-β3$_{FL}$; 5.7-kb proviral DNA; Fig. 5 (top and center panels)), using non-concentrated lentiviral particles. 72 h post transduction, we initiated suspension culture. After 48 h, we induced gene expression for 24 h, using Dox. For both SMO$_{XTAL}$ (Fig. 4c,d) and GABA$_A$R-β3$_{FL}$ (Fig. 5c,d), we determined, using flow cytometry, that ~90% of gated suspension HEK293S GnTI$^-$ TetR cells robustly expressed protein. Interestingly, the analysis also revealed that repression of GABA$_A$R-β3$_{FL}$ expression was more efficient (less 'leaky') than that of SMO$_{XTAL}$, leading to a larger fold change in median fluorescence intensity (MFI) upon Dox application (Figs. 4c and 5c).

To determine the optimal expression parameters for SMO$_{XTAL}$, we expanded the polyclonal stable HEK293S GnTI$^-$ TetR cell line into 6-well format and performed an FSEC screen, varying Dox concentration (0.0, 0.1, 1.0 and 10 μg/mL), expression temperature (30 and 37 °C[44]) and collection

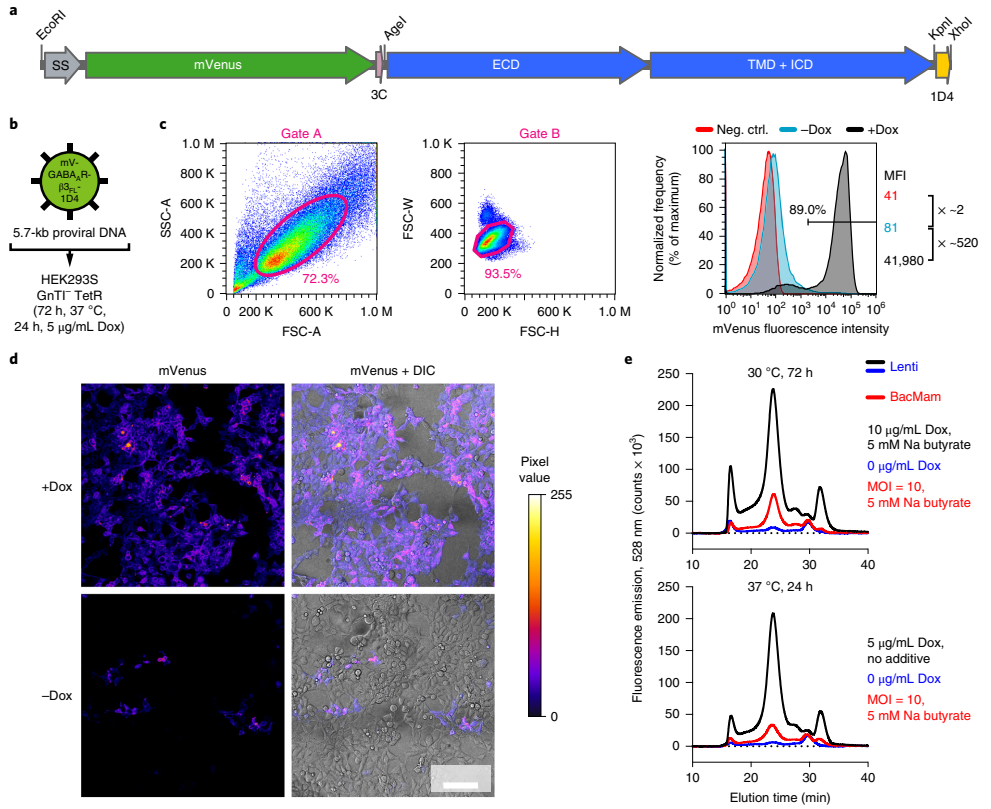

Fig. 5 | Lentiviral transduction and inducible expression of the GABA$_A$ receptor β3 homopentamer (GABA$_A$R-β3$_{FL}$) in HEK293S GnTI⁻ TetR cells, and comparison with BacMam. a, The mVenus-GABA$_A$R-β3$_{FL}$-1D4 construct (5.7-kb proviral DNA). **b**, Non-concentrated lentiviral particles encoding mVenus-GABA$_A$R-β3$_{FL}$-1D4 were used to infect adherent HEK293S GnTI⁻ TetR cells. **c**, Flow cytometry analysis of non-transduced (negative control) and transduced (−Dox and +Dox, respectively) cells after trypsinization and suspension growth. Dox (5 μg/mL Dox for 24 h) was added when the suspension cell density reached ~1.0 × 10^6 cells/mL. **d**, Fluorescence microscopy imaging of transduced (+Dox and −Dox) adherent cells. Images were taken on a Leica SP8 SMD X confocal microscope. Fluorescence emission was detected using hybrid detectors operated in photon-counting mode, meaning that each incident photon gave rise to one gray value. Scale bar, 100 μm. **e**, Comparative lentivirus vs. BacMam FSEC screening. mVenus-GABA$_A$R-β3$_{FL}$-1D4 yield using lentiviral transduction is approximately fivefold greater than using BacMam when comparing the best respective conditions (Supplementary Fig. 7a,b). 1D4, 1D4 tag; 3C, 3C protease cleavage site; DIC, differential interference contrast; ECD, extracellular domain; ICD, intracellular domain; MFI, median fluorescence intensity; MOI, multiplicity of infection; SS, signal sequence; TMD, transmembrane domain.

time (24, 48 and 72 h). From the analysis, we determined that SMO$_{XTAL}$ expression is best when induced using 0.1 or 1.0 μg/mL Dox and collected after 72 h at 37 °C (Fig. 4e). We routinely perform this FSEC analysis for our membrane protein samples; it takes <24 h to screen a total of 24 conditions using an automated HPLC system. The 0.0 μg/mL Dox samples serve as negative controls.

We compared the BacMam procedure[44,45] with our lentiviral procedure for the expression of GABA$_A$R-β3$_{FL}$, using FSEC. Common screening parameters were expression temperature (30 and 37 °C), collection time (24, 48 and 72 h), and additives (5 mM VPA or sodium butyrate). For BacMam and lentiviral transduction, we additionally screened MOI ratios (0, 1, 4 and 10) or Dox concentration (0, 5 and 10 μg/mL), respectively (Supplementary Fig. 7a,b). From this matrix of conditions, we determined that in the case of lentiviral transduction, inducible expression at 37 °C for 24 h without additives or at 30 °C for 72 h with 5 mM sodium butyrate is optimal, whereas in the case

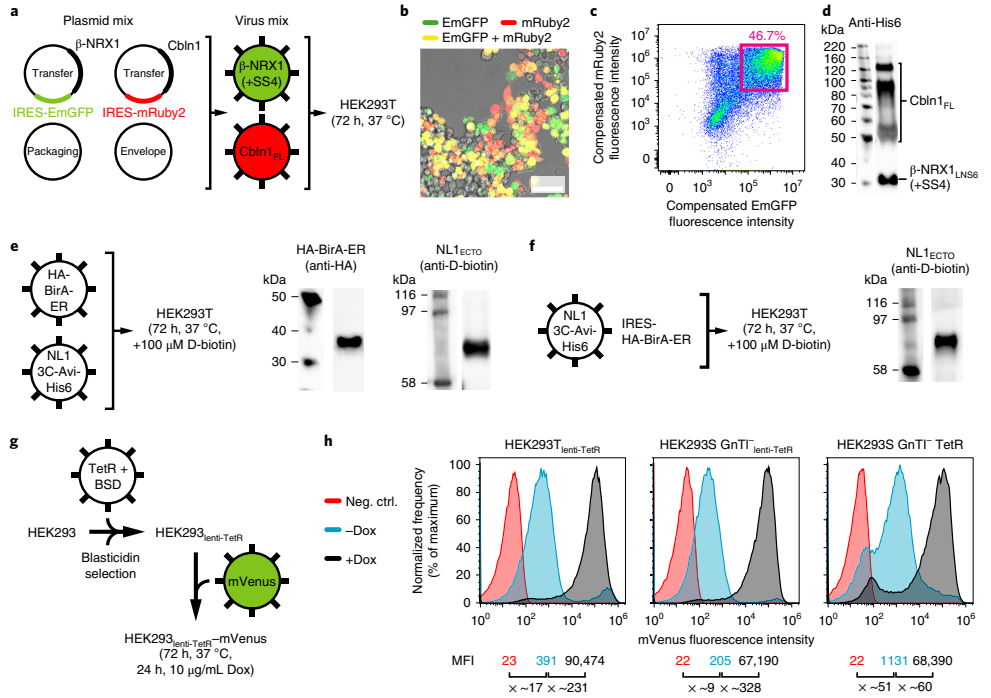

Fig. 6 | Tools for multi-color FACS, in vivo biotinylation and the generation of inducible cell lines. a–d, Multi-color FACS. **a**, Non-concentrated lentiviral particles encoding β-NRX1$_{LNS6}$_IRES-EmGFP (6.1-kb proviral DNA) and Cbln1$_{FL}$_IRES-mRuby2 (6.0-kb proviral DNA) were used to co-infect HEK293T cells. **b**, Fluorescent imaging indicated a mixture of non-, single- and double-transduced cells. The image was taken on a Leica SP8 SMD X confocal microscope. Scale bar, 50 µm. **c**, Two-dimensional compensated fluorescence plot. **d**, Western blot detection of His6-tagged β-NRX1$_{LNS6}$(+SS4) and Cbln1$_{FL}$ secreted from co-infected cells after cell sorting (mouse anti-His6 primary antibody, 1:5,000 dilution; HRP-conjugated goat anti-mouse secondary antibody, 1:5,000 dilution). **e**,**f**, In vivo biotinylation. **e**, Non-concentrated lentiviral particles encoding either HA-BirA-ER (5.1-kb proviral DNA) or 3C-Avi-His6-tagged NL1$_{ECTO}$ (5.9-kb proviral DNA) were used to co-infect HEK293T cells. **f**, Non-concentrated lentiviral particles encoding 3C-Avi-His6-tagged NL1$_{ECTO}$ and IRES_HA-BirA-ER (7.6-kb proviral DNA) were used to infect HEK293T cells. A D-biotin concentration of 100 µM was maintained in the DMEM/F-12/2% FBS medium. Anti-D-biotin western blot detection of in vivo-biotinylated NL1$_{ECTO}$ (high-sensitivity streptavidin-HRP conjugate, 1:4,000 dilution). Anti-HA western blot detection of HA-tagged TetR (mouse anti-HA primary antibody, 1:5,000 dilution; HRP-conjugated goat anti-mouse secondary antibody, 1:5,000 dilution). **g**,**h**, Generation of inducible cell lines. **g**, Non-concentrated lentiviral particles encoding TetR-HA-NLS-P2A-BSD-Myc (5.1-kb proviral DNA) and mVenus (4.7-kb proviral DNA) were used to infect HEK293T and HEK293S GnTI$^-$ cells. **h**, Flow cytometry analysis of the resulting HEK293T$_{lenti-TetR}$ and HEK293S GnTI$^-_{lenti-TetR}$ inducible cell lines, and comparison with the HEK293S GnTI$^-$ TetR cell line[34]. SS4, spliced sequence #4.

of BacMam, expression at 30 °C for 72 h using an MOI ratio of 10 as well as 5 mM sodium butyrate is optimal. However, protein yield using lentiviral transduction was at least fivefold greater than using BacMam when comparing the best respective conditions (Fig. 5e and Supplementary Fig. 7a,b).

For co-infection of cells using lentiviruses encoding distinct transgenes, two strategies can be followed: (i) separately produced lentiviruses can be mixed in the desired stoichiometric ratio after titer determination or (ii) multiple pHR-CMV-TetO$_2$ plasmids can be co-transfected into the HEK293T Lenti-X producer cell line. In both cases, co-transduced cells can then be enriched using multi-color FACS. We applied the second strategy to the secreted Cbln1$_{FL}$–β-NRX1$_{LNS6}$ complex[32] (Fig. 6a); from the total transduced cells pool (Fig. 6b), the subset of cells expressing both transgenes was isolated using FACS and using IRES-EmGFP and IRES-mRuby2 fluorescence (Fig. 6c,d). The approach can be extended to multi-subunit complexes using more fluorochromes; our plasmid suite currently supports up to three colors (IRES-EmGFP, IRES-mRuby2 and IRES-mTurquoise2; Supplementary Fig. 8a,b), but this can be readily modified or extended because the IRES-FP elements can be excised and replaced using the unique *XhoI-BsiWI* restriction sites (Supplementary Fig. 3).

To illustrate in vivo biotinylation, we either (i) co-infected HEK293T cells with non-concentrated lentiviral particles encoding HA-tagged ER-resident BirA (HA-BirA-ER) and lentiviral particles encoding 3C-Avi-His6-tagged $NL1_{ECTO}$ (Fig. 6e) or (ii) performed bicistronic expression of $NL1_{ECTO}$ and HA-BirA-ER using the 3C-Avi-His6_IRES-HA-BirA-ER plasmid (Fig. 6f). D-biotin was maintained in the DMEM/F-12/2% FBS medium at 100 μM. Using western blotting, we confirmed successful biotinylation of secreted $NL1_{ECTO}$ (Fig. 6e,f).

Finally, we generated inducible HEK293T and HEK293S GnTI$^-$ cells by infecting them with non-concentrated lentiviral particles encoding TetR-HA-NLS-P2A-BSD-Myc. After two passages that included selection with 10 μg/mL blasticidin to kill non-transduced cells, we infected the resulting $HEK293T_{lenti\text{-}TetR}$ and HEK293S GnTI$^-_{lenti\text{-}TetR}$ cell lines with non-concentrated lentiviral particles encoding cytosolic mVenus (Fig. 6g). Using flow cytometry, we confirmed inducible mVenus expression in both polyclonal cell lines (Fig. 6h). Interestingly, HEK293S GnTI$^-_{lenti\text{-}TetR}$ cells showed less uninduced ('leaky') mVenus expression than HEK293S GnTI$^-$ TetR cells, leading to a larger fold change in MFI upon Dox application (Fig. 6h).

Reporting Summary

Further information on research design is available in the Nature Research Reporting Summary.

References

1. Aricescu, A. R. & Owens, R. J. Expression of recombinant glycoproteins in mammalian cells: towards an integrative approach to structural biology. *Curr. Opin. Struct. Biol.* **23**, 345–356 (2013).
2. Chang, V. T. et al. Glycoprotein structural genomics: solving the glycosylation problem. *Structure* **15**, 267–273 (2007).
3. Aricescu, A. R., Lu, W. & Jones, E. Y. A time- and cost-efficient system for high-level protein production in mammalian cells. *Acta Crystallogr. D Biol. Crystallogr.* **62**, 1243–1250 (2006).
4. Chaudhary, S. et al. Overexpressing human membrane proteins in stably transfected and clonal human embryonic kidney 293S cells. *Nat. Protoc.* **7**, 453–466 (2012).
5. Naldini, L., Trono, D. & Verma, I. M. Lentiviral vectors, two decades later. *Science* **353**, 1101–1102 (2016).
6. Benabdellah, K. et al. Development of an all-in-one lentiviral vector system based on the original TetR for the easy generation of Tet-ON cell lines. *PLoS ONE* **6**, e23734 (2011).
7. De Groote, P. et al. Generation of a new Gateway-compatible inducible lentiviral vector platform allowing easy derivation of co-transduced cells. *Biotechniques* **60**, 252–259 (2016).
8. Campeau, E. et al. A versatile viral system for expression and depletion of proteins in mammalian cells. *PLoS ONE* **4**, e6529 (2009).
9. Bandaranayake, A. D. et al. Daedalus: a robust, turnkey platform for rapid production of decigram quantities of active recombinant proteins in human cell lines using novel lentiviral vectors. *Nucleic Acids Res.* **39**, e143 (2011).
10. Chang, V. T. et al. Initiation of T cell signaling by CD45 segregation at 'close contacts'. *Nat. Immunol.* **17**, 574–582 (2016).
11. Chang, V. T., Spooner, R. A., Crispin, M. & Davis, S. J. Glycan remodeling with processing inhibitors and lectin-resistant eukaryotic cells. *Methods Mol. Biol.* **1321**, 307–322 (2015).
12. Cronin, J., Zhang, X. Y. & Reiser, J. Altering the tropism of lentiviral vectors through pseudotyping. *Curr. Gene Ther.* **5**, 387–398 (2005).
13. Finkelshtein, D. et al. LDL receptor and its family members serve as the cellular receptors for vesicular stomatitis virus. *Proc. Natl. Acad. Sci. USA* **110**, 7306–7311 (2013).
14. Demaison, C. et al. High-level transduction and gene expression in hematopoietic repopulating cells using a human immunodeficiency virus type 1-based lentiviral vector containing an internal spleen focus forming virus promoter. *Hum. Gene Ther.* **13**, 803–813 (2002).
15. Zufferey, R. et al. Multiply attenuated lentiviral vector achieves efficient gene delivery in vivo. *Nat. Biotechnol.* **15**, 871–875 (1997).
16. Lin, Y. C. et al. Genome dynamics of the human embryonic kidney 293 lineage in response to cell biology manipulations. *Nat. Commun.* **5**, 4767 (2014).
17. Qin, J. Y. et al. Systematic comparison of constitutive promoters and the doxycycline-inducible promoter. *PLoS ONE* **5**, e10611 (2010).
18. Reeves, P. J., Kim, J. M. & Khorana, H. G. Structure and function in rhodopsin: a tetracycline-inducible system in stable mammalian cell lines for high-level expression of opsin mutants. *Proc. Natl. Acad. Sci. USA* **99**, 13413–13418 (2002).
19. Foecking, M. K. & Hofstetter, H. Powerful and versatile enhancer-promoter unit for mammalian expression vectors. *Gene* **45**, 101–105 (1986).
20. Gorman, C. M., Gies, D., McCray, G. & Huang, M. The human cytomegalovirus major immediate early promoter can be trans-activated by adenovirus early proteins. *Virology* **171**, 377–385 (1989).
21. Donello, J. E., Loeb, J. E. & Hope, T. J. Woodchuck hepatitis virus contains a tripartite posttranscriptional regulatory element. *J. Virol.* **72**, 5085–5092 (1998).

22. Garcia-Nafria, J., Watson, J. F. & Greger, I. H. IVA cloning: a single-tube universal cloning system exploiting bacterial In Vivo Assembly. *Sci. Rep.* **6**, 27459 (2016).
23. Schmidt, T. G. et al. Development of the Twin-Strep-tag and its application for purification of recombinant proteins from cell culture supernatants. *Protein Expr. Purif.* **92**, 54–61 (2013).
24. Schmidt, T. G. & Skerra, A. The Strep-tag system for one-step purification and high-affinity detection or capturing of proteins. *Nat. Protoc.* **2**, 1528–1535 (2007).
25. Kumar, M., Keller, B., Makalou, N. & Sutton, R. E. Systematic determination of the packaging limit of lentiviral vectors. *Hum. Gene Ther.* **12**, 1893–1905 (2001).
26. Knox, R. et al. A streamlined implementation of the glutamine synthetase-based protein expression system. *BMC Biotechnol.* **13**, 74 (2013).
27. Mancia, F. et al. Optimization of protein production in mammalian cells with a coexpressed fluorescent marker. *Structure* **12**, 1355–1360 (2004).
28. Oberbek, A., Matasci, M., Hacker, D. L. & Wurm, F. M. Generation of stable, high-producing CHO cell lines by lentiviral vector-mediated gene transfer in serum-free suspension culture. *Biotechnol. Bioeng.* **108**, 600–610 (2011).
29. Shaner, N. C., Patterson, G. H. & Davidson, M. W. Advances in fluorescent protein technology. *J. Cell Sci.* **120**, 4247–4260 (2007).
30. Lam, A. J. et al. Improving FRET dynamic range with bright green and red fluorescent proteins. *Nat. Methods* **9**, 1005–1012 (2012).
31. Goedhart, J. et al. Structure-guided evolution of cyan fluorescent proteins towards a quantum yield of 93%. *Nat. Commun.* **3**, 751 (2012).
32. Elegheert, J. et al. Structural basis for integration of GluD receptors within synaptic organizer complexes. *Science* **353**, 295–299 (2016).
33. Elegheert, J. et al. Structural mechanism for modulation of synaptic neuroligin-neurexin signaling by MDGA proteins. *Neuron* **95**, 896–913.e10 (2017).
34. Reeves, P. J., Callewaert, N., Contreras, R. & Khorana, H. G. Structure and function in rhodopsin: high-level expression of rhodopsin with restricted and homogeneous N-glycosylation by a tetracycline-inducible N-acetylglucosaminyltransferase I-negative HEK293S stable mammalian cell line. *Proc. Natl. Acad. Sci. USA* **99**, 13419–13424 (2002).
35. Yao, F. et al. Tetracycline repressor, tetR, rather than the tetR-mammalian cell transcription factor fusion derivatives, regulates inducible gene expression in mammalian cells. *Hum. Gene Ther.* **9**, 1939–1950 (1998).
36. Brooks, A. R. et al. Transcriptional silencing is associated with extensive methylation of the CMV promoter following adenoviral gene delivery to muscle. *J. Gene Med.* **6**, 395–404 (2004).
37. Hsu, C. C. et al. Targeted methylation of CMV and E1A viral promoters. *Biochem. Biophys. Res. Commun.* **402**, 228–234 (2010).
38. He, J., Yang, Q. & Chang, L. J. Dynamic DNA methylation and histone modifications contribute to lentiviral transgene silencing in murine embryonic carcinoma cells. *J. Virol.* **79**, 13497–13508 (2005).
39. Kim, J. H. et al. High cleavage efficiency of a 2A peptide derived from porcine teschovirus-1 in human cell lines, zebrafish and mice. *PLoS ONE* **6**, e18556 (2011).
40. Li, Z. et al. Simple piggyBac transposon-based mammalian cell expression system for inducible protein production. *Proc. Natl. Acad. Sci. USA* **110**, 5004–5009 (2013).
41. Matasci, M., Baldi, L., Hacker, D. L. & Wurm, F. M. The PiggyBac transposon enhances the frequency of CHO stable cell line generation and yields recombinant lines with superior productivity and stability. *Biotechnol. Bioeng.* **108**, 2141–2150 (2011).
42. Boyce, F. M. & Bucher, N. L. Baculovirus-mediated gene transfer into mammalian cells. *Proc. Natl. Acad. Sci. USA* **93**, 2348–2352 (1996).
43. Dukkipati, A. et al. BacMam system for high-level expression of recombinant soluble and membrane glycoproteins for structural studies. *Protein Expr. Purif.* **62**, 160–170 (2008).
44. Goehring, A. et al. Screening and large-scale expression of membrane proteins in mammalian cells for structural studies. *Nat. Protoc.* **9**, 2574–2585 (2014).
45. Morales-Perez, C. L., Noviello, C. M. & Hibbs, R. E. Manipulation of subunit stoichiometry in heteromeric membrane proteins. *Structure* **24**, 797–805 (2016).
46. Dull, T. et al. A third-generation lentivirus vector with a conditional packaging system. *J. Virol.* **72**, 8463–8471 (1998).
47. Otto, E. et al. Characterization of a replication-competent retrovirus resulting from recombination of packaging and vector sequences. *Hum. Gene Ther.* **5**, 567–575 (1994).
48. Miyoshi, H. et al. Development of a self-inactivating lentivirus vector. *J. Virol.* **72**, 8150–8157 (1998).
49. Zufferey, R. et al. Self-inactivating lentivirus vector for safe and efficient in vivo gene delivery. *J. Virol.* **72**, 9873–9880 (1998).
50. Schermelleh, L., Spada, F. & Leonhardt, H. Visualization and measurement of DNA methyltransferase activity in living cells. *Curr. Protoc. Cell Biol.* Chapter 22, Unit 22.12 (2008).
51. Hattori, M., Hibbs, R. E. & Gouaux, E. A fluorescence-detection size-exclusion chromatography-based thermostability assay for membrane protein precrystallization screening. *Structure* **20**, 1293–1299 (2012).
52. Kawate, T. & Gouaux, E. Fluorescence-detection size-exclusion chromatography for precrystallization screening of integral membrane proteins. *Structure* **14**, 673–681 (2006).

53. Davis, H. E., Rosinski, M., Morgan, J. R. & Yarmush, M. L. Charged polymers modulate retrovirus transduction via membrane charge neutralization and virus aggregation. *Biophys. J.* **86**, 1234–1242 (2004).
54. Backliwal, G. et al. Valproic acid: a viable alternative to sodium butyrate for enhancing protein expression in mammalian cell cultures. *Biotechnol. Bioeng.* **101**, 182–189 (2008).
55. Bell, C. H. et al. Structure of the repulsive guidance molecule (RGM)-neogenin signaling hub. *Science* **341**, 77–80 (2013).
56. Healey, E. G. et al. Repulsive guidance molecule is a structural bridge between neogenin and bone morphogenetic protein. *Nat. Struct. Mol. Biol.* **22**, 458–465 (2015).
57. Byrne, E. F. X. et al. Structural basis of Smoothened regulation by its extracellular domains. *Nature* **535**, 517–522 (2016).
58. Miller, P. S. & Aricescu, A. R. Crystal structure of a human GABAA receptor. *Nature* **512**, 270–275 (2014).
59. Rueden, C. T. et al. ImageJ2: ImageJ for the next generation of scientific image data. *BMC Bioinformatics* **18**, 529 (2017).
60. Meissner, P. et al. Transient gene expression: recombinant protein production with suspension-adapted HEK293-EBNA cells. *Biotechnol. Bioeng.* **75**, 197–203 (2001).
61. Kutner, R. H., Zhang, X. Y. & Reiser, J. Production, concentration and titration of pseudotyped HIV-1-based lentiviral vectors. *Nat. Protoc.* **4**, 495–505 (2009).
62. Telford, W. G. et al. Flow cytometry of fluorescent proteins. *Methods* **57**, 318–330 (2012).
63. Robinson, J. P. & Roederer, M. History of science. Flow cytometry strikes gold. *Science* **350**, 739–740 (2015).
64. Davies, D. Cell separations by flow cytometry. *Methods Mol. Biol.* **878**, 185–199 (2012).
65. Andrell, J. et al. Generation of tetracycline-inducible mammalian cell lines by flow cytometry for improved overproduction of membrane proteins. *Methods Mol. Biol.* **1432**, 63–78 (2016).

Acknowledgements

We thank G. Davies and C. Green (University of Oxford) for assistance with flow cytometry, S. Padilla-Parra and L.A.J. Alvarez (University of Oxford) for assistance with microscopic imaging, D. Laverty (MRC-LMB) for the modified pEZT-BM vector, J. Watson (MRC-LMB) for advice on IVA cloning, and S. Ressl (Indiana University Bloomington) for comments on the manuscript. pMD2.G (Addgene plasmid no.12259) and psPAX2 (Addgene plasmid no. 12260) were a gift from D. Trono (École Polytechnique Fédérale de Lausanne (EPFL)). This work was supported by a Marie-Curie (FP7-328531) long-term postdoctoral fellowship (to J.E.); UK Medical Research Council grants MR/L009609/1 and MC_UP_1201/15 (to A.R.A.) and MR/L017776/1 (to C.S.); a UK Biotechnology and Biological Sciences Research Council grant (BB/M024709/1, to A.R.A.); Cancer Research UK grants C20724/A14414 (to C.S.) and C375/A10976 (to E.Y.J.); a European Research Council (ERC) grant (647278, to C.S.); and Wellcome Trust studentships (105247/Z/14/Z, to S.S., and 203726/Z/16/Z, to R.E.W.). The Wellcome Centre for Human Genetics is funded by Wellcome Trust Core Award 203852/Z/16/2.

Author contributions

J.E. and E.B. designed and constructed the pHR-CMV-TetO_2 plasmid suite. J.E., E.B., B.B. and V.T.C. established and optimized the protocol. J.E., B.B. and E.B. performed the cloning, western blotting, flow cytometry and microscopic imaging. S.S. performed the $GABA_A$-$\beta 3_{FL}$ comparative expression tests. R.E.W. performed the SMO_{XTAL} expression tests. S.C.G. performed the NET1/NEO1 large-scale expressions. E.F.X.B. performed the generation of the inducible $HEK293_{lenti\text{-}TetR}$ cell lines. D.I.S., E.Y.J., C.S. and A.R.A. provided funding and oversaw the research. J.E. and A.R.A. conceptualized the research. J.E. wrote the paper. All authors provided feedback on the final version of the manuscript.

Data availability

The data that support the findings of this study are available from the corresponding authors upon reasonable request.

Competing interests

The authors declare no competing interests.

Additional information

Supplementary information is available for this paper at https://doi.org/10.1038/s41596-018-0075-9.

Reprints and permissions information is available at www.nature.com/reprints.

Correspondence and requests for materials should be addressed to J.E., C.S. or A.R.A.

Publisher's note: Springer Nature remains neutral with regard to jurisdictional claims in published maps and institutional affiliations.

Published online: 19 November 2018

Related link
Key references using this protocol
Chang, V. T. et al. *Nat. Immunol.* **17**, 574–582 (2016): https://www.nature.com/articles/ni.3392

nature protocols

SUPPLEMENTARY INFORMATION

https://doi.org/10.1038/s41596-018-0075-9

In the format provided by the authors and unedited.

Lentiviral transduction of mammalian cells for fast, scalable and high-level production of soluble and membrane proteins

Jonathan Elegheert[1,3,4*], Ester Behiels[1,3,4,6], Benjamin Bishop[1,6], Suzanne Scott[1,2], Rachel E. Woolley[1], Samuel C. Griffiths[1], Eamon F. X. Byrne[1,5], Veronica T. Chang[2], David I. Stuart[1], E. Yvonne Jones[1], Christian Siebold[1*], A. Radu Aricescu[1,2*]

[1]Division of Structural Biology, Wellcome Centre for Human Genetics, University of Oxford, Oxford, UK. [2]MRC Laboratory of Molecular Biology, Cambridge Biomedical Campus, Cambridge, UK. [3]Interdisciplinary Institute for Neuroscience, University of Bordeaux, Bordeaux, France. [4]Present address: Interdisciplinary Institute for Neuroscience, CNRS UMR 5297, Bordeaux, France. [5]Present address: Department of Bioengineering, Stanford University, Stanford, CA, USA. [6]These authors contributed equally: Ester Behiels, Benjamin Bishop. *e-mails: jonathan.elegheert@u-bordeaux.fr; christian@strubi.ox.ac.uk; radu@mrc-lmb.cam.ac.uk

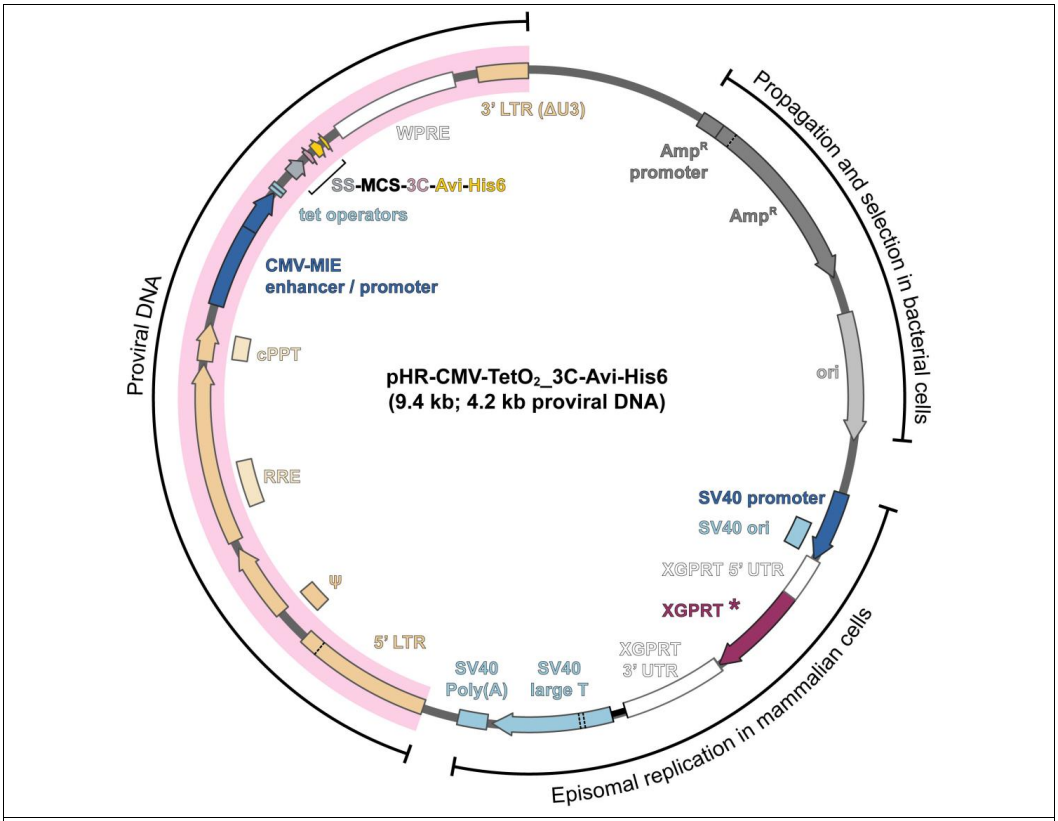

Supplementary Figure 1

The pHR-CMV-$TetO_2$_3C-Avi-His6 transfer plasmid.

LTR: long-terminal repeat; ψ: psi packaging signal; RRE: Rev response element; cPPT: central polypurine tract; CMV-MIE: major immediate early cytomegalovirus enhancer/promoter; SS: signal sequence; MCS: multiple cloning site; 3C: Human Rhinovirus (HRV) 3C protease cleavage site; Avi: Avi-tag; His6: His6-tag; WPRE: Woodchuck Hepatitis Virus posttranscriptional regulatory element; ΔU3: U3 deletion in the 3' LTR; *AmpR*: Ampicillin resistance gene; ori: origin of replication; SV40: Simian vacuolating virus 40; UTR: untranslated region. The genetic elements flanked by the 5' and 3' LTRs will be stably integrated into the host cell genome as proviral DNA, and are highlighted in pink. The gene encoding *E. coli* xanthine-guanine phosphoribosyltransferase (XGPRT, indicated with a star symbol) has been inactivated by deletion of a single base pair, likely to remove an internal *KpnI* site, and resulting introduction of a stop codon. This modification was already present in the pHR-SIN-CSGW lentiviral transfer plasmid on which the pHR-CMV-$TetO_2$ plasmid suite is based. The dominant selectable marker XGPRT is normally used to permit isolation of stably transfected cells using mycophenolic acid, an immunosuppressant drug. We did not correct the open reading frame since our procedure does not require stable maintenance of the lentiviral transfer plasmid in HEK293T Lenti-X cells. The figure was prepared using the SnapGene software (from GSL Biotech; available at http://www.snapgene.com/).

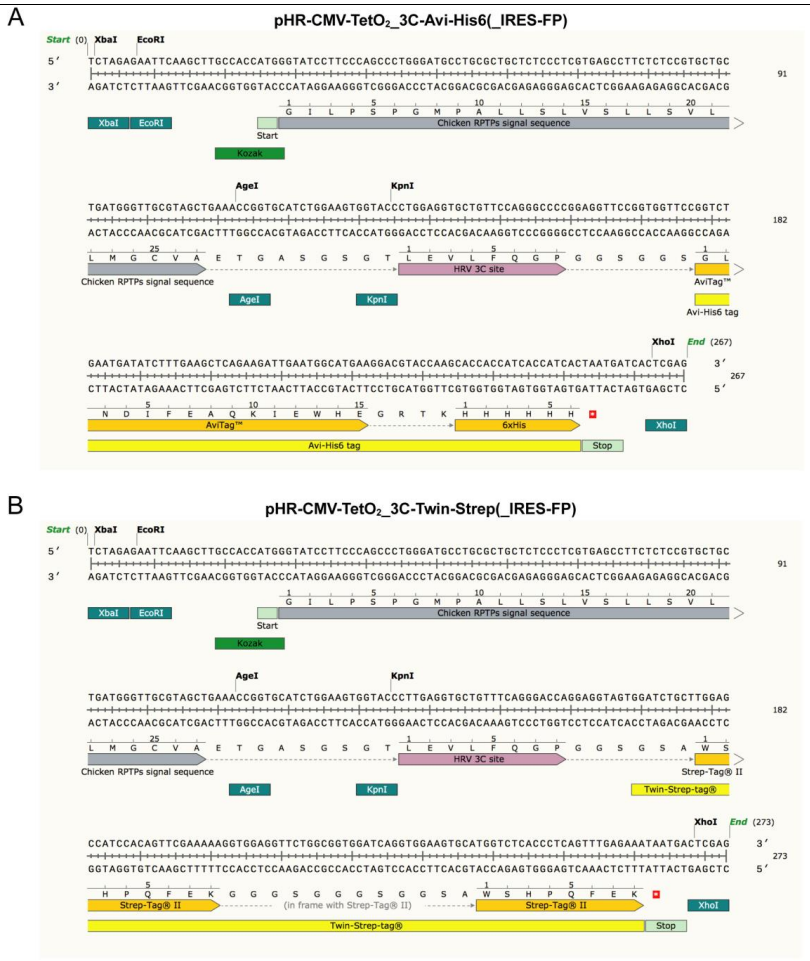

Supplementary Figure 2

The pHR-CMV-TetO$_2$ multiple cloning site.

The pHR-CMV-TetO$_2$ multiple cloning site (MCS) is fully compatible with subcloning of inserts from pHLsec; *XbaI*/*EcoRI* – cRPTPσ signal sequence – *AgeI* – insert – *KpnI* – tag + stop codons – *XhoI*, as well as with *in vivo* assembly (IVA) cloning. **(A)** The pHR-CMV-TetO$_2$_3C-Avi-His6(_IRES-FP) plasmids contain the 3C-Avi-His6 tag inserted between *KpnI* and *XhoI*. **(B)** The pHR-CMV-TetO$_2$_3C-Twin-Strep(_IRES-FP) plasmids contain the 3C-Twin-Strep tag inserted between *KpnI* and *XhoI*. The figure was prepared using the SnapGene software.

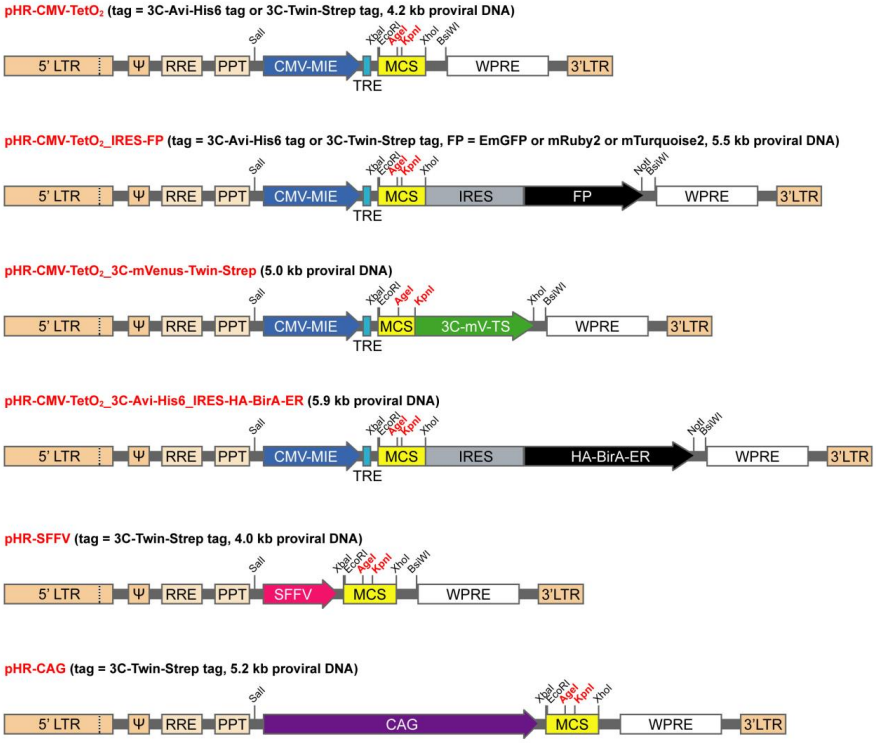

Supplementary Figure 3

Proviral DNA elements of the pHR-CMV-TetO$_2$ plasmids.

Schematic representation of the empty pHR-CMV-TetO$_2$ (4.2 kb proviral DNA), pHR-CMV-TetO$_2$_IRES-FP (5.5 kb proviral DNA), pHR-CMV-TetO$_2$_3C-mVenus-Twin-Strep (5.0 kb proviral DNA), pHR-CMV-TetO$_2$_3C-Avi-His6_HA-BirA-ER (5.9 kb proviral DNA), pHR-SFFV (4.0 kb proviral DNA) and pHR-CAG (5.2 kb proviral DNA) transfer plasmid variants. ψ: psi packaging signal; RRE: Rev response element; PPT: polypurine tract; CMV-MIE: major immediate early cytomegalovirus enhancer/promoter; SFFV: Spleen Focus Forming Virus; CAG: CMV enhancer, chicken β-actin promoter, rabbit β-globin splice acceptor; TRE: tetracycline response element; MCS: multiple cloning site; IRES: internal ribosomal entry site; FP: fluorescent protein; WPRE: Woodchuck Hepatitis Virus posttranscriptional regulatory element; LTR: long-terminal repeat; 3C: Human Rhinovirus (HRV) 3C protease site; mV: mVenus; TS: Twin-Strep. The figure was prepared using the SnapGene software.

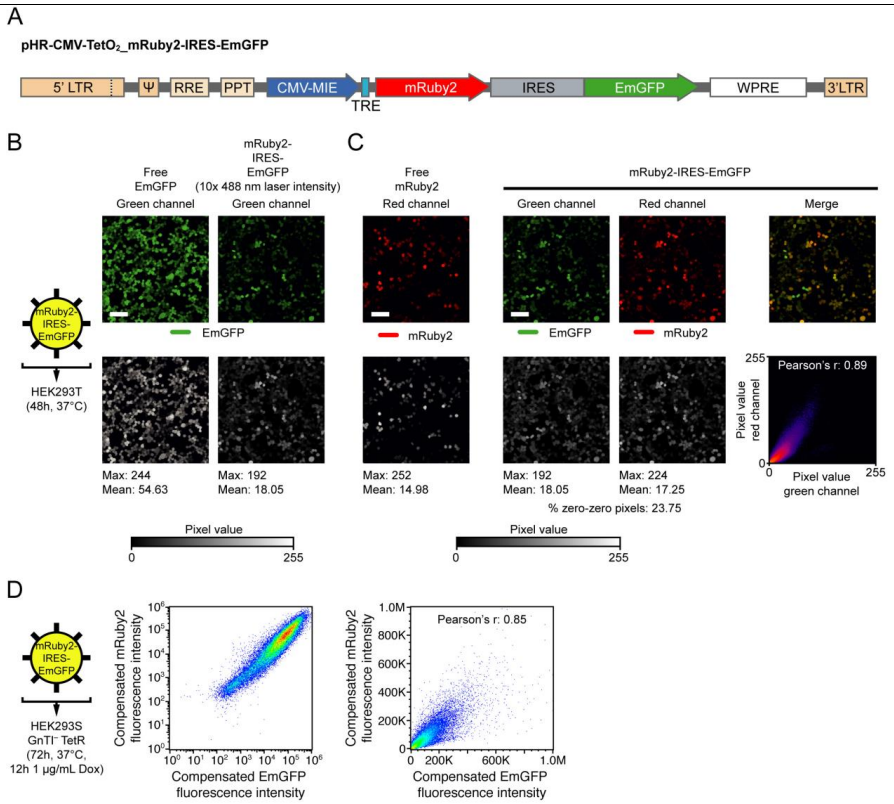

Supplementary Figure 4

Bicistronic expression using IRES-EmGFP.

(A) Schematic representation of the mRuby2-IRES-EmGFP expression construct (2.1 kb insert, 6.0 kb proviral DNA). **(B)** Non-concentrated lentiviral particles encoding mRuby2-IRES-EmGFP were used to infect HEK293T cells. IRES-EmGFP mean fluorescence intensity is ~30-fold lower at identical 488 nm laser power as compared to free EmGFP expression. Scale bar: 100 µm. **(C)** EmGFP and mRuby2 co-localize and their fluorescence intensities show a Pearson correlation coefficient (Pearson's r) of 0.89 between pixel values, implying that IRES-EmGFP is predictive of the presence and expression level of the preceding transgene. Free and bicistronic mRuby2 mean fluorescence intensities are comparable, indicating that IRES-EmGFP does not negatively affect expression of the preceding transgene. Fluorescence images were taken on a Leica SP8 SMD X confocal microscope as sequential scans to avoid spectral crosstalk of EmGFP and mRuby fluorescence into the red and green detection channels, respectively. Fluorescence emission was detected using hybrid detectors (HyD) operated in photon-counting mode, meaning that every incident photon gave rise to one gray value. Scale bar: 100 µm. **(D)** Non-concentrated lentiviral particles encoding mRuby2-IRES-EmGFP were used to infect HEK293S GnTI⁻ TetR cells. Expression was induced using 1 µg/mL Dox for 12 h. Using flow cytometry, we measured a Pearson's r of 0.85 between EmGFP and mRuby2 compensated fluorescence intensities, based on a total of 35,546 single, gated cells.

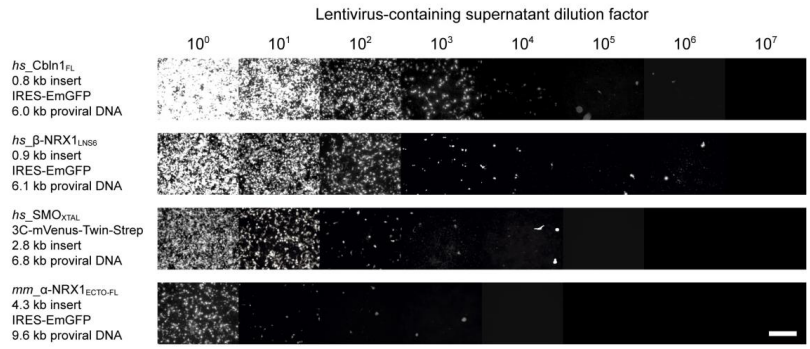

Supplementary Figure 5

Endpoint dilution assay to determine functional lentiviral titer.

The assay was performed as described in Box 2 of the main Protocol. Functional lentiviral titer (and thus MOI) decreases with increasing insert size. Images were taken on a Nikon wide-field TE2000U Microscope. Exposure time was 500 msec and every image was individually enhanced using ImageJ to reveal all cells with fluorescence. Scale bar: 200 µm.

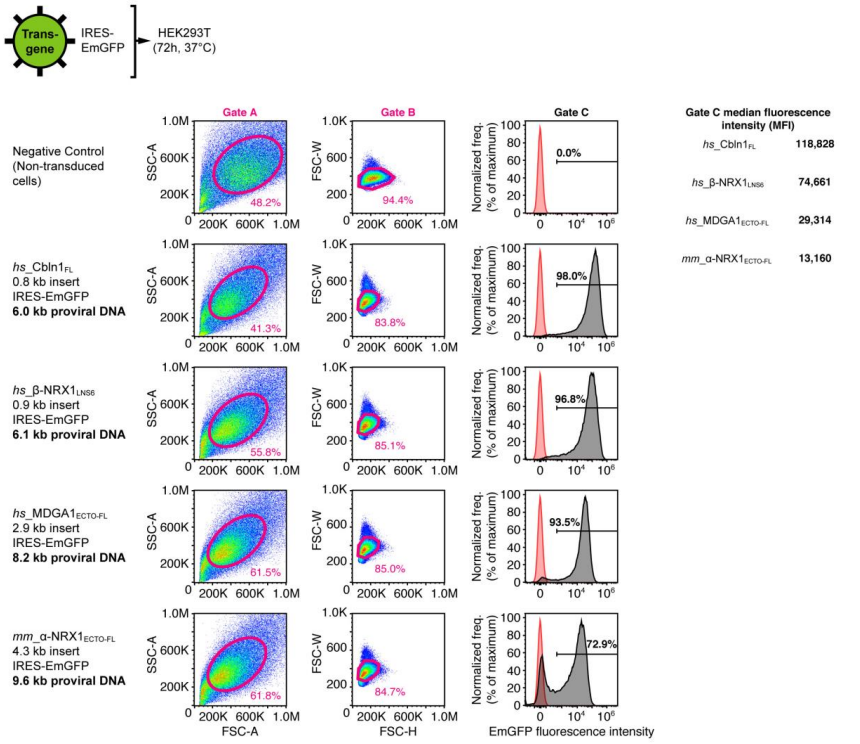

Supplementary Figure 6

Determination of transduction efficiency using flow cytometry.

Non-concentrated lentiviral particles encoding transgene-IRES-EmGFP were used to infect HEK293T cells. The plots show the forward and side scatter area (A), height (H) and width (W), and fluorescence gates used to analyse cells expressing EmGFP. Functional lentiviral titer (and thus MOI) decreases with increasing insert size, leading to decreasing transduction efficiency and also a lower number of integrated gene copies per cell.

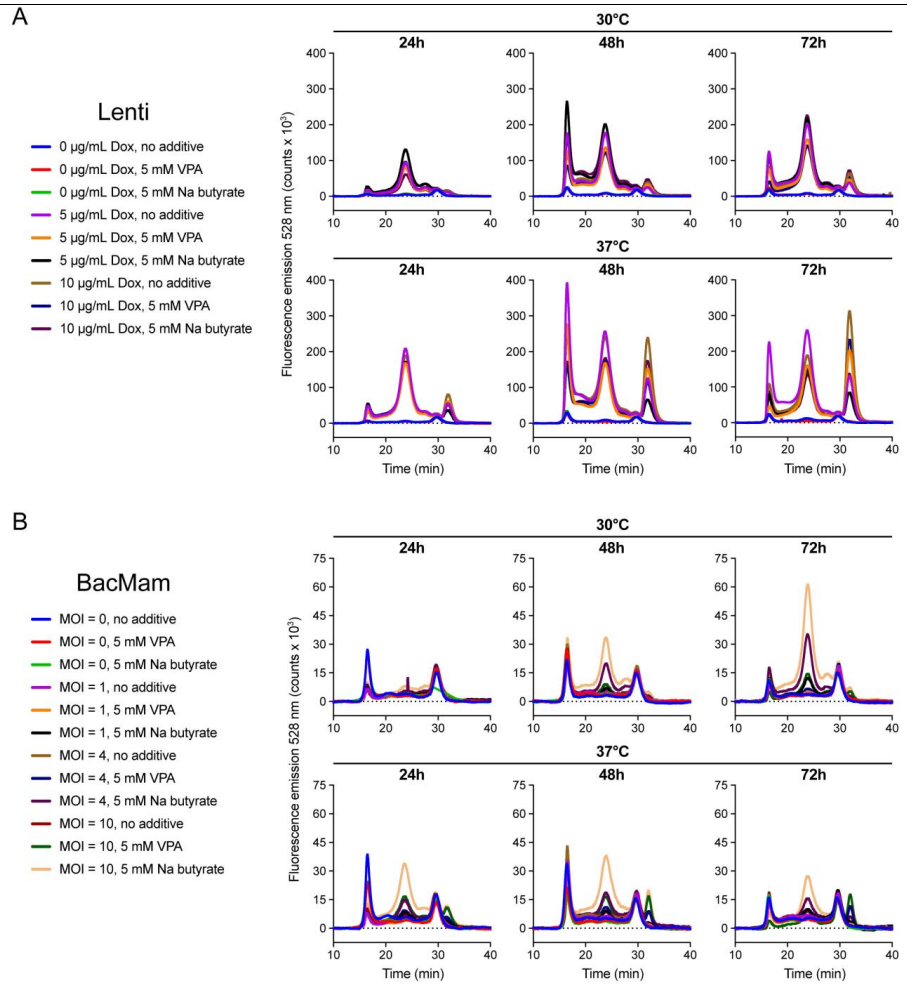

Supplementary Figure 7

$GABA_AR$-$\beta3_{FL}$: comparison of BacMam and lentiviral transduction.

(A) The mVenus-$GABA_AR$-$\beta3_{FL}$-1D4 construct was cloned into the pHR-CMV-$TetO_2$ transfer plasmid. The FSEC analysis shows lentivirus-mediated protein expression in function of expression time (24, 48 h or 72 h), expression temperature (30°C or 37°C), concentration of Dox (0, 5 or 10 µg/mL), and concentration of VPA or sodium butyrate (0 or 5 mM). **(B)** The mVenus-$GABA_AR$-$\beta3_{FL}$-1D4 construct was cloned into a modified pEZT-BM plasmid. The FSEC analysis shows BacMam-mediated protein expression in function of expression time (24, 48 h or 72 h), expression temperature (30°C or 37°C), concentration of VPA or sodium butyrate (0 or 5 mM), and multiplicity of infection (MOI; 0, 1, 4 or 10). Note the difference in scale for the fluorescence emission between panels A and B.

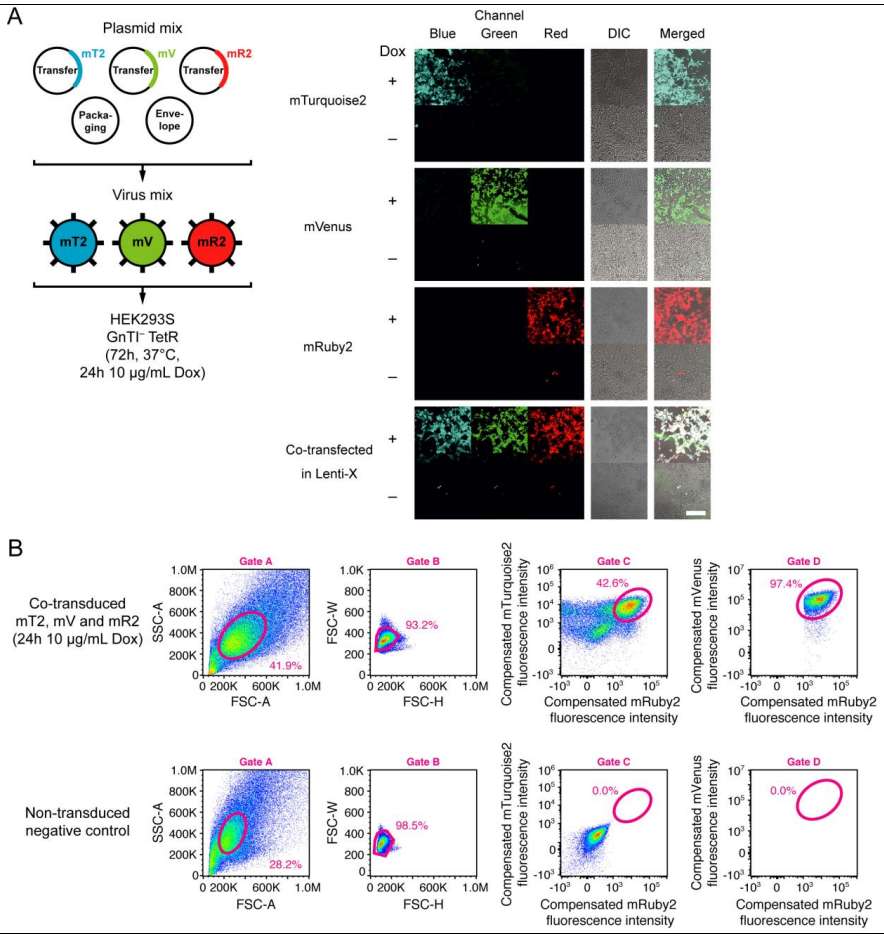

Supplementary Figure 8

Multi-color FACS to enrich co-transduced cells.

(A) Non-concentrated lentiviral particles encoding either mTurquoise2 (mT2; 0.7 kb insert, 4.7 kb proviral DNA), mVenus (mV; 0.7 kb insert, 4.7 kb proviral DNA) or mRuby2 (mR2; 0.7 kb insert, 4.7 kb proviral DNA) were used to co-infect HEK293S GnTI^{-} TetR cells. Fluorescence microscopic imaging of separately infected or co-infected cells, before and after induction with 10 µg/mL Dox, and after 24 h of expression. DIC; differential interference contrast. Fluorescence images were taken on a Leica SP8 SMD X confocal microscope as sequential scans to avoid spectral crosstalk of fluorophores into the separate detection channels. **(B)** The plots show the forward and side scatter area (A), height (H) and width (W), and fluorescence gates used to isolate cells expressing mTurquoise2, mVenus and mRuby2. Scale bar: 200 µm.

Supplementary Methods

Small-scale (6-well) transient transfection procedure for soluble secreted proteins

All procedures are performed in a laminar flow cabinet.

Day 1

- Seed ~1.2 × 10^6 HEK293T or HEK293S GnTI$^-$ cells into one 6-well position, bringing it to ~50% confluency, in a total volume of 2 mL DMEM/F-12/10%FBS.
- Incubate the plate for 24 h at 37°C in a humidified incubator operated with 5% CO_2.

Day 2

- Prepare 4 µg (pHLsec plasmid) or 8 µg (pHR-CMV-TetO_2 plasmid) of plasmid DNA in a sterile 1.5 mL tube; top up with serum-free DMEM-F12 medium to a total volume of ~25 µL and mix gently.
- Prepare 10 µg (pHLsec plasmid) or 20 µg (pHR-CMV-TetO_2 plasmid) of PEI in a separate sterile 1.5 mL tube; top up with serum-free DMEM-F12 medium to a total volume of ~25 µL and mix gently.
- Add the ~25 µL PEI solution to the ~25 µL plasmid DNA solution for a total of ~50 µL. This leads to a 1:2.5 (wt/wt) DNA:PEI ratio.
- Vortex the tube at low speed for 5 sec.
- Centrifuge the tube briefly at low speed to collect the DNA:PEI transfection mix at the bottom of the tube.
- Incubate for 15-20 min.
- The plate with HEK293T or HEK293S GnTI$^-$ cells is now ~90% confluent; take off and discard the complete growth medium and replace with 2 mL DMEM/F-12/2%FBS medium.
- Add the ~50 µL DNA:PEI transfection mix to the 6-well.
- Gently swirl and tilt the plate to distribute the DNA:PEI transfection mix homogenously throughout the 2 mL volume.
- Incubate the plate for the desired amount of time (*e.g.* 24 h, 48 h or 72 h) at the desired temperature (30°C or 37°C) in a humidified incubator operated with 5% CO_2.

Collection

- Collect the secreted protein-containing conditioned medium into a sterile 2 mL tube.
- Centrifuge for 5 min at 20,000 g to pellet debris and dead cells.
- Gently take off the supernatant without disturbing the pellet, and transfer it to a new sterile 2 mL tube.
- Wash the adherent expression cells twice with 1 mL PBS to remove any remaining conditioned medium.
- Prepare the following solution (total volume of 1 mL);
    - 250 µL RIPA lysis and extraction Buffer (ThermoFisher Scientific, cat. no. 89900)
    - 1 µL (~25 U) benzonase nuclease (Merck, cat. no. 70746)
    - 749 µL PBS
- Add the solution to the adherent expression cells.
- Incubate for 5 min.
- Collect the solution into a sterile 1.5 mL tube and centrifuge for 10 min at 20,000 g to pellet debris and nucleic acids.
- This detergent-solubilized, low-viscosity solution is now easy to load into a SDS-PAGE gel slot for Western blotting.
- We usually load 10 µL of non-concentrated conditioned medium and 10 µL of non-concentrated detergent-solubilized expression cells in adjacent gel slots, to comparatively evaluate protein secretion and expression.

To evaluate transfection efficiency, a plasmid expressing a free cytosolic fluorescent marker protein can be co-transfected with the construct of interest. When using the pHR-CMV-TetO_2_IRES-FP transfer plasmid variants, bicistronic expression of such an intracellular fluorescent marker protein occurs automatically.

We like to use PEI as transfection reagent because it is cheap, effective and reliable. In our experience, both the volume in which the DNA:PEI transfection mix is prepared, as well as the DNA:PEI ratio, have a great effect on the transfection efficiency. We recommend adhering to the stated values.

For *in vivo* biotinylation, we maintain a D-biotin concentration of 100 µM (from a 2 mM = 20 × stock) in the DMEM/F-12/2%FBS medium.

Large-scale (roller bottle) transient transfection procedure for soluble secreted proteins

All procedures are performed in a laminar flow cabinet.

Day 1

- Seed ~45 × 10^6 HEK293T or HEK293S GnTI$^-$ cells (*i.e.* all trypsinized cells from one confluent T175 flask) into one 2125 cm^2 roller bottle, bringing it to ~8% confluency, in a total volume of 250 mL DMEM/F-12/10%FBS.
- Place the roller bottle in a roller bottle apparatus operated at 37°C and rotate it at 0.8 revolutions per minute (rpm).

Day 5

- Prepare 250 µg (pHLsec plasmid) or 500 µg (pHR-CMV-$TetO_2$ plasmid) of plasmid DNA.
- At this point, we perform a chloroform extraction to sterilize the plasmid DNA. Add an equal volume of chloroform (Merck, cat. no. C2432) solution to the plasmid DNA, mix well and centrifuge at 10,000 g for 10 min to separate the mixture into a lower organic phase and an upper aqueous phase.
- Transfer the DNA (aqueous phase) to a sterile 50 mL tube; top up with serum-free DMEM-F12 medium to a total volume of ~20 mL and mix gently.
- Prepare 625 µg (pHLsec plasmid) or 1250 µg (pHR-CMV-$TetO_2$ plasmid) of PEI in a separate sterile 50 mL tube; top up with serum-free DMEM-F12 medium to a total volume of ~20 mL and mix gently.
- Add the ~20 mL PEI solution to the ~20 mL plasmid DNA solution for a total of ~40 mL. This leads to a 1:2.5 (wt/wt) DNA:PEI ratio.
- Vortex the tube at low speed for 10 sec.
- Incubate for 15-20 min.
- The roller bottle with HEK293 cells is now ~90% confluent; pour out and discard the complete growth medium and replace with 210 mL DMEM/F-12/2%FBS medium.
- Add the ~40 mL DNA:PEI transfection mix to the roller bottle.
- Incubate the roller bottle at the desired temperature (30°C or 37°C) for the desired amount of time in a roller bottle apparatus; rotating it at 0.80 rpm.

Collection

- In case of HEK293T cells, conditioned medium is usually collected after 4-5 days. In case of HEK293S GnTI$^-$ (TetR) cells, conditioned medium is usually collected after 7-10 days.
- We advise to monitor cell viability throughout the protein expression and to adjust collection times accordingly, *i.e.* to collect sooner if a significant portion of cells has died.
- Centrifuge the secreted protein-containing conditioned medium at 5,000 g for 20 min to remove debris and dead cells.
- Filter-sterilize the secreted protein-containing conditioned medium using a 0.22 µm pore size sterile vacuum bottle-top filter.

Compatibility of pHR-CMV-$TetO_2$ with *in vivo* assembly (IVA) cloning

In vivo assembly (IVA) cloning exploits recA-independent homologous recombination for simplified molecular cloning. For application of IVA cloning with the pHR-CMV-$TetO_2$ plasmids, a PCR amplicon needs to include ~25 bp handles that are homologous to the ends of the linearized pHR-CMV-$TetO_2$ vector. Time-saving advantages of IVA cloning over regular restriction/ligation cloning include that internal restriction sites do not need to be removed from inserts (using *e.g.* overlap-extension PCR), that gel purification of inserts is not needed, and that enzymatic ligation is avoided. The below example describes IVA cloning for cloning of an insert into pHR-CMV-$TetO_2$_3C-Twin-Strep(_IRES-FP) linearized with *AgeI* and *KpnI*.

- Digest and linearize the pHR-CMV-$TetO_2$_3C-Twin-Strep vector with *AgeI* and *KpnI*.
- Gel extract the linearized pHR-CMV-$TetO_2$_3C-Twin-Strep vector.
- Run PCR to amplify insert, using primers that incorporate the suitable handles that are homologous to the ends of the linearized pHR-CMV-$TetO_2$_3C-Twin-Strep vector;
    - 5'-CTGCTGATGGGTTGCGTAGCTGAAA-3' for the forward primer (homologous to sequence upstream of *AgeI*)
    - 5'-GTCCCTGAAACAGCACCTCAAGG-3' for the reverse primer (homologous to sequence downstream of *KpnI*)
- PCR purify the insert.
- Mix insert and vector at an approximate insert:vector molar ratio of 3:1.
- Transform into cloning strain, *e.g.* NEB Stable chemically competent cells (NEB cat. no. C3040)

FSEC screening of the GPCR Smoothened (SMO)

A polyclonal stable HEK293S GnTI$^-$ TetR cell line expressing SMO_{XTAL}-3C-mVenus-Twin-Strep was established using the method described in the main Protocol. The cell line was seeded and expanded in 6-well plates in complete DMEM/F-12/10%FBS. When the cells reached confluency, medium was changed to DMEM/F-12/2%FBS. SMO_{XTAL} expression was induced using Dox (0, 0.1, 1.0 or 10 µg/mL) and cells were incubated for 24, 48 or 72 h at either 30 or 37°C before being harvested by centrifugation (600 g, 3 min, 21°C) and snap frozen in liquid nitrogen.

Thawed cell pellets were resuspended in 50 mM HEPES pH 7.5, 300 mM NaCl, and 1% (vol/vol) mammalian protease inhibitors (Merck, cat. no. P8340). Detergent (*n*-dodecyl-β-D-maltopyranoside, DDM, Anatrace, cat. no. D310) and cholesterol hemisuccinate (CHS, Anatrace, cat. no. CH210) were added to a final concentration of 1% (wt/vol) and 0.2% (wt/vol), respectively. After incubation for 90 min at 4°C, the insoluble fraction was removed by centrifugation (15,000 g, 15 min, 4°C) and the supernatant further clarified (26,000 g, 15 min, 4°C). Each sample was loaded onto a Superose 6 Increase 3.2/300 column (GE Healthcare, cat. no. 29091598) equilibrated in 10 mM HEPES pH 7.5, 150 mM NaCl, 0.03% (wt/vol) DDM and 0.006% (wt/vol) CHS, and attached to an ultra-fast preparative and purification liquid chromatography (UFPLC) system with automated micro-volume loader and in-line fluorescence detection (Shimadzu Prominence UFPLC). mVenus fluorescence was monitored using an excitation wavelength of 515 nm and emission wavelength of 528 nm.

$GABA_AR$-$β3_{FL}$: comparison of BacMam and lentiviral transduction

BacMam

A synthetic construct containing the full-length human $GABA_A$ receptor β3 subunit ($GABA_AR$-$β3_{FL}$) with an N-terminal monoVenus and a C-terminal rho-1D4 tag was subcloned into a modified pEZT-BM vector. In this vector, an *EcoRI* site was removed and a multiple cloning site compatible with that of pHLsec was inserted. The mVenus-$GABA_AR$-$β3_{FL}$-1D4 construct was subcloned into pEZT-BM using *EcoRI* and *XhoI* sites. Bacmid was generated by transforming sequence-verified clones into DH10Bac cells, which were grown on LB-agar plates containing 7 µg/mL gentamicin, 50 µg/mL kanamycin, 10 µg/mL tetracycline, 40 µg/mL IPTG and 300 µg/mL blue gal for two days at 37°C. Bacmid was isolated from white colonies grown in LB media supplemented with 4 µg/mL gentamicin, 25 µg/mL kanamycin and 5 µg/mL tetracycline, and correct recombination of the insert into the bacmid was verified by PCR.

Sf9 cells were maintained in Insect-XPRESS medium (with L-glutamine; Lonza, cat. no. BE12-730Q), in a shaking incubator operated at 27°C and 140 rpm. Prior to transfection, cells were seeded into a 6-well plate at a density of 1×10^6 cells per well. When the cells adhered, they were transfected with 1 µg of bacmid DNA per well, using Cellfectin II (ThermoFisher Scientific, cat. no. 10362100) as a transfection reagent. Insect cell media containing recombinant baculovirus was harvested after four days and passaged twice more in Sf9 cells at a starting density of 1.5×10^6/mL to obtain a high titer stock. After centrifugation at 1,000 g for 15 min, filtration (0.45 µm, PES membrane), and the addition of 2% (vol/vol) FCS, viral stocks were stored at 4°C until further use. Viral titer was determined by end-point dilution assay in Sf9 cells.

HEK293S GnTI$^-$ cells were grown in suspension in FreeStyle 293 medium (Gibco, ThermoFisher Scientific), supplemented with 1% (vol/vol) fetal bovine serum (FBS), non-essential amino acids (NEAA; Gibco, ThermoFisher Scientific) and L-glutamine (L-Gln; Gibco, ThermoFisher Scientific), in conical flasks in a shaking incubator operated at 37°C, 130 rpm and with 8% CO_2. Once a density of 2×10^6 cells/mL was reached, cells were transduced with recombinant baculovirus at a multiplicity of infection (MOI) of 1, 4 or 10, with no more than 5% insect cell media added. 5 mM VPA or 5 mM sodium butyrate were added as specified and cells were grown either at 30°C, 8% CO_2 and 130 rpm or at 37°C, 8% CO_2 and 130 rpm. At 24 h, 48 h and 72 h after transduction, 1 mL of cells was collected and centrifuged at 500 g for 2 min. Cell pellets were snap-frozen in liquid nitrogen and stored at –80°C.

Lentiviral transduction

An identical mVenus-$GABA_AR$-$β3_{FL}$-1D4 construct was subcloned into pHR-CMV-$TetO_2$ using the *EcoRI* and *XhoI* sites. A sequence-verified clone was used to establish a polyclonal cell line in HEK293S GnTI$^-$ TetR cells using the method described in the main Protocol. Suspension HEK293S GnTI$^-$ TetR cells were induced using 5 or 10 µg/mL Dox at a density of 2×10^6 cells/mL. 5 mM VPA or 5 mM sodium butyrate were added as specified and cells were grown either at 30°C, 8% CO_2 and 130 rpm or at 37°C, 8% CO_2 and 130 rpm. At 24 h, 48 h and 72 h after transduction, 1 mL of cells was collected and centrifuged at 500 g for 2 min. Cell pellets were snap-frozen in liquid nitrogen and stored at –80°C.

Fluorescent size-exclusion chromatography (FSEC) screening

For lysate FSEC, cell pellets were briefly thawed in a room-temperature metal block, and then placed on ice. Cells were resuspended in 200 µL ice-cold resuspension buffer containing 300 mM NaCl, 50 mM HEPES pH 7.2, 1 mM $CaCl_2$, 1 mM $MgCl_2$, 5 U/mL benzonase nuclease (Merck, cat. no. 70746) and 1% (vol/vol) mammalian protease inhibitors (Merck, cat. no. P8340). Detergent (*n*-dodecyl-β-D-

maltopyranoside, DDM, Anatrace, cat. no. D310) and cholesterol hemisuccinate (CHS, Anatrace, cat. no. CH210) were added to a final concentration of 1% (wt/vol) and 0.1% (wt/vol), respectively. The cell suspension was rotated for 2 h at 4°C, and then centrifuged at 129,000 g for 20 min at 4°C. The supernatants were loaded onto a Superose 6 Increase 3.2/300 column (GE Healthcare, cat. no. 29091598) equilibrated in 150 mM NaCl, 25 mM HEPES pH 7.2, 0.03% (wt/vol) DDM, 0.003% (wt/vol) CHS, and attached to an ultra-fast preparative and purification liquid chromatography (UFPLC) system with automated micro-volume loader and in-line fluorescence detection (Shimadzu Prominence UFPLC), maintained at 4°C. mVenus fluorescence was monitored using an excitation wavelength of 515 nm and emission wavelength of 528 nm. To avoid prolonged exposure to detergent, lysates were analysed in batches of 12-18.

References

[1] E. Roberts and S. Frankel, "Gamma-Aminobutyric acid in brain: its formation from glutamic acid.", English, *Journal of Biological Chemistry*, vol. 187, no. 1, pp. 55–63, Nov. 1950.

[2] M. G. Erlander, N. J. K. Tillakaratne, S. Feldblum, N. Patel, and A. J. Tobin, "Two genes encode distinct glutamate decarboxylases", English, *Neuron*, vol. 7, no. 1, pp. 91–100, Jul. 1991.

[3] S. L. McIntire, R. J. Reimer, K. Schuske, R. H. Edwards, and E. M. Jorgensen, "Identification and characterization of the vesicular GABA transporter.", English, *Nature*, vol. 389, no. 6653, pp. 870–876, Oct. 1997.

[4] C. Sagné, S. El Mestikawy, M. F. Isambert, M. Hamon, J. P. Henry, B. Giros, and B. Gasnier, "Cloning of a functional vesicular GABA and glycine transporter by screening of genome databases.", English, *FEBS Letters*, vol. 417, no. 2, pp. 177–183, Nov. 1997.

[5] F. A. Chaudhry, R. J. Reimer, E. E. Bellocchio, N. C. Danbolt, K. K. Osen, R. H. Edwards, and J. Storm-Mathisen, "The vesicular GABA transporter, VGAT, localizes to synaptic vesicles in sets of glycinergic as well as GABAergic neurons.", English, *The Journal of neuroscience*, vol. 18, no. 23, pp. 9733–9750, Dec. 1998.

[6] P. E. Kish, C. Fischer-Bovenkerk, and T. Ueda, "Active transport of gamma-aminobutyric acid and glycine into synaptic vesicles.", English, *Proceedings of the National Academy of Sciences of the United States of America*, vol. 86, no. 10, pp. 3877–3881, May 1989.

[7] J. Rizo and J. Xu, "The Synaptic Vesicle Release Machinery", English, *Annual Review of Biophysics*, vol. 44, no. 1, pp. 339–367, Jun. 2015.

[8] I. Mody and R. A. Pearce, "Diversity of inhibitory neurotransmission through GABA(A) receptors", English, *Trends in Neurosciences*, vol. 27, no. 9, pp. 569–575, Sep. 2004.

[9] N. J. Allen, R. Káradóttir, and D. Attwell, "Reversal or reduction of glutamate and GABA transport in CNS pathology and therapy.", English, *Pflugers Archiv (European Journal of Physiology)*, vol. 449, no. 2, pp. 132–142, Nov. 2004.

[10] M. Farrant and Z. Nusser, "Variations on an inhibitory theme: phasic and tonic activation of GABA(A) receptors", English, *Nature Reviews. Neuroscience*, vol. 6, no. 3, pp. 215–229, Mar. 2005.

[11] H. S. Waagepetersen, U. Sonnewald, and A. Schousboe, "The GABA Paradox", English, *Journal of Neurochemistry*, vol. 73, no. 4, pp. 1335–1342, Jan. 2002.

[12] N. M. Rowley, K. K. Madsen, A. Schousboe, and H. Steve White, "Glutamate and GABA synthesis, release, transport and metabolism as targets for seizure control", English, *Neurochemistry International*, vol. 61, no. 4, pp. 546–558, Sep. 2012.

[13] C. Rae, N. Hare, W. A. Bubb, S. R. McEwan, A. Bröer, J. A. McQuillan, V. J. Balcar, A. D. Conigrave, and S. Bröer, "Inhibition of glutamine transport depletes glutamate and GABA neurotransmitter pools: further evidence for metabolic compartmentation", English, *Journal of Neurochemistry*, vol. 85, no. 2, pp. 503–514, Apr. 2003.

[14] E. B. Sequerra, P. Gardino, C. Hedin-Pereira, and F. G. de Mello, "Putrescine as an important source of GABA in the postnatal rat subventricular zone", English, *Neuroscience*, vol. 146, no. 2, pp. 489–493, May 2007.

[15] F. F. Trigo, A. Marty, and B. M. Stell, "Axonal GABAA receptors.", English, *European Journal of Neuroscience*, vol. 28, no. 5, pp. 841–848, Sep. 2008.

[16] J. V. Raimondo, B. A. Richards, and M. A. Woodin, "Neuronal chloride and excitability - the big impact of small changes.", English, *Current Opinion in Neurobiology*, vol. 43, pp. 35–42, Apr. 2017.

[17] J. Szabadics, C. Varga, G. Molnar, S. Olah, P. Barzo, and G. Tamas, "Excitatory effect of GABAergic axo-axonic cells in cortical microcircuits", English, *Science*, vol. 311, no. 5758, pp. 233–235, Jan. 2006.

[18] M. Lopez de Armentia and P. Sah, "Bidirectional synaptic plasticity at nociceptive afferents in the rat central amygdala", *The Journal of physiology*, vol. 581, no. Pt 3, pp. 961–970, Jun. 2007.

[19] Y. Ben-Ari, "Excitatory actions of gaba during development: the nature of the nurture.", English, *Nature Reviews. Neuroscience*, vol. 3, no. 9, pp. 728–739, Sep. 2002.

[20] P. Rorsman, P.-O. Berggren, K. Bokvist, H. Ericson, H. Mohler, C.-G. Östenson, and P. A. Smith, "Glucose-inhibition of glucagon secretion involves activation of GABAA-receptor chloride channels", English, *Nature*, vol. 341, no. 6239, pp. 233–236, Sep. 1989.

[21] A. Tasneem, L. M. Iyer, E. Jakobsson, and L. Aravind, "Identification of the prokaryotic ligand-gated ion channels and their implications for the mechanisms and origins of animal Cys-loop ion channels", English, *Genome biology*, vol. 6, no. 1, R4, 2005.

[22] K. Brejc, W. J. van Dijk, R. V. Klaassen, M. Schuurmans, J. van Der Oost, A. B. Smit, and T. K. Sixma, "Crystal structure of an ACh-binding protein reveals the ligand-binding domain of nicotinic receptors.", English, *Nature*, vol. 411, no. 6835, pp. 269–276, May 2001.

[23] P. H. N. Celie, S. E. van Rossum-Fikkert, W. J. van Dijk, K. Brejc, A. B. Smit, and T. K. Sixma, "Nicotine and carbamylcholine binding to nicotinic acetylcholine receptors as studied in AChBP crystal structures.", English, *Neuron*, vol. 41, no. 6, pp. 907–914, Mar. 2004.

[24] N. Unwin, "Refined structure of the nicotinic acetylcholine receptor at 4A resolution.", English, *Journal of Molecular Biology*, vol. 346, no. 4, pp. 967–989, Mar. 2005.

[25] A. Miyazawa, Y. Fujiyoshi, and N. Unwin, "Structure and gating mechanism of the acetylcholine receptor pore", *Nature*, vol. 423, no. 6943, pp. 949–955, 2003.

[26] C. L. Morales-Perez, C. M. Noviello, and R. E. Hibbs, "X-ray structure of the human $\alpha 4\beta 2$ nicotinic receptor.", English, *Nature*, Oct. 2016.

[27] N. Bocquet, H. Nury, M. Baaden, C. Le Poupon, J. P. Changeux, M. Delarue, and P. J. Corringer, "X-ray structure of a pentameric ligand-gated ion channel in an apparently open conformation", English, *Nature*, vol. 457, no. 7225, pp. 111–114, Jan. 2009.

[28] R. J. Hilf and R. Dutzler, "Structure of a potentially open state of a proton-activated pentameric ligand-gated ion channel", English, *Nature*, vol. 457, no. 7225, pp. 115–118, Jan. 2009.

[29] L. Sauguet, A. Shahsavar, F. Poitevin, C. Huon, A. Menny, A. Nemecz, A. Haouz, J.-P. Changeux, P.-J. Corringer, and M. Delarue, "Crystal structures of a pentameric ligand-gated ion channel provide a mechanism for activation.", English, *Proceedings of the National Academy of Sciences of the United States of America*, vol. 111, no. 3, pp. 966–971, Jan. 2014.

[30] R. J. Hilf and R. Dutzler, "X-ray structure of a prokaryotic pentameric ligand-gated ion channel", English, *Nature*, vol. 452, no. 7185, pp. 375–379, Mar. 2008.

[31] R. E. Hibbs and E. Gouaux, "Principles of activation and permeation in an anion-selective Cys-loop receptor", English, *Nature*, vol. 474, no. 7349, pp. 54–60, 2011.

[32] T. Althoff, R. E. Hibbs, S. Banerjee, and E. Gouaux, "X-ray structures of GluCl in apo states reveal a gating mechanism of Cys-loop receptors.", English, *Nature*, vol. 512, no. 7514, pp. 333–337, Aug. 2014.

[33] G. Hassaine, C. Deluz, L. Grasso, R. Wyss, M. B. Tol, R. Hovius, A. Graff, H. Stahlberg, T. Tomizaki, A. Desmyter, C. Moreau, X. D. Li, F. Poitevin, H. Vogel, and H. Nury, "X-ray structure of the mouse serotonin 5-HT3 receptor", English, *Nature*, vol. 512, no. 7514, pp. 276–281, Aug. 2014.

[34] M. Kudryashev, D. Castaño-Díez, C. Deluz, G. Hassaine, L. Grasso, A. Graf-Meyer, H. Vogel, and H. Stahlberg, "The Structure of the Mouse Serotonin 5-HT3 Receptor in Lipid Vesicles.", English, *Structure*, vol. 24, no. 1, pp. 165–170, Jan. 2016.

[35] J. Du, W. Lu, S. Wu, Y. Cheng, and E. Gouaux, "Glycine receptor mechanism elucidated by electron cryo-microscopy", *Nature*, vol. 526, pp. 224–229, 2015.

[36] X. Huang, P. L. Shaffer, S. Ayube, H. Bregman, H. Chen, S. G. Lehto, J. A. Luther, D. J. Matson, S. I. McDonough, K. Michelsen, M. H. Plant, S. Schneider, J. R. Simard, Y. Teffera, S. Yi, M. Zhang, E. F. DiMauro, and J. Gingras, "Crystal structures of human glycine receptor α3 bound to a novel class of analgesic potentiators.", English, *Nature Structural & Molecular Biology*, vol. 24, no. 2, pp. 108–113, Feb. 2017.

[37] P. S. Miller and A. R. Aricescu, "Crystal structure of a human GABAA receptor.", English, *Nature*, vol. 512, no. 7514, pp. 270–275, Aug. 2014.

[38] S. Phulera, H. Zhu, J. Yu, D. P. Claxton, N. Yoder, C. Yoshioka, and E. Gouaux, "Cryo-EM structure of the benzodiazepine-sensitive alpha1beta1gamma2S tri-heteromeric GABAA receptor in complex with GABA.", English, *eLife*, vol. 7, Jul. 2018.

[39] S. Zhu, C. M. Noviello, J. Teng, R. M. Walsh, J. J. Kim, and R. E. Hibbs, "Structure of a human synaptic GABAA receptor.", English, *Nature*, vol. 179, p. 390, Jun. 2018.

[40] P. Miller, S. Masiulis, T. Malinauskas, A. Kotecha, S. Rao, S. Chavali, L. De Colibus, E. Pardon, S. Hannan, S. Scott, Z. Sun, B. Frenz, G. Klesse, S. Li, J. Diprose, A. Siebert, R. Esnouf, F. DiMaio, S. Tucker, T. Smart, J. Steyaert, M. Babu, M. Sansom, J. Huiskonen, and R. Aricescu, "Heteromeric GABAA receptor structures in positively-modulated active states", *bioRxiv*, 2018.

[41] S. Masiulis, R. Desai, T. Uchański, I. S. Martin, D. Laverty, D. Karia, T. Malinauskas, J. Zivanov, E. Pardon, A. Kotecha, J. Steyaert, K. W. Miller, and A. R. Aricescu, "GABA A receptor signalling mechanisms revealed by structural pharmacology", English, *Nature*, vol. 565, no. 7740, pp. 454–459, Jan. 2019.

[42] D. Laverty, R. Desai, T. Uchański, S. Masiulis, W. J. Stec, T. Malinauskas, J. Zivanov, E. Pardon, J. Steyaert, K. W. Miller, and A. R. Aricescu, "Cryo-EM structure of the human $\alpha 1\beta 3\gamma 2$ GABAA receptor in a lipid bilayer.", English, *Nature*, vol. 565, no. 7740, pp. 516–520, Jan. 2019.

[43] T. Grutter, L. P. de Carvalho, V. Dufresne, A. Taly, M. Fischer, and J.-P. Changeux, "A chimera encoding the fusion of an acetylcholine-binding protein to an ion channel is stabilized in a state close to the desensitized form of ligand-gated ion channels", English, *Comptes Rendus Biologies*, vol. 328, no. 3, pp. 223–234, 2005.

[44] G. Duret, C. Van Renterghem, Y. Weng, M. Prevost, G. Moraga-Cid, C. Huon, J. M. Sonner, and P.-J. Corringer, "Functional prokaryotic-eukaryotic chimera from the pentameric ligand-gated ion channel family.", English, *Proceedings of the National Academy of Sciences of the United States of America*, vol. 108, no. 29, pp. 12 143–12 148, Jul. 2011.

[45] A. M. Hosie, M. E. Wilkins, H. M. A. da Silva, and T. G. Smart, "Endogenous neurosteroids regulate GABAA receptors through two discrete transmembrane sites.", English, *Nature*, vol. 444, no. 7118, pp. 486–489, Nov. 2006.

[46] G. D. Cymes and C. Grosman, "Identifying the elusive link between amino acid sequence and charge selectivity in pentameric ligand-gated ion channels.", English, *Proceedings of the National Academy of Sciences of the United States of America*, vol. 113, no. 45, E7106–E7115, Oct. 2016.

[47] P. S. Miller and T. G. Smart, "Binding, activation and modulation of Cys-loop receptors.", English, *Trends in Pharmacological Sciences*, vol. 31, no. 4, pp. 161–174, Apr. 2010.

[48] M. Gielen and P.-J. Corringer, "The dual-gate model for pentameric ligand-gated ion channels activation and desensitization.", English, *The Journal of physiology*, vol. 596, no. 10, pp. 1873–1902, May 2018.

[49] M. Jansen, M. Bali, and M. H. Akabas, "Modular design of Cys-loop ligand-gated ion channels: functional 5-HT3 and GABA rho1 receptors lacking the large cytoplasmic M3M4 loop", English, *Journal of General Physiology*, vol. 131, no. 2, pp. 137–146, Feb. 2008.

[50] E. Sigel, F. A. Stephenson, C. Mamalaki, and E. A. Barnard, "A gamma-aminobutyric acid/benzodiazepine receptor complex of bovine cerebral cortex", English, *Journal of Biological Chemistry*, vol. 258, no. 11, pp. 6965–6971, Jun. 1983.

[51] P. R. Schofield, M. G. Darlison, N. Fujita, D. R. Burt, F. A. Stephenson, H. Rodriguez, L. M. Rhee, J. Ramachandran, V. Reale, and T. A. Glencorse, "Sequence and functional expression of the GABA A receptor shows a ligand-gated receptor super-family.", English, *Nature*, vol. 328, no. 6127, pp. 221–227, Jul. 1987.

[52] J. Simon, H. Wakimoto, N. Fujita, M. Lalande, and E. A. Barnard, "Analysis of the set of GABA(A) receptor genes in the human genome.", English, *Journal of Biological Chemistry*, vol. 279, no. 40, pp. 41 422–41 435, Oct. 2004.

[53] P. Whiting, R. M. McKernan, and L. L. Iversen, "Another mechanism for creating diversity in gamma-aminobutyrate type A receptors: RNA splicing directs expression of two forms of gamma 2 phosphorylation site.", English, *Proceedings of the National Academy of Sciences of the United States of America*, vol. 87, no. 24, pp. 9966–9970, Dec. 1990.

[54] Z.-W. Chen, K. Fuchs, W. Sieghart, R. R. Townsend, and A. S. Evers, "Deep amino acid sequencing of native brain GABAA receptors using high-resolution mass spectrometry.", English, *Molecular & cellular proteomics : MCP*, vol. 11, no. 1, p. M111.011445, Jan. 2012.

[55] J. Ohlson, J. S. Pedersen, D. Haussler, and M. Ohman, "Editing modifies the GABA(A) receptor subunit alpha3.", English, *RNA*, vol. 13, no. 5, pp. 698–703, May 2007.

[56] E. Y. Rula, A. H. Lagrange, M. M. Jacobs, N. Hu, R. L. Macdonald, and R. B. Emeson, "Developmental modulation of GABA(A) receptor function by RNA editing.", English, *Journal of Neuroscience*, vol. 28, no. 24, pp. 6196–6201, Jun. 2008.

[57] I. Letunic and P. Bork, "Interactive tree of life (iTOL) v3: an online tool for the display and annotation of phylogenetic and other trees.", English, *Nucleic Acids Research*, vol. 44, no. W1, W242–5, Jul. 2016.

[58] F. Sievers, A. Wilm, D. Dineen, T. J. Gibson, K. Karplus, W. Li, R. Lopez, H. McWilliam, M. Remmert, J. Söding, J. D. Thompson, and D. G. Higgins, "Fast, scalable generation of high-quality protein multiple sequence alignments using Clustal Omega.", English, *Molecular Systems Biology*, vol. 7, no. 1, pp. 539–539, Oct. 2011.

[59] R. W. Olsen and W. Sieghart, "International Union of Pharmacology. LXX. Subtypes of gamma-aminobutyric acid(A) receptors: classification on the basis of subunit composition, pharmacology, and function. Update.", English, *Pharmacological Reviews*, vol. 60, no. 3, pp. 243–260, Sep. 2008.

[60] E. Sigel and M. E. Steinmann, "Structure, function, and modulation of GABA(A) receptors", *Journal of Biological Chemistry*, vol. 287, no. 48, pp. 40 224–40 231, Nov. 2012.

[61] S. J. Russek, "Evolution of GABAA receptor diversity in the human genome", English, *Gene*, vol. 227, no. 2, pp. 213–222, Feb. 1999.

[62] N. Nayeem, T. P. Green, I. L. Martin, and E. A. Barnard, "Quaternary structure of the native GABAA receptor determined by electron microscopic image analysis.", English, *Journal of Neurochemistry*, vol. 62, no. 2, pp. 815–818, Feb. 1994.

[63] V. Tretter, N. Ehya, K. Fuchs, and W. Sieghart, "Stoichiometry and assembly of a recombinant GABAA receptor subtype.", English, *The Journal of neuroscience*, vol. 17, no. 8, pp. 2728–2737, Apr. 1997.

[64] S. W. Baumann, R. Baur, and E. Sigel, "Subunit arrangement of gamma-aminobutyric acid type A receptors.", English, *Journal of Biological Chemistry*, vol. 276, no. 39, pp. 36 275–36 280, Sep. 2001.

[65] C. N. Connolly, B. J. Krishek, B. J. McDonald, T. G. Smart, and S. J. Moss, "Assembly and cell surface expression of heteromeric and homomeric gamma-aminobutyric acid type A receptors", English, *Journal of Biological Chemistry*, vol. 271, no. 1, pp. 89–96, Jan. 1996.

[66] D. B. Pritchett, H. Sontheimer, C. M. Gorman, H. Kettenmann, P. H. Seeburg, and P. R. Schofield, "Transient expression shows ligand gating and allosteric potentiation of GABAA receptor subunits", English, *Science*, vol. 242, no. 4883, pp. 1306–1308, Dec. 1988.

[67] Y. Chang, R. Wang, S. Barot, and D. S. Weiss, "Stoichiometry of a recombinant GABAA receptor.", English, *The Journal of neuroscience*, vol. 16, no. 17, pp. 5415–5424, Sep. 1996.

[68] S. W. Baumann, R. Baur, and E. Sigel, "Individual properties of the two functional agonist sites in GABA(A) receptors.", English, *Journal of Neuroscience*, vol. 23, no. 35, pp. 11 158–11 166, Dec. 2003.

[69] A. J. Boileau, "Tandem Subunits Effectively Constrain GABAA Receptor Stoichiometry and Recapitulate Receptor Kinetics But Are Insensitive to GABAA Receptor-Associated Protein", English, *The Journal of neuroscience*, vol. 25, no. 49, pp. 11 219–11 230, Dec. 2005.

[70] R. Baur, F. Minier, and E. Sigel, "A GABA(A) receptor of defined subunit composition and positioning: concatenation of five subunits.", English, *FEBS Letters*, vol. 580, no. 6, pp. 1616–1620, Mar. 2006.

[71] R. Baur and E. Sigel, "Low Expression in Xenopus Oocytes and Unusual Functional Properties of $\alpha 1\beta 2\gamma 2$ GABAA Receptors with Non-Conventional Subunit Arrangement.", English, *PLoS ONE*, vol. 12, no. 1, e0170572, 2017.

[72] M. Jechlinger, R. Pelz, V. Tretter, T. Klausberger, and W. Sieghart, "Subunit composition and quantitative importance of hetero-oligomeric receptors: GABAA receptors containing alpha6 subunits.", English, *The Journal of neuroscience*, vol. 18, no. 7, pp. 2449–2457, Apr. 1998.

[73] S. Pollard, M. J. Duggan, and F. A. Stephenson, "Further evidence for the existence of alpha subunit heterogeneity within discrete gamma-aminobutyric acidA receptor subpopulations.", English, *Journal of Biological Chemistry*, vol. 268, no. 5, pp. 3753–3757, Feb. 1993.

[74] D. Benke, P. Fakitsas, C. Roggenmoser, C. Michel, U. Rudolph, and H. Mohler, "Analysis of the presence and abundance of GABAA receptors containing two different types of alpha subunits in murine brain using point-mutated alpha subunits.", English, *Journal of Biological Chemistry*, vol. 279, no. 42, pp. 43 654–43 660, Oct. 2004.

[75] M. Mortensen and T. G. Smart, "Extrasynaptic $\alpha\beta$ subunit GABA Areceptors on rat hippocampal pyramidal neurons", English, *The Journal of physiology*, vol. 577, no. 3, pp. 841–856, Dec. 2006.

[76] E. Sigel, R. Baur, N. Boulineau, and F. Minier, "Impact of subunit positioning on GABAA receptor function.", English, *Biochemical Society Transactions*, vol. 34, no. Pt 5, pp. 868–871, Nov. 2006.

[77] N. P. Barrera, J. Betts, H. You, R. M. Henderson, I. L. Martin, S. M. J. Dunn, and J. M. Edwardson, "Atomic Force Microscopy Reveals the Stoichiometry and Subunit Arrangement of the $\alpha 4\beta 3\delta$ GABAA Receptor", English, *Molecular Pharmacology*, vol. 73, no. 3, pp. 960–967, Mar. 2008.

[78] B. Patel, M. Mortensen, and T. G. Smart, "Stoichiometry of δ subunit containing GABA(A) receptors.", English, *British Journal of Pharmacology*, vol. 171, no. 4, pp. 985–994, Feb. 2014.

[79] K. R. Wagoner and C. Czajkowski, "Stoichiometry of Expressed α 4β 2δ γ-Aminobutyric Acid Type A Receptors Depends on the Ratio of Subunit cDNA Transfected", English, *Journal of Biological Chemistry*, vol. 285, no. 19, pp. 14 187–14 194, Apr. 2010.

[80] M. M. Eaton, J. Bracamontes, H.-J. Shu, P. Li, S. Mennerick, J. H. Steinbach, and G. Akk, "γ-aminobutyric acid type A $\alpha 4$, $\beta 2$, and δ subunits assemble to produce more than one functionally distinct receptor type.", English, *Molecular Pharmacology*, vol. 86, no. 6, pp. 647–656, Dec. 2014.

[81] W. B. Im, J. F. Pregenzer, J. A. Binder, G. H. Dillon, and G. L. Alberts, "Chloride channel expression with the tandem construct of alpha 6-beta 2 GABAA receptor subunit requires a monomeric subunit of alpha 6 or gamma 2.", English, *Journal of Biological Chemistry*, vol. 270, no. 44, pp. 26 063–26 066, Nov. 1995.

[82] T. P. Bonnert, R. M. McKernan, S. Farrar, B. le Bourdellès, R. P. Heavens, D. W. Smith, L. Hewson, M. R. Rigby, D. J. Sirinathsinghji, N. Brown, K. A. Wafford, and P. J. Whiting, "theta, a novel gamma-aminobutyric acid type A receptor subunit.", English, *Proceedings of the National Academy of Sciences of the United States of America*, vol. 96, no. 17, pp. 9891–9896, Aug. 1999.

[83] K. A. Bollan, R. Baur, T. G. Hales, E. Sigel, and C. N. Connolly, "The promiscuous role of the epsilon subunit in GABAA receptor biogenesis.", English, *Molecular and Cellular Neurosciences*, vol. 37, no. 3, pp. 610–621, Mar. 2008.

[84] M. M. Naffaa, S. Hung, M. Chebib, G. A. R. Johnston, and J. R. Hanrahan, "GABA-ρ receptors: distinctive functions and molecular pharmacology.", English, *British Journal of Pharmacology*, vol. 174, no. 13, pp. 1881–1894, Jul. 2017.

[85] V. E. Wotring, Y. Chang, and D. S. Weiss, "Permeability and single channel conductance of human homomeric rho1 GABAC receptors.", English, *The Journal of physiology*, vol. 521 Pt 2, pp. 327–336, Dec. 1999.

[86] A. Slany, J. Zezula, V. Tretter, and W. Sieghart, "Rat beta 3 subunits expressed in human embryonic kidney 293 cells form high affinity [35S]t-butylbicyclophosphorothionate binding sites modulated by several allosteric ligands of gamma-aminobutyric acid type A receptors.", English, *Molecular Pharmacology*, vol. 48, no. 3, pp. 385–391, Sep. 1995.

[87] C. N. Connolly, J. R. Wooltorton, T. G. Smart, and S. J. Moss, "Subcellular localization of gamma-aminobutyric acid type A receptors is determined by receptor beta subunits", English, *Proceedings of the National Academy of Sciences of the United States of America*, vol. 93, no. 18, pp. 9899–9904, Sep. 1996.

[88] A. Saras, G. Gisselmann, A. K. Vogt-Eisele, K. S. Erlkamp, O. Kletke, H. Pusch, and H. Hatt, "Histamine action on vertebrate GABAA receptors: direct channel gating and potentiation of GABA responses.", English, *Journal of Biological Chemistry*, vol. 283, no. 16, pp. 10 470–10 475, Apr. 2008.

[89] P. Hoerbelt, J. Ramerstorfer, M. Ernst, W. Sieghart, J. L. Thomson, L. B. Hough, and M. W. Fleck, "Mutagenesis and computational docking studies support the existence of a histamine binding site at the extracellular $\beta3$+$\beta3$- interface of homooligomeric $\beta3$ GABAA receptors.", English, *Neuropharmacology*, vol. 108, pp. 252–263, Sep. 2016.

[90] R. L. Macdonald and E. J. Botzolakis, "Biophysical Properties of Recombinant $\gamma2$- and δ-subunit Containing GABAA Receptors", English, in *Extrasynaptic GABAA Receptors*, New York, NY: Springer New York, Sep. 2014, pp. 33–50.

[91] T. N. Vien, S. J. Moss, and P. A. Davies, "Regulating the Efficacy of Inhibition Through Trafficking of gamma-Aminobutyric Acid Type A Receptors.", English, *Anesthesia and analgesia*, vol. 123, no. 5, pp. 1220–1227, Nov. 2016.

[92] P. M. Taylor, P. Thomas, G. H. Gorrie, C. N. Connolly, T. G. Smart, and S. J. Moss, "Identification of amino acid residues within GABA(A) receptor beta subunits that mediate both homomeric and heteromeric receptor expression.", English, *The Journal of neuroscience*, vol. 19, no. 15, pp. 6360–6371, Aug. 1999.

[93] K. Bollan, D. King, L. A. Robertson, K. Brown, P. M. Taylor, S. J. Moss, and C. N. Connolly, "GABA AReceptor Composition Is Determined by Distinct Assembly Signals within α and β Subunits", English, *Journal of Biological Chemistry*, vol. 278, no. 7, pp. 4747–4755, Feb. 2003.

[94] Y. Nakamura, L. M. Darnieder, T. Z. Deeb, and S. J. Moss, "Regulation of GABAARs by phosphorylation.", English, *Advances in Pharmacology*, vol. 72, pp. 97–146, 2015.

[95] E. A. Heller, W. Zhang, F. Selimi, J. C. Earnheart, M. A. Ślimak, J. Santos-Torres, I. Ibañez-Tallon, C. Aoki, B. T. Chait, and N. Heintz, "The biochemical anatomy of cortical inhibitory synapses.", English, *PLoS ONE*, vol. 7, no. 6, e39572, 2012.

[96] Y. Nakamura, D. H. Morrow, A. Modgil, D. Huyghe, T. Z. Deeb, M. J. Lumb, P. A. Davies, and S. J. Moss, "Proteomic Characterization of Inhibitory Synapses Using a Novel pHluorin-tagged γ-Aminobutyric Acid Receptor, Type A (GABAA), α2 Subunit Knock-in Mouse.", English, *Journal of Biological Chemistry*, vol. 291, no. 23, pp. 12 394–12 407, Jun. 2016.

[97] Y. Ge, Y. Kang, R. M. Cassidy, K.-M. Moon, R. Lewis, R. O. L. Wong, L. J. Foster, and A. M. Craig, "Clptm1 Limits Forward Trafficking of GABAA Receptors to Scale Inhibitory Synaptic Strength.", English, *Neuron*, vol. 97, no. 3, pp. 596–610, Feb. 2018.

[98] T. A. Leil, Z.-W. Chen, C.-S. S. Chang, and R. W. Olsen, "GABAA receptor-associated protein traffics GABAA receptors to the plasma membrane in neurons.", English, *Journal of Neuroscience*, vol. 24, no. 50, pp. 11 429–11 438, Dec. 2004.

[99] S. K. Tyagarajan and J. M. Fritschy, "Gephyrin: a master regulator of neuronal function?", English, *Nature Reviews. Neuroscience*, vol. 15, no. 3, pp. 141–156, Mar. 2014.

[100] T. Papadopoulos and T. Soykan, "The Role of Collybistin in Gephyrin Clustering at Inhibitory Synapses: Facts and Open Questions", *Frontiers in Cellular Neuroscience*, vol. 5, p. 11, 2011.

[101] T. Yamasaki, E. Hoyos-Ramirez, J. S. Martenson, M. Morimoto-Tomita, and S. Tomita, "GARLH Family Proteins Stabilize GABA A Receptors at Synapses", English, *Neuron*, vol. 93, no. 5, 1138–1152.e6, Mar. 2017.

[102] E. C. Davenport, V. Pendolino, G. Kontou, T. P. McGee, D. F. Sheehan, G. Lopez-Domenech, M. Farrant, and J. T. Kittler, "An Essential Role for the Tetraspanin LHFPL4 in the Cell-Type-Specific Targeting and Clustering of Synaptic GABAA Receptors.", English, *Cell reports*, vol. 21, no. 1, pp. 70–83, Oct. 2017.

[103] T. P. Angelotti and R. L. Macdonald, "Assembly of GABAA receptor subunits: alpha 1 beta 1 and alpha 1 beta 1 gamma 2S subunits produce unique ion channels with dissimilar single-channel properties.", English, *The Journal of neuroscience*, vol. 13, no. 4, pp. 1429–1440, Apr. 1993.

[104] K. Imoto, C. Busch, B. Sakmann, M. Mishina, T. Konno, J. Nakai, H. Bujo, Y. Mori, K. Fukuda, and S. Numa, "Rings of negatively charged amino acids determine the acetylcholine receptor channel conductance", English, *Nature*, vol. 335, no. 6191, pp. 645–648, Oct. 1988.

[105] G. D. Cymes, Y. Ni, and C. Grosman, "Probing ion-channel pores one proton at a time.", English, *Nature*, vol. 438, no. 7070, pp. 975–980, Dec. 2005.

[106] S. G. Brickley, S. G. Cull-Candy, and M. Farrant, "Single-channel properties of synaptic and extrasynaptic GABAA receptors suggest differential targeting of receptor subtypes.", English, *The Journal of neuroscience*, vol. 19, no. 8, pp. 2960–2973, Apr. 1999.

[107] S. Scott, J. W. Lynch, and A. Keramidas, "Correlating structural and energetic changes in glycine receptor activation", English, *Journal of Biological Chemistry*, vol. 290, no. 9, pp. 5621–5634, Feb. 2015.

[108] J. A. Peters, M. A. Cooper, J. E. Carland, M. R. Livesey, T. G. Hales, and J. J. Lambert, "Novel structural determinants of single channel conductance and ion selectivity in 5-hydroxytryptamine type 3 and nicotinic acetylcholine receptors.", English, vol. 588, no. Pt 4, pp. 587–596, Feb. 2010.

[109] M. Moroni, J. O. Meyer, C. Lahmann, and L. G. Sivilotti, "In glycine and GABA(A) channels, different subunits contribute asymmetrically to channel conductance via residues in the extracellular domain.", English, *Journal of Biological Chemistry*, vol. 286, no. 15, pp. 13 414–13 422, Apr. 2011.

[110] S. P. Kelley, J. I. Dunlop, E. F. Kirkness, J. J. Lambert, and J. A. Peters, "A cytoplasmic region determines single-channel conductance in 5-HT3 receptors", English, *Nature*, vol. 424, no. 6946, pp. 321–324, Jul. 2003.

[111] J. Bormann, O. P. Hamill, and B. Sakmann, "Mechanism of anion permeation through channels gated by glycine and gamma-aminobutyric acid in mouse cultured spinal neurones", English, *The Journal of physiology*, vol. 385, pp. 243–286, Apr. 1987.

[112] V. E. Wotring, T. S. Miller, and D. S. Weiss, "Mutations at the GABA receptor selectivity filter: a possible role for effective charges.", English, *The Journal of physiology*, vol. 548, no. Pt 2, pp. 527–540, Apr. 2003.

[113] M. L. Jensen, D. B. Timmermann, T. H. Johansen, A. Schousboe, T. Varming, and P. K. Ahring, "The beta subunit determines the ion selectivity of the GABAA receptor.", English, *Journal of Biological Chemistry*, vol. 277, no. 44, pp. 41 438–41 447, Nov. 2002.

[114] A. Nemecz, M. S. Prevost, A. Menny, and P.-J. Corringer, "Emerging Molecular Mechanisms of Signal Transduction in Pentameric Ligand-Gated Ion Channels.", English, *Neuron*, vol. 90, no. 3, pp. 452–470, May 2016.

[115] N. Mukhtasimova, W. Y. Lee, H.-L. Wang, and S. M. Sine, "Detection and trapping of intermediate states priming nicotinic receptor channel opening.", English, *Nature*, vol. 459, no. 7245, pp. 451–454, May 2009.

[116] W. Y. Lee and S. M. Sine, "Principal pathway coupling agonist binding to channel gating in nicotinic receptors.", English, *Nature*, vol. 438, no. 7065, pp. 243–247, Nov. 2005.

[117] M. Gielen, P. Thomas, and T. G. Smart, "The desensitization gate of inhibitory Cys-loop receptors", English, *Nature Communications*, vol. 6, p. 6829, 2015.

[118] V. Burzomato, M. Beato, P. J. Groot-Kormelink, D. Colquhoun, and L. G. Sivilotti, "Single-channel behavior of heteromeric alpha1beta glycine receptors: an attempt to detect a conformational change before the channel opens.", English, *Journal of Neuroscience*, vol. 24, no. 48, pp. 10 924–10 940, Dec. 2004.

[119] R. Lape, D. Colquhoun, and L. G. Sivilotti, "On the nature of partial agonism in the nicotinic receptor superfamily.", English, *Nature*, vol. 454, no. 7205, pp. 722–727, Aug. 2008.

[120] S. Basak, N. Schmandt, Y. Gicheru, and S. Chakrapani, "Crystal structure and dynamics of a lipid-induced potential desensitized-state of a pentameric ligand-gated channel.", English, *eLife*, vol. 6, p. 50 151, Mar. 2017.

[121] R. W. Olsen, "GABAA receptor: Positive and negative allosteric modulators.", English, *Neuropharmacology*, vol. 136, no. Pt A, pp. 10–22, Jul. 2018.

[122] L. J. Greenfield, "Molecular mechanisms of antiseizure drug activity at GABAA receptors.", English, *Seizure*, vol. 22, no. 8, pp. 589–600, Oct. 2013.

[123] J. R. Atack, "Development of Subtype-Selective GABAA Receptor Compounds for the Treatment of Anxiety, Sleep Disorders and Epilepsy", English, in *GABA and Sleep*, Basel: Springer Basel, Aug. 2010, pp. 25–72.

[124] T. L. Kash, J. R. Trudell, and N. L. Harrison, "Structural elements involved in activation of the gamma-aminobutyric acid type A (GABAA) receptor.", English, *Biochemical Society Transactions*, vol. 32, no. Pt3, pp. 540–546, Jun. 2004.

[125] A. J. Thompson, H. A. Lester, and S. C. Lummis, "The structural basis of function in Cys-loop receptors", English, *Quarterly Reviews of Biophysics*, vol. 43, no. 4, pp. 449–499, Nov. 2010.

[126] H.-J. Shu, J. Bracamontes, A. Taylor, K. Wu, M. M. Eaton, G. Akk, B. Manion, A. S. Evers, K. Krishnan, D. F. Covey, C. F. Zorumski, J. H. Steinbach, and S. Mennerick, "Characteristics of concatemeric GABA(A) receptors containing $\alpha 4/\delta$ subunits expressed in Xenopus oocytes.", English, *British Journal of Pharmacology*, vol. 165, no. 7, pp. 2228–2243, Apr. 2012.

[127] K. R. Tan, U. Rudolph, and C. Lüscher, "Hooked on benzodiazepines: GABAA receptor subtypes and addiction.", English, *Trends in Neurosciences*, vol. 34, no. 4, pp. 188–197, Apr. 2011.

[128] U. Rudolph and H. Mohler, "Analysis of GABAA receptor function and dissection of the pharmacology of benzodiazepines and general anesthetics through mouse genetics", English, *Annual Review of Pharmacology and Toxicology*, vol. 44, pp. 475–498, 2004.

[129] G. Puia, I. Ducic, S. Vicini, and E. Costa, "Molecular mechanisms of the partial allosteric modulatory effects of bretazenil at gamma-aminobutyric acid type A receptor.", English, *Proceedings of the National Academy of Sciences of the United States of America*, vol. 89, no. 8, pp. 3620–3624, Apr. 1992.

[130] D. J. Nutt and S. M. Stahl, "Searching for perfect sleep: the continuing evolution of GABAA receptor modulators as hypnotics.", English, *Journal of psychopharmacology (Oxford, England)*, vol. 24, no. 11, pp. 1601–1612, Nov. 2010.

[131] R. M. McKernan, T. W. Rosahl, D. S. Reynolds, C. Sur, K. A. Wafford, J. R. Atack, S. Farrar, J. Myers, G. Cook, P. Ferris, L. Garrett, L. Bristow, G. Marshall, A. Macaulay, N. Brown, O. Howell, K. W. Moore, R. W. Carling, L. J. Street, J. L. Castro, C. I. Ragan, G. R. Dawson, and P. J. Whiting, "Sedative but not anxiolytic properties of benzodiazepines are mediated by the GABA(A) receptor alpha1 subtype.", English, *Nature Neuroscience*, vol. 3, no. 6, pp. 587–592, Jun. 2000.

[132] R. Dias, W. F. A. Sheppard, R. L. Fradley, E. M. Garrett, J. L. Stanley, S. J. Tye, S. Goodacre, R. J. Lincoln, S. M. Cook, R. Conley, D. Hallett, A. C. Humphries, S. A. Thompson, K. A. Wafford, L. J. Street, J. L. Castro, P. J. Whiting, T. W. Rosahl, J. R. Atack, R. M. McKernan, G. R. Dawson, and D. S. Reynolds, "Evidence for a Significant Role of $\alpha 3$-Containing GABAA Receptors in Mediating the Anxiolytic Effects of Benzodiazepines", English, *The Journal of neuroscience*, vol. 25, no. 46, pp. 10 682–10 688, Nov. 2005.

[133] F. M. Rivas, J. P. Stables, L. Murphree, R. V. Edwankar, C. R. Edwankar, S. Huang, H. D. Jain, H. Zhou, S. Majumder, S. Sankar, B. L. Roth, J. Ramerstorfer, R. Furtmüller, W. Sieghart, and J. M. Cook, "Antiseizure activity of novel gamma-aminobutyric acid (A) receptor subtype-selective benzodiazepine analogues in mice and rat models.", English, *Journal of Medicinal Chemistry*, vol. 52, no. 7, pp. 1795–1798, Apr. 2009.

[134] D. Zhou, M. Sunzel, M. D. Ribadeneira, M. A. Smith, D. Desai, J. Lin, and S. W. Grimm, "A clinical study to assess CYP1A2 and CYP3A4 induction by AZD7325, a selective GABA(A) receptor modulator - an in vitro and in vivo comparison.", English, *British journal of clinical pharmacology*, vol. 74, no. 1, pp. 98–108, Jul. 2012.

[135] M. M. Poe, K. R. Methuku, G. Li, A. R. Verma, K. A. Teske, D. C. Stafford, L. A. Arnold, J. W. Cramer, T. M. Jones, R. Cerne, M. J. Krambis, J. M. Witkin, E. Jambrina, S. Rehman, M. Ernst, J. M. Cook, and J. M. Schkeryantz, "Synthesis and Characterization of a Novel γ-Aminobutyric Acid Type A (GABAA) Receptor Ligand That Combines Outstanding Metabolic Stability, Pharmacokinetics, and Anxiolytic Efficacy.", English, *Journal of Medicinal Chemistry*, vol. 59, no. 23, pp. 10 800–10 806, Dec. 2016.

[136] B. D. Fischer, R. J. Schlitt, B. Z. Hamade, S. Rehman, M. Ernst, M. M. Poe, G. Li, R. Kodali, L. A. Arnold, and J. M. Cook, "Pharmacological and antihyperalgesic properties of the novel α2/3 preferring GABAA receptor ligand MP-III-024.", English, *Brain research bulletin*, vol. 131, pp. 62–69, May 2017.

[137] S. A. Nickolls, R. Gurrell, G. van Amerongen, J. Kammonen, L. Cao, A. R. Brown, C. Stead, A. Mead, C. Watson, C. Hsu, R. M. Owen, A. Pike, R. L. Fish, L. Chen, R. Qiu, E. D. Morris, G. Feng, M. Whitlock, D. Gorman, J. van Gerven, D. S. Reynolds, P. Dua, and R. P. Butt, "Pharmacology in translation: the preclinical and early clinical profile of the novel α2/3 functionally selective GABA Areceptor positive allosteric modulator PF-06372865", English, *British Journal of Pharmacology*, vol. 175, no. 4, pp. 708–725, Jan. 2018.

[138] N. R. Mirza, J. S. Larsen, C. Mathiasen, T. A. Jacobsen, G. Munro, H. K. Erichsen, A. N. Nielsen, K. B. Troelsen, E. Ø. Nielsen, and P. K. Ahring, "NS11394 [3'-[5-(1-hydroxy-1-methyl-ethyl)-benzoimidazol-1-yl]-biphenyl-2-carbonitrile], a unique subtype-selective GABAA receptor positive allosteric modulator: in vitro actions, pharmacokinetic properties and in vivo anxiolytic efficacy.", English, *Journal of Pharmacology and Experimental Therapeutics*, vol. 327, no. 3, pp. 954–968, Dec. 2008.

[139] S. L. de Haas, K. L. Franson, J. A. J. Schmitt, A. F. Cohen, J. B. Fau, C. Dubruc, and J. M. A. van Gerven, "The pharmacokinetic and pharmacodynamic effects of SL65.1498, a GABA-A alpha2,3 selective agonist, in comparison with lorazepam in healthy volunteers.", English, *Journal of psychopharmacology (Oxford, England)*, vol. 23, no. 6, pp. 625–632, Aug. 2009.

[140] J. R. Atack, P. H. Hutson, N. Collinson, G. Marshall, G. Bentley, C. Moyes, S. M. Cook, I. Collins, K. Wafford, R. M. McKernan, and G. R. Dawson, "Anxiogenic properties of an inverse agonist selective for α3 subunit-containing GABA Areceptors", English, *British Journal of Pharmacology*, vol. 144, no. 3, pp. 357–366, Feb. 2005.

[141] W. Sieghart, J. Ramerstorfer, I. Sarto-Jackson, Z. Varagic, and M. Ernst, "A novel GABA(A) receptor pharmacology: drugs interacting with the α(+) β(-) interface.", English, *British Journal of Pharmacology*, vol. 166, no. 2, pp. 476–485, May 2012.

[142] P. Mirheydari, J. Ramerstorfer, Z. Varagic, P. Scholze, L. Wimmer, M. M. Mihovilovic, W. Sieghart, and M. Ernst, "Unexpected Properties of δ-Containing GABAA Receptors in Response to Ligands Interacting with the α+ β- Site.", English, *Neurochemical Research*, vol. 39, no. 6, pp. 1057–1067, Jun. 2014.

[143] R. W. Olsen, H. J. Hanchar, P. Meera, and M. Wallner, "GABAA receptor subtypes: the "one glass of wine"receptors.", English, *Alcohol*, vol. 41, no. 3, pp. 201–209, May 2007.

[144] I. Sundstrom-Poromaa, D. H. Smith, Q. H. Gong, T. N. Sabado, X. Li, A. Light, M. Wiedmann, K. Williams, and S. S. Smith, "Hormonally regulated alpha(4)beta(2)delta GABA(A) receptors are a target for alcohol.", English, *Nature Neuroscience*, vol. 5, no. 8, pp. 721–722, Aug. 2002.

[145] C. M. Borghese, S. í. Stórustovu, B. Ebert, M. B. Herd, D. Belelli, J. J. Lambert, G. Marshall, K. A. Wafford, and R. A. Harris, "The delta subunit of gamma-aminobutyric acid type A receptors does not confer sensitivity to low concentrations of ethanol.", English, *Journal of Pharmacology and Experimental Therapeutics*, vol. 316, no. 3, pp. 1360–1368, Mar. 2006.

[146] W. Wei, L. C. Faria, and I. Mody, "Low ethanol concentrations selectively augment the tonic inhibition mediated by delta subunit-containing GABAA receptors in hippocampal neurons.", English, *Journal of Neuroscience*, vol. 24, no. 38, pp. 8379–8382, Sep. 2004.

[147] E. Engin, R. S. Benham, and U. Rudolph, "An Emerging Circuit Pharmacology of GABAA Receptors.", English, *Trends in Pharmacological Sciences*, May 2018.

[148] J. J. Lambert, M. A. Cooper, R. D. Simmons, C. J. Weir, and D. Belelli, "Neurosteroids: endogenous allosteric modulators of GABA(A) receptors", English, *Psychoneuroendocrinology*, vol. 34 Suppl 1, S48–58, Dec. 2009.

[149] M. D. Majewska, N. L. Harrison, R. D. Schwartz, J. L. Barker, and S. M. Paul, "Steroid hormone metabolites are barbiturate-like modulators of the GABA receptor.", English, *Science*, vol. 232, no. 4753, pp. 1004–1007, May 1986.

[150] N. L. Harrison, M. D. Majewska, J. W. Harrington, and J. L. Barker, "Structure-activity relationships for steroid interaction with the gamma-aminobutyric acidA receptor complex.", English, *Journal of Pharmacology and Experimental Therapeutics*, vol. 241, no. 1, pp. 346–353, Apr. 1987.

[151] A. M. Hosie, M. E. Wilkins, and T. G. Smart, "Neurosteroid binding sites on GABA(A) receptors.", English, *Pharmacology and Therapeutics*, vol. 116, no. 1, pp. 7–19, Oct. 2007.

[152] M. B. Herd, D. Belelli, and J. J. Lambert, "Neurosteroid modulation of synaptic and extrasynaptic GABA(A) receptors.", English, *Pharmacology and Therapeutics*, vol. 116, no. 1, pp. 20–34, Oct. 2007.

[153] Z. W. Chen, B. Manion, R. R. Townsend, D. E. Reichert, D. F. Covey, J. H. Steinbach, W. Sieghart, K. Fuchs, and A. S. Evers, "Neurosteroid analog photolabeling of a site in the third transmembrane domain of the beta3 subunit of the GABA(A) receptor", English, *Molecular Pharmacology*, vol. 82, no. 3, pp. 408–419, Sep. 2012.

[154] Z.-W. Chen, J. R. Bracamontes, M. M. Budelier, A. L. Germann, D. J. Shin, K. Kathiresan, M.-X. Qian, B. Manion, W. W. L. Cheng, D. E. Reichert, G. Akk, D. F. Covey, and A. S. Evers, "Multiple Functional Neurosteroid Binding Sites on GABA AReceptors", English, *bioRxiv*, p. 357 574, Jan. 2018.

[155] S. Seljeset, D. P. Bright, P. Thomas, and T. G. Smart, "Probing GABAA receptors with inhibitory neurosteroids.", English, *Neuropharmacology*, vol. 136, no. Pt A, pp. 23–36, Jul. 2018.

[156] S. A. Thompson, P. J. Whiting, and K. A. Wafford, "Barbiturate interactions at the human GABAA receptor: dependence on receptor subunit combination", *British Journal of Pharmacology*, vol. 117, no. 3, pp. 521–527, 1996.

[157] M. C. Maldifassi, R. Baur, and E. Sigel, "Functional sites involved in modulation of the GABAA receptor channel by the intravenous anesthetics propofol, etomidate and pentobarbital.", English, *Neuropharmacology*, vol. 105, pp. 207–214, Jun. 2016.

[158] G. D. Li, D. C. Chiara, J. B. Cohen, and R. W. Olsen, "Neurosteroids allosterically modulate binding of the anesthetic etomidate to gamma-aminobutyric acid type A receptors", English, *Journal of Biological Chemistry*, vol. 284, no. 18, pp. 11 771–11 775, May 2009.

[159] T. Lynagh and J. W. Lynch, "Molecular mechanisms of Cys-loop ion channel receptor modulation by ivermectin", English, *Frontiers in Molecular Neuroscience*, vol. 5, 2012.

[160] A. Estrada-Mondragon and J. W. Lynch, "Functional characterization of ivermectin binding sites in $\alpha 1\beta 2\gamma 2$L GABA(A) receptors.", English, *Frontiers in Molecular Neuroscience*, vol. 8, no. 60, p. 55, 2015.

[161] J. K. Hichar, "Effects of gamma-aminobutyric acid and picrotoxin on spontaneous activity in the central nervous system of the crayfish.", English, *Nature*, vol. 188, pp. 1117–1119, Dec. 1960.

[162] R. W. Olsen, "Drug interactions at the GABA receptor-ionophore complex.", English, *Annual Review of Pharmacology and Toxicology*, vol. 22, no. 1, pp. 245–277, 1982.

[163] G. H. Dillon, W. B. Im, D. B. Carter, and D. D. McKinley, "Enhancement by GABA of the association rate of picrotoxin and tert-butylbicyclophosphorothionate to the rat cloned alpha 1 beta 2 gamma 2 GABAA receptor subtype.", English, *British Journal of Pharmacology*, vol. 115, no. 3, pp. 539–545, Jun. 1995.

[164] U. Rudolph, F. Crestani, and H. Mohler, "GABA(A) receptor subtypes: dissecting their pharmacological functions", *Trends in Pharmacological Sciences*, vol. 22, no. 4, pp. 188–194, Apr. 2001.

[165] H. Mohler, "GABAA receptor diversity and pharmacology", English, *Cell and Tissue Research*, vol. 326, no. 2, pp. 505–516, Aug. 2006.

[166] U. Rudolph and H. Mohler, "GABAA receptor subtypes: Therapeutic potential in Down syndrome, affective disorders, schizophrenia, and autism.", English, *Annual Review of Pharmacology and Toxicology*, vol. 54, no. 1, pp. 483–507, 2014.

[167] J. M. Fritschy and P. Panzanelli, "GABAA receptors and plasticity of inhibitory neurotransmission in the central nervous system", English, *European Journal of Neuroscience*, vol. 39, no. 11, pp. 1845–1865, Jun. 2014.

[168] J. R. Atack, "GABAA receptor subtype-selective modulators. I. alpha2/alpha3-selective agonists as non-sedating anxiolytics", English, *Current Topics in Medicinal Chemistry*, vol. 11, no. 9, pp. 1176–1202, 2011.

[169] J. Knabl, R. Witschi, K. Hösl, H. Reinold, U. B. Zeilhofer, S. Ahmadi, J. Brockhaus, M. Sergejeva, A. Hess, K. Brune, J.-M. Fritschy, U. Rudolph, H. Mohler, and H. U. Zeilhofer, "Reversal of pathological pain through specific spinal GABAA receptor subtypes.", English, *Nature*, vol. 451, no. 7176, pp. 330–334, Jan. 2008.

[170] K. R. Tan, M. Brown, G. Labouèbe, C. Yvon, C. Creton, J.-M. Fritschy, U. Rudolph, and C. Lüscher, "Neural bases for addictive properties of benzodiazepines", *Nature*, vol. 463, no. 7282, pp. 769–774, Feb. 2010.

[171] U. Rudolph, F. Crestani, D. Benke, I. Brunig, J. A. Benson, J. M. Fritschy, J. R. Martin, H. Bluethmann, and H. Mohler, "Benzodiazepine actions mediated by specific gamma-aminobutyric acid(A) receptor subtypes", English, *Nature*, vol. 401, no. 6755, pp. 796–800, Oct. 1999.

[172] K. Low, F. Crestani, R. Keist, D. Benke, I. Brunig, J. A. Benson, J. M. Fritschy, T. Rulicke, H. Bluethmann, H. Mohler, and U. Rudolph, "Molecular and neuronal substrate for the selective attenuation of anxiety", English, *Science*, vol. 290, no. 5489, pp. 131–134, Oct. 2000.

[173] R. R. Griffiths and M. W. Johnson, "Relative abuse liability of hypnotic drugs: a conceptual framework and algorithm for differentiating among compounds.", English, *The Journal of clinical psychiatry*, vol. 66 Suppl 9, pp. 31–41, 2005.

[174] H. U. Zeilhofer, W. T. Ralvenius, and M. A. Acuña, "Restoring the spinal pain gate: GABA(A) receptors as targets for novel analgesics.", English, *Advances in Pharmacology*, vol. 73, pp. 71–96, 2015.

[175] B. Luscher, Q. Shen, and N. Sahir, "The GABAergic deficit hypothesis of major depressive disorder", English, *Molecular psychiatry*, vol. 16, no. 4, pp. 383–406, Nov. 2010.

[176] W. Wisden, D. J. Laurie, H. Monyer, and P. H. Seeburg, "The distribution of 13 GABAA receptor subunit mRNAs in the rat brain. I. Telencephalon, diencephalon, mesencephalon", English, *The Journal of neuroscience*, vol. 12, no. 3, pp. 1040–1062, Mar. 1992.

[177] D. J. Laurie, P. H. Seeburg, and W. Wisden, "The distribution of 13 GABAA receptor subunit mRNAs in the rat brain. II. Olfactory bulb and cerebellum", English, *The Journal of neuroscience*, vol. 12, no. 3, pp. 1063–1076, Mar. 1992.

[178] J.-M. Fritschy and H. Mohler, "GABAA-receptor heterogeneity in the adult rat brain: Differential regional and cellular distribution of seven major subunits", *The Journal of Comparative Neurology*, vol. 359, no. 1, pp. 154–194, 1995.

[179] J. M. Fritschy, J. Paysan, A. Enna, and H. Mohler, "Switch in the expression of rat GABAA-receptor subtypes during postnatal development: an immunohistochemical study", English, *The Journal of neuroscience*, vol. 14, no. 9, pp. 5302–5324, Sep. 1994.

[180] J. Paysan, A. Kossel, J. Bolz, and J. M. Fritschy, "Area-specific regulation of gamma-aminobutyric acid type A receptor subtypes by thalamic afferents in developing rat neocortex", English, *Proceedings of the National Academy of Sciences of the United States of America*, vol. 94, no. 13, pp. 6995–7000, Jun. 1997.

[181] J.-M. Fritschy and I. Brünig, "Formation and plasticity of GABAergic synapses: physiological mechanisms and pathophysiological implications", English, *Pharmacology and Therapeutics*, vol. 98, no. 3, pp. 299–323, Jun. 2003.

[182] T. Klausberger, J. D. Roberts, and P. Somogyi, "Cell type- and input-specific differences in the number and subtypes of synaptic GABA(A) receptors in the hippocampus", English, *The Journal of neuroscience*, vol. 22, no. 7, pp. 2513–2521, Apr. 2002.

[183] G. Nyiri, T. F. Freund, and P. Somogyi, "Input-dependent synaptic targeting of alpha2-subunit-containing GABAA receptors in synapses of hippocampal pyramidal cells of the rat", English, *European Journal of Neuroscience*, vol. 13, no. 3, pp. 428–442, Feb. 2001.

[184] K. Kerti-Szigeti and Z. Nusser, "Similar GABAA receptor subunit composition in somatic and axon initial segment synapses of hippocampal pyramidal cells.", English, *eLife*, vol. 5, e18426, Aug. 2016.

[185] J. Paul, H. U. Zeilhofer, and J.-M. Fritschy, "Selective distribution of GABA(A) receptor subtypes in mouse spinal dorsal horn neurons and primary afferents.", English, *Journal of Comparative Neurology*, vol. 520, no. 17, pp. 3895–3911, Dec. 2012.

[186] J. Knabl, U. B. Zeilhofer, F. Crestani, U. Rudolph, and H. U. Zeilhofer, "Genuine antihyperalgesia by systemic diazepam revealed by experiments in GABAA receptor point-mutated mice", English, *Pain*, vol. 141, no. 3, pp. 233–238, Feb. 2009.

[187] D. M. Dirig and T. L. Yaksh, "Intrathecal baclofen and muscimol, but not midazolam, are antinociceptive using the rat-formalin model.", English, *Journal of Pharmacology and Experimental Therapeutics*, vol. 275, no. 1, pp. 219–227, Oct. 1995.

[188] A. Di Lio, D. Benke, M. Besson, J. Desmeules, Y. Daali, Z.-j. Wang, R. Edwankar, J. M. Cook, and H. U. Zeilhofer, "HZ166, a novel GABAA receptor subtype-selective benzodiazepine site ligand, is antihyperalgesic in mouse models of inflammatory and neuropathic pain.", English, *Neuropharmacology*, vol. 60, no. 4, pp. 626–632, Mar. 2011.

[189] G. Munro, J. A. Lopez-Garcia, I. Rivera-Arconada, H. K. Erichsen, E. Ø. Nielsen, J. S. Larsen, P. K. Ahring, and N. R. Mirza, "Comparison of the novel subtype-selective GABAA receptor-positive allosteric modulator NS11394 [3'-[5-(1-hydroxy-1-methyl-ethyl)-benzoimidazol-1-yl]-biphenyl-2-carbonitrile] with diazepam, zolpidem, bretazenil, and gaboxadol in rat models of inflammatory and neuropathic pain.", English, *Journal of Pharmacology and Experimental Therapeutics*, vol. 327, no. 3, pp. 969–981, Dec. 2008.

[190] S. Nickolls, H. Mace, R. Fish, M. Edye, R. Gurrell, M. Ivarsson, T. Pitcher, S. Tanimoto-Mori, D. Richardson, C. Sweatman, J. Nicholson, C. Ward, J. Jinks, C. Bell, K. Young, H. Rees, A. Moss, R. Kinloch, and G. McMurray, "A Comparison of the α2/3/5 Selective Positive Allosteric Modulators L-838,417 and TPA023 in Preclinical Models of Inflammatory and Neuropathic Pain.", English, *Adv Pharmacol Sci*, vol. 2011, no. 1, pp. 608 912–12, 2011.

[191] M. Hofmann, K. S. Kordás, A. Gravius, K. Bölcskei, C. G. Parsons, A. Dekundy, W. Danysz, L. Dézsi, I. M. Wittko-Schneider, K. Sághy, I. Gyertyán, and C. Horváth, "Assessment of the effects of NS11394 and L-838417, α2/3 subunit-selective GABA(A) [corrected] receptor-positive allosteric modulators, in tests for pain, anxiety, memory and motor function.", English, *Behavioural pharmacology*, vol. 23, no. 8, pp. 790–801, Dec. 2012.

[192] G. Griebel, G. Perrault, J. Simiand, C. Cohen, P. Granger, H. Depoortere, D. Françon, P. Avenet, H. Schoemaker, Y. Evanno, M. Sevrin, P. George, and B. Scatton, "SL651498, a GABAA Receptor Agonist with Subtype-Selective Efficacy, as a Potential Treatment for Generalized Anxiety Disorder and Muscle Spasms", *CNS Drug Reviews*, vol. 9, no. 1, pp. 3–20, 2006.

[193] J. Paul, G. E. Yévenes, D. Benke, A. Di Lio, W. T. Ralvenius, R. Witschi, L. Scheurer, J. M. Cook, U. Rudolph, J.-M. Fritschy, and H. U. Zeilhofer, "Antihyperalgesia by α2-GABAA receptors occurs via a genuine spinal action and does not involve supraspinal sites.", English, *Neuropsychopharmacology*, vol. 39, no. 2, pp. 477–487, Jan. 2014.

[194] R. Gurrell, P. Dua, G. Feng, M. Sudworth, M. Whitlock, D. S. Reynolds, and R. P. Butt, "A randomised, placebo-controlled clinical trial with the α2/3/5 subunit selective GABAA positive allosteric modulator PF-06372865 in patients with chronic low back pain", English, *Pain*, p. 1, May 2018.

[195] H. U. Zeilhofer, E. Neumann, and G. Munro, "Spinal GABAA receptors for pain control-Lost in translation?", English, *Pain*, p. 1, Apr. 2018.

[196] J. Nagy, "Anti-anxiety action op diazepam after intraamygdaloid application in the rat", English, *Neuropharmacology*, vol. 18, no. 6, pp. 573–576, Jun. 1979.

[197] H. V. Morris, G. R. Dawson, D. S. Reynolds, J. R. Atack, and D. N. Stephens, "Both alpha2 and alpha3 GABAA receptor subtypes mediate the anxiolytic properties of benzodiazepine site ligands in the conditioned emotional response paradigm.", English, *European Journal of Neuroscience*, vol. 23, no. 9, pp. 2495–2504, May 2006.

[198] C. I. Dixon, T. W. Rosahl, and D. N. Stephens, "Targeted deletion of the GABRA2 gene encoding alpha2-subunits of GABA(A) receptors facilitates performance of a conditioned emotional response, and abolishes anxiolytic effects of benzodiazepines and barbiturates.", English, *Pharmacology, Biochemistry and Behavior*, vol. 90, no. 1, pp. 1–8, Jul. 2008.

[199] E. Engin, K. S. Smith, Y. Gao, D. Nagy, R. A. Foster, E. Tsvetkov, R. Keist, F. Crestani, J.-M. Fritschy, V. Y. Bolshakov, M. Hajos, S. A. Heldt, and U. Rudolph, "Modulation of anxiety and fear via distinct intrahippocampal circuits.", English, *eLife*, vol. 5, e14120, Mar. 2016.

[200] G. Griebel and A. Holmes, "50 years of hurdles and hope in anxiolytic drug discovery", English, *Nature Reviews. Drug Discovery*, vol. 12, no. 9, pp. 667–687, Sep. 2013.

[201] J. R. Atack, "Subtype-Selective GABAA Receptor Modulation Yields a Novel Pharmacological Profile: The Design and Development of TPA023", *Advances in Pharmacology*, vol. 57, pp. 137–185, Jan. 2009.

[202] L. M. Behlke, R. A. Foster, J. Liu, D. Benke, R. S. Benham, A. J. Nathanson, B. K. Yee, H. U. Zeilhofer, E. Engin, and U. Rudolph, "A Pharmacogenetic 'Restriction-of-Function' Approach Reveals Evidence for Anxiolytic-Like Actions Mediated by α5-Containing GABAA Receptors in Mice", English, *Neuropsychopharmacology*, vol. 41, no. 10, pp. 2492–2501, Apr. 2016.

[203] A. N. Duke, Z. Meng, D. M. Platt, J. R. Atack, G. R. Dawson, D. S. Reynolds, V. V. N. P. B. Tiruveedhula, G. Li, M. R. Stephen, W. Sieghart, J. M. Cook, and J. K. Rowlett, "Evidence That Sedative Effects of Benzodiazepines Involve Unexpected GABAA Receptor Subtypes: Quantitative Observation Studies in Rhesus Monkeys.", English, *Journal of Pharmacology and Experimental Therapeutics*, vol. 366, no. 1, pp. 145–157, Jul. 2018.

[204] J. K. Rowlett, D. M. Platt, S. Lelas, J. R. Atack, and G. R. Dawson, "Different GABAA receptor subtypes mediate the anxiolytic, abuse-related, and motor effects of benzodiazepine-like drugs in primates.", English, *Proceedings of the National Academy of Sciences of the United States of America*, vol. 102, no. 3, pp. 915–920, Jan. 2005.

[205] C. Victorri-Vigneau, E. Dailly, G. Veyrac, and P. Jolliet, "Evidence of zolpidem abuse and dependence: results of the French Centre for Evaluation and Information on Pharmacodependence (CEIP) network survey.", English, *British journal of clinical pharmacology*, vol. 64, no. 2, pp. 198–209, Aug. 2007.

[206] N. M. Shinday, E. K. Sawyer, B. D. Fischer, D. M. Platt, S. C. Licata, J. R. Atack, G. R. Dawson, D. S. Reynolds, and J. K. Rowlett, "Reinforcing effects of compounds lacking intrinsic efficacy at α1 subunit-containing GABAA receptor subtypes in midazolam- but not cocaine-experienced rhesus monkeys.", English, *Neuropsychopharmacology*, vol. 38, no. 6, pp. 1006–1014, May 2013.

[207] L. M. Reynolds, E. Engin, G. Tantillo, H. M. Lau, J. W. Muschamp, W. A. Carlezon, and U. Rudolph, "Differential roles of GABA(A) receptor subtypes in benzodiazepine-induced enhancement of brain-stimulation reward.", English, *Neuropsychopharmacology*, vol. 37, no. 11, pp. 2531–2540, Oct. 2012.

[208] E. Engin, K. I. Bakhurin, K. S. Smith, R. M. Hines, L. M. Reynolds, W. Tang, R. Sprengel, S. J. Moss, and U. Rudolph, "Neural basis of benzodiazepine reward: requirement for α2 containing GABAA receptors in the nucleus accumbens.", English, *Neuropsychopharmacology*, vol. 39, no. 8, pp. 1805–1815, Jul. 2014.

[209] C. Hamers-Casterman, T. Atarhouch, S. Muyldermans, G. Robinson, C. Hamers, E. B. Songa, N. Bendahman, and R. Hamers, "Naturally occurring antibodies devoid of light chains.", English, *Nature*, vol. 363, no. 6428, pp. 446–448, Jun. 1993.

[210] H. Nicolls, "The camel factor: nanobody revolution", English, *New Scientist*, no. 2624, Oct. 2007.

[211] A. S. Greenberg, D. Avila, M. Hughes, A. Hughes, E. C. McKinney, and M. F. Flajnik, "A new antigen receptor gene family that undergoes rearrangement and extensive somatic diversification in sharks", English, *Nature*, vol. 374, no. 6518, pp. 168–173, Mar. 1995.

[212] S. Muyldermans, "Nanobodies: natural single-domain antibodies.", English, *Annual Review of Biochemistry*, vol. 82, no. 1, pp. 775–797, 2013.

[213] T. N. Baral, R. MacKenzie, and M. Arbabi Ghahroudi, "Single-domain antibodies and their utility.", English, *Current protocols in immunology*, vol. 103, Unit 2.17. Nov. 2013.

[214] E. Pardon, T. Laeremans, S. Triest, S. G. F. Rasmussen, A. Wohlkönig, A. Ruf, S. Muyldermans, W. G. J. Hol, B. K. Kobilka, and J. Steyaert, "A general protocol for the generation of Nanobodies for structural biology.", English, *Nature Protocols*, vol. 9, no. 3, pp. 674–693, Mar. 2014.

[215] D. P. Staus, R. T. Strachan, A. Manglik, B. Pani, A. W. Kahsai, T. H. Kim, L. M. Wingler, S. Ahn, A. Chatterjee, A. Masoudi, A. C. Kruse, E. Pardon, J. Steyaert, W. I. Weis, R. S. Prosser, B. K. Kobilka, T. Costa, and R. J. Lefkowitz, "Allosteric nanobodies reveal the dynamic range and diverse mechanisms of G-protein-coupled receptor activation.", English, *Nature*, vol. 535, no. 7612, pp. 448–452, Jul. 2016.

[216] H. D. Herce, D. Schumacher, A. F. L. Schneider, A. K. Ludwig, F. A. Mann, M. Fillies, M.-A. Kasper, S. Reinke, E. Krause, H. Leonhardt, M. C. Cardoso, and C. P. R. Hackenberger, "Cell-permeable nanobodies for targeted immunolabelling and antigen manipulation in living cells", English, *Nature Chemistry*, vol. 9, no. 8, pp. 762–771, Jul. 2017.

[217] A. M. Ring, A. Manglik, A. C. Kruse, M. D. Enos, W. I. Weis, K. C. Garcia, and B. K. Kobilka, "Adrenaline-activated structure of β2-adrenoceptor stabilized by an engineered nanobody.", English, *Nature*, vol. 502, no. 7472, pp. 575–579, Oct. 2013.

[218] J. Sun and R. Mackinnon, "Cryo-EM Structure of a KCNQ1/CaM Complex Reveals Insights into Congenital Long QT Syndrome", English, *Cell*, vol. 169, no. 6, 1042–1050.e9, Jun. 2017.

[219] A. R. Aricescu, W. Lu, and E. Y. Jones, "A time- and cost-efficient system for high-level protein production in mammalian cells.", English, *Acta Crystallographica Section D*, vol. 62, no. Pt 10, pp. 1243–1250, Oct. 2006.

[220] C. L. Morales-Perez, C. M. Noviello, and R. E. Hibbs, "Manipulation of Subunit Stoichiometry in Heteromeric Membrane Proteins.", English, *Structure*, vol. 24, no. 5, pp. 797–805, May 2016.

[221] J. Elegheert, E. Behiels, B. Bishop, S. Scott, R. E. Woolley, S. C. Griffiths, E. F. X. Byrne, V. T. Chang, D. I. Stuart, E. Y. Jones, C. Siebold, and A. R. Aricescu, "Lentiviral transduction of mammalian cells for fast, scalable and high-level production of soluble and membrane proteins", *Nature Methods*,

[222] L. L. Molday and R. S. Molday, "1D4: A Versatile Epitope Tag for the Purification and Characterization of Expressed Membrane and Soluble Proteins", in *Electron Crystallography of Soluble and Membrane Proteins*, New York, NY: Springer New York, May 2014, pp. 1–15.

[223] E. Itakura, C. Chen, and M. de Bono, "Purification of FLAG-tagged Secreted Proteins from Mammalian Cells", English, *Bio-protocol*, vol. 7, no. 15, e2430, 2017.

[224] T. G. M. Schmidt, L. Batz, L. Bonet, U. Carl, G. Holzapfel, K. Kiem, K. Matulewicz, D. Niermeier, I. Schuchardt, and K. Stanar, "Development of the Twin-Strep-tag(R) and its application for purification of recombinant proteins from cell culture supernatants.", English, *Protein expression and purification*, vol. 92, no. 1, pp. 54–61, Nov. 2013.

[225] D. S. Wilson, A. D. Keefe, and J. W. Szostak, "The use of mRNA display to select high-affinity protein-binding peptides.", English, *Proceedings of the National Academy of Sciences of the United States of America*, vol. 98, no. 7, pp. 3750–3755, Mar. 2001.

[226] M. H. Kubala, O. Kovtun, K. Alexandrov, and B. M. Collins, "Structural and thermodynamic analysis of the GFP:GFP-nanobody complex.", English, *Protein Science*, vol. 19, no. 12, pp. 2389–2401, Dec. 2010.

[227] M. Howarth and A. Y. Ting, "Imaging proteins in live mammalian cells with biotin ligase and monovalent streptavidin", English, *Nature Protocols*, vol. 3, no. 3, pp. 534–545, Mar. 2008.

[228] D. G. Gibson, L. Young, R.-Y. Chuang, J. C. Venter, C. A. Hutchison, and H. O. Smith, "Enzymatic assembly of DNA molecules up to several hundred kilobases.", English, *Nature Methods*, vol. 6, no. 5, pp. 343–345, May 2009.

[229] J. García-Nafría, J. F. Watson, and I. H. Greger, "IVA cloning: A single-tube universal cloning system exploiting bacterial In Vivo Assembly.", English, *Sci Rep*, vol. 6, no. 1, p. 27 459, Jun. 2016.

[230] R. Zell and H. J. Fritz, "DNA mismatch-repair in Escherichia coli counteracting the hydrolytic deamination of 5-methyl-cytosine residues.", English, *EMBO Journal*, vol. 6, no. 6, pp. 1809–1815, Jun. 1987.

[231] F. L. Graham, J. Smiley, W. C. Russell, and R. Nairn, "Characteristics of a human cell line transformed by DNA from human adenovirus type 5.", English, *Journal of General Virology*, vol. 36, no. 1, pp. 59–74, Jul. 1977.

[232] R. B. DuBridge, P. Tang, H. C. Hsia, P. M. Leong, J. H. Miller, and M. P. Calos, "Analysis of mutation in human cells by using an Epstein-Barr virus shuttle system.", English, *Molecular and Cellular Biology*, vol. 7, no. 1, pp. 379–387, Jan. 1987.

[233] W. S. Pear, G. P. Nolan, M. L. Scott, and D. Baltimore, "Production of high-titer helper-free retroviruses by transient transfection.", English, *Proceedings of the National Academy of Sciences of the United States of America*, vol. 90, no. 18, pp. 8392–8396, Sep. 1993.

[234] P. J. Reeves, N. Callewaert, R. Contreras, and H. G. Khorana, "Structure and function in rhodopsin: high-level expression of rhodopsin with restricted and homogeneous N-glycosylation by a tetracycline-inducible N-acetylglucosaminyltransferase I-negative HEK293S stable mammalian cell line.", English, *Proceedings of the National Academy of Sciences of the United States of America*, vol. 99, no. 21, pp. 13 419–13 424, Oct. 2002.

[235] A. Goehring, C. H. Lee, K. H. Wang, J. C. Michel, D. P. Claxton, I. Baconguis, T. Althoff, S. Fischer, K. C. Garcia, and E. Gouaux, "Screening and large-scale expression of membrane proteins in mammalian cells for structural studies", English, *Nature Protocols*, vol. 9, no. 11, pp. 2574–2585, Nov. 2014.

[236] G. Backliwal, M. Hildinger, V. Hasija, and F. M. Wurm, "High-density transfection with HEK-293 cells allows doubling of transient titers and removes need for a priori DNA complex formation with PEI.", English, *Biotechnology and Bioengineering*, vol. 99, no. 3, pp. 721–727, Feb. 2008.

[237] G. Backliwal, M. Hildinger, I. Kuettel, F. Delegrange, D. L. Hacker, and F. M. Wurm, "Valproic acid: a viable alternative to sodium butyrate for enhancing protein expression in mammalian cell cultures.", English, *Biotechnology and Bioengineering*, vol. 101, no. 1, pp. 182–189, Sep. 2008.

[238] R. Karlsson, P. S. Katsamba, H. Nordin, E. Pol, and D. G. Myszka, "Analyzing a kinetic titration series using affinity biosensors.", English, *Analytical biochemistry*, vol. 349, no. 1, pp. 136–147, Feb. 2006.

[239] D. Frenzel and D. Willbold, "Kinetic titration series with biolayer interferometry.", English, *PLoS ONE*, vol. 9, no. 9, e106882, 2014.

[240] R. Karlsson, K. Andersson, C. Wass, and GE Healthcare Bio-Sciences AB, "Method and System for Determination of Molecular Interaction Parameters", Aug. 2016.

[241] R. Fernandez-Leiro and S. H. W. Scheres, "Unravelling biological macromolecules with cryo-electron microscopy.", English, *Nature*, vol. 537, no. 7620, pp. 339–346, 2016.

[242] Y. Cheng, R. M. Glaeser, and E. Nogales, *How Cryo-EM Became so Hot.* English. Nov. 2017, vol. 171.

[243] Y. Cheng, N. Grigorieff, P. A. Penczek, and T. Walz, "A primer to single-particle cryo-electron microscopy", English, *Cell*, vol. 161, no. 3, pp. 438–449, Apr. 2015.

[244] M. Ohi, Y. Li, Y. Cheng, and T. Walz, "Negative staining and image classification — powerful tools in modern electron microscopy", English, *Biological Procedures Online*, vol. 6, no. 1, pp. 23–34, Jan. 2004.

[245] J. Dubochet and A. W. McDowall, "VITRIFICATION OF PURE WATER FOR ELECTRON MICROSCOPY", English, *Journal of Microscopy*, vol. 124, no. 3, pp. 3–4, Dec. 1981.

[246] J. Dubochet, M. Adrian, J.-J. Chang, J.-C. Homo, J. Lepault, A. W. McDowall, and P. Schultz, "Cryo-electron microscopy of vitrified specimens", English, *Quarterly Reviews of Biophysics*, vol. 21, no. 02, pp. 129–228, 1988.

[247] R. M. Glaeser, "Specimen Behavior in the Electron Beam", *Methods in Enzymology*, vol. 579, pp. 19–50, Jan. 2016.

[248] L. A. Passmore and C. J. Russo, "Specimen Preparation for High-Resolution Cryo-EM", in *The Resolution Revolution: Recent Advances In cryoEM*, Elsevier, 2016, pp. 51–86.

[249] C. J. Russo and L. A. Passmore, "Electron microscopy: Ultrastable gold substrates for electron cryomicroscopy.", English, *Science*, vol. 346, no. 6215, pp. 1377–1380, Dec. 2014.

[250] R. S. Pantelic, J. C. Meyer, U. Kaiser, W. Baumeister, and J. M. Plitzko, "Graphene oxide: a substrate for optimizing preparations of frozen-hydrated samples.", English, *Journal of structural biology*, vol. 170, no. 1, pp. 152–156, Apr. 2010.

[251] M. Bokori-Brown, T. G. Martin, C. E. Naylor, A. K. Basak, R. W. Titball, and C. G. Savva, "Cryo-EM structure of lysenin pore elucidates membrane insertion by an aerolysin family protein.", English, *Nature Communications*, vol. 7, p. 11 293, Apr. 2016.

[252] E. Palovcak, F. Wang, S. Q. Zheng, Z. Yu, S. Li, D. Bulkley, D. A. Agard, and Y. Cheng, "A simple and robust procedure for preparing graphene-oxide cryo-EM grids", English, *bioRxiv*, p. 290 197, 2018.

[253] J. Snijder, A. J. Borst, A. Dosey, A. C. Walls, A. Burrell, V. S. Reddy, J. M. Kollman, and D. Veesler, "Vitrification after multiple rounds of sample application and blotting improves particle density on cryo-electron microscopy grids.", English, *Journal of structural biology*, vol. 198, no. 1, pp. 38–42, Apr. 2017.

[254] R. M. Glaeser and B.-G. Han, "Opinion: hazards faced by macromolecules when confined to thin aqueous films.", English, *Biophysics reports*, vol. 3, no. 1, pp. 1–7, 2017.

[255] S. H. W. Scheres, "Chapter Six - Processing of Structurally Heterogeneous Cryo-EM Data in RELION", in *Guide to Protein Purification, 2nd Edition*, R. A. Crowther, Ed., Academic Press, 2016, pp. 125–157.

[256] K. Naydenova and C. J. Russo, "Measuring the effects of particle orientation to improve the efficiency of electron cryomicroscopy", English, *Nature Communications*, vol. 8, no. 1, p. 450, Sep. 2017.

[257] D. J. Johnson and D. Crawford, "Defocusing phase contrast effects in electron microscopy", English, *Journal of Microscopy*, vol. 98, no. 3, pp. 313–324, Aug. 2011.

[258] P. N. Unwin and R. Henderson, "Molecular structure determination by electron microscopy of unstained crystalline specimens.", English, *Journal of Molecular Biology*, vol. 94, no. 3, pp. 425–440, May 1975.

[259] J. Frank, *Three-Dimensional Electron Microscopy of Macromolecular Assemblies*. Oxford University Press, 2006.

[260] R. Henderson, "Overview and future of single particle electron cryomicroscopy.", English, *Archives of biochemistry and biophysics*, vol. 581, pp. 19–24, Sep. 2015.

[261] G. McMullan, A. R. Faruqi, and R. Henderson, "Direct Electron Detectors", *Methods in Enzymology*, vol. 579, pp. 1–17, Jan. 2016.

[262] M. A. Herzik, M. Wu, and G. C. Lander, "Achieving better-than-3-Å resolution by single-particle cryo-EM at 200 keV", English, *Nature Methods*, vol. 14, no. 11, pp. 1075–1078, Oct. 2017.

[263] R. Henderson, "The potential and limitations of neutrons, electrons and X-rays for atomic resolution microscopy of unstained biological molecules.", English, *Quarterly Reviews of Biophysics*, vol. 28, no. 2, pp. 171–193, May 1995.

[264] R. Danev and K. Nagayama, "Phase plates for transmission electron microscopy.", English, *Methods in Enzymology*, vol. 481, pp. 343–369, 2010.

[265] R. Danev and W. Baumeister, "Expanding the boundaries of cryo-EM with phase plates.", English, *Current opinion in structural biology*, vol. 46, pp. 87–94, Oct. 2017.

[266] R. Danev, B. Buijsse, M. Khoshouei, J. M. Plitzko, and W. Baumeister, "Volta potential phase plate for in-focus phase contrast transmission electron microscopy.", English, *Proceedings of the National Academy of Sciences of the United States of America*, vol. 111, no. 44, pp. 15 635–15 640, Nov. 2014.

[267] R. Danev and W. Baumeister, "Cryo-EM single particle analysis with the Volta phase plate", English, *eLife*, vol. 5, p. 439, Mar. 2016.

[268] R. Danev, D. Tegunov, and W. Baumeister, "Using the Volta phase plate with defocus for cryo-EM single particle analysis.", English, *eLife*, vol. 6, p. 1823, Jan. 2017.

[269] G. McMullan, A. R. Faruqi, D. Clare, and R. Henderson, "Comparison of optimal performance at 300keV of three direct electron detectors for use in low dose electron microscopy.", English, *Ultramicroscopy*, vol. 147, pp. 156–163, Dec. 2014.

[270] G. McMullan, S. Chen, R. Henderson, and A. R. Faruqi, "Detective quantum efficiency of electron area detectors in electron microscopy", English, *Ultramicroscopy*, vol. 109, no. 9, pp. 1126–1143, Aug. 2009.

[271] G. C. Farnell and B. Flint, "The response of photographic materials to electrons with particular reference to electron micrography", English, *Journal of Microscopy*, vol. 97, no. 3, pp. 271–291, 1973.

[272] M. Kuijper, G. van Hoften, B. Janssen, R. Geurink, S. De Carlo, M. Vos, G. van Duinen, B. van Haeringen, and M. Storms, "FEI's direct electron detector developments: Embarking on a revolution in cryo-TEM.", English, *Journal of structural biology*, vol. 192, no. 2, pp. 179–187, Nov. 2015.

[273] X. Li, P. Mooney, S. Zheng, C. R. Booth, M. B. Braunfeld, S. Gubbens, D. A. Agard, and Y. Cheng, "Electron counting and beam-induced motion correction enable near-atomic-resolution single-particle cryo-EM", English, *Nature Methods*, vol. 10, no. 6, pp. 584–590, May 2013.

[274] R. M. Glaeser, D. Typke, P. C. Tiemeijer, J. Pulokas, and A. Cheng, "Precise beam-tilt alignment and collimation are required to minimize the phase error associated with coma in high-resolution cryo-EM.", English, *Journal of structural biology*, vol. 174, no. 1, pp. 1–10, Apr. 2011.

[275] A. Punjani, J. L. Rubinstein, D. J. Fleet, and M. A. Brubaker, "cryoSPARC: algorithms for rapid unsupervised cryo-EM structure determination.", English, *Nature Methods*, vol. 14, no. 3, pp. 290–296, Mar. 2017.

[276] T. Grant, A. Rohou, and N. Grigorieff, "cisTEM, user-friendly software for single-particle image processing.", English, *eLife*, vol. 7, e14874, Mar. 2018.

[277] D. Tegunov and P. Cramer, "Real-time cryo-EM data pre-processing with Warp", Jan. 2018.

[278] S. Q. Zheng, E. Palovcak, J.-P. Armache, K. A. Verba, Y. Cheng, and D. A. Agard, "MotionCor2: anisotropic correction of beam-induced motion for improved cryo-electron microscopy.", English, *Nature Methods*, vol. 14, no. 4, pp. 331–332, Apr. 2017.

[279] A. Rohou and N. Grigorieff, "CTFFIND4: Fast and accurate defocus estimation from electron micrographs.", English, *Journal of structural biology*, vol. 192, no. 2, pp. 216–221, Nov. 2015.

[280] K. Zhang, "Gctf: Real-time CTF determination and correction.", English, *Journal of structural biology*, vol. 193, no. 1, pp. 1–12, Jan. 2016.

[281] T. Wagner, F. Merino, M. Stabrin, T. Moriya, C. Gatsogiannis, and S. Raunser, "SPHIRE-crYOLO: A fast and well-centering automated particle picker for cryo-EM", English, *bioRxiv*, p. 356 584, 2018.

[282] Z. A. Ripstein and J. L. Rubinstein, "Processing of Cryo-EM Movie Data", in *The Resolution Revolution: Recent Advances In cryoEM*, Elsevier, 2016, pp. 103–124.

[283] J. Zivanov, T. Nakane, and S. Scheres, "A Bayesian approach to beam-induced motion correction in cryo-EM single-particle analysis", Jan. 2018.

[284] R. Henderson, "Avoiding the pitfalls of single particle cryo-electron microscopy: Einstein from noise.", English, *Proceedings of the National Academy of Sciences of the United States of America*, vol. 110, no. 45, pp. 18 037–18 041, Nov. 2013.

[285] S. H. W. Scheres, "A Bayesian view on cryo-EM structure determination.", English, *Journal of Molecular Biology*, vol. 415, no. 2, pp. 406–418, Jan. 2012.

[286] P. B. Rosenthal and R. Henderson, "Optimal Determination of Particle Orientation, Absolute Hand, and Contrast Loss in Single-particle Electron Cryomicroscopy", English, *Journal of Molecular Biology*, vol. 333, no. 4, pp. 721–745, Oct. 2003.

[287] T. Nakane, D. Kimanius, E. Lindahl, and S. H. Scheres, "Characterisation of molecular motions in cryo-EM single-particle data by multi-body refinement in RELION.", English, *eLife*, vol. 7, Jun. 2018.

[288] G. N. Murshudov, "Refinement of Atomic Structures Against cryo-EM Maps.", English, *Methods in Enzymology*, vol. 579, pp. 277–305, 2016.

[289] P. Emsley, B. Lohkamp, W. G. Scott, and K. Cowtan, "Features and development of Coot.", English, *Acta Crystallographica Section D*, vol. 66, no. Pt 4, pp. 486–501, Apr. 2010.

[290] P. V. Afonine, B. K. Poon, R. J. Read, O. V. Sobolev, T. C. Terwilliger, A. Urzhumtsev, and P. D. Adams, "Real-space refinement in PHENIX for cryo-EM and crystallography.", English, *Acta crystallographica. Section D, Structural biology*, vol. 74, no. Pt 6, pp. 531–544, Jun. 2018.

[291] G. N. Ramachandran, C. Ramakrishnan, and V. Sasisekharan, "Stereochemistry of polypeptide chain configurations.", English, *Journal of Molecular Biology*, vol. 7, pp. 95–99, Jul. 1963.

[292] S. H. W. Scheres, "RELION: implementation of a Bayesian approach to cryo-EM structure determination.", English, *Journal of structural biology*, vol. 180, no. 3, pp. 519–530, Dec. 2012.

[293] T. De Meyer, S. Muyldermans, and A. Depicker, "Nanobody-based products as research and diagnostic tools.", English, *Trends in biotechnology*, vol. 32, no. 5, pp. 263–270, May 2014.

[294] U. Rothbauer, K. Zolghadr, S. Tillib, D. Nowak, L. Schermelleh, A. Gahl, N. Backmann, K. Conrath, S. Muyldermans, M. C. Cardoso, and H. Leonhardt, "Targeting and tracing antigens in live cells with fluorescent nanobodies.", English, *Nature Methods*, vol. 3, no. 11, pp. 887–889, Nov. 2006.

[295] T. Li, J.-P. Bourgeois, S. Celli, F. Glacial, A.-M. Le Sourd, S. Mecheri, B. Weksler, I. Romero, P.-O. Couraud, F. Rougeon, and P. Lafaye, "Cell-penetrating anti-GFAP VHH and corresponding fluorescent fusion protein VHH-GFP spontaneously cross the blood-brain barrier and specifically recognize astrocytes: application to brain imaging.", English, *FASEB Journal*, vol. 26, no. 10, pp. 3969–3979, Oct. 2012.

[296] S. Masiulis, "Structural Studies of Human GABA-A Receptors", PhD thesis, Apr. 2018.

[297] A. Kirchhofer, J. Helma, K. Schmidthals, C. Frauer, S. Cui, A. Karcher, M. Pellis, S. Muyldermans, C. S. Casas-Delucchi, M. C. Cardoso, H. Leonhardt, K.-P. Hopfner, and U. Rothbauer, "Modulation of protein properties in living cells using nanobodies", *Nature Structural & Molecular Biology*, vol. 17, no. 1, pp. 133–138, Dec. 2009.

[298] A. Manglik, B. K. Kobilka, and J. Steyaert, "Nanobodies to Study G Protein–Coupled Receptor Structure and Function", English, *Annual Review of Pharmacology and Toxicology*, vol. 57, no. 1, pp. 19–37, Jan. 2017.

[299] R. Doshi, B. R. Chen, C. R. T. Vibat, N. Huang, C.-W. Lee, and G. Chang, "In vitro nanobody discovery for integral membrane protein targets.", English, *Sci Rep*, vol. 4, p. 6760, Oct. 2014.

[300] Fridy, P. C., Y. Li, S. Keegan, M. K. Thompson, I. Nudelman, J. F. Scheid, M. Oeffinger, M. C. Nussenzweig, D. Fenyo, B. T. Chait, and M. P. Rout, "A robust pipeline for rapid production of versatile nanobody repertoires", *Nature Methods*, vol. 11, no. 12, pp. 1253–1260, Dec. 2014.

[301] M. B. Gorbet and M. V. Sefton, "Endotoxin: The uninvited guest", English, *Biomaterials*, vol. 26, no. 34, pp. 6811–6817, Dec. 2005.

[302] L. Mack, B. Brill, N. Delis, and B. Groner, "Endotoxin depletion of recombinant protein preparations through their preferential binding to histidine tags.", English, *Analytical biochemistry*, vol. 466, pp. 83–88, Dec. 2014.

[303] J. T. Kittler, P. Rostaing, G. Schiavo, J. M. Fritschy, R. Olsen, A. Triller, and S. J. Moss, "The subcellular distribution of GABARAP and its ability to interact with NSF suggest a role for this protein in the intracellular transport of GABA(A) receptors.", English, *Molecular and Cellular Neurosciences*, vol. 18, no. 1, pp. 13–25, Jul. 2001.

[304] J. Andréll and C. G. Tate, "Overexpression of membrane proteins in mammalian cells for structural studies.", English, *Molecular Membrane Biology*, vol. 30, no. 1, pp. 52–63, Feb. 2013.

[305] V. T. Chang, M. Crispin, A. R. Aricescu, D. J. Harvey, J. E. Nettleship, J. A. Fennelly, C. Yu, K. S. Boles, E. J. Evans, D. I. Stuart, R. A. Dwek, E. Y. Jones, R. J. Owens, and S. J. Davis, "Glycoprotein structural genomics: solving the glycosylation problem.", English, *Structure*, vol. 15, no. 3, pp. 267–273, Mar. 2007.

[306] Z. Dostalova, A. Liu, X. Zhou, S. L. Farmer, E. S. Krenzel, E. Arevalo, R. Desai, P. L. Feinberg-Zadek, P. A. Davies, I. H. Yamodo, S. A. Forman, and K. W. Miller, "High-level expression and purification of Cys-loop ligand-gated ion channels in a tetracycline-inducible stable mammalian cell line: GABAA and serotonin receptors.", English, *Protein Science*, vol. 19, no. 9, pp. 1728–1738, Sep. 2010.

[307] Z. Dostalova, X. Zhou, A. Liu, X. Zhang, Y. Zhang, R. Desai, S. A. Forman, and K. W. Miller, "Human alpha1beta3gamma2L gamma-aminobutyric acid type A receptors: High-level production and purification in a functional state.", English, *Protein Science*, vol. 23, no. 2, pp. 157–166, Feb. 2014.

[308] X. Zhou, R. Desai, Y. Zhang, W. J. Stec, K. W. Miller, and Y. Jounaidi, "High-level production and purification in a functional state of an extrasynaptic gamma-aminobutyric acid type A receptor containing $\alpha 4\beta 3\delta$ subunits", English, *PLoS ONE*, vol. 13, no. 1, e0191583, Jan. 2018.

[309] T. A. Kost and J. P. Condreay, "Recombinant baculoviruses as mammalian cell gene-delivery vectors.", English, *Trends in biotechnology*, vol. 20, no. 4, pp. 173–180, Apr. 2002.

[310] T. Kawate and E. Gouaux, "Fluorescence-detection size-exclusion chromatography for precrystallization screening of integral membrane proteins.", English, *Structure*, vol. 14, no. 4, pp. 673–681, Apr. 2006.

[311] J. Fitzgerald, P. Leonard, E. Darcy, S. Sharma, and R. O'Kennedy, "Immunoaffinity Chromatography: Concepts and Applications.", English, *Methods in Molecular Biology*, vol. 1485, pp. 27–51, 2017.

[312] M. Lorch and R. Batchelor, *Stabilizing Membrane Proteins in Detergent and Lipid Systems*, English, ser. Strategies for Expression and Isolation. Weinheim, Germany: Wiley-Blackwell, 2011, vol. 61.

[313] M. Zoonens, F. Zito, K. L. Martinez, and J.-L. Popot, "Amphipols: A General Introduction and Some Protocols", English, in *Membrane Proteins Production for Structural Analysis*, New York, NY: Springer New York, Jun. 2014, pp. 173–203.

[314] D. P. Claxton and E. Gouaux, "Expression and purification of a functional heteromeric GABAA receptor for structural studies.", English, *PLoS ONE*, vol. 13, no. 7, e0201210, 2018.

[315] W. Lu, J. Du, A. Goehring, and E. Gouaux, "Cryo-EM structures of the triheteromeric NMDA receptor and its allosteric modulation.", English, *Science*, eaal3729, Feb. 2017.

[316] I. G. Denisov and S. G. Sligar, "Nanodiscs in Membrane Biochemistry and Biophysics.", English, *Chemical reviews*, vol. 117, no. 6, pp. 4669–4713, Mar. 2017.

[317] J. Frauenfeld, R. Löving, J.-P. Armache, A. F.-P. Sonnen, F. Guettou, P. Moberg, L. Zhu, C. Jegerschöld, A. Flayhan, J. A. G. Briggs, H. Garoff, C. Löw, Y. Cheng, and P. Nordlund, "A saposin-lipoprotein nanoparticle system for membrane proteins.", English, *Nature Methods*, vol. 13, no. 4, pp. 345–351, Apr. 2016.

[318] J. M. Dorr, S. Scheidelaar, M. C. Koorengevel, J. J. Dominguez, M. Schafer, C. A. van Walree, and J. A. Killian, "The styrene-maleic acid copolymer: a versatile tool in membrane research.", English, *European Biophysics Journal*, vol. 45, no. 1, pp. 3–21, Jan. 2016.

[319] D. Kimanius, B. O. Forsberg, S. Scheres, and E. Lindahl, "Accelerated cryo-EM structure determination with parallelisation using GPUs in RELION-2", English, *bioRxiv*, p. 059 717, 2016.

[320] J. Zivanov, T. Nakane, B. Forsberg, D. Kimanius, W. J. H. Hagen, E. Lindahl, and S. H. W. Scheres, "RELION-3: new tools for automated high-resolution cryo-EM structure determination", English, *bioRxiv*, p. 421 123, 2018.

[321] E. D'Imprima, D. Floris, M. Joppe, R. Sánchez, M. Grininger, and W. Kühlbrandt, "The deadly touch: protein denaturation at the water-air interface and how to prevent it", English, *bioRxiv*, p. 400 432, 2018.

[322] M. Khoshouei, R. Danev, J. M. Plitzko, and W. Baumeister, "Revisiting the Structure of Hemoglobin and Myoglobin with Cryo-Electron Microscopy", English, *Journal of Molecular Biology*, vol. 429, no. 17, pp. 2611–2618, Aug. 2017.

[323] R. Danev and W. Baumeister, "Cryo-EM single particle analysis with the Volta phase plate.", English, *eLife*, vol. 5, p. 439, Mar. 2016.

[324] J. García-Nafría, R. Nehmé, P. C. Edwards, and C. G. Tate, "Cryo-EM structure of the serotonin 5-HT1B receptor coupled to heterotrimeric Go", English, *Nature*, vol. 558, no. 7711, pp. 620–623, Jun. 2018.

[325] C. J. Draper-Joyce, M. Khoshouei, D. M. Thal, Y.-L. Liang, A. T. N. Nguyen, S. G. B. Furness, H. Venugopal, J.-A. Baltos, J. M. Plitzko, R. Danev, W. Baumeister, L. T. May, D. Wootten, P. M. Sexton, A. Glukhova, and A. Christopoulos, "Structure of the adenosine-bound human adenosine A1 receptor–Gi complex", English, *Nature*, vol. 63, p. 1, Jun. 2018.

[326] M. Khoshouei, M. Radjainia, W. Baumeister, and R. Danev, "Cryo-EM structure of haemoglobin at 3.2 Å determined with the Volta phase plate", English, *Nature Communications*, vol. 8, p. 16 099, Jun. 2017.

[327] S. Liu, L. Xu, F. Guan, Y.-T. Liu, Y. Cui, Q. Zhang, X. Zheng, G.-Q. Bi, Z. H. Zhou, X. Zhang, and S. Ye, "Cryo-EM structure of the human $\alpha 5\beta 3$ GABAA receptor.", English, *Cell research*, p. 1, Aug. 2018.

[328] I. Drulyte, R. M. Johnson, E. L. Hesketh, D. L. Hurdiss, C. A. Scarff, S. A. Porav, N. A. Ranson, S. P. Muench, and R. F. Thompson, "Approaches to altering particle distributions in cryo-electron microscopy sample preparation.", English, *Acta crystallographica. Section D, Structural biology*, vol. 74, no. Pt 6, pp. 560–571, Jun. 2018.

[329] Y. Gao, E. Cao, D. Julius, and Y. Cheng, "TRPV1 structures in nanodiscs reveal mechanisms of ligand and lipid action.", English, *Nature*, vol. 534, no. 7607, pp. 347–351, Jun. 2016.

[330] M. L. Carlson, J. W. Young, Z. Zhao, L. Fabre, D. Jun, J. Li, J. Li, H. S. Dhupar, I. Wason, A. T. Mills, J. T. Beatty, J. S. Klassen, I. Rouiller, and F. Duong, "The Peptidisc, a simple method for stabilizing membrane proteins in detergent-free solution", English, *eLife*, vol. 7, p. 215, Aug. 2018.

[331] A. Casañal, A. Kumar, C. H. Hill, A. D. Easter, P. Emsley, G. Degliesposti, Y. Gordiyenko, B. Santhanam, J. Wolf, K. Wiederhold, G. L. Dornan, M. Skehel, C. V. Robinson, and L. A. Passmore, "Architecture of eukaryotic mRNA 3′-end processing machinery", English, *Science*, vol. 358, no. 6366, pp. 1056–1059, Nov. 2017.

[332] D. Laverty, P. Thomas, M. Field, O. J. Andersen, M. G. Gold, P. C. Biggin, M. Gielen, and T. G. Smart, "Crystal structures of a GABAA-receptor chimera reveal new endogenous neurosteroid-binding sites.", English, *Nature Structural & Molecular Biology*, vol. 24, no. 11, pp. 977–985, Nov. 2017.

[333] J. Helma, M. C. Cardoso, S. Muyldermans, and H. Leonhardt, "Nanobodies and recombinant binders in cell biology", English, *The Journal of cell biology*, vol. 209, no. 5, pp. 633–644, Jun. 2015.

[334] Z. Debyser, F. Christ, J. De Rijck, and R. Gijsbers, "Host factors for retroviral integration site selection", English, *Trends in Biochemical Sciences*, vol. 40, no. 2, pp. 108–116, Feb. 2015.